

Seismic Isolation of Nuclear Power Plants using Elastomeric Bearings

AVAILABILITY OF REFERENCE MATERIALS IN NRC PUBLICATIONS

NRC Reference Material

As of November 1999, you may electronically access NUREG-series publications and other NRC records at NRC's Library at www.nrc.gov/reading-rm.html. Publicly released records include, to name a few, NUREG-series publications; *Federal Register* notices; applicant, licensee, and vendor documents and correspondence; NRC correspondence and internal memoranda; bulletins and information notices; inspection and investigative reports; licensee event reports; and Commission papers and their attachments.

NRC publications in the NUREG series, NRC regulations, and Title 10, "Energy," in the *Code of Federal Regulations* may also be purchased from one of these two sources.

1. The Superintendent of Documents

U.S. Government Publishing Office
Washington, DC 20402-0001
Internet: bookstore.gpo.gov
Telephone: (202) 512-1800
Fax: (202) 512-2104

2. The National Technical Information Service

5301 Shawnee Road
Alexandria, VA 22312-0002
www.ntis.gov
1-800-553-6847 or, locally, (703) 605-6000

A single copy of each NRC draft report for comment is available free, to the extent of supply, upon written request as follows:

Address: **U.S. Nuclear Regulatory Commission**
Office of Administration
Multimedia, Graphics, and Storage &
Distribution Branch
Washington, DC 20555-0001
E-mail: distribution.resource@nrc.gov
Facsimile: (301) 415-2289

Some publications in the NUREG series that are posted at NRC's Web site address www.nrc.gov/reading-rm/doc-collections/nuregs are updated periodically and may differ from the last printed version. Although references to material found on a Web site bear the date the material was accessed, the material available on the date cited may subsequently be removed from the site.

Non-NRC Reference Material

Documents available from public and special technical libraries include all open literature items, such as books, journal articles, transactions, *Federal Register* notices, Federal and State legislation, and congressional reports. Such documents as theses, dissertations, foreign reports and translations, and non-NRC conference proceedings may be purchased from their sponsoring organization.

Copies of industry codes and standards used in a substantive manner in the NRC regulatory process are maintained at—

The NRC Technical Library

Two White Flint North
11545 Rockville Pike
Rockville, MD 20852-2738

These standards are available in the library for reference use by the public. Codes and standards are usually copyrighted and may be purchased from the originating organization or, if they are American National Standards, from—

American National Standards Institute

11 West 42nd Street
New York, NY 10036-8002
www.ansi.org
(212) 642-4900

Legally binding regulatory requirements are stated only in laws; NRC regulations; licenses, including technical specifications; or orders, not in NUREG-series publications. The views expressed in contractor prepared publications in this series are not necessarily those of the NRC.

The NUREG series comprises (1) technical and administrative reports and books prepared by the staff (NUREG-XXXX) or agency contractors (NUREG/CR-XXXX), (2) proceedings of conferences (NUREG/CP-XXXX), (3) reports resulting from international agreements (NUREG/IA-XXXX), (4) brochures (NUREG/BR-XXXX), and (5) compilations of legal decisions and orders of the Commission and Atomic and Safety Licensing Boards and of Directors' decisions under Section 2.206 of NRC's regulations (NUREG-0750).

DISCLAIMER: This report was prepared as an account of work sponsored by an agency of the U.S. Government. Neither the U.S. Government nor any agency thereof, nor any employee, makes any warranty, expressed or implied, or assumes any legal liability or responsibility for any third party's use, or the results of such use, of any information, apparatus, product, or process disclosed in this publication, or represents that its use by such third party would not infringe privately owned rights.

Seismic Isolation of Nuclear Power Plants using Elastomeric Bearings

Manuscript Completed: February 2016
Date Published: February 2019

Prepared by:
M. Kumar
A. Whittaker
M. Constantinou

Multidisciplinary Center for Earthquake Engineering Research (MCEER)
University at Buffalo, State University of New York
212 Ketter Hall
Buffalo, NY 14260

Ramón L. Gascot-Lozada, NRC Project Manager

ABSTRACT

Seismic isolation using low damping rubber (LDR) and lead-rubber (LR) bearings is a viable strategy for mitigating the effects of extreme earthquake shaking on safety-related nuclear structures. Although seismic isolation has been deployed in nuclear structures in France and South Africa, it has not seen widespread use. This has been attributed to, in part, limited new build nuclear construction in the past 30 years and a lack of guidelines, codes and standards for the analysis, design and construction of isolation systems specific to nuclear structures.

The nuclear accident at Fukushima Daiichi in March 2011 has led the nuclear community to consider seismic isolation for new large light water and small modular reactors to withstand the effects of extreme earthquakes. The mechanical properties of LDR and LR bearings are not expected to change substantially in design basis shaking. However, under shaking more intense than design basis, the properties of the lead cores in lead-rubber bearings may degrade due to heating associated with energy dissipation, some bearings in an isolation system may experience net tension, and the compression and tension stiffness may be affected by the horizontal displacement of the isolation system.

The effects of variation in mechanical properties of lead-rubber bearing on the response of base-isolated nuclear power plants (NPPs) were investigated using an advanced numerical model of lead-rubber bearing. The model was verified and validated, and implemented in OpenSees and ABAQUS. A series of experiments were conducted at University at Buffalo to characterize the behavior of elastomeric bearings in tension. The test data was used to validate a phenomenological model of an elastomeric bearing in tension. The value of three times the shear modulus of rubber in the elastomeric bearing was found to be a reasonable estimate of the cavitation stress of a bearing. The sequence of loading did not change the behavior of an elastomeric bearing under cyclic tension, and there was no significant change in the shear modulus, compressive stiffness, and buckling load of a bearing following cavitation.

Response-history analysis of base-isolated NPP structures was performed using a two-node macro model and a lumped-mass stick model. A comparison of responses obtained from analysis using simplified and advanced isolator models showed that the variation in buckling load due to horizontal displacement and strength degradation due to heating of lead cores affect the responses of a base-isolated NPP most significantly. The two-node macro model can be used to estimate the horizontal displacement response of a base-isolated NPP, but a three-dimensional model that explicitly considers all of the bearings in the isolation system will be required to estimate demands on individual bearings, and to investigate rocking and torsional responses. The use of the simplified LR bearing model underestimated the torsional and rocking response of the base-isolated NPP. Vertical spectral response at the top of containment building was very sensitive to how damping was defined for the response-history analysis.

FOREWORD

As part of their 2008-2011 Seismic Research Program Plan, the Office of Regulatory Research (RES) of the U.S. Nuclear Regulatory Commission (USNRC) initiated an effort to investigate seismic base isolation technology. Base isolation is a technology developed to protect a structure from the damaging effects of earthquake shaking, by essentially decoupling the structure from high frequency, horizontal earthquake shaking. Operating seismically isolated nuclear power plants already exist in France and South Africa. Although base isolation has been effectively used on bridges, commercial buildings and other structures in the United States, there have been no applications to safety-related nuclear facilities in the United States.

The research studied technical bases that would inform design and review guidance for the possible use of seismic base isolation technology in nuclear power plants. The focus of the research was new surface-mounted large light water reactor designs but many of its products also are relevant for isolation of structures and components of next generation nuclear power plants. To conduct this research RES sponsored research at the University of Buffalo (UB) and Lawrence Berkeley National Laboratory (LBNL) under a contract to LBNL. This report is a deliverable for that contract that documents the research done on elastomeric seismic isolation bearings and, specifically, on lead-rubber and low-damping rubber bearings. A companion report, NUREG/CR-7254, documents the research done on another type of bearings, sliding bearings, namely the single concave Friction Pendulum™ bearing.

This research developed numerical models of low-damping rubber and lead-rubber elastomeric bearings, which permit extensive sensitivity analysis of base-isolated nuclear power plants subjected to a wide range of earthquake shaking. The report also documents the results of sensitivity analyses conducted with those models that provide data and insights on the performance of the two types of isolators studied and relate that performance to the design features of the isolators. The information in this report could help form the basis for regulatory guidance on seismic base isolation although such work is not planned at present.

Specifically, the research documented in this report prepared numerical models following best practice standards and implement them in commercial software. Physical experiments also were conducted to characterize the behavior of the elastomeric bearings under tensile and shear loadings, and to enable validation of the numerical models. The sensitivity analyses used two representations of a nuclear power plant isolated with lead-rubber bearings, a two-node macro model and a lumped-mass stick model, subjected to design and beyond basis earthquake shaking. The results reported inform which representation of an isolated nuclear power plant and which features of the isolator model are needed to accurately compute responses for a wide range of earthquake shaking.

The data and results in this report inform the technical basis to ensure readiness of the NRC infrastructure for potential applications that would utilize seismic isolation technologies. A third report, NUREG/CR-7253, "Technical Considerations for Seismic Isolation of Nuclear Facilities," provides technical considerations, as well as performance and design recommendations addressing the design, construction, and operational needs for SI systems that consider the seismic, risk-informed, performance of structures, systems, and components (SSC). Technical considerations and regulatory challenges identified in that report include performance criteria to address the full scope of seismic demands, methods appropriate for the seismic soil-structure interaction analysis of a seismically isolated plant, defense in depth, reliability of the isolators during the operating life of the plant, and inspection and maintenance procedures.

TABLE OF CONTENTS

ABSTRACT	iii
FOREWORD	v
TABLE OF CONTENTS	vii
LIST OF FIGURES	xiii
LIST OF TABLES	xxi
EXECUTIVE SUMMARY	xxvii
ACKNOWLEDGMENTS	xxix
ABBREVIATIONS AND ACRONYMS	xxxii
1 INTRODUCTION	1-1
1.1 General	1-1
1.2 Motivation	1-1
1.3 Scope of Work.....	1-3
1.4 Report Organization	1-3
2 LITERATURE REVIEW	2-1
2.1 Introduction.....	2-1
2.2 Historical Developments	2-1
2.2.1 Introduction	2-1
2.2.2 France	2-1
2.2.3 South Africa	2-2
2.2.4 Italy.....	2-4
2.2.5 United Kingdom	2-5
2.2.6 New Zealand.....	2-5
2.2.7 Japan.....	2-5
2.2.8 United States	2-6
2.3 Standardized Designs of Seismically Isolated Nuclear Reactors	2-8
2.3.1 Advanced Liquid Metal Reactor	2-8
2.3.2 Super-Power Reactor Inherently Safe Module (S-PRISM)	2-8
2.3.3 Sodium Advanced Fast Reactor.....	2-9
2.3.4 Secure Transportable Autonomous Reactor	2-9
2.3.5 DFBR.....	2-11
2.3.6 Super Safe, Small and Simple (4S).....	2-13
2.3.7 Jules Horowitz Reactor (RJH).....	2-15
2.3.8 International Thermonuclear Experimental Reactor (ITER)	2-17

2.3.9 International Reactor Innovative and Secure (IRIS)	2-18
2.4 Review of Experimental Work.....	2-20
2.4.1 General	2-20
2.4.2 Iwabe <i>et al.</i> (2000)	2-22
2.4.3 Kato <i>et al.</i> (2003)	2-22
2.4.4 Shoji <i>et al.</i> (2004).....	2-23
2.4.5 Feng <i>et al.</i> (2004).....	2-24
2.4.6 Warn (2006).....	2-24
2.4.7 Constantinou <i>et al.</i> (2007).....	2-24
2.5 Review of Mathematical Models	2-25
2.5.1 Hyperelastic models.....	2-25
2.5.2 Linear and nonlinear stiffness models	2-28
2.6 Modeling in Contemporary Software Programs	2-32
2.6.1 General.....	2-32
2.6.2 SAP2000.....	2-33
2.6.3 3D-BASIS	2-34
2.6.4 PERFORM-3D	2-35
2.6.5 ABAQUS, LS-DYNA, and ANSYS.....	2-37
2.6.6 OpenSees.....	2-41
2.6.7 Summary	2-42
3 MATHEMATICAL MODELS OF ELASTOMERIC BEARINGS	3-1
3.1 Introduction.....	3-1
3.2 Mechanical Behavior in Vertical Direction	3-1
3.2.1 General	3-1
3.2.2 Coupling of horizontal and vertical response.....	3-1
3.2.3 Buckling in compression	3-3
3.2.4 Cavitation in tension.....	3-5
3.2.5 Post-cavitation behavior	3-6
3.2.6 Strength degradation in cyclic loading	3-9
3.2.7 Mathematical model	3-10
3.3 Mechanical Behavior in the Horizontal Direction.....	3-11
3.3.1 General	3-11
3.3.2 Coupled horizontal response.....	3-11
3.3.3 Heating of the lead core	3-12
3.3.4 Equivalent damping	3-14

3.3.5	Variation in shear modulus.....	3-15
3.3.6	Mathematical model.....	3-16
3.4	Mechanical Behavior in Rotation and Torsion.....	3-19
4	IMPLEMENTATION OF THE MATHEMATICAL MODELS IN OPENSEES AND ABAQUS.....	4-1
4.1	Introduction.....	4-1
4.2	Physical Model.....	4-1
4.2.1	Reference coordinate systems.....	4-3
4.3	Numerical Model and Code Implementation.....	4-9
4.3.1	General.....	4-9
4.3.2	Material models.....	4-9
4.3.3	Nonlinear geometric effects.....	4-19
4.4	Implementation in OpenSees.....	4-22
4.4.1	General.....	4-22
4.4.2	OpenSees framework.....	4-23
4.4.3	Variables and functions in OpenSees elements.....	4-24
4.4.4	User elements.....	4-27
4.5	Implementation in ABAQUS.....	4-29
4.5.1	General.....	4-29
4.5.2	ABAQUS framework.....	4-29
4.5.3	Variables in ABAQUS subroutines.....	4-32
4.5.4	User input interface of the elements.....	4-35
4.5.5	User elements.....	4-35
5	VERIFICATION AND VALIDATION.....	5-1
5.1	Introduction.....	5-1
5.2	Background.....	5-2
5.3	Elastomeric Bearing Model Development.....	5-5
5.3.1	General.....	5-5
5.3.2	Model development.....	5-6
5.4	Verification and Validation Criteria.....	5-7
5.5	Verification of the Model.....	5-8
5.5.1	Verification model.....	5-8
5.5.2	Code verification.....	5-10
5.5.3	Solution verification.....	5-25
5.5.4	Conclusions on verification.....	5-44

5.6 Validation of the Model	5-45
5.6.1 General	5-45
5.6.2 Sensitivity analysis	5-46
5.6.3 Available test data	5-49
5.6.4 Validation plan	5-53
5.7 Accuracy Criteria	5-55
6 SPECIMEN SELECTION AND EXPERIMENTAL PROGRAM.....	6-1
6.1 Introduction.....	6-1
6.2 Model Bearing Properties	6-1
6.2.1 Target and reported properties, and predicted capacities.....	6-1
6.3 Test Program.....	6-15
6.3.1 General.....	6-15
6.3.2 Description.....	6-15
6.4 Instrumentation and Data Acquisition	6-22
6.4.1 General.....	6-22
6.4.2 Single Bearing Testing Machine.....	6-22
6.4.3 Five channel load cell.....	6-25
6.4.4 Potentiometers.....	6-26
6.4.5 Krypton tracking system.....	6-26
6.4.6 Video monitoring system.....	6-28
6.4.7 Concrete strength tester.....	6-30
7 EXPERIMENTAL RESULTS.....	7-1
7.1 Introduction.....	7-1
7.2 Data Processing	7-1
7.2.1 General.....	7-1
7.2.2 Filtering	7-1
7.2.3 Axial displacement	7-3
7.2.4 Actuator comparison	7-7
7.3 Characterization Testing.....	7-10
7.3.1 General.....	7-10
7.3.2 Shear properties	7-10
7.3.3 Compression properties	7-19
7.3.4 Tensile properties	7-23
7.4 Effect of Lateral Offset on Tensile Properties.....	7-24
7.5 Effect of Tensile Loading History on Cavitation.....	7-28

7.6 Effect of Cavitation on Mechanical Properties.....	7-32
7.6.1 General.....	7-32
7.6.2 Shear properties	7-32
7.6.3 Axial properties	7-36
7.6.4 Critical buckling load capacity	7-36
7.7 Failure mode in tension	7-40
7.8 Validation of Mathematical Model	7-41
7.9 Conclusions and Recommendations.....	7-42
8 RESPONSE OF THE TWO-NODE MACRO MODEL OF BASE-ISOLATED NUCLEAR POWER PLANT.....	8-1
8.1 Introduction.....	8-1
8.2 Numerical Model	8-1
8.3 Results of Analysis using the Simplified Isolator Model	8-5
8.4 Results of Analysis using the Advanced Isolator Model	8-10
8.4.1 Strength degradation in shear due to heating of the lead core	8-10
8.4.2 Variation in buckling load due to horizontal displacement	8-14
8.4.3 Cavitation and post-cavitation behavior.....	8-16
8.4.4 Variation in axial stiffness due to horizontal displacement.....	8-17
8.4.5 Variation in shear stiffness due to axial load	8-18
8.4.6 Cumulative effects	8-20
8.5 Summary and Conclusions.....	8-25
9 RESPONSE OF A LUMPED-MASS MODEL OF A BASE-ISOLATED NUCLEAR POWER PLANT.....	9-1
9.1 Introduction.....	9-1
9.2 Fixed-base Model of a Nuclear Power Plant.....	9-1
9.2.1 Modal analysis	9-3
9.3 Base-isolated Model of the Nuclear Power Plant.....	9-6
9.4 Response-history Analysis	9-8
9.5 Results of Analysis using the Simplified Isolator Model	9-10
9.6 Results of Analysis using the Advanced Isolator Model	9-12
9.7 Comparison with Macro-model Analysis	9-16
9.8 Vertical Accelerations in the Superstructure	9-18
9.8.1 Modal properties	9-21
9.8.2 Damping	9-22
9.8.3 Substructuring.....	9-29

9.9 Conclusions.....	9-41
10 SUMMARY, CONCLUSIONS AND RECOMMENDATIONS	10-1
10.1 Summary.....	10-1
10.2 Conclusions.....	10-2
10.3 Recommendations for Future Research	10-3
11 REFERENCES.....	11-1
APPENDIX A EXPERIMENTAL PROGRAM AND RESULTS.....	A-1
APPENDIX B RESPONSE OF THE TWO-NODE MACRO MODEL OF BASE-ISOLATED NUCLEAR POWER PLANT.....	B-1
APPENDIX C RESPONSE OF THE LUMPED-MASS STICK MODEL OF BASE-ISOLATED NUCLEAR POWER PLANT.....	C-1

LIST OF FIGURES

Figure 1-1	Seismically isolated nuclear power plant (Kammerer <i>et al.</i> , 2019).....	1-2
Figure 2-1	Cut-away view of seismic isolator used for the Cruas NPP; dimensions in mm (Labbe, 2010)	2-3
Figure 2-2	Vertical cross section through the isolator and pedestal in the Cruas NPP (Labbe, 2010)	2-3
Figure 2-3	Four units of seismically isolated NPP at Cruas, France (Forni and Poggianti, 2011)	2-3
Figure 2-4	Historical development of PRISM.....	2-7
Figure 2-5	ALMR reactor & steam generator facility general arrangement (Forni, 2010)	2-8
Figure 2-6	Cut-away view of the PRISM reactor (GE, 2012)	2-9
Figure 2-7	Vertical cross section through the seismically isolated STAR (Yoo and Kulak, 2002)	2-10
Figure 2-8	3D isolation system for the STAR (Yoo <i>et al.</i> , 1999)	2-11
Figure 2-9	Vertical layout of seismically isolated demonstration FBR (Forni, 2010).....	2-12
Figure 2-10	2D isolation system for the demonstration FBR (Forni, 2010)	2-12
Figure 2-11	3D isolation system for the demonstration FBR (Forni, 2010)	2-13
Figure 2-12	Vertical cross section through the seismically isolated 4S reactor, dimensions in mm (Shimizu, 2009).....	2-14
Figure 2-13	Layout of lead-rubber bearings in the 4S reactor (Shimizu, 2009).....	2-15
Figure 2-14	Elastomeric bearing used for the RJH (NUVIA, 2011)	2-15
Figure 2-15	Cut-away view of Jules Horowitz Reactor (NUVIA, 2011)	2-16
Figure 2-16	Layout of the isolators for the RJH (NUVIA, 2011)	2-16
Figure 2-17	Isolator layout for the seismically isolated ITER (www.iter.org)	2-17
Figure 2-18	Cross-section through the elastomeric bearing used for ITER and RJH (NUVIA, 2011)	2-17
Figure 2-19	Isolators installed on the site of ITER (http://www.iter.org)	2-18
Figure 2-20	Vertical section through IRIS (Forni and Poggianti, 2011)	2-19
Figure 2-21	Layout of isolators for IRIS (Poggianti, 2011)	2-19
Figure 2-22	Variation of cavitation stress with the thickness of rubber discs of different Young's modulus (Gent and Lindley, 1959b)	2-21
Figure 2-23	Hysteresis in tension loading with 200 % shear strain (Iwabe <i>et al.</i> , 2000).....	2-22
Figure 2-24	Effect of offset shear strain on tensile behavior (Kato <i>et al.</i> , 2003).....	2-23
Figure 2-25	Lateral force versus lateral displacement under tensile and compressive loading (Shoji <i>et al.</i> , 2004)	2-23
Figure 2-26	Load-deformation behavior of LDR bearings under tensile loading with zero lateral offset (Warn, 2006)	2-24
Figure 2-27	Load-displacement behavior in tension (Constantinou <i>et al.</i> , 2007).....	2-25
Figure 2-28	Components of energy dissipation in the tensile loading of elastomeric bearings.....	2-28
Figure 2-29	Linear stiffness model of elastomeric bearing in vertical direction	2-29
Figure 2-30	Vertical stiffness model for an elastomeric bearing (Constantinou <i>et al.</i> , 2007)	2-31
Figure 2-31	Axial stress-strain model (Yamamoto <i>et al.</i> , 2009)	2-32
Figure 2-32	Three of the six independent springs in a Link/Support element	2-33
Figure 2-33	Link/Support property data input to SAP2000 (CSI, 2011)	2-34
Figure 2-34	Model that can be analyzed in 3D-BASIS-ME-MB (Tsopelas <i>et al.</i> , 2005).....	2-35
Figure 2-35	Degrees of freedom in 3D-BASIS-ME-MB (Tsopelas <i>et al.</i> , 2005).....	2-36
Figure 2-36	Finite element model of a low damping rubber bearing	2-37

Figure 2-37	Properties definition of rubber material in ABAQUS	2-38
Figure 2-38	Conceptual illustration of connector behaviors (Dassault, 2010a)	2-39
Figure 2-39	Type of connectors used for seismic isolators	2-40
Figure 2-40	Definition of connector's behavior	2-40
Figure 2-41	OpenSees isolator model	2-41
Figure 3-1	Model of an elastomeric bearing (Constantinou <i>et al.</i> , 2007).....	3-2
Figure 3-2	Stress softening under compression	3-2
Figure 3-3	Reduced area of elastomeric bearings (adapted from Constantinou <i>et al.</i> (2007)).....	3-5
Figure 3-4	Bilinear variation of buckling load	3-5
Figure 3-5	Post-cavitation variation of tensile force in the bearing.....	3-8
Figure 3-6	Load-deformation behavior of rubber bearings under tension	3-10
Figure 3-7	Mathematical model of elastomeric bearings in axial direction	3-10
Figure 3-8	Mathematical model of elastomeric bearings in shear	3-11
Figure 3-9	Schematic of a LR bearing (Kalpakidis <i>et al.</i> , 2010).....	3-13
Figure 3-10	Idealized behavior of elastomeric bearings in shear (Warn and Whittaker, 2006)	3-14
Figure 3-11	Effective stiffness of elastomeric bearings (Constantinou <i>et al.</i> , 2007)	3-16
Figure 3-12	Stress and strain dependency of LDR bearings (courtesy of DIS Inc.)	3-16
Figure 3-13	Mathematical model of lead rubber bearings in horizontal direction	3-17
Figure 3-14	Alternative representation of the mathematical model	3-17
Figure 4-1	Physical model of an elastomeric bearing	4-1
Figure 4-2	Discrete spring representation of an elastomeric bearing	4-2
Figure 4-3	Coordinate systems used in OpenSees and ABAQUS.....	4-4
Figure 4-4	Three of the six basic deformations in the 1-2 plane (adapted from CSI (2007)).....	4-4
Figure 4-5	Orientation of local and global coordinate axis systems	4-6
Figure 4-6	Components of the numerical model of elastomeric bearing	4-12
Figure 4-7	Overturning loads due to translation of story weights (Wilson, 2002)	4-21
Figure 4-8	High-level OpenSees objects in the software framework (Mazzoni <i>et al.</i> (2006)).....	4-23
Figure 4-9	The components of the Domain object (Mazzoni <i>et al.</i> , 2006).....	4-23
Figure 4-10	The components of the Analysis object (Mazzoni <i>et al.</i> , 2006).....	4-24
Figure 4-11	Internal construction of an elastomeric bearing	4-27
Figure 4-12	Local and global coordinates used in OpenSees for the elements	4-28
Figure 4-13	Outline of a general analysis step in ABAQUS (adapted from Dassault (2012)).....	4-31
Figure 4-14	Programming structure of user elements (adapted from Dassault (2012)).....	4-37
Figure 5-1	Model development, verification and validation (Thacker <i>et al.</i> , 2004).....	5-4
Figure 5-2	Hierarchy of the model for an elastomeric bearing	5-5
Figure 5-3	Verification, validation and model calibration plan for elastomeric bearings	5-7
Figure 5-4	Two-node macro model of a base-isolated NPP	5-9
Figure 5-5	Analyses cases used for the symmetry test	5-10
Figure 5-6	Force-displacement response in shear at the free node.....	5-11
Figure 5-7	Shear strength degradation due to heating of the lead core (large size bearing in Kalpakidis <i>et al.</i> (2010)).....	5-12
Figure 5-8	Shear force history (large size bearing in Kalpakidis <i>et al.</i> (2010))	5-13
Figure 5-9	Cavitation and post-cavitation behavior (LDR5 in Warn (2006))	5-14
Figure 5-10	Cavitation and post-cavitation behavior (KN2 in Iwabe <i>et al.</i> (2000)).....	5-14
Figure 5-11	Axial behavior under increasing amplitude triangular loading and linearly increasing lateral loading ($\Delta t = 0.01$ sec, LDR5 in Warn (2006))	5-15

Figure 5-12	Axial behavior under increasing amplitude triangular loading and linearly increasing lateral loading ($\Delta t = 0.005$ sec, LDR5 in Warn (2006))	5-15
Figure 5-13	Order of accuracy test (Roy and Oberkamp, 2011)	5-17
Figure 5-14	Observed order of accuracy at a crossover point (Oberkamp and Roy, 2010)	5-21
Figure 5-15	Order of accuracy in the vertical direction ($a_g = g \sin(\pi t)$)	5-23
Figure 5-16	Order of accuracy in the horizontal direction ($a_g = 0.001g \sin(\pi t)$)	5-23
Figure 5-17	Order of accuracy in horizontal direction ($a_g = 0.1g \sin(\pi t)$ for LDR and $a_g = 0.5g \sin(\pi t)$ for LR bearing)	5-23
Figure 5-18	Observed order of accuracy of the heating model	5-24
Figure 5-19	Discretization error in the shear displacement	5-30
Figure 5-20	Discretization error in the temperature rise of the lead core	5-30
Figure 5-21	Horizontal shear response of a LDR bearing	5-31
Figure 5-22	Force-displacement loops for a LR bearing	5-31
Figure 5-23	Temperature increase in the lead core	5-32
Figure 5-24	Discretization error in shear displacement	5-32
Figure 5-25	Free vibration response of a LDR bearing in the horizontal direction ($u_o = 0.01$ mm, $\zeta = 2\%$)	5-34
Figure 5-26	Free vibration response of a LDR bearing in the vertical direction ($u_o = 0.01$ mm, $\zeta = 2\%$)	5-34
Figure 5-27	Bending moments in a two node element	5-35
Figure 5-28	Integrators in OpenSees	5-36
Figure 5-29	Shear displacement response of a LDR bearing ($\Delta t/T_n = 0.1$)	5-38
Figure 5-30	Shear displacement response of a LDR bearing ($\Delta t/T_n = 0.01$)	5-39
Figure 5-31	Variation of numerical damping with time-discretization ($T_n = 2$ sec)	5-40
Figure 5-32	Shear displacement response obtained using Central Difference integrator	5-41
Figure 5-33	Shear displacement obtained using Newmark Linear Acceleration integrator	5-42
Figure 5-34	Effect of Newmark parameter, γ , on the shear displacement history of a LDR bearing ($\Delta t = 0.1$ sec, $T_n = 2$ sec)	5-42
Figure 5-35	Effect of Newmark parameter, γ , on the shear displacement history of a LDR bearing ($\beta = 0.25$, $\Delta t = 0.01$ sec, $T_n = 2$ sec)	5-43
Figure 5-36	Effect of Newmark parameter, β , on the shear displacement history of a LDR bearing ($\gamma = 0.5$, $\Delta t = 0.1$ sec, $T_n = 2$ sec)	5-43
Figure 5-37	Effect of Newmark parameter, β , on the shear displacement history of a LDR bearing ($\gamma = 0.5$, $\Delta t = 0.01$ sec, $T_n = 2$ sec)	5-44
Figure 5-38	Effect of various parameters on axial behavior of a LDR bearing	5-47
Figure 5-39	Effect of the strength degradation parameter on the tensile behavior	5-47
Figure 5-40	Effect of different parameters on yield strength of a LDR bearing	5-48
Figure 5-41	Effect of parameters on the shear behavior (LR5 bearing in Warn (2006))	5-48
Figure 5-42	Effect of parameters on the shear behavior (large size LR bearing of Kalpakidis <i>et al.</i> (2010))	5-49
Figure 5-43	Calibration of the mathematical model in tension with test data	5-49
Figure 5-44	Calibration of the mathematical model in tension with test data of Clark (1996)	5-50
Figure 5-45	Shear force-displacement behavior of a LR bearing under harmonic loading	5-51
Figure 5-46	Shear force history of a LR bearing under harmonic loading	5-51
Figure 5-47	Shear force-displacement behavior of a LR bearing under random loading	5-52
Figure 5-48	Shear force history of a LR bearing under random loading	5-52

Figure 6-1	Geometric details of bearing type A	6-5
Figure 6-2	Geometric details of bearing type B	6-6
Figure 6-3	DIS bearing type A, DA (courtesy of DIS, Inc.).....	6-7
Figure 6-4	DIS bearing type B, DB (courtesy of DIS, Inc.).....	6-8
Figure 6-5	Mageba bearing type A, MA (courtesy of Mageba)	6-9
Figure 6-6	Mageba bearing type B, MB (courtesy of Mageba)	6-10
Figure 6-7	Signals used for the experiments	6-21
Figure 6-8	Schematic of Single Bearing Testing Machine (Warn, 2006).....	6-23
Figure 6-9	Photograph of Single Bearing Testing Machine.....	6-23
Figure 6-10	Layout of experimental setup (top-view).....	6-24
Figure 6-11	Capacity nomogram for load cell cross-section (SEESL, 2010).....	6-24
Figure 6-12	Five channel load cell.....	6-25
Figure 6-13	String potentiometer used for the measurement of axial displacement.....	6-26
Figure 6-14	Components of the Krypton tracking system	6-27
Figure 6-15	Locations monitored by the Krypton camera during testing	6-28
Figure 6-16	Cameras used for the video monitoring system.....	6-29
Figure 6-17	Location of the four cameras on the columns of the SBTM	6-29
Figure 6-18	Compression Strength Tester at SEESL, University at Buffalo.....	6-30
Figure 6-19	Potentiometers.....	6-31
Figure 7-1	Effect of cutoff frequency on the shear response (bearing DA3, test 1).....	7-2
Figure 7-2	Effect of cutoff frequency on the tensile response (bearing DA3, test 6)	7-2
Figure 7-3	Top view of the instrumentation setup of SBTM	7-3
Figure 7-4	Locations of LEDs for Krypton tracking system	7-3
Figure 7-5	Axial deformation obtained using string potentiometers (bearing DA3, test 2)	7-5
Figure 7-6	Axial deformation obtained using string potentiometers (bearing MA3, test 3)	7-5
Figure 7-7	Axial deformation obtained using potentiometers and Krypton camera (bearing DA3, test 2)	7-6
Figure 7-8	Axial deformation obtained using potentiometers and Krypton camera (bearing DA3, test 3)	7-6
Figure 7-9	Shear force obtained using the MTS actuator and five channel load cell (bearing DB4, test 4a).....	7-8
Figure 7-10	Shear force-displacement response obtained using the MTS actuator and the five channel load cell (bearing DB4, test 4a).....	7-8
Figure 7-11	Shear displacement obtained using the MTS actuator and the Krypton camera (bearing DB4, test 4a).....	7-9
Figure 7-12	Shear force-displacement loops obtained using the MTS actuator and the Krypton camera (bearing DB4, test 4a).....	7-9
Figure 7-13	Idealized force-displacement behavior of an elastomeric bearing in shear (Warn and Whittaker, 2006).....	7-10
Figure 7-14	A general hysteretic system (Chopra, 2007)	7-11
Figure 7-15	Statistical distributions of shear moduli	7-15
Figure 7-16	Statistical distributions of damping ratios.....	7-15
Figure 7-17	Variation of effective shear modulus of MA1 with frequency and strain	7-16
Figure 7-18	Variation of shear modulus of DIS bearings with shear strain.....	7-17
Figure 7-19	Variation of effective shear modulus of Mageba bearings with shear strain.....	7-17
Figure 7-20	Variation of effective shear modulus of DIS bearings with axial pressure	7-18
Figure 7-21	Variation of effective shear modulus of Mageba bearings with axial pressure	7-18
Figure 7-22	Compression characterization tests of bearings	7-20

Figure 7-23	Load-deformation behavior in cyclic tensile loading at different lateral offsets.....	7-26
Figure 7-24	Variation of tensile stiffness with lateral offset strain.....	7-26
Figure 7-25	Variation of tensile stiffness with number of cycles for bearing DA1	7-27
Figure 7-26	Variation of tensile stiffness with number of cycles for bearing DB4 ($\Delta/R = 0$).....	7-27
Figure 7-27	Effect of lateral offset on tensile hysteresis	7-28
Figure 7-28	Behavior of DIS bearings under cyclic tensile loading	7-29
Figure 7-29	Behavior of Mageba bearings under cyclic tensile loading	7-30
Figure 7-30	Behavior of DIS and Mageba bearings under cyclic tensile loading.....	7-30
Figure 7-31	Behavior of the trial bearing under cyclic tensile loading	7-31
Figure 7-32	Variation of effective shear modulus with shear strain for bearing DB4	7-33
Figure 7-33	Variation of effective shear modulus with axial pressure for bearing DA4.....	7-33
Figure 7-34	Variation of effective shear modulus with axial pressure for bearing DB4.....	7-34
Figure 7-35	Variation of effective shear modulus with axial pressure for bearing MB1	7-34
Figure 7-36	Slippage across the damaged interface of bearing MA4 in a shear test (axial pressure = 0.5 MPa).....	7-35
Figure 7-37	Shear response of bearing MA4 at different axial loads	7-36
Figure 7-38	Compression failure tests of DA bearings	7-38
Figure 7-39	Compression failure tests of DB bearings	7-38
Figure 7-40	Compression failure tests of MA bearings.....	7-39
Figure 7-41	Compression failure tests of MB bearings.....	7-39
Figure 7-42	Failure mechanism in rubber bearings under tension.....	7-41
Figure 7-43	Misaligned groves in top and bottom bearing plates of the bearing MA4	7-41
Figure 7-44	Validation of the mathematical model in tension, normalized force versus displacement	7-43
Figure 8-1	Two-node macro model of a base-isolated NPP	8-1
Figure 8-2	Acceleration response spectra of ground motions.....	8-5
Figure 8-3	Simplified model of LR bearing	8-5
Figure 8-4	Percentiles of horizontal displacement for LR bearing models	8-10
Figure 8-5	Percentiles of horizontal shear force for LR bearing models.....	8-11
Figure 8-6	Ratio of minimum characteristic shear strength to initial strength	8-12
Figure 8-7	Maximum temperature rise in the lead core	8-13
Figure 8-8	Histories of temperature increase in the lead cores.....	8-13
Figure 8-9	Normalized axial load ratios	8-15
Figure 8-10	Demand-capacity ratios for the constant buckling load model, P_{cr0}	8-15
Figure 8-11	Demand-capacity ratios for the displacement-dependent buckling load model, P_{cr}	8-16
Figure 8-12	Axial response of bearing LR5 in Warn (2006) subject to harmonic vertical excitation	8-18
Figure 8-13	Influence of axial stiffness model on the vertical response of T3Q6	8-19
Figure 8-14	Effect of the variation of axial compressive stiffness on T3Q6.....	8-19
Figure 8-15	Response of T2Q6 to ground motion 1 at 167% DBE	8-20
Figure 8-16	Ratios of percentiles of peak horizontal displacement to the median DBE displacement; simplified and advanced models	8-21
Figure 8-17	Ratios of the percentiles of peak horizontal displacement calculated using the advanced model to the median DBE displacement calculated using the simplified model.....	8-21
Figure 9-1	Stick model of the nuclear power plant (EPRI, 2007)	9-2
Figure 9-2	Orientation of the coordinate axes.....	9-3

Figure 9-3	Orientation of local axes in OpenSees	9-4
Figure 9-4	Stick model of a base-isolated NPP in OpenSees.....	9-6
Figure 9-5	Plan view of the layout of isolated basemat showing (node, bearing) pairs	9-7
Figure 9-6	Acceleration response spectra of ground motions.....	9-9
Figure 9-7	Ratios of percentiles of peak horizontal displacement to the median DBE displacement; simplified and advanced models	9-15
Figure 9-8	Ratios of the percentiles of peak horizontal displacement calculated using the advanced model to the median DBE displacement calculated using the simplified model.....	9-15
Figure 9-9	Ratios of the percentiles of peak horizontal displacement calculated using the stick model to the two-node macro model; simplified model.....	9-17
Figure 9-10	Ratios of the percentiles of peak horizontal displacement calculated using the stick model to the two-node macro model; advanced model	9-17
Figure 9-11	Mean peak zero-period accelerations (g) for 30 ground motion sets in the superstructure along the height for the model T2Q6; 100% DBE shaking.....	9-19
Figure 9-12	Acceleration histories at node 2137 of model T2Q6 subject to GM1; 100% DBE shaking.....	9-20
Figure 9-13	Acceleration response spectra at node 2137 of model T2Q6 subject to GM1; 100% DBE shaking	9-21
Figure 9-14	Power spectral density of vertical acceleration for model T2Q6 subject to GM1; 100% DBE shaking	9-21
Figure 9-15	Variation of modal damping ratios with frequency	9-22
Figure 9-16	Mean peak zero-period accelerations (g) for 30 ground motion sets in the superstructure along the height of the base-isolated NPP model T2Q6; 100% DBE shaking.....	9-27
Figure 9-17	Mean floor response spectra for 30 ground motion sets at the center of the isolated basemat (node 2137) for three damping models and corresponding modal damping ratios in the superstructure; T2Q6, 100% DBE shaking.....	9-28
Figure 9-18	Acceleration histories at node 417 of model T2Q6 subject to GM1; 100% DBE shaking.....	9-31
Figure 9-19	Acceleration histories at node 310 of model T2Q6 subject to GM1; 100% DBE shaking.....	9-33
Figure 9-20	Acceleration histories at node 538 of model T2Q6 subject to GM1; 100% DBE shaking.....	9-35
Figure A-1	Tension in a single constrained rubber layer.....	A-14
Figure A-2	Shear strain and tensile stress in a constrained solid rubber layer in tension.....	A-16
Figure A-3	Shear strain and tensile stress in a constrained annular rubber layer in tension.....	A-17
Figure A-4	Distribution of shear strain in the radial direction.....	A-18
Figure C-1	The plan view of the representative reactor model (Roche-Rivera, 2013).....	C-2
Figure C-2	The plan view of the representative reactor model	C-3
Figure C-3	A two-dimensional representation of base-isolated NPP	C-13
Figure C-4	Spatial profile for mean of peak axial displacements (mm) for sets of 30 ground motion sets, 200% DBE.....	C-28
Figure C-5	Mean peak zero-period accelerations (g) for the 30 ground motion sets, T2Q6	C-30
Figure C-6	Mean peak zero-period accelerations (g) for the 30 ground motion sets, T2Q12	C-31
Figure C-7	Floor response spectra, simplified model, node 2137, X direction	C-33
Figure C-8	Floor response spectra, simplified model, node 2137, Y direction	C-34

Figure C-9	Floor response spectra, simplified model, node 2137, Z direction.....	C-35
Figure C-10	Floor response spectra, advanced model, node 2137, X direction.....	C-37
Figure C-11	Floor response spectra, advanced model, node 2137, Y direction.....	C-38
Figure C-12	Floor response spectra, advanced model, node 2137, Z direction.....	C-39

LIST OF TABLES

Table 2-1	Properties of the lead-rubber bearings used for the 4S reactor (Shimizu, 2009).....	2-13
Table 2-2	Experimental work on the tensile properties of elastomeric bearings.....	2-21
Table 2-3	Hyperelastic models used in ABAQUS (Dassault, 2010d).....	2-26
Table 2-4	Modeling of elastomeric seismic isolators and software programs	43
Table 3-1	Typical value of lead and steel related parameters (Kalpakidis et al., 2010).....	3-13
Table 4-1	Direction cosines of axes (adapted from Cook (2001)).....	4-6
Table 4-2	Array indices	4-9
Table 4-3	Axial force and stiffness as a function of displacement.....	4-11
Table 4-4	Functions used in an OpenSees Element.....	4-25
Table 4-5	Description of the user input arguments for the elements.....	4-26
Table 4-6	Default values of optional parameters	4-29
Table 4-7	Overview of variables used in ABAQUS user subroutines (contd.).....	4-33
Table 4-8	Analysis cases used in ABAQUS	4-34
Table 4-9	Parameter definitions used for UEL interface	4-35
Table 4-10	Properties of UELs that need to be defined as PROPS array.....	4-36
Table 5-1	Description of model input parameters (Roy and Oberkamp, 2011)	5-4
Table 5-2	Scope of the V&V for the elastomeric bearing models.....	5-6
Table 5-3	Phenomenon ranking and identification table for models of elastomeric bearings	5-7
Table 5-4	Geometrical and mechanical properties of elastomeric bearings.....	5-9
Table 5-5	Code-to-code verification for different component of the mathematical models.....	5-12
Table 5-6	Discretization errors for numerical model in the axial direction	5-29
Table 5-7	Discretization errors for numerical model in the shear direction.....	5-29
Table 5-8	Damping ratios (%) calculated from numerical response.....	5-33
Table 5-9	Bending moments at the two nodes of the element (N-m).....	5-35
Table 5-10	Stability requirements for the response obtained using different integrators	5-37
Table 5-11	Numerical damping in shear displacement response of a LDR bearing using different Newmark parameters (%).....	5-41
Table 5-12	Properties of the bearings used for experimental comparison	5-50
Table 5-13	Error associated with computational model	5-51
Table 5-14	Response quantities to be measured during the experiments	5-54
Table 6-1	Target model bearing properties	6-2
Table 6-2	DIS model bearing properties.....	6-3
Table 6-3	Mageba model bearing properties.....	6-4
Table 6-4	Geometrical and mechanical properties of elastomeric bearings (SI units).....	6-13
Table 6-5	Geometrical and mechanical properties of elastomeric bearings (US units)	6-14
Table 6-6	Summary of single bearing testing program (contd.)	6-17
Table 6-7	Trial bearing test sequence (SI units).....	6-20
Table 6-8	Single bearing testing machine actuator capabilities	6-25
Table 6-9	Details of the camera used for video monitoring system.....	6-28
Table 7-1	Shear properties obtained from shear characterization tests (contd.).....	7-13
Table 7-2	Averaged shear properties of bearings.....	7-14
Table 7-3	Summary of averaged shear properties	7-14
Table 7-4	Effect of frequency on effective shear modulus	7-16
Table 7-5	Compression properties obtained from characterization tests (contd.)	7-21
Table 7-6	Summary of averaged compression properties of bearings.....	7-22

Table 7-7	Theoretical and experimentally obtained compressive stiffness	7-22
Table 7-8	Summary of tensile properties obtained from tensile tests.....	7-23
Table 7-9	Average tensile properties of bearings	7-23
Table 7-10	Compressive and tensile stiffness of bearings.....	7-24
Table 7-11	Experimental and theoretical cavitation strengths.....	7-25
Table 7-12	Location of rupture plane in bearings failed due to cavitation	7-31
Table 7-13	Pre- and post-cavitation shear properties of elastomeric bearings	7-32
Table 7-14	Coefficient of kinetic friction between rubber layers.....	7-36
Table 7-15	Pre- and post-cavitation axial properties of elastomeric bearings	7-37
Table 7-16	Theoretical and experimental values of critical buckling load.....	7-40
Table 8-1	Geometrical and mechanical properties of elastomeric bearings.....	8-2
Table 8-2	Geometric and material properties of LR bearing models.....	8-3
Table 8-3	Rayleigh damping ratios in the six directions of motion of the isolation system.....	8-4
Table 8-4	Percentiles of peak horizontal displacement (mm) for 30 ground motion sets; simplified model ¹	8-7
Table 8-5	Percentiles of peak horizontal shearing force (% <i>W</i>) for 30 ground motion sets; simplified model ^{1, 2}	8-7
Table 8-6	Percentiles of peak compressive displacement (mm) for 30 ground motion sets; simplified model ¹	8-8
Table 8-7	Percentiles of peak compressive force (% <i>W</i>) for 30 ground motion sets; simplified model ^{1, 2}	8-8
Table 8-8	Percentiles of peak tensile displacement (mm) for 30 ground motion sets; simplified model ¹	8-9
Table 8-9	Percentiles of peak tensile force (% <i>W</i>) for 30 ground motion sets; simplified model ^{1, 2}	8-9
Table 8-10	Number of ground motions (of 30) triggering buckling failures; using P_{cr0}	8-16
Table 8-11	Number of ground motions (of 30) triggering buckling failures; using P_{cr}	8-16
Table 8-12	Number of ground motions (of 30) that cavitate isolators.....	8-17
Table 8-13	Number of ground motion sets (of 30) for which cavitation is predicted; advanced model	8-22
Table 8-14	Number of ground motion sets (of 30) for which buckling is predicted; advanced model	8-22
Table 8-15	Percentiles of peak horizontal displacement (mm) for 30 ground motion sets; advanced model.....	8-23
Table 8-16	Percentiles of peak shearing force; advanced model (% <i>W</i>) for thirty ground motion sets; advanced model	8-23
Table 8-17	Percentiles of peak compressive force (% <i>W</i>) for 30 ground motion sets; advanced model	8-25
Table 8-18	Mean peak tensile force (% <i>F_c</i>); of 30 ground motion sets; advanced model.....	8-25
Table 9-1	Modal properties of the stick models in OpenSees.....	9-4
Table 9-2	Modal properties of Auxiliary Shield Building (ASB)	9-5
Table 9-3	Modal properties of Steel Containment Vessel (SCV)	9-5
Table 9-4	Modal properties of Containment Internal Structure (CIS)	9-5
Table 9-5	Geometrical and mechanical properties of elastomeric bearings.....	9-7
Table 9-6	Geometric and material properties of LR bearing isolation system models.....	9-8
Table 9-7	Mean peak displacements (mm) for the 30 ground motion sets at the center and four corners of the basemat (model T2Q6); simplified model	9-11
Table 9-8	Mean peak rotations (degrees) for the 30 ground motion sets; simplified model	9-11

Table 9-9	Mean peak zero-period accelerations (g) for the 30 ground motion sets at center of basemat (node 2137); simplified model.....	9-11
Table 9-10	Mean peak spectral accelerations (g) for the 30 ground motion sets at center of basemat (node 2137); simplified model.....	9-11
Table 9-11	Mean peak displacements (mm) for 30 ground motion sets at the center and four corners of the basemat (model T2Q6); advanced model	9-13
Table 9-12	Mean peak rotations (degrees) for 30 ground motion sets; advanced model.....	9-13
Table 9-13	Mean peak zero-period accelerations (g) for 30 ground motion sets at the center of the basemat (node 2137); advanced model	9-13
Table 9-14	Mean peak spectral accelerations (g) for 30 ground motion sets at center of basemat (node 2137); advanced model.....	9-13
Table 9-15	Median number of bearings (of 273) for 30 ground motion sets for which buckling is predicted; advanced model	9-14
Table 9-16	Median number of bearings (of 273) for 30 ground motion sets for which cavitation is predicted; advanced model	9-14
Table 9-17	Mean peak ground acceleration (g) for 30 ground motion sets	9-18
Table 9-18	Mean peak zero-period accelerations (g) for 30 ground motion sets at the center of the basemat; base-isolated NPP	9-18
Table 9-19	Damping ratios corresponding to isolation frequency	9-24
Table 9-20	Damping ratios corresponding to the frequencies of the ASB.....	9-24
Table 9-21	Damping ratios corresponding to the frequencies of the SCV.....	9-24
Table 9-22	Damping ratios corresponding to the frequencies of the CIS.....	9-24
Table 9-23	Mean peak zero-period accelerations (g) for 30 ground motion sets at the center of the basemat (node 2137); Rayleigh damping.....	9-25
Table 9-24	Mean peak zero-period accelerations (g) for 30 ground motion sets at the center of the basemat (node 2137); mass proportional damping	9-25
Table 9-25	Mean peak zero-period accelerations (g) for 30 ground motion sets at the center of the basemat (node 2137); stiffness proportional damping.....	9-25
Table 9-26	Percentiles of peak horizontal displacement (mm) for 30 ground motion sets at the center of the basemat (node 2137); Rayleigh damping.....	9-26
Table 9-27	Percentiles of peak horizontal displacement (mm) for 30 ground motion sets at the center of the basemat (node 2137); mass proportional damping.....	9-26
Table 9-28	Percentiles of peak horizontal displacement (mm) for 30 ground motion sets at the center of the basemat (node 2137); stiffness proportional damping	9-26
Table 9-29	Rayleigh damping in the horizontal and vertical modes of the fixed-base superstructures in OpenSees	9-29
Table 9-30	Mean peak zero-period accelerations (g) for 30 ground motion sets at node 417; lumped-mass stick model	9-30
Table 9-31	Mean peak zero-period accelerations (g) for 30 ground motion sets at node 417; equivalent fixed-base model in OpenSees (EFB_OpenSees)	9-30
Table 9-32	Percentage reduction in means of peak zero-period accelerations (g) for 30 ground motion sets at node 417 obtained using the lumped-mass stick model and the equivalent fixed-base model in OpenSees (EFB_OpenSees).....	9-30
Table 9-33	Mean peak zero-period accelerations (g) for 30 ground motion sets at node 310; lumped-mass stick model	9-32
Table 9-34	Mean peak zero-period accelerations (g) for 30 ground motion sets at node 310; equivalent fixed-base model in OpenSees (EFB_OpenSees)	9-32
Table 9-35	Percentage reduction in means of peak zero-period accelerations (g) for 30 ground motion sets at node 310 obtained using the lumped-mass stick model and the equivalent fixed-base model in OpenSees (EFB_OpenSees).....	9-32

Table 9-36	Mean peak zero-period accelerations (g) for 30 ground motion sets at node 538; lumped-mass stick model	9-34
Table 9-37	Mean peak zero-period accelerations (g) for 30 ground motion sets at node 538; equivalent fixed-base model in OpenSees (EFB_OpenSees)	9-34
Table 9-38	Percentage reduction in means of peak zero-period accelerations (g) for 30 ground motion sets at node 538 obtained using the lumped-mass stick model and the equivalent fixed-base model in OpenSees (EFB_OpenSees).....	9-34
Table 9-39	Mean peak zero-period accelerations (g) for 30 ground motion sets at node 2137 (isolated basemat); lumped-mass stick model, 2% Rayleigh damping	9-37
Table 9-40	Mean peak zero-period accelerations (g) for 30 ground motion sets at node 2137 (isolated basemat); lumped-mass stick model, 10% Rayleigh damping	9-37
Table 9-41	Percentage reduction in means of peak zero-period accelerations (g) for 30 ground motion sets at node 2137 (isolated basemat) obtained using 2% and 10% Rayleigh damping, lumped-mass stick model	9-37
Table 9-42	Mean peak zero-period accelerations (g) for 30 ground motion sets at node 310; lumped-mass stick model (ASB), 2% Rayleigh damping	9-38
Table 9-43	Mean peak zero-period accelerations (g) for 30 ground motion sets at node 310; lumped-mass stick model (ASB), 10% Rayleigh damping	9-38
Table 9-44	Percentage reduction in means of peak zero-period accelerations (g) for 30 ground motion sets at node 310 (ASB) obtained using 2% and 10% Rayleigh damping, lumped-mass stick model	9-38
Table 9-45	Mean peak zero-period accelerations (g) for 30 ground motion sets at node 417 (SCV); lumped-mass stick model, 2% Rayleigh damping.....	9-39
Table 9-46	Mean peak zero-period accelerations (g) for 30 ground motion sets at node 417 (SCV); lumped-mass stick model, 10% Rayleigh damping.....	9-39
Table 9-47	Percentage reduction in means of peak zero-period accelerations (g) for 30 ground motion sets at node 417 (SCV) obtained using 2% and 10% Rayleigh damping, lumped-mass stick model	9-39
Table 9-48	Mean peak zero-period accelerations (g) for 30 ground motion sets at node 538 (CIS); lumped-mass stick model, 2% Rayleigh damping	9-40
Table 9-49	Mean peak zero-period accelerations (g) for 30 ground motion sets at node 538 (CIS); lumped-mass stick model, 10% Rayleigh damping	9-40
Table 9-50	Percentage reduction in means of peak zero-period accelerations (g) for 30 ground motion sets at node 538 (CIS) obtained using 2% and 10% Rayleigh damping, lumped-mass stick model	9-40
Table A-1	Single bearing test sequence (contd.).....	A-2
Table A-2	Failure states of bearings under tensile load (contd.).....	A-20
Table B-1	Percentiles of peak horizontal displacement (mm) for 30 ground motion sets; heating effects ¹	B-2
Table B-2	Percentiles of peak horizontal shearing force (% <i>W</i>) for 30 ground motion sets; heating effects ^{1, 2}	B-2
Table C-1	Nodes and mass properties for structural model (units: kip, feet, seconds).....	C-5
Table C-2	Element properties for structural model (units: kip, feet, seconds)	C-7
Table C-3	Modal properties of the Auxiliary Shield Building (ASB)	C-10
Table C-4	Modal properties of the Steel Containment Vessel (SCV).....	C-11
Table C-5	Modal properties of the Containment Internal Structure (CIS).....	C-12
Table C-6	Location of the center of gravities	C-14
Table C-7	Percentiles of peak horizontal displacement (mm) for 30 ground motion sets; simplified model ¹	C-16
Table C-8	Percentiles of peak horizontal shearing force (% <i>W</i>) for 30 ground motion sets; simplified model ^{1, 2}	C-16

Table C-9	Percentiles of peak compressive displacement (mm) for 30 ground motion sets; simplified model ¹	C-17
Table C-10	Percentiles of peak compressive force (% <i>W</i>) for 30 ground motion sets; simplified model ^{1,2}	C-17
Table C-11	Percentiles of peak tensile displacement (mm) for 30 ground motion sets; simplified model ¹	C-18
Table C-12	Percentiles of peak tensile force (% <i>W</i>) for 30 ground motion sets; simplified model ^{1,2}	C-18
Table C-13	Percentiles of peak torsion (degrees) for 30 ground motion sets; simplified model ¹	C-19
Table C-14	Percentiles of peak rotation (degrees) about X axis for 30 ground motion sets; simplified model ¹	C-19
Table C-15	Percentiles of peak rotation (degrees) about Y axis for 30 ground motion sets; simplified model ¹	C-19
Table C-16	Percentiles of peak horizontal displacement (mm) for 30 ground motion sets; advanced model ¹	C-20
Table C-17	Percentiles of peak horizontal shearing force (% <i>W</i>) for 30 ground motion sets; advanced model ^{1,2}	C-20
Table C-18	Percentiles of peak compressive displacement (mm) for 30 ground motion sets; advanced model ¹	C-21
Table C-19	Percentiles of peak compressive force (% <i>W</i>) for 30 ground motion sets; advanced model ^{1,2}	C-21
Table C-20	Percentiles of peak tensile displacement (mm) for 30 ground motion sets; advanced model ¹	C-22
Table C-21	Percentiles of peak tensile force (% <i>W</i>) for 30 ground motion sets; advanced model ^{1,2}	C-22
Table C-22	Percentiles of peak torsion (degrees) for 30 ground motion sets; simplified model ¹	C-23
Table C-23	Percentiles of peak rotation (degrees) about X axis for 30 ground motion sets; simplified model ¹	C-23
Table C-24	Percentiles of peak rotation (degrees) about Y axis for 30 ground motion sets; simplified model ¹	C-23
Table C-25	Percentiles of temperature rise (°C) in the lead core for 30 ground motion sets; advanced model.....	C-24
Table C-26	Percentiles of shear characteristic strength (ratio of initial) for 30 ground motion sets; advanced model ¹	C-24
Table C-27	Number of bearings (of 273) for which buckling is predicted due to each ground motion set at four shaking intensities; advanced model	C-25
Table C-28	Number of bearings (of 273) for which cavitation is predicted due to each ground motion set at four shaking intensities; advanced model	C-26

EXECUTIVE SUMMARY

Seismic (base) isolation is a viable strategy to mitigate the damaging effects of extreme earthquakes on nuclear power plant (NPP) structures. This report addresses key technical challenges associated with the seismic isolation of nuclear power plants (NPPs) using two types of elastomeric bearings: 1) low damping rubber (LDR), and 2) lead-rubber (LR). A focus of the study is surface-mounted large light water reactors, although many of the research products are also directly relevant for isolation of components of next generation nuclear plants, most of which will likely be deeply embedded.

This report can be parsed into four subject areas: 1) development of advanced numerical models of LDR and LR bearings, 2) cross-platform implementation of the numerical models to three contemporary software programs, namely, OpenSees, ABAQUS, and LS-DYNA, 3) comprehensive verification and validation of the numerical models as per the ASME best practices, and 4) performance assessment of the base-isolated NPP subject to different intensities of earthquake shaking.

The mechanical properties of LDR and LR bearings are not expected to change substantially in design basis shaking. However, under shaking more intense than design basis, the properties of the lead cores in lead-rubber bearings may degrade due to heating associated with energy dissipation, some bearings in an isolation system may experience net tension, and the compression and tension stiffness of a bearing may be affected by the horizontal displacement of the isolation system. Mathematical models of low damping rubber (LDR) and lead rubber (LR) bearings suitable for analysis of safety-related nuclear structures subjected to design basis and beyond design basis earthquake shaking are developed to accommodate the following five characteristics or behaviors that may be important for US plants sited in regions of moderate to high seismic hazard: 1) strength degradation in shear due to heating of the lead core (LR bearings), 2) variation in buckling load due to horizontal displacement, 3) cavitation and post-cavitation behavior due to tensile loading, 4) variation in axial stiffness due to horizontal displacement, and 5) variation in shear stiffness due to axial load.

The advanced numerical models are now implemented as new User Elements (UEs) in the open-source platform OpenSees, and the commercial finite element codes ABAQUS and LS-DYNA. The user elements ElastomericX for the LDR bearing and LeadRubberX for the LR bearing are available in OpenSees and ABAQUS. The mathematical model of the LR bearing is implemented in LS-DYNA as a user material (UMAT), providing a third UMAT for isolator elements. The performance of the UEs, in terms of their capabilities and computational expense is discussed. A mathematical model for high-damping rubber bearings, HDRX, is implemented in OpenSees; the model includes many of the features of ElastomericX but implements the Grant et al. model in shear. HDRX was written for completeness and not in support of application to NPPs in the United States. These user elements and materials are publically available to enable and encourage use by researchers and the design professional community.

The models of LDR and LR bearings were verified and validated following ASME best practices. Those isolator characteristics crucial to robust estimates of performance are identified, which includes heating of the lead core in the LR bearing. Modeling errors due to different sources are quantified, and if possible, minimized or eliminated. The discretization errors in the peak horizontal and vertical response are less than 2%. The V+V activities helped establish confidence in these models and identified possible errors in the response due to use of these models, if any. The mathematical models in the shear (horizontal) and axial directions were

validated using existing experimental data. A series of validation experiments was conducted at the University at Buffalo to characterize behavior of elastomeric bearing under tensile and shear loadings. The test data was used to validate a phenomenological model of an elastomeric bearing in tension. Sixteen low damping rubber bearings from two manufacturers, with similar geometric properties but different shear moduli, were tested under various loading conditions to identify those factors that affect cavitation in an elastomeric bearing. The value of three times shear modulus (determined by testing bearings at 100% shear strain) is a good estimate of the cavitation stress in the rubber of a bearing. The effect of cavitation on the compressive stiffness, shear stiffness (under service axial load), and buckling load is negligible.

A model of a base-isolated nuclear island was analyzed using response-history techniques for design and beyond design basis earthquake shaking. Thirty three-component ground motions, selected and spectrally matched to be consistent with uniform hazard response spectra (UHRS) for design basis earthquake (DBE) shaking at the site of the Diablo Canyon Nuclear Generating Station, were used for response-history analysis. The model of the NPP nuclear island was derived from an early version of the Westinghouse AP1000 reactor but is considered to be representative of large light water reactors currently under construction in the United States. Two representations of the base-isolated NPP isolated with LR bearings were analyzed: 1) a two-node macro model, and 2) a lumped-mass stick model. The two representations of base-isolated NPP provided same horizontal displacement response, but the lumped-mass stick model provided additional information on torsional and rocking response and the spatial distribution of cavitation and buckling in the bearings comprising the isolation system. Simplified and advanced representations of LR bearing behavior were considered. The simplified model, with equal axial stiffness in compression and tension (and independent of shear displacement), represents the state-of-the-practice for response-history analyses of seismically isolated structures using contemporary software programs. The advanced isolator model considers the five characteristics of LR bearings identified previously. The effect of each of the five characteristics on the response of the isolated structure is quantified.

Heating of the lead core in a LR bearing has a relatively small effect ($< 10\%$) on horizontal DBE (shear) displacements but the influence increases at higher intensities of shaking. The buckling load of a LR bearing varies substantially during earthquake shaking. The displacement-dependent model for buckling load predicts failure for many more ground motions than the constant buckling load model, and is thus recommended for use in design practice. Isolation systems of different combinations of isolation period and strength-to-supported weight were analyzed. For a given isolation period, the effect of lead core heating decreases with an increase in the ratio of characteristic strength to weight, whereas for a given value of the ratio, the effect decreases with an increase in isolation period. Floor response spectra in two orthogonal horizontal directions were obtained at different locations in the stick model. Vertical accelerations in the superstructure of the base-isolated NPP are very sensitive to the definition of damping. A substructuring method is proposed that allows the use of different damping values for the isolation system and the superstructure and provides a more realistic estimate of vertical acceleration without overdamping the horizontal response. The reported data allows a reader to judge which representation of an isolated NPP (macro model or lumped-mass stick) and which features, if any, of the advanced isolator model are needed to compute response for different intensities of earthquake shaking.

ACKNOWLEDGMENTS

Financial support for this research project was provided the the United Stated Nuclear Regulatory Commission (USNRC) to MCEER via a contract led by Dr. Robert Budnitz at the Lawrence Berkeley National Laboratory (LBNL). The financial support provided by the USNRC and LBNL, and the technical leadership of Dr. Budnitz, is gratefully acknowledged.

A review panel was formed by LBNL to help guide our work and to provide timely feedback on interim deliverables. We sincerely thank members of the panel for their intellectual contributions to the project: Nilesh Chokshi, Antonio Godoy, James Johnson, Annie Kammerer, Robert Kennedy, Don Moore, and Johnathan Stewart.

Dynamic Isolation Systems (DIS), Inc. and Mageba provided bearings at no cost for the tests conducted as part of the project. Former University at Buffalo graduate students, Dr. Ioannis Kalpakidis of Energo Engineering, Dr. Amarnath Kasalananti of DIS, Inc., and Dr. Gordon Warn of Penn State University provided test data on elastomeric bearings. The staff of the Structural Engineering and Earthquake Simulation Laboratory at the University at Buffalo, including Scot Weinreber, Bob Staniszewski, Jeffrey Cizdziel, Christopher Budden and Mark Pitman, helped with the experimental studies. The authors are extremely grateful for this support.

Any opinions, finding and conclusion or recommendations expressed in this publication are those of the authors and do not necessarily reflect the views of MCEER, the University at Buffalo, LBNL or the USNRC.

ABBREVIATIONS AND ACRONYMS

α	Ratio of post-elastic shear stiffness to initial elastic stiffness
α_s	Thermal diffusivity of steel
β_{eff}	Effective damping
σ_{YL}	Effective yield stress of the lead-core
ρ_L	Density of lead
σ_{YLO}	Effective yield stress of lead at the reference temperature
τ	Dimensionless time parameter
ω	Angular frequency
ϕ, ϕ_{max}	Cavitation damage index and its maximum value
γ, β	Parameters of the Bouc-Wen Model that control the shape of the hysteresis loop
A_o	Bonded rubber area including cover thickness
a_c	Strength degradation parameter
A_L	Area of the lead-core
A_r	Reduced effective area of a bearing due to lateral displacement
c_d	Damping parameter
c_L	Specific heat of lead
E_D	Energy dissipated per cycle
D_o	Outer diameter
D_i	Inner diameter
f_b, f_l, f_g	Nodal force vector in basic, local and global coordinate systems
F_c	Initial cavitation force
F_{cn}	Cavitation force at any instance
F_{max}	Maximum tension force at any instance
F_Y	Yield strength
G_{eff}	Effective shear modulus
h	Total height of a bearing (rubber+shim)
I	Area moment of inertia
K	Bulk modulus of rubber
k_c	Cavitation parameter
K_d	Post-elastic shear stiffness
K_{eff}	Effective shear stiffness
K_{el}	Initial shear stiffness
K_b, K_l, K_g	Element stiffness matrix in basic, local and global coordinate systems

K_{H0}	Horizontal stiffness at zero axial load
K_{H0}	Horizontal stiffness
k_s	Thermal conductivity of steel
K_r	Rotational stiffness
K_t	Torsional stiffness
K_{v0}	Vertical stiffness at zero lateral displacement
K_v	Vertical stiffness
L_{int}	Total height (including int. plate)
L_{ext}	Total height (including ext. plate)
n	Number of rubber layers
P_{cr}	Critical buckling load
p_{static}	Static pressure on a bearing
Q_d	Characteristic strength
$sDratio$	Ratio of distance of the shear center from bottom node
S	Shape factor (without cover)
t_c	Rubber cover thickness around the perimeter of a bearing
T_{eff}	Effective time period
t_{ext}	External plate thickness
t_{int}	Internal plate thickness
T_{gl}	Transformation matrix from global to local coordinate system
T_{lb}	Transformation matrix from local to basic coordinate system
T_L	Temperature rise in the lead-core
t_r	Single rubber layer thickness
T_r	Total rubber layer thickness
t_s	Steel shim thickness
u_b, u_l, u_g	Nodal displacement vector in basic, local and global coordinate systems
u_c	Initial cavitation displacement
u_{cn}	Cavitation deformation at any instance
u_{max}	Maximum tensile deformation at any instance
u_{cr}	Critical buckling deformation
Y	Yield displacement
f	Frequency
Z_x, Z_y	Hysteretic parameters of the Bouc-Wen model
AASHTO	American Association of State Highway and Transportation Officials
ALMR	Advanced Liquid Metal Reactor

ANL	Argonne National Laboratory
ASB	Auxiliary and Shield Building
ASCE	American Society of Civil Engineering
ASME	American Society of Mechanical Engineering
CEA	Commissariat a L'Energie Atomique
CFD	Computational Fluid Dynamics
CIS	Containment Internal Structure
CRIEPI	Central Research Institute of Electric Power Industry
CSI	Computer and Structures, Incorporated
CST	Concrete Strength Tester
DA, DB	DIS type A and B bearings
DFBR	Demonstration Fast Breeder Reactor
DIS	Dynamic Isolation Systems
DoE	Department of Energy
EdF	Electricite de France
EFB	Equivalent Fixed Base
EPR	European Fast Reactor
EPRI	Electric Power Research Institute
ESFR	European Sodium Fast Reactor
ETEC	Energy Technology Engineering Center
FEA	Finite Element Analysis
FEM	Finite Element Method
FP	Friction Pendulum
GE	General Electric
GRE	Generalized Richardson Exploration
HDR	High Damping Rubber
HHT	Hilber-Hughes-Taylor
IEEE	Institute of Electrical and Electronics Engineers
IRIS	International Reactor Innovative and Secure
ITER	International Thermonuclear Experimental Reactor
JHR	Jules Horowitz Reactor
JNES	Japan Nuclear Energy Safety
LR	Lead rubber
LVDT	Linear variable displacement transducer
MA, MB	Mageba type A and B bearings
MCEER	Multidisciplinary Center for Earthquake Engineering Research

MODF	Multi-Degree-of-Freedom
NIST	National Institute of Standards Testing
NPP	Nuclear power plant
NRA	Nuclear Regulatory Authority
NSSS	Nuclear Steam Supply System
PIRT	Phenomena Identification and Ranking Table
PRISM	Power Reactor Inherently Safe Module
PWR	Pressurized Water Reactor
SAFR	Sodium Advanced Fast Reactor
SBTM	Single Bearing Testing Machine
SCV	Steel Containment Vessel
SDOF	Single-Degree-of-Freedom
SEESL	Structural Engineering and Earthquake Simulation Laboratory
SER	Safety Evaluation Report
SQA	Software Quality Assurance
SSE	Safe Shutdown Earthquake
TxQy	Isolation System of Time Period x and Strength to Supported Weight Ratio of y
UEL	User Element
UHRS	Uniform Hazard Response Spectra
UMAT	User Material
USNRC	United States Nuclear Regulatory Council
V&V	Verification and Validation

1 INTRODUCTION

1.1 General

Seismic (base) isolation is a relatively mature technology for protecting structures from the effects of moderate and severe earthquake shaking. Although the technology has been widely deployed for buildings, bridges and certain classes of mission-critical infrastructure, it has yet to be routinely adopted for the seismic protection of safety-related nuclear structures, including nuclear power plants. The limited numbers of applications to nuclear structures to date have been in France and South Africa, for which synthetic rubber (neoprene) bearings, including flat sliders in one installation, have been used. Limited use of seismic isolation has been attributed to a) a significant downturn in nuclear power plant construction in the thirty-year period from 1980 to 2010, b) construction of nuclear facilities in regions of low to moderate seismic hazard for which isolation is not necessarily needed, and c) the lack of consensus standards for the analysis and design of seismic isolation systems for nuclear facilities and companion requirements for testing of prototype and production bearings.

Early studies on isolation of nuclear structures showed mixed results, which pointed to the need for additional research and development (Buckle, 1985; Eidingner and Kelly, 1985; Gueraud *et al.*, 1985; Hadjian and Tseng, 1983; Kelly, 1979; Plichon and Jolivet, 1978; Plichon *et al.*, 1980; Skinner *et al.*, 1976b; Wu *et al.*, 1987; Wu *et al.*, 1988). US federal government support for research programs supporting isolation of nuclear power plants finished in the 1990s. Related research efforts declined accordingly. The nuclear accident at Fukushima Daiichi in March 2011 rekindled interest in the use of seismic isolation to protect nuclear structures from the effects of moderate to severe earthquake shaking. One impediment to the implementation of seismic isolation to NPPs was a lack of guidance for the analysis, design, and regulation of seismically isolated nuclear structures. Such guidance is now available in Chapter 12 of ASCE/SEI Standard 4-16 (ASCE, 2017) and NUREG/CR 7253 entitled “*Technical Considerations for Seismic Isolation of Nuclear Facilities*” (Kammerer *et al.*, 2019). Much of the technical basis in these documents can be traced to the research of Huang (Huang *et al.*, 2008; Huang *et al.*, 2010; Huang *et al.*, 2011a; Huang *et al.*, 2011b; Huang *et al.*, 2011c). Warn and Whittaker (2006) conducted experiments and analytical studies to understand the coupling between the horizontal and the vertical response of elastomeric bearings. Kalpakidis and Constantinou (2008) investigated the heating of the lead core in LR bearing, and proposed an analytical model to calculate shear strength as a function of temperature rise in the lead core.

The study presented in this report builds on the available knowledge and addresses the issues that are critical to seismic isolation of NPPs. Much of this is reproduced from Kumar *et al.* (2015), which in turn is based on the PhD dissertation of the first author.

This NUREG/CR addresses elastomeric seismic isolation bearings. A companion sliding isolation NUREG/CR (Kumar *et al.*, 2019) addresses sliding isolation bearings and seismic risk assessment of isolated nuclear power plants.

1.2 Motivation

Figure 1-1 identifies components of a seismically isolated nuclear structure. The isolators (also termed isolator units and bearings) are assumed installed in a near horizontal plane beneath a basemat that supports the nuclear construction, which is defined as the *superstructure*.

The isolators are installed atop pedestals and a foundation, which is defined as the *substructure*. The moat is a space in which the isolated superstructure can move without restriction in the event of earthquake shaking. Only horizontal isolation is considered because there are no viable three-dimensional isolation systems available in the marketplace at the time of this writing for large, surface mounted building structures such as nuclear power plants.

A focus of the study is large light water nuclear reactors: the backbone of the US nuclear fleet at the time of this writing. That said, much of the research product discussed in this report is more broadly applicable, to large components of light water reactors and advanced reactors, including high temperature gas reactors, which will likely be deeply embedded.

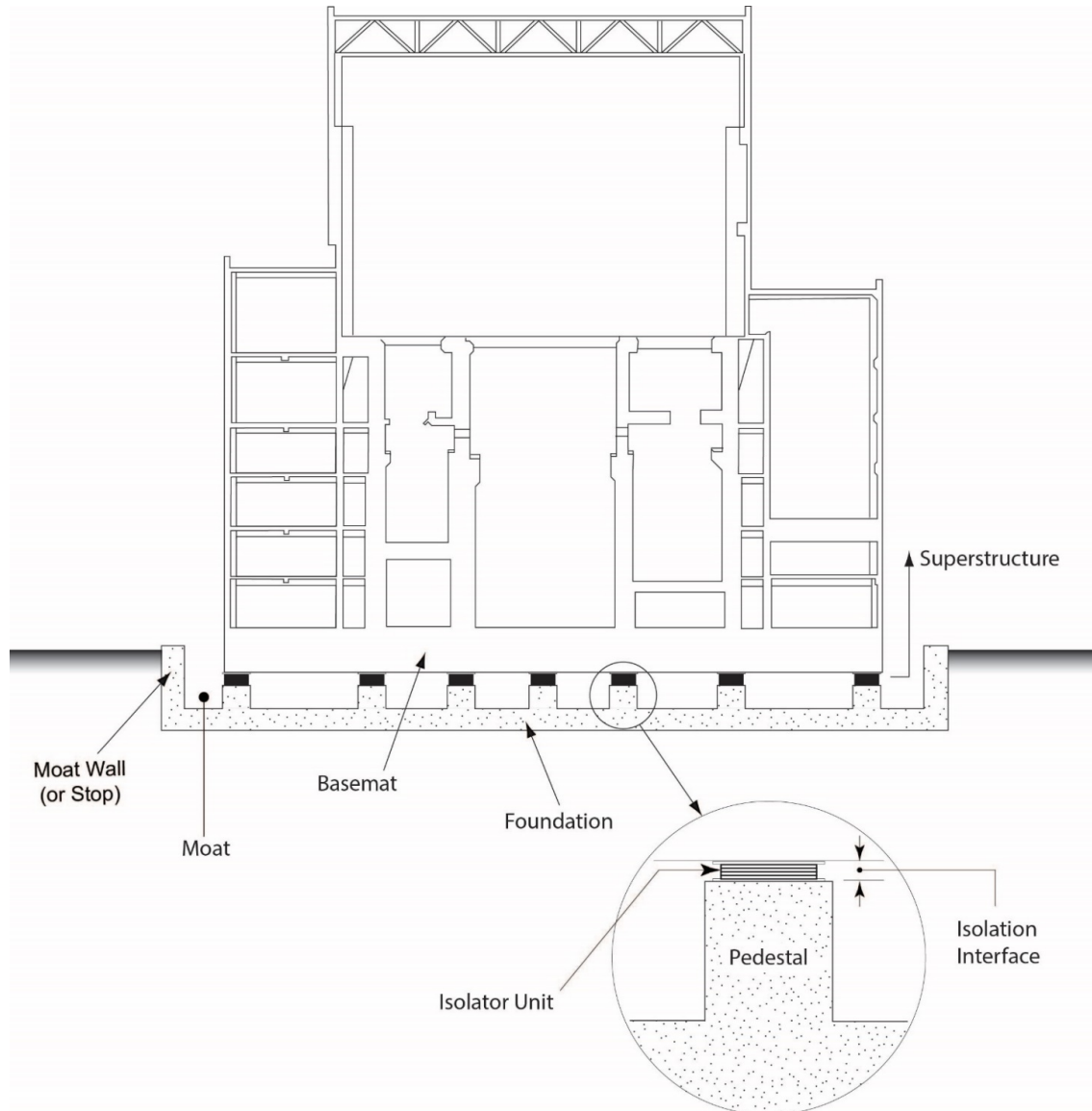


Figure 1-1 Seismically isolated nuclear power plant (Kammerer *et al.*, 2019)

The nuclear accident at Fukushima Daiichi in March 2011 focused the attention of the nuclear energy industry on the effects of extreme earthquakes: shaking more intense than design basis. Although the mechanical properties of LDR and LR bearings are not expected to change substantially in design basis shaking, under shaking more intense than design basis, the

properties of the lead cores in lead-rubber bearings may degrade due to heating associated with energy dissipation, some bearings in an isolation system may experience net tension, and the compression and tension stiffness may be affected by the horizontal displacement of the isolation system. The implementation of seismic isolation in US NPPs will likely only be possible if these changes in mechanical properties can be tracked in analysis.

The key components of the study described in this report are:

1. Experimental investigation of the behavior of elastomeric bearings in tension
2. Development of verified and validated numerical models of elastomeric bearings for analysis of seismically isolated NPPs
3. Quantification of the response of base-isolated NPPs subject to design basis and beyond-design basis earthquake shaking
4. Investigation of the effects of vertical excitation
5. Investigation of rocking and uplift in base-isolated NPP subject to design and beyond-design basis earthquake shaking

1.3 Scope of Work

The scope of work for this study is as follows:

1. Investigate existing application of the seismic isolation to nuclear structures and models of elastomeric bearings used for analysis of seismically isolated structures.
2. Perform experiments to characterize the behavior of elastomeric seismic isolation bearings in tension.
3. Develop mathematical models that can be used to analyze base-isolated NPPs subject to extreme earthquake shaking.
4. Implement the mathematical models in contemporary software programs used for structural analysis.
5. Verify and validate the numerical models.
6. Analyze base-isolated NPPs subject to design and beyond-design basis earthquake shaking.
7. Address numerical issues associated with the specification of damping in response-history analysis of base-isolated nuclear power plants.

1.4 Report Organization

This report has eleven chapters, the appendices and list of references. Seismic isolation of NPPs and experimental studies and numerical models available for analysis of elastomeric bearings are reviewed in Chapter 2. Chapter 3 presents mathematical models of LDR and LR bearings that can be used to analyze base-isolated NPPs. Implementation of these mathematical models in OpenSees and ABAQUS is presented in Chapter 4. The models are verified and validated in Chapter 5. The experimental program and the test results to characterize the behavior of elastomeric bearings in tension are presented in Chapter 6 and Chapter 7, respectively. Chapter 8 and Chapter 9 discuss the results of response-history analysis of a base-isolated NPP using a two-node macro model and a lumped-mass stick model, respectively. A substructuring approach to specify damping and estimate acceleration response in an isolated superstructure is described in Chapter 9. Summary, conclusions, and recommendations are provided in Chapter 10. A list of references is presented in Chapter 11. Three appendices present the experimental program and results (A), response of the two-node macro model of a base-isolated NPP (B), and the response of a base-isolated NPP (C).

2 LITERATURE REVIEW

2.1 Introduction

Although seismic isolation has been deployed in nuclear structures in France and South Africa, it has not been used in the United States. This is attributed to limited new build nuclear construction in the past 30 years and a lack of guidelines, codes and standards for the analysis, design and construction of isolation systems specific to nuclear structures.

The behavior of natural rubber-based bearings in horizontal shear and vertical compression is well established and robust mathematical models exist that have been validated experimentally. However, knowledge of bearing response in tension is rather limited and the mathematical models that have been proposed do not capture those behaviors that have been observed experimentally.

This chapter summarizes the application of and research on base-isolated NPPs, and reviews experimental work on the behavior of elastomeric bearings under tensile loading and numerical models that have been used to analyze behavior in tension. Section 2.2 introduces research and application of base-isolated NPPs in different countries around the world. The isolation systems for these NPPs are described in Section 2.3. Section 2.4 summarizes experiments on behavior of bearings in tension. Only relevant work on seismic isolation bearings is discussed and the work on bonded rubber cylinders (e.g., Dorfmann and Burtscher (2000) and Dorfmann (2003)) is not considered. Mathematical models of elastomeric bearings that represent the state-of-the-art for response-history analysis of seismically isolated structures and their usage in contemporary software programs are discussed in Section 2.5 and Section 2.6, respectively.

2.2 Historical Developments

2.2.1 Introduction

The idea of substantially decoupling a structure from the destructive effects of high frequency earthquake ground motion has existed for a long time. Early developments are not reported here. Applications of isolation to nuclear power plant have been somewhat recent, and followed the development of analysis, design and fabrication procedures. An attractive feature of seismic isolation is its application to standardized reactor designs that traditionally have been designed for a low level of seismic hazard (often a peak ground acceleration of 0.2 or 0.3 g). The isolation of such standardized reactors enables their deployment in regions of higher seismic hazard because the isolators serve to reduce the horizontal inertial forces that can develop in the isolated superstructure. Early studies on isolation of nuclear structures showed mixed results, which pointed to the need for additional research and development (Buckle, 1985; Eiding and Kelly, 1985; Gueraud *et al.*, 1985; Hadjian and Tseng, 1983; Kelly, 1979; Plichon and Jolivet, 1978; Plichon *et al.*, 1980; Skinner *et al.*, 1976b; Wu *et al.*, 1987; Wu *et al.*, 1988).

Developments in seismic isolation of nuclear power plants and related research in the major nuclear power depending countries are summarized in the following sections.

2.2.2 France

Seismic isolation of NPPs using rubber bearing pads was studied during late 1970s with a focus on applications to reactors in France (Jolivet and Richli, 1977; Plichon, 1975; Plichon and Jolivet, 1978). France was the first country to implement seismic isolation in nuclear power plants, although their approaches to design and construction vary substantially from practice in

the United States, with one utility, one isolator vendor, and one architect/engineer/contractor, which allowed France to implement seismic isolation earlier than other countries. Framatome (now AREVA NP) had developed a standardized design for a 900 MWe Pressurized Water Reactor (PWR) that was suitable for most sites in France where the peak ground acceleration for the Safe Shutdown Earthquake (or design-basis earthquake) was less than 0.2g. For sites with higher seismicity, the standard plant was seismically isolated to limit the demand on the NPP and its structures, systems, and components. Licensing objections from the Commissariat à l'Énergie Atomique (CEA, French counterpart of USNRC) were addressed (Delfosse, 1977; Derham and Plunkett, 1976).

Four PWR units were seismically isolated at Cruas in France between 1978 and 1984. Construction began in 1978 and the reactors were built in 1983 and 1984. Framatome was the Nuclear Steam Supply System (NSSS) vendor and Electricite de France (EdF) was the utility owner. The isolation system was developed by Spie-Batignolles Batiment Travaux Publics (SBTP) and EdF (Plichon *et al.*, 1980). Each unit was isolated using 1,800 neoprene isolators (500 × 500 × 66.5 mm) that are shown in Figure 2-1. A vertical cross section through an isolator and its pedestal is shown in Figure 2-2. The peak ground acceleration for the Safe Shutdown Earthquake (SSE) at the site was 0.3g. The four units at Cruas are shown in Figure 2-3. The shear modulus of the elastomer was reported as 1.10 MPa in 1978. Periodical testing of elastomer kept at site revealed a 37% increase in its shear modulus to 1.51 MPa by 2005 (Labbe, 2010).

France has conducted research on standardized NPP design concepts, collaborating with other European countries, since its first application of isolation to nuclear power plants. These research programs have resulted in the development of the seismically isolated European Sodium Fast Reactor (ESFR) and the seismically isolated European Pressurized Reactor (EPR).

A 100 MWe materials-research Jules Horowitz Reactor (RJH), is being built at Cadarache, France and is being base isolated. The reactor is being built by an international consortium of research institutions from France (CEA and EdF), the Czech Republic (NRI), Spain (CIEMAT), Finland (VTT), Belgium (SCKCEN), and European Commission. India (DAE) and Japan (JAEA) are participating as associate members. The utility-owner EdF and Vattenfall, and the Nuclear Steam Supply System (NSSS) vendor AREVA are the utilities and industrial partners. The isolation system is composed of 195 elastomeric bearing pads (900 × 900 × 181 mm) that were manufactured by Freyssinet. Construction began in 2007 and operation is expected to start in 2021. Technical details of the isolation system proposed for RJH are presented in Section 2.3.7.

Another nuclear facility, the International Thermonuclear Experimental Reactor (ITER), is also under construction at Cadarache. ITER is an international nuclear fusion experimental facility, and is being isolated by 493 elastomeric pads of a similar design to that used for the RJH. The construction of ITER began in 2008 and it is expected to begin operation in 2019. Technical details of isolation system in ITER are presented in Section 2.3.8.

2.2.3 South Africa

The isolation of the French standardized plant enabled it to be used at sites where the earthquake hazard was more severe than that for which the standardized plant was designed. Two seismically isolated reactors were constructed at Koeberg, South Africa. The peak horizontal ground acceleration for design basis earthquake shaking (SSE) was 0.3g.

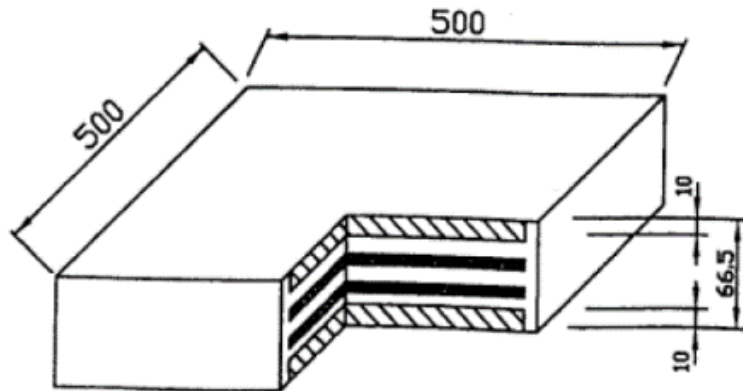


Figure 2-1 Cut-away view of seismic isolator used for the Cruas NPP; dimensions in mm (Labbe, 2010)

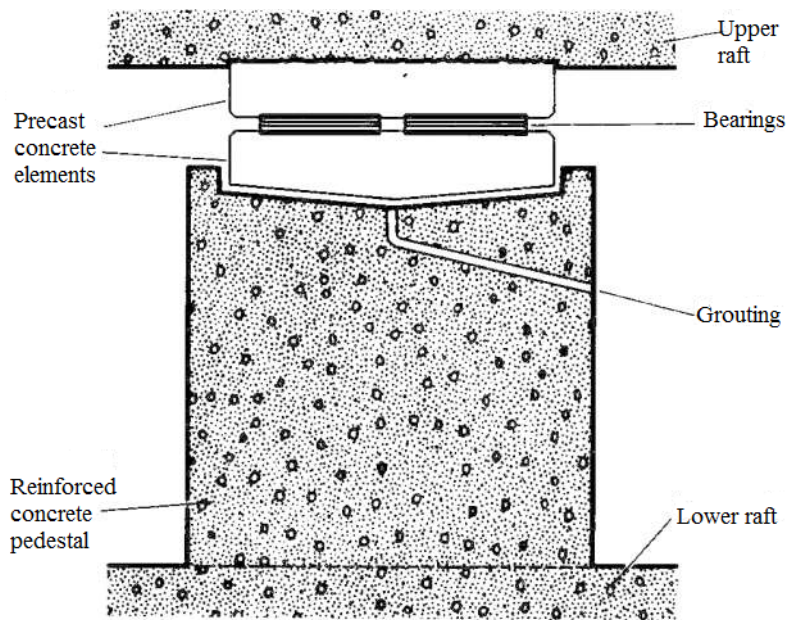


Figure 2-2 Vertical cross section through the isolator and pedestal in the Cruas NPP (Labbe, 2010)



Figure 2-3 Four units of seismically isolated NPP at Cruas, France (Forni and Poggianti, 2011)

A modified version of the isolators used for the Cruas NPPs was used for the Koeberg plant to limit the shear strain in the neoprene pads (Gueraud *et al.*, 1985). A flat slider was installed between the top of the pad and the upper mat. The flat sliders used a lead-bronze alloy lower plate and a polished stainless steel upper plate. A total of 2000 neoprene pads (700 × 700 × 100 mm) were used to isolate each reactor at Koeberg. Tajirian and Kelly (1989) note that a similar type of isolator was proposed for the Karun River plant in Iran.

The isolators used at Koeberg are considered inappropriate for application to NPPs in the United States. Flat sliders cannot provide the minimum lateral restoring force that is required from a SI system to limit the residual earthquake displacement. Moreover, sliding bimetallic interfaces are prone to load dwell-creep induced increases in the static coefficient of friction (Constantinou *et al.*, 1996; Constantinou *et al.*, 2007). Lee (1993) reported on the changes in the properties of the flat sliders used in the Koeberg isolators and noted an increase in the static coefficient of friction from 0.2 to 0.4 after 14 years of service.

2.2.4 Italy

Research on the use of seismic isolation for Italian nuclear power plants started in late 1980s. The focus of the Italian research was isolation of fast breeder reactors. The only fast reactor under development at that time was PEC (Prova Elementi di Combustibile), a fuel element test reactor, which was an Italian contribution to European Fast Breeder Reactor (EFR) development program.

The Italian Committee for Nuclear and Alternative Energy Sources (ENEA), in collaboration with International Working Group on Fast Reactors (IWGFR) of the International Atomic Energy Agency (IAEA), organized the Specialists' Meeting on "Fast Breeder Reactor-Block Antiseismic Design and Verification" in 1987 to discuss the application of seismic isolation to Fast Reactors (Martelli, 1988). A framework for research and development of standardized NPP units with seismic isolation was prepared. Work on the seismic isolation of fast reactors began in 1988 by ENEA and ISMES (Istituto Sperimentale Modelli e Strutture) and involved proposals for development of guidelines for seismically isolated NPPs using high damping rubber (HDR) bearings (Martelli *et al.*, 1989), static and dynamic experiments using shake tables, determination of qualification procedures for seismic isolation systems, and development and verification of finite element nonlinear models for single bearing and simplified tools for dynamic analysis of seismically isolated structures (Martelli *et al.*, 1991). Research conducted between 1993 and 1996 at the Italian electric utility company ENEL (Ente Nazionale per l'Energia eLettrica) and supported by the European Commission (EC) aimed at development of optimized design features for HDR bearings. Research focused on improvement of bearing materials, analysis and design tools, manufacturing process and quality control. Scragging and recovery in HDR bearings were not addressed. Other research programs were conducted in the framework of national collaboration among members of the Italian Working Group on Seismic Isolation (GLIS, "Gruppo di Lavoro Isolamento Sismico") and international collaboration between GLIS and EU and non-EU members (Martelli *et al.*, 1999).

Italy had an active role in the development of the International Reactor Innovative and Secure (IRIS). IRIS is a smaller version of the pressurized water reactor being developed by international team of companies, laboratories, universities and is being coordinated by Westinghouse. ENEA proposed seismic isolation of the IRIS reactor building in 2006 and developed it in collaboration with the Politecnico di Milano and Pisa University in 2010 (Forni and Poggianti, 2011).

2.2.5 United Kingdom

The United Kingdom is characterized by low to moderate seismicity, which is similar to much of France. The UK Central Electricity Generating Board (CEGB) collaborated with the CRIEPI-EPRI seismic isolation program in its second phase of work to develop a standardized design of a seismically isolated nuclear power plant (Austin *et al.*, 1991). The proposed seismic isolation system consisted of natural rubber bearings and viscous dampers. The goal of this isolation system was analyzability, with the bearings being modeled as linear elements and the dampers as viscous elements.

2.2.6 New Zealand

New Zealand has implemented seismic isolation in their civil structures. Some of very first studies on isolation of NPPs were undertaken by researchers in New Zealand although there are no nuclear power plants in New Zealand. The main purpose was to develop technologies such as the lead-rubber bearing that could be sold abroad. Skinner *et al.* (1976a), Skinner *et al.* (1976b), and Buckle (1985) reported studies on the application of isolation to nuclear structures.

2.2.7 Japan

The application of seismic isolation in Japan grew quickly in the 1980s and 1990s but was limited to non-nuclear structures. The application of isolation and standardization of nuclear power plants received significant attention from the government and private construction companies in the 1980s. Advanced experimental facilities, including the largest shake table in the world at the time, facilitated research and development of various types of isolation systems in Japan. Initial studies focused on fast breeder reactors, because it was hoped that isolation would reduce the capital cost associated with design against the effects of earthquakes, allow standardization of fast breeder reactors for all siting conditions in Japan, and make fast breeder reactors an economical alternative to pressurized water reactors.

In 1987, the Central Research Institute of Electric Power Industry (CRIEPI), under contract from Ministry of International Trade and Industry (MITI) of Japan, started a seven-year research program to develop a technical basis for application of seismic isolation to fast breeder reactors. Two dimensional (horizontal) system and 3D isolation systems were studied (Shiojiri, 1991). CRIEPI drafted FBR Seismic Isolation System Design Methods in 1990 based on the results obtained from the research program (Ishida *et al.*, 1995). The CRIEPI test program finished in 1996.

A study was conducted by the Japan Atomic Power Company (JAPC) and a design was developed for the 2D seismic isolation of the Demonstration Fast Breeder Reactor (DFBR) using different 2D isolation systems (Inagaki *et al.*, 1996).

CRIEPI coordinated a research program with the Electric Power Research Institute (EPRI) of the USA and CEGB of the UK to study the feasibility of selected isolation systems and their application to liquid metal reactors. Five isolation systems were considered: 1) elastomeric bearings with friction plates (France), 2) lead-rubber bearings (New Zealand), 3) coil springs with viscous dampers (Germany), 4) Teflon bearings with elastic restraint (Greece), and 5) bearings with hysteretic dampers. A comparison of the performance of these isolation systems suggested the lead-rubber bearing was the best of the five considered. CEGB of the UK joined this program later. An isolation system consisting of elastomeric bearings (150×150×70 mm) and German GERB type viscous dampers was suggested by CEGB for further study.

In 2000, and based on prior studies, the Japan Electric Association published JEAG 4614-2000, “Technical guideline on seismic base isolated system for structural safety and design of nuclear power plants” (JEA, 2000). The Japan Nuclear Energy Safety (JNES) organization, established in 2003, coordinated isolation related research in Japan. JNES was reorganized recently as the Nuclear Regulatory Authority (NRA).

2.2.8 United States

Studies were conducted in the late 1970s and early 1980s to assess the feasibility of available seismic isolation systems to nuclear structures (DIS, 1983; Kunar and Maini, 1979; Vaidya and Eggenberger, 1984) but the results of these studies were not pursued by the nuclear community following the downturn in nuclear power plant construction following the accident at Three Mile Island in 1979.

A number of authors identified issues that had to be resolved before any application of seismic isolation was possible in the nuclear industry in the United States (Eidinger and Kelly, 1985; Hadjian and Tseng, 1983). One of the important issues was reliability. At that time there was insufficient data on the performance of seismically isolated conventional structures during major earthquakes to provide the necessary confidence that isolation would deliver the proposed benefits. A cost-benefit analysis was also needed to understand the financial implications of using isolation. Hadjian and Tseng (1983) noted that this cost-benefit analysis should not be based on initial capital cost only but should also consider the probability of success or failure and resulting consequences (Stevenson, 1978). Some of the major concerns regarding the use of isolation were (Eidinger and Kelly, 1985; Hadjian and Tseng, 1983; Tajirian and Kelly, 1989):

1. Long term reliability of isolators
2. Inability to define beyond design basis earthquake criteria
3. Deployment of a failsafe mechanism in case of failure of the isolation system
4. Unavailability of performance data of isolated structures during earthquakes
5. Lack of understanding of ground motion data with respect to long period components and directivity effects
6. Inspection and replacement requirements of isolators
7. Unavailability of design codes

There have been considerable advances in the understanding of these issues and all of these concerns have been addressed.

The US Department of Energy (DoE) and EPRI sponsored projects in the 1980s to study the application of seismic isolation to fast breeder reactors. The feasibility of several isolation systems were assessed, including the French system employed at Cruas, lead-rubber bearings (Freskakis and Sigal, 1985), and the Alexisimon sliding system (Ikonou, 1985). The DOE then sponsored projects to develop three advanced reactors: 1) Power Reactor Inherently Safe Module (PRISM), 2) Sodium Advanced Fast Reactor (SAFR), and 3) Modular High Temperature Gas Cooled Reactor (MHTGR). All three designs included passive safety features and incorporated seismic isolation to the standardize design (Tajirian and Kelly, 1989).

The Energy Technology Engineering Center (ETEC, 1988) coordinated the Seismic Technology Program Plan (STPP) sponsored by Department of Energy. The goal of the research program was to reduce the impact of seismic design on the cost of liquid metal reactors. Seismic isolation was identified as a key element to meet this goal. The five objectives of the STPP were: 1) seismic isolation verification, 2) seismic qualification of standardized plants,

3) utilization of inherent strength, 4) validation of core seismic analysis, and 5) validation of piping design. The ALMR development program was started in 1989 to meet the objectives of STPP. Experimental and analytical studies were performed to develop standardized nuclear reactor design concepts that were economically competitive with other domestic energy sources and have passive safety features (Clark *et al.*, 1995; Gluekler, 1997; Kelly *et al.*, 1990; Snyder and Tajirian, 1990).

PRISM was chosen in 1989 by DOE for further development as part of ALMR program. The development of PRISM was managed by a team lead by General Electric (GE) Nuclear Energy and included Argonne National Laboratory (ANL), Energy Technology Engineering Center (ETEC), the University of California at Berkeley, and Bechtel National, Inc. (BNI) (Gluekler *et al.*, 1989). The qualification and testing of the proposed isolation system was performed with full-scale and reduced-scale bearings. Kelly *et al.* (1990) noted the high damping rubber bearings stiffened at shear strains greater than 200% and bolted connections perform better than doweled connections allowing higher horizontal displacement capacity and restoring force. However, experiments on high damping rubber bearings identified scragging effects and significant nonlinear behavior at high shear strains. The ALMR program was cancelled in 1994. The US Nuclear Regulatory Commission, in its pre-application safety evaluation report (SER) in 1994, concluded that there was no obvious impediments to licensing the PRISM (ALMR) design (NRC, 1994). General Electric continued development of PRISM after the ALMR program was terminated as the Super-PRISM (S-PRISM) project. A key difference between PRISM and S-PRISM was that in PRISM, each of the two reactors was placed on separate isolated mat, whereas in S-PRISM a single isolated mat supported both reactors. The progress of research activities on PRISM is cartooned in Figure 2-4.

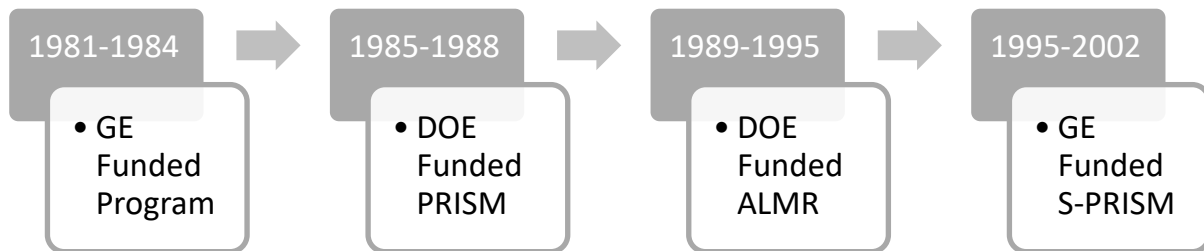


Figure 2-4 Historical development of PRISM

SAFR was a sodium-cooled reactor designed by Rockwell International Corp. This design concept included low shape factor bearings, which provided horizontal and some vertical isolation (Aiken *et al.*, 1989; Tajirian *et al.*, 1990). The Nuclear Regulatory Commission issued pre-application safety evaluation reports for SAFR and PRISM in 1991 and 1994.

US federal government support for research programs supporting isolation of nuclear power plants finished in the 1990s. Related research efforts declined accordingly. Malushte and Whittaker (2005) noted that one impediment to implementation was a lack of guidance for the analysis, design and regulation of seismically isolated nuclear structures. Such guidance is now available in Chapter 12 of ASCE/SEI Standard 4-16 (ASCE, 2017). Recommendations for NPP structures are provided in Kammerer *et al.* (2019). Much of the technical basis in these documents can be traced to the research of Huang (Huang *et al.*, 2008; Huang *et al.*, 2010; Huang *et al.*, 2011a; Huang *et al.*, 2011b; Huang *et al.*, 2011c).

2.3 Standardized Designs of Seismically Isolated Nuclear Reactors

2.3.1 Advanced Liquid Metal Reactor

The Advanced Liquid Metal Reactor (ALMR) project was started in 1984 by the Argonne National Laboratory and supported by Department of Energy (DOE). The reactor was isolated in the horizontal direction. The isolation system consisted of 66 high damping rubber bearings. The fundamental frequencies of the isolated structure were 0.7 Hz in the horizontal direction and 20 Hz in the vertical direction. The ALMR was designed for shaking associated with spectra anchored to peak ground accelerations in the horizontal and vertical directions of 0.5 g. Figure 2-5 presents a cut-away view of the isolated reactor. The ALMR program was discontinued in 1994.

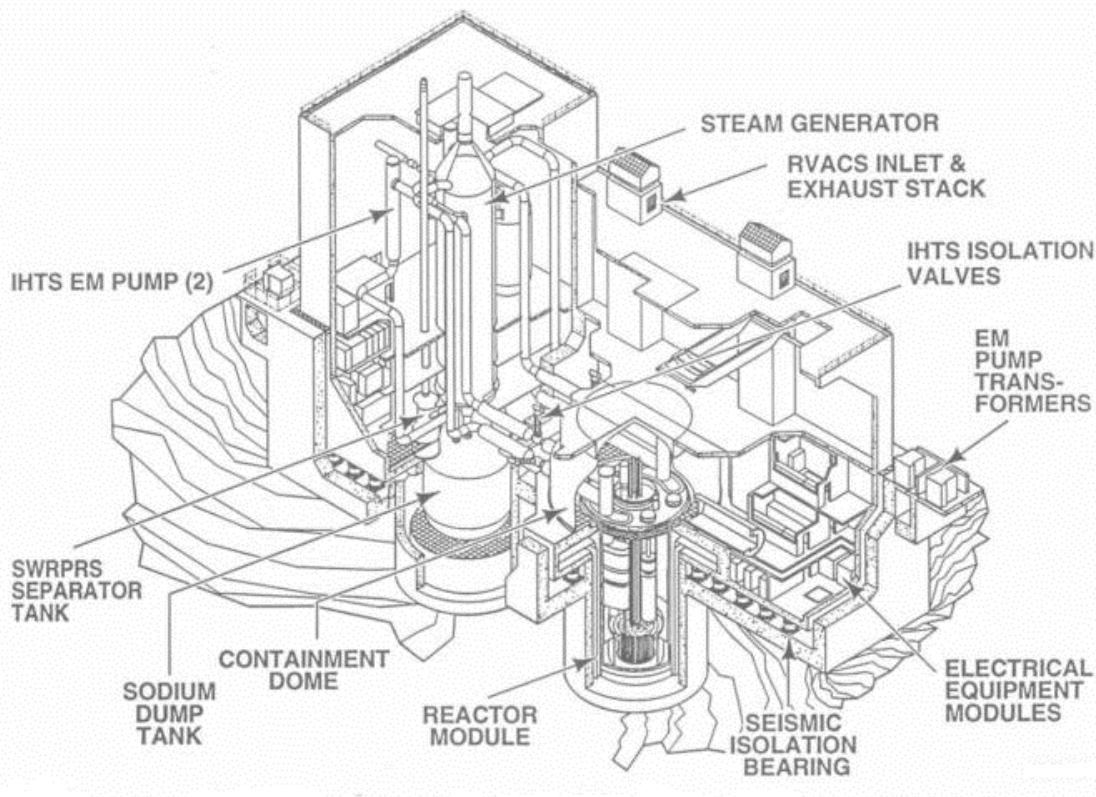


Figure 2-5 ALMR reactor & steam generator facility general arrangement (Forni, 2010)

2.3.2 Super-Power Reactor Inherently Safe Module (S-PRISM)

The Super-Power Reactor Inherently Safe Module (S-PRISM) is a compact standardized liquid metal reactor, with 622 MWe capacity. It was developed by GE Hitachi Nuclear Energy. S-PRISM is an advanced version of the PRISM concept developed in the 1980s and 1990s as part of the ALMR program. It retains the key design features of ALMR, and its seismic isolation system is that of the original PRISM reactor (Tajirian and Kelly, 1989). The design is modular with a number of reactor modules per power unit. Each reactor module is isolated in the horizontal direction using 20 high damping rubber bearings with a diameter of 1320 mm and a total height of 587 mm. Each bearing consists of 30 layers of rubber (30 × 12.7 mm) and 29 steel shims (29 × 3.2 mm). The fundamental frequencies in the horizontal and vertical directions were

0.7 Hz and 21 Hz, respectively. The isolation system was design for shaking characterized by horizontal peak ground acceleration of up to 0.5 g and vertical peak ground acceleration of up to 0.3 g.

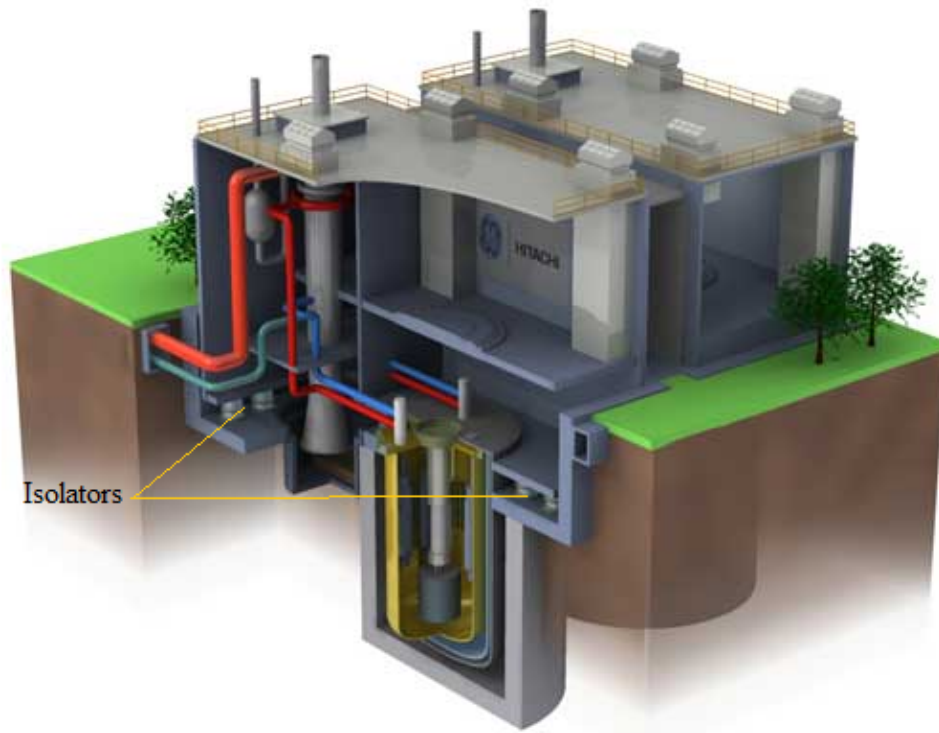


Figure 2-6 Cut-away view of the PRISM reactor (GE, 2012)

2.3.3 Sodium Advanced Fast Reactor

Rockwell International developed the DOE-sponsored Sodium Advanced Fast Reactor (SAFR) in 1988. SAFR featured a pool type liquid metal reactor as its primary module. It was designed for shaking characterized by standard-shaped spectra anchored to horizontal and vertical peak ground accelerations of 0.3 g. The seismic isolation system used 100 low-shape factor, high damping rubber (HDR) bearings to isolate in the horizontal and vertical directions. The bearings had diameter of 970 mm and total height of 426 mm, and included four 100-mm thick layers of rubber and 3.2-mm thick steel shims. The low shape factor (≈ 2.4) of the rubber layers provided flexibility in vertical direction but the vertical load capacity was limited as a result. The estimated fundamental frequencies of the isolated structure were 0.5 Hz and 3 Hz in the horizontal and vertical directions, respectively. Reduced-scale tests on these low shape factor bearings were performed with doweled and fixed connections (Kelly *et al.*, 1990).

2.3.4 Secure Transportable Autonomous Reactor

Argonne National Laboratory (ANL) developed the Secure Transportable Autonomous Reactor (STAR), a liquid metal reactor. Two types of isolation system were developed for this reactor (Yoo and Kulak, 2002). A vertical cross section through the isolated structure is shown in Figure 2-7. A 2D isolation system provides isolation in horizontal direction with high damping rubber (HDR) bearings, each 1200 mm in diameter and 500 mm tall. Each bearing consists of 29

rubber layers and 28 steel shims, with a total height of rubber of 278 mm. The fundamental frequencies of the isolated structure in the horizontal and vertical directions are 0.5 Hz and 21 Hz, respectively.

Studies on 3D isolation systems were performed for STAR-LM. Vertical isolation was achieved by helicoidal springs, as shown in Figure 2-8 (Yoo *et al.*, 1999). The 3D isolated structure had fundamental frequencies of 0.5 Hz and 1.1 Hz in the horizontal and vertical directions, respectively. Design basis shaking for the STAR-LM reactor was described by a spectrum anchored to a peak ground acceleration of 0.3g and a vertical peak ground acceleration of 0.2g.

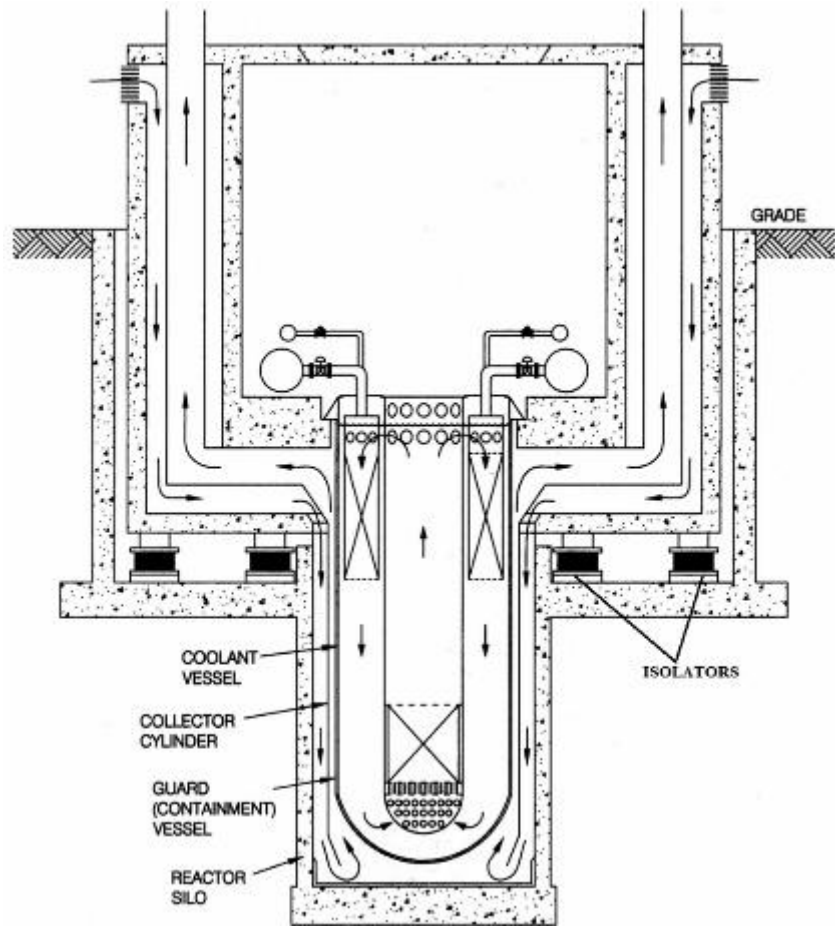


Figure 2-7 Vertical cross section through the seismically isolated STAR (Yoo and Kulak, 2002)

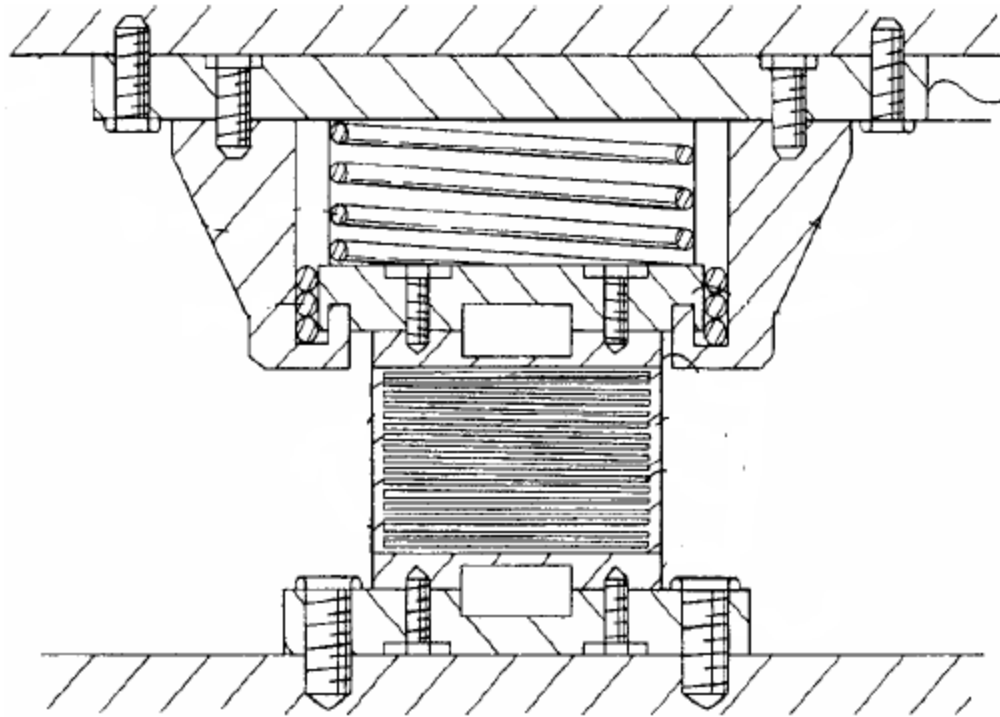


Figure 2-8 3D isolation system for the STAR (Yoo *et al.*, 1999)

2.3.5 DFBR

A demonstration fast breeder reactor (DFBR) was designed by CRIEPI in Japan. The design included 2D (horizontal) and 3D (horizontal and vertical) isolation systems. The 2D isolation system consists of 246 elastomeric bearings (diameters up to 1600 mm) with steel dampers for supplemental energy dissipation. The fundamental frequencies of the isolated structure were 0.5 Hz and 20 Hz in the horizontal and vertical directions, respectively.

The 3D isolation system was realized by using elastomeric bearings for horizontal isolation and air springs for vertical isolation, as shown in Figure 2-11. The elastomeric bearings had a diameter of 1600 mm and a height of 225 mm. The fundamental frequencies in the horizontal and vertical directions were 0.4 Hz and 0.5 Hz, respectively. The air compartment operated at a service pressure of 1.6 MPa and resisted a vertical service load of 9800 kN.

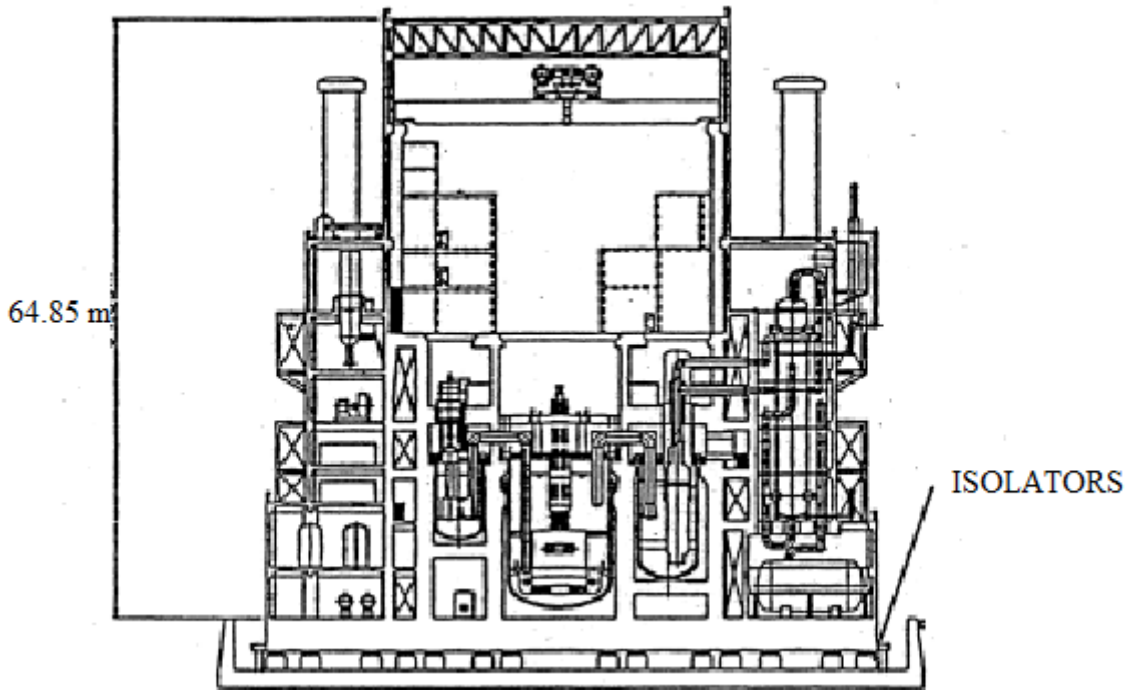


Figure 2-9 Vertical layout of seismically isolated demonstration FBR (Forni, 2010)

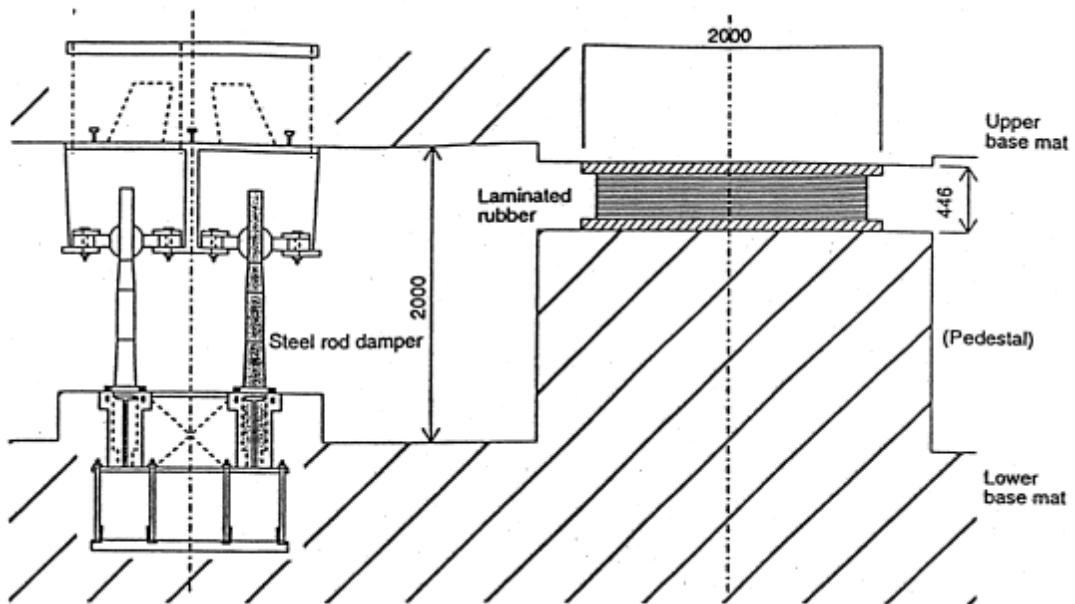


Figure 2-10 2D isolation system for the demonstration FBR (Forni, 2010)

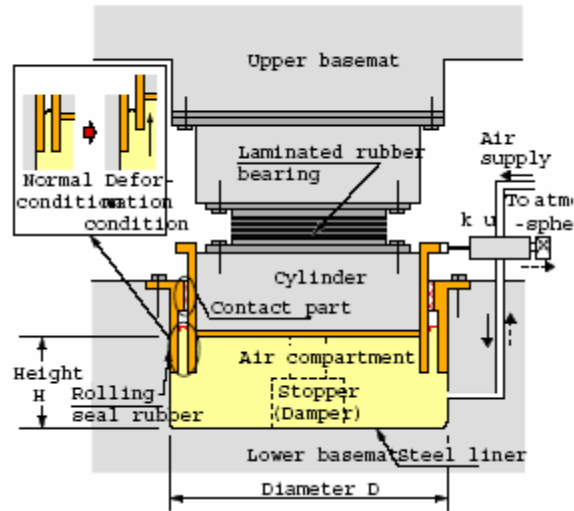


Figure 2-11 3D isolation system for the demonstration FBR (Forni, 2010)

2.3.6 Super Safe, Small and Simple (4S)

The 4S reactor is described as an ultra-compact design and was developed by Toshiba and CRIEPI of Japan. This design was proposed for a site in the state of Alaska. The capacity of the 4S was 10 MWe, with a possible increase up to 50 MWe. The 4S reactor has enhanced passive safety features, including seismic isolation. The reactor module is installed in a sealed cylindrical vault 30 m below grade level, as shown in Figure 2-12. The analysis and design of the seismic isolation system is based on Japanese guidelines JAEG 4614-200 (JEA, 2000), which was introduced previously. Lead-rubber bearings of three different geometries were proposed and the layout of the isolators was based on the axial capacities listed in the first column of Table 2-1. The geometry of the lead-rubber bearings is presented in Table 2-1. The fundamental frequency of the isolated structure in the horizontal direction was 0.5 Hz. The isolation system for the 4S reactor was designed for earthquake shaking with a horizontal peak ground acceleration of 0.3g (Shimizu, 2009).

Table 2-1 Properties of the lead-rubber bearings used for the 4S reactor (Shimizu, 2009)

Axial capacity (kN)	Bonded diameter (mm)	Isolator diameter (mm)	Rubber layer thickness (mm)	Number of rubber layers	Overall height (mm)
3250	1050	1450	220	16	440
4750	1250	1650	200	13	420
6250	1450	1850	196	12	416

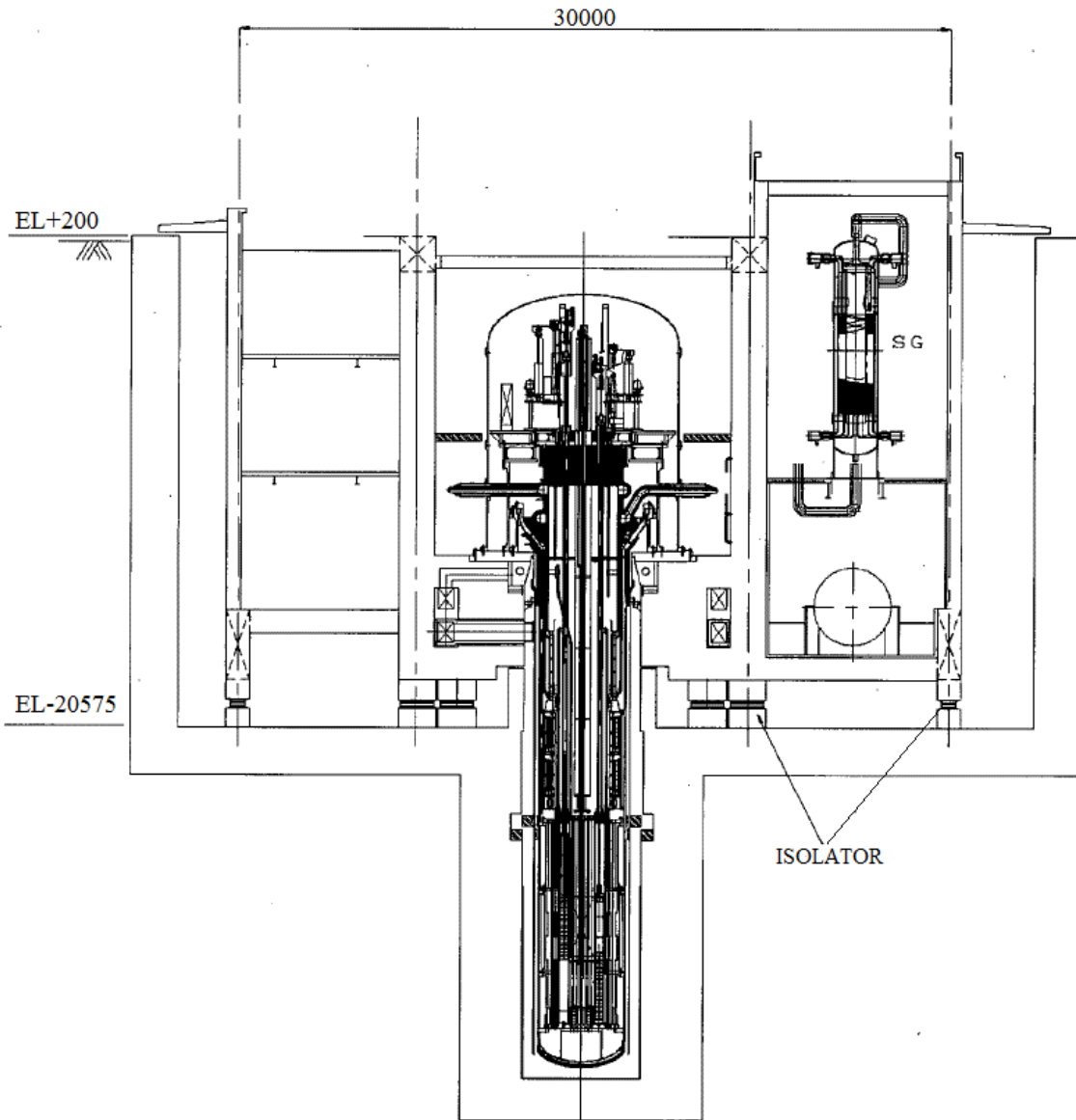


Figure 2-12 Vertical cross section through the seismically isolated 4S reactor, dimensions in mm (Shimizu, 2009)

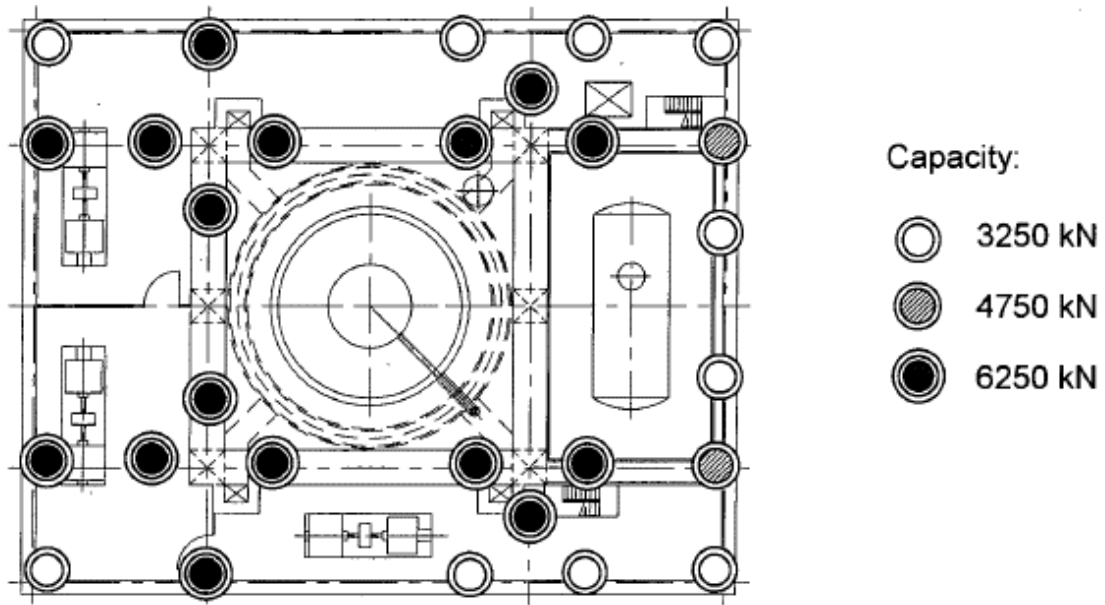


Figure 2-13 Layout of lead-rubber bearings in the 4S reactor (Shimizu, 2009)

2.3.7 Jules Horowitz Reactor (RJH)

The Jules Horowitz Reactor is a material testing and research reactor that is being built at Cadarache in France. The reactor building is equipped with a horizontal isolation system. One hundred and ninety-five synthetic rubber bearings ($900 \times 900 \times 181$ mm), manufactured by Freyssinet comprised the now installed isolation system. In each bearing, the total thickness of synthetic rubber is 120 mm (6×20 mm), the total thickness of the shims is 25 mm (5×5 mm), the total thickness of the end plates is 30 mm (2×15 mm), and 3 mm thickness of cover rubber was used to provide environmental protection. The photographs of the rubber bearings and the model of the reactor is shown in Figure 2-14 and Figure 2-15, respectively. The dynamic shear modulus of the rubber and damping ratio are 1.1 MPa and 5%, respectively (NUVIA, 2011). The layout of the isolators are shown in Figure 2-16. The fundamental frequency of the isolated structure in the horizontal direction is 0.6 Hz. The design basis earthquake shaking was designed by a spectrum anchored to a peak horizontal acceleration of 0.35g.

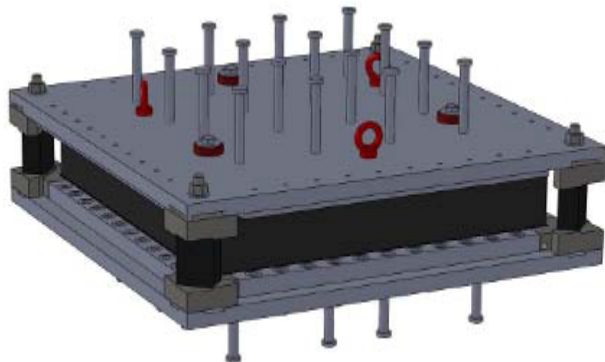
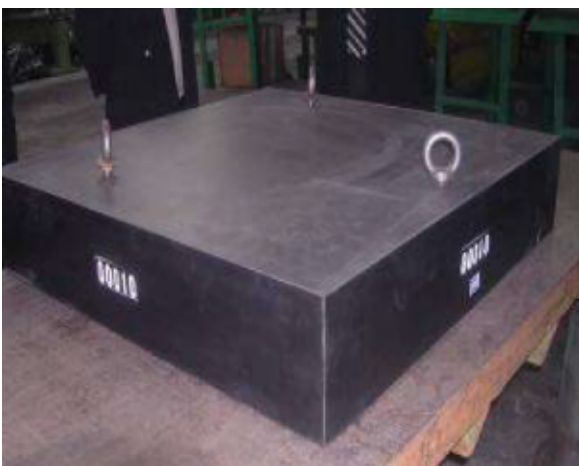


Figure 2-14 Elastomeric bearing used for the RJH (NUVIA, 2011)

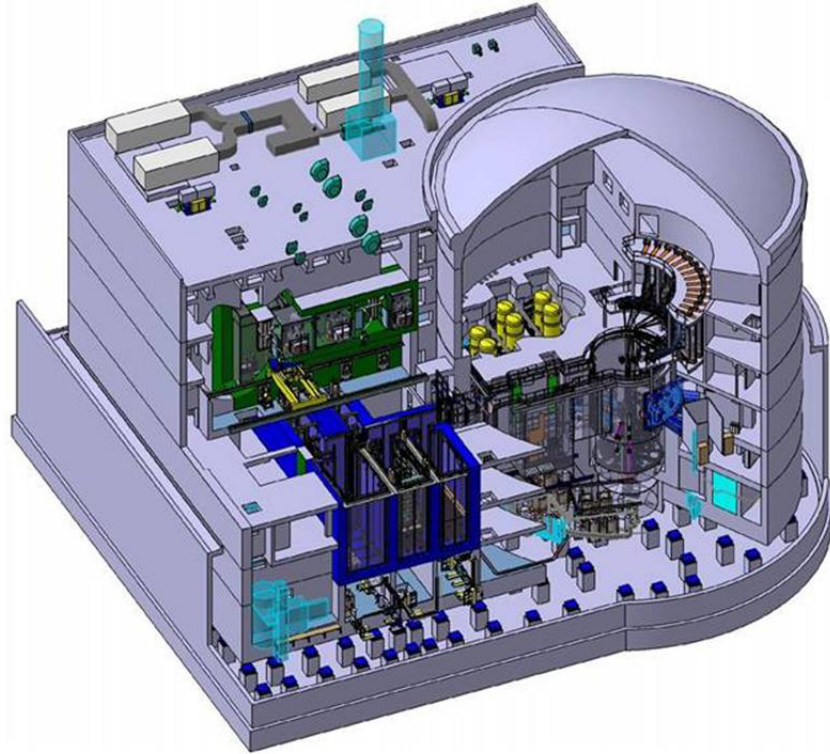


Figure 2-15 Cut-away view of Jules Horowitz Reactor (NUVIA, 2011)

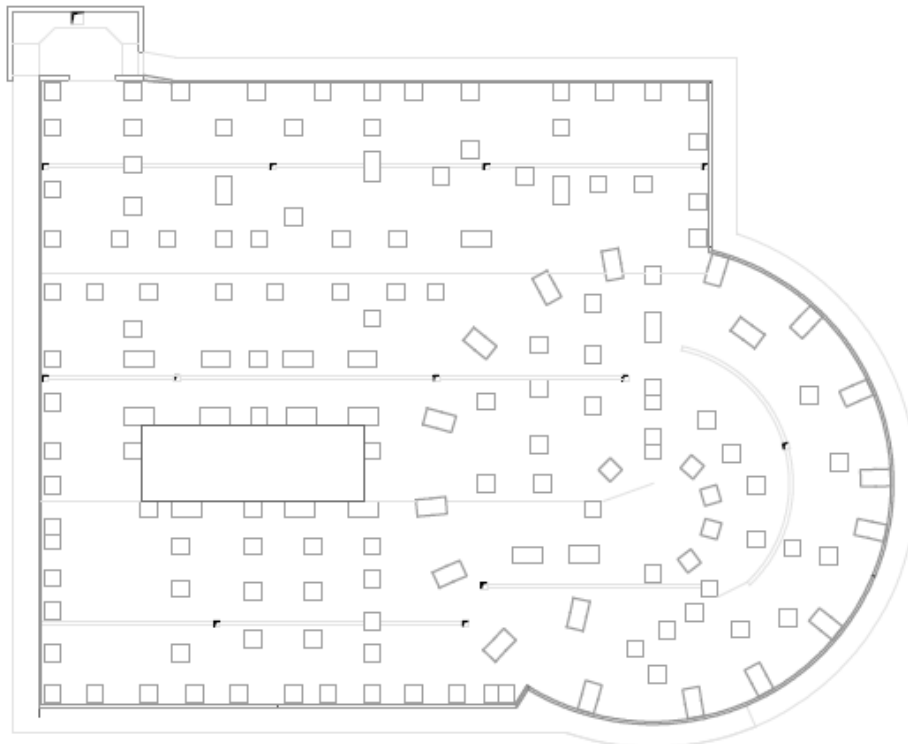


Figure 2-16 Layout of the isolators for the R/JH (NUVIA, 2011)

2.3.8 International Thermonuclear Experimental Reactor (ITER)

The International Thermonuclear Experimental Reactor (ITER) is a research nuclear fusion reactor being constructed at Cadarache, France, and is located 3 km from the site of the RJH. The reactor building is isolated using 493 elastomeric bearings of the same design used for the RJH. The installation of the bearings was completed in March 2012.

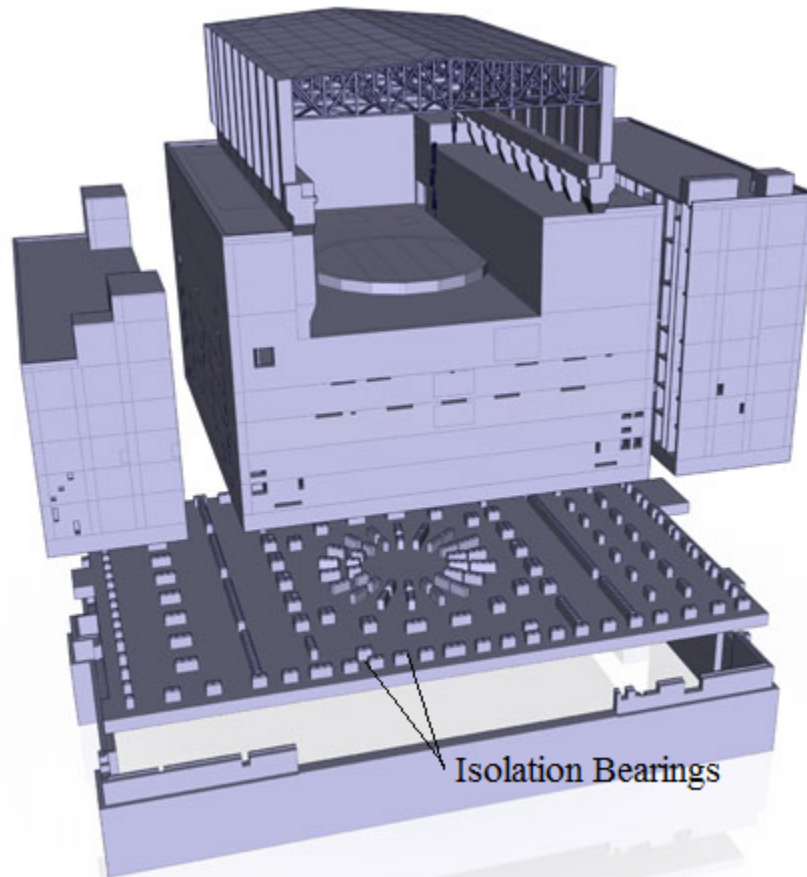


Figure 2-17 Isolator layout for the seismically isolated ITER (www.iter.org)

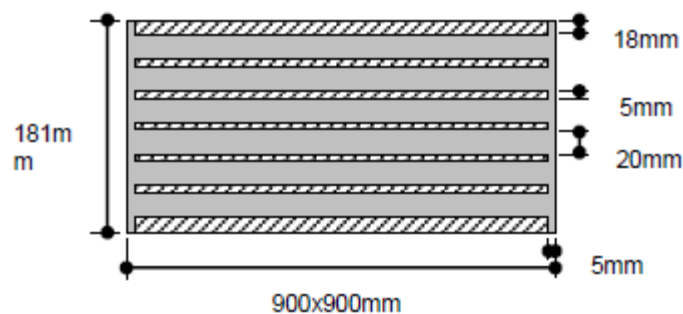


Figure 2-18 Cross-section through the elastomeric bearing used for ITER and RJH (NUVIA, 2011)



Figure 2-19 Isolators installed on the site of ITER (<http://www.iter.org>)

2.3.9 International Reactor Innovative and Secure (IRIS)

IRIS is a small-scale Pressurized Water Reactor (PWR) being developed by group of companies, laboratories, and universities, and is led by Westinghouse Electric Company. Seismic isolation has been considered for the design of this plant (Poggianti, 2011). The seismic isolation system is composed of 99 High Damping Rubber (HDR) bearings with two different diameters, 1000 mm and 1300 mm, and a height of 100 mm. The shear modulus of rubber is reported as 1.4 MPa (Poggianti, 2011). The fundamental frequency of isolated reactor in the horizontal direction is 0.7 Hz. It was designed for safe shutdown earthquake shaking (design basis) shaking characterized by spectra with horizontal and vertical peak ground accelerations of 0.3g and 0.2g, respectively. The proposed layout of the isolators is shown in Figure 2-21.

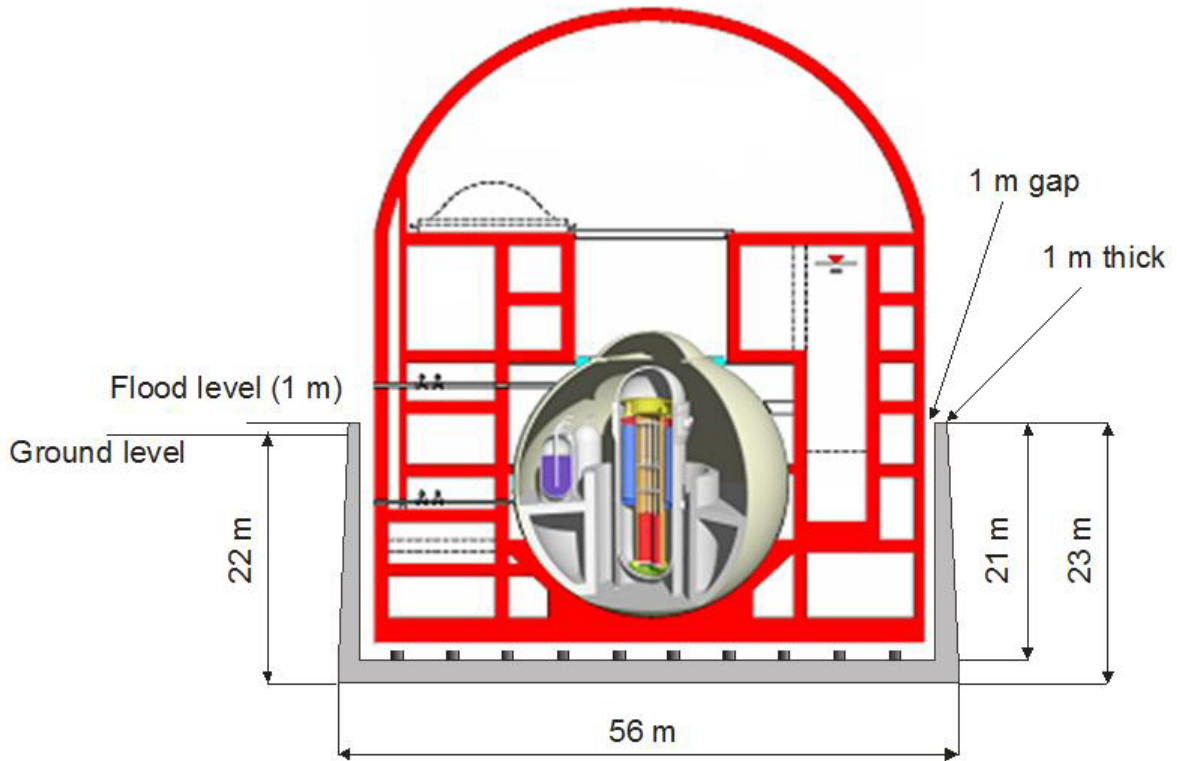


Figure 2-20 Vertical section through IRIS (Forni and Poggianti, 2011)

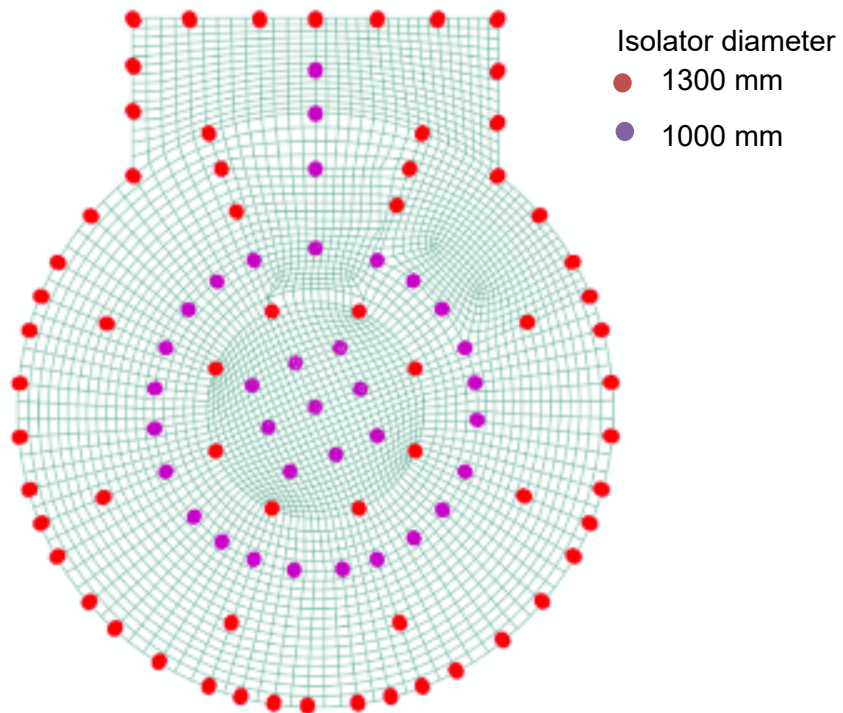


Figure 2-21 Layout of isolators for IRIS (Poggianti, 2011)

2.4 Review of Experimental Work

2.4.1 General

Tensile deformation in elastomeric bearings has traditionally been considered undesirable. Design codes and standards that explicitly consider response in axial tension do not allow tensile loading or limit the value of allowable tensile stress in elastomeric bearings under design-basis loading. The Japanese specifications for design of highway bridges (JRA, 2011) limit the tensile stress in G8 and G10 rubber¹ to 2 MPa. Eurocode 8 restricts the use of elastomeric bearings if axial tensile force is expected during seismic loadings. New Zealand and Chinese seismic design codes limit the tensile stress to 3 times the shear modulus (G) and 1 MPa, respectively (Mangerig and Mano, 2009; Yang *et al.*, 2010).

Recent experiments have shown that elastomeric bearings can sustain large tensile strains of up to 100% following cavitation, without rupture of the bearing (Iwabe *et al.*, 2000). The design codes for seismic isolation of nuclear facilities in the United States (ASCE, 2017; Kammerer *et al.*, 2019) considers the effects of extreme earthquakes. Seismic isolation is being considered for new build nuclear power plants and these isolation systems will have to be designed to accommodate these extreme loadings, which may include net tensile force in bearings. In order to consider tensile loading in seismic isolation design, robust mathematical models are required to simulate the load-deformation behavior in tension.

Much of the initial work on cavitation of elastomers was done by Gent and Lindley (1959b). They used bonded rubber cylinders in their experiments to investigate behavior under tensile loading. The cavitation stress (or cracking stress as defined in Gent and Lindley (1959b)) is defined as the tensile stress at which microcracks form in the volume of rubber. The variation of cavitation stress with the thickness of the rubber discs is presented in Figure 2-22.

As evident from Figure 2-22, the tensile properties of rubber are highly dependent on its thickness, or more appropriately the shape factor, S^2 , which is defined as the loaded area divided by the perimeter area that is free to bulge. Only elastomeric bearings with high shape factors, between 5 and 30, are discussed here, because these are used for seismic isolation applications. Experimental programs on the tensile behavior of rubber bearings are summarized in Table 2-2. Very few experiments have investigated the cyclic load-deformation behavior of elastomeric bearings in tension and most have only considered the effect of constant axial load on the shear properties of elastomeric bearings.

¹ G8 and G10 denote rubber classes with shear modulus 0.8 and 1 MPa, respectively. More information is presented in Japan Road Association (JRA). (2011). "Bearing support design guide for highway bridges (In Japanese)." Japan.

² The first shape factor, S , for a circular bearing is equal to the $D / 4t_r$, where D is the bonded diameter and t_r is the thickness of the individual rubber layer.

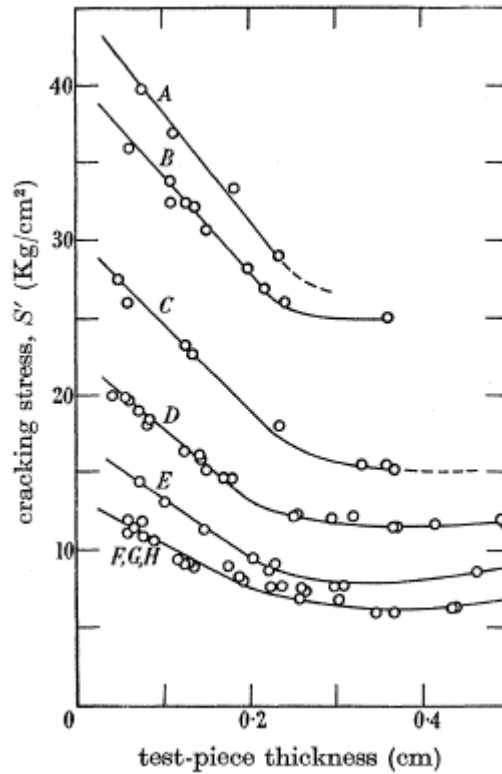


Figure 2-22 Variation of cavitation stress with the thickness of rubber discs of different Young's modulus (Gent and Lindley, 1959b)

Table 2-2 Experimental work on the tensile properties of elastomeric bearings

Research reference	Bearing properties	Focus
Iwabe <i>et al.</i> (2000)	LDR, LR, HDR bearings, diameter 500 mm and 1000 mm, shape factor ~30	Tension, shear-tension, post-cavitation mechanical properties
Kato <i>et al.</i> (2003)	LDR, diameter 500 mm and 1000 mm, varying bearing plate thickness, shape factor~33	Tension, scale effect, bearing plate thickness
Shoji <i>et al.</i> (2004)	LR, 240×240 mm, shape factor~8	Cyclic deterioration under tension
Feng <i>et al.</i> (2004)	LR, diameter 100 mm, shape factor~15	Tension, mechanical properties, three-dimensional dynamic loading
Warn (2006)	LDR, LR, outer diameter 152 mm, inner diameter 30 mm, shape factor~12	Tension, coupling of horizontal and vertical motion
Constantinou <i>et al.</i> (2007)	LDR, diameter 250 mm, shape factor~9	Single cycle tensile loading
Iwabe <i>et al.</i> (2000)	LDR, LR, HDR bearings, diameter 500 mm and 1000 mm, shape factor ~30	Tension, shear-tension, post-cavitation mechanical properties

2.4.2 Iwabe *et al.* (2000)

Iwabe *et al.* (2000) performed a series of tests that focused on the tensile loading of low-damping rubber (LDR), lead rubber (LR), and high-damping rubber (HDR) bearings. Bearings with high shape factor, $S = 30$, were subjected to cyclic tensile loading with and without lateral displacements. The load-deformation behavior in tension was recorded and changes in the mechanical characteristics before and after tensile loading were monitored.

Bearings experienced cavitation and sustained tensile strains up to 100% under shear strains of 200% without rupture. Cyclic tensile loading showed a) nonlinear hysteretic behavior following cavitation, and b) the cavitation strength decreasing by half following large tensile strains, typically greater than 100%. Hysteresis was more pronounced in HDR bearings than LDR and LR bearings. The hysteresis in a LDR bearing under tensile loading subjected to 200% shear displacement is shown in Figure 2-23. Characteristic tests to monitor mechanical properties showed no significant change in shear characteristics following tensile loading.

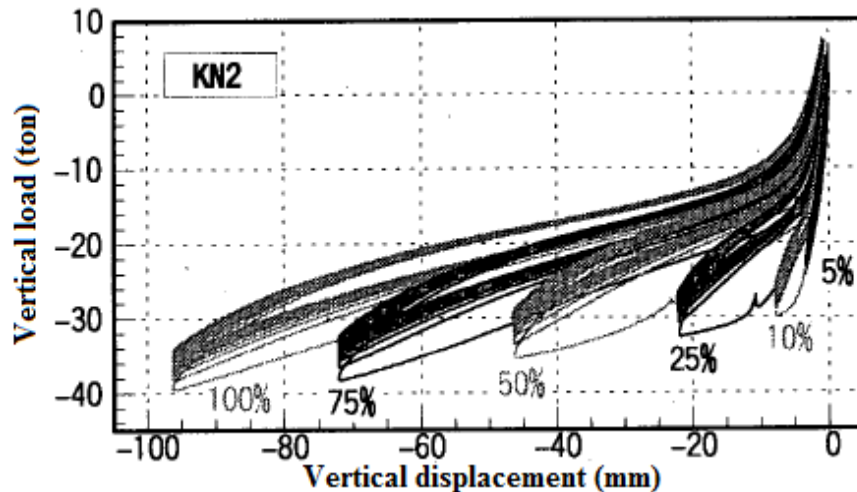


Figure 2-23 Hysteresis in tension loading with 200 % shear strain (Iwabe *et al.*, 2000)

2.4.3 Kato *et al.* (2003)

Kato *et al.* (2003) tested LDR bearings of different diameters with shape factors of approximately 33 to obtain vertical and horizontal characteristics under cyclic loading, and to investigate the effects of end plate thickness and size on the mechanical properties of elastomeric bearings. Tensile-compressive tests at constant shear strain and shear testing under constant tensile strains were performed. The tensile stiffness was measured including the stiffness contributions from the end plates. The experiments showed an increase in tensile stiffness with increasing end plate thickness (and hence stiffness); but shear stiffness was not dependent on end plate thickness or the tensile state of load or deformation. Figure 2-24 shows four load-deformation curves in tension at offset shear strains³ of 0%, 100%, 200% and 300%, respectively. The cavitation strength decreased with an increase in offset shear strain, as shown by the dashed arrow in Figure 2-24, and the maximum tensile deformation increased at higher offset shear strains. The bearing failed at a tensile strain of 50% at an offset shear strain of 300%. Scale effects on tensile properties were investigated using a 500-mm diameter and a

³ The shear strain imposed prior to testing and maintained during testing in tension.

1000-mm diameter bearing with almost identical shape factors. Minimal effects of the overall shape of the bearing, which is characterized by the second shape factor S_2 (= bonded diameter divided by total rubber height, (D/T_r)) were observed on the tensile properties of the bearings, which is expected as properties of bearings in tension are more appropriately represented as functions of the first shape factor.

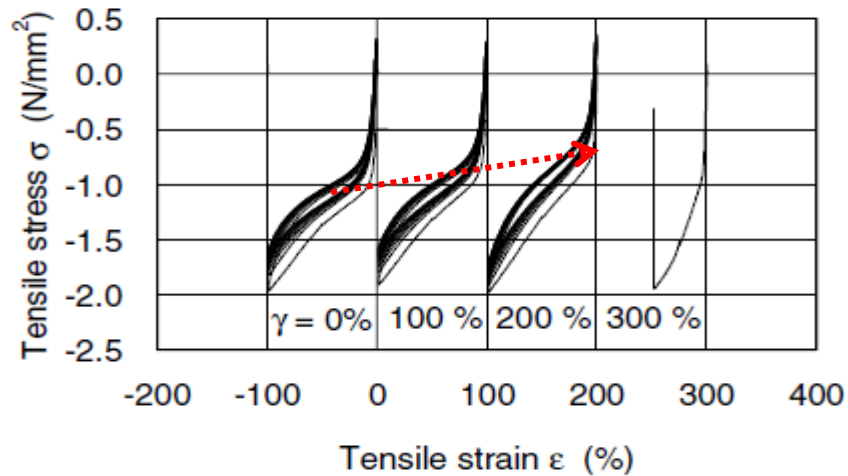


Figure 2-24 Effect of offset shear strain on tensile behavior (Kato *et al.*, 2003)

2.4.4 Shoji *et al.* (2004)

Experiments were performed by Shoji *et al.* (2004) to evaluate effect of axial load on the shear behavior of elastomeric bearings. Low-shape factor bearings, $S \sim 8$, were subjected to cyclic shear loading under constant tensile or compressive load. The effect of axial load on the response in shear was monitored. An image analysis technique was used for strain measurements. Hysteresis in shear, as measured by the area contained within the force-displacement loop, under constant compressive load was greater than in shear under constant tensile load, as shown in Figure 2-25.

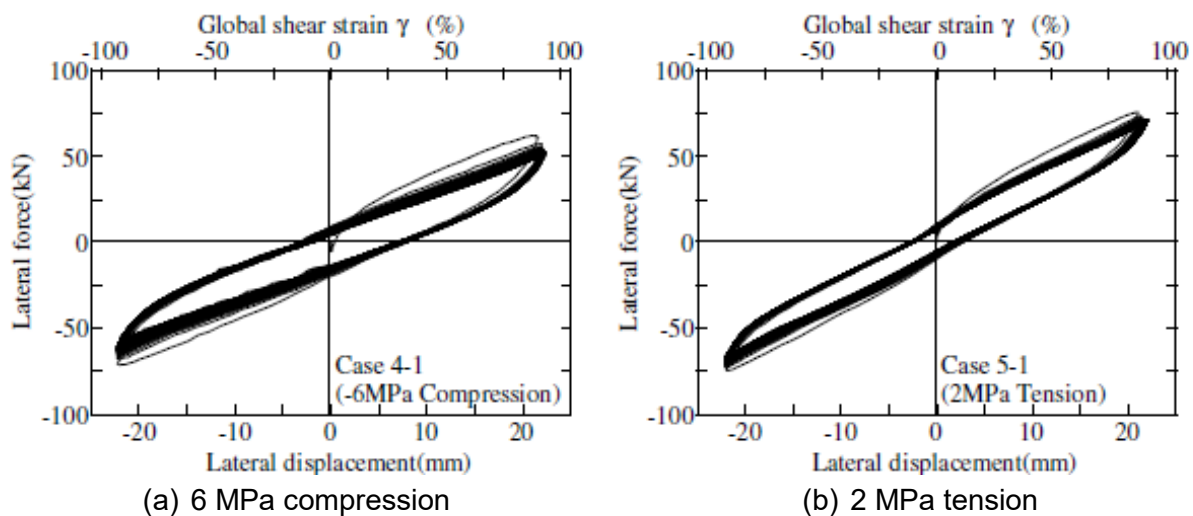


Figure 2-25 Lateral force versus lateral displacement under tensile and compressive loading (Shoji *et al.*, 2004)

2.4.5 Feng *et al.* (2004)

Feng *et al.* (2004) conducted three-dimensional shaking table tests on a 1/12 scale model of a 24-story building using 8 LR bearings of 100 mm diameter and a first shape factor of about 15. The variation of axial load was monitored and effect of axial load variation on hysteresis in shear was investigated. Axial loads were observed to vary, and tension occurred in LR bearings in 14 of the 55 tests, with a maximum tensile stress in a bearing of 2.2 MPa. A difference in hysteresis in shear due to axial load variation (3-D versus 2-D excitation) was seen in the experimental results.

2.4.6 Warn (2006)

Warn (2006) and Warn and Whittaker (2006) investigated the coupled horizontal-vertical response of LDR and LR bearings through a series of static and dynamic tests using a quarter-scale isolated bridge model. LDR and LR bearings with low shape factors, $S \sim 12$, were used for the tests. The results obtained showed clear dependency of vertical stiffness on shear displacement. The experimental results for vertical stiffness were in good agreement with analytical and empirical models. The shear hysteresis of the LR bearings was influenced by variation of axial load. Large tensile deformation tests, with and without a lateral offset, were performed to investigate the tensile load-deformation behavior of LDR and LR bearings. One of the obtained tensile load-deformation curves for LDR bearings is presented in Figure 2-26.

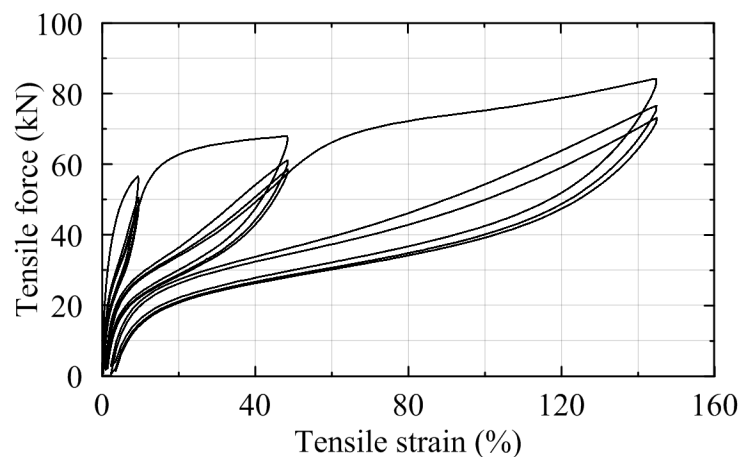


Figure 2-26 Load-deformation behavior of LDR bearings under tensile loading with zero lateral offset (Warn, 2006)

2.4.7 Constantinou *et al.* (2007)

A low shape factor bearing, $S \sim 9$, was subjected to single-cycle tensile loading to obtain tensile properties. The value of axial stiffness obtained from the experiment was in good agreement with the vertical stiffness obtained using the two-spring model (Koh and Kelly, 1987). The bearing cavitated at tensile load of $3 GA$, where G is the shear modulus at shear strain of 75%, and A is the bonded rubber area. The force-displacement curve obtained for the tensile loading is shown in Figure 2-27.

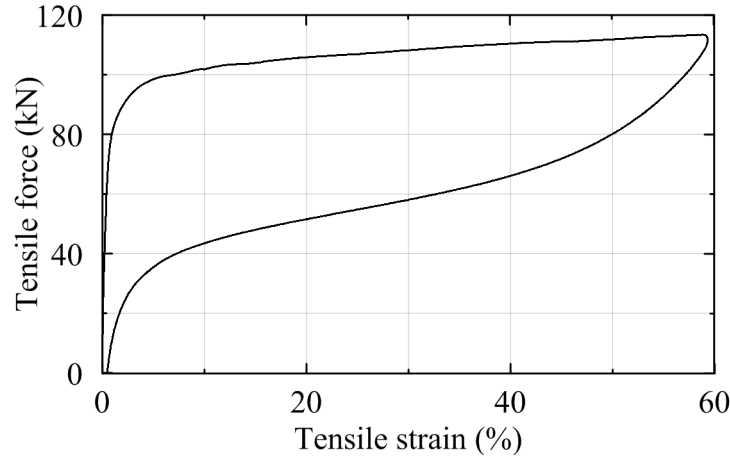


Figure 2-27 Load-displacement behavior in tension (Constantinou *et al.*, 2007)

2.5 Review of Mathematical Models

Elastomeric bearings have been conventionally modeled using a linear spring in the vertical direction. However, experiments have shown highly nonlinear response associated with cavitation, hysteresis, and coupling with horizontal displacement under tensile loading. Mathematical models have been proposed to capture the load-deformation behavior of elastomeric bearings in tension and these can be divided in two groups:

1. Continuum hyperelastic models using strain energy density functions
2. Discrete linear and nonlinear models using analytical or empirical formulations

2.5.1 Hyperelastic models

Hyperelastic models are used for rubber when finite element methods are used to model elastomeric bearings. Hyperelastic models make use of a strain energy potential, U , to obtain constitutive relationships. The general formulation of hyperelastic models is given by:

$$U = U(F) \quad (2.1)$$

$$S = \frac{\partial U(F)}{\partial F} \quad (2.2)$$

where S is the measure of stress and F is the measure of strain. The underlying assumption is that the material is elastic and isotropic. It is shown later that these models can be modified to include energy dissipation characteristics.

The strain energy potential, U , can be decoupled into a deviatoric (shear) component W , and a dilatational (volumetric) component $U_{dilatation}$:

$$U = W + U_{dilatation} \quad (2.3)$$

$$U = W(I_1, I_2) + U_{dilatational}(I_3) \quad (2.4)$$

Strain invariants are expressed in terms of three principal stretch ratios (deformed length divided by original length), λ_1 , λ_2 and λ_3 as: $I_1 = \lambda_1^2 + \lambda_2^2 + \lambda_3^2$, $I_2 = \lambda_1^2 \lambda_2^2 + \lambda_2^2 \lambda_3^2 + \lambda_3^2 \lambda_1^2$, and $I_3 = \lambda_1^2 \lambda_2^2 \lambda_3^2$. The strain energy potential can be rewritten in terms of principal stretch ratios as:

$$U = W(\lambda_1, \lambda_2, \lambda_3) + U_{dilatational}(J) \quad (2.5)$$

where $J = \lambda_1 \lambda_2 \lambda_3$ is a measure of volumetric strain.

Various hyperelastic models have been proposed using different deviatoric and dilatation functions that relate strain invariants to strain energy potential using unknown parameters. These models make use of experimental data to obtain unknown parameters using curve-fitting and are applicable for a certain range and state of strain. Some of the hyperelastic models available in the finite element program ABAQUS are identified in Table 2-3.

Table 2-3 Hyperelastic models used in ABAQUS (Dassault, 2010d)

Physical models	Material parameters
Arruda-Boyce	2
Van der waals	4
Phenomenological models	
Polynomial (order N)	$\geq 2N$
Mooney-Rivlin (1 st order)	2
Reduced polynomial (independent of I_2)	N
Neo-Hookean (1 st order)	1
Yeoh (3 rd order)	3
Ogden (order N)	2N
Marlow (independent of I_2)	n.a. ¹

1. n.a.: not applicable

One of the earliest proposed hyperelastic models was the Mooney-Rivlin model (Mooney, 1940; Rivlin, 1948). The model considered only incompressible materials ($I_3 = 1$, $J = \lambda_1 \lambda_2 \lambda_3 = 1$) and ignored the dilatational component of the strain energy potential. In its simplest form, the Mooney-Rivlin model can be expressed as:

$$U = C_1(I_1 - 3) + C_2(I_2 - 3) \quad (2.6)$$

where C_1 and C_2 are temperature-dependent material parameters related to the initial shear modulus of the material by the expression:

$$2(C_1 + C_2) = G \quad (2.7)$$

For small tensile strains, the contribution from second strain invariant, I_2 , can be neglected, and the Neo-Hookean model (Rivlin, 1948) is formulated as:

$$U = C_1(I_1 - 3) \quad (2.8)$$

where $2C_1 = G$. The Neo-Hookean model captures the behavior of hyperelastic material for moderate tensile strains of 40%.

Both of the above models are applicable only for incompressible materials (Poisson's ratio, $\nu = 0.5$; Young's modulus, $E = 3G$). However, rubber exhibits some compressibility. Moreover, an infinitely incompressible material presents numerical stability problems in finite element calculations. A dilatational term is often added to the strain energy potential to model the "almost incompressible" behavior of rubber, taking into account its bulk modulus, K . The dilatational component is given by the expression:

$$U_{dilatational} = \frac{K}{2}(J - 1)^2 \quad (2.9)$$

The Mooney-Rivlin model and the Neo-Hookean model, modified to account for the compressibility of rubber, are given by:

$$\text{Mooney-Rivlin:} \quad U = C_1(I_1 - 3) + C_2(I_2 - 3) + \frac{K}{2}(J - 1)^2 \quad (2.10)$$

$$\text{Neo-Hookean:} \quad U = C_1(I_1 - 3) + \frac{K}{2}(J - 1)^2 \quad (2.11)$$

If the initial shear modulus of rubber is known, the Neo-Hookean model can be applied directly without the need for experimental data, which makes the Neo-Hookean model one of the popular hyperelastic models in finite element analysis.

Most of the hyperelastic models developed after Rivlin (1948) use more generalized formulations of the Mooney-Rivlin model with a larger number of parameters. Although these models capture the response more accurately for a greater range of strain, having large number of parameters (N in Table 2-3) requires more experimental data and calibration. Dorfmann and Burtcher (2000) suggested a cavitation-based damage model to simulate the load-deformation behavior of elastomeric bearings in tension. They used the modified Mooney-Rivlin equation (2.10) for strain energy potential, and pre-cavitation and post-cavitation bulk modulus in the dilatational component to allow for the sharp change in stiffness after cavitation.

Models proposed after Rivlin (1948) have tried to capture the hysteresis under tensile loading due to Mullin's effect (scragging). Although low shape factor bearings might show little energy dissipation due to Mullin's effect, the nature of hysteresis in tensile loading of seismic isolation bearing is primarily due to cavitation or internal damage that cannot be captured by any of the proposed models. Figure 2-28 shows the contributions of damage and Mullin's effect (scragging) to the total energy dissipation under tensile loading. The area between the loading and unloading branches represents the energy dissipated due to damage. Subsequent loading follows the prior unloading path elastically until the strain exceeds the prior maximum value, below which loading has the effect of only opening and closing existing cavities within the rubber, and small energy dissipation due to Mullin's effect.

Hyperelastic models can be used to simulate nonlinear tensile behavior of rubber. However, limitations in terms of the large number of unknown parameters, dependency on experimental data, and inability to reproduce the hysteretic behavior due to damage, restricts their

widespread use. Finite element analysis is computationally intensive and is not a popular method for analysis of large structures with many structural components. Contemporary software programs for structural analysis use simplified models that are discussed in the following section.

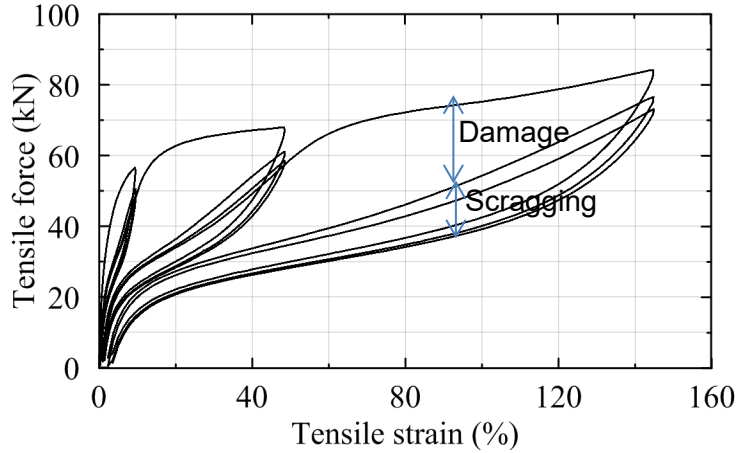


Figure 2-28 Components of energy dissipation in the tensile loading of elastomeric bearings

2.5.2 Linear and nonlinear stiffness models

Elastomeric bearings in the axial direction have been conventionally modeled as a linear spring with a constant stiffness, as shown in Figure 2-29.

The axial stiffness of multilayer elastomeric bearings is given by the expression:

$$K_{vo} = \left(\sum_1^n \frac{1}{K_i} \right)^{-1} = \left(\frac{t_i}{AE_i} \right)^{-1} \quad (2.12)$$

which, for bearings with rubber layers of the same thickness, is simplified to:

$$K_{vo} = \frac{AE}{T_r} \quad (2.13)$$

where K_{vo} is the vertical stiffness at zero lateral displacement, A is the bonded rubber area, T_r is the total rubber thickness, and E is the elastic modulus in the vertical direction. The same expression is used for compression and tension but with a different definition of elastic modulus: compression modulus E_c and tension modulus E_t .

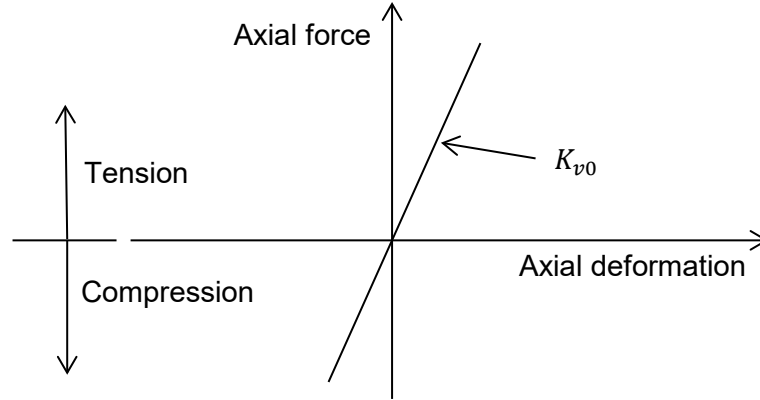


Figure 2-29 Linear stiffness model of elastomeric bearing in vertical direction

Analytical expressions for the compression modulus of elastomeric bearings were developed by Chalhoub and Kelly (1990) and Constantinou *et al.* (1992) for different shapes. The compression modulus for a circular elastomeric bearing with finite compressibility is given by (Constantinou *et al.*, 2007):

$$E_c = \left(\frac{1}{6GS^2} + \frac{4}{3K} \right)^{-1} \quad (2.14)$$

where S is the first shape factor of the bearing and K is the bulk modulus of the rubber. As suggested by experiments, the tension modulus before cavitation is the same as the value in compression, namely, $E_c = E_t$. Hence, a single value of stiffness in compression and tension, given by Equation (2.13), is used in linear-stiffness model.

Koh and Kelly (1987) and Kelly (1993) proposed two vertical stiffness models for elastomeric bearings that take into account the height reduction due to shear deformation. The coupling of vertical stiffness with lateral displacement is captured by these models. The first model, known as a two-spring model, considers a simplified physical representation of elastomeric bearing. The second models a bearing as a continuous beam with equivalent properties and assumes that plane sections remain plane but not necessarily perpendicular to the neutral axis. This model can also be used to explain the concept of tension buckling and increased tensile deformation capacity of bearings in tension with lateral shear offset (Kelly, 2003). The vertical stiffness obtained from the two models are:

Two-spring model:

$$K_v = \frac{AE_c}{T_r} \frac{1}{\left[1 + \frac{3}{\pi^2} \left(\frac{u}{r} \right)^2 \right]} \quad (2.15)$$

Exact model:

$$K_v = \frac{AE_c}{T_r} \frac{1}{\left[1 + \frac{3}{4} f'(\pi p) \left(\frac{u}{r} \right)^2 \right]} \quad (2.16)$$

where u is the lateral displacement of elastomeric bearing, r is the radius of gyration of bonded rubber area, $p = P / P_{cr}$, P is the axial load, and P_{cr} is the critical buckling load

accounting for area reduction. The function $f(\pi p)$ is a trigonometric function with f and f' given by:

$$f(x) = \frac{(x - \sin x)}{(1 - \cos x)}; f'(x) = \frac{(1 - \cos x) - x \sin x}{(1 - \cos x)^2} \quad (2.17)$$

and $f'(\pi p)$ is a symmetric function that varies between 1/3 to 1 as πp varies between 0 to π , or P varies between 0 to buckling load P_{cr} . For tensile loading, the axial load P is much less than the critical buckling loading in tension; and a bearing cavitates at loads much less than P_{cr} . The value of $f'(\pi p)$ is closer to 1/3 than 1 in tensile loading. The two-spring model and the continuous beam model are linear with respect to vertical displacement but show nonlinear characteristics with increasing lateral displacements. The two-spring model proposed above shows good agreement with experimental results (Warn and Whittaker, 2006). In addition, Warn and Whittaker (2006) also suggested vertical stiffness expressions based on the overlapping area method and a linear approximation of overlapping area method to capture the coupling of vertical stiffness and horizontal displacement.

None of the linear or nonlinear models discussed above considers cavitation. The calculation of cavitation stress and post-cavitation stiffness remains an open issue. Gent (1990) suggests that cavitation occurs at a negative pressure of about $3G$. This value is however a good approximation only for certain range of radii of initial voids present in the rubber.

Constantinou *et al.* (2007) suggested a bilinear model and included cavitation strength and post-cavitation stiffness. The model ignores coupling of vertical stiffness and horizontal displacement in tensile loading. Tensile stiffness is given by:

$$K_{vt} = \frac{E_t A}{T_r} \quad (2.18)$$

where E_t is the tensile modulus. The modulus E_t before cavitation is same as E_c , given by Equation (2.14). The modulus, E_t , after cavitation takes the value of Young's modulus, E , of rubber, as the state of stress in the rubber after cavitation reduces to that of uniaxial tension. Elastomers used in seismic isolation (filled rubber) have Young's modulus of about $E = 4G$ (Ciesielski, 1999; Gent, 2001). Hence, the ratio of tensile stiffness before and after cavitation is given by the expression:

$$\frac{K_{vt,pre-cavitation}}{K_{vt,post-cavitation}} = \frac{E_c}{E} = \frac{1}{\frac{2}{3S^2} + \frac{16G}{3K}} \quad (2.19)$$

with the values in the range of 100 to 200 for typical intermediate and high shape factor bearings constructed using low damping natural rubber.

The vertical stiffness model suggested by Constantinou *et al.* (2007) is presented in Figure 2-30.

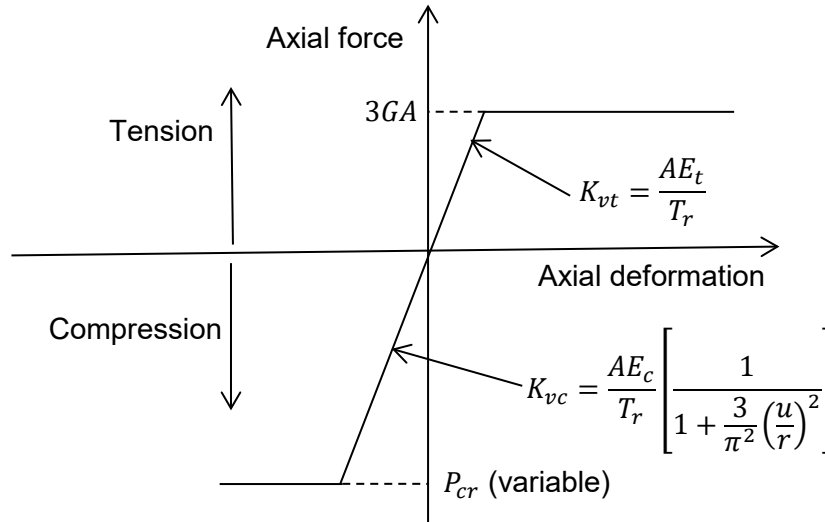


Figure 2-30 Vertical stiffness model for an elastomeric bearing (Constantinou *et al.*, 2007)

Yamamoto *et al.* (2009) used a similar backbone curve to Figure 2-30 and included hysteresis in compression and tension, as shown in Figure 2-31. The model uses the compression modulus proposed by Gent and Lindley (1959a) and an arbitrarily small value of post-cavitation modulus. Following unloading in tension (c-d-a), it traces back to a target point (d) defined by the user and then follows the compression curve. It defines a yield zone in compression (a-e), and assumes the post-buckling modulus as half of the compression modulus.

The model proposed by Yamamoto *et al.* (2009) seeks to capture the hysteresis in axial loading in addition to other features of the vertical stiffness model. However, the model fails to capture the permanent damage and reduction in cavitation strength observed in experiments (Iwabe *et al.*, 2000; Warn, 2006). It does not consider effects of loading history on load-deformation behavior in tension and does not provide a technical basis for choosing a particular post-cavitation stiffness. Also, it does not consider coupling of vertical and horizontal motion confirmed by experimental studies (e.g., Warn and Whittaker (2006)). Moreover, use of too many unknown parameters limits its utility for numerical simulations.

In addition to the models discussed above, other researchers have proposed empirical formulae for stiffness and cavitation strength (Iwabe *et al.*, 2000; Yang *et al.*, 2010). However, these formulae are based on limited experimental results and involve a number of unknown parameters. A robust mathematical formulation for use in structural analysis cannot be obtained from these models.

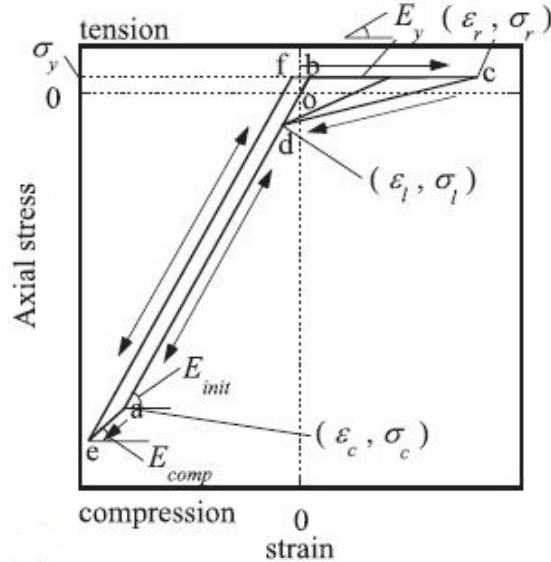


Figure 2-31 Axial stress-strain model (Yamamoto *et al.*, 2009)

2.6 Modeling in Contemporary Software Programs

2.6.1 General

This section describes how elastomeric bearings are modeled in computer codes that are widely used in the United States, noting that numerical models of seismic isolation systems should a) include all isolators in the seismic isolation system, and b) the account for the spatial distribution of the isolators across the footprint of the isolated structure.

There are two ways to represent the physical model of an isolator: 1) a full three-dimensional continuum model, and 2) a three-dimensional discrete model in which two nodes are connected by six springs to represent the mechanical behavior in each of the six directions (three translation and three rotation).

General-purpose Finite Element Analysis (FEA) programs such as ABAQUS (Dassault, 2010e), LS-DYNA (LSTC, 2012a) and ANSYS (ANSYS, 2011), enable the use of discrete and continuum models of seismic isolation bearings. The special-purpose software programs used for structural analysis of base-isolated structures such as SAP2000 (Wilson, 1997), OpenSees (McKenna *et al.*, 2006), PERFORM-3D (CSI, 2006), and 3D-BASIS (Nagarajaiah *et al.*, 1989), model an elastomeric bearing as a two-node discrete element with stiffness in each of the six principal directions represented by linear or nonlinear springs between the two nodes. Analytical expressions for force and stiffness can be used to define a spring in any direction.

The modeling techniques for different types of isolator in seven software programs (SAP2000, OpenSees, PERFORM-3D, 3D-BASIS, LS-DYNA, ABAQUS, and ANSYS) are discussed in the following sections. Two types of rubber-based isolator are considered: 1) Low Damping Rubber (LDR) bearing, and 2) Lead Rubber (LR) bearing. The discrete modeling techniques discussed for these isolators can be extended for friction-based isolators.

2.6.2 SAP2000

In SAP2000, isolators are modeled using Link/Support element option. Link is a two-node element connected by six springs. Each node has six degrees of freedom. A description of the Link element is given in Figure 2-32.

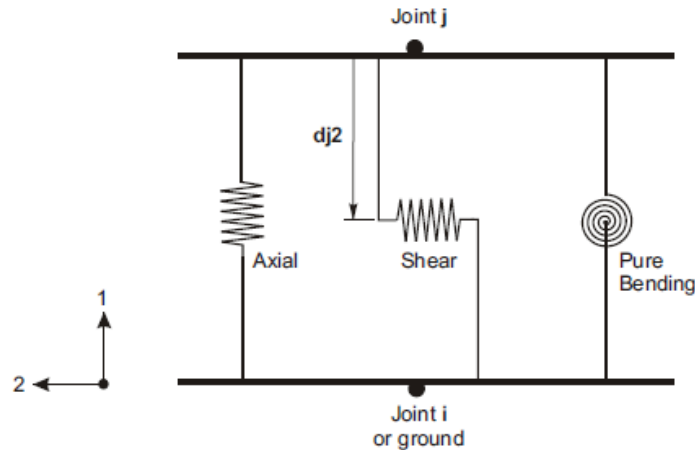
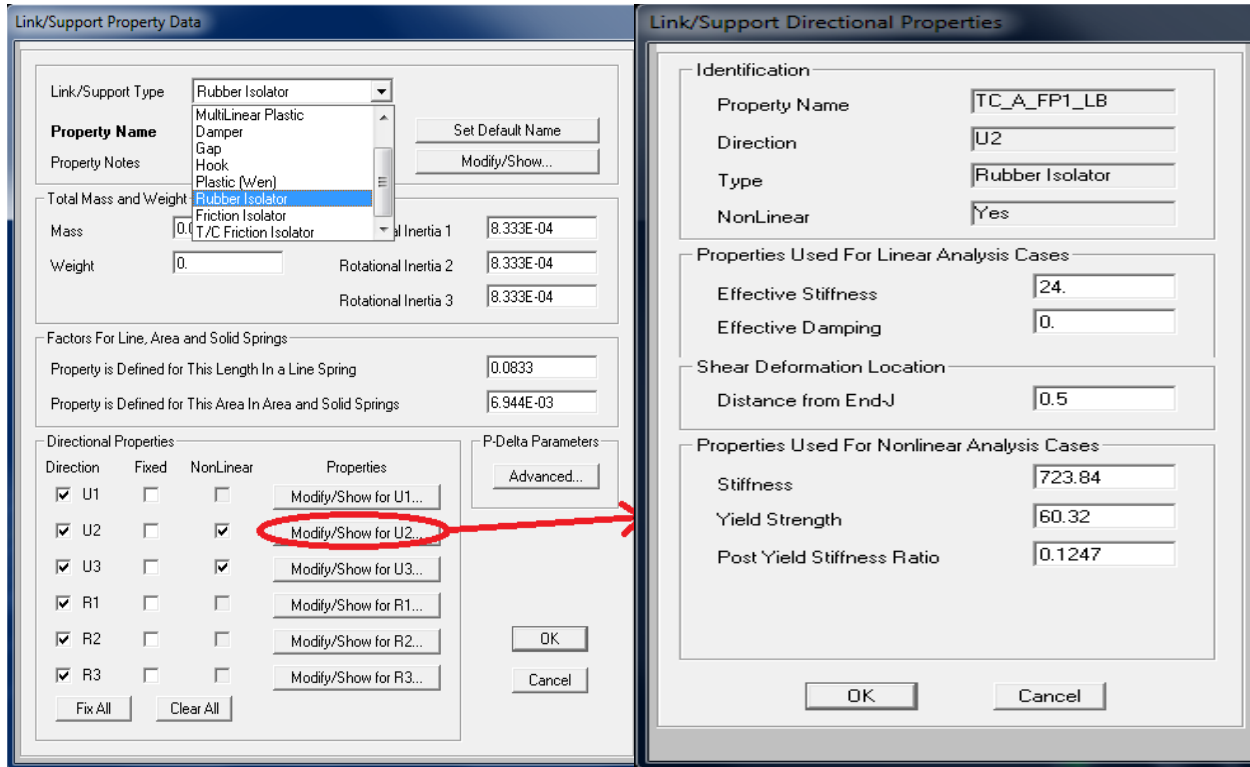


Figure 2-32 Three of the six independent springs in a Link/Support element

SAP2000 provides the option to use the link element to model any structural element that can be represented as 2-node element. The property data form for the link element is shown in Figure 2-33. Low damping rubber (LDR), lead rubber (LR), flat sliders, single Friction Pendulum (FP), and double FP bearings can be modeled using the link element. The shearing behavior is based on the model proposed by Park *et al.* (1986) and extended for seismic isolation bearings by Nagarajaiah *et al.* (1991). For nonlinear force-deformation response, either a) elastic and post-elastic stiffness values, or b) equivalent linear stiffness, is assigned.

For the *elastomeric bearing* (rubber isolator) option in the link element, nonlinear (bilinear) properties can be assigned to the two horizontal shear directions, but only linear elastic behavior is accommodated for the remaining axial and three rotational directions.



a) Link/support property data form

b) Nonlinear directional properties for U2

Figure 2-33 Link/Support property data input to SAP2000 (CSI, 2011)

2.6.3 3D-BASIS

The computer program 3D-BASIS (also 3D-BASIS-M, 3D-BASIS-TABS, and 3D-BASIS-ME-MB) is used for the nonlinear dynamic analysis of seismically isolated structures (Nagarajaiah *et al.*, 1989; Tsopelas *et al.*, 2005). The analysis model and reference frames of a base-isolated structure in 3D-BASIS-ME-MB are shown in Figure 2-34 and Figure 2-35. The software program provides the option to use elastomeric (LDR and LR) bearings and friction-based isolators that include the single FP bearing, the double FP bearing, and the XY-FP bearing.

The isolators in 3D-BASIS are modeled using explicit nonlinear force-displacement relationships. The isolators are considered rigid in vertical direction and do not offer any torsional resistance. The following elements are available in the program 3D-BASIS-ME-MB for modeling the behavior of elastomeric bearings (Tsopelas *et al.*, 2005):

1. Linear elastic element.
2. Linear and nonlinear viscous elements for fluid viscous dampers or other devices displaying viscous behavior.
3. Hysteretic element for elastomeric bearings and steel dampers.
4. Stiffening (biaxial) hysteretic element for elastomeric bearings.

The model proposed by Park *et al.* (1986) and extended for analysis of seismic isolators by Nagarajaiah *et al.* (1989) is used for the unidirectional and bi-directional hysteretic elements.

2.6.4 PERFORM-3D

PERFORM-3D is a software program used for the nonlinear dynamic analysis of structures. PERFORM-3D has powerful capabilities for inelastic analysis. The nonlinear model proposed by Park *et al.* (1986) and extended for analysis of seismic isolators is used in the two horizontal (shear) directions. Elastic stiffness is used in the vertical (axial) direction with the option to provide different values in compression and tension. The local-axis orientation of the isolators must be assigned to seismic isolator elements in PERFORM 3D. Axis 3 is usually defined as the vertical (axial) direction of an isolator, and Axes 1 and 2 are the horizontal (shear) directions.

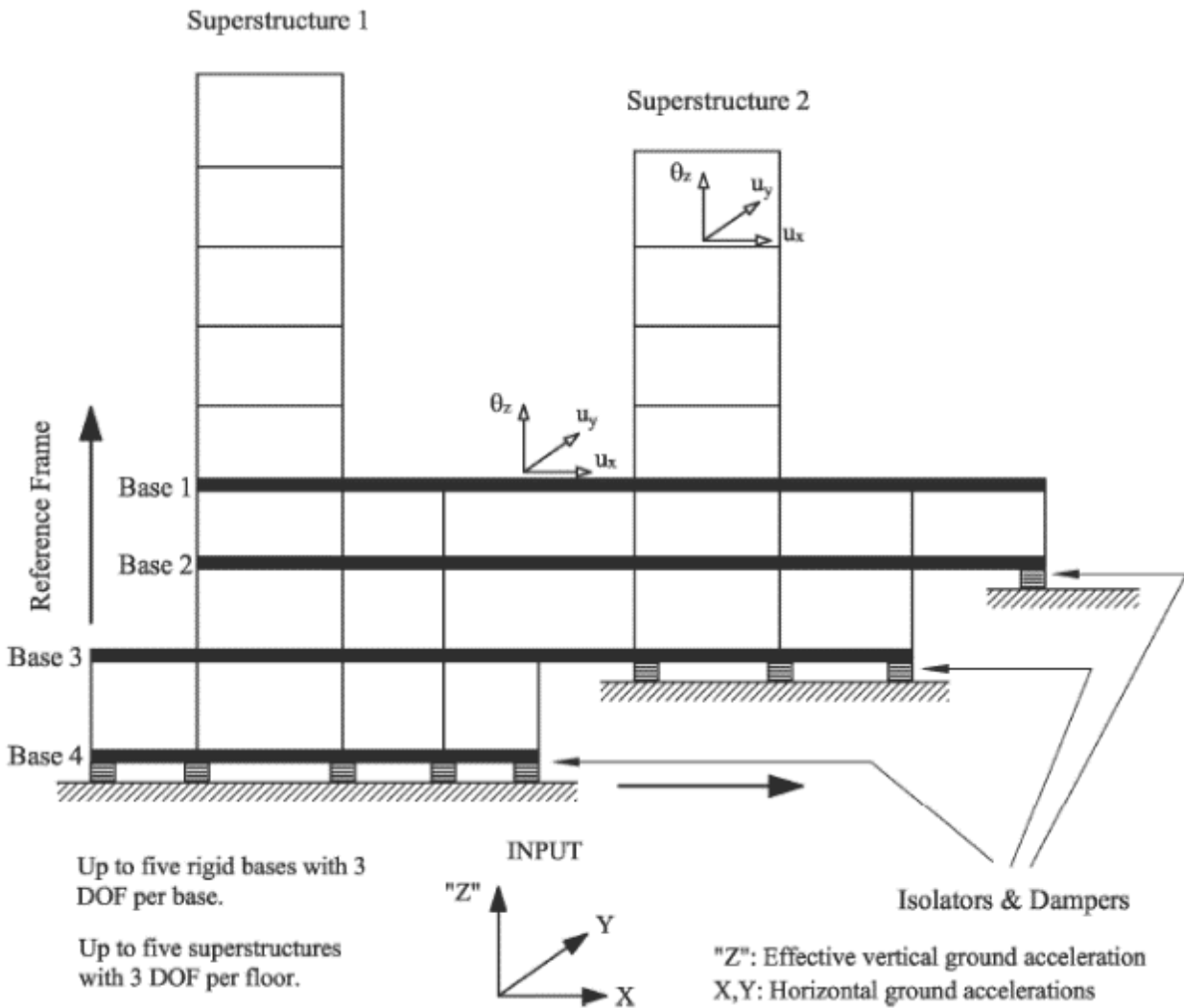


Figure 2-34 Model that can be analyzed in 3D-BASIS-ME-MB (Tsopelas *et al.*, 2005)

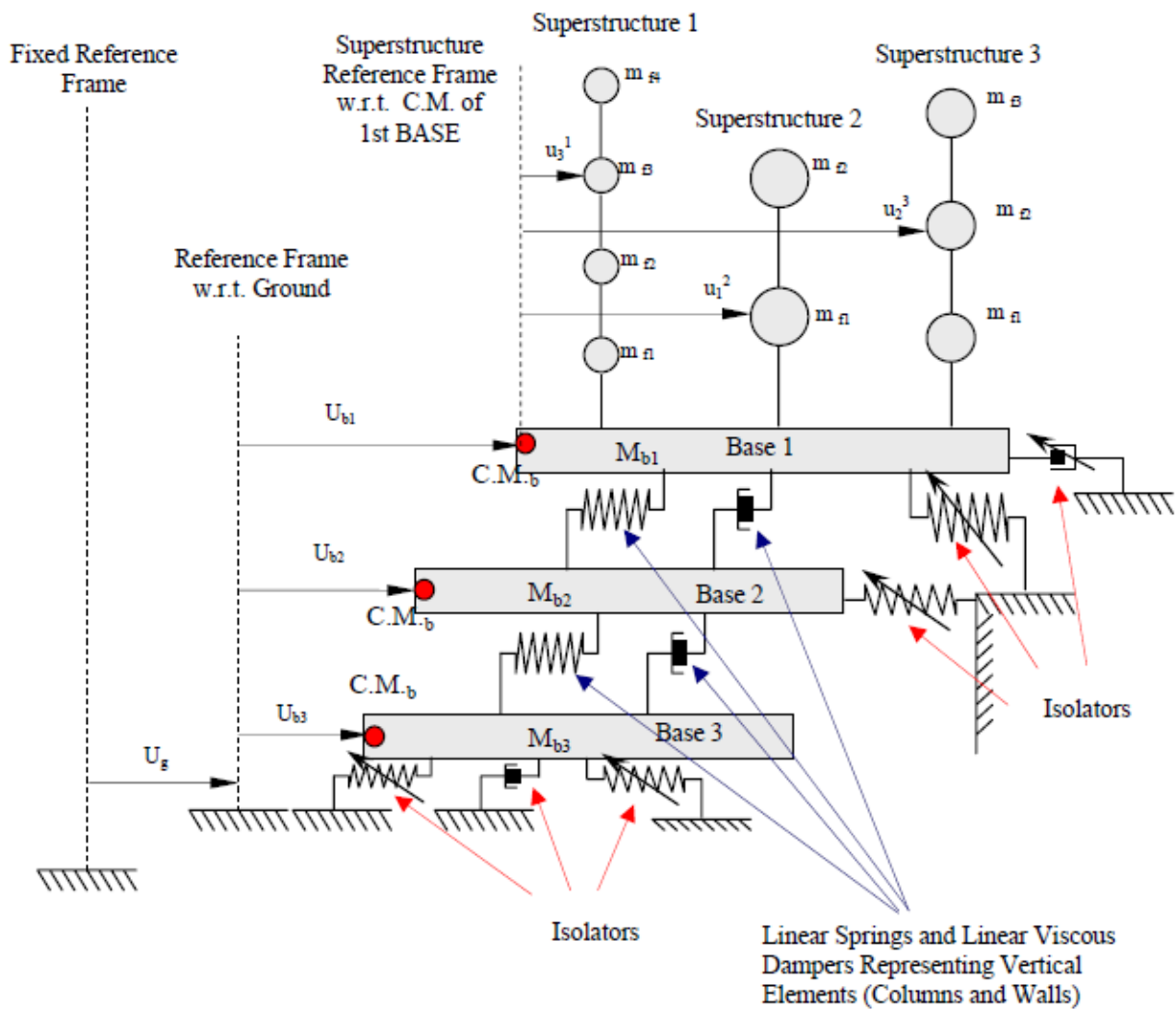


Figure 2-35 Degrees of freedom in 3D-BASIS-ME-MB (Tsopeles et al., 2005)

2.6.5 ABAQUS, LS-DYNA, and ANSYS

2.6.5.1 Continuum Modeling

In the continuum modeling approach, an isolator is modeled as a three-dimensional continuous object with appropriate material and geometrical properties assigned to different components of the isolator. All three FEA software programs, ABAQUS, LS-DYNA, and ANSYS use a similar approach to model an elastomeric seismic isolation bearing. The wide range of capabilities of FEA allows a user to model complex phenomena like heating of the lead core in LR bearings. The capability of a FEA model of a bearing to simulate the actual behavior depends on how detailed a model is constructed. Very detailed models will increase the computational effort.

An elastomeric bearing is modeled as a multilayer object of alternating rubber and steel. Rubber layers are usually meshed using solid elements and the steel layers can be modeled using either solid or shell elements. A finite element model of an elastomeric bearing constructed in ABAQUS is shown in Figure 2-36.

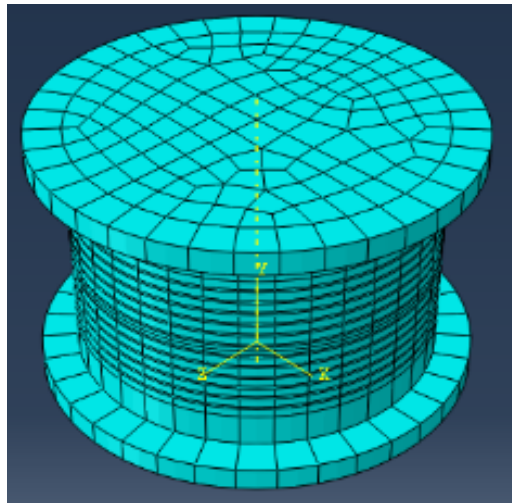
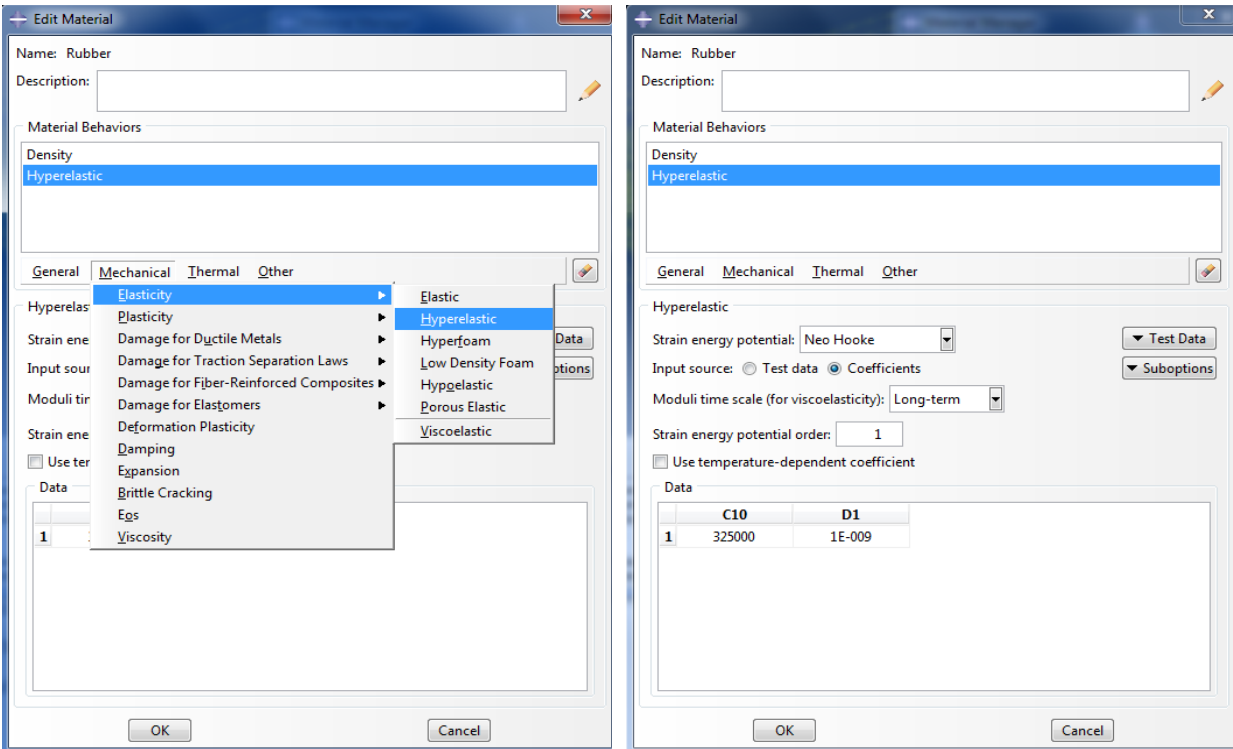


Figure 2-36 Finite element model of a low damping rubber bearing

Steel is modeled as a linear elastic material. Kinematic plastic or any other metal plasticity material model can be used if yielding in the internal steel shims is expected. Rubber can be modeled either as hyperelastic material or a viscoelastic material. A viscoelastic model can be used if experimental data on stress-strain, strain-rate, creep, and stress relaxation are available. If only stress-strain data are available from an experiment, a hyperelastic material model is recommended. The property data form of rubber defined using a hyperelastic material is shown in Figure 2-37.

Hyperelastic material models require experimental data to determine the unknown parameters required to model the rubber. If the initial shear modulus of the rubber is known, the Neo-Hookean model (Rivlin, 1948) is an appropriate model for tensile shear strains of up to 40%, in which case no experimental data are required. A high value is assigned to the bulk modulus of rubber to account for its incompressibility. If a viscoelastic material model is used for the rubber, LS-DYNA requires the user to input a short-term and long-term shear modulus; in ABAQUS it can be modeled in the frequency domain using complex modulus or in the time domain by constructing a Prony series.



a) Selection of mechanical properties

b) Definition of a Neo-Hookean material

Figure 2-37 Properties definition of rubber material in ABAQUS

The behavior of rubber in high shape factor bearings differs from the experimental behavior observed from rubber coupon tests. When an elastomeric bearing is subjected to vertical tension, cavities form inside the volume of rubber: cavitation. Cavitation is followed by the substantial reduction in the vertical stiffness. Although rubber damage models are available in ABAQUS (e.g., Mullins damage model), the cavitation phenomenon in elastomeric bearings is different and cannot be captured using these models. Cavitation in elastomeric bearings cannot be captured by ABAQUS, LS-DYNA, or ANSYS using a continuum modeling approach.

Convergence is often an issue with the use of hyperelastic material models due to their highly nonlinear characteristics. The single-parameter Neo-Hookean hyperelastic material, although easy to use, is not suitable for very large deformation analysis in which strains exceeds 40%. Hyperelastic models using a larger number of parameters (e.g., Yeoh (1993), Ogden (1972)) provide better numerical stability but require experimental data to determine the parameters.

2.6.5.2 Discrete Modeling

2.6.5.2.1 General

Finite element analysis (FEA) software programs also provide option to create discrete model of isolators. Although the continuum approach modeling of isolators among different FEA software programs is similar, the modeling options for creating discrete models of isolators vary across the platforms. Some of the software programs provide a direct option to model a bearing based on its geometrical and material properties, whereas others use different techniques to create a two-node, twelve degree-of-freedom element with six principal directions. The discrete modeling

techniques in ABAQUS and LS-DYNA are discussed here. ANSYS does not provide a direct option for discrete modeling of isolators, but link and spring elements can be used.

2.6.5.2.2 Discrete Modeling in ABAQUS

ABAQUS provides the option to use a “connector” element to create discrete models of isolators. The connector element in ABAQUS is similar to Link/support element in SAP2000. ABAQUS provides a comprehensive list of “connector” elements that can be used to model an elastic spring, a dashpot, friction, plasticity, and damage. Different directions between two nodes can be coupled, uncoupled or combined. An illustration of connector behaviors in ABAQUS is shown in Figure 2-38.

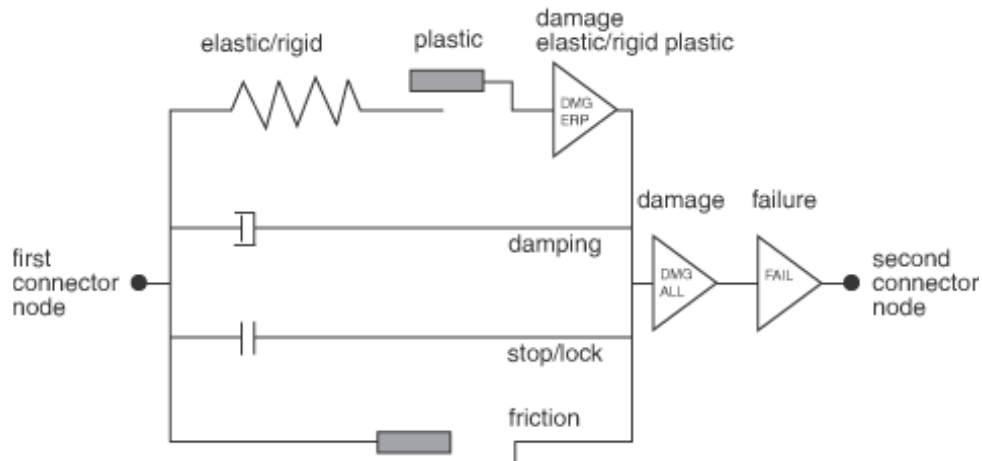


Figure 2-38 Conceptual illustration of connector behaviors (Dassault, 2010a)

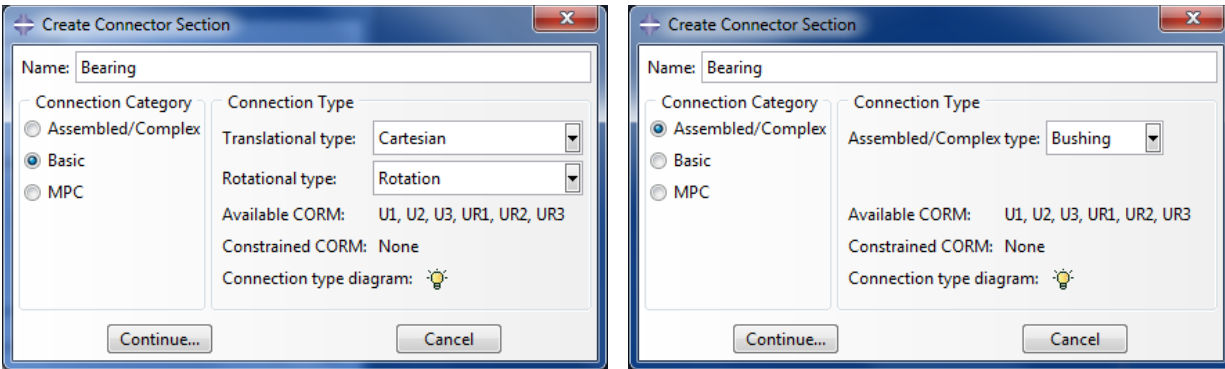
The first step in developing a connector is to define a connection type that represents the physical model of the isolator. There are two ways to create two-node, twelve degree-of-freedom discrete element that is characterized by six local directions: 1) a basic category connection with a translational connection type assigned to Cartesian and rotational connection type assigned to Rotation, or 2) an assembled/complex category Bushing connection. Both options are shown in Figure 2-39.

Once the connection type is defined, connection behavior can be defined in each of the six local directions for the seismic isolator. ABAQUS provides the option to use an isotropic or a kinematic hardening model. A direct option to use the Bouc-Wen model extended by Nagarajaiah *et al.* (1991) for seismic isolators is not available. Figure 2-40 shows the data form for a connector. Additional information on use of connector elements in ABAQUS is provided in Section 28 of ABAQUS Analysis User’s Manual (Dassault, 2010a) and Section 15.7, 15.8 and 15.17 of ABAQUS/CAE User’s Manual (Dassault, 2010b).

The use of a discrete model using connector elements in ABAQUS reduces the computational effort drastically from that associated with a continuum model, and most of the nonlinear behaviors can still be captured. However, modeling of isolators using connector elements in ABAQUS is involved by comparison with the discrete models available in structural analysis software programs such as SAP2000 and OpenSees.

ABAQUS also allows the user to define a model, which is not available in ABAQUS, through user subroutine code and then to integrate (link) it to ABAQUS for analysis. The two-node

discrete model of elastomeric bearings can be implemented in ABAQUS by creating new subroutines called User Elements (UELs). The computational efficiency can be increased significantly, and it can capture all of the behaviors of seismic isolators observed experimentally that are defined by the user in the subroutine.



a) Basic connection

b) Assembled

Figure 2-39 Type of connectors used for seismic isolators

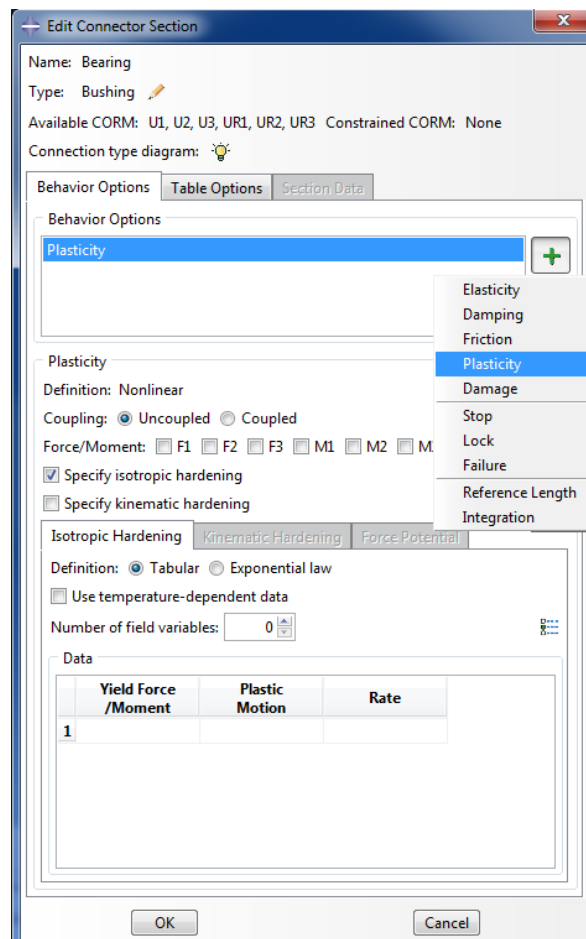


Figure 2-40 Definition of connector's behavior

2.6.5.2.3 Discrete Modeling in LS-DYNA

LS-DYNA provides a direct option to model an elastomeric bearing through a material model option `*MAT_SEISMIC_ISOLATOR`. The corresponding element and section is created using options `*ELEMENT_BEAM` and `*SECTION_BEAM`, respectively. `ELFORM` is set to 6 (discrete beam), and the local axes of the isolator is defined in `*SECTION_BEAM` option. This material can be used to model elastomeric bearings, flat slider bearings, single FP bearings, double FP bearings and XY-FP bearings. Behavior in two horizontal (shear) directions is similar to SAP2000 and OpenSees, which is based on the model proposed by Park *et al.* (1986) and extended for seismic isolators by Nagarajaiah *et al.* (1989). The vertical stiffness for all types of isolators is linear elastic, with the option to provide different values in compression and tension. The element has no rotational or torsional stiffness and a pinned joint is assumed. However, if required, moments can be calculated according to the vertical load times the lateral displacement of the isolator by assigning the moment factors in the `*MAT` definition. Additional details on modeling a seismic isolator using `*MAT_SEISMIC_ISOLATOR` material model is provided in `*MAT_197` of LS-DYNA Keyword User's Manual (LSTC, 2012b).

2.6.6 OpenSees

OpenSees provides more flexibility to model isolators because of its code-based approach to construct the finite element model of the structure. Currently OpenSees has one element to model elastomeric bearings (LDR and LR). These OpenSees elements can be used for two-dimensional or three-dimensional model of isolators. The three-dimensional representation of an isolator and associated degrees of freedom are shown in Figure 2-41.

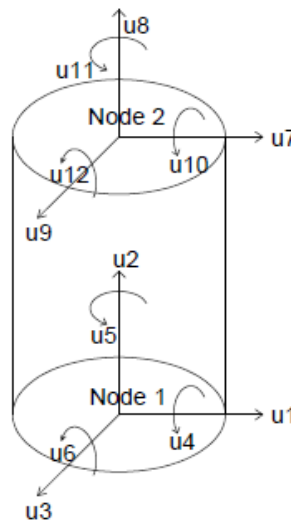


Figure 2-41 OpenSees isolator model

All elements use the model proposed by Park *et al.* (1986), as extended for seismic isolation bearings by Nagarajaiah *et al.* (1991), to capture coupled behavior in the two horizontal shear directions. The elastomeric bearing element (Schellenberg, 2006) uses the mechanical properties of an elastomeric bearing as input parameters to describe the force-deformation relationships. A user can assign any material model available in the OpenSees material library in the vertical (axial) direction. A linear elastic material with vertical stiffness calculated from a two-spring model (Koh and Kelly, 1988; Warn *et al.*, 2007) or a bilinear model (Constantinou *et al.*, 2007) is usually used in the vertical direction. This element cannot capture coupling of

horizontal and vertical motion, cavitation in tension, strength reduction in cyclic tensile loading, heating of the lead core (in LR bearings) under large cyclic displacements, and variations in the critical buckling load of the bearing with horizontal displacement.

2.6.7 Summary

All of the available software programs discussed here are capable of modeling seismic isolators with varying degrees of sophistication. Although, the effort required also depends on user's familiarity with the particular software program, some programs provide a direct option to model an isolator element based on their material, geometrical and mechanical properties, whereas in others, several elements need to be combined to produce isolator-like behavior, or a continuum-based approach needs to be used. The special-purpose software programs used for structural analysis (e.g., SAP2000, OpenSees, PERFORM-3D, and 3D-BASIS) enable modeling of simple isolator behaviors, but complex behaviors (e.g., cavitation, interaction between axial compression and shear stiffness, strength degradation) cannot be captured, except in the open-source code, OpenSees. The general-purpose software programs (LS-DYNA, ABAQUS, and ANSYS) can model complex isolator behaviors using either discrete or continuum approaches. Of the three general-purpose FEA programs discussed here, only LS-DYNA provides a direct option to model an isolator based on its material and geometrical properties. The continuum approach is recommended when the behavior of an individual isolator is to be studied. For analysis of large base-isolated structures, the discrete model will generally have to be used. Table 2-4 presents the capability of the seven programs summarized in this section to model elastomeric bearings. Two new elements have been created by Kumar (2014) for LDR and LR bearing to incorporate these features. Moreover, the new elements take only the geometrical and material properties of elastomeric bearing as input arguments and the appropriate mechanical properties are calculated by the element.

Table 2-4 Modeling of elastomeric seismic isolators and software programs

Properties	3DBASIS	SAP2000	PERFORM3D	LSDYNA	ABAQUS	OpenSees	New elements ¹
Coupled horizontal directions	Yes	Yes	Yes	Yes	Yes	Yes	Yes
Coupled horizontal and vertical directions	No	No	No	No	No	No	Yes
Different tensile and compressive stiffness	No	No	Yes	Yes	Yes	Yes	Yes
Nonlinear tensile behavior	No	No	No	No	Yes	Yes	Yes
Cavitation and post-cavitation	No	No	No	No	No	No	Yes
Nonlinear compressive behavior	No	No	No	No	Yes	Yes	Yes
Varying buckling capacity	No	No	No	No	No	No	Yes
Heating of lead core	No	No	No	No	No	No	Yes

1. New elements created for LDR and LR bearings in OpenSees, ABAQUS, and LS-DYNA at the University at Buffalo, with funding from USNRC

3 MATHEMATICAL MODELS OF ELASTOMERIC BEARINGS

3.1 Introduction

Analysis of elastomeric bearings for extreme loadings requires robust mathematical models that consider all of the properties that are expected to be critical under such loadings. At the same time, these models should be sufficiently simple to be implemented in numerical tools for the analysis of base-isolated structures.

This chapter addresses important aspects of the loading of elastomeric bearings that are expected to affect the response of the isolated structure under extreme loadings. Mathematical formulations to model the considered aspects are presented. These mathematical formulations include numerically robust expressions that have been validated experimentally and new phenomenological equations to model behavior in axial tension. The mechanical behavior in the vertical direction is discussed in Section 3.2, which includes discussion on the behavior of elastomeric bearings in tension and formulation of phenomenological models to simulate the behavior observed experimentally. A mathematical model for mechanical behavior in the vertical direction, applicable to both LDR and LR bearings, is presented at the end of the section. The mechanical behavior in the horizontal direction is discussed in Section 0, and mathematical models are presented at the end of the section.

3.2 Mechanical Behavior in Vertical Direction

3.2.1 General

LDR and LR bearings show similar behavior in the axial direction assuming no contribution from the lead core in either compression or tension. The behavior of elastomeric bearings in pure compression is well established and experimentally validated, and available mathematical models capture the behavior reasonably accurately for regular loading. These models are however not appropriate for extreme loadings where large variations in axial loads and coupling of horizontal and vertical responses needs to be considered. Available mathematical models are extended here to address extreme loadings.

Unlike in compression, no robust mathematical model exists for load-deformation behavior in tension. Response in tension is characterized by highly nonlinear behavior that need to be investigated to formulate an accurate mathematical model.

3.2.2 Coupling of horizontal and vertical response

The coupling of horizontal and vertical response is considered by: 1) variation of shear stiffness with axial load, and 2) dependence of axial stiffness on lateral displacement.

Two models are used for the elastic analysis of elastomeric bearings under axial loading. The continuous beam model (Kelly, 1993; Stanton and Roeder, 1982) is an extension of work of Haringx (1948). The two-spring model (Koh and Kelly, 1987), presented in Figure 3-1, is a simplification of continuous beam model.

The two-spring model provides results that are close to the continuous beam model and is used here to obtain expressions for mechanical properties of elastomeric bearings. The two-spring model has been validated experimentally by Warn *et al.* (2007) and used here owing to its robust formulation and ease of numerical implementation.

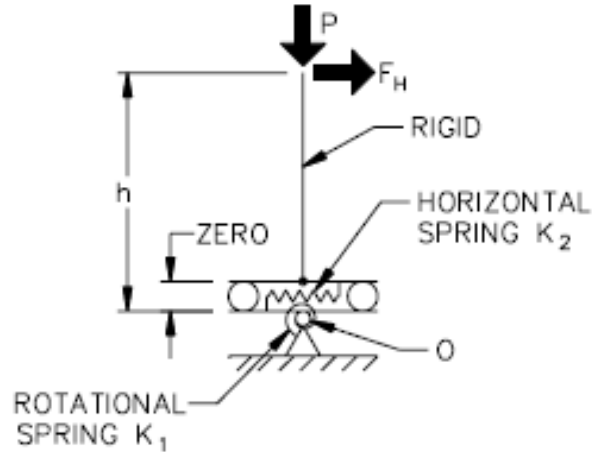


Figure 3-1 Model of an elastomeric bearing (Constantinou *et al.*, 2007)

The vertical stiffness of the elastomeric bearing obtained from the two-spring model is given as:

$$K_v = \frac{AE_c}{T_r} \left[1 + \frac{3}{\pi^2} \left(\frac{u_h}{r_g} \right)^2 \right]^{-1} = K_{v0} \left[1 + \frac{3}{\pi^2} \left(\frac{u_h}{r_g} \right)^2 \right]^{-1} \quad (3.1)$$

where A is the bonded rubber area; E_c is the compression modulus of the bearing calculated as average axial stress divided by the average axial strain in a rubber layer; T_r is the total rubber thickness; u_h is the lateral displacement of the bearing; r_g is the radius of gyration of the bonded rubber area; and K_{v0} is the axial compressive stiffness at zero lateral displacement. The axial load-deformation curve in compression is shown in Figure 3-2. The instantaneous value of the buckling load, P_{cr} , is discussed in the following section.

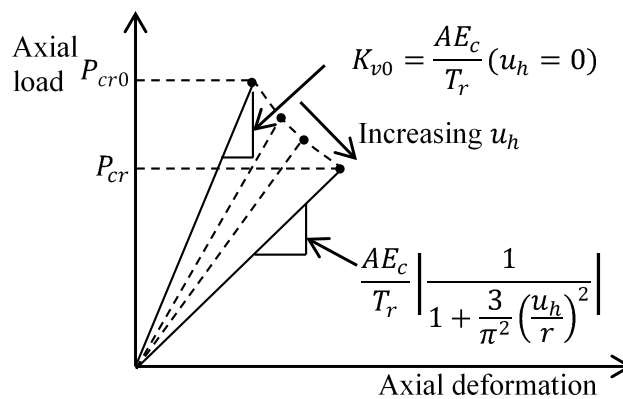


Figure 3-2 Stress softening under compression

The effect of axial load on the horizontal stiffness of an elastomeric bearing becomes important only when the axial load, P , is close to the critical buckling load capacity. Koh and Kelly (1987) provided an analytical expression for the horizontal stiffness, K_H , as a function of the axial load using a two-spring model.

An approximation of the analytical expression for the horizontal stiffness that provides very accurate result is given as (Kelly, 1993):

$$K_H = \frac{GA}{T_r} \left[1 - \left(\frac{P}{P_{cr}} \right)^2 \right] = K_{H0} \left[1 - \left(\frac{P}{P_{cr}} \right)^2 \right] \quad (3.2)$$

where K_{H0} is the shear stiffness at zero axial load, and other terms have been previously defined.

3.2.3 Buckling in compression

The critical buckling load in compression is given by the expression derived from the two-spring model (Koh and Kelly, 1987):

$$P_{cr} = \sqrt{P_S P_E} \quad (3.3)$$

where P_E is the Euler buckling load and is given by:

$$P_E = \frac{\pi^2 E I_s}{h^2} \quad (3.4)$$

and

$$P_S = G A_s \quad (3.5)$$

where A_s and I_s are the shear area and moment of inertia after accounting for the rigidity of steel shims, and are given as:

$$A_s = A \frac{h}{T_r} \quad (3.6)$$

$$I_s = I \frac{h}{T_r} \quad (3.7)$$

where A is the bonded rubber area, I is the area moment of inertia, T_r is total rubber thickness, and h is the total height including the rubber and steel shims but excluding the end plates. The modulus of elasticity here is the rotation modulus:

$$E = E_r \quad (3.8)$$

A list of rotation moduli for different shapes and obtained using different solutions is provided in Constantinou *et al.* (2007). Rotation moduli and compression moduli of an incompressible material of circular and square bearings follow the relationship:

$$E_r = \frac{E_c}{3} \quad (3.9)$$

where E_c is the compression modulus. For circular bearings rotation modulus is $E_r = 2GS^2$.

The critical buckling load in Equation (3.3) varies with lateral displacement. The area reduction method has been shown to provide conservative results (Buckle and Liu, 1993; Buckle *et al.*, 2002; Warn and Whittaker, 2006; Weisman and Warn, 2012). The reduced critical buckling load is:

$$P_{cr} = P_{cr0} \frac{A_r}{A} \quad (3.10)$$

For rectangular bearings of bonded area dimension $B_1 \times B_2$:

$$A_r = B_2 (B_1 - \Delta) \quad (3.11)$$

For circular bearings of bonded area of diameter D :

$$A_r = \frac{D^2}{4} (\delta - \sin \delta) \quad (3.12)$$

where $\delta = 2 \cos^{-1}(\Delta / D)$, and Δ is the lateral displacement of the bearing.

Figure 3-3 shows the overlap area of an elastomeric bearing.

Substituting the value of δ in Equation (3.12), the reduced area can be written as:

$$A_r = \frac{D^2}{4} \left[2 \cos^{-1} \left(\frac{\Delta}{D} \right) - 2 \frac{\Delta \sqrt{D^2 - \Delta^2}}{D^2} \right] \quad (3.13)$$

The area reduction method suggests zero capacity for a bearing at a horizontal displacement equal to the diameter of bearing. However, experiments have shown that a bearing does not lose all of its capacity at $\Delta = D$ but rather retains a residual capacity. The model proposed by Warn and Whittaker (2006) is considered here, which uses a linear approximation of area reduction method and takes into account the finite buckling capacity of a bearing at zero overlap area. The piecewise linear approximation of reduced area model is illustrated in Figure 3-4. The mathematical formulation of model is given by set of equations:

$$P_{cr} = \begin{cases} P_{cr0} \frac{A_r}{A} & \frac{A_r}{A} \geq 0.2 \\ 0.2 P_{cr0} & \frac{A_r}{A} < 0.2 \end{cases} \quad (3.14)$$

where P_{cr0} is the buckling load at zero displacement, and P_{cr} is the buckling load at overlapping area A_r of a bearing with an initial bonded rubber area of A .

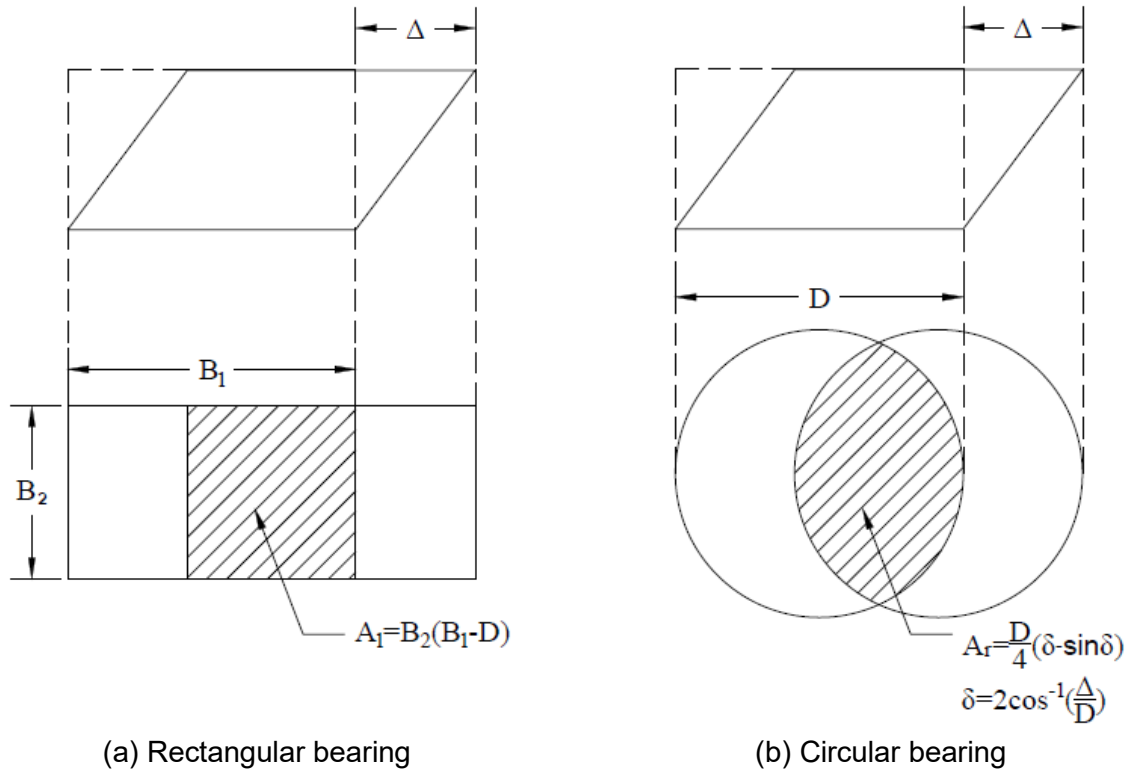


Figure 3-3 Reduced area of elastomeric bearings (adapted from Constantinou *et al.* (2007))

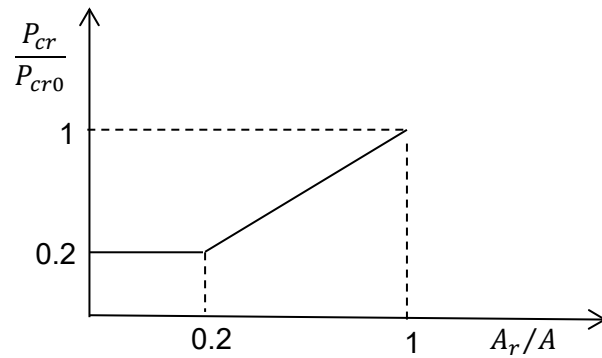


Figure 3-4 Bilinear variation of buckling load

3.2.4 Cavitation in tension

An elastomeric bearing under tensile loading is characterized by the formation of cavities in the volume of rubber. Gent and Lindley (1959b) explained that the fracture inside a rubber layer occurs at a critical hydrostatic stress value that is related to critical value of applied tensile stress. This critical tensile stress is equal to the hydrostatic stress for high shape factor bearings where critical hydrostatic stress is attained uniformly over most of the bonded area, except at the boundaries. This is in contrast to low shape factor bearings where the critical hydrostatic stress is attained only in the central area and value of the critical tensile stress is about half of the critical hydrostatic stress. The critical stress, known as cavitation stress, depends mainly on the rubber compound.

Cavitation is followed by the substantial reduction of the vertical stiffness indicated by a highly discernible transition on the tensile load-deformation curve. The transition becomes smoother as the shape factor decreases and it is generally difficult to locate a cavitation point on load-deformation curve. Gent (1990) suggested that cavitation occurs at a negative pressure of about $3G$, where G is the shear modulus. The cavitation force is given by the expression:

$$F_c = 3GA_0 \quad (3.15)$$

where A_0 is the bonded rubber area and G is the shear modulus of rubber obtained experimentally from the testing of elastomeric bearings at *large shear deformation* under nominal axial loads. The *large shear deformation* is the region in which the shear modulus G is relatively constant, as is explained in a later section.

3.2.5 Post-cavitation behavior

The nonlinear characteristic of natural rubber is influenced by amount of fillers and cross-linking of the polymer chains. The reduction in stiffness after cavitation is due to breakage of rubber-filler bonds. The subsequent increase in stiffness at large strains is due to the limited extensibility of polymer chains and strain crystallization.

Most of the available mathematical models use a very small value of post-cavitation stiffness of an arbitrary magnitude. Constantinou *et al.* (2007) suggested an expression for post-cavitation stiffness as:

$$K_{post-cavitation} = \frac{EA}{T_r} \quad (3.16)$$

where E is the elastic modulus of rubber. Following formation of cracks after cavitation, rubber loses its triaxial state of stress and experiences uniaxial tensile stress. Hence, the elastic modulus used in Equation (3.16) is the Young's modulus of rubber. Elastomers used in seismic isolation (filled rubber) have Young's modulus of about $E = 4G$ (Ciesielski, 1999; Gent, 2001). Here, it is assumed that bonded area of rubber remains the same even after the formation of cracks due to cavitation.

Experiments have shown that the post-cavitation stiffness of elastomeric bearings decreases with increasing tensile deformation. The assumption of constant post-cavitation stiffness needs to be revisited. Assume that area used in Equation (3.16) is the *true area* of bearing excluding the total area of cavities that change with tensile deformation. The *true area* of a bearing is equal to the bonded rubber area at the onset of cavitation and decreases as the number and size of the cavities increase with tensile deformation. The reduction in true area can be attributed to two factors: 1) number of cavities, and 2) size of cavities. The reduction in area of low shape factor bearings is mainly due to the increase in the size of cavities. For high shape factor bearings used in seismic isolation applications, it is due to increase in the number of cavities. A theory is presented below to simulate the observed post-cavitation behavior in elastomeric bearings.

Consider the rubber area to be made up of infinite number of small area elements. Every time a cavity is formed, the area element is eroded. The greater the area, the greater the rate of destruction of area elements. So the rate of reduction of total area with respect to tensile deformation would be proportional to the instantaneous true area at any moment.

Mathematically, the above hypothesis can be expressed as:

$$\frac{\partial A}{\partial u} \propto -A \quad (3.17)$$

$$\frac{\partial A}{\partial u} = -k_c A \quad (3.18)$$

where k_c is defined as cavitation parameter, which is constant for a particular elastomeric bearing and describes the post-cavitation variation of tensile stiffness. The true area of the bearing is equal to the bonded rubber area A_o at onset of cavitation ($u = u_c$) and decreases with tensile deformation. Integrating Equation (3.18), the variation of area with tensile deformation is obtained as:

$$A = A_o e^{-k_c(u-u_c)} \quad (3.19)$$

Instantaneous post-cavitation stiffness of bearing is given by:

$$K_{post-cavitation} = \frac{EA}{T_r} = \frac{EA_o}{T_r} e^{-k_c(u-u_c)} \quad (3.20)$$

If $K_o = \frac{EA_o}{T_r}$ is the initial post-cavitation stiffness just after the cavitation, above equation can be rewritten as:

$$K_{post-cavitation} = K_o e^{-k_c(u-u_c)} \quad (3.21)$$

Equation (3.21) describes the post-cavitation variation of tensile stiffness of an elastomeric bearing. It decreases exponentially, and rate of decrease is controlled by the parameter k_c . To obtain the tensile load variation, post-cavitation stiffness can also be expressed as:

$$K_{post-cavitation} = \frac{\partial F}{\partial u} \quad (3.22)$$

where F is the tensile force in the bearing. Substituting the expression for post-cavitation stiffness in Equation (3.22):

$$\frac{\partial F}{\partial u} = \frac{EA}{T_r} = \frac{EA_o}{T_r} e^{-k_c(u-u_c)} \quad (3.23)$$

The above equation can be integrated to obtain force, F , at any tensile deformation u . Noting that $E = 3G$ for rubber and the cavitation strength $F_c = 3GA_o$, Equation (3.23) can be written as:

$$K_{post-cavitation} = \frac{F_c}{T_r} e^{-k_c(u-u_c)} \quad (3.24)$$

Equation (3.24) can be integrated with limits (F_c, u_c) to (F, u) , to obtain tensile force in the bearing as:

$$F = F_c \left[1 + \frac{1}{k_c T_r} (1 - e^{-k_c(u-u_c)}) \right] \quad (3.25)$$

The relationship in Equation (3.25) can be formulated in terms of stress, σ , and strain, ε . Using the expression $F = \sigma A$, Equation (3.22) can be rewritten as:

$$A \frac{\partial \sigma}{\partial u} + \sigma \frac{\partial A}{\partial u} = \frac{EA_o}{T_r} e^{-k_c(u-u_c)} \quad (3.26)$$

Substituting $\frac{\partial A}{\partial u} = -k_c A$ and $u = k_c T_r \varepsilon$, the above equation is simplified to:

$$\frac{\partial \sigma}{\partial \varepsilon} = E + k_c T_r \sigma \quad (3.27)$$

where $\partial \sigma / \partial \varepsilon$ is the post-cavitation modulus, E_{post} , of an elastomeric bearing. Solving the above differential equation, the expression for post-cavitation stress is obtained as:

$$\sigma = \sigma_c \left[e^{k_c T_r (\varepsilon - \varepsilon_c)} + \frac{1}{k_c T_r} (e^{k_c T_r (\varepsilon - \varepsilon_c)} - 1) \right] \quad (3.28)$$

where $\sigma_c = 3G$ is the cavitation stress in the bearing. The same expression for stress is obtained if the post-cavitation tensile force, F , in Equation (3.25) is divided by the corresponding area, A , in Equation (3.19). The variation of tensile force with tensile deformation is shown in Figure 3-5.

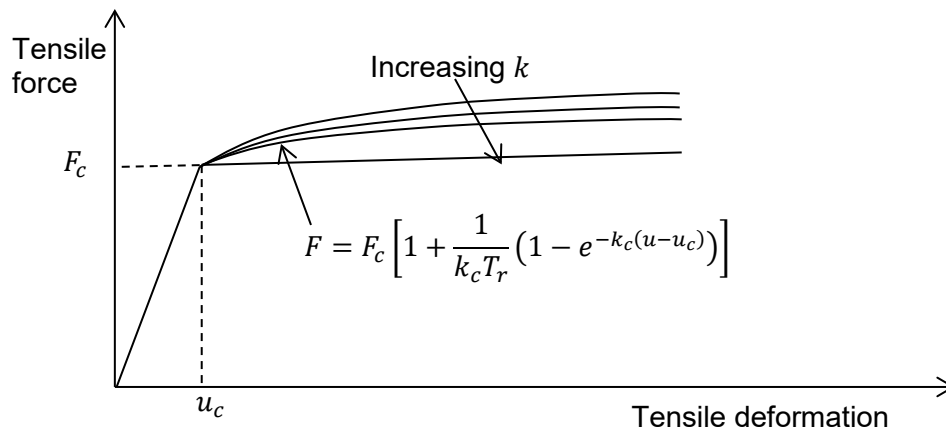


Figure 3-5 Post-cavitation variation of tensile force in the bearing

The constant k_c is obtained by calibration with experimental data and is usually greater than 1. As k_c increases, the slope of the post-cavitation tensile force is reduced and for a very large value of k_c , the bilinear stiffness model discussed in Constantinou *et al.* (2007) is recovered. The proposed model does not capture minor stiffening effects that are observed during tensile loading of elastomeric bearing at large tensile strains (>100%) due to limited extensibility of the polymer chains in rubber.

3.2.6 Strength degradation in cyclic loading

Cavitation in elastomeric bearings is accompanied by the irreversible damage due to the formation of micro cracks in the volume of rubber. When bearing is loaded beyond the point of cavitation and unloaded, it returns along a new path and its cavitation strength is reduced. The area enclosed between the loading and unloading branches is the energy dissipated due to damage. Subsequent loading follows the latest unloading path elastically until the tensile deformation exceeds the prior maximum value u_{max} , below which loading has the effect of only opening and closing existing cavities within the rubber. Once loading exceeds the past maximum value of tensile strain, the formation of new cavities leads to increased damage, and follows the post cavitation behavior defined previously by Equation (3.25). Upon load reversal, the force-displacement relationship traces a new unloading path and the cavitation strength is further reduced. The unloading paths can be approximated by straight lines between the points of maximum force and displacement (F_{max}, u_{max}) and the point of reduced force and displacement (F_{cn}, u_{cn}) . Points (F_{max}, u_{max}) and (F_{cn}, u_{cn}) change with repeated cycling. To capture this behavior mathematically, a damage index ϕ is introduced such that the cavitation force is:

$$F_{cn} = F_c(1 - \phi) \quad (3.29)$$

The damage index ϕ represents the cumulative damage in the bearing ($0 \leq \phi \leq 1$). It is a function of the maximum deformation experienced by the bearing under tensile loading. Mathematically, it can be expressed as $\phi = f(u_{max})$, where f satisfies the following relations: 1) $f(u_c) = 0$ (no strength reduction up to cavitation deformation), and 2) $f(u_{max}) \rightarrow \phi_{max}$ (damage index converges to a maximum value after large deformations). This implies that function f is a nonlinear and monotonically increasing function that is continuous in its domain. Moreover, the damage index converges to a maximum value, ϕ_{max} , requiring f to be an asymptotic function. A function satisfying these properties is given by:

$$\phi = \phi_{max} \left[1 - e^{-a \left(\frac{u - u_c}{u_c} \right)} \right] \quad (3.30)$$

where parameter a is a strength degradation parameter that defines the rate of damage and ϕ_{max} is the maximum damage that can be expected in a bearing. The load-deformation behavior of elastomeric bearings under cyclic tensile loading is summarized in Figure 3-6.

The cavitation strength of bearings decreases from F_c to $F_c(1 - \phi_{max})$ following large strains. The history of loading plays an important role in the characteristics of the response. If the bearing experiences large tensile strains (and hence damage) early in the loading, the subsequent response of bearing will be primarily elastic. If the tensile strain increases incrementally during cyclic loading, damage and energy dissipation would build up progressively.

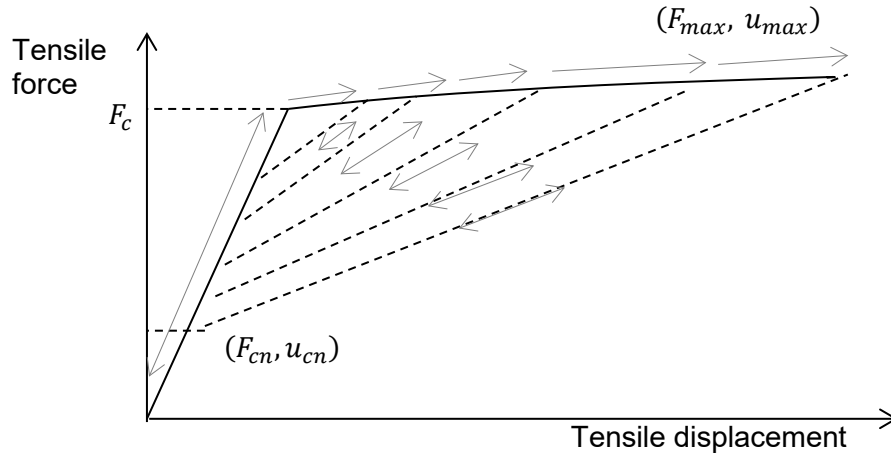


Figure 3-6 Load-deformation behavior of rubber bearings under tension

3.2.7 Mathematical model

A mathematical model of an elastomeric bearing in the axial direction is presented in Figure 3-7. The model captures the following characteristics in the axial direction:

- 1) Buckling in compression
- 2) Coupling of vertical and horizontal motion
- 3) Cavitation
- 4) Post-cavitation variation
- 5) Strength degradation due to cyclic loading

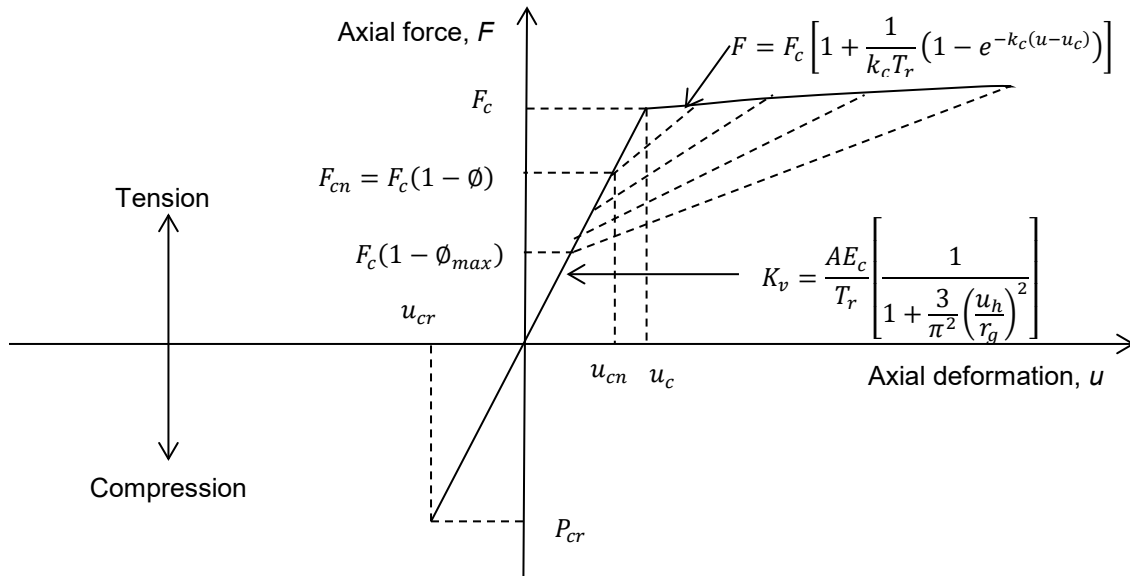


Figure 3-7 Mathematical model of elastomeric bearings in axial direction

The model uses three unknown parameters: 1) a cavitation parameter, k , 2) a strength degradation parameter, a , and 3) a damage index, ϕ_{max} . These parameters should be determined experimentally. However, if an experimental evaluation of parameters is not possible, the user can assign suitable values to the parameters based on previous experimental results on bearings of similar properties.

3.3 Mechanical Behavior in the Horizontal Direction

3.3.1 General

The behavior of elastomeric bearings in shear is well established, and mathematical models exist to reasonably capture the response expected for design basis earthquake for regular structures. These mathematical models use simplified load-deformation relationships and ignore behaviors that might be important under beyond design basis earthquakes during which elastomeric bearings may experience large strains and lateral displacements under time-varying three-dimensional loadings. These models are modified here to include the effects of heating of lead core in LR bearings. The characteristic shear strength of LDR bearing is estimated from an assumed value of equivalent viscous damping, which is discussed in the following sections.

3.3.2 Coupled horizontal response

A smooth hysteretic model is used for elastomeric bearings in horizontal shear, which is based on the model proposed by Park *et al.* (1986) and extended for the analysis of elastomeric bearings under bidirectional motion. The bidirectional smooth bilinear hysteretic model by Park *et al.* (1986) has already been implemented in software programs 3D-BASIS (Nagarajaiah *et al.*, 1989) and SAP2000 (Wilson, 1997).

The model used here is shown in Figure 3-8. Parameters used in the model proposed by Park *et al.* (1986) have been expressed here in the form that is typical of seismic isolation design, namely, initial elastic stiffness K_{el} , characteristic strength Q_d , yield strength F_y , yield displacement Y , and post-elastic stiffness K_d .

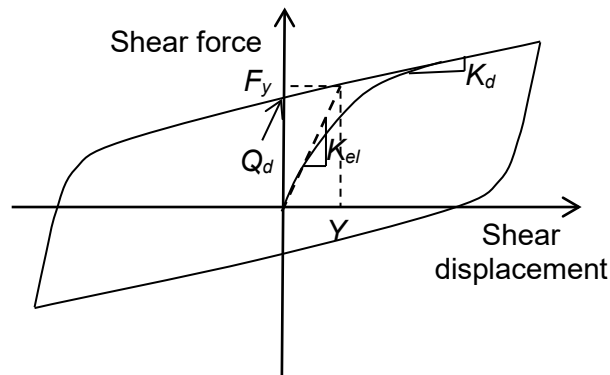


Figure 3-8 Mathematical model of elastomeric bearings in shear

The isotropic formulation of the model in terms of restoring forces in orthogonal directions, F_x and F_y , is given by the equation:

$$\begin{Bmatrix} F_x \\ F_y \end{Bmatrix} = c_d \begin{Bmatrix} \dot{U}_x \\ \dot{U}_y \end{Bmatrix} + K_d \begin{Bmatrix} U_x \\ U_y \end{Bmatrix} + (\sigma_{YL} A_L) \begin{Bmatrix} Z_x \\ Z_y \end{Bmatrix} \quad (3.31)$$

where σ_{YL} is the effective yield stress of confined lead; A_L is the cross sectional area of the lead core, and c_d is a parameter that accounts for the viscous energy dissipation in rubber; and

Z_x and Z_y represent the hysteretic components of the restoring forces. Both Z_x and Z_y have units of displacement and are function of the histories of u_x and u_y .

The biaxial interaction, or coupling, is given by the following differential equation:

$$Y \begin{Bmatrix} \dot{Z}_x \\ \dot{Z}_y \end{Bmatrix} = \left(A[I] - \begin{bmatrix} Z_x^2 (\gamma \text{Sign}(\dot{U}_x Z_x) + \beta) & Z_x Z_y (\gamma \text{Sign}(\dot{U}_y Z_y) + \beta) \\ Z_x Z_y (\gamma \text{Sign}(\dot{U}_x Z_x) + \beta) & Z_y^2 (\gamma \text{Sign}(\dot{U}_y Z_y) + \beta) \end{bmatrix} \right) \begin{Bmatrix} \dot{U}_x \\ \dot{U}_y \end{Bmatrix} \quad (3.32)$$

Parameters γ and β control the shape of the hysteresis loop and A is the amplitude of the restoring force.

When yielding commences, the solution of Equation (3.32) is given by the following equations, provided the parameters satisfy the relationship $A/(\beta + \gamma) = 1$ (Constantinou and Adnane, 1987):

$$Z_x = \cos \theta, \quad Z_y = \sin \theta \quad (3.33)$$

where θ represents the direction of the resultant force with respect to the direction of motion, and is given by expression:

$$\theta = \tan^{-1}(\dot{U}_y / \dot{U}_x) \quad (3.34)$$

The interaction curve given by Equation (3.33) is circular and Z_x and Z_y are bounded by the values of ± 1 .

The first two terms in Equation (3.31) represents the contributions of rubber, and the third term represents the contribution of the lead core, to the total resisting force in the elastomeric bearing.

3.3.3 Heating of the lead core

The effective yield stress of lead used in Equation (3.31) is not constant but decreases with number of cycles of loading due to heating of the lead core (Importantly, it also varies as a function of its confinement by the rubber and steel shims, and the end plates). The extent of the reduction depends on the geometric properties of the bearing and the speed of motion. Kalpakidis and Constantinou (2009b) characterized the dependency of the characteristic strength of a LR bearing on the instantaneous temperature of its lead core, which itself is a function of time.

The set of equations describing heating of the lead core are:

$$\dot{T}_L = \frac{\sigma_{yL}(T_L) \sqrt{Z_x^2 + Z_y^2} \sqrt{\dot{U}_x^2 + \dot{U}_y^2}}{\rho_L c_L h_L} - \frac{k_s T_L}{a \rho_L c_L h_L} \left(\frac{1}{F} + 1.274 \left(\frac{t_s}{a} \right) (\tau)^{-1/3} \right) \quad (3.35)$$

$$F = \begin{cases} 2\left(\frac{\tau}{\pi}\right)^{1/2} - \left(\frac{\tau}{\pi}\right) \left[2 - \left(\frac{\tau}{4}\right) - \left(\frac{\tau}{4}\right)^2 - \frac{15}{4}\left(\frac{\tau}{4}\right)^3 \right], \tau < 0.6 \\ \frac{8}{3\pi} - \frac{1}{2(\pi\tau)^{1/2}} \left[1 - \frac{1}{3(4\tau)} + \frac{1}{6(4\tau)^2} - \frac{1}{12(4\tau)^3} \right], \tau \geq 0.6 \end{cases} \quad (3.36)$$

$$\tau = \frac{\alpha_s t}{a^2} \quad (3.37)$$

$$\sigma_{YL}(T_L) = \sigma_{YL0} e^{-E_2 T_L} \quad (3.38)$$

where h_L is the height of lead core, a is the radius of the lead core, t_s is the total of the shim plates thickness in the bearing, c_L is the specific heat of lead, ρ_L is the density of lead, α_s is the thermal diffusivity of steel, k_s is the thermal conductivity of steel, σ_{YL0} is the effective yield stress of lead at the reference temperature, τ is a dimensionless time parameter and t is the time since the beginning of motion. Figure 3-9 illustrates some of the variables.

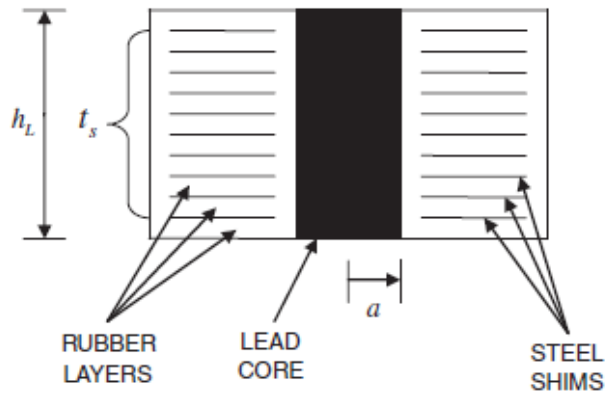


Figure 3-9 Schematic of a LR bearing (Kalpakidis *et al.*, 2010)

Equation (3.38) predicts the characteristic strength of a LR bearing, normalized by the area A_L , as a function of instantaneous temperature obtained from Equation (3.35) through parameter E_2 . Typical values of parameters related to lead and steel are listed in Table 3-1.

Table 3-1 Typical value of lead and steel related parameters (Kalpakidis *et al.*, 2010)

Parameter	Value
ρ_L	11200 kg/m ³
c_L	130 J/(kg°C)
k_s	50 W/(m°C)
α_s	1.4×10^{-5} m ² /s
E_2	0.0069/°C

The term $\sqrt{Z_x^2 + Z_y^2}$ in Equation (3.35) is equal to 1 following yielding under large inelastic deformations, but less than 1 under small elastic deformations. To simplify the numerical

computations, $\sqrt{Z_x^2 + Z_y^2}$ is taken as 1. This assumption has an effect of overestimating the energy dissipation in the lead when displacements are less than the yield displacement, which is not significant because lead-rubber bearings are intended to undergo large inelastic deformations under design basis earthquake loadings.

3.3.4 Equivalent damping

The damping in LR bearings is primarily contributed by energy dissipation in the lead core and contribution of viscous damping due to rubber is typically neglected. The force-displacement loop of an elastomeric bearing is idealized as in Figure 3-10, and the effective period and effective damping of the isolated system are calculated using following equations (AASHTO, 2010; ASCE, 2010):

$$T_{eff} = 2\pi \sqrt{\frac{W}{K_{eff}g}} \quad (3.39)$$

$$K_{eff} = K_d + \frac{Q_d}{D} \quad (3.40)$$

$$\beta_{eff} = \frac{1}{2\pi} \left[\frac{E_D}{K_{eff}D^2} \right] \quad (3.41)$$

where D is the displacement of the system due to earthquake shaking obtained from smoothed response spectra, and E_D is the energy dissipated per cycle at displacement D .

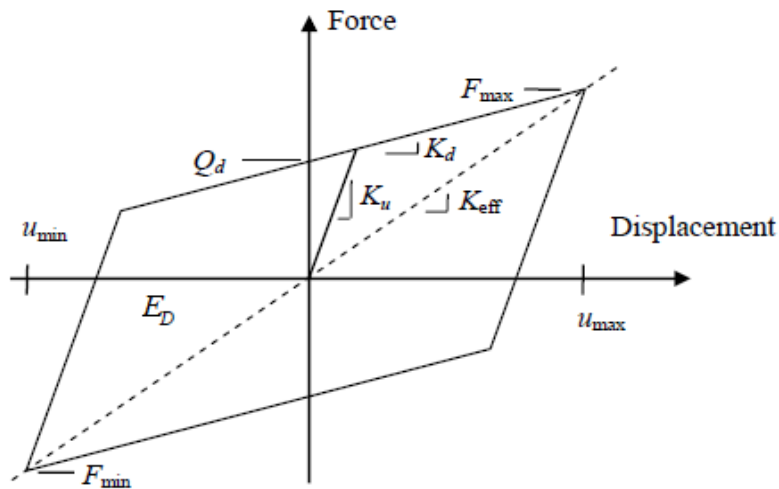


Figure 3-10 Idealized behavior of elastomeric bearings in shear (Warn and Whittaker, 2006)

For the idealized behavior shown in Figure 3-10, E_D is given as:

$$E_D = 4Q_d(D - Y) \quad (3.42)$$

where Y is the yield displacement.

The characteristic strength of a LR bearing is determined using the effective yield stress of the lead. For LDR bearings, the characteristic strength cannot be obtained directly; an effective damping of system is assumed and the characteristic strength is determined as:

$$\beta_{eff} = \frac{1}{2\pi} \left[\frac{4Q_d (D - Y)}{K_{eff} D^2} \right] \leq \frac{2Q_d}{\pi K_d D} \quad (3.43)$$

$$Q_d \geq \frac{\pi}{2} \times \beta_{eff} \times K_d \times D \quad (3.44)$$

If the value of displacement D due to earthquake shaking is known, the characteristic strength of a LDR bearing can be estimated and used in the detailed analysis. A simplified method of analysis for isolated structures is discussed in Constantinou *et al.* (2011).

If the analysis for the estimation of damping in isolated system is not performed, a nominal damping of 2% to 3% can be assumed.

3.3.5 Variation in shear modulus

The effective shear modulus of an elastomeric bearing is obtained from experimental data. Low damping rubber and lead-rubber bearings show viscoelastic and hysteretic behaviors in shear, respectively. The effective stiffness, K_{eff} , is calculated using:

$$K_{eff} = \frac{|F^+| + |F^-|}{|\Delta^+| + |\Delta^-|} \quad (3.45)$$

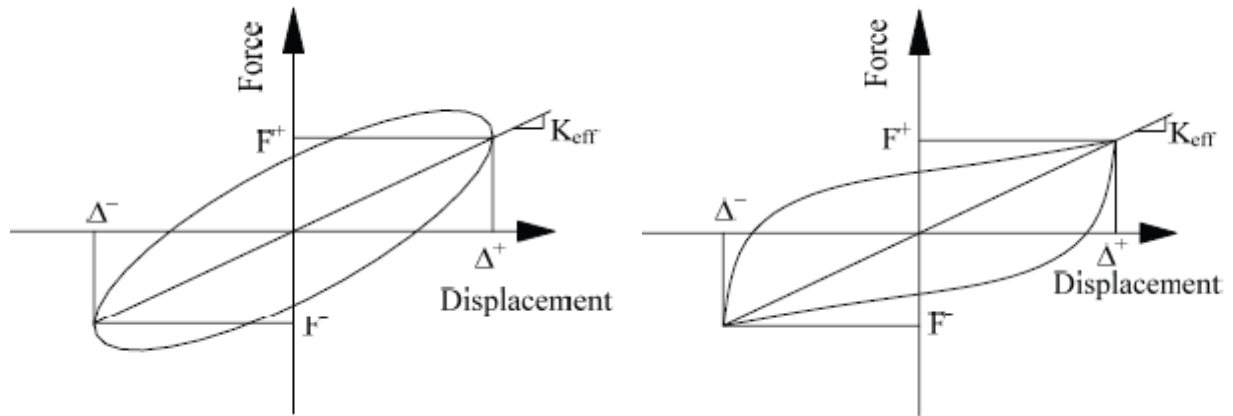
where Δ^+ and Δ^- are the maximum and minimum horizontal displacements obtained from an experiment, and F^+ and F^- are the corresponding forces. Values F^+ and F^- are the maximum and minimum force for the hysteresis case, as shown in Figure 3-11.

The effective shear modulus is subsequently determined using the expression:

$$G_{eff} = \frac{K_{eff} T_r}{A} \quad (3.46)$$

A typical variation of shear modulus with strain is shown in Figure 3-12 for a LDR bearing (bonded diameter = 35.5 inch, shape factor = 26).

Most of the available mathematical models use a constant shear modulus for an elastomeric bearing, although shear modulus varies with strain and axial loads. Increasing the axial pressure reduces the shear modulus. However, if the shear modulus, G , is determined from testing at large strains and under nominal axial pressure, the value of G already includes some effects of axial load. The shear modulus of natural rubber decreases with increasing strain up to 100%, remains relatively constant for shear strain between 100 and 200%, and increases again at shear strains of 200 to 250%. The shear modulus obtained from testing of elastomeric bearings at large strains is used for calculation of shear stiffness of LDR bearings, post-elastic stiffness of LR bearings, and buckling load.



(a) Viscoelastic behavior

(b) Hysteretic behavior

Figure 3-11 Effective stiffness of elastomeric bearings (Constantinou *et al.*, 2007)

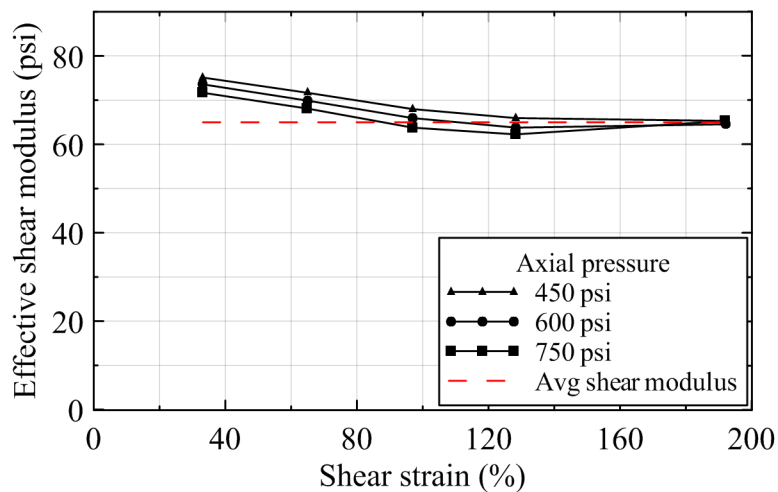


Figure 3-12 Stress and strain dependency of LDR bearings (courtesy of DIS Inc.)

3.3.6 Mathematical model

3.3.6.1 Lead rubber bearings

A mathematical model of LR bearings in horizontal shear is presented in Figure 3-13. The model captures the following characteristics of lead-rubber bearings:

- 1) Nonlinear shear force-deformation behavior
- 2) Bi-directional interaction in the horizontal plane
- 3) Strength degradation due to heating of the lead core

The parameters used here have been defined in previous sections. For numerical implementation, the model is represented as sum of two sub-models: 1) a viscoelastic model of rubber, and 2) an elasto-plastic model of lead, shown in Figure 3-14. The contribution of the rubber to the total resisting force is given by the first two terms in Equation (3.31) and the third terms represents the contribution of the lead core. The sum of all three terms is the restoring force in the LR bearing.

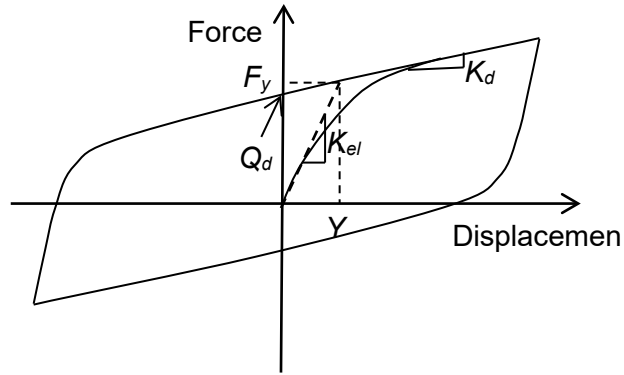


Figure 3-13 Mathematical model of lead rubber bearings in horizontal direction

$$c_d \begin{Bmatrix} \dot{U}_x \\ \dot{U}_y \end{Bmatrix} + K_d \begin{Bmatrix} U_x \\ U_y \end{Bmatrix} + (\sigma_{yL} A_L) \begin{Bmatrix} Z_x \\ Z_y \end{Bmatrix} = \begin{Bmatrix} F_x \\ F_y \end{Bmatrix}$$

Figure 3-14 Alternative representation of the mathematical model

The characteristic strength, or yield stress of the lead core, decreases with the number of cycles under large shear deformation according to Eqns. (3.35) through (3.38). The yield stress of the lead core at the reference temperature (beginning of motion) is obtained experimentally as it depends on the degree of confinement of the lead core in the bearing (Kalpakidis and Constantinou, 2009a).

3.3.6.2 Low damping rubber bearings

The same mathematical model used for the LR bearing is used for the LDR bearing with one modification. The hysteretic term in Equation (3.31), $(\sigma_{yL} A_L) \begin{Bmatrix} Z_x \\ Z_y \end{Bmatrix}$, is replaced by the yield strength of the LDR bearing obtained using the assumed value of effective damping of the system, as explained in Section 3.3.4.

3.3.6.3 High damping rubber bearing

The strain rate-independent bidirectional model proposed by Grant *et al.* (2004) is used to capture the behavior of HDR bearings in shear. This model can capture stiffness and damping degradation in HDR bearings due to short-term (Mullins') effect and long-term (scragging) effects. The model decomposes the resisting force vector into an elastic component parallel to displacement vector and a hysteretic component parallel to the velocity vector. The bidirectional

behavior is described in terms of shear force vector F , displacement vector U , and a unit vector n given as:

$$F = \begin{Bmatrix} F_x \\ F_y \end{Bmatrix} \quad U = \begin{Bmatrix} U_x \\ U_y \end{Bmatrix} \quad n = \frac{\dot{U}}{\|\dot{U}\|} \quad (3.47)$$

where X and y subscript refers to the two perpendicular horizontal directions of a bearing and n is a unit vector in the direction of the velocity.

The bidirectional force vector is:

$$F(U, n, D_S, D_M) = F_1(U, D_S, D_M) + F_2(U, n, D_S) \quad (3.48)$$

where F_1 and F_2 are the elastic and plastic parts of the shear force vector, respectively; and D_S and D_M are the scalar history variables that account for the stiffness and damping degradation.

The mathematical formulation of the elastic component is developed from generalized Mooney-Rivlin strain energy function as following:

$$F_1 = K_{S,1} K_M \left[a_1 + a_2 \|U\|^2 + a_3 \|U\|^4 \right] U \quad (3.49)$$

where a_1 , a_2 , and a_3 are material parameters, and $K_{S,1}$ and K_M are reduction factors to account for stiffness and damping degradation.

The plastic component is given as:

$$F_2 = Rn - \delta\mu \quad (3.50)$$

where R is the radius of a bounding surface in the force space, δ is a scaled distance variable, and μ is a unit distance vector along which distance is measured. The radius R is:

$$R = b_1 + K_{S,2} b_2 \|U\|^2 \quad (3.51)$$

where b_1 and b_2 are material parameters, and $K_{S,2}$ is reduction factor to account for the effect of scragging on hysteretic force.

An *image force* is defined by projecting the unit vector, n , onto the bounding surface:

$$\hat{F} = Rn \quad (3.52)$$

The parameters δ and μ are defined as the magnitude and the direction, respectively, of the vector pointing from the current force to the image force.

$$\delta = \|\hat{F} - F_2\| \quad \mu = \frac{\hat{F} - F_2}{\|\hat{F} - F_2\|} \quad (3.53)$$

The rate of change of direction of the hysteretic force in the F_2 space is defined using:

$$\frac{\dot{F}_2}{\|\dot{F}_2\|} = \mu \quad (3.54)$$

The magnitude of change is defined in terms of the scalar parameter δ using following:

$$\dot{\delta} = -b_3 \delta \|\dot{U}\| \quad (3.55)$$

The numerical implementation of the model is presented in Grant *et al.* (2005).

3.4 Mechanical Behavior in Rotation and Torsion

The torsional and rotational behaviors of elastomeric bearing do not significantly affect the overall response of a seismically isolated structure. Hence, behavior in rotation and torsion are represented by linear elastic springs with stiffnesses calculated as:

Rotation:
$$K_r = \frac{E_r I_s}{T_r} \quad (3.56)$$

Torsion:
$$K_t = \frac{G I_t}{T_r} \quad (3.57)$$

where E_r is the rotation modulus of the bearing, I_s is the moment of inertia about an axis of rotation in the horizontal plane, and I_t is the moment of inertia about the vertical axis. The perpendicular axis theorem implies that for symmetric bearings, $I_t = 2I_s$. Constantinou *et al.* (2007) provides a list of rotation moduli for different shapes of elastomeric bearings. For circular bearings of incompressible rubber, the relationship between compression modulus and rotation modulus is $E_r = E_c / 3$.

4 IMPLEMENTATION OF THE MATHEMATICAL MODELS IN OPENSEES AND ABAQUS

4.1 Introduction

The implementation of the mathematical models of Low Damping Rubber (LDR) and Lead Rubber (LR) bearings presented in Chapter 3 and High Damping Rubber (HDR) bearing proposed by Grant *et al.* (2004) in OpenSees (McKenna *et al.*, 2006) and ABAQUS (Dassault, 2010a) is discussed in this chapter. ABAQUS is a general purpose Finite Element Analysis (FEA) package. New capabilities are added to ABAQUS through user subroutines written in the FORTRAN 77 programming language. The mathematical models of LDR and LR bearings are implemented through a special type of subroutine called User Elements (UELs). OpenSees is an open source platform for computational simulations in earthquake engineering. New capabilities to OpenSees are added by implementation of Element classes using the C++ programming language. Three Element classes are written for the mathematical models of LDR, LR, and HDR bearings.

This chapter describes the addition of new user elements¹ to OpenSees and ABAQUS. The physical model of the elastomeric bearings considered in these software programs is discussed in Section 4.2. Section 4.3 discusses how the algorithms are implemented. The implementation in OpenSees and ABAQUS is discussed in Section 4.4 and 4.5, respectively.

4.2 Physical Model

The 3D continuum geometry of an elastomeric bearing is modeled as a 2-node, 12 DOF discrete element, as shown in Figure 4-1. The two nodes are connected by six springs, which represent the material models in the six basic directions: axial, shear (2), torsional and rotational (2) directions. The discrete spring representation of three-dimensional continuum model is shown in Figure 4-2.

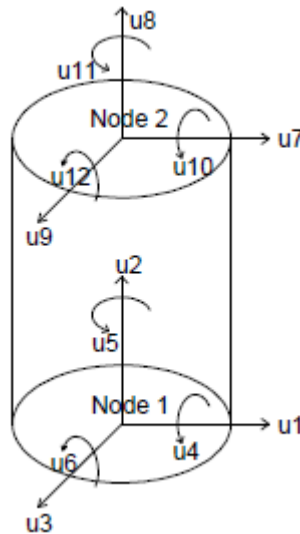


Figure 4-1 Physical model of an elastomeric bearing

¹ The term “user elements” will be used from here on to collectively refer the new elements in OpenSees and ABAQUS, unless a specific distinction is made.

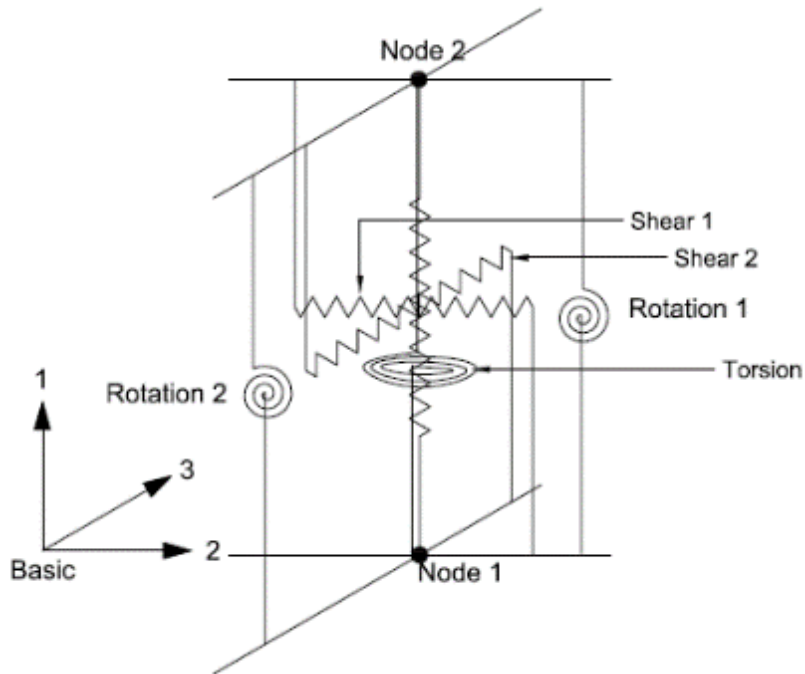


Figure 4-2 Discrete spring representation of an elastomeric bearing

The general form of the element stiffness matrix, K_b , in the basic coordinate system for the element representation considered above is:

$$K_b = \begin{bmatrix} Axial & 0 & 0 & 0 & 0 & 0 \\ 0 & Shear1 & Shear12 & 0 & 0 & 0 \\ 0 & Shear21 & Shear2 & 0 & 0 & 0 \\ 0 & 0 & 0 & Torsion & 0 & 0 \\ 0 & 0 & 0 & 0 & Rotation1 & 0 \\ 0 & 0 & 0 & 0 & 0 & Rotation2 \end{bmatrix} \quad (4.1)$$

and the element force vector in the basic coordinate system is:

$$f_b = \begin{bmatrix} Axial \\ Shear1 \\ Shear2 \\ Torsion \\ Rotation1 \\ Rotation2 \end{bmatrix} \quad (4.2)$$

As discussed in Chapter 3, the coupling of the two horizontal (shear) directions is considered explicitly. The coupling of vertical and horizontal response is accommodated indirectly by using expressions for vertical and shear stiffness that depend on the horizontal shearing displacement and axial load, respectively. Linear uncoupled springs are considered in the torsion and the two rotational springs as they are not expected to significantly affect the response of an elastomeric bearing. The off-diagonal terms due to coupling between axial and shear, and axial and rotation, are not considered in the two-spring model (Koh and Kelly, 1987) used here. An exact model would have non-zero values of these off-diagonal terms. A discussion on the formulation of the two-spring model and the exact model is presented in Ryan *et al.* (2005).

4.2.1 Reference coordinate systems

The force vector and the tangent stiffness matrix are formulated at component level in the element's basic coordinate system. The system of equations for the whole model is solved in the global coordinate system to obtain the model response. Coordinate transformations are used to switch between basic, local, and global coordinates. The quantities in basic, local and global coordinates are designated using subscripts b , l , and g , respectively. A matrix that transforms any vector from coordinate system a to coordinate system b is denoted as T_{ab} . Hence, the transformation matrices, T_{gl} and T_{lb} transform any vector from global to local and local to basic coordinate systems, respectively². Figure 4-3 presents the orientation of coordinate axes used in OpenSees and ABAQUS. The element (or component) forces, displacements, and stiffness matrices are formulated in element's basic coordinate system and transformed from basic to local and then local to global coordinate system. The contribution from each element of the model in the global coordinate system is assembled to obtain the systems of equations for the whole model and solved to obtain nodal responses (e.g., forces, displacements). The nodal response quantities obtained in the global coordinate system are transformed back to the element's basic and local coordinate systems to obtain forces and displacements in the components.

To obtain the transformation matrix, T_{lb} , element deformations in the basic coordinate system are expressed as a function of the element's local displacements. Shear deformations in elastomeric bearings can be caused by rotations as well as translations. Figure 4-4 presents the definitions of axial, shear and bending deformation. These definitions ensure that all deformations will be zero under rigid body motion of the elastomeric bearing. Similar definitions have been used in OpenSees (elastomericBearing element (Schellenberg, 2006)) and SAP2000 (Link/Support element). The shear distance ratio, $sDratio$, is the ratio of distance from Node 1 to the height of bearing where the shear deformations ($u_b(2)$ and $u_b(3)$) are measured. This point is located at the shear center³ of the elastomeric bearing in the 1-2 plane. In most cases, elastomeric bearings are fixed against rotation at both nodes and the shear center is located at the mid-height of the bearing ($sDratio = 0.5$).

² Transformation matrices T and T^T are referred to as element compatibility matrix, b , and T^T is referred to as force compatibility matrix, a , in conventional matrix structural analysis. These two matrices satisfy the contragradience relationship $a = b^T$.

³ The shear center of a cross section is defined as the point about which transverse forces do not produce any rotation. The location of the shear center of a column is the inflection point along the height.

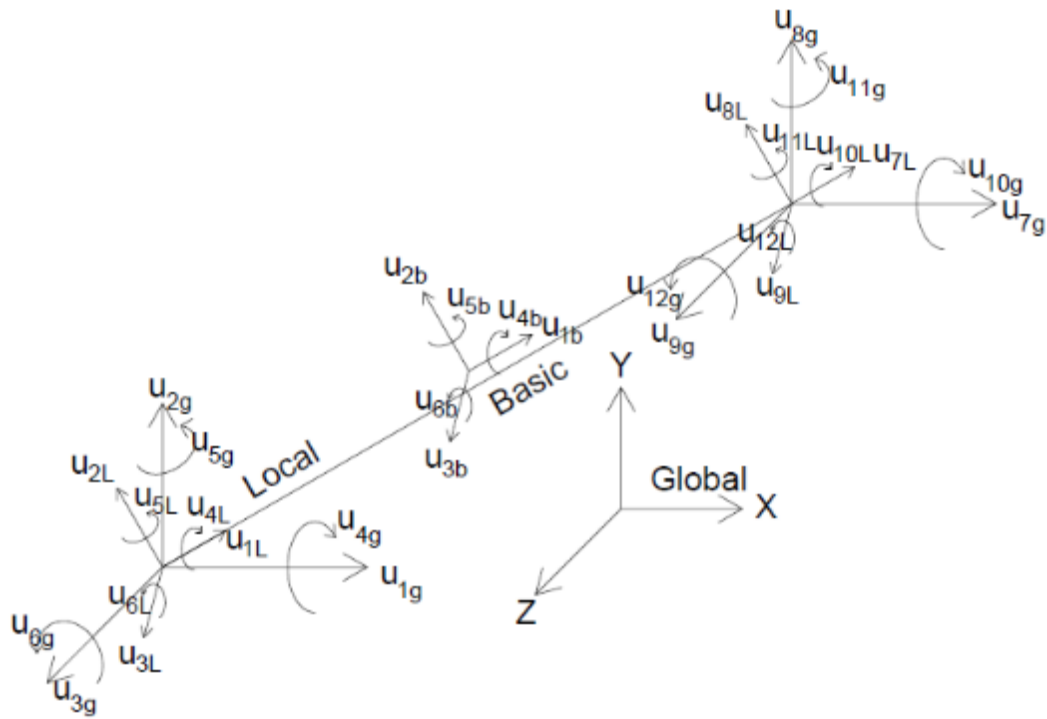


Figure 4-3 Coordinate systems used in OpenSees and ABAQUS

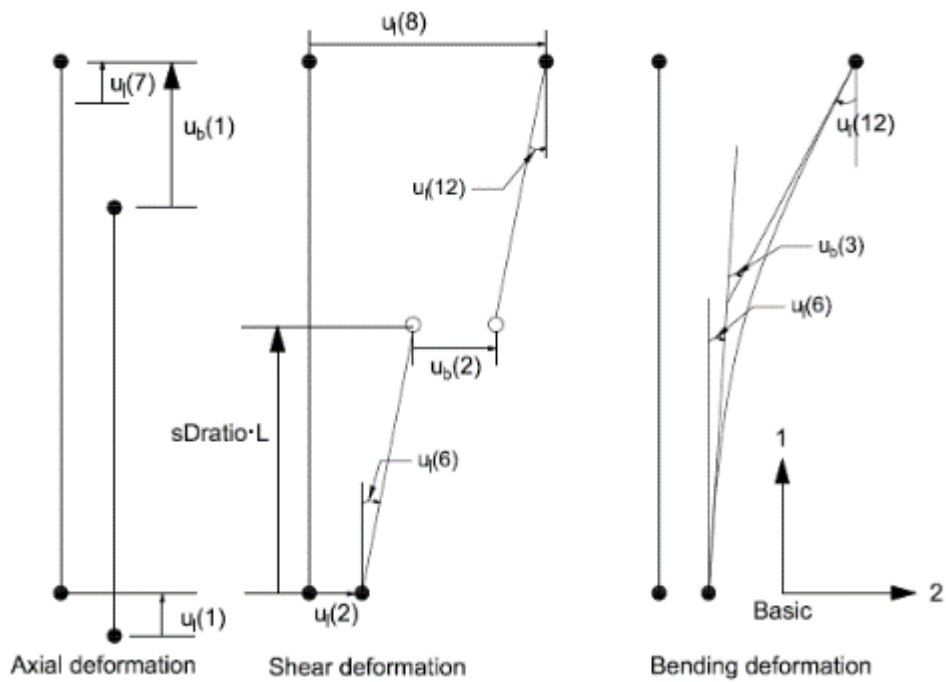


Figure 4-4 Three of the six basic deformations in the 1-2 plane (adapted from CSI (2007))

The relationships between basic and local deformations are given by:

$$\begin{aligned}
u_b(1) &= u_l(7) - u_l(1) \\
u_b(2) &= u_l(8) - u_l(2) - sDratio \cdot L \cdot u_l(6) - (1 - sDratio)L \cdot u_l(12) \\
u_b(3) &= u_l(9) - u_l(3) + sDratio \cdot L \cdot u_l(5) + (1 - sDratio)L \cdot u_l(11) \\
u_b(4) &= u_l(10) - u_l(4) \\
u_b(5) &= u_l(11) - u_l(5) \\
u_b(6) &= u_l(12) - u_l(6)
\end{aligned} \tag{4.3}$$

which can be written in a matrix format as:

$$u_b = T_{lb} u_l \tag{4.4}$$

where T_{lb} is the local-to-basic coordinate transformation matrix that is given by:

$$T_{lb} = \begin{bmatrix} -1 & 0 & 0 & 0 & 0 & 0 & 1 & 0 & 0 & 0 & 0 & 0 \\ 0 & -1 & 0 & 0 & 0 & -sDratio \cdot L & 0 & 1 & 0 & 0 & 0 & -(1 - sDratio)L \\ 0 & 0 & -1 & 0 & sDratio \cdot L & 0 & 0 & 0 & 1 & 0 & (1 - sDratio)L & 0 \\ 0 & 0 & 0 & -1 & 0 & 0 & 0 & 0 & 0 & 1 & 0 & 0 \\ 0 & 0 & 0 & 0 & -1 & 0 & 0 & 0 & 0 & 0 & 1 & 0 \\ 0 & 0 & 0 & 0 & 0 & -1 & 0 & 0 & 0 & 0 & 0 & 1 \end{bmatrix} \tag{4.5}$$

Similarly the relationships between basic and local forces are given by:

$$\begin{aligned}
f_l(1) &= -f_b(1) \\
f_l(2) &= -f_b(2) \\
f_l(3) &= -f_b(3) \\
f_l(4) &= -f_b(4) \\
f_l(5) &= sDratio \cdot L \cdot f_b(3) - f_b(5) \\
f_l(6) &= -sDratio \cdot L \cdot f_b(2) - f_b(6) \\
f_l(7) &= f_b(1) \\
f_l(8) &= f_b(2) \\
f_l(9) &= f_b(3) \\
f_l(10) &= f_b(4) \\
f_l(11) &= (1 - sDratio) \cdot L \cdot f_b(3) + f_b(5) \\
f_l(12) &= -(1 - sDratio) \cdot L \cdot f_b(2) + f_b(6)
\end{aligned} \tag{4.6}$$

which can be written as:

$$f_l = T_{lb}^T f_b \tag{4.7}$$

where f_l and f_b are 6×1 and 12×1 force vectors in local and global coordinates, respectively.

For the transformation between local and global coordinates, consider the two coordinate axis systems and angles between their axes, as presented in Figure 4-5.

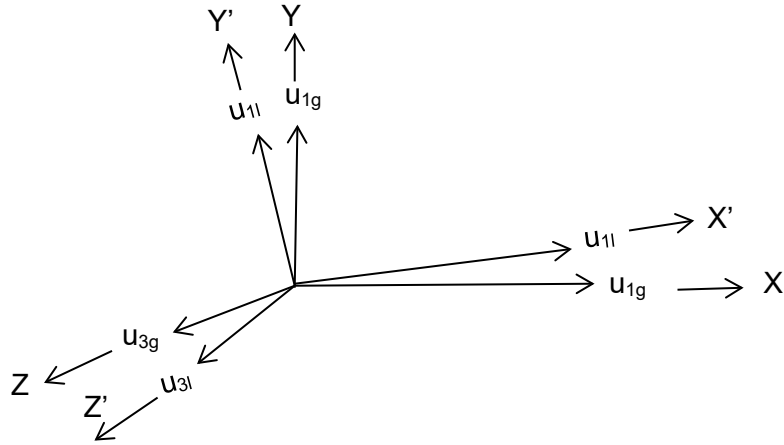


Figure 4-5 Orientation of local and global coordinate axis systems

The global coordinate axes are represented as X , Y , and Z . The local coordinate axes are represented as X' , Y' , and Z' . The direction cosines of the angles between axes are presented in Table 4-1.

Table 4-1 Direction cosines of axes (adapted from Cook (2001))

	X	Y	Z
X'	l_1	m_1	n_1
Y'	l_2	m_2	n_2
Z'	l_3	m_3	n_3

If T_{dc} is a 3×3 direction cosines matrix consisting of the direction cosines presented in Table 4-1, and T_{gl} is the global-to-local coordinate transformation matrix, the relationship between the local and global deformations is:

$$u_l = T_{gl} u_g \quad (4.8)$$

where T_{gl} is 12×12 matrix given as:

$$T_{gl} = \begin{bmatrix} T_{dc} & 0 & 0 & 0 \\ 0 & T_{dc} & 0 & 0 \\ 0 & 0 & T_{dc} & 0 \\ 0 & 0 & 0 & T_{dc} \end{bmatrix} \quad (4.9)$$

The X -axis in the local coordinate system (element's principal axis), which is a vector joining the two nodes of an elastomeric bearing, is obtained as the difference of the nodal coordinates:

$$x = (X_2 - X_1)\hat{i} + (Y_2 - Y_1)\hat{j} + (Z_2 - Z_1)\hat{k} = (X_2 - X_1, Y_2 - Y_1, Z_2 - Z_1) \quad (4.10)$$

In order to obtain the orientation of other two local coordinate axes (y and Z), one of the two coordinate axis vectors needs to be assumed in the beginning, and the other coordinate axis can be obtained as a cross-product of the two known coordinate axis vectors. Finally, the correct orientation of the assumed coordinate axis vector can be obtained as the cross-product of other two coordinate axis vectors.

If the y -axis vector is assumed for the element, the Z -axis vector is obtained as:

$$\begin{aligned} z(1) &= x(2)y(3) - x(3)y(2) \\ z(2) &= x(3)y(1) - x(1)y(3) \\ z(3) &= x(1)y(2) - x(2)y(1) \end{aligned} \quad (4.11)$$

The correct orientation of the y -axis vector is finally obtained as the cross product of the Z and X axis vectors:

$$\begin{aligned} y(1) &= z(2)x(3) - z(3)x(2) \\ y(2) &= z(3)x(1) - z(1)x(3) \\ y(3) &= z(1)x(2) - z(2)x(1) \end{aligned} \quad (4.12)$$

The three local coordinate axis vectors are divided by their respective norms to obtain the unit vectors representing the orientation of three coordinate local axes. The components of unit vectors represent the direction cosines with respect to global coordinate system, and the direction cosines matrix, T_{dc} , and transformation matrix, T_{gl} , can be obtained:

$$T_{dc} = \begin{bmatrix} x(1)/x_n & x(2)/x_n & x(3)/x_n \\ y(1)/y_n & y(2)/y_n & y(3)/y_n \\ z(1)/z_n & z(2)/z_n & z(3)/z_n \end{bmatrix} \quad (4.13)$$

$$T_{gl} = \begin{bmatrix} T_{dc} & 0 & 0 & 0 \\ 0 & T_{dc} & 0 & 0 \\ 0 & 0 & T_{dc} & 0 \\ 0 & 0 & 0 & T_{dc} \end{bmatrix} \quad (4.14)$$

where x_n , y_n , and z_n are the norm of vectors X , y , and Z , respectively.

In OpenSees, same global coordinate system is used for most of the problems (although this is not necessary), which provides an opportunity to assume local y -axis vector to be global X -axis as the default option in the user elements. It also means that orientation of a bearing (local X -axis) cannot be along global X -axis using the default arguments. The user must override default option with their own set of X and y axis vectors to use an arbitrary orientation of bearing in an analysis.

The user elements created in ABAQUS do not allow an arbitrary orientation of elastomeric bearings. The principal axis of a bearing must be along one of the global coordinate axes, X , Y , or Z , which accommodates virtually all cases for seismic isolation in structural analysis.

The direction cosines matrix, T_{dc} , for each of the global coordinate axis are:

$$T_X = \begin{bmatrix} 1 & 0 & 0 \\ 0 & 1 & 0 \\ 0 & 0 & 1 \end{bmatrix}; T_Y = \begin{bmatrix} 0 & 1 & 0 \\ -1 & 0 & 0 \\ 0 & 0 & 1 \end{bmatrix}; T_Z = \begin{bmatrix} 0 & 0 & 1 \\ -1 & 0 & 0 \\ 0 & -1 & 0 \end{bmatrix}; \quad (4.15)$$

If the principal axis (local X -axis) of a bearing is along global Y -axis (vertical direction), the T_Y matrix can be used to obtain T_{gl} using Equation (4.14). Once the transformation matrices are obtained, system of equations can be set up in global coordinates.

The relationship between the local and global forces is given by:

$$f_g = T_{gl}^T f_l \quad (4.16)$$

The load-deformation relationship for the user elements in basic coordinate is:

$$f_b = K_b u_b \quad (4.17)$$

Multiplying both sides of equations by T_{lb}^T and using $u_b = T_{lb} u_l$:

$$T_{lb}^T f_b = T_{lb}^T K_b T_{lb} u_l \quad (4.18)$$

Again multiplying both sides of equations by T_{gl}^T , and noting that $T_{lb}^T f_b = f_l$ and $u_l = T_{gl} u_g$:

$$T_{gl}^T f_l = T_{gl}^T T_{lb}^T K_b T_{lb} T_{gl} u_g \quad (4.19)$$

In Equation (4.19), the expression $T_{gl}^T f_l$ is the force vector in the global coordinate system, f_g . The equation can be written as:

$$f_g = K_g u_g \quad (4.20)$$

where K_g is the global stiffness matrix of the elastomeric bearing and obtained as:

$$K_g = T_{gl}^T T_{lb}^T K_b T_{lb} T_{gl} \quad (4.21)$$

The relationship between global nodal force vector and element's basic forces is:

$$f_g = T_{gl}^T T_{lb}^T f_b \quad (4.22)$$

The stiffness matrix in the global coordinate system, K_g , can be obtained using the element's stiffness matrix, K_b , in the basic coordinate system and transformation matrices using Equation (4.21). Equation (4.20) is solved to obtain nodal forces and displacements in the global coordinate system, which can be transferred back to local and basic coordinates using transformation matrices.

4.3 Numerical Model and Code Implementation

4.3.1 General

The numerical model is constructed from the mathematical model and an algorithm is devised to code the numerical model in OpenSees and ABAQUS using the C++ and FORTRAN programming languages, respectively. The code of a user element includes three main components:

1. Material models definition
2. Geometry definition
3. Mechanical formulation

The primary task of a UEL is to provide the force vector and the stiffness matrix in the global coordinate system. The material models for an elastomeric bearing represented by springs, in the six basic directions, as presented in Chapter 3. The material and geometric properties are used to obtain a mechanical formulation represented by the load-deformation relationship in the global coordinate system. The implementation of the mathematical models for the load-deformation relationships in each direction are presented below.

4.3.2 Material models

4.3.2.1 General

The mechanical behaviors of elastomeric bearings in six directions are represented by linear and nonlinear springs, also referred to as material models. The mathematical models are discretized into numerical models and the algorithms for implementation of the numerical models in software programs are discussed.

Force vectors and stiffness matrices in C++ (OpenSees) and FORTRAN 77 (ABAQUS) are represented by one and two dimensional arrays, respectively. In C++, array elements start with index 0, and in FORTRAN 77 with 1. The indices of array elements correspond to the each of six basic directions. Table 4-2 presents the array indices used to represent the six basic directions in OpenSees and ABAQUS.

The numerical implementation presented in following sections use the array index convention discussed in Section 4.2, which is also the index convention used in ABAQUS (FORTRAN 77).

Table 4-2 Array indices

Direction	OpenSees (C++)	ABAQUS (FORTRAN 77)
Vertical (Axial)	0	1
Horizontal (Shear) 1	1	2
Horizontal (Shear) 2	2	3
Rotation about vertical (Torsion)	3	4
Rotation about horizontal 1	4	5
Rotation about horizontal 2	5	6

4.3.2.2 Vertical (axial) direction

The material behavior of an elastomeric bearing is linear elastic (for zero horizontal displacement) in compression up to buckling. The critical buckling load for an elastomeric bearing depends on the overlap area, which is a function of horizontal displacement. The critical buckling load must be updated after each analysis step. The bilinear approximation to the linear area reduction method (Buckle and Liu, 1993), suggested by Warn and Whittaker (2006), is used.

The horizontal displacement, u_h , in the bearing is calculated as:

$$u_h = \sqrt{u_b(2)^2 + u_b(3)^2} \quad (4.23)$$

The angle subtended by the chord of the overlap area at the center of the bearing is:

$$\delta = 2 \cos^{-1} \frac{u_h}{D_2} \quad (4.24)$$

where D_2 is the outer diameter of the bearing. The reduced overlap area, A_r , is calculated as:

$$A_r = \frac{(D_2)^2}{4} (\delta - \sin \delta) \quad (4.25)$$

The critical load, P_{cr} , at lateral displacement, u_h , is obtained as:

$$P_{cr} = \begin{cases} P_{cr0} \frac{A_r}{A} & \frac{A_r}{A} \geq 0.2 \\ 0.2P_{cr0} & \frac{A_r}{A} < 0.2 \end{cases} \quad (4.26)$$

where P_{cr0} is the buckling load at zero displacement, and P_{cr} is the buckling load at overlapping area A_r of a bearing with an initial bonded rubber area of A .

The vertical stiffness, K_v , depends on the lateral displacement, and is updated at each time-step:

$$K_v = \frac{AE_c}{T_r} \left[1 + \frac{3}{\pi^2} \left(\frac{u_h}{r} \right)^2 \right]^{-1} = K_{v0} \left[1 + \frac{3}{\pi^2} \left(\frac{u_h}{r_g} \right)^2 \right]^{-1} \quad (4.27)$$

where E_c is the compression modulus (Constantinou *et al.*, 2007), u_h is the horizontal displacement, r_g is the radius of gyration of the bonded rubber area, and K_{v0} is the axial compressive stiffness at zero lateral displacement. When the compressive load exceeds the buckling load, the bearing is assumed to have failed and offer no resistance. A very small value of post-buckling axial stiffness (e.g., $K_{v0} / 1000$) is assumed to avoid numerical problems.

Table 4-3 Axial force and stiffness as a function of displacement

Initialization	$F_{cm} = F_{cr}; F_{cr \min} = F_{cr}$ $u_{cr} = F_{cr} / K_{v0}; u_{cm} = u_{cr}$ $F_c = 3GA; F_{cn} = F_c; F_{\max} = F_c$ $u_c = F_c / K_{v0}; u_{cn} = u_c; u_{\max} = u_c$	
State variables update	$u_h = \sqrt{u_b(2)^2 + u_b(3)^2}$	
	$K_v = K_{v0} \left[1 + \frac{3}{\pi^2} \left(\frac{u_h}{r_g} \right)^2 \right]^{-1}$ $u_c = F_c / K_v$	
	$\text{IF } u_b(1) \geq u_{\max} \left\{ \begin{array}{l} u_{\max} = u_b(1) \\ F_{cn} = F_c \left(1 - \left[1 - \exp \left(-a_c \frac{(u_b(0) - u_c)}{u_c} \right) \right] \right) \right\}$	
	$\delta = 2 \cos^{-1} \frac{u_h}{D_2}; A_r = \frac{(D_2 + t_c)^2 - D_1^2}{4} (\delta - \sin \delta)$ $F_{cm} = \begin{cases} F_{cr} \frac{A_r}{A} & \text{IF } \frac{A_r}{A} \geq 0.2 \\ 0.2 F_{cr} & \text{IF } \frac{A_r}{A} < 0.2 \text{ or } \frac{u_h}{D_2} \geq 1.0 \end{cases}$ $\text{IF } F_{cr \min} < F_{cm} \left\{ \begin{array}{l} F_{cr \min} = F_{cm} \\ u_{cn} = \frac{F_{cm}}{K_v} \end{array} \right.$	
	$F_{\max} = F_c \left[1 + \frac{1}{k_c T_r} (1 - \exp(-(u_{\max} - u_c))) \right]$ $u_{cn} = F_{cn} / K_v$	
Force and stiffness update	$u_b(1) \leq u_{cm}$	$K_b(1,1) = K_{v0} / 1000$ $f_b(1) = F_{cr \min} + K_b(1,1)(u_b(1) - u_{cn})$
	$u_{cm} < u_b(1) \leq u_{cn}$	$K_b(1,1) = K_v$ $f_b(1) = K_b(1,1) \times u_b(1)$
	$u_{cn} < u_b(1) \leq u_{\max}$	$K_b(1,1) = (F_{\max} - F_{cn}) / (u_{\max} - u_{cn})$ $f_b(1) = K_b(1,1)(u_b(1) - u_{cn})$

	$u_b(1) > u_{max}$	$K_b(1,1) = \frac{F_c}{T_r} \exp(-k_c(u_b(1) - u_c))$ $F = F_c \left[1 + \frac{1}{k_c T_r} (1 - \exp(-k_c(u_b(1) - u_c))) \right]$
--	--------------------	---

The material behavior is linear elastic (for zero horizontal displacement) in tension up to cavitation followed by linear or nonlinear post-elastic behavior depending on the history of tensile loading. The two transition points in tensile loading are the cavitation (u_{cn} , F_{cn}) and the point of prior maximum tensile displacement (u_{max} , F_{max}). The transition points are updated every time the tensile displacement exceeds the prior maximum value, u_{max} . The cavitation point (u_{cn} , F_{cn}) starts with initial values of (u_c , F_c), the initial cavitation point, and then changes under cyclic loading. Table 4-3 presents the entries in the stiffness matrix, K_b , and nodal force vector, f_b , corresponding to axial direction as a function of axial displacement.

4.3.2.3 Horizontal Direction

4.3.2.3.1 General

The horizontal shear behavior of LDR and LR bearings is modeled using an extension of the Bouc-Wen model (Park *et al.*, 1986; Wen, 1976). The model proposed by Grant *et al.* (2004) is used for HDR bearings. The numerical formulations start with the construction of a stiffness matrix, and force and displacements vectors in the basic coordinate system. The stiffness matrix and nodal response quantities are converted from the basic to the global coordinate system through transformation matrices described previously. The formulation of these models are presented in the following sections.

4.3.2.3.2 Low damping and lead rubber bearings

Two numerical models and their implementation algorithms are presented here. The bidirectional formulation of the Bouc-Wen model and the plasticity model are used. Both models are represented as the sum of a viscoelastic model of rubber and a hysteretic model of the lead core, as shown in Figure 4-6. The key difference between the two models is the smooth transition from elastic to plastic force-displacement behavior in Bouc-Wen model. Figure 4-6 shows the sharp transition in the plasticity formulation.

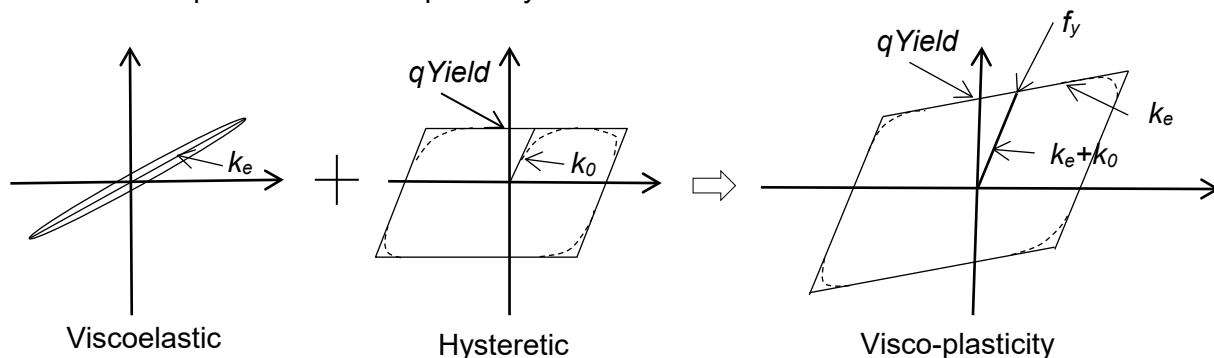


Figure 4-6 Components of the numerical model of elastomeric bearing

The viscoelastic component has the elastic stiffness, k_e , and the hysteretic component has an initial elastic stiffness k_0 . The sum of these two models (the mathematical model of elastomeric

bearing in shear) has initial stiffness $k_e + k_0$ and post-yield stiffness k_e . A parameter α is often assumed in an analysis, which is the ratio of the post-yield stiffness to the initial stiffness of an elastomeric bearing:

$$\alpha = \frac{k_e}{k_e + k_0} \quad (4.28)$$

The post-yield stiffness, k_e , of an elastomeric bearing is:

$$k_e = \frac{GA}{T_r} \quad (4.29)$$

For given value of α , the initial stiffness of hysteretic component can be calculated using:

$$k_0 = \left(\frac{1}{\alpha} - 1 \right) k_e \quad (4.30)$$

The yield strength of hysteretic component (or characteristic strength of elastomeric bearing), $qYield$, is calculated as product of yield stress of lead and the area A_L of the lead core for LR bearing, while for LDR bearing it is calculated by assuming a nominal value of damping (described in Chapter 3). If $qYield$ is known, the yield strength, f_y , of elastomeric bearing can be obtained using:

$$f_y = \frac{qYield}{1 - \alpha} \quad (4.31)$$

The formulations the Bouc-Wen model and the plasticity model using the parameters obtained from Equation (4.28) through (4.31) are discussed in the following sections.

4.3.2.3.3 Bouc-Wen formulation

A smooth hysteretic model is used for elastomeric bearings in horizontal shear, which is based on the model proposed by Park *et al.* (1986) and extended for the analysis of elastomeric bearings under bidirectional motion (Nagarajaiah *et al.*, 1989). The bidirectional smooth hysteretic model by Park *et al.* (1986) has already been implemented in software programs 3D-BASIS (Nagarajaiah *et al.*, 1989) and SAP2000 (Wilson, 1997). A detailed discussion on this mathematical model was presented in Chapter 3. The numerical implementation is presented here.

The isotropic formulation of the model in terms of restoring forces in two horizontal orthogonal directions, represented by indices 2 and 3, is given by the equation:

$$\begin{Bmatrix} f_b(2) \\ f_b(3) \end{Bmatrix} = c_d \begin{Bmatrix} \dot{u}_b(2) \\ \dot{u}_b(3) \end{Bmatrix} + k_e \begin{Bmatrix} u_b(2) \\ u_b(3) \end{Bmatrix} + (qYield) \begin{Bmatrix} z(1) \\ z(2) \end{Bmatrix} \quad (4.32)$$

where f_b , u_b and \dot{u}_b are the force, displacement and velocity in the basic coordinate system, k_e is the elastic stiffness of rubber (also the post-elastic stiffness of the bearing), c_d is a parameter

that accounts for the viscous energy dissipation in the rubber, and $qYield$ is the yield strength of hysteretic part (also the characteristic shear strength of the bearing).

The first two terms in Equation (4.32) represent the resisting force in the rubber and the third term represents the resisting force in the hysteretic component (the lead core in the LR bearing). The hysteretic evolution parameter, $\mathbf{Z} = [z(1) \ z(2)]^T$, is used to calculate the resisting force in the bearing due to the hysteretic component using the following equation:

$$u_y \begin{Bmatrix} \dot{z}(1) \\ \dot{z}(2) \end{Bmatrix} = (A[I] - [\Omega]) \begin{Bmatrix} \dot{u}_b(2) \\ \dot{u}_b(3) \end{Bmatrix} \quad (4.33)$$

where matrix Ω is given by:

$$\Omega = \begin{bmatrix} z(1)^2 (\gamma \text{Sign}(\dot{u}_b(2)z(1)) + \beta) & z(1)z(2) (\gamma \text{Sign}(\dot{u}_b(3)z(2)) + \beta) \\ z(1)z(2) (\gamma \text{Sign}(\dot{u}_b(2)z(1)) + \beta) & z(2)^2 (\gamma \text{Sign}(\dot{u}_b(3)z(2)) + \beta) \end{bmatrix} \quad (4.34)$$

The above equations are solved numerically using the Newton-Raphson method, which provides a single expression for \mathbf{Z} and allows for a smooth transition from the elastic to the plastic region.

Noting that $x \cdot \text{sgn}(x) = |x|$, and $|\dot{x}| = \left| \frac{\Delta x}{\Delta t} \right| = \frac{|\Delta x|}{\Delta t} = \frac{\Delta x \cdot \text{sgn}(\Delta x)}{\Delta t}$, the incremental form of Equation (4.33) describing the evolution of hysteretic parameter \mathbf{Z} is:

$$\begin{Bmatrix} \Delta z(1) \\ \Delta z(1) \end{Bmatrix} = \frac{1}{u_y} (A[I] - [\Delta\Omega]) \begin{Bmatrix} \Delta u_b(2) \\ \Delta u_b(3) \end{Bmatrix} \quad (4.35)$$

where matrix $\Delta\Omega$ is given by:

$$\Delta\Omega = \begin{bmatrix} z(1)^2 (\gamma \text{Sign}(\Delta u(2)z(1)) + \beta) & z(1)z(2) (\gamma \text{Sign}(\Delta u(3)z(2)) + \beta) \\ z(1)z(2) (\gamma \text{Sign}(\Delta u(2)z(1)) + \beta) & z(2)^2 (\gamma \text{Sign}(\Delta u(3)z(2)) + \beta) \end{bmatrix} \quad (4.36)$$

where Δ is the increment from step n to $n+1$ given as $\Delta(\) = \Delta(\)_{n+1} - \Delta(\)_n$. Hence, for variable \mathbf{Z} , $\Delta z(1) = z_{n+1}(1) - z_n(1)$ and $\Delta z(2) = z_{n+1}(2) - z_n(2) = z_{n+1}(2) - z_c(2)$, where \mathbf{Z} represents the $(n+1)$ th step and z_c the n th step (also referred to as committed or converged step in OpenSees).

Define three temporary variables as:

$$tmp1 = \gamma \text{Sign}(\Delta u_b(2)z(1)) + \beta \quad (4.37)$$

$$tmp2 = \gamma \text{Sign}(\Delta u_b(3)z(2)) + \beta \quad (4.38)$$

$$tmp3 = z(1)\Delta u_b(2)tmp1 + z(2)\Delta u_b(3)tmp2 \quad (4.39)$$

Using the Newton-Raphson method, a solution of equation $f = 0$ is sought, where f is:

$$f = \begin{Bmatrix} \Delta z(1) \\ \Delta z(2) \end{Bmatrix} - \frac{1}{u_y} (A[I] - [\Delta\Omega]) \begin{Bmatrix} \Delta u_b(2) \\ \Delta u_b(3) \end{Bmatrix} \quad (4.40)$$

which can be written in terms of temporary variables as:

or,

$$f = \begin{Bmatrix} z(1) - z_c(1) - \frac{1}{u_y} (A\Delta u(2) - z(1)tmp3) \\ z(2) - z_c(2) - \frac{1}{u_y} (A\Delta u(3) - z(2)tmp3) \end{Bmatrix} \quad (4.41)$$

The gradient Df is then calculated as:

$$Df = \begin{bmatrix} \frac{\partial f(1)}{\partial z(1)} & \frac{\partial f(1)}{\partial z(2)} \\ \frac{\partial f(2)}{\partial z(1)} & \frac{\partial f(2)}{\partial z(2)} \end{bmatrix} \quad (4.42)$$

where,

$$Df(1,1) = \frac{\partial f(1)}{\partial z(1)} = 1 + \frac{1}{u_y} (2z(1)\Delta u_b(2)tmp1 + z(2)\Delta u_b(3)tmp2) \quad (4.43)$$

$$Df(1,2) = \frac{\partial f(1)}{\partial z(2)} = \frac{tmp2}{u_y} z(1)\Delta u_b(3) \quad (4.44)$$

$$Df(2,1) = \frac{\partial f(2)}{\partial z(1)} = \frac{tmp1}{u_y} z(2)\Delta u_b(2) \quad (4.45)$$

$$Df(2,2) = \frac{\partial f(2)}{\partial z(2)} = 1 + \frac{1}{u_y} (2z(1)\Delta u_b(2)tmp1 + z(2)\Delta u_b(3)tmp2) \quad (4.46)$$

The first estimate of the solution Z of equation $f = 0$, is obtained using:

$$\Delta z = \frac{f}{Df} \quad (4.47)$$

The solution of above equation is:

$$\Delta z(0) = \frac{f(1)Df(2,2) - f(2)Df(1,2)}{Df(1,1)Df(2,2) - Df(1,2)Df(2,1)} \quad (4.48)$$

$$\Delta z(1) = \frac{f(1)Df(2,1) - f(2)Df(1,1)}{Df(1,2)Df(2,1) - Df(1,1)Df(2,2)} \quad (4.49)$$

The above steps are repeated and the value of Z after a number of iteration is:

$$z = z - \frac{f}{Df} \quad (4.50)$$

The number of iterations is dictated by accuracy desired for the solution Z . When Δz becomes smaller than a defined tolerance, the solution is assumed to have converged.

Once the value of the hysteretic parameter is obtained, its derivatives with respect to horizontal displacements ($dzdu$ matrix) are obtained using following sets of equations:

$$\frac{\partial u_b(2)}{\partial u_b(3)} = \frac{\Delta u_b(2)}{\Delta u_b(3)}, \quad \frac{\partial u_b(3)}{\partial u_b(2)} = \frac{\Delta u_b(3)}{\Delta u_b(2)} \quad (4.51)$$

$$dzdu(1,1) = \frac{\partial z(1)}{\partial u(2)} = \frac{1}{u_y} \left(A - z(1) \left(z(1)tmp1 + z(2)tmp2 \frac{\partial u_b(3)}{\partial u_b(2)} \right) \right) \quad (4.52)$$

$$dzdu(1,2) = \frac{\partial z(1)}{\partial u(3)} = \frac{1}{u_y} \left(A \frac{\partial u_b(2)}{\partial u_b(3)} - z(1) \left(z(1)tmp1 \frac{\partial u_b(2)}{\partial u_b(3)} + z(2)tmp2 \right) \right) \quad (4.53)$$

$$dzdu(2,1) = \frac{\partial z(2)}{\partial u(2)} = \frac{1}{u_y} \left(A \frac{\partial u_b(3)}{\partial u_b(2)} - z(2) \left(z(1)tmp1 + z(2)tmp2 \frac{\partial u_b(3)}{\partial u_b(2)} \right) \right) \quad (4.54)$$

$$dzdu(2,2) = \frac{\partial z(2)}{\partial u(3)} = \frac{1}{u_y} \left(A - z(2) \left(z(1)tmp1 \frac{\partial u_b(2)}{\partial u_b(3)} + z(2)tmp2 \right) \right) \quad (4.55)$$

The shear force in two the horizontal directions are:

$$f_b(2) = c_d \cdot \dot{u}_b(2) + qYield \cdot z(1) + k_e \cdot u_b(2) \quad (4.56)$$

$$f_b(3) = c_d \cdot \dot{u}_b(3) + qYield \cdot z(2) + k_e \cdot u_b(3) \quad (4.57)$$

The coupled tangent stiffness terms of the basic stiffness matrix in the two horizontal directions are:

$$\begin{aligned}
 K_b(2,2) &= \frac{c_d}{\Delta t} + qYield \frac{\partial z(1)}{\partial u_b(2)} + k_e \\
 K_b(2,3) &= qYield \frac{\partial z(1)}{\partial u_b(3)} \\
 K_b(3,2) &= qYield \frac{\partial z(2)}{\partial u_b(2)} \\
 K_b(3,3) &= \frac{c_d}{\Delta t} + qYield \frac{\partial z(2)}{\partial u_b(3)} + k_e
 \end{aligned} \tag{4.58}$$

4.3.2.3.4 Plasticity formulation

For the plasticity model, the displacements of the hysteretic component, $u_{bPlastic}$ in the two horizontal directions are used as state variables. The 2×1 vector $qTrial$ of trial shear forces of the hysteretic component in two horizontal directions is calculated as:

$$\begin{aligned}
 qTrial(1) &= k_0 (u_b(2) - u_{bPlastic}(1)) \\
 qTrial(2) &= k_0 (u_b(3) - u_{bPlastic}(2))
 \end{aligned} \tag{4.59}$$

The resultant of trial shear forces is:

$$qTrialNorm = \sqrt{qTrial(1)^2 + qTrial(2)^2} \tag{4.60}$$

A dummy parameter Y is defined to determine transition from elastic to plastic behavior.

$$Y = qTrialNorm - qYield \tag{4.61}$$

where $Y \leq 0$ represents the elastic region and $Y \geq 0$ represents the plastic region. For the elastic region, the nodal forces in basic coordinate system are:

$$\begin{aligned}
 f_b(2) &= k_e u_b(2) + qTrial(1) \\
 f_b(3) &= k_e u_b(3) + qTrial(2)
 \end{aligned} \tag{4.62}$$

and shear stiffnesses in two horizontal directions are:

$$\begin{aligned}
K_b(2,2) &= \frac{\partial(f_b(2))}{\partial(u_b(2))} = k_e + k_0 \\
K_b(3,3) &= \frac{\partial(f_b(3))}{\partial(u_b(3))} = k_e + k_0 \\
K_b(2,3) &= \frac{\partial(f_b(2))}{\partial(u_b(3))} = 0 \\
K_b(3,2) &= \frac{\partial(f_b(3))}{\partial(u_b(2))} = 0
\end{aligned} \tag{4.63}$$

For the plastic region ($Y \geq 0$), the hysteretic components of the forces in each direction are distributed in the ratios of their trial shear forces. The nodal forces in each direction are given as:

$$\begin{aligned}
f_b(2) &= c_d \dot{u}_b(2) + k_e u_b(2) + \frac{qYield \times qTrial(1)}{qTrialNorm} \\
f_b(3) &= c_d \dot{u}_b(3) + k_e u_b(3) + \frac{qYield \times qTrial(2)}{qTrialNorm}
\end{aligned} \tag{4.64}$$

The shear stiffnesses in two directions are given as:

$$K_b(2,2) = \frac{\partial(f_b(2))}{\partial(u_b(2))} = \frac{\partial(f_b(2))}{\partial(\dot{u}_b(2))} \times \frac{\partial(\dot{u}_b(2))}{\partial(u_b(2))} + \frac{\partial(f_b(2))}{\partial(u_b(2))} = \frac{c_d}{\Delta t} + k_e + k_0 \times \frac{qYield \times qTrial(2)^2}{qTrialNorm^3} \tag{4.65}$$

$$K_b(3,3) = \frac{\partial(f_b(3))}{\partial(\dot{u}_b(3))} \times \frac{\partial(\dot{u}_b(3))}{\partial(u_b(3))} + \frac{\partial(f_b(3))}{\partial(u_b(3))} = \frac{c_d}{\Delta t} + k_e + k_0 \times \frac{qYield \times qTrial(1)^2}{qTrialNorm^3} \tag{4.66}$$

$$K_b(2,3) = \frac{\partial(f_b(2))}{\partial(u_b(3))} = -k_0 \times \frac{qYield \times qTrial(1) \times qTrial(2)}{qTrialNorm^3} \tag{4.67}$$

$$K_b(3,2) = \frac{\partial(f_b(3))}{\partial(u_b(2))} = -k_0 \times \frac{qYield \times qTrial(1) \times qTrial(2)}{qTrialNorm^3} \tag{4.68}$$

Note that $\partial(\dot{u}_b(2)) / \partial(u_b(2)) = 1 / \Delta t$ is the stiffness contribution from the viscous component of the rubber.

The resultant plastic displacement is calculated by dividing the parameter Y by the initial elastic stiffness of hysteretic component, k_0 . The parameter Y is the excess force above the yield strength in the elastomeric bearing and dividing it by k_0 gives the equivalent plastic

displacement, $dGamma$, which is another dummy parameter (known as the return-mapping parameter). This plastic displacement is then distributed between the two horizontal directions in the ratio of their trial hysteretic forces. The plastic displacements are updated after every step as:

$$\begin{aligned} u_{bPlastic}(1) &= u_{bPlasticC}(1) + dGamma \frac{qTrial(1)}{qTrialNorm} \\ u_{bPlastic}(2) &= u_{bPlasticC}(2) + dGamma \frac{qTrial(2)}{qTrialNorm} \end{aligned} \quad (4.69)$$

where $u_{bPlasticC}$ is the plastic displacement from the last time step.

4.3.2.4 Rotational and torsional directions

The other three directions of the physical model of an elastomeric bearing are torsion about the axial direction and rotations about the two horizontal directions. The torsional and rotational behaviors of elastomeric bearings do not significantly affect the overall response of a seismically isolated structure. Accordingly, the three directions are represented by springs with linear elastic stiffnesses as:

$$\text{Torsional direction:} \quad K_b(4,4) = \frac{2GI_r}{T_r} \quad (4.70)$$

$$\text{Rotational directions} \quad K_b(5,5) = K_b(6,6) = \frac{E_r I_r}{T_r} \quad (4.71)$$

where parameters are defined in Chapter 3.

The nodal forces in the basic coordinate system are:

$$\begin{aligned} f_b(4) &= K_b(4,4) \times u_b(4) \\ f_b(5) &= K_b(5,5) \times u_b(5) \\ f_b(6) &= K_b(6,6) \times u_b(6) \end{aligned} \quad (4.72)$$

4.3.2.5 High damping rubber bearings

The model of HDR bearings in shear proposed by Grant *et al.* (2004) is used. A detailed discussion on the numerical implementation of the model is provided in Grant *et al.* (2005) and is not repeated here.

4.3.3 Nonlinear geometric effects

For analysis of structures assuming linear geometry, the element equilibrium equations are satisfied in the undeformed configuration and the compatibility relationship between element deformations (in the basic coordinate system) and end displacements in the global coordinate system does not depend on the displacements. Elastomeric bearings may experience large displacements under beyond design earthquake shaking, and the effects of the geometric nonlinearity should be considered by satisfying the element equilibrium equations in the

deformed configuration and using nonlinear compatibility relationship between element deformations and end displacements in the global coordinate system.

There are two ways to consider geometric nonlinearity in the analysis of elastomeric bearings: 1) considering $P - \Delta$ effects to satisfy the element equilibrium equations in the deformed condition, or, 2) using analytical expressions for the mechanical properties of elastomeric bearings that have been derived considering geometrical nonlinearity.

For applications in earthquake engineering, considering $P - \Delta$ effects is an approximate method to account for geometric nonlinearity. The axial load, P , at a lateral displacement, Δ , results in a $P - \Delta$ moment. This moment can be replaced by an equivalent force couple. Figure 4-7 shows the inclusion of $P - \Delta$ in the analysis of a multistory building. The lateral force-displacement relationship that should be included in the formulation to account for $P - \Delta$ effects is:

$$\begin{Bmatrix} f_i \\ f_{i+1} \end{Bmatrix} = \frac{W_i}{h_i} \begin{bmatrix} 1.0 & -1.0 \\ -1.0 & 1.0 \end{bmatrix} \begin{Bmatrix} u_i \\ u_{i+1} \end{Bmatrix} \quad (4.73)$$

$$f_{P\Delta} = K_G u \quad (4.74)$$

where K_G is $P - \Delta$ geometric stiffness matrix.

The lateral forces due to $P - \Delta$ moments are evaluated for all the stories of the building and are added to the overall lateral equilibrium of building to solve for the nodal displacements.

$$F = (K + K_G) u \quad (4.75)$$

When internal forces in the members are obtained from these displacements using linear theory, equilibrium equations are found to be satisfied in the deformed configuration. Hence, including $P - \Delta$ effects allows one to satisfy equilibrium in the deformed configuration without any explicit consideration of geometric nonlinearity in the element equilibrium and compatibility equations.

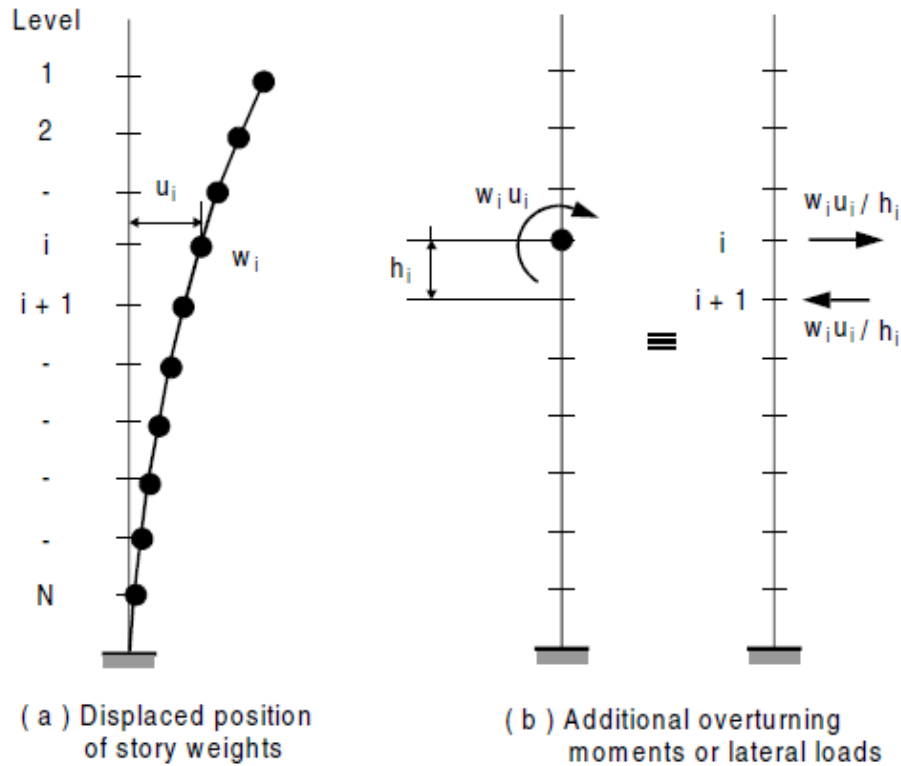


Figure 4-7 Overturning loads due to translation of story weights (Wilson, 2002)

Analytical expressions for mechanical properties are obtained using explicit considerations of geometric nonlinearity in the second approach. These analytical expressions are used to define the six springs that connect the two nodes of an elastomeric bearing. The element equilibrium and compatibility equations are satisfied in the deformed configuration to obtain expressions for mechanical properties.

The axial stiffness and two shear stiffnesses of an elastomeric bearing are obtained here including the effects of geometric nonlinearity (Koh and Kelly, 1987). These three stiffness expressions depend on axial load and lateral displacements of a bearing. The critical buckling capacity of a bearing also depends on the lateral displacement. The bilinear approximation to the linear area reduction method suggested by Warn *et al.* (2007) is used to calculate the critical buckling capacity of a bearing. The moment due to the axial load of the superstructure at a horizontal displacement is equally divided between the two ends of the bearing.

The horizontal elastic stiffness of a bearing, k_e , at an axial load P is given by:

$$k_e = \frac{GA}{T_r} \left(1 - \frac{P^2}{P_{cr}^2} \right) \quad (4.76)$$

where P_{cr} is the critical buckling load capacity of the bearing at zero lateral displacement. This expression is a simplified approximation of the exact expression derived by Koh and Kelly (1987) and has been shown produce to accurate results.

The vertical stiffness of a bearing at a lateral displacement u_h is given by:

$$K_v = \frac{AE_c}{T_r} \left[1 + \frac{3}{\pi^2} \left(\frac{uh}{r} \right)^2 \right]^{-1} \quad (4.77)$$

where $u_h = \sqrt{u_b(2)^2 + u_b(3)^2}$ is the resultant horizontal displacement of the bearing.

The critical buckling load capacity of a bearing is given by expression:

$$P_{cr} = \begin{cases} P_{cr0} \frac{A_r}{A} & \text{for } \frac{A_r}{A} \geq 0.2 \\ 0.2P_{cr0} \frac{A_r}{A} & \text{for } \frac{A_r}{A} < 0.2 \end{cases} \quad (4.78)$$

where P_{cr0} is the buckling load at zero displacement, and P_{cr} is the buckling load at overlapping area A_r of a bearing with an initial bonded rubber area of A . Additional information on the calculation of the reduced area is provided in Chapter 3.

The torsional and two rotational stiffnesses are not expected to significantly affect the response of elastomeric bearings. Linear expressions are used for these three stiffnesses.

4.4 Implementation in OpenSees

4.4.1 General

The Open System for Earthquake Engineering Simulation (OpenSees) is an object-oriented, open-source software framework for simulations in earthquake engineering using finite element methods. OpenSees is not a code. OpenSees has a modular architecture that allows users to add additional functionalities without much dependence on other components of the program. The user can focus on the changes and improvements in the program relevant to them without needing to know the whole framework (e.g., changing stress-strain relationship in a material model without knowing about equations solvers and integration methods).

The Tcl/Tk programming language is used to support the OpenSees commands. The OpenSees interpreter (OpenSees.exe) is an extension of the Tcl/Tk programming language that adds commands to Tcl for finite element analysis. Each of these commands is a one-line statement associated with a C++ procedure, which is used to define the problem geometry, loading, formulation and solution. The procedure is called upon by the OpenSees interpreter (OpenSees.exe) to parse the command. Additional functionalities are added to OpenSees through these C++ procedures. The most basic example of these procedures is an element in finite element analysis. In OpenSees, the Element is a procedure that maintains the state of the finite element model of a component and computes its contribution of resisting force, and tangent matrix to the structure.

Three elements are created for LDR, LR, and HDR bearings. Section 4.4.2 describes the general framework of OpenSees and presents the theoretical background of the formulation of user elements in OpenSees. The presentation is based on the discussion presented in Mazzoni

et al. (2006) and Fenves *et al.* (2004). The wiki version of the user documentation of OpenSees is available on the website <http://opensees.berkeley.edu/wiki>.

4.4.2 OpenSees framework

In OpenSees the analysis model is created through set of modules that construct the finite element model, specify the analysis procedure, and select the quantities to be monitored during an analysis procedure and the output of results. The four types of high-level objects created in OpenSees during each finite element analysis are presented in Figure 4-8.

The Domain object holds the state of the finite element model at time t_i and $t_i + dt$ and stores the objects created by the ModelBuilder object when the Analysis object advances the state from t_i and $t_i + dt$. The information from the Domain object is accessed by the Analysis and Recorder objects. The ModelBuilder object is used to construct the objects in the model and adds them to the domain. Different ModelBuilders may be used to construct and add a model to the Domain, such as a text based model building language (Tcl/Tk) or a graphical user interface (OpenSees Navigator). A simulation may use one of many solution procedures available in the Analysis object to invoke solvers to solve the systems of equations, which moves the model from state at time t_i and $t_i + dt$. The user-defined parameters are monitored during the analysis using the Recorder object for post-processing and visualization of simulation results.

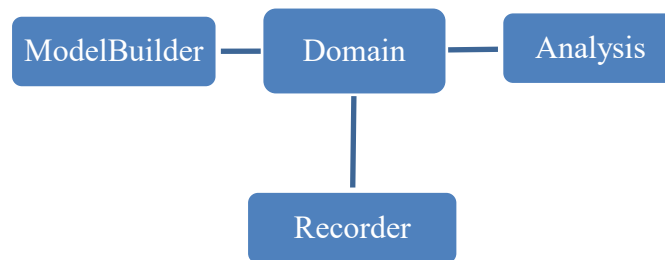


Figure 4-8 High-level OpenSees objects in the software framework (Mazzoni *et al.* (2006))

The high-level objects discussed above are constructed using many small objects. The Domain object contains all the information on the finite element model, such as nodes, boundary conditions, loads, and single and multi-point constrains, as shown in Figure 4-9. The components of the Analysis object are shown in Figure 4-10.

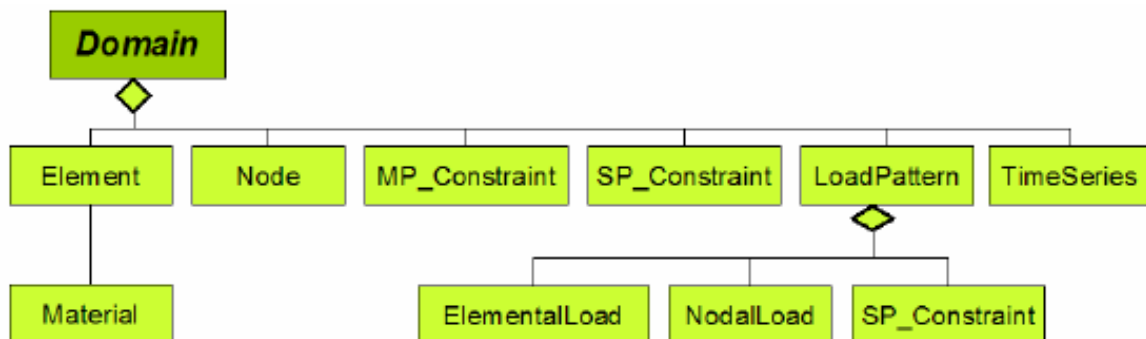


Figure 4-9 The components of the Domain object (Mazzoni *et al.*, 2006)

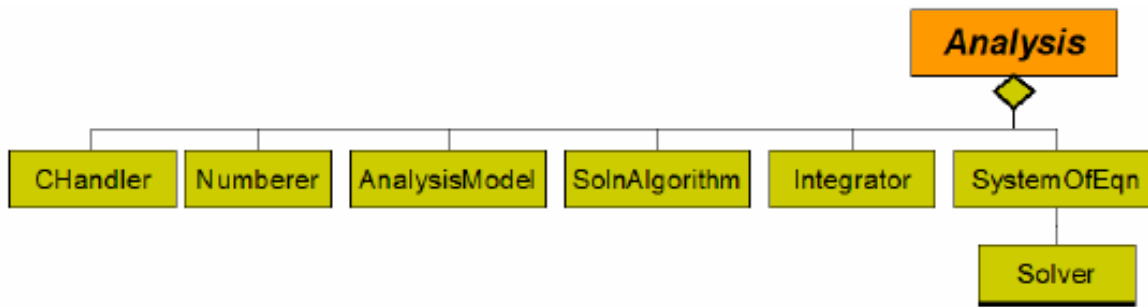


Figure 4-10 The components of the Analysis object (Mazzoni *et al.*, 2006)

The Element object is created here using C++ procedures. As discussed before, the main function of the Element is to provide the nodal force vector and stiffness matrix. Trial displacements are made available to the element at each step by OpenSees. The Element uses these trial displacements to advance the state of the model from t_i to $t_i + dt$ and assembles the force vector and stiffness matrix at $t_i + dt$. Iterations are performed at each time-step to achieve convergence. The converged state is also referred to as the committed step. The nodal force vector and stiffness matrix provided by the Element correspond to the committed step.

Procedures (or Class) used to write an Element in C++ follow an object-oriented approach, which means that each class in C++ has specific tasks (functions) and certain properties (data). In this way, the object-oriented approach tries to simulate a physical object. For example, a class Person created in C++ will have certain properties (e.g., name, height, weight, and ethnicity) and specific tasks (e.g., teaching) represented by data and functions. The data and functions of the Person class might be available to other classes depending upon whether they are declared public (available to all), private (only available inside the class), or protected (available for obtaining information but properties cannot be modified). The data and functions are declared and initialized through a header file (.h file), which is also responsible for calling pre-compiled libraries that are used in the procedure. A header file can be thought of declaration of intent of a class. The actual tasks of a class are described in cplusplus (.cpp) file through functions and data.

4.4.3 Variables and functions in OpenSees elements

The modular architecture of OpenSees means that the Element has very few generalized variables that should be defined for each element. Each element can define its own variables and user input arguments. The primary task of element is to provide a nodal force vector and a stiffness matrix. The variables that must always be defined for an element are: 1) an element tag and 2) tags of the nodes that define the element. All of these tags must be unique in the finite element model created in OpenSees. For the elastomeric bearing element created here, two node tags must be defined.

All the elements have a similar set of functions that are called to perform a task or obtain parameter values. For example, the function getTangentStiff() is called to get the tangent stiffness matrix in the global coordinate system. The list of functions used in an Element in OpenSees is shown presented in Table 4-4.

Table 4-4 Functions used in an OpenSees Element

Function	Task
getNumExternalNodes	returns number of nodes in the element
getExternalNodes	returns an array containing the node ids
getNodePtrs	returns pointers to the node ids
getNumDOF	returns number of DOF of the element
setDomain	adds the element object to the domain
commitState	commits state variables, the converged state variables are copied to new trial variables
revertToLastCommit	if step is not converged, model state is returned back to last committed state
revertToStart	resets the state of the model to the beginning of the analysis
update	takes the state of the model from t to $t + dt$, nodal force vector and stiffness matrix are calculated
getTangentStiff	returns the stiffness matrix in global coordinates
getInitialStiff	returns the initial tangent stiffness matrix
getMass	returns the mass matrix for the element
zeroLoad	sets the nodal force vector to zero
addLoad	checks if the compatible loads have been assigned to the element
addInertiaLoadToUnbalance	adds inertial load to the nodal force vector
getResistingForce	returns the nodal force vector in the global coordinates excluding inertial loads
getResistingForceInclInertia	returns the nodal force vector in the global coordinates including inertial loads
sendSelf	sends element parameters to a data array, required for a parallel processing option
recvSelf	receives element parameters from a data array, required for a parallel processing option
displaySelf	displays the deformed shape of the bearing
print	prints the output on the command line of OpenSees interpreter (OpenSees.exe)
setResponse	prints the response invoked by recorders to ASCII files
getResponse	prints the response on the command line of OpenSees interpreter (OpenSees.exe)
setUp	assemble the transformation matrices

Table 4-5 Description of the user input arguments for the elements

Argument priority	Data type	Input arguments		Definition
		<i>ElastomericX</i>	<i>LeadRubberX</i>	
Required	int	tag	tag	Element tag
Required	int	Nd1	Nd1	First node tag of the element
Required	int	Nd2	Nd2	Second node tag of the element
Required	double	fy	fy	Yield stress of bearing
Required	double	alpha	alpha	Yield displacement of bearing
Required	double	G	G	Shear modulus of rubber
Required	double	Kbulk	Kbulk	Bulk modulus of rubber
Required	double	D1	D1	Lead (or internal) diameter
Required	double	D2	D2	Outer diameter
Required	double	ts	ts	Single shim layer thickness
Required	double	tr	tr	Single rubber layer thickness
Required	int	n	n	Number of rubber layers
Optional	double	x	x	Local x direction
Optional	double	y	y	Local y direction
Optional	double	kc	kc	Cavitation parameter
Optional	double	PhiM	PhiM	Damage parameter
Optional	double	ac	ac	Strength reduction parameter
Optional	double	sDratio	sDratio	Shear distance ratio
Optional	double	m	m	Mass of the bearing
Optional	double	cd	cd	Viscous damping parameter
Optional	double	tc	tc	Cover thickness
Optional	double		qL	Density of lead
Optional	double		cL	Specific heat of lead
Optional	double		kS	Thermal conductivity of steel
Optional	double		aS	Thermal diffusivity of steel
Optional	int	tag1	tag1	Cavitation
Optional	int	tag2	tag2	Buckling load variation
Optional	int	tag3	tag3	Shear stiffness variation
Optional	int	tag4	tag4	Axial stiffness variation
Optional	int		tag5	Shear strength degradation

4.4.4 User elements

Two elements, *ElastomericX* and *LeadRubberX*, were created for LDR and LR bearings, respectively. Both element classes use similar structure and input arguments, except *LeadRubberX* has additional parameters and functions to capture the heating of the lead core under large cyclic displacements. These elements can only be used with three-dimensional finite element models in OpenSees. The input arguments of the two elements are summarized in Table 4-5. The elements take basic geometric and material parameters of elastomeric bearings as input arguments. Input arguments include mandatory and optional parameters. The default values of the option argument are provided in the element. The elements can be used in three type of analysis with OpenSees, namely: 1) eigenvalue analysis, 2) static analysis, and 3) transient (dynamic) analysis.

The geometric details of an elastomeric bearing is presented in Figure 4-11.

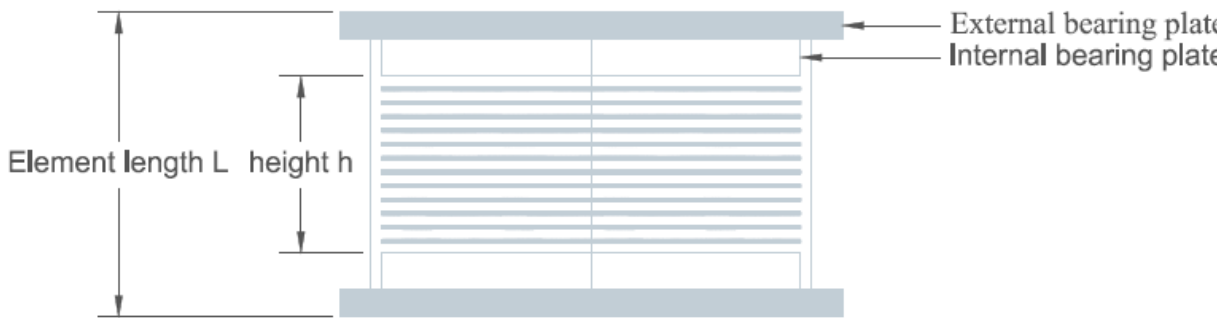


Figure 4-11 Internal construction of an elastomeric bearing

The length of the element, L , is calculated using the coordinates of its two nodes, Nd1 and Nd2. This length is used in the calculation of geometric stiffness and to consider $P-\Delta$ effects. The height of the bearing used in the calculations of mechanical properties is given by:

$$h = nt_r + (n - 1)t_s \quad (4.79)$$

where t_r is the thickness of single rubber layer, t_s is the thickness of steel shim, and n is the number of rubber layers. The length of the element (distance between Nd1 and Nd2) includes two internal and two external bearing plates at each ends, and is given by:

$$L = nt_r + (n - 1)t_s + 2t_{int} + 2t_{ext} \quad (4.80)$$

where t_{int} and t_{ext} are the thicknesses of the internal and external bearing plate, respectively.

The default orientations of the local X and y axes are shown in Figure 4-12. The vector defining the local X axis is obtained from the coordinates of the two nodes of the bearing. The local y axis is aligned to global X axis and a vector along this direction is assumed to be an unit vector $(-1, 0, 0)$. The vector defining the Z axis is then obtained as cross product of X and y . Finally, the vector defining y is obtained as the cross product of Z and X .

An arbitrary orientation of an elastomeric bearing can be modeled by providing vectors that define the local X and y directions, which overrides the default orientation of the local

coordinate axes. The shear distance ratio is the distance of the shear center from node 1 of the elastomeric bearing as a fraction of the element length. For symmetrical circular and square bearings, this ratio is 0.5, which is the default value. The bearing is assumed to be massless and a default value of 0 is assigned to the parameter m_b .

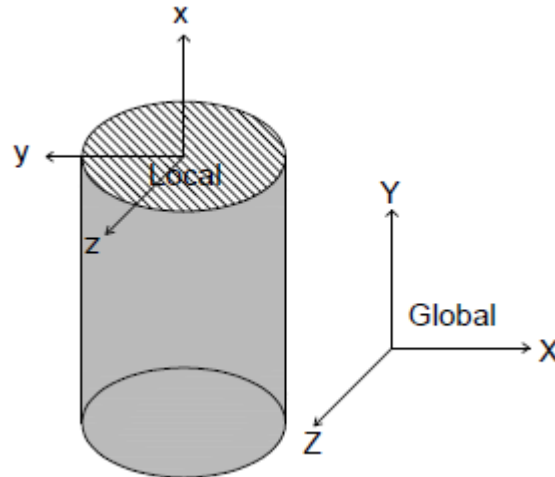


Figure 4-12 Local and global coordinates used in OpenSees for the elements

For *LeadRubberX*, additional heating parameters are used. The default values of these parameters used in the elements are from Kalpakidis *et al.* (2010). The default values of heating parameters are in the SI system of units, and should be overridden if the Imperial/US units are used.

Four and five tags are used in *ElastomericX* and *LeadRubberX*, respectively, to include the following characteristics of an elastomeric bearing under extreme loading:

1. Cavitation and post-cavitation behavior due to tensile loading
2. Variation in buckling load due to horizontal displacement
3. Variation in shear stiffness due to axial load
4. Variation in axial stiffness due to horizontal displacement
5. Strength degradation in shear due to heating of the lead core (LR bearings)

The tag value is set 1 or 0 to include or exclude a characteristic. Default values of the optional parameters are summarized in Table 4-6.

The user input interface of *ElastomericX* and *LeadRubberX* to be used in a Tcl/Tk input file are:

```
element ElastomericX $tag $Nd1 $Nd2 $fy $alpha $Gr $Kbulk $D1 $D2 $tr $ts $n <$x1 $x2
$x3 $y1 $y2 $y3> <$kc> <$PhiM> <$ac> <$sDratio> <$m> <$cd> <$tc> <$tag1> <$tag2>
<$tag3> <$tag4>
```

```
element LeadRubberX $tag $Nd1 $Nd2 $fy $alpha $Gr $Kb $D1 $D2 $tr $ts $n <$x1 $x2 $x3
$y1 $y2 $y3> <$kc> <$PhiM> <$ac> <$sDratio> <$m> <$cd> <$alphaS $kS $qL $cL>
<$tag1> <$tag2> <$tag3> <$tag4> <$tag5>
```

where the parameters are defined in Table 4-5. The \$ sign refers to the value of the parameter followed by it. The input parameters enclosed in < > are optional parameters, whose default values are presented in Table 4-6.

Table 4-6 Default values of optional parameters

Parameter	Value
kc	10
PhiM	0.75
ac	1.0
sDratio	0.5
m	0.0
tc	0.0
cd	128000 N-s/m
qL	11200 kg/m ³
cL	130 J/(kg°C)
kS	50 W/(m°C)
aS	1.4×10 ⁻⁵ m ² /s
tag1	0
tag2	0
tag3	0
tag4	0
tag5	0

4.5 Implementation in ABAQUS

4.5.1 General

ABAQUS provides the user with the capability to define special purpose subroutines or elements. Capabilities are added to ABAQUS through the creation of subroutines written in the FORTRAN 77 programming language. A subroutine is a FORTRAN procedure that can be compiled and tested separately from its host program. Subroutines can be added to the ABAQUS for various tasks such as defining material models, load distributions, frictional properties, and contact interface behavior. However, the focus here is a special type of user subroutine called User Elements (UEL). A UEL can be a finite element that represents the geometry (e.g., beam, truss, solid) of the model, or can be feedback links, which provide response at certain points as a function of displacements, velocities, accelerations at some other points in the model.

The user elements considered here represents a geometric model of the elastomeric bearing and hence the discussion is focused on the geometry based user elements. Section 4.5.2 describes the general framework of ABAQUS and presents the theoretical background of the formulation of user elements in ABAQUS. The presentation is based on the discussion presented in Section 29.16.1 of the ABAQUS Analysis User's Manual (Dassault, 2010a), and Section 1.1.23 of the ABAQUS User Subroutines Reference Manual (Dassault, 2010c).

4.5.2 ABAQUS framework

The response of a system modeled in ABAQUS is obtained by solution of equilibrium equations in incremental steps. User elements are coded to define the element's contribution to the whole model. The user element is called every time element calculations are required and it must perform all the calculations appropriate for the current step in the analysis. Information about the

model, which includes model definition, nodes and joint connectivity, geometrical and material parameters, loads definition and analysis requirements are defined through an ABAQUS input (.inp) file. This input file can be written by the user, or the ABAQUS pre-processor can be used to generate this input file interactively through a graphical user interface. The input file is then passed through the ABAQUS solver, which generates a set of equilibrium equations to be solved. The solver calls the user element every time information is required from user-defined elements. When user elements are called, ABAQUS provides these subroutines with the values of nodal coordinates, all solution-dependent nodal variables (e.g., displacements, velocities, accelerations, incremental displacements), solution dependent state variables at the start of the increment, and the user-defined properties in input file for this element. ABAQUS also passes an array of control flags to the element that indicates what tasks the element need to perform. Depending upon the flags, the element defines its contribution to the nodal force vector and the Jacobian (stiffness)⁴ matrix of the whole model and also updates the solution dependent state variables. A typical process flow of an analysis step and role of user element in ABAQUS is shown in Figure 4-13.

The element during the analysis step provides nodal forces F^N and the element's contribution to the total Jacobian matrix, $-dF^N/du^M$. Both of these depend on the nodal variables u^M and solution dependent state variables H^α . The nodal forces are given by:

$$F^N = F^N(u^M, H^\alpha, \text{geometry, attributes, predefined field variables, distributed loads}) \quad (4.81)$$

If a finite element is in equilibrium subject to surface tractions t and body forces f with stress σ , and with interpolation $\delta u = N^N \delta u^N$, $\delta \varepsilon = \beta^N \delta u^N$, the nodal forces are given by:

$$F^N = \int_S N^N \cdot t dS + \int_V N^N \cdot f dV - \int_V \beta^N : \sigma dV \quad (4.82)$$

To solve the equilibrium equations using the Newton-Raphson method:

$$\begin{aligned} \tilde{K}^{NM} c^M &= R^N \\ u^N &= u^N + c^N \end{aligned} \quad (4.83)$$

where R^N is the residual force at degree of freedom N and

$$\tilde{K}^{NM} = -\frac{dR^N}{du^M} \quad (4.84)$$

is the Jacobian matrix. The indices N and M are the degrees of freedom of the element.

During each iteration in the Newton-Raphson method, F^N and $-dF^N/du^M$ must be defined by the element, which are element's contribution to the residual R^N and Jacobian K^{NM} , respectively.

⁴ Stiffness matrix is for displacement-based formulations. However, a more generalized term "Jacobian" is used when multi-physics problems are solved in which additional independent variables are considered (e.g., a thermo-mechanical problem using temperature as an independent variable).

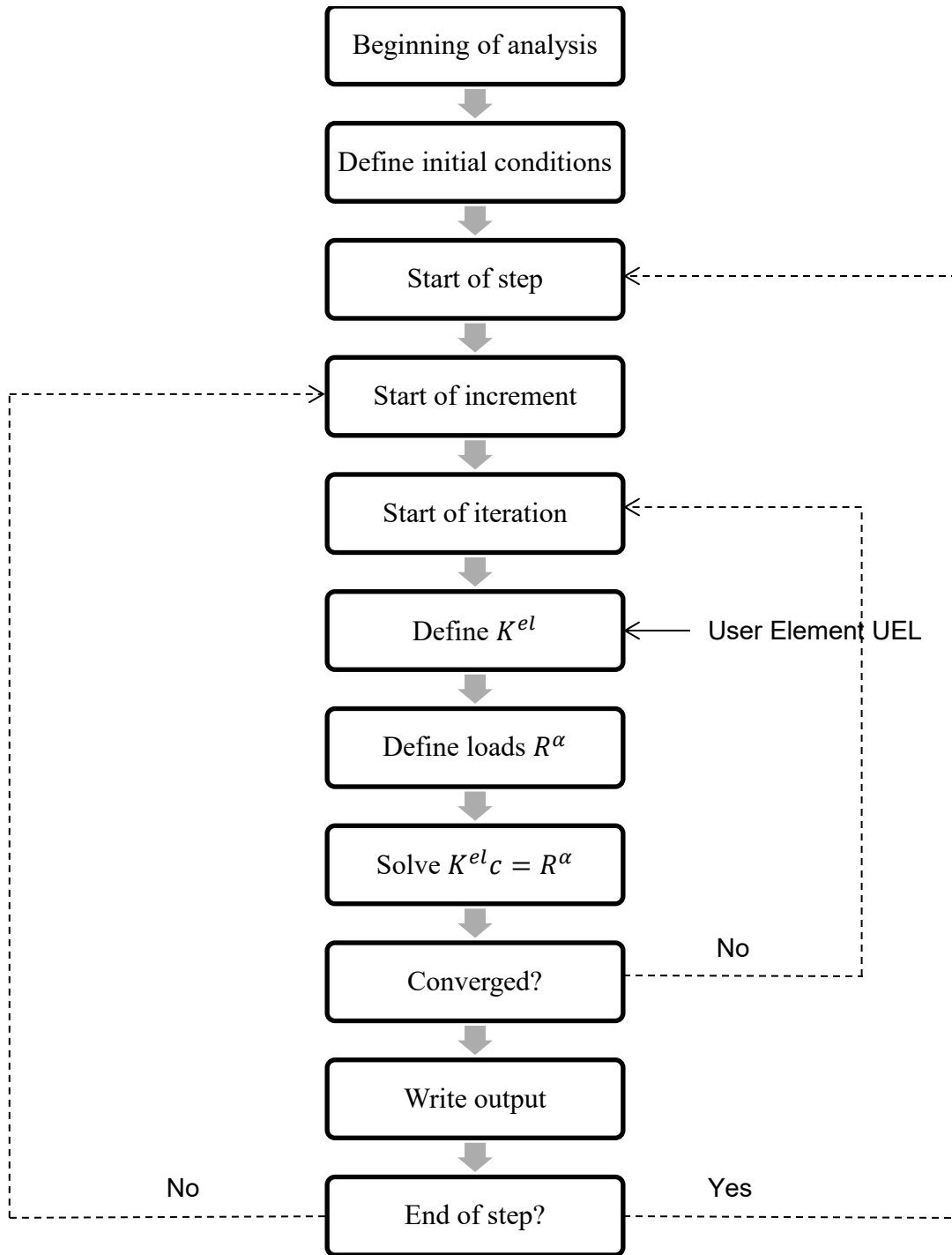


Figure 4-13 Outline of a general analysis step in ABAQUS (adapted from Dassault (2012))

The element's contribution $-dF^N / du^M$ to the Jacobian matrix must consider all the direct and indirect dependencies of F^N on u^M . If the solution dependent state variables H^α depend on u^M , $-dF^N / du^M$ is given as:

$$K_{ele} = -\frac{dF^N}{du^M} = -\frac{\partial F^N}{\partial H^\alpha} \frac{\partial H^\alpha}{\partial u^M} \quad (4.85)$$

In the case of direct-integration dynamic analysis, F^N depends on the velocity, \dot{u}^M , and acceleration, \ddot{u}^M . Hence nodal velocity and acceleration histories must be stored by the element in addition to the displacement history. Where implicit integration is used for integration of the dynamic equations, the element's contribution to the Jacobian is given as:

$$K_{ele} = -\frac{dF^N}{du^M} - \frac{dF^N}{d\dot{u}^M} \left(\frac{d\dot{u}}{du} \right)_{t+\Delta t} - \frac{dF^N}{d\ddot{u}^M} \left(\frac{d\ddot{u}}{du} \right)_{t+\Delta t} \quad (4.86)$$

The Hilber-Hughes-Taylor (HHT) implicit integration scheme is used in ABAQUS for integration of the dynamic equations of motion. For this scheme:

$$\begin{aligned} \left(\frac{d\dot{u}}{du} \right)_{t+\Delta t} &= \frac{\gamma}{\beta\Delta t} \\ \left(\frac{d\ddot{u}}{du} \right)_{t+\Delta t} &= \frac{1}{\beta\Delta t^2} \end{aligned} \quad (4.87)$$

where γ and β are Newmark integration parameters. The term $-dF^N/d\dot{u}^M$ represents the damping matrix and $-dF^N/du^M$ represents the mass matrix of the element. The HHT scheme is unconditionally stable and there is no limit on the size of the time step for stability. The size of the time step is governed by accuracy. The overall dynamic equilibrium equation in HHT scheme is written as:

$$-M^{NM}\ddot{u}_{t+\Delta t} + (1+\alpha)G_{t+\Delta t}^N - \alpha G_t^N = 0 \quad (4.88)$$

where α is a parameter to control numerical damping in the model, and G^N is the total force at degree of freedom N , excluding inertia forces, and is termed the static residual. Equation (4.88) requires static residuals at the current and previous time step. ABAQUS provides information only at the current time step and static residual values from previous time steps need to be stored as the solution dependent state variables, H^α , which can be accessed at the current time step for the required calculations.

4.5.3 Variables in ABAQUS subroutines

ABAQUS defines a general set of variables and depending on the model and analysis requirements, some, or all of these variables, are used. These variables can be categorized in different groups based on their functions as presented in Table 4-7.

The variables RHS, AMATRIX, and SVARS must be defined in the user element, which correspond to F^N , $-dF^N/du^M$, and H^α defined earlier, respectively. Variable ENERGY can be defined depending upon the significance of the element energy in the overall model. If the user defines an integration scheme that requires a different time step for stability and accuracy, the user can suggest a new time step within the element using the variable PNEWDT. The set of variables passed to the user element for obtaining information about the analysis model in ABAQUS must not be modified by the user element.

The variables RHS, AMATRIX, and SVARS are populated based on the entries in the LFLAGS array, which defines the analysis type. A description of general analysis cases based on LFLAGS array is presented in Table 4-8.

Table 4-7 Overview of variables used in ABAQUS user subroutine:

Category	Name	Description
Must be defined	RHS	An array containing contributions of the element to the right hand side vector of the overall system of equations.
	AMATRX	An array containing contribution of the element to the Jacobian (stiffness) of the overall system of equations. The particular matrix required at any instant depends on the entries in LFLAGS array.
	SVARS	An array containing values of NSVARS number of solution-dependent state variables.
Can be defined	ENERGY	An array containing values of energy quantities associated with the element
Can be updated	PNEWDT	Ratio of time increment required by user to the time increment (DTIME) currently being used by ABAQUS.
Passed in for information	PROPS	A floating point array containing NPROPS values of geometrical and material properties defined by user for the element.
	JPROPS	An integer array containing NJPROP of integer values of geometrical and material properties defined by user for the element.
	COORDS	An array containing original coordinates of the nodes of the element. COORDS(K1, K2) represents the K1th coordinate of the K2th node of the element
	U, DU, V, A	Arrays containing the current estimate of the basic solution variables (displacements, incremental displacements, velocities, accelerations) at the nodes of the element at the end of current increment.
	JDLTYPE	An array containing the integers used to define distributed load types for the element.
	DDL MAG	An array containing increments in the magnitudes of the distributed loads currently active on the element.
	PREDEF	An array containing values of predefined field variables at the nodes of the element.
	PARAMS	An array containing the parameters associated with the solution procedure defined by entries in the LFLAGS array. $PARAMS(1) = \alpha$, $PARAMS(2) = \beta$, $PARAMS(3) = \gamma$
	LFLAGS	An array containing the flags that define the current solution procedure and requirements for element calculations.
	TIME(1)	Current value of step time
	TIME (2)	Current value of total time
	DTIME	Time increment
	PERIOD	Time period of the current step
	NDOFEL	Number of degrees of freedom in the element
	MLVARX	Dimensioning parameter used when several displacement or right-hand-side vectors are used.
	NRHS	Number of load vectors (1 in most nonlinear problems)
NSVARS	User defined number of solution dependent state variables in the element	

Table 4-7 Overview of variables used in ABAQUS user subroutines (contd.)

	NPROPS	Number of user-defined real property values constituting the array PROPS
	NJPROPS	Number of user-defined integer property values constituting the array PROPS
	MCRD	Greater of the user-defined maximum number of coordinates needed at any node point and the value of the largest active degree of freedom of the user element that is less than or equal to 3
	NNODE	User-defined number of nodes on the element
	JTYPE	Integer defining the element type
	KSTEP	Current step number
	KINC	Current increment number
	JELEM	User-assigned element number
	NDLOAD	Identification number of the distributed load or flux currently active on the element
	MDLOAD	Total number of distributed loads and/or fluxes on the element
	NPREFD	Number of predefined field variables

Table 4-8 Analysis cases used in ABAQUS

		Normal implicit time incrementation procedure. User subroutine UEL must define the residual vector in RHS and the Jacobian matrix in AMATRX
LFLAGS(3) = 1	LFLAGS(1) = 1, 2	Static analysis $RHS = F^N(u^M, H^\alpha, \text{other variables})$ $AMATRX = -dF^N / du^M$
	LFLAGS(1) = 11, 12	Direct-integration dynamic analysis $RHS = -M^{NM}\ddot{u}_{t+\Delta t} + (1+\alpha)G_{t+\Delta t}^N - \alpha G_t^N$ $AMATRX = M^{NM}d\ddot{u} / du + (1+\alpha)C^{NM}d\dot{u} / du + (1+\alpha)K^{NM}$
LFLAGS(3) = 2	Define the current stiffness matrix only	$AMATRX = K^{NM} = -\partial F^N / \partial u^M$
LFLAGS(3) = 3	Define the current damping matrix only	$AMATRX = C^{NM} = -\partial F^N / \partial \dot{u}^M$
LFLAGS(3) = 4	Velocity jump calculation	Define the current mass matrix $AMATRX = M^{NM}$
LFLAGS(3) = 5	Half increment calculation	Define the current half-step residual or load vector $RHS = F_{1/2}^N = -M^{NM}\ddot{u}_{t+\Delta t} + (1+\alpha)G_{t+\Delta t}^N - \alpha / 2(G_t^N + G_t^N)$
LFLAGS(3) = 6	Initial acceleration calculation	Define current mass matrix and the residual vector $AMATRX = M^{NM}$
		$RHS = G^N$

For the default time increment option provided in the ABAQUS input file, the element must define the half-increment residual load vector, $F_{1/2}^N$. ABAQUS adjusts the time increment so that residual load vector at the half time step is within the tolerance defined for convergence ($\max |F_{1/2}^N| \leq \textit{tolerance}$). The solution-dependent state variables are calculated at the half step, $H_{1/2}^\alpha$, to calculate $F_{1/2}^N$, but these values are not saved. The DTIME variable contains Δt , and not $\Delta t / 2$. The values contained in U , V , A , and DU are half-increment values.

4.5.4 User input interface of the elements

The user needs to define the element in the input (.inp) file through the *USER ELEMENT option. The ABAQUS preprocessor does not allow user element definition through the graphical user interface and the user must enter the element definition directly into the input file. The *USER ELEMENT option must be defined before the user element is invoked with the *ELEMENT option. The syntax for interfacing UEL is:

```
*USER ELEMENT, TYPE=Un, NODES=, COORDINATES=, PROPERTIES=, I PROPERTIES=,
VARIABLES=, UNSYMM
Data line(s)
*ELEMENT,TYPE=Un, ELSET=UEL
Data line(s)
*UEL PROPERTY, ELSET=UEL
Data line(s)
*USER SUBROUTINES, (INPUT=file_name)
```

The parameters used in above interface are defined in Table 4-9. A detailed discussion on the user input interface for user elements is presented in Section 29.16.1 of the ABAQUS Analysis User's Manual (Dassault, 2010a).

Table 4-9 Parameter definitions used for UEL interface

Parameter	Definition
TYPE	(User-defined) element type of the form Un , where n is a number
NODES	Number of nodes in the element
COORDINATES	Maximum number of coordinates at any node
PROPERTIES	Number of floating point properties
I PROPERTIES	Number of integer properties
VARIABLES	Number of solution dependent variables
UNSYMM	Flag to indicate that the Jacobian is unsymmetric

4.5.5 User elements

Two ABAQUS user subroutines, UELs, were created for elastomeric bearings: *ElastomericX* for Low Damping Rubber (LDR) bearing, and *LeadRubberX* for Lead Rubber (LR) bearing. The *LeadRubberX* element builds on the formulation of *ElastomericX* and adds thermo-mechanical properties to capture strength degradation due to heating of the lead core.

The primary task of user elements is to provide the RHS and AMATRX arrays during the analysis step and to update SVARS array. The user elements can be used for:

- 1) Static analysis

- 2) Direct integration dynamic analysis
- 3) Eigenfrequency extraction analysis

The user can specify any arbitrary length of the element, however a length representative of the actual height of the elastomeric bearing is recommended. If the ABAQUS preprocessor is used to generate the input file, the user can start by defining a dummy element in place of the elastomeric bearing, and after the user input file has been generated by the preprocessor, the dummy element can be deleted by manually editing the input file and replacing it with the definition of *ElastomericX* or *LeadRubberX*, as discussed in Section 4.5.4.

The mechanical properties of the material (or material definitions) are defined in both user elements. Twelve and eighteen real property values (NPROPS=12, 18) and one integer property value (NJPROP=1) must be defined for the *ElastomericX* and *LeadRubberX*, respectively. The entries of PROPS array for both elements are presented in Table 4-10.

Table 4-10 Properties of UELs that need to be defined as PROPS array

PROPS(i)	<i>ElastomericX</i>	<i>LeadRubberX</i>	Definition
1	qRubber	qYield	Yield strength of bearing
2	Uy	Uy	Yield displacement of bearing
3	G	G	Shear modulus of rubber
4	Kbulk	Kbulk	Bulk modulus of rubber
5	D1	D1	Lead (or internal) diameter
6	D2	D2	Outer diameter
7	t	t	Single rubber layer thickness
8	ts	ts	Single shim layer thickness
9	ac	ac	Cavitation parameter
10	phi	phi	Damage parameter
11	sDratio	sDratio	Shear distance ratio ⁵
12	m	m	Mass of the bearing
13	cd	cd	Rubber damping parameter
14		alphaS	Thermal diffusivity of steel
15		kS	Thermal conductivity of steel
16		qL	Density of lead
17		cL	Specific heat of lead
18		TL1	Initial reference temperature of lead
JPROPS(i)			
1	n	n	Number of shim layers

ABAQUS does not store a history of internal parameters between step increments. Solution-dependent state variables must be defined to store parameter values that are required for calculations at the next step. This is done through storing solution-dependent state variables in SVARS and updating them at the end of each step. Twenty-seven and twenty-eight state variables are defined in *ElastomericX* and *LeadRubberX*, respectively, with *LeadRubberX* containing an extra variable to store the temperature of the lead core. The variable SRESID in ABAQUS stores the static residual of total nodal forces at time $t + dt$. The first 12 elements of SVARS contains the static residual at time t . Entries of SRESID are copied to SVARS(1-12)

⁵ It is the distance of shear center from node 1 of the elastomeric bearing as a fraction of the total element length. For symmetrical circular and square bearings, this ratio is 0.5.

after the dynamic residual has been calculated in the user element. In the case of half-increment residual calculations, entries from 13-24 of SVARS contain the static residual at the beginning of the previous increment. SVARS(1-12) is copied into SVARS(13-24) after the dynamic residual has been calculated. SVARS(25) contains the variable u_{\max} , which is the maximum past axial deformation of the bearing under tensile loading. SVARS(26-27) contains the plastic horizontal shear displacements in the bearing. The temperature of lead core is stored in SVARS(28) for *LeadRubberX*.

The user elements must define its contribution to the right hand side vector (RHS), and to the Jacobian of overall model (AMATRIX) (see Section 4.5.2). For the user elements considered here, the RHS variable is the nodal force vector, f_b , calculated using Equation (4.2), and AMATRIX is the stiffness matrix, K_b , obtained using Equation (4.1) for the most calculation steps except in half step residual calculations and initial acceleration calculation where mass matrix is passed for AMATRIX and the static residual is passed for RHS. RHS and AMATRIX are needed in global coordinates. The element nodal force and stiffness arrays are first formulated below in basic coordinates and then transformed to global coordinates using transformation matrices. Individual entries of the K_b and f_b are calculated per Section 4.3. Once, K_b and f_b are obtained, their contribution in the global coordinate system are $f_g = T_{gl}^T T_{lb}^T f_b$, and $K_g = T_{gl}^T T_{lb}^T K_b T_{lb} T_{gl}$, respectively.

The programming structure of the UEL subroutine is shown in Figure 4-13. The main body of executable statements, which consists of set of tasks that need to be performed for each analysis case, is supplemented by two internal user subroutines: 1) ForceStiffness – to calculate the nodal force and stiffness matrix of the element in global coordinates, and 2) Transformation – to transform the quantities from one coordinate system to other.

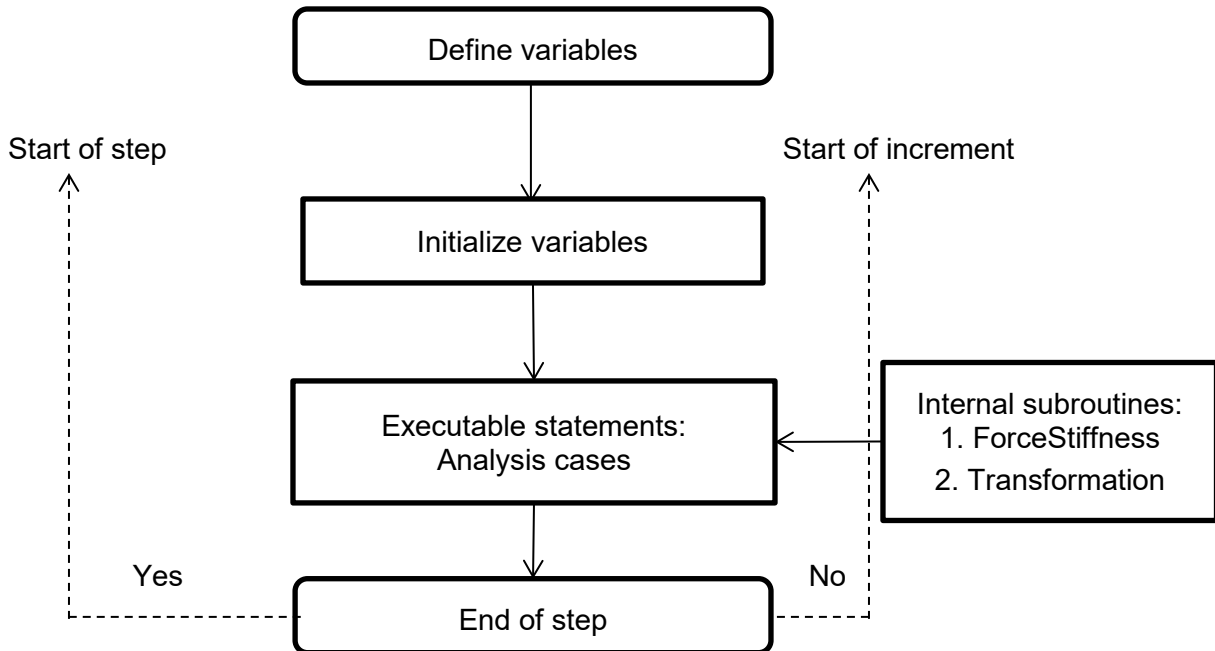


Figure 4-14 Programming structure of user elements (adapted from Dassault (2012))

5 VERIFICATION AND VALIDATION

5.1 Introduction

The models developed for the analysis of engineered systems are always approximations of the physical reality, and are limited by knowledge of physical processes, available data, mathematical formulations and numerical tools of analysis. The degree of accuracy to which these models predict the response of a system is addressed by the process of Verification and Validation (V&V). The prediction of response of a physical event through engineering models consists of many steps, and each step is accompanied by sources of error. The magnitude of the error depends on the assumptions, tools and techniques used for the analysis and an acceptance criterion is established with an acceptable level of error.

The credibility, reliability and consistency of models used for solving complex systems should be established to identify the confidence in their implementation. For low-consequence events there is additional room for accommodating higher error due to the low risk involved, and most times V&V activities are not performed because the resources cannot be justified. Given that actual high-consequence events may never be studied in a controlled environment, it becomes important that high confidence is established in the models that are used to study and predict the outcomes of such events. The design basis and beyond design basis earthquake shaking of Nuclear Power Plants (NPPs) are examples of high-consequence events. The models used to predict the outcome of these events need to be verified and validated to establish a high level of confidence. The system of interest here is an isolation system for a NPP that includes models of low damping rubber (LDR) and lead-rubber (LR) bearings.

The behavior of elastomeric bearings under extreme loadings is modeled using mathematical models and numerical formulations presented in Chapter 3 and Chapter 4, respectively. Chapter 3 discusses the theoretical background (conceptual models) of LDR and LR bearings based on available knowledge and the formulation of mathematical models in the horizontal and vertical directions. Mathematical models express physical behavior with mathematical equations using a set of assumptions. Each assumption introduces a source of error in the mathematical model. All sources of error in the mathematical need to be quantified, and if possible, should be minimized or removed. The accuracy of a mathematical model is assessed through validation procedures to determine if the mathematical model is a sufficiently good representation of behavior of the system.

Chapter 4 discusses the computational model, which include formulation of numerical models from the mathematical models and the implementation of the numerical models in the software programs OpenSees (McKenna *et al.*, 2006) and ABAQUS (Dassault, 2010e). The degree of accuracy with which the computational model represents the mathematical models is assessed through verification procedures. Verification and validation (V&V) is a cyclic process that quantifies the error in a model due to different sources. Quantification of the error helps prioritize V&V activities, and enables the assessment of the effect of a particular feature of the model on the behavior of the system.

Verification and validation is introduced in Section 5.2, which includes definitions of standard terms and describes the approach used for the development of a V&V plan. Section 5.3 provides a brief description of the model of an elastomeric bearing. Section 5.4 through Section 5.6 describe the step-by-step application of V&V methods to the elastomeric bearing models. The general background of V&V procedures presented in this chapter builds on the information presented in Oberkampf and Roy (2010), Oberkampf *et al.* (2004), Thacker *et al.* (2004) and

Roache (1998). The definitions of the standard terms presented in the ASME Guide for Verification and Validation in Computational Solid Mechanics (ASME, 2006) have been used here.

5.2 Background

The development of computer methods to simulate physical events prompted researchers to question the reliability, credibility and consistency of mathematical models and numerical tools and techniques. The computational physics and engineering community faced two major challenges: 1) development of guidelines to verify and validate simulations used for predication of outcomes of a physical event, and 2) standardization of terminologies and methodologies used in V&V across various disciplines. The interdisciplinary nature of V&V procedures demands that those involved communicate using terminologies that are consistent across the disciplines to minimize confusion in the decision-making process.

The Institute of Electrical and Electronics Engineers (IEEE) was one of the first institutions to define verification and validation methods (IEEE, 1984; IEEE, 1991). The definitions, however, considered only computer-implementation aspects of a broad range of V&V procedures that evolved later, and were intended for developers involved in Software Quality Assurance (SQA). The Defense Modeling and Simulation Office (DMSO) of the US Department of Defense (DoD) published their definitions of V&V activities in 1994 (DMSO, 1994). The DoD guidelines were more suitable for large-scale models, and were not appropriate for applications to more basic computational physics and engineering simulations (Oberkampf and Roy, 2010). The Computational Fluid Dynamics (CFD) community of the American Institute of Aeronautics and Astronautics (AIAA) coordinated a project in 1992 for the development and standardization of basic terminologies and methodologies used in V&V of computational fluid dynamics simulations. Their guide was published in 1998 (AIAA, 1998) and it used the DMSO (1994) definition of validation methods but modified the definition of verification to reflect the importance of accuracy of the numerical solution of the mathematical model.

The V&V committee of American Society of Mechanical Engineering (ASME) was formed in 2001 to draft guidelines on V&V in computational solid mechanics. The ASME Guide for Verification and Validation in Computational Solid Mechanics was published in 2006. It used the same definition of validation as AIAA (1998) but slightly modified the definition of verification. The ASME guide is used here to define terms, to the degree possible. It defines verification and validation as:

Verification: The process of determining that a computational model accurately represents the underlying mathematical model and its solution.

Validation: The process of determining the degree to which a model is an accurate representation of the real world from the perspective of the intended uses of the model.

Verification is concerned with the accurate representation of the mathematical model through software implementation of a numerical model, and a relationship to the physical reality is not of concern. Validation considers the degree of accuracy to which the mathematical model represents the physical reality, which is represented by experimental data.

ASME (2006) provides a list of standard terms used in V&V, some of which are reproduced below:

Prediction: The output from a model that calculates the response of a physical system before experimental data are available to the user.

Model: The conceptual, mathematical, and numerical representations of the physical phenomena needed to represent specific real-world conditions and scenarios. Thus, the model includes the geometrical representation, governing equations, boundary and initial conditions, loadings, constitutive models and related material parameters, spatial and temporal approximations, and numerical solution algorithms.

Conceptual Model: The collection of assumptions and descriptions of physical processes representing the solid mechanics behavior of the reality of interest from which the mathematical model and validation experiments can be constructed.

Computational model: The numerical implementation of the mathematical model, usually in the form of numerical discretization, solution algorithm, and convergence criteria.

Mathematical model: The mathematical equations, boundary values, initial conditions, and modeling data needed to describe the conceptual model.

Calibration: The process of adjusting physical modeling parameters in the computational model to improve agreement with experimental data.

The process of model development and V&V procedures is summarized in Figure 5-1.

The V&V process starts with the definition of the domain of interest, which is the physical system and associated environment for which the model is to be created. This helps to define the scope of various activities and the formulation of suitable assumptions. For high-consequence events, it is advisable to define a domain of interest that is precise and detailed. Although this action limits the applicability of the model to a small range of problems, it reduces the uncertainty associated with a wide range of working environments and thus increases confidence in the model. Moreover, simplifying a model by excluding minor details, which are not expected to have a major influence on the behavior of the system, increases robustness and decreases sources of error in the computational model. The ASME Guide realizes the limitations of contemporary modeling techniques used in computational solid mechanics, and limits the scope of V&V activities to the model's intended use for the response quantities of interest.

Once the domain of interest is defined, a conceptual model of the physical problem is formulated through a set of features that are expected to play a role in the physical event for which the model is to be used. A mechanics-based representation of the physical problem that is amenable to mathematical and computational modeling is created, which includes: 1) geometrical details of the model, 2) material definition, 3) initial and boundary conditions, 4) external loads, and 5) modeling and analysis approach. Conceptual models are developed through engineering expertise and judgment, and it is important that the rationale for each decision and the basis of each assumption are properly documented.

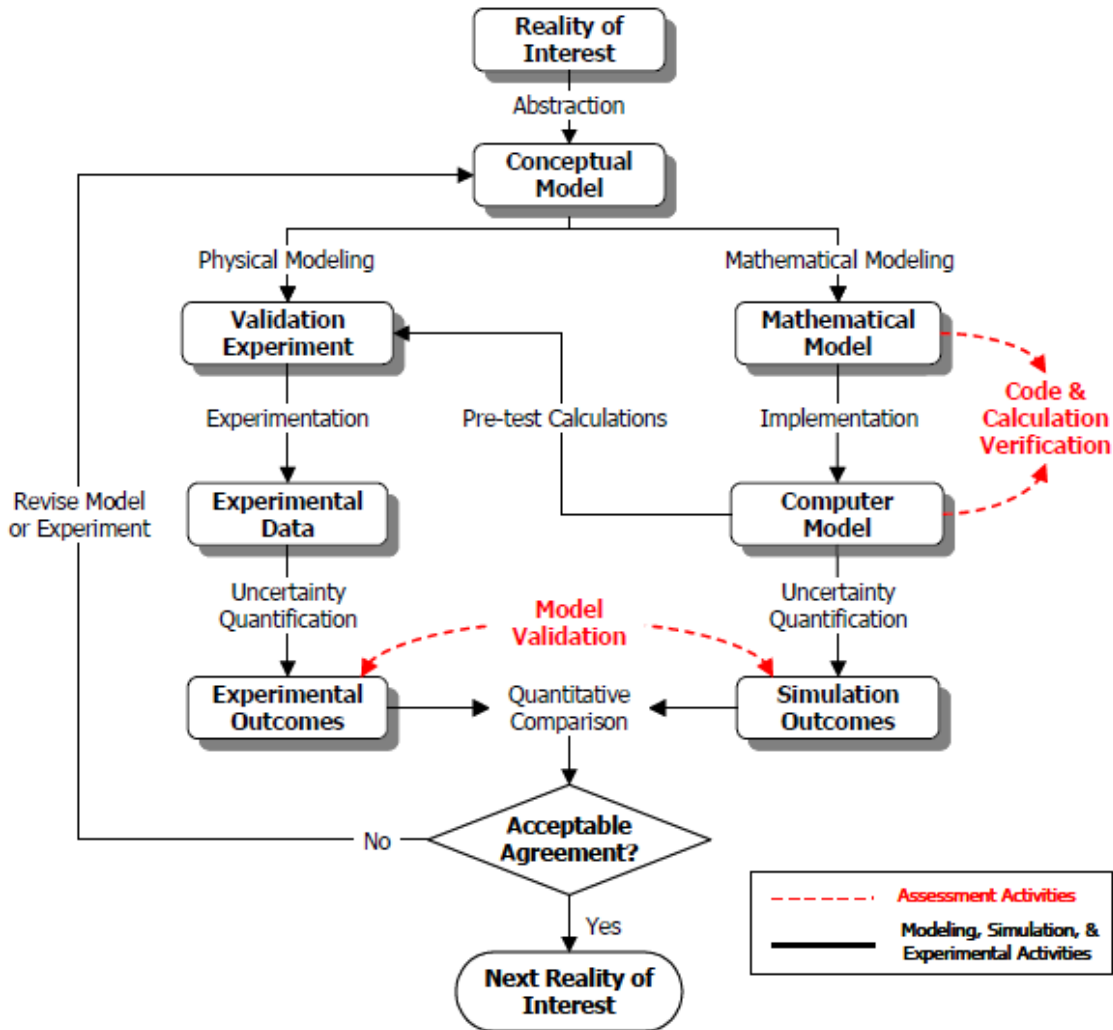


Figure 5-1 Model development, verification and validation (Thacker *et al.*, 2004)

The development of a conceptual model sets the stage for the creation of a mathematical model. A mathematical description of the conceptual model is formulated through a set of equations and statements that describes the physical problem. The mathematical model uses parameters that are one of the major sources of uncertainty that affects its accuracy. These parameters can be divided in three categories based on the method used for their determination, and are presented in Table 5-1.

Table 5-1 Description of model input parameters (Roy and Oberkamp, 2011)

Parameter type	Description	Level of confidence
Measured	Measurable properties of the system or surroundings that can be independently measured	High
Estimated	Physical modeling parameters that cannot be independently measured separate from the model of the system	Medium
Calibrated	Ad-hoc parameters that have little or no physical justification outside of the model of the system	Low

A computational model is developed using the mathematical model to predict the system's response through computer programs. The process involves spatial and temporal discretization of the mathematical model to a numerical model, and implementation of the numerical model in a computer program using a numerical algorithm that solves the model through direct or iterative solution techniques. Domain discretization and solution techniques are the major sources of the error in the computational model in addition to computer round-off error and coding bugs.

Verification activities are performed to improve the accuracy of the computational results. The system response obtained from analysis of verified models is compared with data obtained from validation experiments. The test data must be processed to remove measurement errors. If the computational results are within acceptable error per an established accuracy criteria, the model is deemed validated. If not, the model needs to be revised. The revision can be made by: 1) updating the model parameters that are determined using calibration with experimental results, and 2) improving the mathematical or conceptual model to better represent the underlying mechanics of the system that will result in better agreement with the experimental results.

5.3 Elastomeric Bearing Model Development

5.3.1 General

A V&V plan for the elastomeric bearing models discussed in Chapter 3 and 4 is presented here. The hierarchy of the model of an elastomeric bearing and its components are shown in Figure 5-2. The mechanical behavior in moment and torsion do not significantly affect the response quantities of interest in the shear and axial directions. The V&V tasks are performed only for the mechanical behavior of the LDR and LR bearings in the horizontal (shear) and the vertical (axial) directions, as identified by the shading. The conceptual and mathematical models are presented in Chapter 3 and the computational model is discussed in Chapter 4.

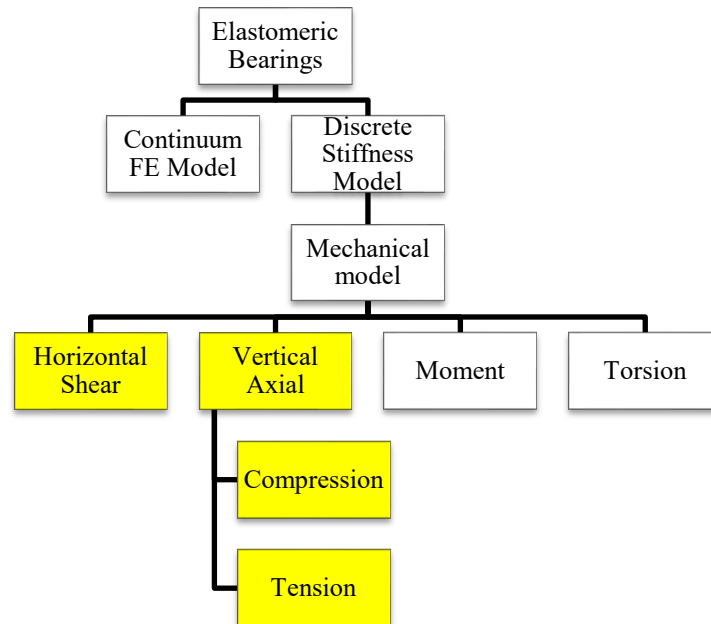


Figure 5-2 Hierarchy of the model for an elastomeric bearing

5.3.2 Model development

The physical model of an elastomeric bearing is formulated as a two node, twelve-degree of freedom system. The two nodes are connected by six springs, which represent the material models in the six basic directions. The six material models capture the behavior in the axial, shear (2), torsional and rotational (2) directions. The mathematical models and computational models of elastomeric bearings are discussed in detail in Chapter 3 and Chapter 4, respectively. The mathematical model of the elastomeric bearing is implemented in OpenSees and ABAQUS as user elements. A user element is the implementation of a numerical model in a computer program using a programming language. Two elements are created in each program for LDR and LR bearings. A user element for high damping rubber (HDR) bearings was also created in OpenSees. The HDR user element has the same axial formulation as LDR and LR bearings, but uses the model proposed by Grant *et al.* (2004) in shear. The V&V of the HDR user element is not discussed here.

The scope of the model and its intended use must be defined for V&V activities, which helps in prioritizing tasks and allocating resources for each activity. Table 5-2 presents the information required on the model to begin the V&V process.

Table 5-2 Scope of the V&V for the elastomeric bearing models

Feature	Description
Domain of interest	Seismic isolation of NPPs
Intended use of the model	Response-history analysis of a NPP under design and beyond design basis earthquake loadings
Response features of interest	1) Acceleration, velocity, displacement a) of the structure b) of secondary systems <ul style="list-style-type: none"> • 2) displacement in the isolators • 3) energy dissipation (damping) in the isolators • a) due to heating in the lead core of LR bearings • b) due to cavitation under tension
Accuracy requirements	To be developed after consultations with stakeholders

One of the important steps in the development of the model of an elastomeric bearing is to identify the processes that are expected to have significant effects on the response of the base-isolated NPP. This is achieved by constructing a Phenomena Identification and Ranking Table (PIRT). The PIRT for the models of elastomeric bearings is presented in Table 5-3. The confidence and importance levels assigned to the different components of the mathematical model in Table 5-3 are based on preliminary information available on the mathematical models of elastomeric bearings.

The PIRT helps to prioritize those physical processes that should be investigated experimentally for validation. Heating of the lead core and coupling effects are assigned a low priority for validation as they are based on robust mechanical formulations and have already been validated under similar conditions (Kalpakidis and Constantinou, 2009a; Warn *et al.*, 2007). The two-spring model by Koh and Kelly (1987) describes the elastic behavior of elastomeric bearing in the vertical direction and can be modeled with high confidence. The model for the variation in the buckling load capacity with lateral displacement is expected to be of high importance. Buckling is modeled using the linear approximation of the area-reduction method, which is

numerically robust and has been validated experimentally (Warn and Whittaker, 2006). A new phenomenological model is used for cavitation, post-cavitation and strength reduction in cyclic tension. The parameters of the phenomenological model are obtained from calibration with test data. The uncertainty associated with these parameters is high, and so a low confidence of modeling is assigned in Table 5-3. The effect of cavitation and post-cavitation behavior on the system's response is not yet known but is expected to be of medium importance to the response quantities of interest. Phenomena with medium or high importance to response quantities of interest and low level of confidence in modeling are given high priority for the experimental validation activities. The phenomenological model that describes the behavior of an elastomeric bearing in cyclic tension is validated experimentally. The parameters associated with cavitation, post-cavitation, strength reduction in cyclic tension are estimated.

Table 5-3 Phenomenon ranking and identification table for models of elastomeric bearings

Phenomenon	Importance to response of interest	Level of confidence in model
Coupled horizontal directions	High	High
Heating of lead core in LR bearing	High	High
Varying buckling capacity	High	Medium
Coupled horizontal and vertical directions	Medium	Medium
Nonlinear tensile behavior	Medium	Low
Cavitation and post-cavitation	High	Low
Nonlinear compressive behavior	Low	Low
Post-buckling behavior	Low	Low

The model development and V&V plan for the model of elastomeric bearings is presented in Figure 5-3.

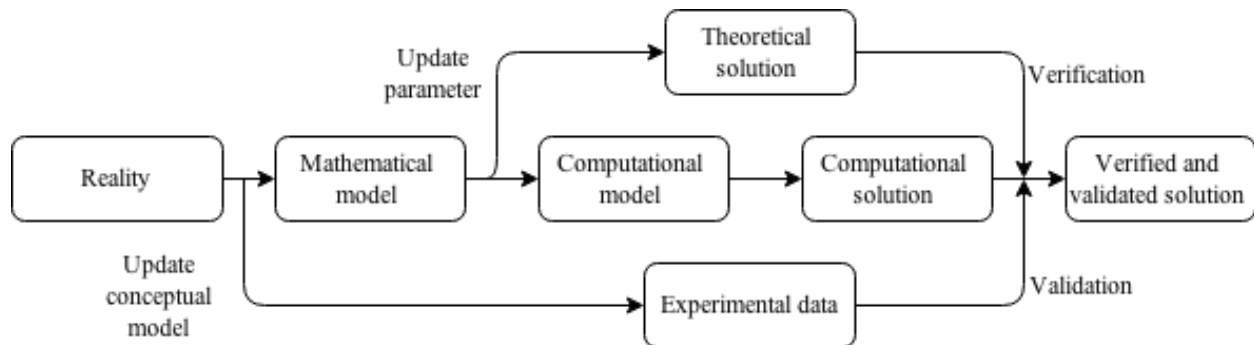


Figure 5-3 Verification, validation and model calibration plan for elastomeric bearings

5.4 Verification and Validation Criteria

A criterion needs to be established to obtain a quantitative measure of accuracy in verification and validation activities. The criterion can be defined in terms of an objective norm function that includes all the values of a response quantity of interest over the domain and provides a cumulative difference. A computational solution is compared against a reference solution, which, in the case of verification, can be an exact or a high order estimate of the exact solution, and in validation, must be the test data.

The L_1 difference norm over a discretized domain provides an average value of absolute difference, and is given as:

$$\xi_1 = \frac{1}{N} \sum_{i=1}^N |f_{2i} - f_{1i}| \quad (5.1)$$

where f_{1i} and f_{2i} are the reference solution and the solution for the response quantity of interest, respectively, at the i th sample point, and N is the total number of sample points. The L_1 norm is appropriate when the response quantities contain several discontinuities and singularities in their domain (Oberkampf and Roy, 2010).

The L_2 (Euclidean) norm provides the root mean square of difference over the domain:

$$\xi_2 = \sqrt{\frac{1}{N} \sum_{i=1}^N (f_{2i} - f_{1i})^2} \quad (5.2)$$

A third approach is to plot a statistical distribution of the difference and obtain a mean, median and standard deviation.

5.5 Verification of the Model

Verification of the model is performed to assess the degree of accuracy with which the computational model represents the mathematical model. A model must be verified before it can be used for any validation activity. The errors associated with the computational model should be separated from the errors arising from use of an inadequate mathematical model formulation based on a set of assumptions. The phenomenological model in tension has three parameters that are determined by calibration with experimental data. If an unverified computational model is used to compare numerical results with experimental outcomes, the errors associated with the unverified computational model are absorbed in the value of unknown parameters during model calibration. A bias in response is obtained when these parameters are used to predict the response of a system.

Verification can be categorized as: 1) code verification and 2) solution verification. Code verification deals with the programming aspects of the computational model and checks whether the discretized numerical model is implemented correctly in the computer program. Solution verification checks for the discretization (temporal and spatial), iterative convergence, and round-off error. The computational model of an elastomeric bearing is implemented in OpenSees and ABAQUS. Although OpenSees allows greater control of an analysis with the ability to control many aspects of the computational process, the absence of a user-interface also means that there is a greater possibility of coding errors. ABAQUS, on the other hand, has an interactive user-interface that reduces the possibility of coding errors but it also provides less flexibility to the user to control the modeling and analysis process.

5.5.1 Verification model

The verification activities are performed using a two-node macro model shown in Figure 5-4. All six degrees of freedom of the bottom node (node 1) are fixed to the ground, as are the three rotational degrees of freedom at the top node. The two nodes are joined by the user element (*ElastomericX* or *LeadRubberX*).

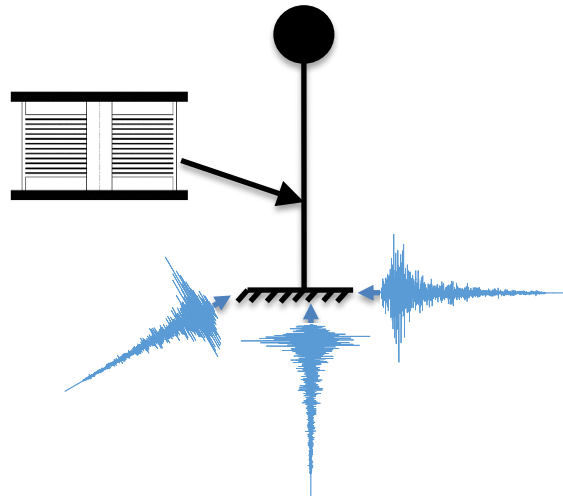


Figure 5-4 Two-node macro model of a base-isolated NPP

The LDR5 in Warn (2006) and larger size LR bearing in Kalpakidis *et al.* (2010) are used for *ElastomericX* and *LeadRubberX*, respectively. The properties of the two bearings are presented in Table 5-4. A static (gravity load) pressure on the bearing of 3 MPa is used for all analyses. The total gravity weight W on the bearing is calculated by multiplying the static pressure by the bonded rubber area. The total weight W is divided by g to obtain the equivalent mass M , which is lumped in the three translational directions at node 2 for static and dynamic analyses.

Table 5-4 Geometrical and mechanical properties of elastomeric bearings

Property	Notations (units)	Value	
		LDR	LR
Single rubber layer thickness	t_r (mm)	3	9.53
Number of rubber layers	n	20	16
Total rubber thickness	T_r (mm)	60	152.4
Steel shim thickness	t_s (mm)	3	4.76
Outer diameter	D_o (mm)	152	508
Inner/lead core diameter	D_i (mm)	30	139.7
Rubber cover thickness	t_c (mm)	12	12.7
Yield stress of lead	σ_L (MPa)	n.a. ¹	13
Static pressure due to gravity loads	p_{static} (MPa)	3.0	3.0
Shear modulus	G (MPa)	0.80	0.87

1. not applicable

5.5.2 Code verification

Code verification assesses the mathematical correctness and implementation of the numerical algorithms in a source code using a programming language. Code verification can further be divided into: 1) numerical code verification, and 2) software quality assurance (SQA).

5.5.2.1 Numerical code verification

Numerical code verification ensures that the solution algorithms are implemented correctly in the source code and are working as intended. Three techniques are employed here for numerical code verification: 1) symmetry test, 2) code-to-code comparison, and 3) order of accuracy test.

5.5.2.1.1 Symmetry test

If a code is provided with symmetric geometry, initial conditions and boundary conditions, it should produce symmetric response. The elastomeric bearing model is circular in shape and has radial symmetry. The models in OpenSees and ABAQUS are subjected to two symmetry conditions: 1) the bearing is fixed at its base and ground motion is applied to the free node at its top in the x-direction, and 2) the bearing fixed at its top and ground motion applied to the free node at its bottom in the negative x-direction. The two analysis cases are shown in Figure 5-5.

Sinusoidal loading is applied at the free node of a LDR (LDR5 in Warn (2006)) and a LR bearing (large size bearing in Kalpakidis *et al.* (2010)) for the two analysis cases. The responses at the free node in the two cases are presented in Figure 5-6 for the LDR and LR bearing, respectively. The L1 and L2 norm of the percentage difference is 0% for the *ElastomericX* and the *LeadRubberX* elements.

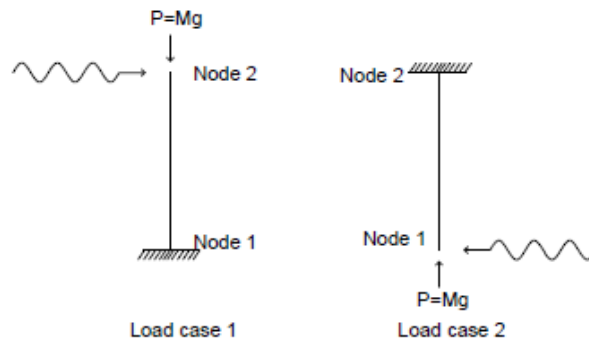


Figure 5-5 Analyses cases used for the symmetry test

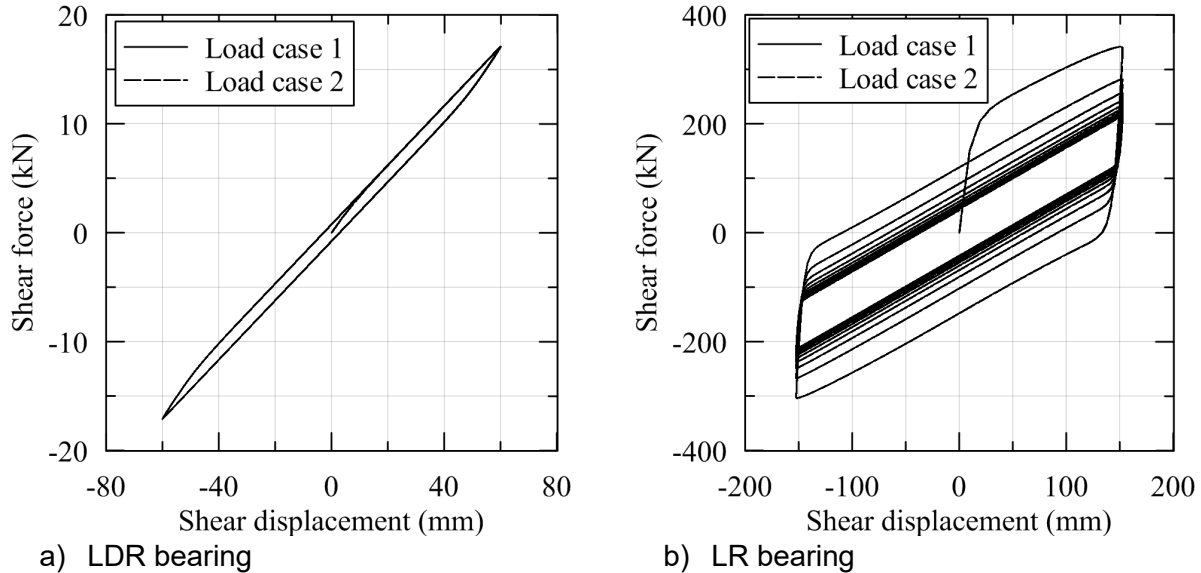


Figure 5-6 Force-displacement response in shear at the free node

5.5.2.1.2 Code-to-code comparison

Code-to-code comparison is the most widely used verification method to establish confidence in the codes implementing a mathematical model. The two prerequisites for code-to-code comparison are (Trucano *et al.*, 2003): 1) the two codes should implement the same mathematical model, and 2) one of the codes should have undergone rigorous code verification activities. The mathematical model of an elastomeric bearing is implemented in OpenSees and ABAQUS (refer to Chapter 4). ABAQUS is a commercial product that has well-documented software quality assurance through a verification manual (Dassault, 2010f) and a benchmarks manual (Dassault, 2010g), which provide a high confidence in the software. Good agreement between the results obtained from the models of elastomeric bearings implemented in OpenSees and ABAQUS increases confidence in the codes. A summary of the components of the mathematical model verified using code-to-code comparison is presented in Table 5-5, and plots of comparisons are shown in Figure 5-7 through Figure 5-12.

The code-to-code comparison shows good agreement for the components of the mathematical models of elastomeric bearing listed in Table 5-5. The percentage difference between the responses obtained using OpenSees and ABAQUS are less than 10% for all components of the mathematical model except in the strength degradation of LR bearing in shear due to heating of the lead core. The L1 and L2 norm of the difference between OpenSees and ABAQUS is 10% and 21%, respectively, for the strength degradation model of LR bearing under harmonic loading. A comparison of the plots of shear response obtained using OpenSees and ABAQUS in Figure 5-7 and Figure 5-8 show that the difference is primarily due to the reversal of motion. Although the magnitude of absolute difference are small, the percentage difference becomes large when responses values are close to zero during the reversal of motion. The percentage difference accumulates over 25 cycles of loading. Warn and Whittaker (2004) report that actual energy demand imposed on isolators in maximum earthquake excitation are far less than that imposed by codes (e.g., ASCE (2010)) in prototype testing, and recommend only four fully reversed cycles to the total design displacement at a frequency equal to the inverse of the effective period of isolated structures. Decreasing the number of cycles from 25 to 4 for the LR bearing reduces the L1 and L2 norms of the percentage difference to 3% and 12%, respectively.

Table 5-5 Code-to-code verification for different component of the mathematical models

Investigated property	Bearing used in the analysis	Loading protocol		Time step (sec)	L1 difference norm (%)	L2 difference norm (%)
		Horizontal	Vertical			
Heating	Large size bearing in Kalpakidis <i>et al.</i> (2010)	Harmonic loading	Constant compression	0.01	9.75	21.28
Cavitation	LDR 5 in Warn (2006)	Zero offset	Increasing triangular	0.01	0.43	6.57
Cavitation	KN2 in Iwabe <i>et al.</i> (2000)	Constant offset (200%)	Increasing sinusoidal	0.01	0.01	0.12
Buckling	LDR 5 in Warn (2006)	Linearly increasing	Increasing triangular	0.01	0.00	0.13
Buckling	LDR 5 in Warn (2006)	Linear increasing	Sinusoidal	0.01	0.53	7.07

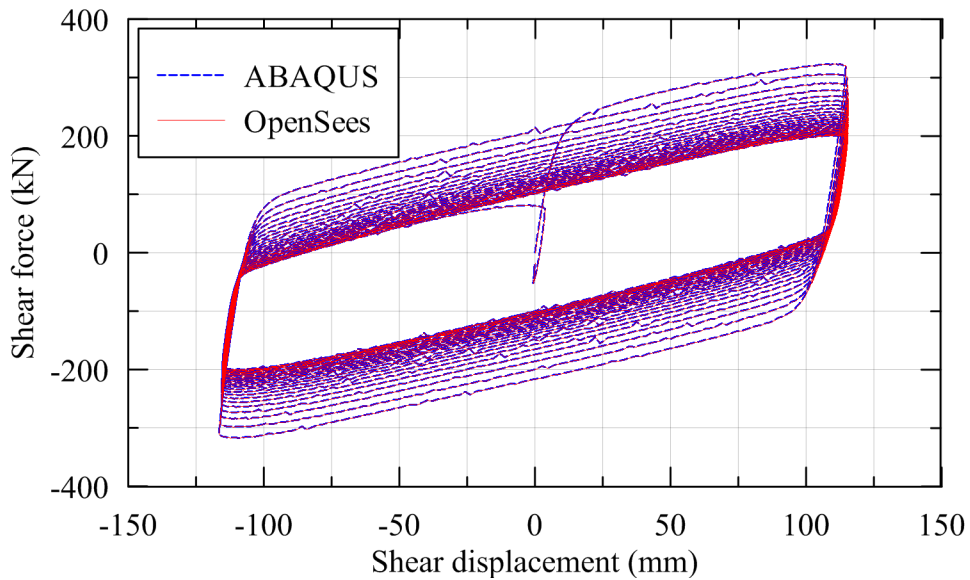


Figure 5-7 Shear strength degradation due to heating of the lead core (large size bearing in Kalpakidis *et al.* (2010))

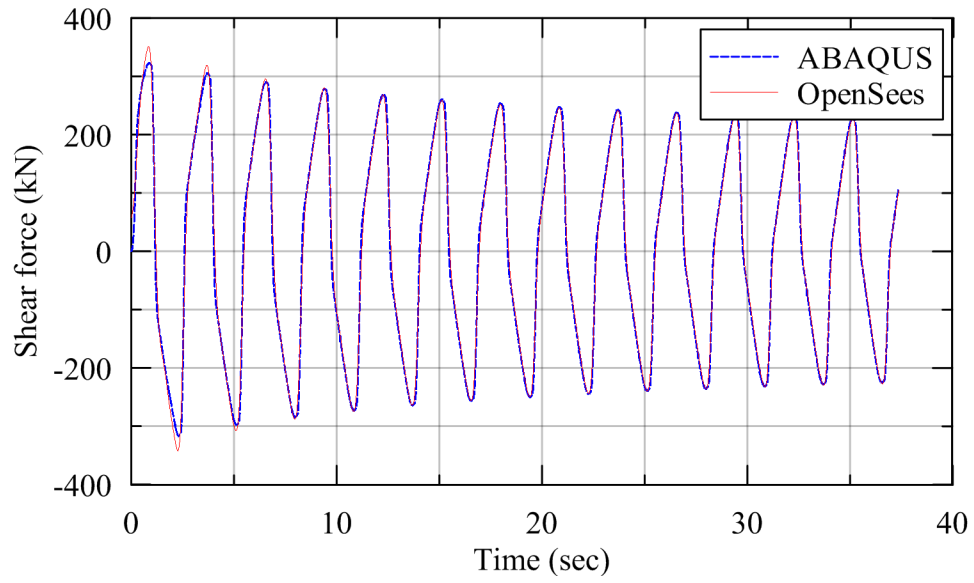


Figure 5-8 Shear force history (large size bearing in Kalpakidis *et al.* (2010))

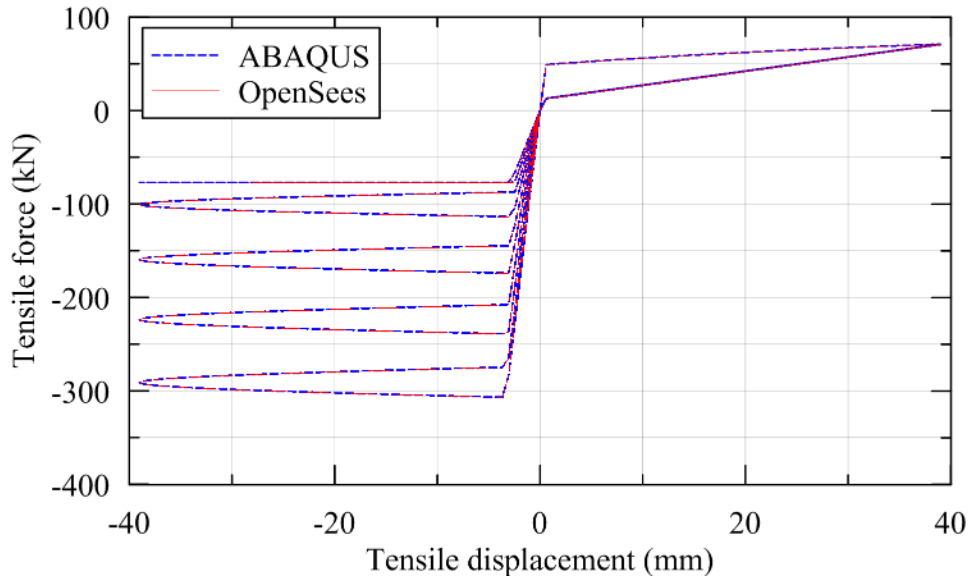


Figure 5-9 Cavitation and post-cavitation behavior (LDR5 in Warn (2006))

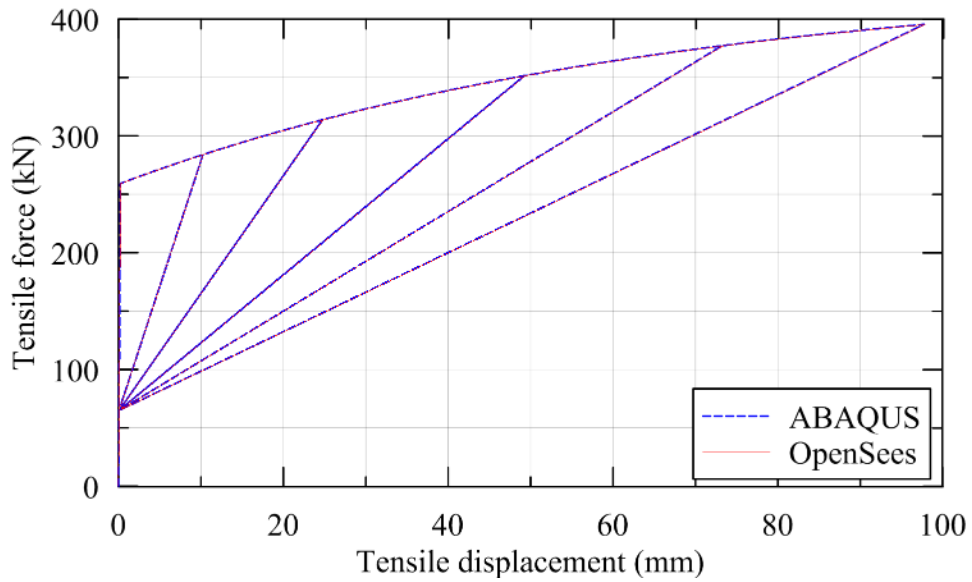


Figure 5-10 Cavitation and post-cavitation behavior (KN2 in Iwabe *et al.* (2000))

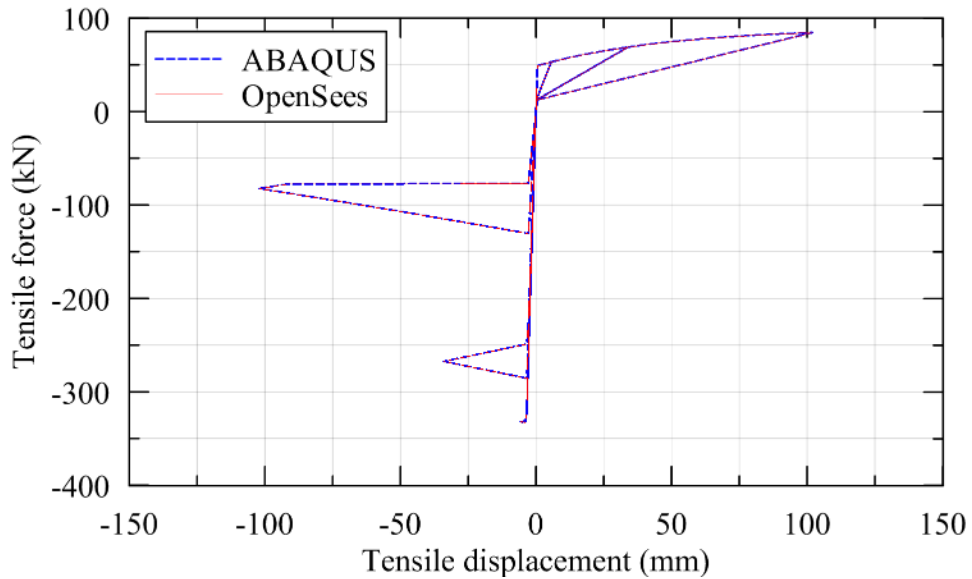


Figure 5-11 Axial behavior under increasing amplitude triangular loading and linearly increasing lateral loading ($\Delta t = 0.01$ sec, LDR5 in Warn (2006))

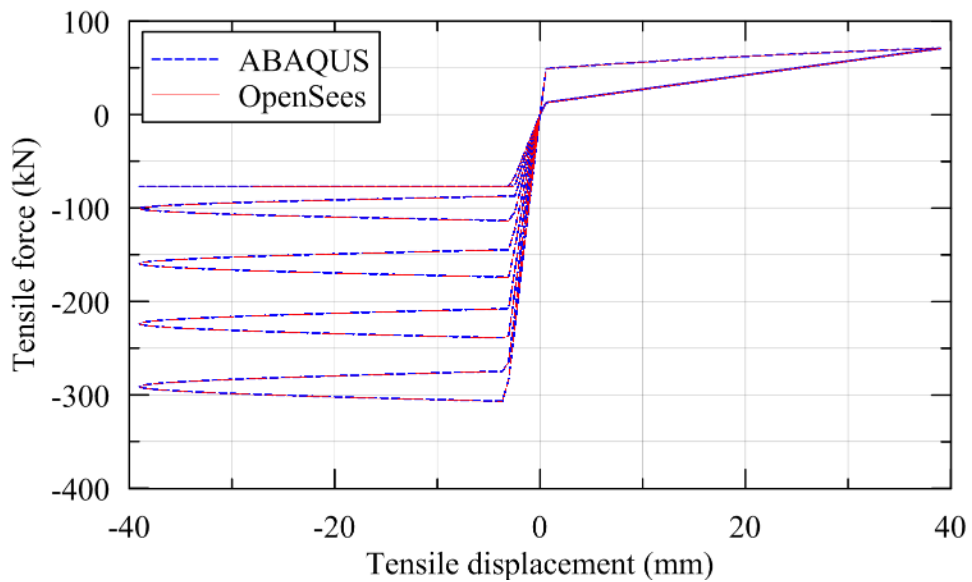


Figure 5-12 Axial behavior under increasing amplitude triangular loading and linearly increasing lateral loading ($\Delta t = 0.005$ sec, LDR5 in Warn (2006))

5.5.2.1.3 Order of accuracy test

The order of accuracy test is the most rigorous code verification activity. The results of the order of accuracy test is very sensitive to small mistakes in the code or deficiencies in the numerical algorithm. It examines the rate at which discrete numerical solution approaches the exact solution of the mathematical model as mesh discretization parameters (spatial and temporal) are refined. The order of the spatial and temporal convergence rates are determined to assess the accuracy of the code.

The order of accuracy can be determined as a formal order of accuracy and observed order of accuracy. The formal order of accuracy is the theoretical order of convergence of the discrete solution to the exact solution of the mathematical model. The observed order of accuracy is the rate at which computational solution converges to the exact solution of the mathematical model as the mesh size is refined. The formal order of accuracy of a numerical algorithm can be obtained through power series expansion, and is not necessarily the same as the observed order of accuracy due to errors associated with the code implementation of the discrete numerical solution. For the purpose of calculations here, the exact solution can be obtained from either a closed-form analytical solution or a high-confidence numerical solution with a fine discretization. An alternative to these two methods of obtaining an exact solution is to obtain a higher order estimate of the exact solution of the mathematical model through the Richardson Exploration method, which is discussed later in this chapter. Roy and Oberkampf (2011) provides a detailed discussion on calculation of formal and observed order-of-accuracies. The flowchart of the order of accuracy test is shown in Figure 5-13.

Elastomeric bearings are modeled as two-node, twelve degree-of-freedom, discrete elements. Hence no spatial discretization is involved, and only temporal discretization is used for the static and dynamic analysis. The dynamic equilibrium of a system is given by the following differential equation:

$$m \frac{d^2 u}{dt^2} + f_s(u, \dot{u}) = p(t) \quad (5.3)$$

where $f_s(u, \dot{u})$ is the resisting force that depends on the displacement and the velocity, and $p(t)$ is the external load applied to the system. For a linear system the resisting force is a sum of a spring force, ku , and a damping force, $c\dot{u}$. The discretized numerical form of the Equation (5.3) can be solved exactly for linear system, but requires iterative techniques for nonlinear systems.

A Central Difference solution scheme is used here to illustrate the procedure for determination of formal order of accuracy. A similar but more involved approach can be followed for other integrators (e.g., Newmark, HHT). The discretized form of Equation (5.3) is:

$$m \frac{u_{i+1} - 2u_i + u_{i-1}}{\Delta t^2} + c \frac{u_{i+1} - u_{i-1}}{2\Delta t} + ku_i = p_i \quad (5.4)$$

where subscript i represents the time step.

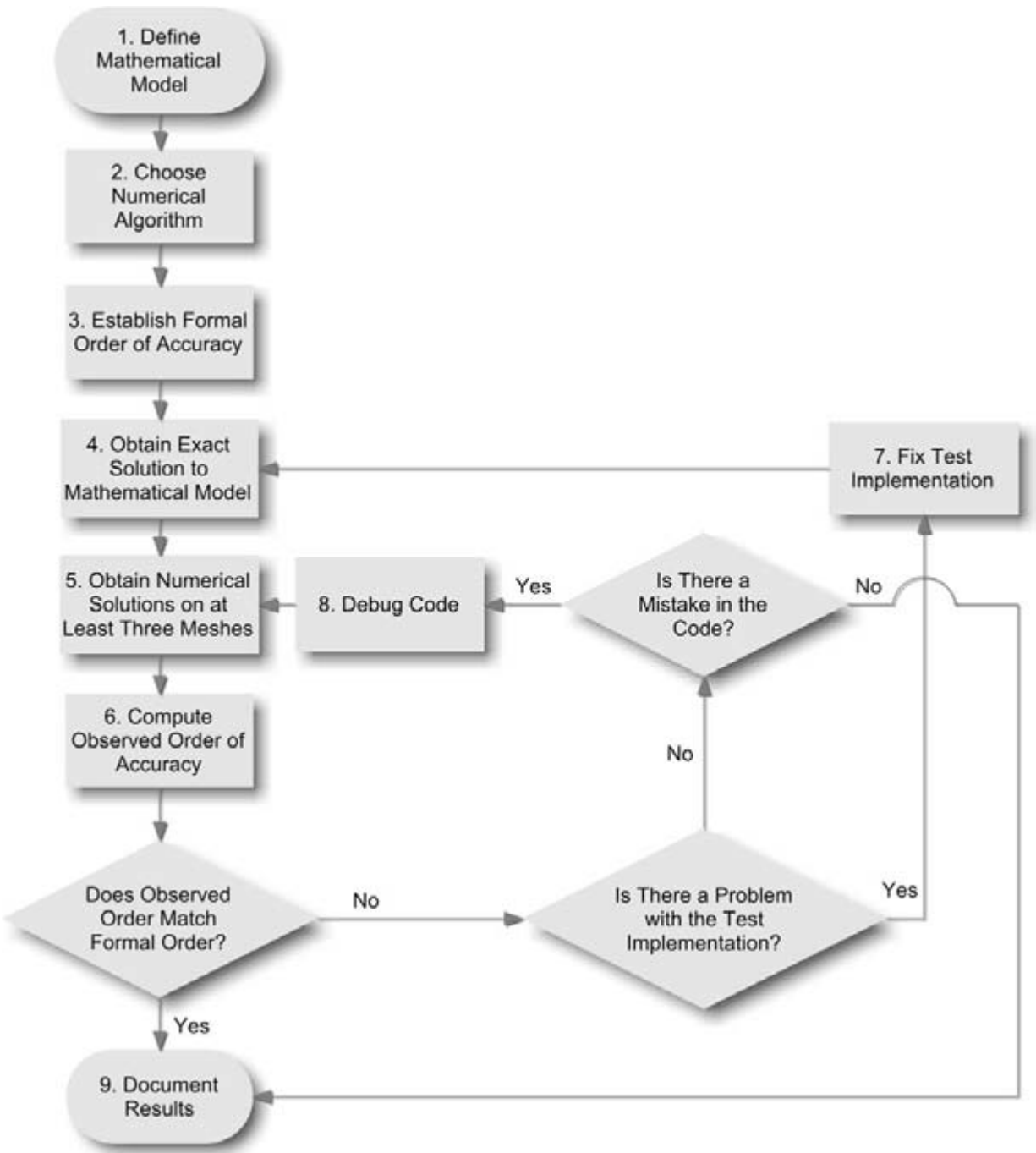


Figure 5-13 Order of accuracy test (Roy and Oberkampf, 2011)

The Taylor series expansion of u_{i+1} and u_{i-1} around u_i are:

$$u_{i+1} = u_i + \frac{\partial u_i}{\partial t} \frac{(\Delta t)}{1} + \frac{\partial^2 u_i}{\partial t^2} \frac{(\Delta t)^2}{2} + \frac{\partial^3 u_i}{\partial t^3} \frac{(\Delta t)^3}{6} + O(\Delta t^4) \quad (5.5)$$

$$u_{i-1} = u_i + \frac{\partial u_i}{\partial t} \frac{(-\Delta t)}{1} + \frac{\partial^2 u_i}{\partial t^2} \frac{(-\Delta t)^2}{2} + \frac{\partial^3 u_i}{\partial t^3} \frac{(-\Delta t)^3}{6} + O(\Delta t^4) \quad (5.6)$$

Substituting the values of u_{i+1} and u_{i-1} into Equation (5.4):

$$\underbrace{m \frac{u_{i+1} - 2u_i + u_{i-1}}{\Delta t^2} + c \frac{u_{i+1} - u_{i-1}}{2\Delta t} + ku_i - p_i}_{L_h(u)} = \underbrace{m \frac{d^2 u}{dt^2} + c\dot{u} + ku - p(t)}_{L(u)} + \underbrace{\left(\frac{m}{12} \frac{\partial^4 u_i}{\partial t^4} + \frac{c}{6} \frac{\partial^3 u_i}{\partial t^3} \right) \Delta t^2 + O(\Delta t^3)}_{\text{truncation error: } TE_h(u)} \quad (5.7)$$

$$\underbrace{m \frac{u_{i+1} - 2u_i + u_{i-1}}{\Delta t^2} + c \frac{u_{i+1} - u_{i-1}}{2\Delta t} + ku_i - p_i}_{L_h(u)} = \underbrace{m \frac{d^2 u}{dt^2} + c\dot{u} + ku - p(t)}_{L(u)} + \underbrace{\left(\frac{m}{12} \frac{\partial^4 u_i}{\partial t^4} + \frac{c}{6} \frac{\partial^3 u_i}{\partial t^3} \right) \Delta t^2 + O(\Delta t^3)}_{\text{truncation error: } TE_h(u)} \quad (5.8)$$

or,
$$L_h(u) = L(u) + TE_h(u) \quad (5.9)$$

where $L_h(u)$ represents the discretized model, $L(u)$ is the mathematical model and $TE_h(u)$ is the truncation error. The parameter h defines the systematic mesh refinement over space and time. For the discretization considered here, h is the time step Δt used in the static and dynamic analysis. The formal order of accuracy is defined as the smallest exponent of the discretization parameter, Δt , in the truncation error, $TE_h(u)$. Hence the discretized numerical model described by Equation (5.4) is second-order accurate, or has a formal order of accuracy $p = 2$.

If u_h is the exact solution to the discrete expression $L_h(u)$, then $L_h(u_h) = 0$, and if \tilde{u} is the exact solution to the mathematical model, then $L(\tilde{u}) = 0$.

Substituting $u = u_h$ in Equation (5.9) and subtracting $L(\tilde{u}) = 0$ from it:

$$L(u_h) - L(\tilde{u}) + TE_h(u_h) = 0 \quad (5.10)$$

The discretization error, ε_h , is the difference between the solution to the discretized equations and the exact solution of the mathematical model:

$$\varepsilon_h = u_h - \tilde{u} \quad (5.11)$$

If the operator L is linear, then $L(u_h) - L(\tilde{u}) = L(u_h - \tilde{u}) = L(\varepsilon_h)$. Substituting into Equation (5.10) gives:

$$L(\varepsilon_h) = -TE_h(u_h) \quad (5.12)$$

The above equation implies that discretization error is propagated in same manner as the original solution u_h .

To obtain the observed order of accuracy, consider a Taylor series expansion of the solution u_h to the discretized equations:

$$u_h = u_{h=0} + \left. \frac{\partial u}{\partial h} \right|_{h=0} h + \left. \frac{\partial^2 u}{\partial h^2} \right|_{h=0} \frac{(h)^2}{2!} + \left. \frac{\partial^3 u}{\partial h^3} \right|_{h=0} \frac{(h)^3}{3!} + O(h^4) \quad (5.13)$$

where $h = \Delta t$ is the discretization parameter and $u_{h=0} = \tilde{u}$ is the exact solution to the mathematical model. For a formal p^{th} -order accurate solution scheme, by definition $\partial^k u / \partial h^k = 0$ for $k < p$ since the order of terms less than p does not contribute to the truncation error. Equation (5.13) is reduced to:

$$\varepsilon_h = u_h - u_{h=0} = g_p h^p + O(h^{p+1}) \quad (5.14)$$

where g_p is a function of the spatial and temporal variables, and ε_h is the discretization error. If $O(h^{p+1})$ is neglected, the logarithmic form of Equation (5.14) can be written as:

$$\log(\varepsilon_h) = p \log(h) + \log(g_p) \quad (5.15)$$

which is the equation of a straight line in log-space. The slope of the straight line provides the order of accuracy, p .

Equation (5.14) is used to calculate the observed order of accuracy by replacing the formal order of accuracy p with the observed order of accuracy \hat{p} . The asymptotic zone of the solution of a discretized equation is defined where the discretization parameter h approaches to zero. If two different time steps $h = \Delta t$ and $h = r\Delta t$ are used in the asymptotic solution zone, where terms of order $p+1$ vanish, two equations are obtained:

$$\varepsilon_{\Delta t} = g_p (\Delta t)^{\hat{p}} \quad (5.16)$$

$$\varepsilon_{r\Delta t} = g_p (r\Delta t)^{\hat{p}} \quad (5.17)$$

The observed order of accuracy \hat{p} is obtained by eliminating g_p from Equation (5.17) and Equation (5.16) as:

$$\hat{p} = \frac{\ln\left(\frac{\varepsilon_{r\Delta t}}{\varepsilon_{\Delta t}}\right)}{\ln(r)} \quad (5.18)$$

If an exact solution to the mathematical model is available, the observed order of accuracy can be obtained by obtaining response values for only two values of mesh discretization parameters using Equation (5.18). However, if an exact solution to a mathematical model is not available, which is usually the case with most of the mathematical models used for the nonlinear analysis of structures, three values of the response parameter can be evaluated for time discretization of Δt , $r\Delta t$ and $r^2\Delta t$, respectively:

$$\begin{aligned} u_1 &= u_{\Delta t} = u_{\Delta t=0} + g_p \Delta t^{\hat{p}} \\ u_2 &= u_{r\Delta t} = u_{\Delta t=0} + g_p (r\Delta t)^{\hat{p}} \\ u_3 &= u_{r^2\Delta t} = u_{\Delta t=0} + g_p (r^2\Delta t)^{\hat{p}} \end{aligned} \quad (5.19)$$

where u is a response quantity (e.g, displacement, velocity, acceleration, temperature), and $O(h^{p+1})$ is zero in the asymptotic zone of the solution. Solving the above equations, the observed order of accuracy is obtained as:

$$\hat{p} = \frac{\ln\left(\frac{\|u_3 - u_2\|}{\|u_2 - u_1\|}\right)}{\ln(r)} \quad (5.20)$$

If the observed order of accuracy is found equal to the formal order of accuracy, then the code is considered to be verified. The process described in flowchart of Figure 5-13 is followed.

For response-history analysis the observed order of accuracy is evaluated locally on a point-by-point basis in the domain. The observed order of accuracy cannot be evaluated at crossover points where the difference between responses obtained at different mesh discretization changes its sign, as shown in Figure 5-14. The observed order determined locally might produce unrealistic values. The global norm of the discretization error should be used for order verification tests.

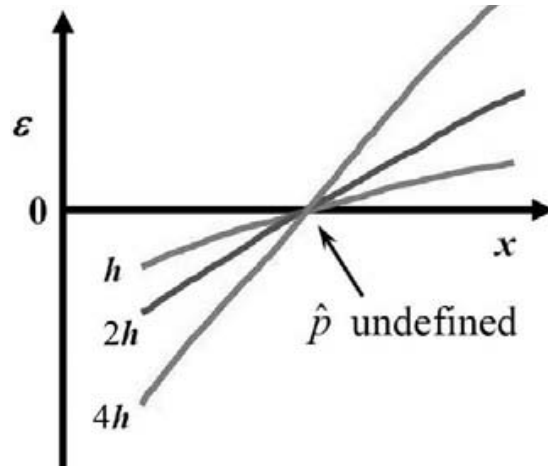


Figure 5-14 Observed order of accuracy at a crossover point (Oberkampf and Roy, 2010)

The procedure above describes calculation of formal and observed order of accuracies for a linear system using the Central Difference integration scheme. The formal order of accuracy cannot easily be calculated for nonlinear systems.

The observed order of accuracy of the computational models in the axial and shear directions are determined in the following sections. Loads are applied such that the response is linear. The formal order of accuracy for the linear system was obtained as two; it could not be determined for nonlinear problems. The observed order of accuracy is obtained for nonlinear problems to illustrate the difficulty associated with order verification tests of nonlinear problems.

A two-node bearing element, fixed at its base, is subjected to uniform sinusoidal excitation in axial and shear directions. The shear displacement response is obtained for several time discretization values. Response-history analyses were performed to obtain the variation of the order of accuracy with time discretization. Equation (5.20) is used to calculate the order of accuracy. A value of Δt and r are chosen and then response quantities are obtained at ten time discretization values $r^j \Delta t$ ($1 \leq j \leq 11$). Using the response quantity available at six time steps, eight orders ($1 \leq j \leq 9$) of accuracy are obtained to demonstrate that the observed order of accuracy is converging to a value as the mesh discretization parameter, Δt , approaches zero. The observed order of accuracy is calculated as:

$$\text{Order} = \frac{\log \left(\frac{\|u(r^j \Delta t) - u(r^{j-1} \Delta t)\|}{\|u(r^{j-1} \Delta t) - u(r^{j-2} \Delta t)\|} \right)}{\log(r)} \quad (5.21)$$

The L_1 and L_2 norms of the difference in response on point-by-point basis were obtained over the history of response and the orders of accuracy were calculated.

A series of analyses were performed on LDR and LR bearings to obtain the variations of orders of accuracy with time discretization in the shear direction. The Newmark average acceleration method was used for integration scheme. Results are presented in Figure 5-15 and Figure 5-16 for the axial and shear directions, respectively. The observed orders of accuracy converge to two for numerical models of LDR and LR bearings in the axial and shear directions. As the

observed order of accuracy matches the formal order of accuracy, the code correctness can be confirmed for the numerical models when the response is linear.

The observed order of accuracy was also determined for nonlinear response. It was found that as the magnitude of the applied loads is increased, such that the response changes from linear to nonlinear, the order of accuracy is decreased from two to one in the shear direction. However, the order of accuracy for the numerical model in the axial direction did not converge to a fixed value. Results are presented in Figure 5-17.

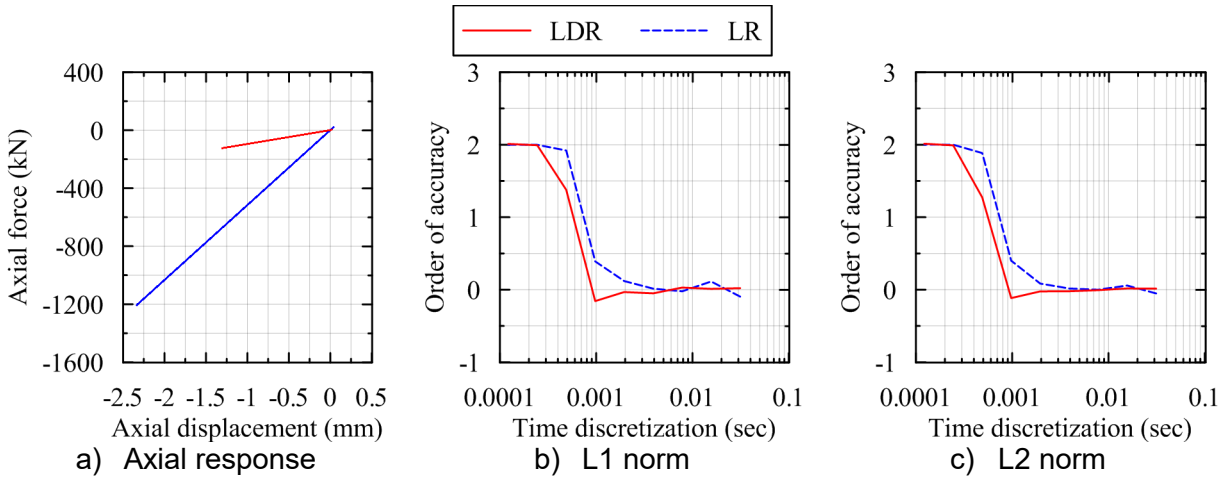


Figure 5-15 Order of accuracy in the vertical direction ($a_g = g \sin(\pi t)$)

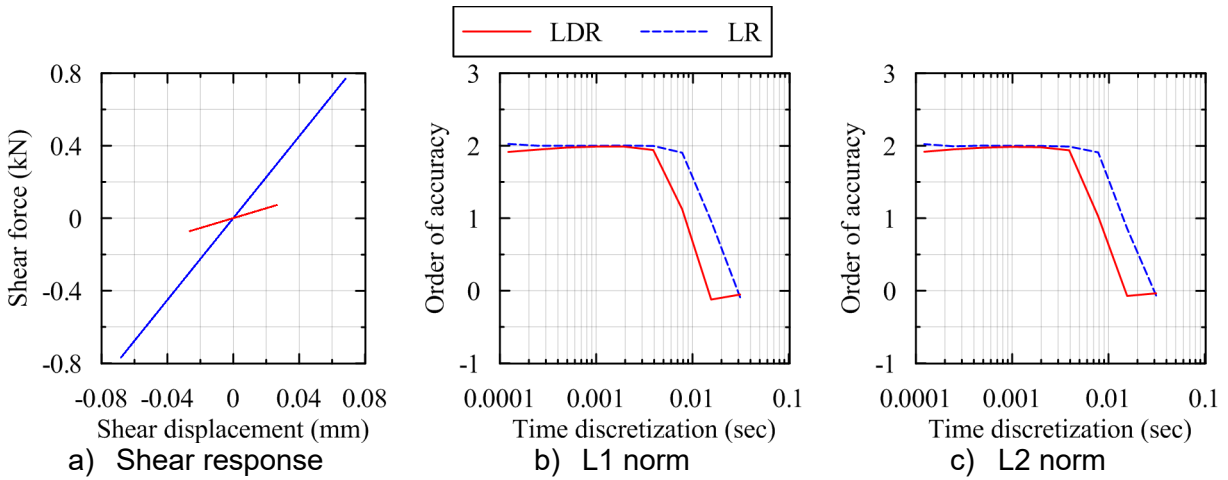


Figure 5-16 Order of accuracy in the horizontal direction ($a_g = 0.001g \sin(\pi t)$)

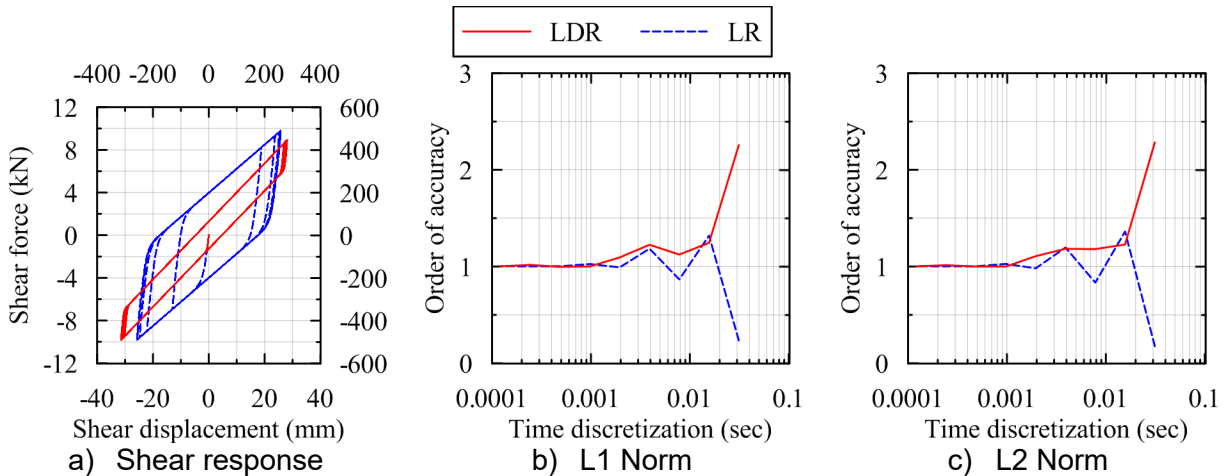


Figure 5-17 Order of accuracy in horizontal direction ($a_g = 0.1g \sin(\pi t)$ for LDR and $a_g = 0.5g \sin(\pi t)$ for LR bearing)

Heating of the lead core

The temperature increase in the lead core of the LR bearing was calculated at different values of Δt to estimate the observed orders of accuracy of the numerical model of the LR bearing for the linear and nonlinear response discussed above. Results are presented in Figure 5-18.

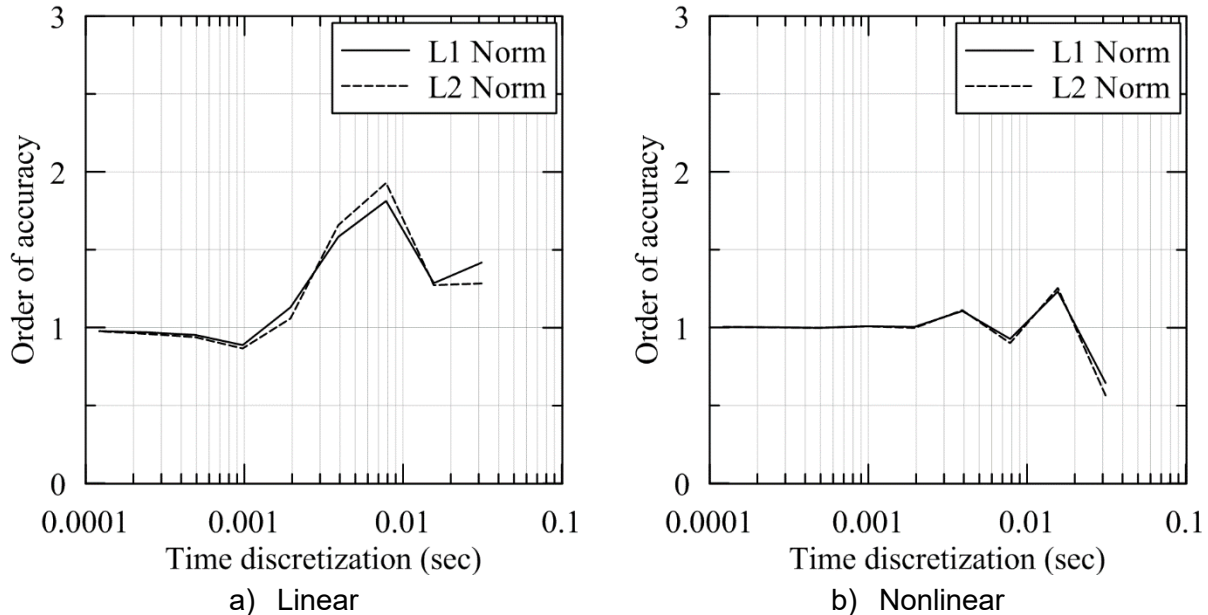


Figure 5-18 Observed order of accuracy of the heating model

5.5.2.2 Software Quality Assurance

The software program ABAQUS and the software framework OpenSees provide a modular framework for implementation of new mathematical models through user subroutines. The user subroutines (user elements for LDR and LR bearings) are written using one of the programming languages, and form a part of the software program that can be used to perform an analysis (e.g., response-history analysis of a NPP). The code verification of user subroutines was discussed in the previous sections. However, errors might be present due to the global framework of OpenSees and ABAQUS. The Software Quality Assurance (SQA) check, identify, and remove errors associated with the global framework and ensure that the user subroutines are free from programming errors.

Errors are most likely due to the source code of a software program, but can also be introduced due to the compiler (e.g., limited precision, undeclared variables). For example, C++ and FORTRAN77 treat uninitialized variables differently when used in an executable statement. The adequacy of a software program to produce reliable results with a specified set of libraries using a specific compiler is assessed. Software quality assurance must always be performed during development of the software product and before it is used for the verification of a computational model that has been created using the framework of the software program. Most of the commercial software programs publish their verification or benchmark manuals as part of their SQA. ABAQUS has a verification manual (Dassault, 2010f) and a benchmark manual (Dassault, 2010g). The verification manual evaluates the accuracy of numerical algorithm implementation, and the benchmark manual assesses the performance of the software program.

The scope of work for addressing programming errors is limited to user subroutines. It is assumed that OpenSees and ABAQUS have been checked for programming errors by their developers. Some of the commonly encountered sources of programming errors are:

1. Default parameters values
2. Units of measurements
3. Uninitialized variables
4. Division by zero
5. Values of constants
6. Incompatible divisions

The user elements in OpenSees and ABAQUS were checked for errors arising from such sources and all identified issues were addressed.

5.5.3 Solution verification

Solution verification (also called calculation verification) assesses the accuracy of the approximate discretized numerical solution of a mathematical model that is implemented for computational predictions. Solution verification activities commence only after code verification is completed. The error associated with the numerical model are discussed in the following sections.

5.5.3.1 Round-off error

Round-off error is contributed by the finite arithmetic used by a computer program. For example, the value of $2.0 \times (1.0 / 2.0)$ should ideally be 1.0 if infinite precision is used, however, it is often calculated less than 1.0 (say 0.999 999) in a single-precision computation. Most programming languages require the user to initialize the type of variable (text, number, boolean etc). The C/C++ source code in OpenSees needs the user to define the numeric type of variable as int, float, double or long. Each variable type uses a different precision in the computations. Specifying the largest precision type for each variable is not desirable as it slows down the execution of the program. If appropriate variable precision is used in a source code, errors due to round off are usually very small when compared to those associated with discretization. Round-off error is not investigated here because it is not expected to have any significant effect on the results obtained using the mathematical models of elastomeric bearings.

5.5.3.2 Iterative convergence error

Iterative methods are employed to solve the system of equations obtained after discretization of the mathematical model. The system of equations takes the form $Ax = b$, where A is the coefficient matrix, b is the column vector and X is the desired solution. The iterative error is the difference between the solution obtained using iterative methods and the exact solution ($x = A^{-1}b$) of the system of equations. The iterative method is employed because exact solution obtained using direct methods is computationally expansive. The solution process in iterative methods begins with an initial estimate of the value of X and iterations are then performed until the iterative residual, $R^k = b - Ax^k$, becomes acceptably small. The Newton-Raphson method is one of iterative techniques that is used in OpenSees to solve a system of equation. The iterative error is usually much smaller than the discretization error. OpenSees provides the option to specify the iterative step convergence criteria. The user can always control the iterative error by specifying a very small iterative residual for convergence.

5.5.3.3 Discretization error

Discretization error is often one of the largest source of numerical errors, which is the most difficult to estimate. An appropriate temporal discretization needs to be assumed for an OpenSees analysis. Most of the ground motions available through PEER ground motion database are sampled at intervals of either 0.005 or 0.01 sec. If a smaller analysis time step is used, OpenSees linearly interpolates the ground motion data to provide values at intermediate points. Providing a smaller time step often increases the stability of a computational solution. The increased resolution of response data due to smaller analysis time step helps to capture response in a region of very high stiffness (in axial direction), which might be missed if a larger time step is used. The most notable effect of discretization in dynamic analysis is numerical damping due to use of implicit transient integrators (e.g., Newmark, Hilber-Hughes-Taylor methods), which will be discussed later. In response-history analysis, transient integrators provide an additional source of damping that is undesirable.

There are numerous methods to estimate discretization error. The Generalized Richardson Exploration (GRE) is used here because of its ease of application. This method is useful when an exact solution to the mathematical model is either unavailable or difficult to evaluate. The five conditions that need to be satisfied for application of this method are (Oberkampf and Roy, 2010):

1. The formal order of accuracy should match the observed order of accuracy.
2. Uniform mesh spacing should be used in the numerical model.
3. Discretization should be refined systematically.
4. The obtained solution should be smooth in nature.
5. Other numerical error sources should be small compared to the discretization error.

The GRE uses a systematic discretization refinement to obtain a higher order estimate (order of accuracy $> p$) of the exact solution to the mathematical model, which can be used in place of the exact solution to obtain error estimates. The information presented below extends the discussion presented in Section 5.5.2.1. The discretization error of an p^{th} -order accurate response quantity u is given by:

$$\varepsilon_h = u_h - \tilde{u} = g_p h^p + g_{p+1} h^{p+1} + O(h^{p+2}) \quad (5.22)$$

where u_h is the exact solution to the discretized differential equation (numerical model) and \tilde{u} is the exact solution to the differential equation (mathematical model). The errors are estimated for two discretization values $h = \Delta t$ and $h = r\Delta t$ as:

$$u_{\Delta t} = \tilde{u} + g_p \Delta t^p + g_{p+1} (r\Delta t)^{p+1} + O(\Delta t^{p+2}) \quad (5.23)$$

$$u_{r\Delta t} = \tilde{u} + g_p (r\Delta t)^p + g_{p+1} (r\Delta t)^{p+1} + O(\Delta t^{p+2}) \quad (5.24)$$

The term g_p is eliminated from the two equations to obtain:

$$\tilde{u} = u_{\Delta t} + \frac{u_{\Delta t} - u_{r\Delta t}}{r^p - 1} + g_{p+1} \Delta t^{p+1} \frac{r^p (r - 1)}{r^p - 1} + O(\Delta t^{p+2}) \quad (5.25)$$

Combining the higher order terms with the exact solution gives a higher order estimate of the exact solution:

$$\bar{u} = \tilde{u} - g_{p+1} \Delta t^{p+1} \frac{r^p (r-1)}{r^p - 1} - O(\Delta t^{p+2}) \quad (5.26)$$

where \bar{u} is the higher order estimate ($p+1$ order accurate) of the exact solution to the mathematical model and is given by the expression:

$$\bar{u} = u_{\Delta t} + \frac{u_{\Delta t} - u_{r\Delta t}}{r^p - 1} \quad (5.27)$$

Hence, \bar{u} is a higher order accurate solution of the exact solution \tilde{u} than u . In most cases, the exact solution \tilde{u} of a mathematical model is not available. If the five conditions for the application of Richardson extrapolation method are satisfied, then \bar{u} calculated in the asymptotic zone of the discretized numerical solution can replace \tilde{u} . The discretization error is calculated using $\varepsilon_{\Delta t} = u_{\Delta t} - \bar{u}$ to give:

$$\varepsilon_{\Delta t} = -\frac{u_{\Delta t} - u_{r\Delta t}}{r^p - 1} \quad (5.28)$$

To confirm the reliability of the discretization error, calculations should be performed for different discretization values to obtain at least three estimates of the discretization error.

Ten estimates of discretization error are obtained here. The response quantities of interest, u_i , are calculated at several time discretization values, $r^i \Delta t$. The higher order estimate of exact solution, \bar{u} , are determined using response quantities u_i and u_{i+1} available at the analysis time step of $r^i \Delta t$ and $r^{i+1} \Delta t$, respectively. The percentage discretization error is given as:

$$\% \varepsilon_{\Delta t} = \frac{u_i - \bar{u}}{\bar{u}} \times 100\% \quad (5.29)$$

where \bar{u} is calculated using u_i and u_{i+1} as:

$$\bar{u} = u_i + \frac{u_i - u_{i+1}}{r^p - 1} \quad (5.30)$$

Substituting the value of \bar{u} in Equation (5.29), the discretization error is obtained as:

$$\% \varepsilon_{\Delta t} = \frac{\varepsilon_{\Delta t}}{\bar{u}} \times 100\% = \frac{u_i - u_{i+1}}{u_{i+1} r^p - u_i} \times 100\% \quad (5.31)$$

The index, i , is varied from 1 to 10 to obtain error estimates for the ten values of time discretization. The observed orders of accuracy of the mathematical models of the elastomeric bearing were calculated and reported in Figure 5-16. Ensuring that the observed order of accuracy is equal to the formal order of accuracy is one of the criteria for applying the Richardson extrapolation method to obtain the discretization error. The formal order of accuracy

of the numerical models in the axial shear direction was obtained as two for linear response of LDR and LR bearings, while it could not be calculated for nonlinear response. Oberkampff and Roy (2010) suggest that if the solutions at the three time discretization values used for the calculation of the observed order of accuracy are in the asymptotic range, the observed order of accuracy can replace the formal order of accuracy to calculate the discretization error. The observed orders of accuracy of two and one are used to calculate the discretization errors for linear and nonlinear response, respectively. The value of refinement ratio r is 2. The L_1 norm of the discretization errors calculated on point-by-point basis over the history of response are obtained. Only the first two cycles of the response is used to calculate the discretization error in the axial direction because unrealistic values of discretization error might be obtained due to period lengthening in the numerical response: an issue with implicit integrators and finite time discretization that is discussed in a later section.

The discretization error in the displacements for the analyses cases presented in Section 5.5.2.1 are reported in Table 5-6 and Table 5-7 for the axial and shear directions, respectively. The plots are presented here only for nonlinear response, noting that linear response in shear is seldom observed in elastomeric bearings during earthquake shaking. The plot of the variation of the discretization error in shear displacement with time step is presented in Figure 5-19 and Figure 5-20. The plot of the shear force-displacement loops of the LDR and LR bearings obtained using different time steps are presented in Figure 5-21 and Figure 5-22, respectively. The variation of the temperature rise in the lead core of a LR bearing obtained using different analysis time steps are presented in Figure 5-23.

The discretization error in the response quantities decreases as the analysis time step is reduced. The reduction in the discretization error with the time step suggests a monotonic convergence of the solution to the numerical model. Reliable estimates of the discretization error can only be obtained in the asymptotic zone of the solution. The asymptotic zone of solution for shear displacement and temperature was obtained in Section 5.5.2.1.3 for time discretization values smaller than 0.01 sec. A time step of 0.01 sec provides discretization error in the response quantities (e.g., displacement, force, temperature) less than 5%, except in the nonlinear axial response. A larger discretization error in nonlinear axial response is observed due to local instability in the numerical response around cavitation, although it does not affect the maximum value of axial force or displacements.

Table 5-6 Discretization errors for numerical model in the axial direction

Δt (sec)	LDR		LR	
	Linear	Nonlinear	Linear	Nonlinear
0.125	4.93	--	5.60	125.58
0.0625	4.04	60.55	4.51	46.79
0.03125	19.53	34.22	4.71	34.32
0.015625	4.27	79.61	4.86	89.99
0.007813	5.20	85.70	5.60	34.57
0.003906	5.01	111.15	5.16	40.24
0.001953	4.95	6.14	8.92	11.60
0.000977	2.91	4.62	1.04	130.11
0.000488	0.57	0.79	0.43	2.08
0.000244	0.14	0.04	0.19	0.23

Table 5-7 Discretization errors for numerical model in the shear direction

Δt (sec)	LDR		LR		Temperature	
	Linear	Nonlinear	Linear	Nonlinear	Linear	Nonlinear
0.125	10.99	25.48	130.27	80.80	3.88	14.30
0.0625	13.40	8.38	21.58	16.43	1.38	7.91
0.03125	53.36	2.60	9.62	4.54	0.53	2.63
0.015625	7.13	2.61	4.76	2.21	0.19	1.22
0.007813	2.87	1.24	0.77	0.98	0.08	0.56
0.003906	0.43	0.40	0.17	0.48	0.04	0.27
0.001953	0.11	0.18	0.04	0.24	0.02	0.13
0.000977	0.03	0.09	0.01	0.12	0.01	0.07
0.000488	0.01	0.04	0.00	0.06	0.01	0.03
0.000244	0.00	0.02	0.00	0.03	0.00	0.02

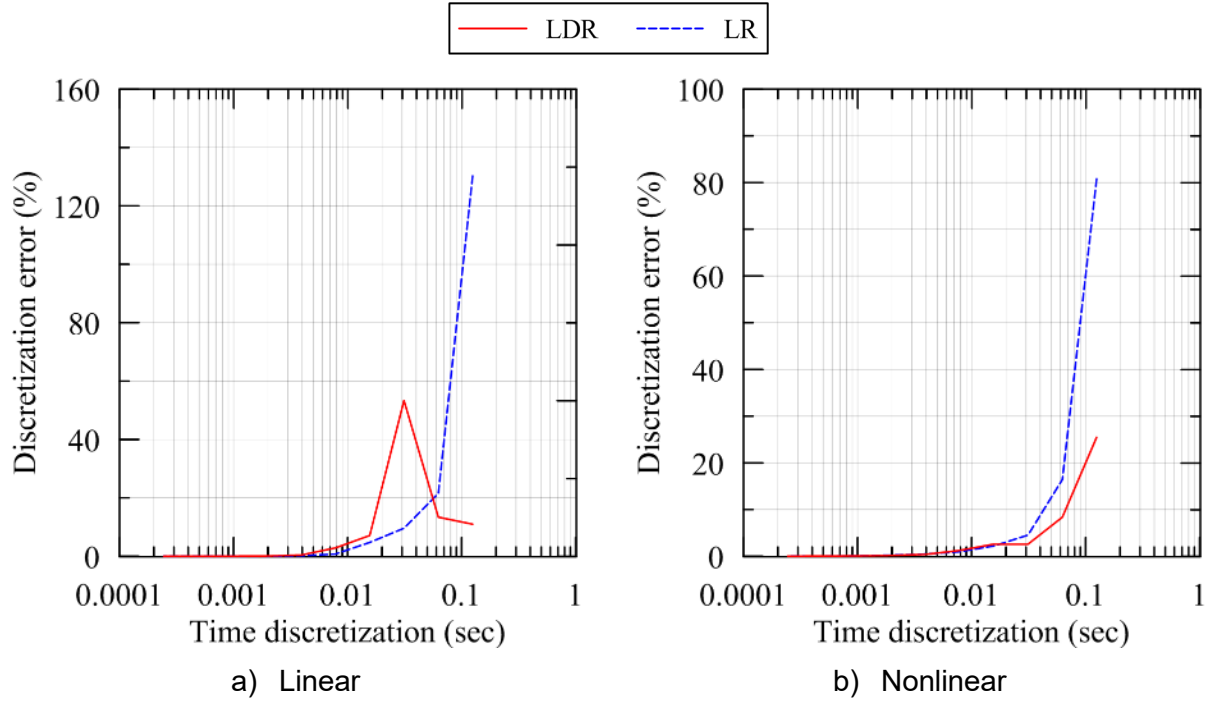


Figure 5-19 Discretization error in the shear displacement

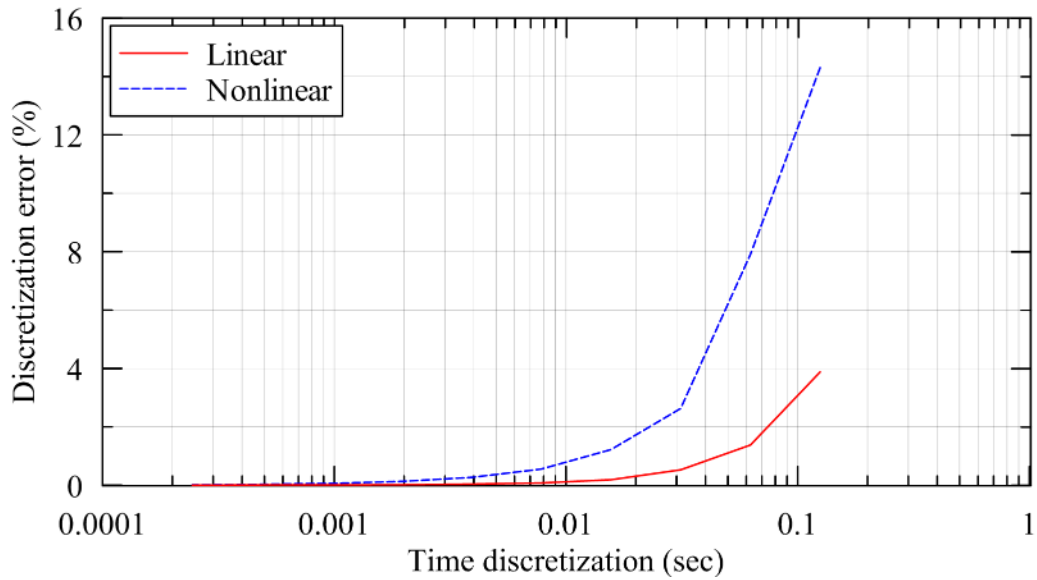


Figure 5-20 Discretization error in the temperature rise of the lead core

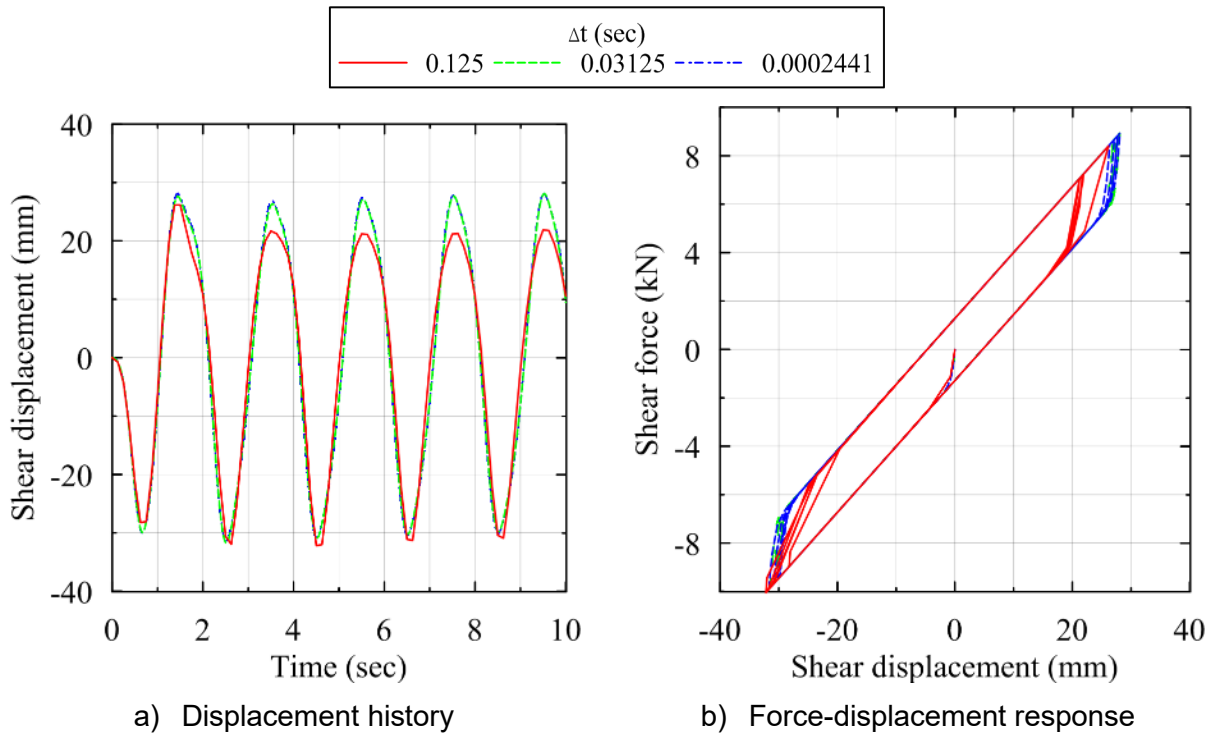


Figure 5-21 Horizontal shear response of a LDR bearing

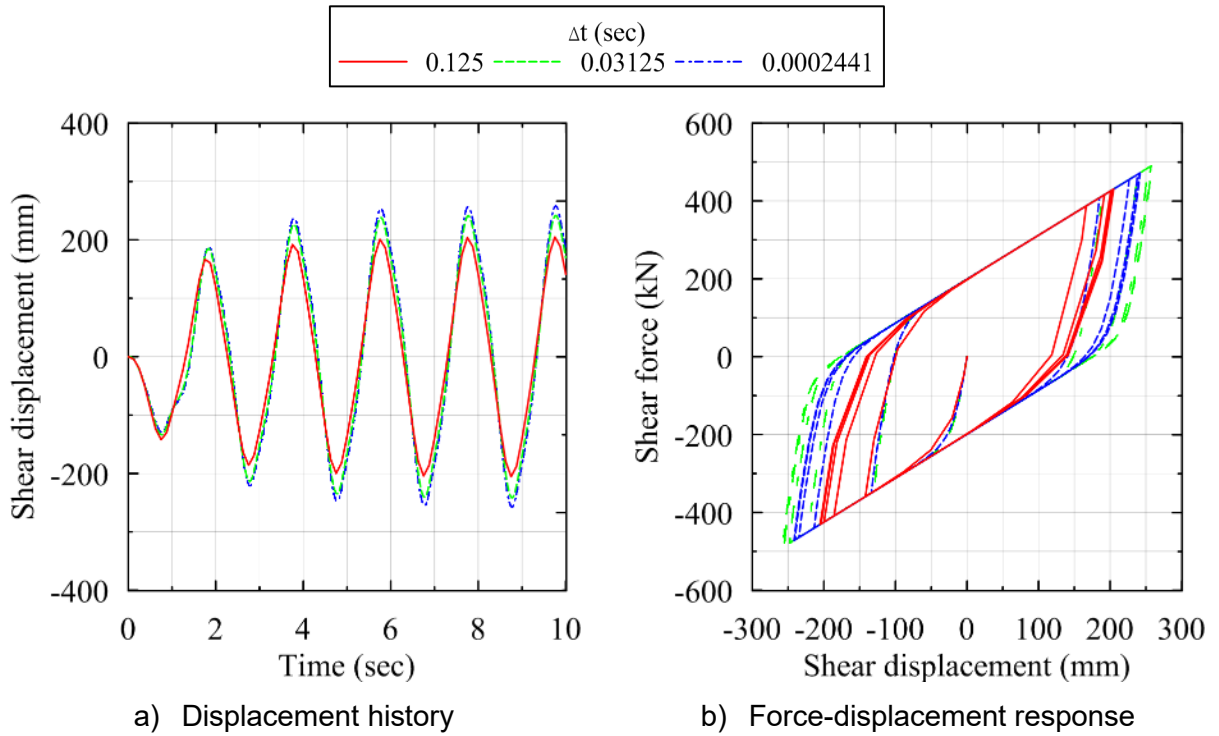


Figure 5-22 Force-displacement loops for a LR bearing

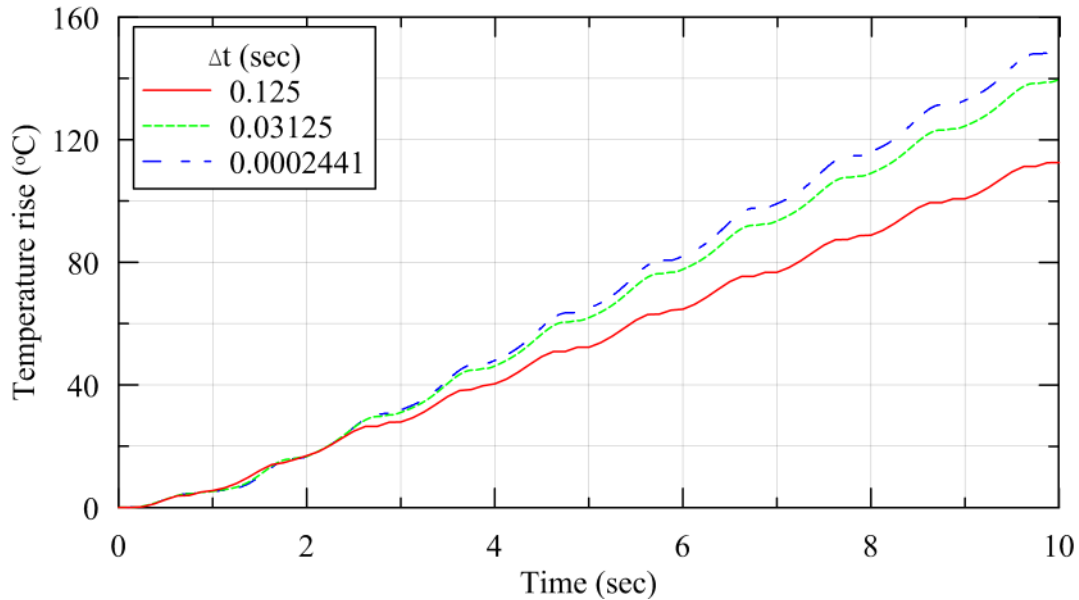


Figure 5-23 Temperature increase in the lead core

An observed order of accuracy of 1 was assumed in the absence of a formal order of accuracy for the calculation of the discretization error in the numerical models of the nonlinear axial and shear behavior. If the observed order of accuracy is higher than the formal order of accuracy, the discretization error obtained using the observed order of accuracy provides an unconservative estimate.

The discretization error in shear displacement at each time step for different values of the temporal discretization is shown in Figure 5-24 for LDR and LR bearings. Local spikes in the discretization error might contribute substantially to the global norm of the discretization error, but do not affect the maximum value of a response quantity. The maximum horizontal displacement for the three analysis time step of Figure 5-24a are 31.4 mm, 31.5 mm, and 31.6 mm, respectively, whereas for Figure 5-24b they are 249 mm, 257 mm, and 257 mm, respectively. Hence, discretization error in a numerical model should always be interpreted carefully and the contributions of local discretization error must be checked.

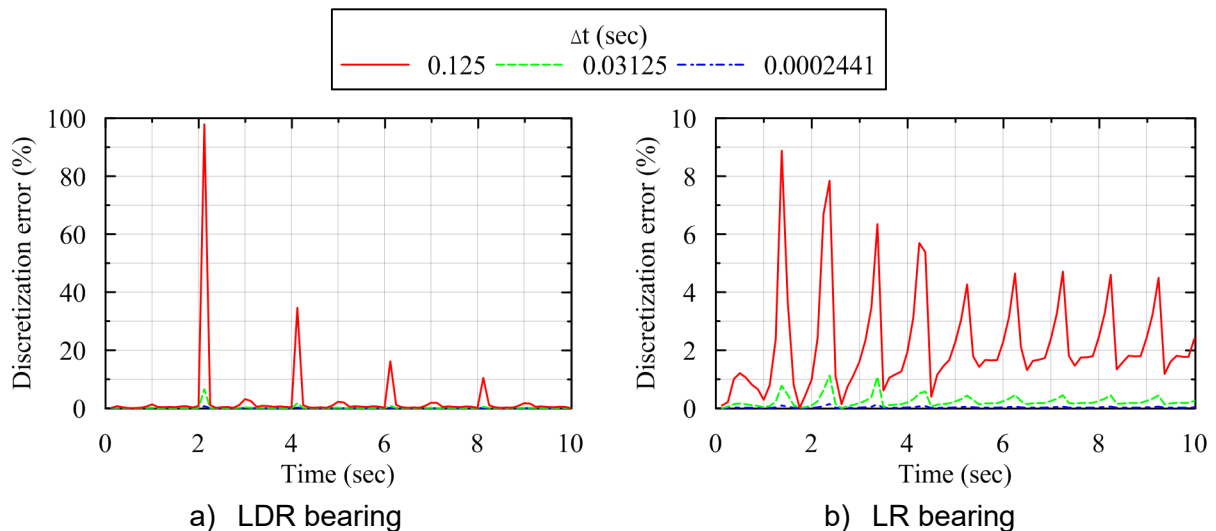


Figure 5-24 Discretization error in shear displacement

5.5.3.4 Damping in OpenSees

OpenSees provides option to use three types of damping: 1) Rayleigh damping, 2) mass proportional damping, and 3) stiffness proportional damping. There is no option to use modal damping unlike other structural analysis software programs (e.g., SAP2000). Analyses are performed to verify damping calculations performed by OpenSees. The LDR5 bearing of Warn (2006) is assigned 2% damping in the horizontal direction using the three damping definitions listed above. An initial displacement of 0.01 mm is imposed and the bearing is then allowed to go into free vibration response. The same analyses are performed in axial direction. A small initial displacement is used to ensure linear elastic behavior to avoid any contribution of viscous damping. The free-vibration displacement response of a single-degree-of-freedom system is:

$$u(t) = e^{-\xi\omega_n t} \left[u(0) \cos \omega_D t + \frac{\dot{u}(0) + \xi\omega_n u(0)}{\omega_D} \sin \omega_D t \right] \quad (5.32)$$

where ξ is the damping ratio; $u(0)$ and $\dot{u}(0)$ are the initial displacement and velocity, respectively; ω_n is the natural frequency, and $\omega_D = \omega_n \sqrt{1 - \xi^2}$. The response of the bearing for the three damping options and the analytical response is presented in Figure 5-25 and Figure 5-26 for horizontal and vertical directions, respectively. Numerical damping values are calculated from the free vibration response using (Chopra, 2007):

$$\xi = \frac{1}{2\pi j} \ln \frac{u_i}{u_{i+j}} \quad (5.33)$$

where u_i and u_{i+j} are the i th and $(i + j)$ th peak displacement response. The damping values calculated from numerical response are summarized in Table 5-8. No difference is observed between the assigned damping and the damping calculated from the numerical response.

Table 5-8 Damping ratios (%) calculated from numerical response

Direction	Damping definition		
	Rayleigh	Mass proportional	Stiffness proportional
Horizontal	1.997	1.997	1.997
Vertical	1.994	1.994	1.994

5.5.3.5 Geometric nonlinearity in OpenSees

The elements for elastomeric bearings (*ElastomericX* and *LeadRubberX*) include the second order effects of geometric nonlinearity on stiffness by using analytical expressions for mechanical properties derived using explicit consideration for geometric nonlinearity (details are in Chapter 3). The $P - \Delta$ moments are divided equally among the two nodes of the bearing.

To verify the $P - \Delta$ calculations, the two-node macro model was analyzed with different user elements for the elastomeric bearing: 1) *ElastomericX*, 2) *elastomericBoucWen*, and 3) *TwoNodeLink*. The results obtained using *ElastomericX* (and *LeadRubberX*) are compared with existing bearing elements, *elastomericBoucWen* and *TwoNodeLink*, in OpenSees, and against theoretical calculations. The properties of LDR5 bearing in Warn (2006) are used for the user elements.

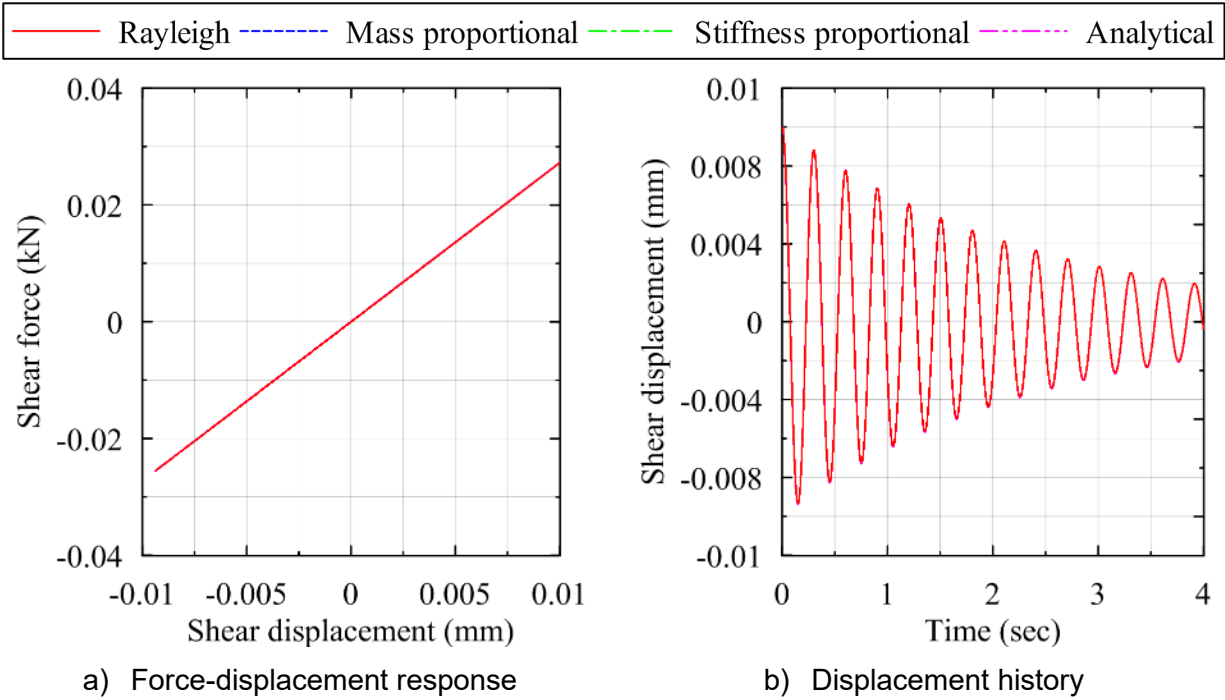


Figure 5-25 Free vibration response of a LDR bearing in the horizontal direction ($u_0 = 0.01$ mm, $\zeta = 2\%$)

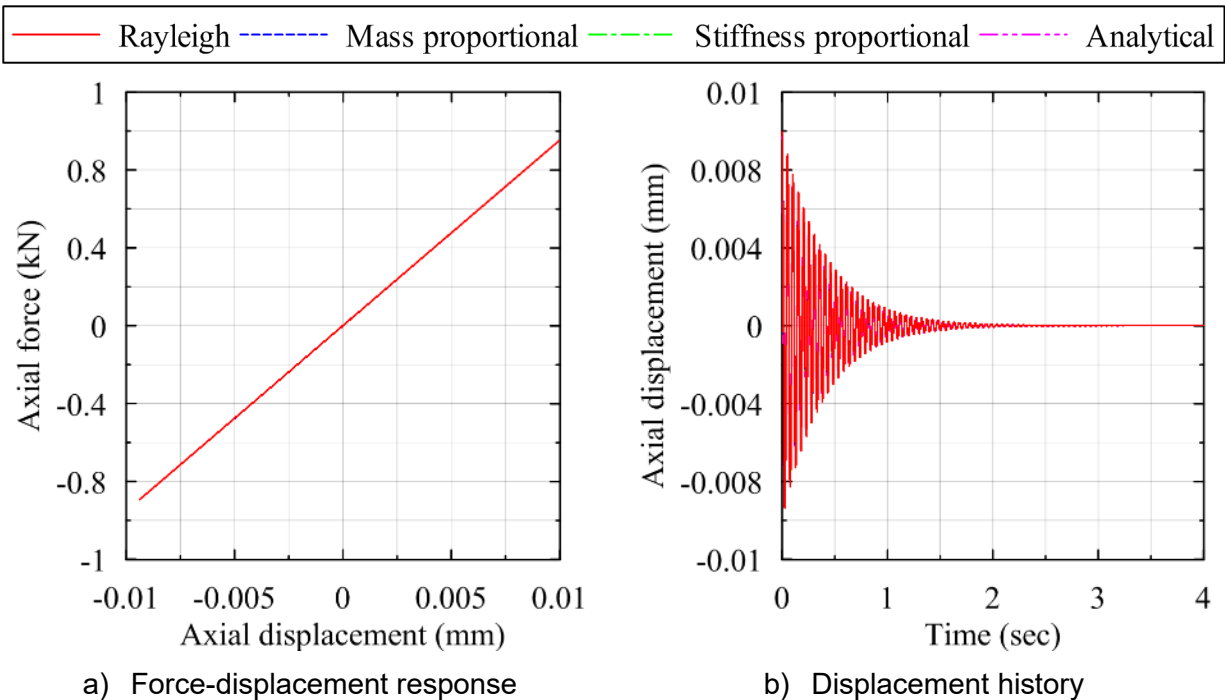


Figure 5-26 Free vibration response of a LDR bearing in the vertical direction ($u_0 = 0.01$ mm, $\zeta = 2\%$)

A horizontal strain of 100% and an axial load of 10% of critical buckling load are applied to the top node (Node 2) of the macro model. The distribution of the bending moment at the two nodes of the element is shown in Figure 5-27.

The values of the parameters F , P , Δ , and h are 16846 N, 38491 N, 0.06 m, and 0.117 m, respectively. The theoretical value of the end moments is obtained as:

$$M = \frac{Fh}{2} + \frac{P\Delta}{2} \quad (5.34)$$

The force and the moments at the two nodes of the elastomeric bearing are compared in Table 5-9. No difference is observed between the results.

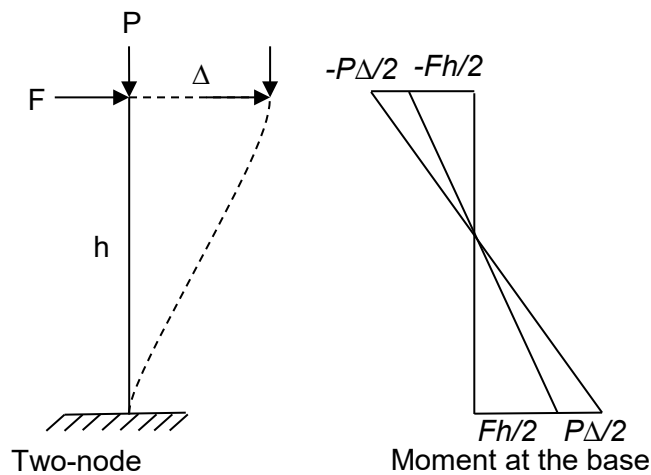


Figure 5-27 Bending moments in a two node element

Table 5-9 Bending moments at the two nodes of the element (N-m)

Calculation source	Node 1	Node 2
Theoretical	2140	2140
<i>ElastomericX</i>	2140	2140
elastomericBearingBoucWen	2140	2140
twoNodeLink	2140	2140

5.5.3.6 Integrators in OpenSees

OpenSees provides the option to use different integrators for static and dynamic analysis. The integrators used in static and dynamic analysis are referred to as static and transient integrators, respectively. Transient integrators are further divided into implicit and explicit integrators. The integrators available in OpenSees are summarized in Figure 5-28.

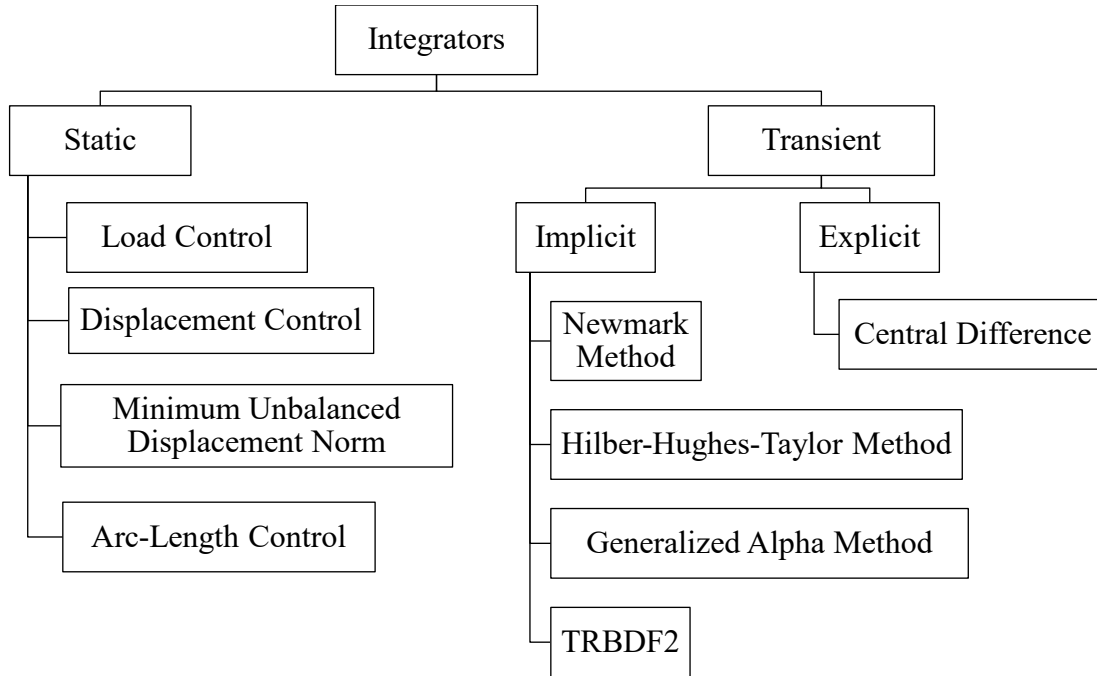


Figure 5-28 Integrators in OpenSees

Integrators are the time stepping procedures that advance the state of analysis from time t to $t + \Delta t$. An integrator determines the meaning of the terms in the system of equations $Ax = B$. The integrators discussed here are either based on finite difference of velocity and acceleration (e.g., Central Difference method) or on assumed variations of acceleration (e.g., Newmark, HHT).

The Newmark family of integrations are most widely used for earthquake engineering applications, and are given by the following equations (Chopra, 2007):

$$\dot{u}_{i+1} = \dot{u}_i + [(1 - \gamma)\Delta t]\ddot{u}_i + (\gamma\Delta t)\ddot{u}_{i+1} \quad (5.35)$$

$$u_{i+1} = u_i + (\Delta t)\dot{u}_i + [(0.5 - \beta)(\Delta t)^2]\ddot{u}_i + [\beta(\Delta t)^2]\ddot{u}_{i+1} \quad (5.36)$$

where u is displacement and γ and β are the Newmark integration parameters. The stability and accuracy of response depends on parameters γ and β . Two special cases of Newmark integrators are: 1) Newmark Average Acceleration, and 2) Newmark Linear Acceleration. The Newmark Average Acceleration ($\gamma = 0.5$, $\beta = 0.25$) and the Newmark Linear Acceleration ($\gamma = 0.5$, $\beta = 0.167$) integrator assumes a constant average acceleration and linearly varying acceleration, respectively, between steps i and $i + 1$. The stability of the solution obtained using these integrators depends on the time step Δt used for dynamic analysis. An unconditionally stable integrator provides a stable solution for all values of Δt . Integrators and their conditions of stability are presented in Table 5-10. The stability conditions are applicable only for linear problems. The stability of these methods over a wide range of nonlinear problems is not always guaranteed.

Table 5-10 Stability requirements for the response obtained using different integrators

Integrator	Parameters	Condition of stability
Newmark (general)	$\beta \geq \gamma / 2 \geq 1/4$	Unconditionally stable
Newmark Average Acceleration	$\gamma = 1/2, \beta = 1/4$	Unconditionally stable
Newmark Linear Acceleration	$\gamma = 1/2, \beta = 1/6$	$\Delta t \leq 0.55T_n$
Hilber-Hughes-Taylor (HHT)	$2/3 \leq \alpha \leq 1$	Unconditionally stable
Central Difference	---	$\Delta t \leq 0.318T_n$

The integrators used in a dynamic analysis have the tendency to provide numerical energy dissipation depending on the values of integrator's parameters and the analysis time step. The numerical energy dissipation due to integrators introduces numerical damping in the system¹. An integrator can also shorten or elongate the period of a structure obtained from the numerical response. The numerical damping and the period elongation introduce errors in the numerical response, which need to be quantified and removed. The effects of using different transient integrators, associated parameters, and time discretization values on the numerical response of elastomeric bearings are discussed below.

The selection of an integrator for a response-history analysis is dictated by stability and accuracy of the numerical solution. An integration scheme that is stable for a linear system might not be stable for nonlinear system. Moreover, the numerical damping is difficult to quantify in a nonlinear system due to contribution of hysteretic damping. The performance of different integrators is benchmarked against a linear elastic SDOF system in the following sections. It provides insight into the use of elastomeric bearing elements with different integration schemes, and sets a stage for a discussion on performance of integration schemes using different values of integrator's parameters and time step.

The two-node macro model is used for analyses. Properties of the LDR 5 bearing of Warn (2006) is used for the element connecting the two nodes. The mass is calculated from the given value of the period of oscillation in the horizontal direction. The node 2 of the macro model is subjected to an initial displacement of 1 mm and then allowed to undergo free vibration. The yield shear displacement for the bearing is assumed to be 7 mm to ensure a linear elastic response. The exact solution for the free vibration of a SDOF system is:

$$u_{exact} = u_0 \cos\left(\frac{2\pi}{T}t\right) \quad (5.37)$$

where u_0 is the initial displacement and T is the fundamental period of the SDOF system.

The user elements for LDR and LR bearings adopt the same mathematical model in the horizontal direction except for the mathematical model for heating of the lead core in the LR

¹ In some cases (e.g., impact, contact problems) numerical damping is provided deliberately in the analysis of a MDOF system to reduce response from the high frequency modes, also called zero-energy spurious modes.

bearing. Results of analyses using the LDR bearing are presented here. For small (elastic) response, the conclusions obtained using *ElastomericX* are also applicable to *LeadRubberX*.

5.5.3.6.1 Effect of integrator

The Newmark family of integrators are the most widely used for response-history analysis involving earthquake shaking. However, if a problem involves impact, or if high frequency modes are of interest, other integrators may have to be used. The effect of using different integrators on the accuracy and the stability of a response quantity is investigated here. Four integrators are considered: 1) Newmark Average, 2) Newmark Linear, 3) Central Difference, and 4) Hilber-Hughes-Taylor (HHT).

Figure 5-29 presents the shear displacement history obtained using different integrators with an analysis time step of $\Delta t / T_n = 0.1$ ($\Delta t = 0.2$ sec, $T_n = 2$ sec). The central difference integrator shortens the period, while the implicit integrators elongates the period of the numerical response when compared to exact response obtained from analytical solutions. The difference between theoretical period and the numerical periods using different integrators vanishes for small values of $\Delta t / T_n$. For example, no difference in numerical periods is observed for $\Delta t / T_n = 0.01$.

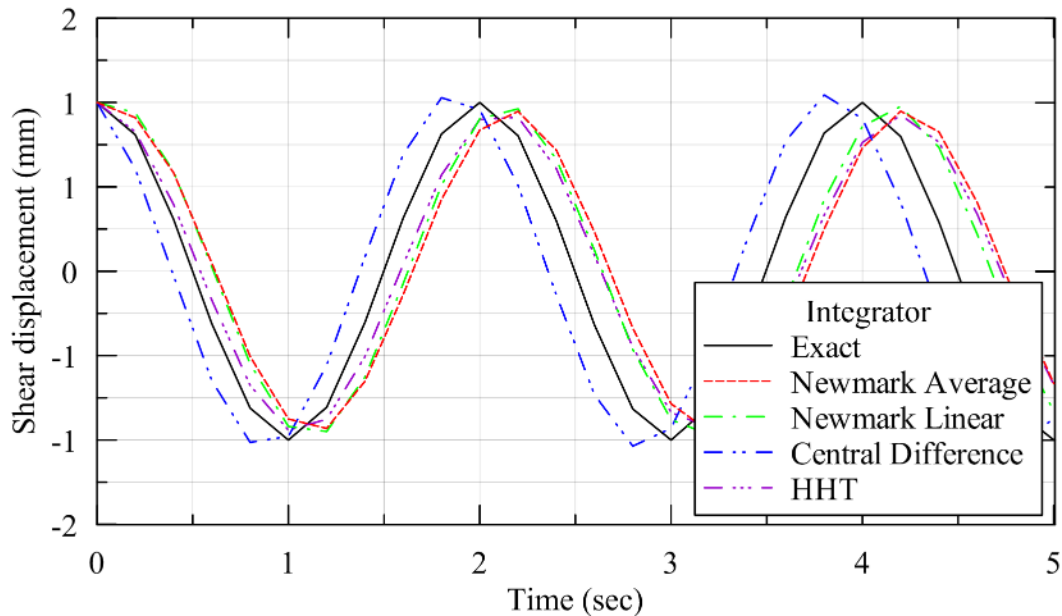


Figure 5-29 Shear displacement response of a LDR bearing ($\Delta t / T_n = 0.1$)

The numerical energy dissipation in the response due to integrators is shown in Figure 5-30. The numerical energy dissipation amounts to an equivalent numerical damping in the response, which can be calculated by obtaining the ratios of successive amplitudes in the displacement history and using Equation (5.33). The variation of numerical damping with time step Δt is presented in Figure 5-31. For a given value of the period of oscillation, no significant change in numerical damping is observed with time discretization for the Newmark Average, Newmark Linear, and Central Difference integrators. Numerical damping of response obtained using HHT integrator increases with increasing time discretization. Analyses were also performed for a range of natural period, T_n , of the model (1 to 4 sec), and similar results were observed.

Instability in the solution is observed when using Central Difference method with an analysis time step $\Delta t \geq 0.318T_n$ and Newmark Linear Acceleration method with $\Delta t \geq 0.55T_n$, where T_n is the smallest period of a mode of interest (Chopra, 2007). Figure 5-32 and Figure 5-33 present shear displacement responses obtained using the Central Difference and Newmark Linear Acceleration integrator at a very small time step and a time step value slightly greater than the stability limit for each integrator. The instability in responses obtained at time steps greater than the stability limits can be observed. The Newmark Average Acceleration method is unconditionally stable. Conditionally stable integrators might need to be used when an accurate solution cannot be obtained or convergence is not achieved by using unconditionally stable integrators.

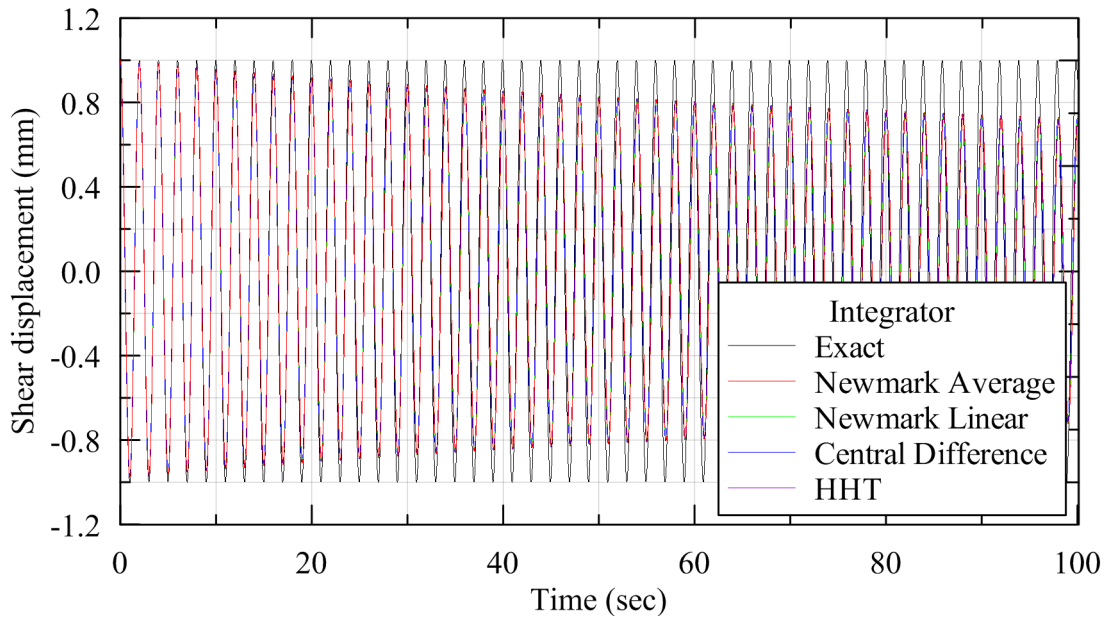


Figure 5-30 Shear displacement response of a LDR bearing ($\Delta t/T_n = 0.01$)

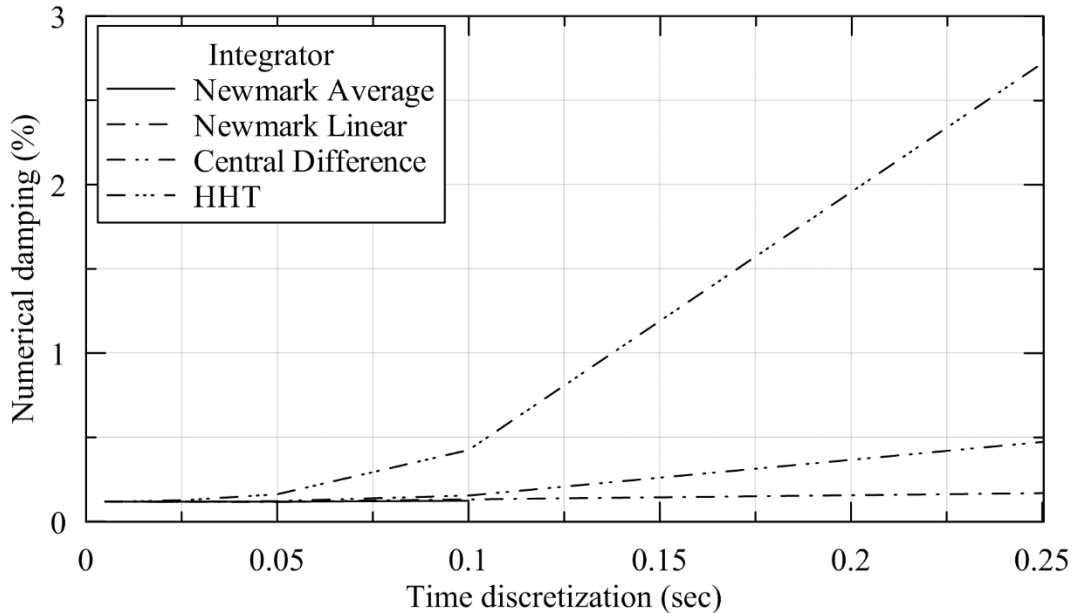


Figure 5-31 Variation of numerical damping with time-discretization ($T_n = 2$ sec)

5.5.3.6.2 Newmark Average Acceleration integrator

The Newmark Average Acceleration integrator ($\gamma = 0.5$, $\beta = 0.25$) is further investigated here. The numerical damping provided by an integrator depends on the ratio $\Delta t / T_n$, where Δt is the time step used in the analysis and T_n is time period. A value of $\Delta t / T_n$ that provides accurate response in the lower modes of oscillations might not be able to accurately capture response in higher modes. If higher modes are of interest, the values of Δt and T_n should be selected such that response of higher modes can be captured. The period of an isolation system typically varies between 1.0 to 4.0 sec in the horizontal direction and 0.01 to 0.2 sec in the vertical direction. As discussed in the previous section, the numerical damping provided by the Newmark Average Acceleration integrator is insensitive to $\Delta t / T_n$ for a wide range of values when compared to other integrators (refer to Figure 5-31). A very small numerical damping was obtained for $\Delta t / T_n$ less than 0.1. For an isolation system with a horizontal time period of 2 sec and a vertical time period of 0.1 sec, a time step smaller than 0.01 sec should minimize the numerical damping in the response. The contribution of numerical damping becomes significant when damping provided by other sources are small. For example, viscous damping provided by LR and LDR bearings in the vertical direction, and LDR bearings in the horizontal direction is typically between 2 to 4%. If analysis is performed using Newmark Average Acceleration integrator with $\Delta t = 0.01$ sec, the additional numerical damping in the axial response for a very stiff isolation system can be as much as 1%.

5.5.3.6.3 Effect of Newmark parameters

For the general Newmark integrator, the values of parameters γ and β are provided by the user. The effect of Newmark's parameters γ and β on the response of an elastomeric bearing is investigated here. The shear displacement history of the macro model is obtained using different values of γ and β using two values of $\Delta t / T_n$ (0.05 and 0.005). Results are presented in Figure 5-34 through Figure 5-37. The numerical damping in the response for each value of the parameter using two different time steps is presented in Table 5-11.

As the parameter γ is increased, the numerical energy dissipation (damping) in the response increases. The effect of increased damping due to a higher value of γ is more pronounced with coarser time discretization. Analysis with $\gamma = 0.9$ and $\Delta t = 0.1$ sec produce numerical damping as high as 5.97%. The Newmark parameter β does not significantly affect the shear displacement history even for a coarse time discretization. A minor increase in numerical damping due to β is observed with increasing time step.

Table 5-11 Numerical damping in shear displacement response of a LDR bearing using different Newmark parameters (%)

Time step (Δt) (sec)	γ ($\beta = 0.25$)			β ($\gamma = 0.5$)		
	0.5	0.7	0.9	0.25	0.50	0.75
0.1	0.15	3.06	5.97	0.15	0.13	0.10
0.01	0.14	0.44	0.73	0.14	0.14	0.14

A special case of general Newmark integrator is the Newmark Average Acceleration integrator ($\gamma = 0.5$, $\beta = 0.25$), which is expected to provide the least numerical energy dissipation in the response.

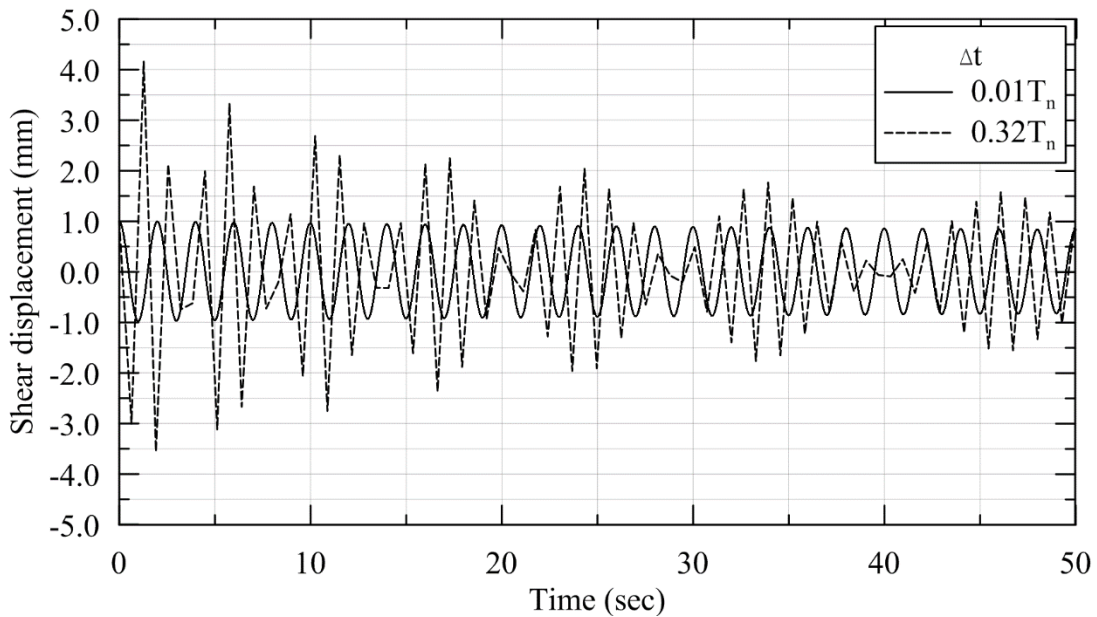


Figure 5-32 Shear displacement response obtained using Central Difference integrator

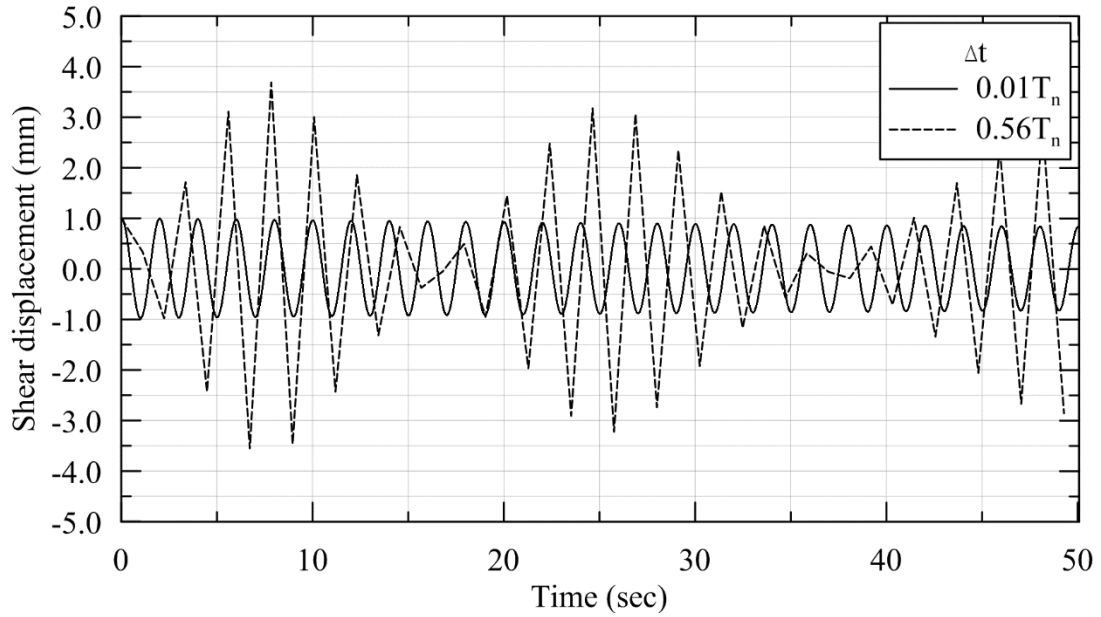


Figure 5-33 Shear displacement obtained using Newmark Linear Acceleration integrator

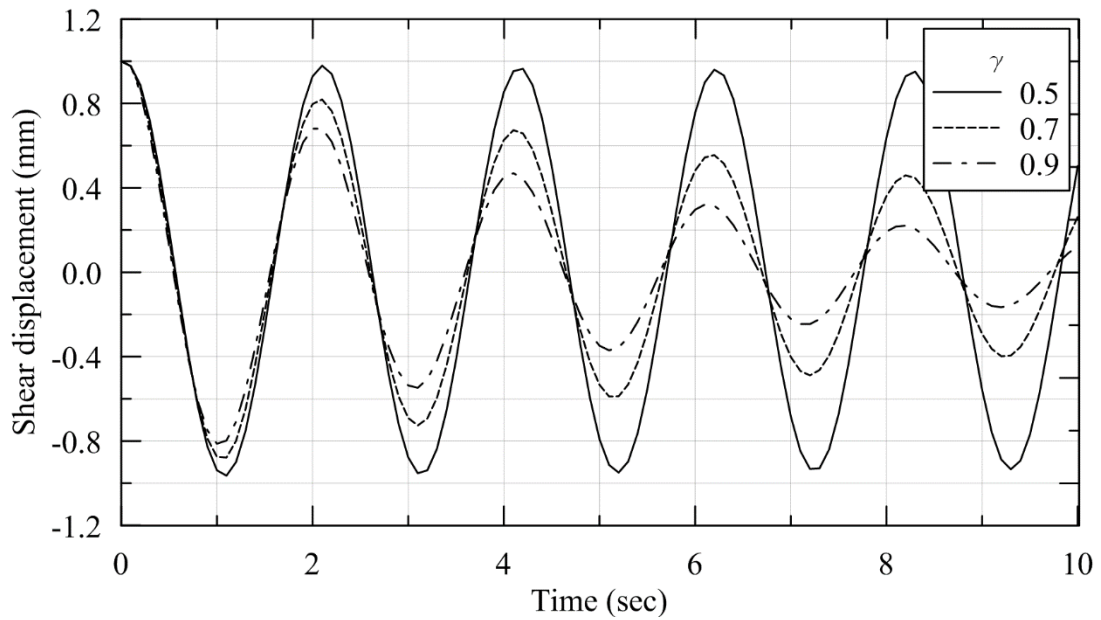


Figure 5-34 Effect of Newmark parameter, γ , on the shear displacement history of a LDR bearing ($\Delta t = 0.1$ sec, $T_n = 2$ sec)

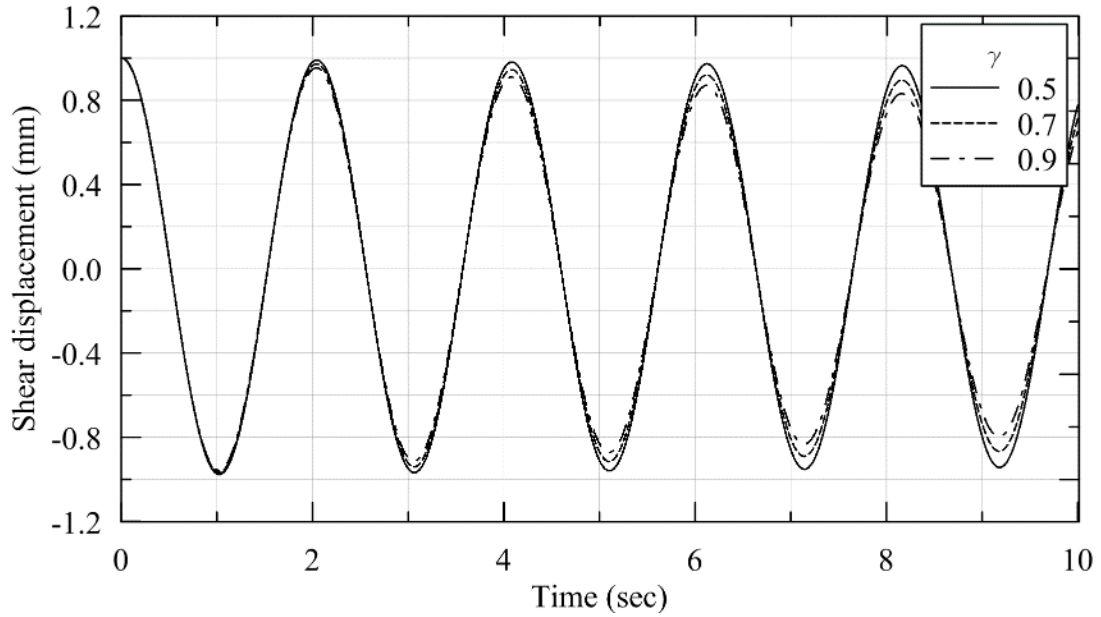


Figure 5-35 Effect of Newmark parameter, γ , on the shear displacement history of a LDR bearing ($\beta = 0.25$, $\Delta t = 0.01$ sec, $T_n = 2$ sec)

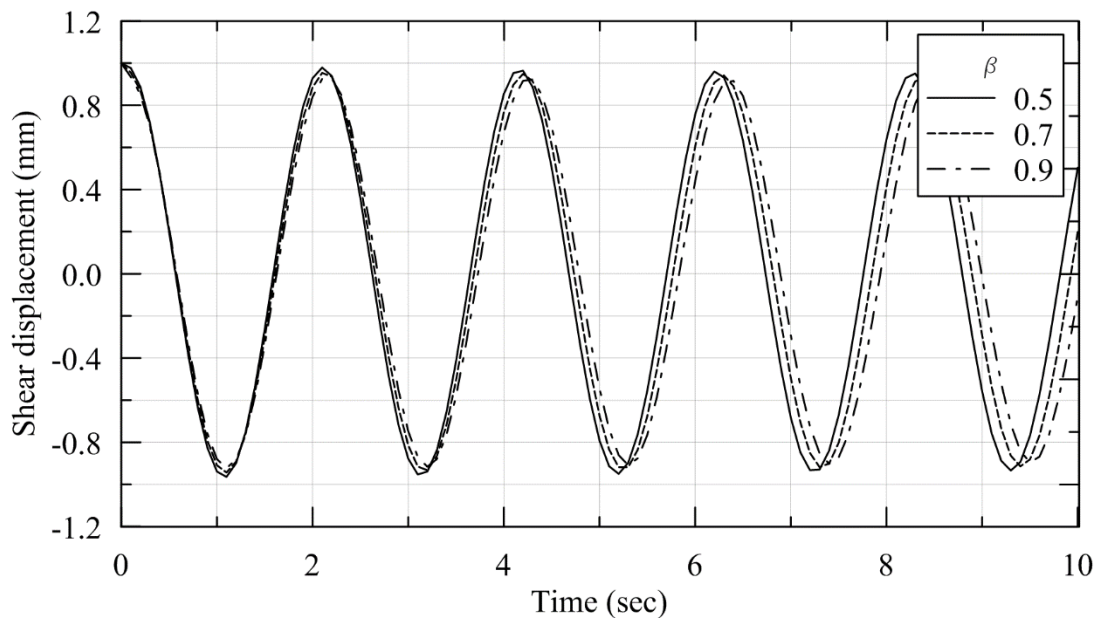


Figure 5-36 Effect of Newmark parameter, β , on the shear displacement history of a LDR bearing ($\gamma = 0.5$, $\Delta t = 0.1$ sec, $T_n = 2$ sec)

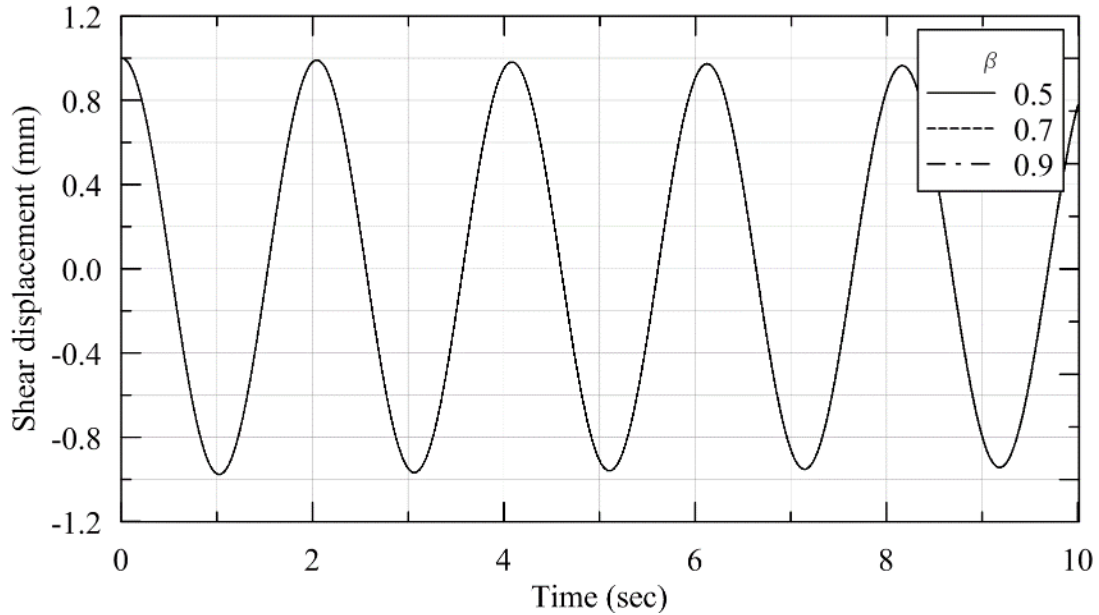


Figure 5-37 Effect of Newmark parameter, β , on the shear displacement history of a LDR bearing ($\gamma = 0.5$, $\Delta t = 0.01$ sec, $T_n = 2$ sec)

5.5.4 Conclusions on verification

A verification plan was prepared for the computational model of elastomeric bearings. The computational model is represented here by user elements of LR and LDR bearings implemented in the software framework OpenSees. Several sets of analyses were performed using these user elements to identify error sources and quantify them. Where possible, errors were minimized by removing error sources (e.g., programming bugs), or by sensitivity analyses to arrive at a set of parameters that minimize the associated error.

Some of the important conclusions from these verification activities are:

1. The component of the mathematical model that contributes most to the error was heating of the lead core in the LR bearing.
2. Code-to-code verification shows good agreement between OpenSees and ABAQUS using an analysis time step of 0.01 sec.
3. The discretization errors in the shear force, including heating effects (LR bearing), are 1% (L1 norm) and 15% (L2 norm) using an analysis time step of 0.01 sec.
4. The discretization error in the shear force excluding heating effects (LDR bearing) is less than 0.2% (L1 and L2 norm) using an analysis time step of 0.01 sec.
5. For values of the ratio $\Delta t / T_n$ (analysis time step/time period) less than 0.1, insignificant numerical energy dissipation is observed.
6. Numerical damping provided by the Newmark Average Acceleration integrator was the least sensitive to the time step.
7. Instability in the numerical response of a MDOF system might be encountered with conditionally stable integration schemes (e.g., Central Difference, Newmark Linear Acceleration method) if the analysis time step is not within the stability limit for that particular scheme.

8. The Newmark Average Acceleration method is an appropriate choice of integrator for seismic analysis of isolated structures. However, if higher modes are of interest, or if the problem involves sudden change in the stiffness matrix (e.g. impact), other integrators (e.g., Central Difference) should be evaluated.
9. For an isolation system of horizontal and vertical period greater than 1 sec and 0.05 sec, respectively, a time step of 0.005 sec or smaller is recommended for response-history analysis.

5.6 Validation of the Model

5.6.1 General

The validation process assesses the accuracy with which a mathematical model represents the physical reality for its intended use. Experiments are considered the best available representation of the reality of interest for which the model is constructed. Preexisting experimental data cannot be used if it inadequately represents the intended use of a model. Experiments are performed simulating the initial conditions, boundary conditions, material properties and applied loads as close as possible to model's intended use, while also characterizing the anomalies where present and quantifying the uncertainties in measurements. The outcomes of these specifically designed experiments are compared with the predictions of the verified computational models to assess the accuracy of a mathematical model. These are termed as validation experiments. The primary goal of a validation experiment is to assess the predictive capability of the computational model by comparing computational results to the experimental outcomes for the response quantities of interest. For validation activities, three conditions must be satisfied:

1. A clear definition of the model that includes the reality of interest, its intended use and the response quantities of interest
2. A verified computational model
3. Quantification of uncertainties in the experimental outcomes

The scope and intended use of the mathematical models of elastomeric bearing were defined in Table 5-3. The computational models were verified in the previous section. A plan for experimental validation is developed here based on the PIRT presented in Table 5-3 and sensitivity analyses. The sources of error (e.g., unknown parameters) in the mathematical model are identified. The goal of validation experiment is to investigate the behavior of the mathematical model that are expected to significantly affect the response quantities of interest.

The cavitation parameters are expected to have high uncertainty. The unknown cavitation parameters in the mathematical model of elastomeric bearing were estimated by calibration with the experimental data of Warn (2006), Warn and Whittaker (2006), Constantinou *et al.* (2007) and Iwabe *et al.* (2000). A validation experiment is required to assess the predictive capability of the computational model with these cavitation parameters. If the model shows good agreement with the results obtained from the validation experiments, the elastomeric bearing model would be considered verified and validated. However, if the numerical response prediction differs from the experimental results by an amount greater than the accuracy criteria, one of two options can be considered:

1. Refine the model using new data obtained from validation experiments, which involves calibration to update cavitation parameters and change any underlying assumption that

is not found appropriate based on information obtained from validation experiment, and then repeat the validation activities with a new set of experiments and the updated model of elastomeric bearings.

2. Restrict the use of model only for the conditions under which it satisfies the accuracy criteria.

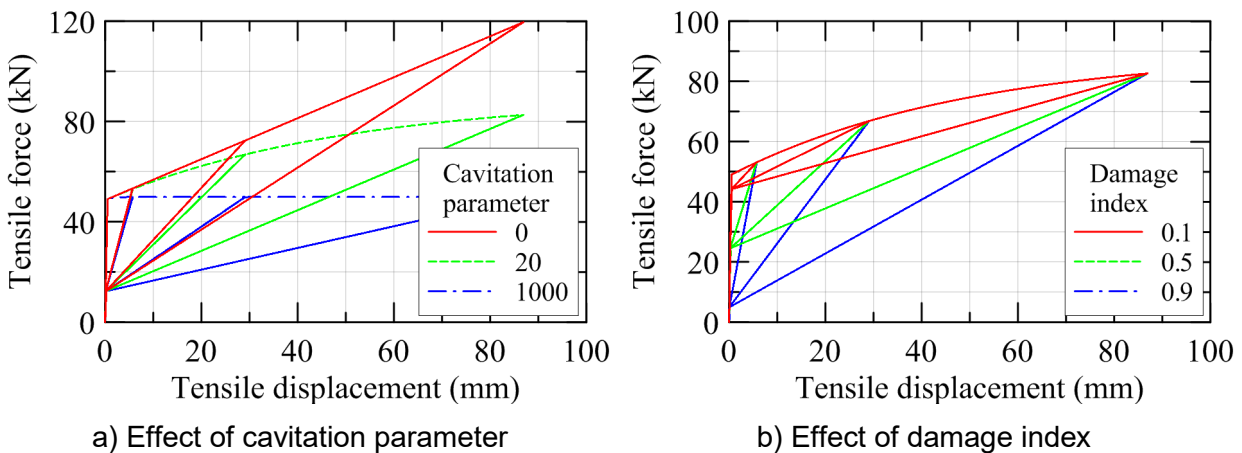
The choice of option will depend on the available resources and on the risk associated with the use of a model to predict the outcome of an event (e.g., beyond design-basis shaking of base-isolated NPPs). The calibration results using available experimental data are presented here. An experimental program to investigate behavior of elastomeric bearing under tensile loading is prepared based on the criteria and considerations presented in the following sections.

5.6.2 Sensitivity analysis

A sensitivity analysis of the model is performed to identify parameters or phenomena which significantly affect the response quantities of interest. It also assists in deciding on behaviors of elastomeric bearing that should be investigated through the validation experiments.

The effect of cavitation, lateral displacement and axial force on the load-deformation behavior of an elastomeric bearing (LDR 5 in Warn (2006)) is shown in Figure 5-38. The effect of strength degradation parameter on load-deformation behavior in cyclic tension is shown in Figure 5-39.

The bilinear stiffness model of Constantinou *et al.* (2007) ($k \rightarrow 0$) overestimates the tensile load, and a very small value of the post-cavitation stiffness ($k \rightarrow \infty$) underestimates the tensile load at large tensile displacements. The value of $k = 20$ in Figure 5-38a was determined using experimental data of Warn (2006). The damage index ϕ converges to its maximum value ϕ_{max} . The maximum damage index, ϕ_{max} , directly affects the energy dissipation capacity and determines the final cavitation strength. Experiments suggest that the value of maximum damage index varies between 0.5 and 0.9 (e.g., Iwabe *et al.* (2000), Warn (2006)). If the energy dissipation capacity due to cavitation is to be neglected in the analysis of elastomeric bearings, a very small value of the maximum damage index can be used. The vertical stiffness of the bearing decreases with lateral displacement, but the magnitude remains very high, and changes are not expected to significantly affect the tensile response, as shown in Figure 5-38c. The buckling load capacity of the bearing is affected substantially by the lateral displacement.



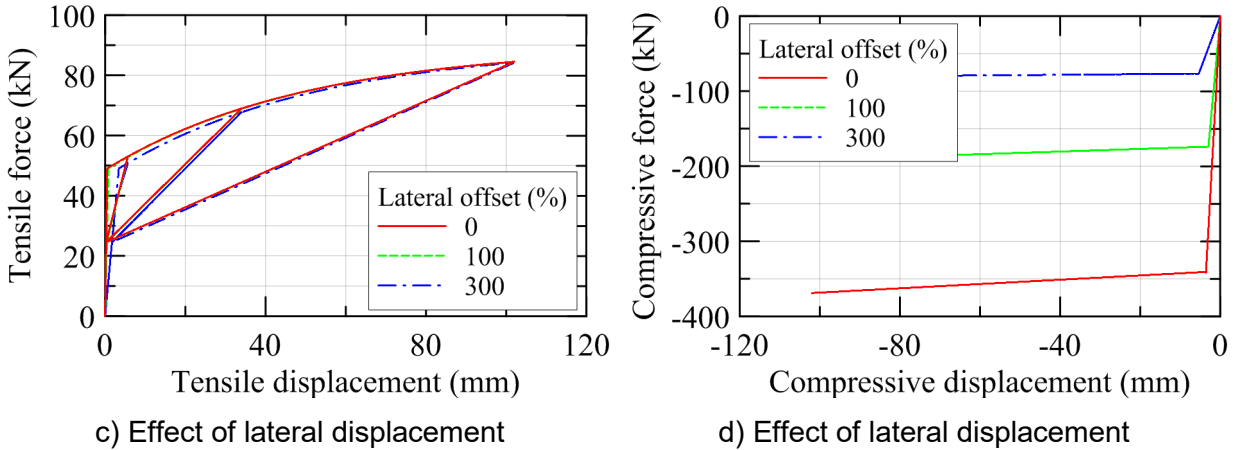


Figure 5-38 Effect of various parameters on axial behavior of a LDR bearing

The strength degradation parameter, a_c , determines the rate at which the damage index converges to its maximum value, ϕ_{max} , which directly affects the cavitation strength in subsequent cycles in tension. A value of $a_c = 1$ provides a close match with experimental observations, as shown in Figure 5-39.

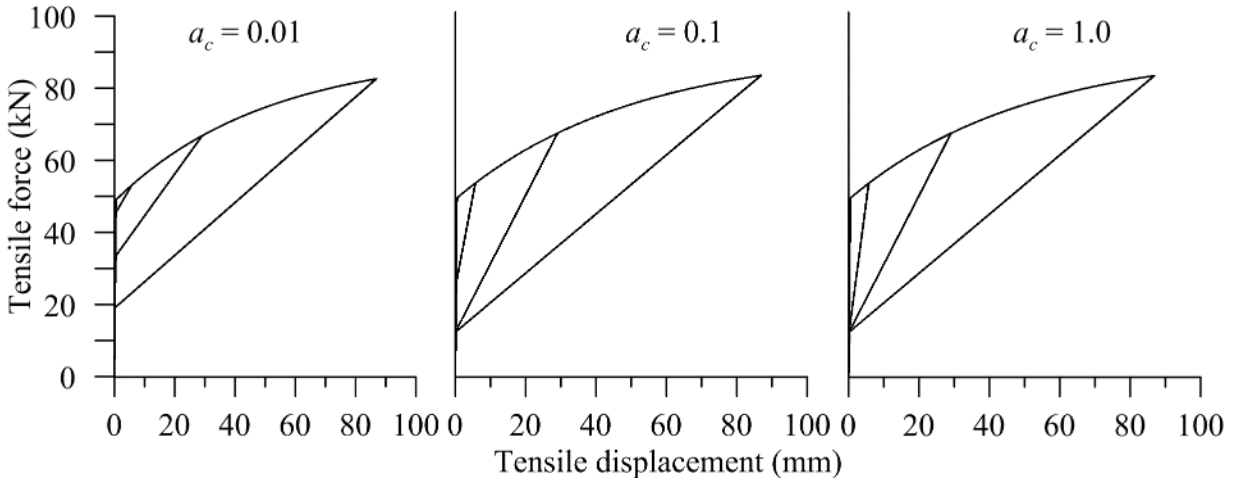


Figure 5-39 Effect of the strength degradation parameter on the tensile behavior

As discussed in Chapter 4, the yield strength of a LDR bearing is determined using an assumed value of damping and maximum displacement. The effect of the damping ratio (β_{eff}) and the displacement (D) used in the calculation of yield strength on the shear hysteresis loop of the LDR 5 bearing in Warn (2006) is shown in Figure 5-40. Warn (2006) reports damping ratios of LDR bearings in the range of 2 to 4%. The energy dissipation capacity of a LDR bearing in this damping range, as evident from Figure 5-40(a), is insignificant, and is not expected to significantly affect the shear response. Hence, the response of a LDR bearing is not sensitive to the damping ratio used for the calculation of yield strength. The other effect of damping ratio on shear behavior of a LDR bearing is the increase in effective stiffness with damping. However, calculation of effective shear modulus of a LDR bearing using test data already accounts for the effect of damping on shear stiffness. For an assumed value of damping ratio, the energy

dissipation capacity of a LDR bearing increases with displacement (D) used in the calculation of the yield strength. However, at small value of damping ratio (3%), the response of LDR bearing is not expected to be sensitive to D .

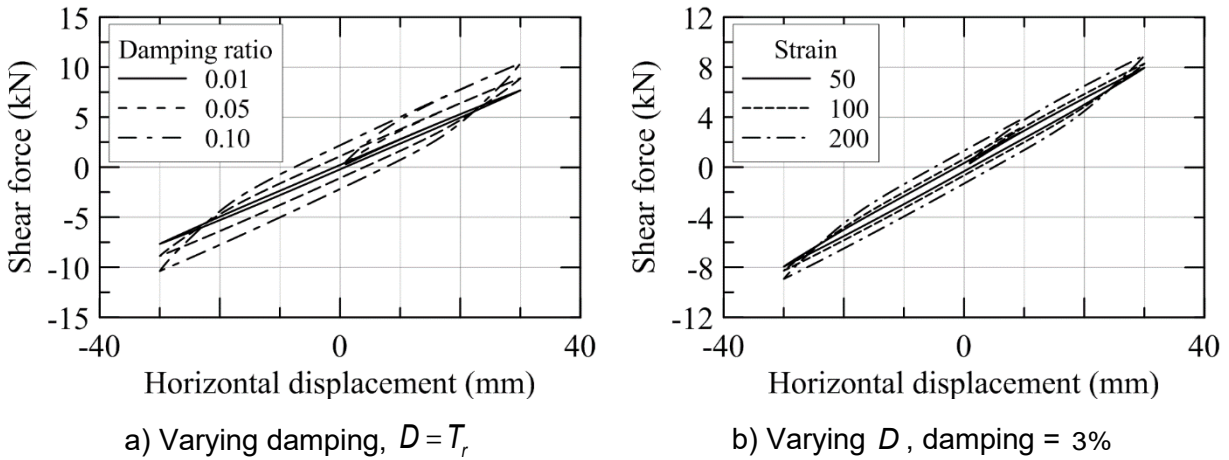


Figure 5-40 Effect of different parameters on yield strength of a LDR bearing

The effect of axial load on LR5 bearing of Warn (2006) and the large size bearing in Kalpakidis *et al.* (2010) is shown in Figure 5-41 and Figure 5-42, respectively. The shear stiffness decreases with axial load, but the effect only becomes apparent when the axial load is close to the critical buckling load. The energy dissipation capacity of LR bearing is primarily due to the lead core and the contribution of viscous damping can be neglected. The effect of the viscous damping term ($c_d U$) on the load-deformation behavior of a LR bearing is minor at small displacements.

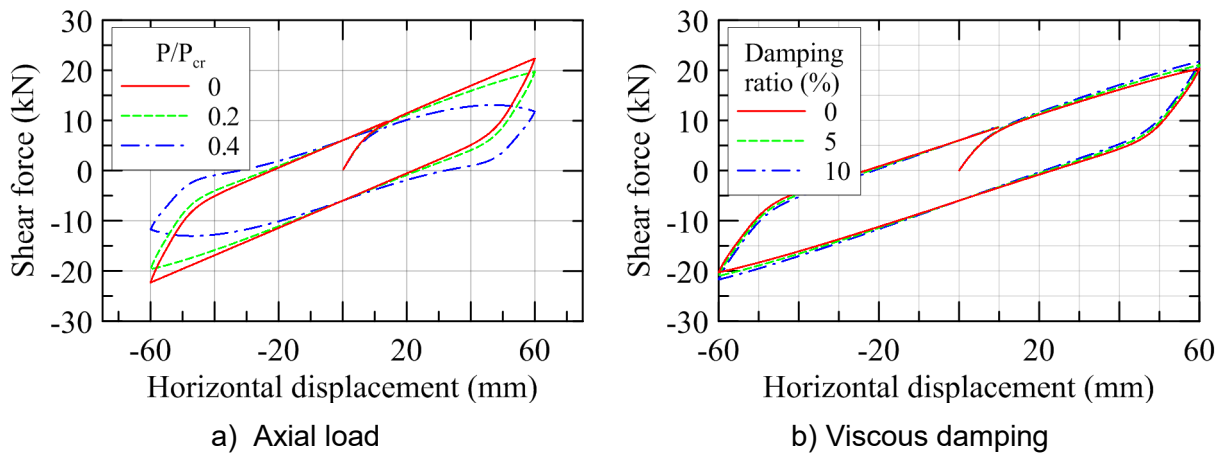


Figure 5-41 Effect of parameters on the shear behavior (LR5 bearing in Warn (2006))

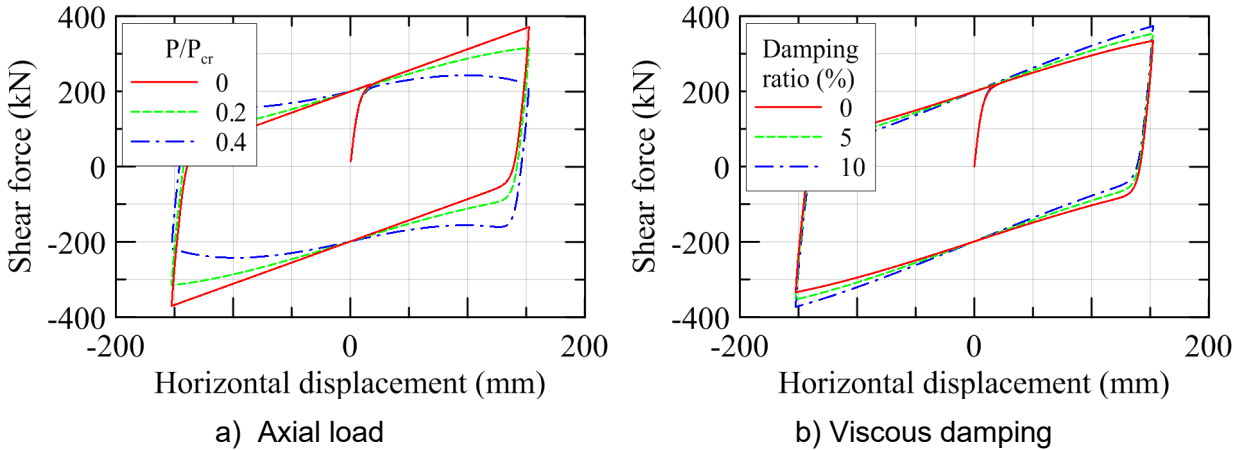


Figure 5-42 Effect of parameters on the shear behavior (large size LR bearing of Kalpakidis *et al.* (2010))

5.6.3 Available test data

5.6.3.1 Calibration

The three unknown parameters of the phenomenological model of an elastomeric bearing in tension are determined through calibration with test data. The computational model was verified before calibration to quantify and remove errors associated with the implementation of the mathematical model. Four sets of available test data in the literature are used for calibration: 1) Constantinou *et al.* (2007), 2) Iwabe *et al.* (2000), 3) Warn (2006), and 4) Clark (1996). The calibration plots are presented in Figure 5-44 and Figure 5-45.

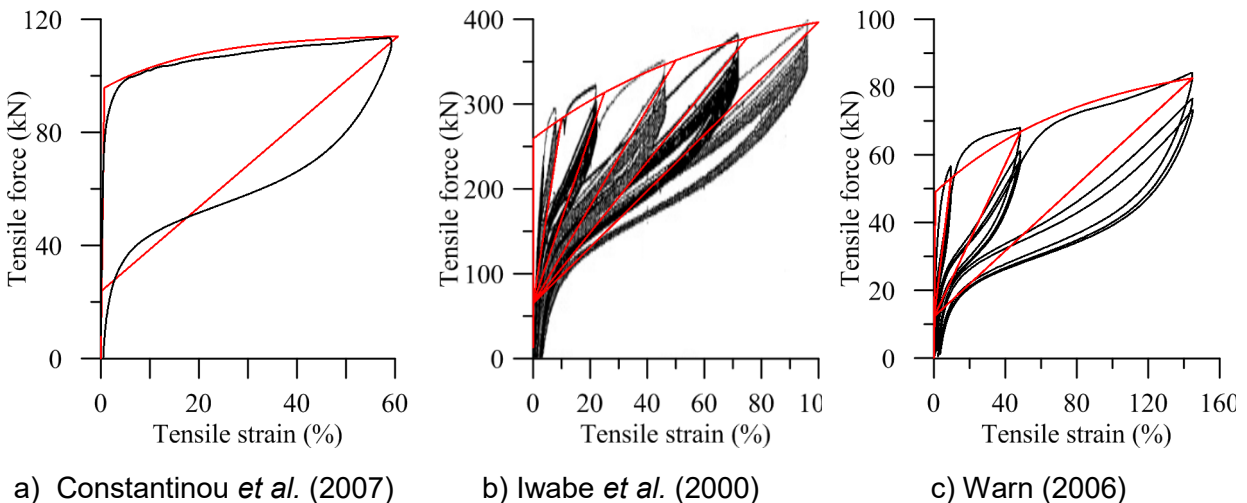


Figure 5-43 Calibration of the mathematical model in tension with test data

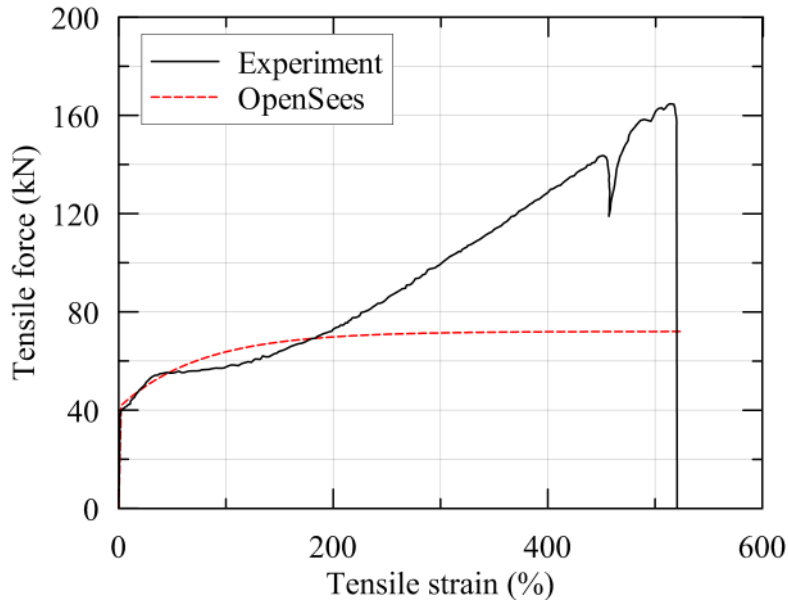


Figure 5-44 Calibration of the mathematical model in tension with test data of Clark (1996)

The details of the bearings and the values of parameters estimated by calibration against experimental data are presented in Table 5-12.

Table 5-12 Properties of the bearings used for experimental comparison

	Constantinou <i>et al.</i> (2007)	Iwabe <i>et al.</i> (2000)	Warn (2006)	Clark (1996)
Diameter (mm)	250	500	164	176
Shape factor (S)	9.8	33	10.2	20
Cavitation parameter (k)	60	15	20	30
Maximum damage index (ϕ_{\max})	0.75	0.75	0.75	--
Strength degradation parameter (a_c)	1.0	1.0	1.0	--
Error (%) ^{1,2} , L1, L2 Norm	9.02, 14.64	--	18.2, 24.6	7.29, 7.99

1. Experimental data was not available for Iwabe *et al.* (2000).

2. Error norms were evaluated for Clark (1996) for response only up to 200% tensile strain.

5.6.3.2 Experimental comparison

The ability of the verified computational model to predict the response of an elastomeric bearing in shear is investigated through a comparison with available test data. The heating parameters of LR bearings are known, and do not require calibration with experimental data. The available test data can be used for validation of the mathematical model used to describe the shear behavior of an elastomeric bearing. Comparisons of computational results with experimental data for the LR bearing in the horizontal (shear) direction are presented in Figure 5-45 through Figure 5-48.

The errors in the computational results with respect to the experimental data are presented in Table 5-13.

Table 5-13 Error associated with computational model

Experiment	Type of loading	L1 error (%)	L2 error (%)
Kalpakidis <i>et al.</i> (2010)	harmonic	14.60	25.94
Kalpakidis <i>et al.</i> (2010)	random	31.05	39.82

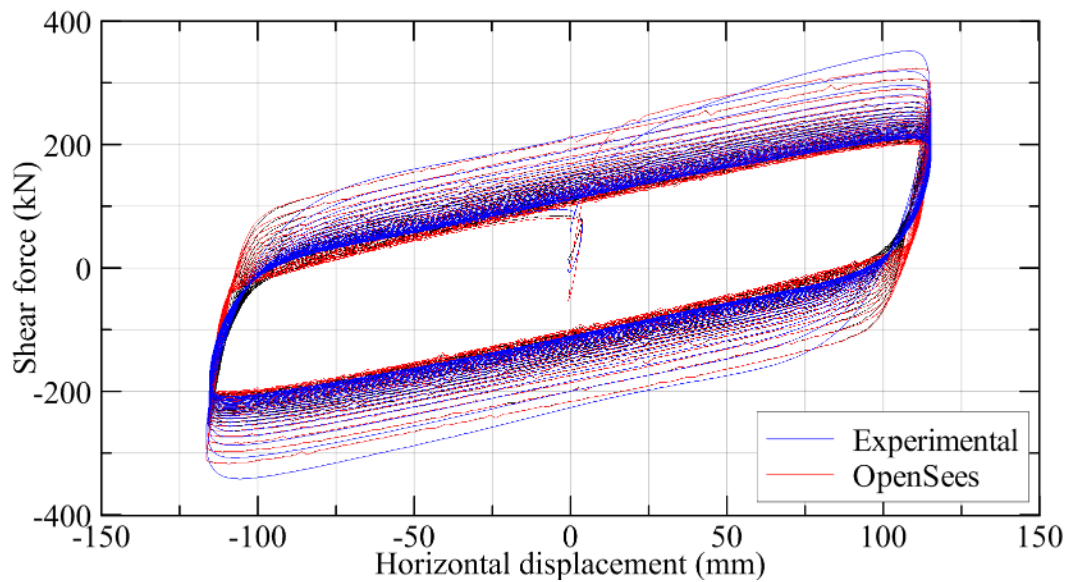


Figure 5-45 Shear force-displacement behavior of a LR bearing under harmonic loading

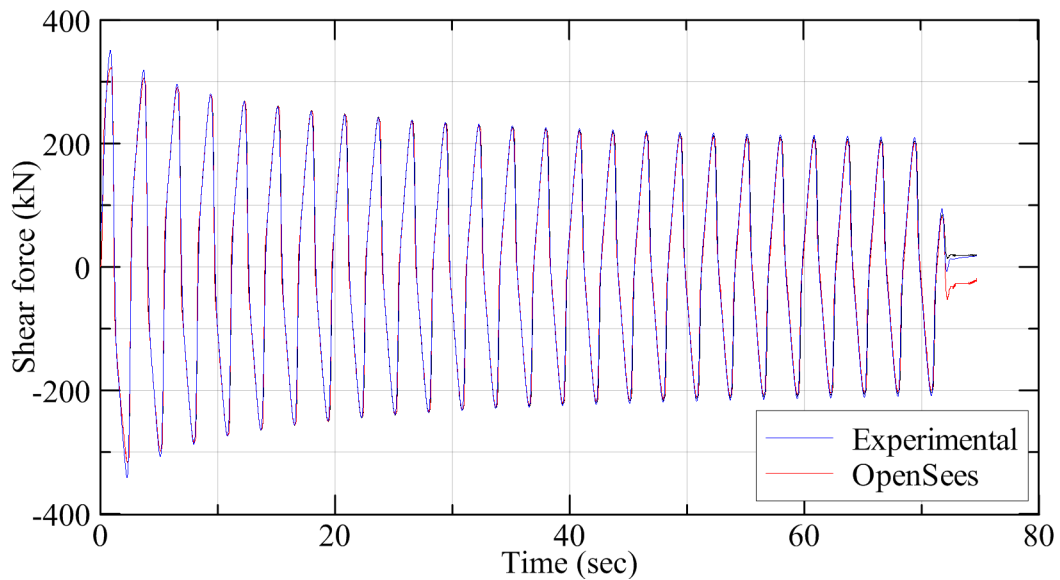


Figure 5-46 Shear force history of a LR bearing under harmonic loading

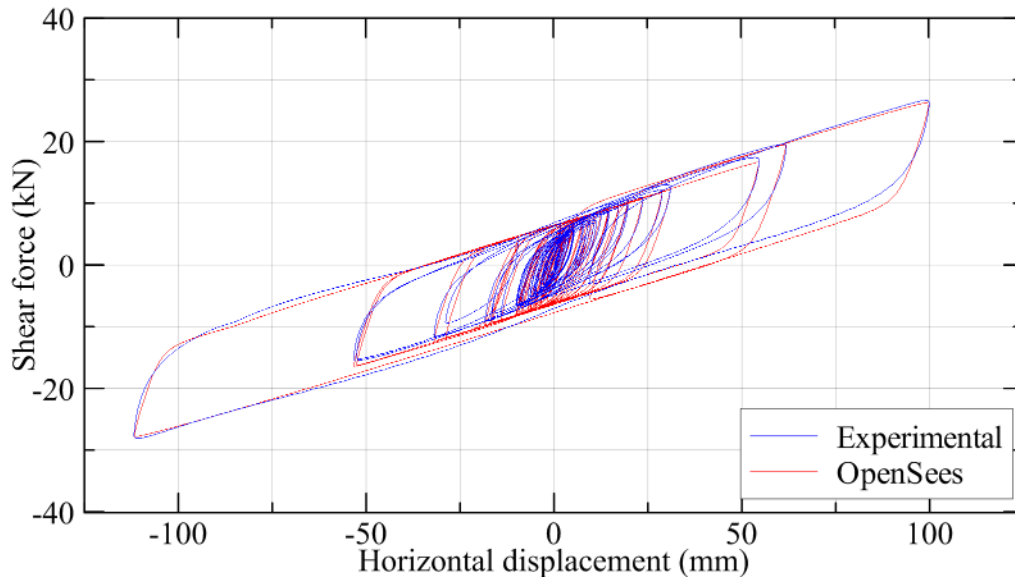


Figure 5-47 Shear force-displacement behavior of a LR bearing under random loading

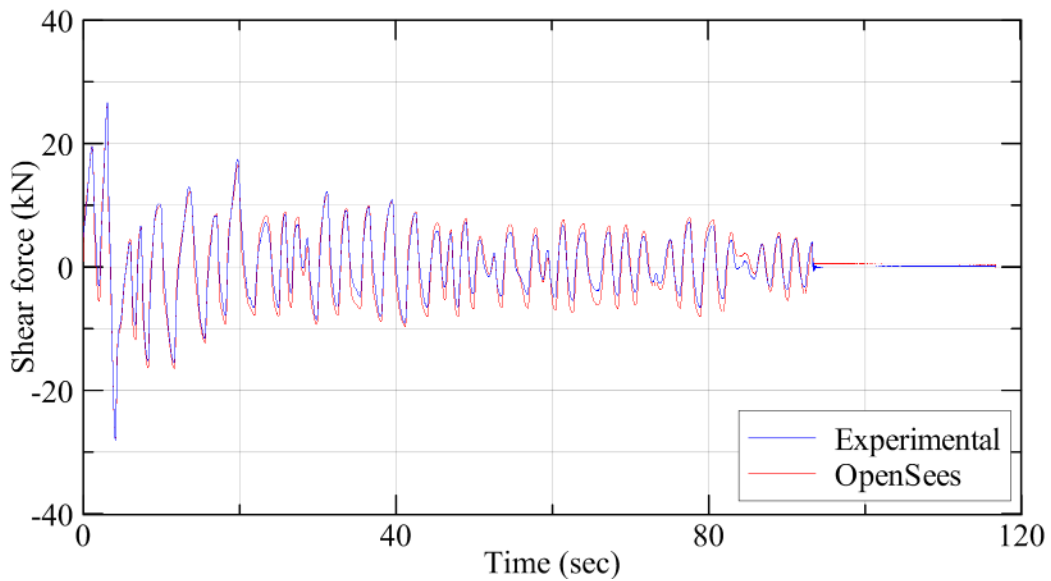


Figure 5-48 Shear force history of a LR bearing under random loading

5.6.4 Validation plan

Experiments are considered the best available representation of the physical reality subject to the limitations of experimental error. It is not always possible and feasible to include all the details of physical reality into the mathematical model. Engineering judgment is often used to decide which features will have a significant effect on the response quantities of interest for the intended use. A mathematical model is formulated based on a set of assumptions to reduce a physical reality to a mathematical construct and preliminary values are assigned to unknown parameters based on available experimental data. The validity of these assumptions is investigated through validation experiments. If results are found to be unsatisfactory, these assumptions must be revisited.

The preliminary step in the design of an experiment is to determine which features of the model need to be investigated. One way of deciding the importance and reliability of a feature is to construct the PIRT, as shown in Table 5-1. However, the information required to construct a PIRT is not always available. A more common approach is to perform sensitivity analyses of the computational model, which was presented in Section 5.6.2. The mathematical model of the heating of the lead core in a LR bearing has been validated by Kalpakidis and Constantinou (2009a). The good agreement between the mathematical model and the experimental results established confidence in the model to a sufficient degree. Moreover, the mathematical model of the behavior in horizontal direction is a physics-based model and does not involve any unknown parameters. The mathematical model of the mechanical behavior in compression is also physics-based, and has been validated experimentally (Warn and Whittaker, 2006; Warn *et al.*, 2007). Hence, the validation experiment of Chapter 6 does not focus on the mechanical behaviors in shear and compression.

The mathematical model of the mechanical behavior of elastomeric bearings in tension is based on the observations from experiments. A phenomenological formulation was proposed in Chapter 3 to capture this behavior. The model uses three parameters to capture the behavior in tension under cyclic loading. The three cavitation parameters are determined through calibration process, as discussed in the previous section. The key assumptions that are expected to affect the response are:

- Exponential post-cavitation variation
- Exponential cyclic strength degradation
- Linear unloading path
- No strain hardening

The five features of the model to be investigated in the validation experiments are:

1. Cavitation and post-cavitation behavior under tensile loading
2. Effect of loading history on tensile properties
3. Dependence of load-deformation behavior on the shape factor
4. Change in shear and compression properties following tensile loading
5. Influence of shear displacement on tensile force response

The selection of these features is based on the available knowledge about the behavior of elastomeric bearings in tension and the associated uncertainty in its modeling. The response quantities to be measured during the experiments are summarized in Table 5-14.

Table 5-14 Response quantities to be measured during the experiments

Response quantity	Location	Method of measurement
Shear displacement	At top and bottom of the bearing	Direct
Axial displacement	At top and bottom of the bearing	Direct
Rotation angle	Through relative displacements along the circumference of the bearing	Derived
Axial load	At the bottom of the bearing through load cell	Direct
Shear force	At the bottom of the bearing through load cell and at the top bearing by horizontal actuator	Direct
Moment	At the bottom of the bearing through load cell	Direct

It is highly recommended that the response quantities be measured directly rather than derived from other measurements. For example, the center of an elastomeric bearing is not available for measurements in an experimental setup. Hence, axial displacement at the center is determined by interpolation of the axial displacements measured at other locations around the bearing. The consistency of the output data can be established by corroborating different measurements such as measuring accelerations of displacements to corroborate velocity, or measuring axial loads at different locations to corroborate moments.

Sources of error in the experimental setup need to be identified. Some common sources of error in the testing of elastomeric bearing are:

- Calibration of measurement devices
- Inertia of components in the test setup
- High frequency noise in response
- Rigidity of supports
- Load application

Sources of error should either be removed or accounted for in the experimental results. If a source of error is discovered after the experiment, the test data should be processed to remove bias.

Redundant measurements are often required to verify accuracy of the response data. It helps to quantify uncertainty in experimental measurements. Redundant measurements can be obtained by:

1. Repeating the same test using different specimens
2. Repeating the test using the same specimen
3. Using different measurement techniques for the same response
4. Placing similar transducers at symmetrical locations

The first strategy cannot be used for elastomeric bearing because the properties of elastomeric bearings are expected to degrade following cyclic loading. The second strategy is not considered here due to limited resources. The third and fourth strategies are employed here.

The steps discussed above help to design a meaningful validation procedure. However, the experimental results will still contain errors and uncertainties, which need to be quantified. Errors in the experimental outcomes can be classified as random errors (precision) or

systematic errors (accuracy). Random errors are due to the measurement error, design tolerances, construction uncertainty, variability in material properties, and other sources specific to an experiment. Random errors cannot be removed from the system; however, the uncertainty in the results due to random errors can be quantified. Systematic errors can be present due to calibration error, data acquisition error and testing technique. Systematic errors produce bias in the results that is difficult to detect and estimate. Wherever possible, uncertainties in experimental results should be represented through a distribution of test data at each point with a mean value and a standard deviation.

A detailed experimental program is prepared based on the considerations presented above, and is presented in Chapter 6. Results of the validation experiments are discussed in Chapter 7.

5.7 Accuracy Criteria

Verification and validation is performed with respect to a specific series of tests and tolerances that have been deemed to provide sufficient accuracy. The accuracy criteria for the results obtained using the mathematical models of elastomeric bearings are developed based on the intended use of the model and the reality of interest. The intended use of these models of elastomeric bearings is the response-history analysis of seismically isolated nuclear power plants. The reality of interest here is the seismic isolation of nuclear power plants. Although application to nuclear power plants demands that stringent accuracy criteria be adopted, it has been found that uncertainties associated with model of elastomeric bearings is overwhelmed by the uncertainties in the definition of the seismic hazard and the input ground motion (Huang *et al.*, 2009). Hence, practical rather than an ambitious accuracy criterion should be formulated.

The following steps can be used to estimate acceptable error in a response quantity:

1. Identify response quantities of interest
2. Identify the error sources and quantify the errors associated with the model that significantly affect each response quantity
3. Quantify the sensitivity of the response quantity with respect to parameters associated with error sources identified in step 2
4. Establish the acceptable error for response quantity with respect to each source of error
5. Combine the errors from various sources in a probabilistic or deterministic framework to establish an acceptable level of error for each response quantity

6 SPECIMEN SELECTION AND EXPERIMENTAL PROGRAM

6.1 Introduction

Scaled models of elastomeric bearings were designed for testing to validate the proposed mathematical model for load-deformation behavior in the vertical direction proposed in Chapter 3 and to estimate cavitation and damage parameters. The selection of the model bearings was primarily based on typical bearing properties that have been used, or are expected to be used, in the nuclear industry, but was limited by the capacity of the Single Bearing Testing Machine (SBTM) at the University at Buffalo.

Details of the model bearings that were selected for the experiment are presented in Section 6.2. The test program, presented in Section 6.3, describes the goals and the sequence of tests. Section 6.4 presents the details of the instrumentation and the data acquisition system used for the experiments.

6.2 Model Bearing Properties

6.2.1 Target and reported properties, and predicted capacities

The seismic isolation systems of the Cruas Nuclear Power Plant (NPP) in France and the Koeberg NPP in South Africa have used synthetic rubber bearings with a shape factor of around 10. Two of the reactors under construction in France, the International Thermonuclear Experimental Reactor and the Jules Horowitz Reactor, use bearings of a similar design. However, most of the seismic isolation design concepts developed for NPPs in the US and Japan (discussed in Chapter 1) use circular natural rubber bearings with shape factors greater than 20 (refer to Chapter 1). The selection of the model bearings for this testing program were based on typical designs that have been used for seismic isolation designs developed for nuclear power plants in the US and Japan. A goal of these experiments is to characterize the behavior of rubber bearings under tensile loading. Low damping rubber (LDR) bearing and lead-rubber (LR) bearing are expected to show similar load-deformation behavior under tensile loading so only LDR bearings were tested. The target properties of the model bearings, the reported properties of the model bearings, and the predicted capacities of the model bearings, based on the reported properties are presented below.

Two manufacturers, Dynamic Isolation Systems, Inc. (DIS) and Magedba, each provided eight bearings for the experiments. The maximum diameter of the bearings was limited by the capacity of the load cell used to measure forces in the vertical direction. Details of LDR bearings manufactured by DIS and Magedba are provided in Table 6-2 and Table 6-3, respectively. The bearings from the two manufacturers had differences in their bonded diameters, shear moduli, and cover thickness. The DIS bearings had a central hole; the Magedba bearings did not. The effect of the central hole is discussed in Appendix A.5.

Each set of eight bearings had the same diameter but were further divided into two groups of four bearings according to their shape factor. The two groups of four bearings with rubber layer thicknesses of 7 mm and 4 mm were identified by the letters A and B, respectively. The LDR bearings were named DA1, DB1, MA1, MB1, DA2, etc., where the first letter refers to the manufacturer (D for DIS and M for Magedba), the second letter identifies the rubber layer thickness (or shape factor), and the number identifies a specific bearing. Accordingly, DA1 refers to a bearing manufactured by DIS from the group of bearings with a rubber layer thickness 7 mm.

A summary of the target properties for the model bearings is presented in Table 6-1. The properties of the model bearings supplied by DIS are presented in Table 6-2. The schematic drawings provided by DIS are presented in Figure 6-3 and Figure 6-4. The properties of the Mageba model bearings are presented in Table 6-3, and the schematic drawings provided by Mageba are shown in Figure 6-5 and Figure 6-6.

Table 6-1 Target model bearing properties

Parameter			Bearing type	
Description	Notation	Unit	LDR A	LDR B
Number of bearings	N.A.	N.A.	4	4
Outer diameter	D_o	mm	300	300
Inner diameter ¹	D_i	mm	N.A.	N.A.
Individual rubber layer thickness	t_r	mm	6	3
Number of rubber layers	n	-	20	20
Individual steel shim thickness	t_s	mm	3	3
Number of steel layers	n	-	19	19
Shape factor	S	-	12.5	25.0
Cover rubber thickness	t_c	mm	3	3
Target shear modulus	G	MPa	0.55	0.55
Internal plate thickness ²	t_{int}	mm	25	25

1. A central hole is not required for testing but may be needed for manufacture. The presence of a central hole does not affect the goals of the experiment, because tensile properties of a bearing depend only on the bonded rubber area.

2. See Figure 6.1

Table 6-2 DIS model bearing properties

Parameter			Bearing type	
Description	Notation	Unit	LDR A	LDR B
Number of bearings	N.A.	N.A.	4	4
Outer diameter	D_o	mm	296.8±4	296.8±4
Inner diameter	D_i	mm	19.05±2	19.05±2
Individual rubber layer thickness	t_r	mm	7	4
Number of rubber layers	n	-	20	20
Individual steel shim thickness	t_s	mm	3.04	3.04
Number of steel layers	n	-	19	19
Shape factor	S	-	9.92	17.36
Cover rubber thickness	t_c	mm	4	4
Reported shear modulus	G	MPa	0.45	0.45
Internal plate thickness ¹	t_{int}	mm	25.4±1.6	25.4±1.6
Estimated mass	m	kg	72	67

1. See Figure 6.1

Table 6-3 Mageba model bearing properties

Parameter			Bearing type	
Description	Notation	Unit	LDR A	LDR B
Number of bearings	N.A.	N.A.	4	4
Outer diameter	D_o	mm	299	299
Inner diameter	D_i	mm	n.a.	n.a.
Individual rubber layer thickness	t_r	mm	7	4
Number of rubber layers	n	-	20	20
Individual steel shim thickness	t_s	mm	3	3
Number of steel layers	n	-	19	19
Shape factor	S	-	10.7	18.7
Cover rubber thickness	t_c	mm	5	5
Reported shear modulus	G	MPa	0.55	0.55
Internal plate thickness ¹	t_{int}	mm	25	25
Estimated mass	m	kg	74	68

1. See Figure 6.1

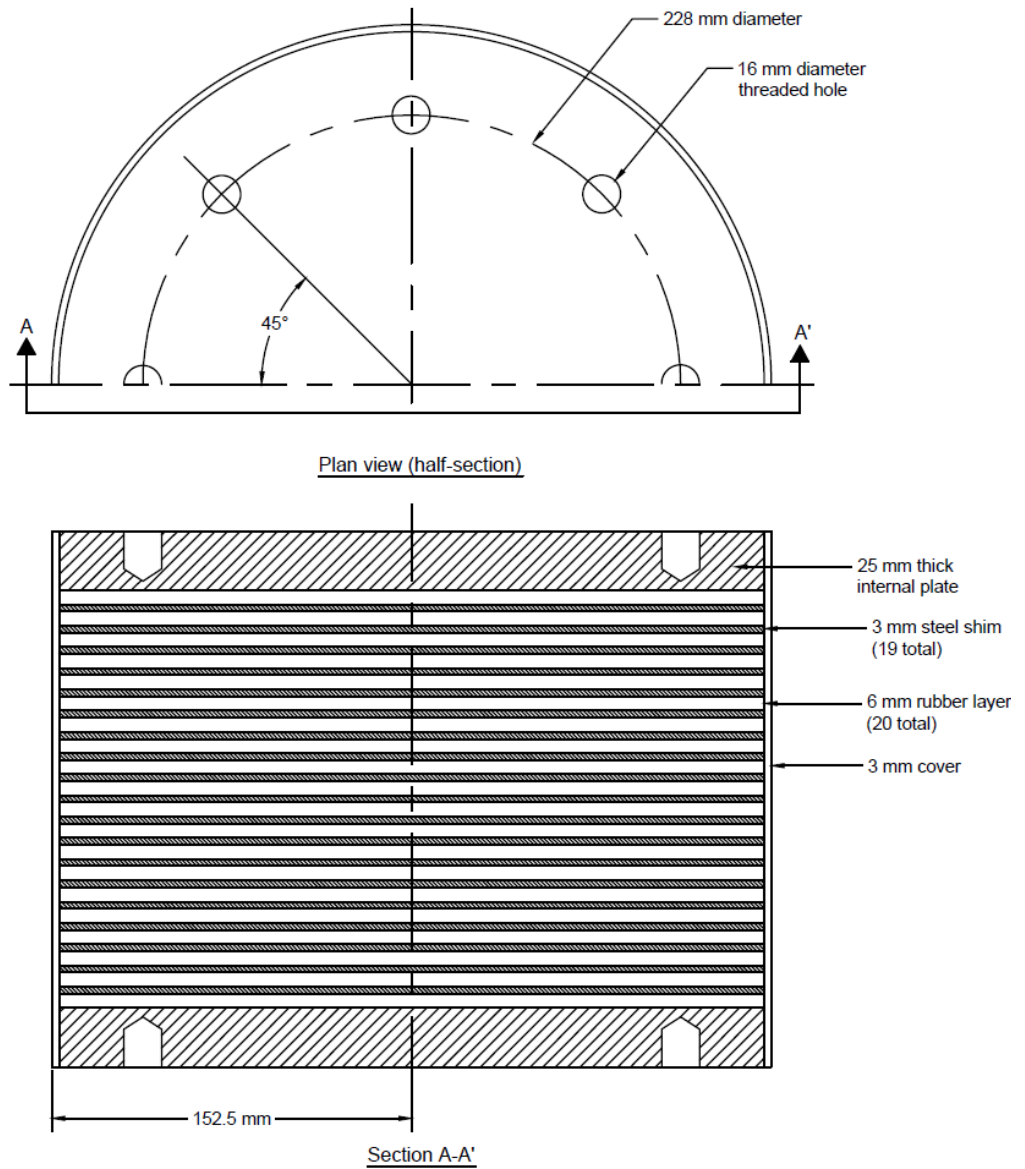


Figure 6-1 Geometric details of bearing type A

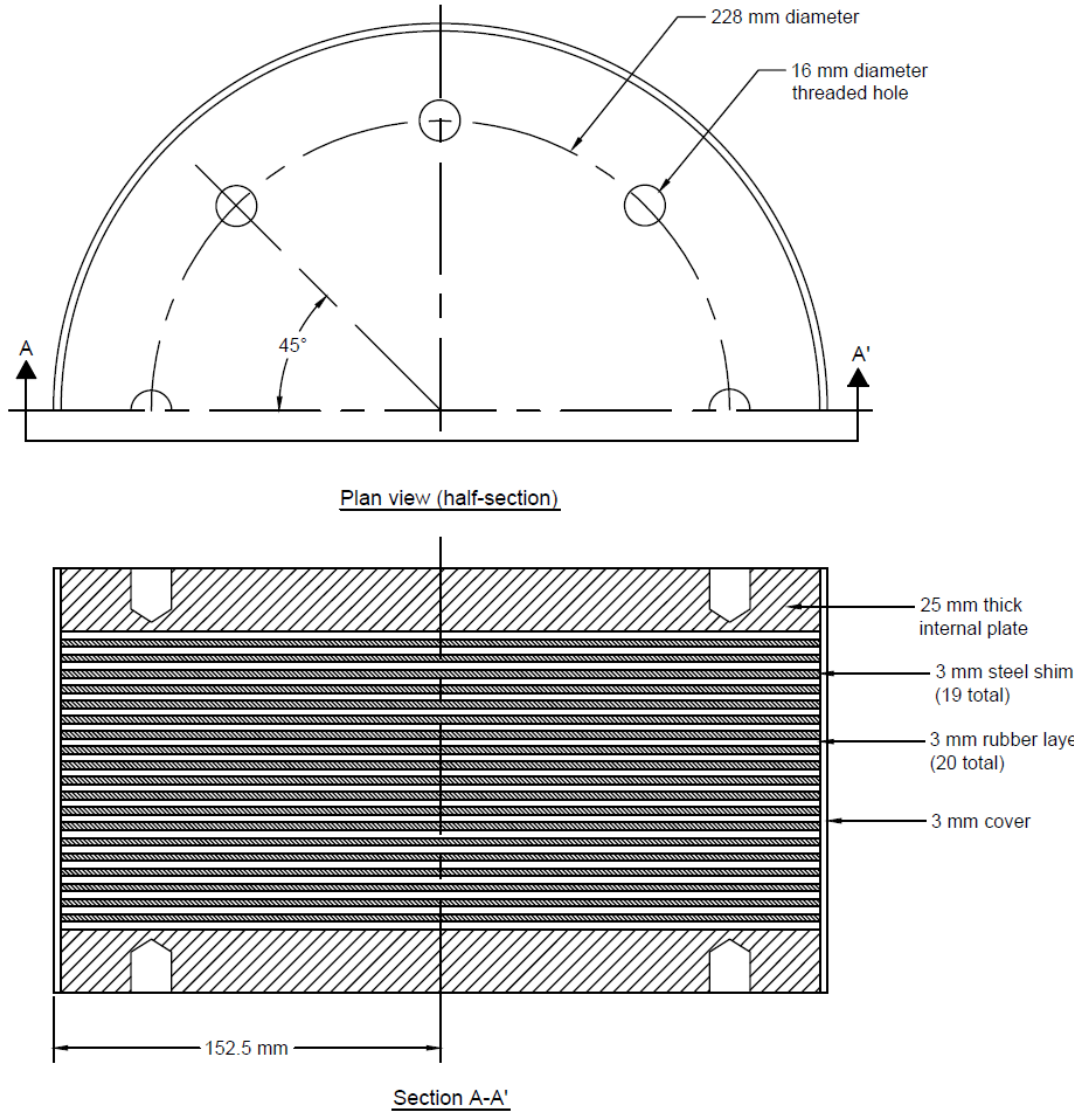


Figure 6-2 Geometric details of bearing type B

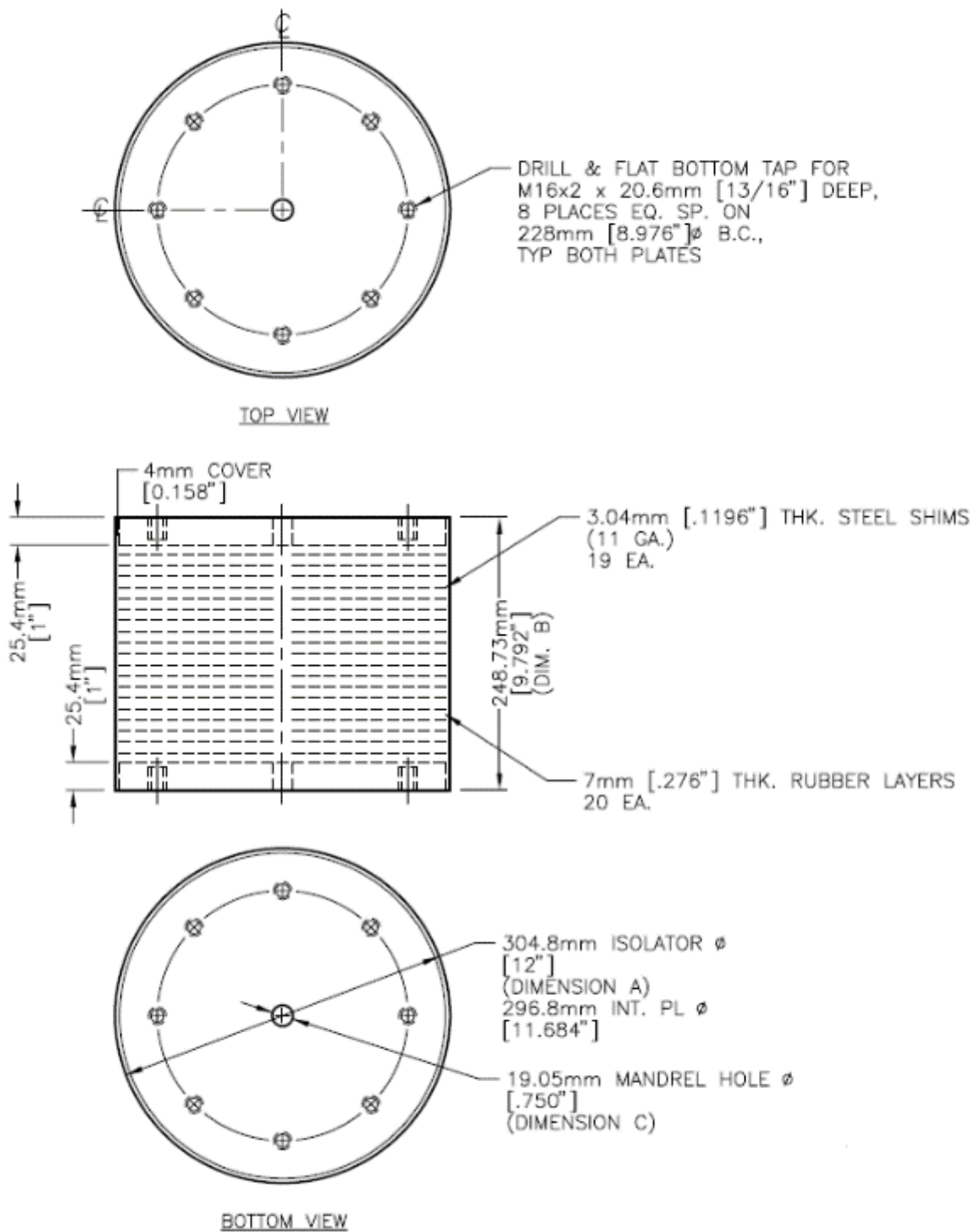


Figure 6-3 DIS bearing type A, DA (courtesy of DIS, Inc.)

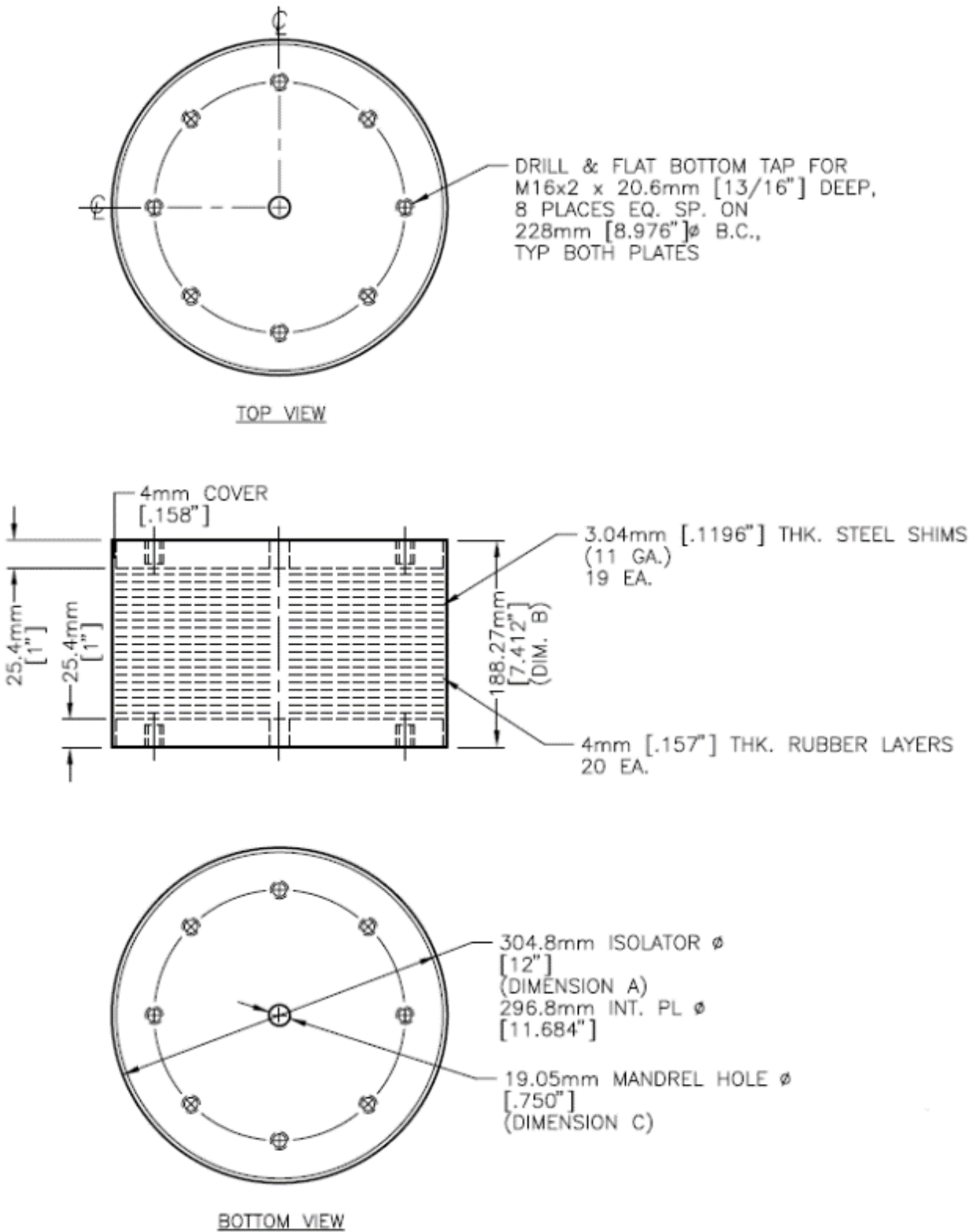


Figure 6-4 DIS bearing type B, DB (courtesy of DIS, Inc.)

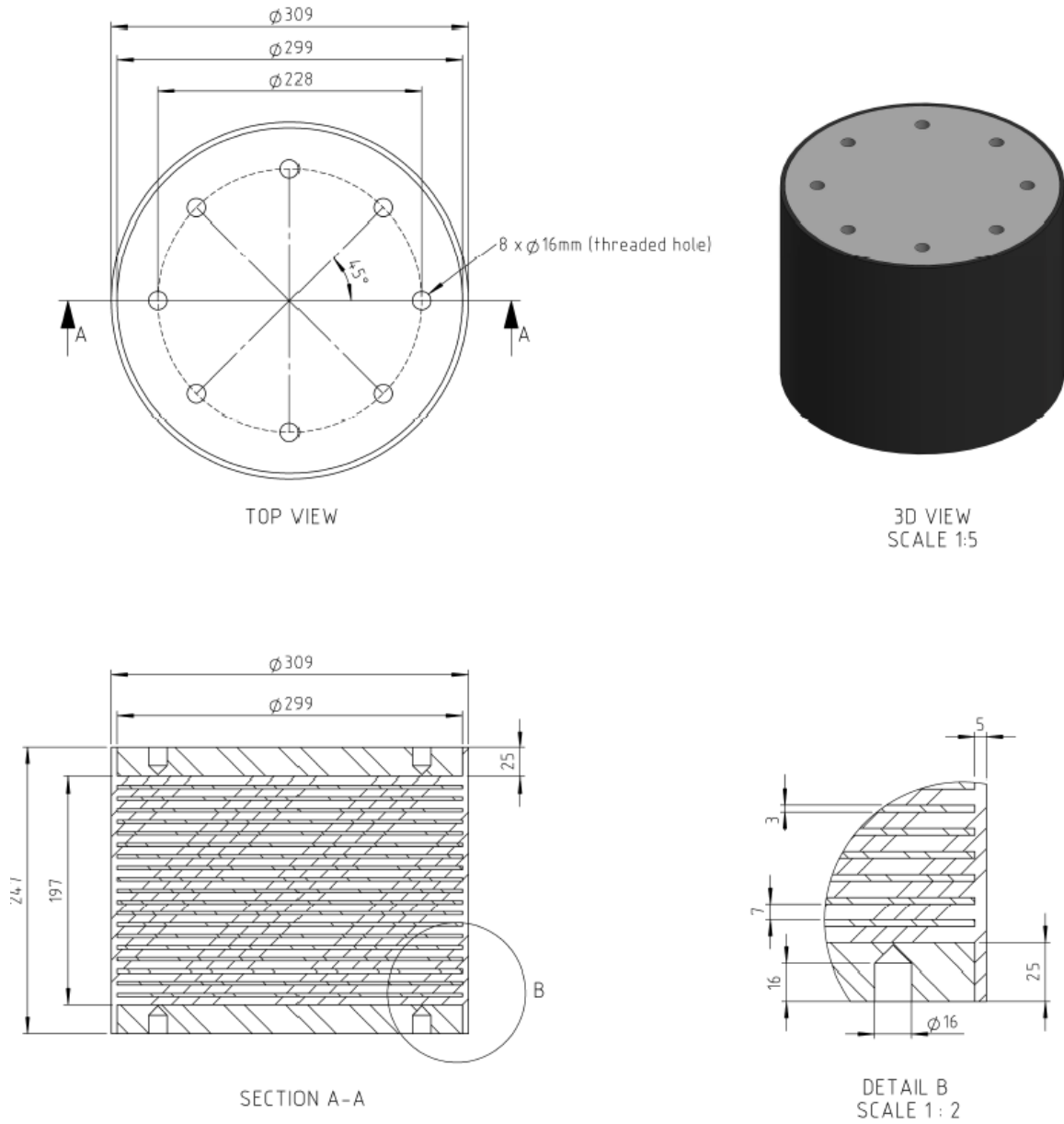


Figure 6-5 Mageba bearing type A, MA (courtesy of Mageba)

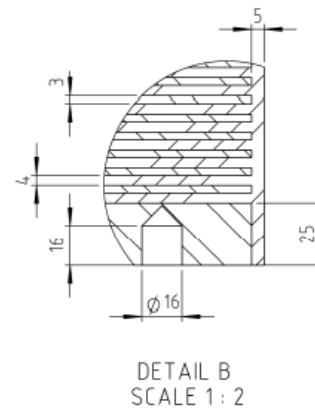
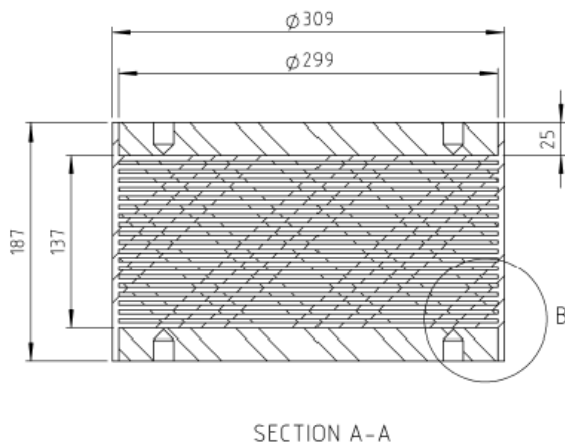
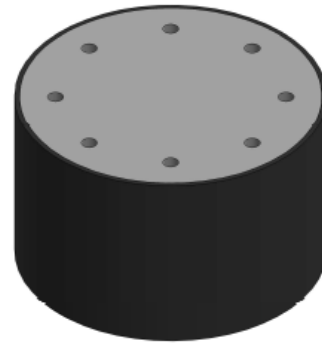
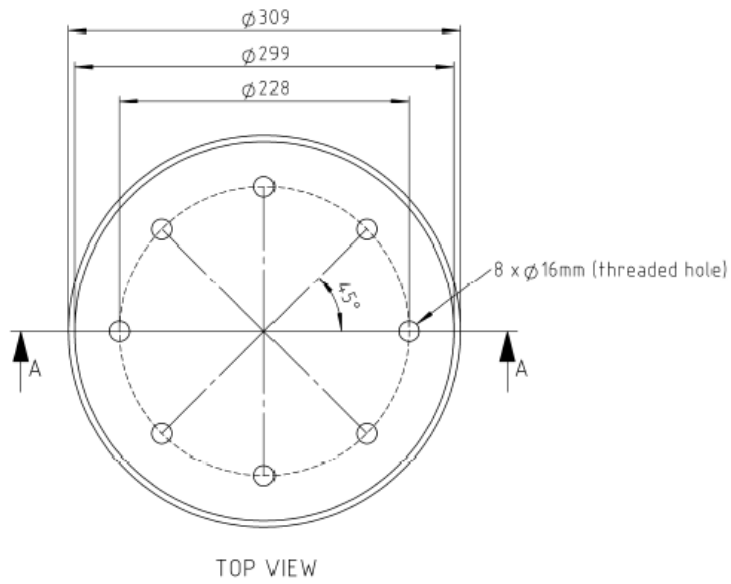


Figure 6-6 Mageba bearing type B, MB (courtesy of Mageba)

The theoretical mechanical properties of elastomeric bearings are presented in Table 6-4 and Table 6-5 in SI and US customary systems of units, respectively. The shear modulus of the rubber, G , bearings is required to estimate mechanical properties. The shear modulus reported by the manufacturer is not used here. The effective shear modulus of each type of bearing obtained at 100% shear strain is used to calculate the mechanical properties, as described in Chapter 3. The shape factor, S , of the bearings with a central hole (DA and DB) is obtained using:

$$S = \frac{D_o - D_i}{4t_r} \quad (6.1)$$

where D_o is the outer diameter excluding the cover thickness, D_i is the internal diameter, and t_r is the thickness of single rubber layer.

The shape factor of the bearings without a central hole (MA and MB) are obtained using:

$$S = \frac{D_o^2 - D_i^2}{4D_o t_r} \quad (6.2)$$

The moment of inertia, I , is calculated as:

$$I = \frac{\pi}{64} \left[(D_o + t_c)^4 - D_i^4 \right] \quad (6.3)$$

where t_c is added to the outer diameter to include a contribution from half of the cover rubber thickness to the moment of inertia.

The compression modulus, E_c , is obtained as:

$$E_c = \left(\frac{1}{6GS^2F} + \frac{4}{3K} \right)^{-1} \quad (6.4)$$

where F is a factor to account for the central hole in a circular bearing, K is the bulk modulus of rubber, and G is the effective shear modulus of rubber. The value of F is 1 for bearings without a central hole, and for bearings with a central hole is (Constantinou *et al.*, 2007):

$$F = \frac{\left(\frac{D_o}{D_i} \right)^2 + 1}{\left(\frac{D_o}{D_i} - 1 \right)^2} + \frac{1 + \frac{D_o}{D_i}}{\left(1 - \frac{D_o}{D_i} \right) \ln \left(\frac{D_o}{D_i} \right)} \quad (6.5)$$

The vertical stiffness, K_{v0} , and the horizontal stiffness, K_{H0} , are given by:

$$K_{v0} = \frac{A_0 E_c}{T_r} \quad (6.6)$$

$$K_{H0} = \frac{GA_0}{T_r} \quad (6.7)$$

where A_0 is the bonded rubber area of a bearing, and T_r is the total thickness of rubber layers in a bearing.

The critical buckling load, P_{cr} , and critical displacement, u_{cr} , in compression are:

$$P_{cr} = \sqrt{P_E GA_S} = \frac{\pi \sqrt{E_r G I A_0}}{T_r} \quad (6.8)$$

$$u_{cr} = \frac{P_{cr}}{K_{v0}} \quad (6.9)$$

where A_S is the shear area and E_r is the rotational modulus of a bearing.

The cavitation force, F_c , and cavitation displacement, u_c , in tension are:

$$F_c = 3GA_0 \quad (6.10)$$

$$u_c = \frac{F_c}{K_{v0}} \quad (6.11)$$

Table 6-4 Geometrical and mechanical properties of elastomeric bearings (SI units)

Property	Notation (units)	DA	DB	MA	MB
Single rubber layer thickness	t_r (mm)	7	4	7	4
Number of rubber layers	n	20	20	20	20
Total rubber layer thickness	T_r (mm)	140	80	140	80
Steel shim thickness	t_s (mm)	3	3	3	3
Outer diameter	D_o (mm)	296.8	296.8	299	299
Inner diameter	D_i (mm)	19	19	0	0
Cover thickness	t_c (mm)	4	4	5	5
Internal plate thickness (mm)	t_{int} (mm)	25.4	25.4	25	25
External plate thickness (mm)	t_{ext} (mm)	38.1	38.1	38.1	38.1
Total height (rubber+shim)	h (mm)	198	138	197	137
Total height (including int. plate)	L_{int} (mm)	249	189	247	187
Total height (including ext. plate)	L_{ext} (mm)	325	265	323	263
Bonded area (including cover)	A_o (mm ²)	70778	70778	72583	72583
Shear modulus	G (MPa)	0.41	0.45	0.79	0.77
Shape factor (without cover)	S	9.9	17.4	10.7	18.7
Moment of inertia	I (mm ⁴)	4.0E+08	4.0E+08	4.2E+08	4.2E+08
Bulk modulus	K (MPa)	2000	2000	2000	2000
Compression modulus	E_c (MPa)	159	427	397	777
Vertical stiffness	K_{vo} (kN/m)	80161	377341	205999	705255
Horizontal stiffness	K_{Ho} (kN/m)	207	398	410	699
Critical buckling load	P_{cr} (kN)	557	1675	1266	3060
Critical buckling displacement	u_{cr} (mm)	6.9	4.4	6.1	4.3
Cavitation force	F_c (kN)	87	96	172	168
Cavitation displacement	u_c (mm)	1.1	0.3	0.8	0.2

Table 6-5 Geometrical and mechanical properties of elastomeric bearings (US units)

Property	Notation (units)	DA	DB	MA	MB
Single rubber layer thickness	t_r (in)	0.276	0.157	0.276	0.157
Number of rubber layers	n	20	20	20	20
Total rubber layer thickness	T_r (in)	5.512	3.150	5.512	3.150
Steel shim thickness	t_s (in)	0.120	0.120	0.118	0.118
Outer diameter	D_o (in)	11.685	11.685	11.772	11.772
Inner diameter	D_i (in)	0.750	0.750	0.000	0.000
Cover thickness	t_c (in)	0.157	0.157	0.197	0.197
Internal plate thickness (mm)	t_{int} (in)	1.000	1.000	0.984	0.984
External plate thickness (mm)	t_{ext} (in)	1.500	1.500	1.500	1.500
Total height (rubber+shim)	h (in)	7.786	5.424	7.756	5.394
Total height (including int. plate)	L_{int} (in)	9.786	7.424	9.724	7.362
Total height (including ext. plate)	L_{ext} (in)	12.786	10.424	12.724	10.362
Bonded area (including cover)	A_o (in ²)	110	110	113	113
Shear modulus	G (psi)	68	71	123	117
Shape factor (without cover)	S	9.9	17.4	10.7	18.7
Moment of inertia	I (in ⁴)	915	915	943	943
Bulk modulus	K (psi)	290000	290000	290000	290000
Compression modulus	E_c (psi)	25954	65680	60767	115458
Vertical stiffness	K_{vo} (kips/in)	517	2288	1241	4125
Horizontal stiffness	K_{Ho} (kips/in)	1.36	2.47	2.52	4.20
Critical buckling load	P_{cr} (kips)	139	394	293	691
Critical buckling displacement	u_{cr} (inch)	0.268	0.172	0.236	0.167
Cavitation force	F_c (kips)	22	23	42	40
Cavitation displacement	u_c (inch)	0.043	0.010	0.034	0.010

6.3 Test Program

6.3.1 General

The goal of the experimental program was to characterize the behavior of LDR bearings under pure tension and shear-tension loading, and to observe the effects of material parameters, geometrical parameters, and loading conditions. The six objectives of the test program were to understand and characterize:

1. Cavitation and post-cavitation behavior of rubber bearings under tensile loading
2. Effect of loading history on tensile properties
3. Change in shear and compression properties following tensile loading
4. Influence of shear displacement on tensile-force response
5. Effect of cavitation on buckling load capacity

6.3.2 Description

The test program consisted of a series of tensile and shear-tension loading tests. Lateral and vertical benchmark tests were conducted before and after each series of tensile loadings to monitor any change in the mechanical properties of the bearings. A benchmark unidirectional shear test at a 100% shear strain under a constant axial pressure of 1 MPa, and a benchmark compressive test with an axial load amplitude of 100 kN and zero lateral offset were conducted in the horizontal and vertical directions, respectively.

Past experimental observations (Iwabe *et al.*, 2000; Warn, 2006) have shown that the shear properties of elastomeric bearings determined under nominal axial compressive pressure do not change substantially following cavitation. A possible explanation for this observation is that post-cavitation shear strength and stiffness are provided by the friction in the volume of damaged rubber under service axial loads. Tests by Iwabe *et al.* (2000) and Warn (2006) used a nominal value of axial pressure to determine the shear properties of elastomeric bearings. Friction depends strongly on axial pressure. The shear properties of two of the model bearings were calculated at different axial pressures, before and after cavitation, to investigate the effect of axial pressure on the change in shear properties following cavitation.

The effective shear modulus of seismic isolation bearings obtained using experimental data depends on the value of axial pressure and shear strain at which it is calculated. Experiments were conducted at different values of axial pressure subjected to varying shear strain amplitudes to obtain the variation of the effective shear modulus with axial pressure and shear strain. These tests were performed before and after cavitation to investigate if the variation of shear modulus with axial pressure and shear strain amplitude changes due to cavitation.

Illustrations of the input signals to the actuators are presented in Figure 6-7. The amplitude and frequency of the signals vary for the different tests. Tensile tests that involved cavitation and shear tests were conducted under displacement control. Compression tests were conducted under force control. Most of the experiments were quasi-static tests conducted at an excitation frequency of 0.01 Hz. Some characterization tests were also conducted at frequencies of 0.1 and 1 Hz to investigate the effects of loading rate on mechanical properties.

The five types of test that were conducted are described below:

- 1. Characterization tests:** The mechanical properties of all the model bearings were determined from benchmark characterization tests in shear and compression. The shear characterization tests were conducted at 100% shear strain under nominal axial load. An axial load representative of service load conditions is often used for shear characterization tests. Typical service design loads for elastomeric bearings used for seismic isolation of structures vary in the range of 3 MPa to 7 MPa. However, a nominal axial load of 70 kN corresponding to axial pressure of 1 MPa was used for the shear characterization tests because the moment capacity of the load cell was limited. This value of axial load allowed the bearings to undergo shear strains greater than 100% without exceeding the moment capacity of the load cell. Force-controlled compression characterization tests were conducted at amplitude of 300 kN, which corresponds to axial stress of approximately 4.3 MPa.
- 2. Effect of lateral offset on behavior in tension:** Tests were conducted to understand the effects of lateral offset on the pre-cavitation and post-cavitation behavior of elastomeric bearings in tension. Force-controlled tests were conducted at an amplitude equal to the half of the estimated cavitation strength to obtain the variation of tensile stiffness with lateral offset. Tests involving cavitation were also conducted at different lateral offsets under displacement control to investigate the effect of lateral offset on cavitation properties, namely, cavitation strength, post-cavitation stiffness, and strength degradation. Elastomeric bearings with different rubber layer thicknesses and shear modulus were tested to understand the effects of shape factor and shear modulus on cavitation properties.
- 3. Effect of shear loading history on cavitation:** The loading history in the shear direction might affect the cavitation behavior of an elastomeric bearing. Two model bearings were subjected to shear displacement histories of a varying number of cycles and amplitudes followed by cyclic tensile loading.
- 4. Effect of tensile loading history on cavitation:** The effect of tensile loading history on cavitation was investigated using two triangular excitation signals: 1) increasing displacement amplitude after every three cycles (IT), and 2) decreasing amplitude after every three cycles (DT).
- 5. Effect of cavitation on critical buckling load capacity:** All model bearings were subjected to linearly increasing compressive loads up to failure to assess the effect of cavitation on the critical buckling load capacity of a bearing at zero lateral displacement.

The summary of the testing program is presented in Table 6-6. The detailed sequence is presented in Appendix A.1.

Table 6-6 Summary of single bearing testing program

Test	Bearing	Type	Signal ¹	Preload P_0 (kN)	Axial load amplitude ² P (kN)	Static lateral offset Δ / R (%)	Displ. Amplitude u, δ (%)	Freq. f (Hz)	No. of cycles
1. Characterization tests									
1	DA1, MA1	Shear	S	70	n.a. ³	n.a.	$\pm 25, \pm 50, \pm 75, \pm 100$	0.01	4
2	MB1, DB4	Shear	S	70	n.a.	n.a.	$\pm 25, \pm 50, \pm 100, \pm 125, \pm 175$	0.01	4
3	DB1, MB1, DB4	Shear	S	35, 70, 105, 140, 175	n.a.	n.a.	± 100	0.01	4
4	DA4	Shear	S	11, 22, 33, 44, 70, 90, 140	n.a.	n.a.	± 100	0.01	4
5	DA1, MA1	Shear	S	70	n.a.	n.a.	$\pm 25, \pm 50, \pm 75$	1	4
6	DA1, MA1	Tension	T	0	-25	n.a.	n.a.	0.01	4
7	All	Shear	S	70	n.a.	n.a.	± 100	0.01	4
8	All	Compression	T	0	300	n.a.	n.a.	0.01	4
2. Effect of lateral offset on behavior in tension									
1	DA1, MA1	Tension	T	0	-50 kN	0, 50, 100, 150, 200	n.a.	0.01	4
2	DA4, MA4	Tension	T	0	-50 kN	0, 25, 50, 75, 100	n.a.	0.01	4
3	DB1, DB2	Tension	IT	0	n.a.	100	5, 10, 25, 50, 100	0.01	3
4	DB1, DB2	Shear	S	35, 70, 105, 140, 175	n.a.	n.a.	± 100	0.01	4
5	DB1, DB2	Shear	S	70	n.a.	n.a.	$\pm 25, \pm 50, \pm 100, \pm 125, \pm 175$	0.01	4

Table 6-6 Summary of single bearing testing program (contd.)

Test	Bearing	Type	Signal ¹	Preload P_0 (kN)	Axial load amplitude ² P (kN)	Static lateral offset Δ / R (%)	Displ. Amplitude u, δ (%)	Freq. f (Hz)	No. of cycles
6	DA4, MA4	Tension	IT	0	n.a.	0	5, 10, 25, 50, 65	0.01	3
7	DA4, MA4	Shear	S	70	n.a.	n.a.	± 100	0.01	4
8	DA4, MA4	Compression	T	0	300	n.a.	n.a.	0.01	4
3. Effect of shear loading history on cavitation									
1	MB1, MB2, DB4	Tension	IT	0	n.a.	0	5, 10, 25, 50, 100	0.01	3
2	MB4	Tension	DT	0	n.a.	0	100, 50, 25, 10, 5	0.01	3
3	MB1, DB4	Shear	S	35, 70, 105, 140, 175	n.a.	n.a.	± 100	0.01	4
4	DB4	Shear	S	70	n.a.	n.a.	$\pm 25, \pm 50, \pm 100, \pm 125, \pm 175$	0.01	4
5	MB2, MB4	Shear	S	70	n.a.	n.a.	± 100	0.01	4
6	MB2, MB4	Compression	T	0	300	n.a.	n.a.	0.01	4
4. Effect of tensile loading history on cavitation									
1	DA3, MA3	Tension	DT	0	n.a.	0	50, 25, 10, 5	0.01	3
2	DA3, MA3	Shear	S	70	n.a.	n.a.	± 100	0.01	4
3	DA3, MA3	Compression	T	0	300	n.a.	n.a.	0.01	4
4	DA3, MA3	Tension	IT	0	n.a.	0	5, 10, 25, 50, 65	0.01	3
5	DA3, MA3	Shear	S	70	n.a.	n.a.	± 100	0.01	4
6	DA3, MA3	Compression	T	0	300	n.a.	n.a.	0.01	4
7	DA2, MA2	Tension	IT	0	n.a.	0	5, 10, 25, 50, 65	0.01	3
8	DA2, MA2	Shear	S	70	n.a.	n.a.	± 100	0.01	4
9	DA2, MA2	Compression	T	0	300	n.a.	n.a.	0.01	4
10	DA2, MA2	Tension	DT	0	n.a.	0	65, 50, 25, 10, 5	0.01	3
11	DA2, MA2	Shear	S	70	n.a.	n.a.	± 100	0.01	4

Table 6-6 Summary of single bearing testing program (contd.)

Test	Bearing	Type	Signal ¹	Preload P_0 (kN)	Axial load amplitude ² P (kN)	Static lateral offset Δ / R (%)	Displ. Amplitude u, δ (%)	Freq. f (Hz)	No. of cycles
12	DA2, MA2	Compression	T	0	300	n.a.	n.a.	0.01	4
13	DB3, MB3	Tension	IT	0	n.a.	0	5, 10, 25, 50	0.01	3
14	DB3, MB3	Shear	S	70	n.a.	n.a.	±100	0.01	4
15	DB3, MB3	Compression	T	0	300	n.a.	n.a.	0.01	4
16	DB3, MB3	Tension	DT	0	n.a.	0	50, 25, 10, 5	0.01	3
17	DB3, MB3	Shear	S	70	n.a.	n.a.	±100	0.01	4
18	DB3, MB3	Compression	T	0	300	n.a.	n.a.	0.01	4
5. Effect of cavitation on critical buckling load capacity									
1	ALL	Compression	L	0	n.a.	0	Failure	n.a.	n.a.

1. S = Sinusoidal, T = Triangular, IT = Increasing Triangular, DT = Decreasing Triangular

2. Negative value indicates loading in tension

3. n.a.: not applicable

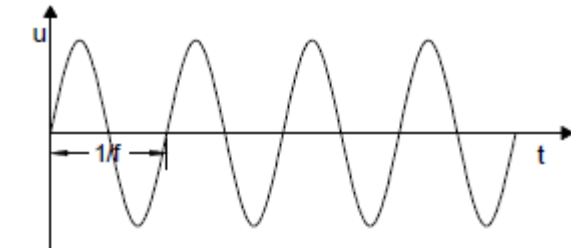
Table 6-7 Trial bearing test sequence (SI units)

Test no	Test type	Bearing	Type	Signal ¹	Preload P_0 (kN)	Axial load amplitude ² P (kN)	Static lateral offset Δ (mm)	Displ. Amplitude u, δ (mm)	Freq. f (Hz)	No. of cycles
Characterization tests										
1	1	Trial	Shear	S	51	n.a.	n.a. ³	±82.5	0.01	4
2	1	Trial	Compression	T	25	300	n.a.	n.a.	0.01	4
3	1	Trial	Compression	T	0	300	n.a.	n.a.	0.01	4
4	4	Trial	Tension	IT	0	n.a.	0	7, 35, 82.5	0.01	3
5	4	Trial	Shear	S	51	n.a.	n.a.	±82.5	0.01	4
6	4	Trial	Compression	T	25	300	n.a.	n.a.	0.01	4
7	4	Trial	Tension	DT	0	n.a.	0	82.5, 35, 7	0.01	3
8	4	Trial	Shear	S	51	n.a.	n.a.	±82.5	0.01	4
9	4	Trial	Compression	T	25	300	n.a.	n.a.	0.01	4
10	4	Trial	Shear	S	25.3	n.a.	n.a.	±80	0.01	4
11	4	Trial	Shear	S	51	n.a.	n.a.	±82.3	0.01	4
12	4	Trial	Shear	S	101	n.a.	n.a.	±82.3	0.01	4
13	4	Trial	Shear	S	152	n.a.	n.a.	±82.3	0.01	4
14	4	Trial	Tension	IT	0	n.a.	0	7, 35, 82.3	0.01	3

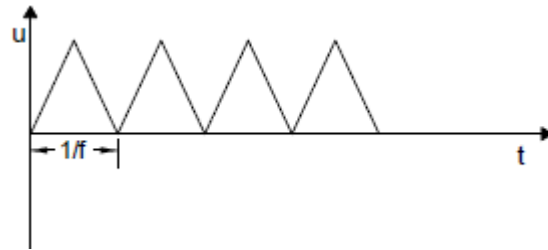
1. S = Sinusoidal, T = Triangular, IT = Increasing Triangular, DT = Decreasing Triangular

2. Negative value indicates loading in tension

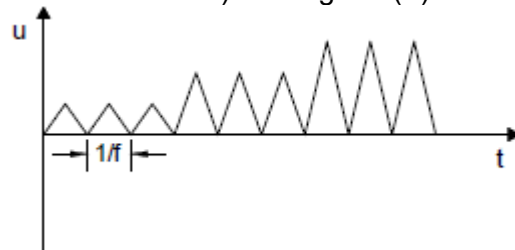
3. n.a.: not applicable



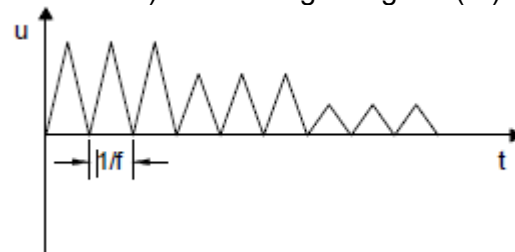
a) Sinusoidal signal (S)



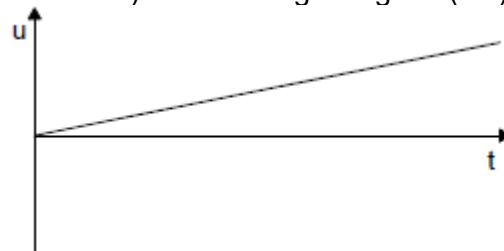
b) Triangular (T)



c) Increasing triangular (IT)



d) Decreasing triangular (DT)



e) Linear (L)

Figure 6-7 Signals used for the experiments

6.4 Instrumentation and Data Acquisition

6.4.1 General

A Single Bearing Testing Machine (SBTM) was used to perform tensile tests and shear and compression characterization tests. The compression failure tests were performed using a Concrete Strength Tester (CST).

For tests performed using the SBTM, twelve data channels were used to record the performance of the actuators and the response of the seismic isolation bearing during testing. Nine of these data collection channels were stationary instruments, and one data channel recorded time. Although, ten data channels are sufficient to operate the SBTM, two additional data channels, both assigned to string potentiometers, were used to measure relative vertical displacement across the bearing. The deformations in the bearings were also measured using a Krypton camera that tracked the locations of seven LEDs installed on bearings. Five video cameras were used to capture the behavior of elastomeric bearings from different locations.

Six data channels were used for compression failure tests of elastomeric bearings using the CST. Five of these channels were stationary instruments, and one data channel recorded time. The stationary instruments included four linear potentiometers and one load cell to measure axial displacement and axial force, respectively. The instrumentation and the data acquisition systems are described in the following sections.

6.4.2 Single Bearing Testing Machine

The SBTM is used to test single elastomeric bearing under unidirectional shear and axial loading. A schematic of the SBTM showing its dimensions and using standard U.S. section sizes is presented in Figure 6-8. Figure 6-9 is a photograph of the SBTM during testing. Figure 6-10 presents its spatial orientation. All tests discussed in Section 6.3, except the compression failure tests, were performed in the SBTM. The SBTM consists of a pedestal frame, a reaction frame, a loading beam, a horizontal (dynamic) MTS™ actuator, two vertical Parker actuators and a 5-channel reaction load cell.

The SBTM can impose shearing and axial loads and displacements, and combinations thereof. The capacity of the load cell, in terms of first yield, to simultaneously resist shear, axial and bending moment is presented as a nomogram in Figure 6-11. The actuators' capacities in terms of maximum stroke, velocity, and force are presented in Table 6-8. The maximum velocity of the vertical Parker actuators was not known. The maximum velocity of vertical actuators in the SBTM is expected to be different from the rated capacity of individual actuators. Triangular signals of different frequencies in increments were applied to the vertical actuators, and the amplitude of the command signal and response of the actuators were compared. The response of the actuators increase proportional to the command signal before reaching its maximum value. The frequency (and hence velocity) at which the difference between the actuator response and the command signal started to increase abruptly, was accepted as the maximum velocity that could safely be applied to the vertical actuators. This maximum velocity was determined as 50 mm/s for the vertical actuators. The capacity of the SBTM is generally limited by the capacity of the reaction load cell. Warn (2006) reported the elastic capacity of the 5-channel reaction load cell subjected to simultaneous actions as, 89 kN shearing force, 22.5 kN-m bending moment, and 222 kN axial force.

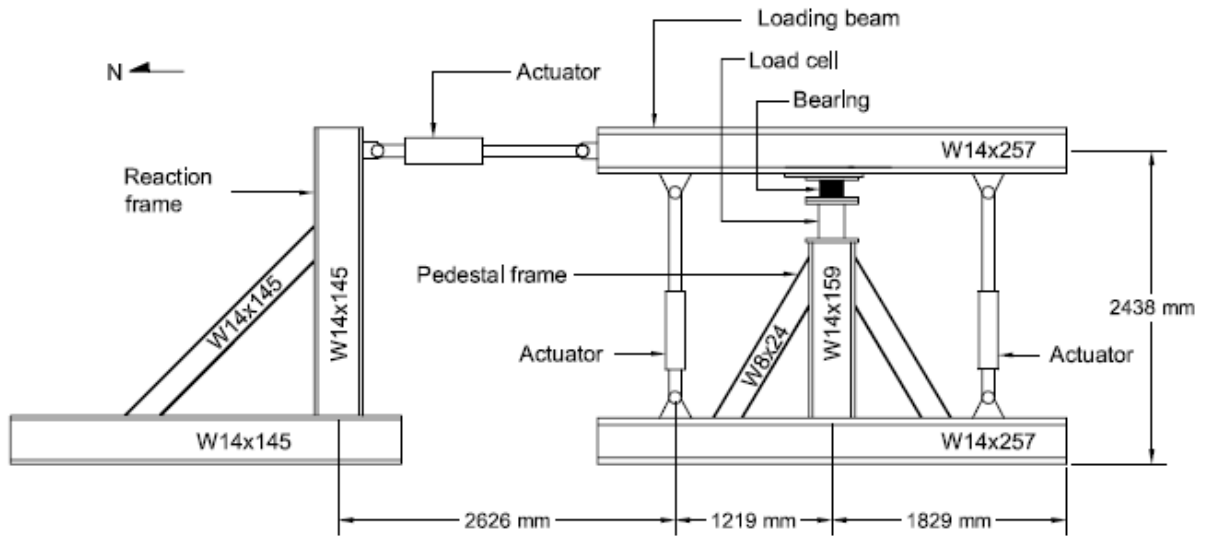


Figure 6-8 Schematic of Single Bearing Testing Machine (Warn, 2006)

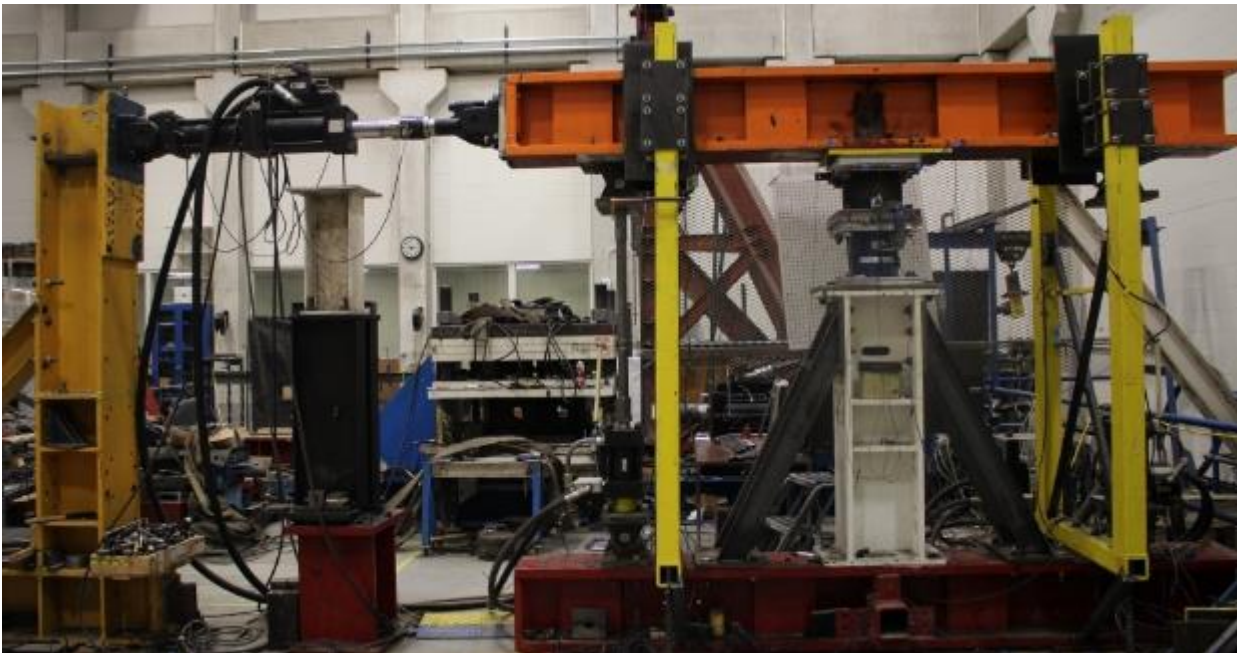


Figure 6-9 Photograph of Single Bearing Testing Machine

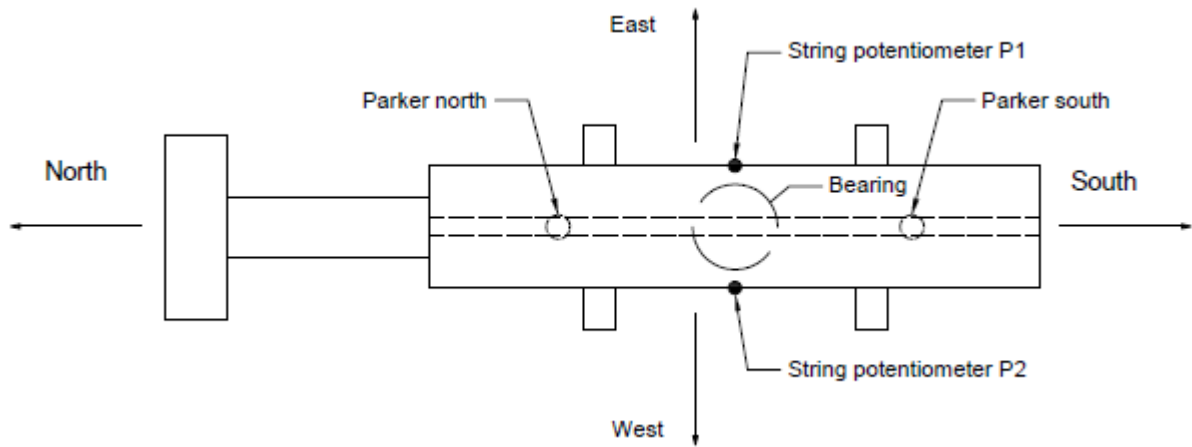


Figure 6-10 Layout of experimental setup (top-view)

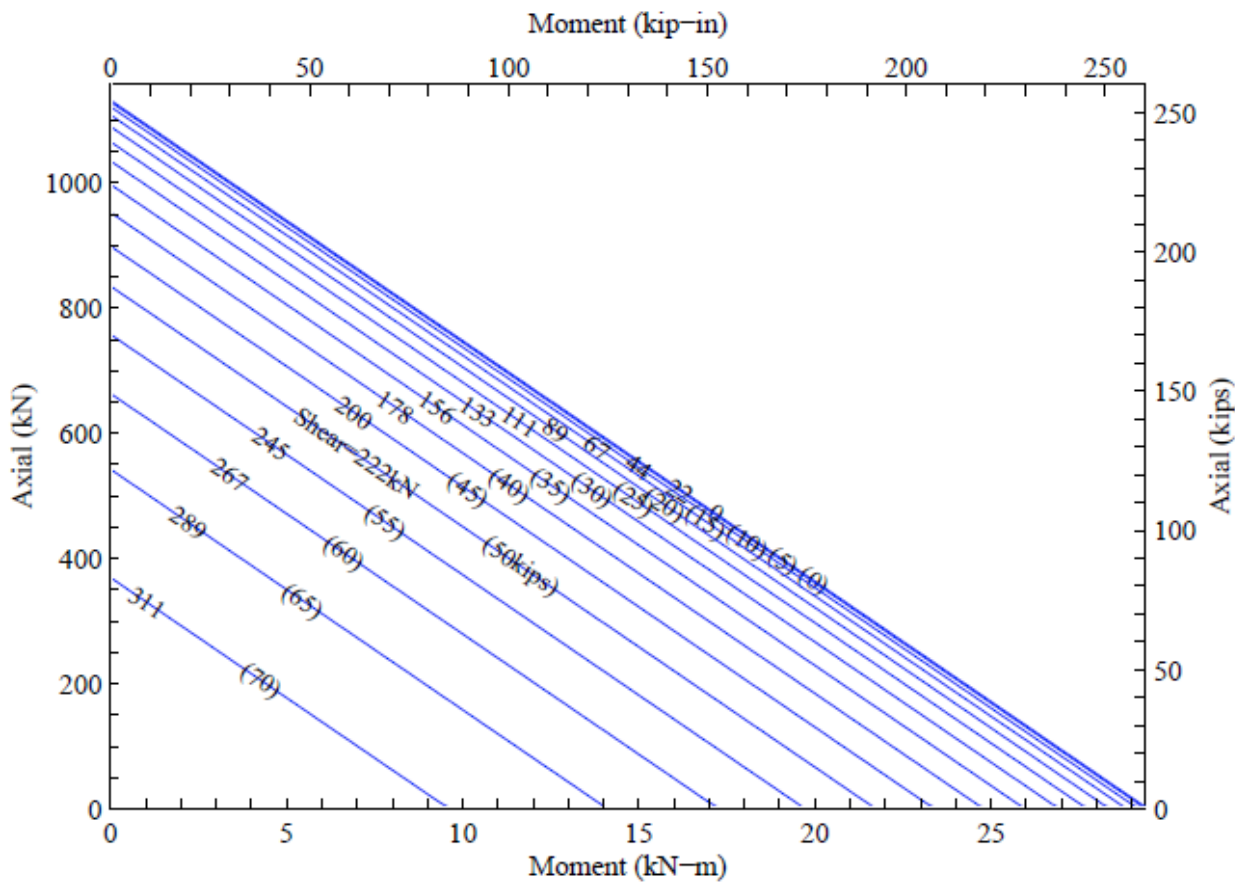


Figure 6-11 Capacity nomogram for load cell cross-section (SEESL, 2010)

Table 6-8 Single bearing testing machine actuator capabilities

Actuator ¹	Stroke (mm)	Velocity (mm/s)	Force (kN)
Horizontal (MTS)	±152	635	245
North vertical (Parker)	±50	50	317 Compression 300 Tension
South vertical (Parker)	±50	50	317 Compression 300 Tension

1. Actuator orientation is shown in Figure 6-8

6.4.3 Five channel load cell

The five channel load cell shown in Figure 6-12 was used to measure reactions during the tests. The load cell was built at the University at Buffalo by the Structural Engineering and Earthquake Simulation Laboratory (SEESL), and was calibrated against a National Institute of Standards and Technology (NIST) traceable reference load cell (Calibration Certificate: UB-2005-03-02). The original design sheet of the load cell is presented in Appendix A6.1. A detailed discussion on calibration process used for the load cell can be found in the appendix of Warn (2006). The load cell measures shear in two horizontal directions (S_x and S_y), moment about two horizontal axes (M_x and M_y), and the axial force.



Figure 6-12 Five channel load cell

6.4.4 Potentiometers

String potentiometers manufactured by Celesco (model no: SP1-12), with stroke ± 300 mm, were used to measure axial deformations on the east and the west side of bearings. The data sheet for the string potentiometer, obtained from the manufacture's website, is presented in Appendix A6.2. The location of a string potentiometer on one side of the bearing and a close up view are shown in Figure 6-13.



a) Location (west-side)

b) Close up view

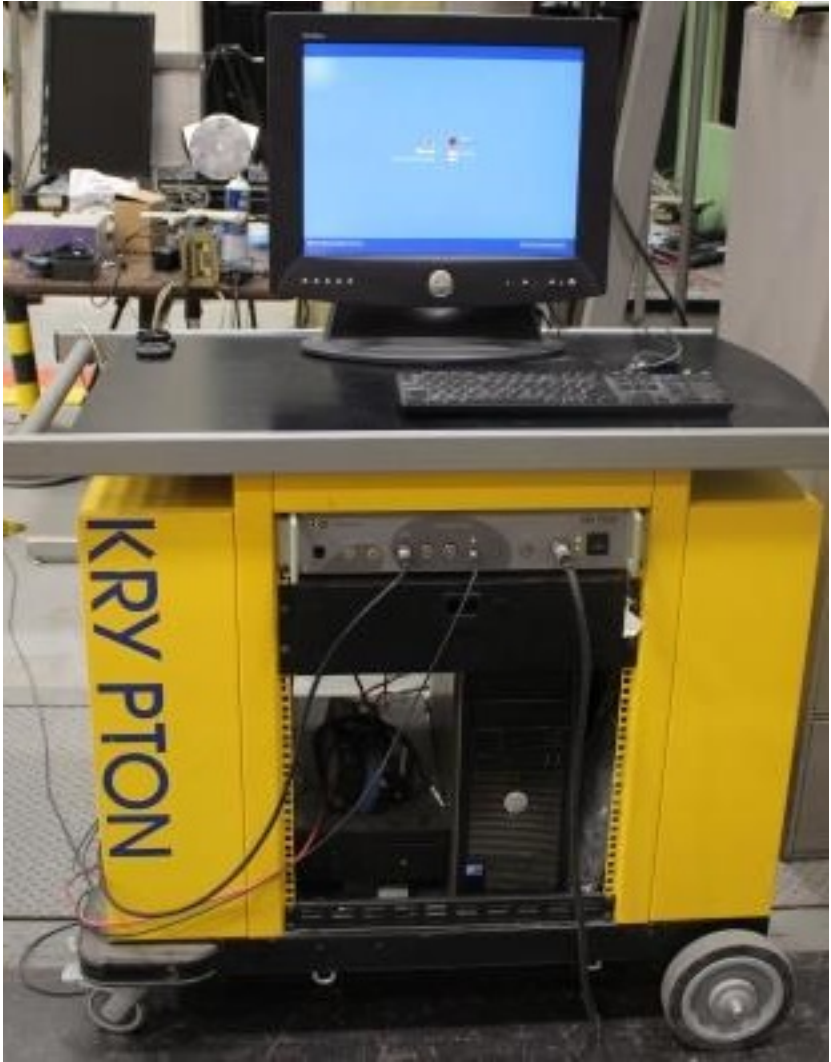
Figure 6-13 String potentiometer used for the measurement of axial displacement

6.4.5 Krypton tracking system

A portable coordinate tracking machine, known as Krypton Tracking System (KTS), was used to measure the deformation of a bearing in the shear and axial directions (SEESL, 2014). The components of the KTS is shown in Figure 6-14. The Krypton camera tracks the coordinates of the LEDs attached to the bearing. Seven locations were tracked during the experiments, as shown in Figure 6-15, three on each of the lower and upper bearing plates, and a location on the opposite face of the bearing during testing. The (x,y,z) coordinates of each location were monitored.



a) Camera



b) Controller

Figure 6-14 Components of the Krypton tracking system

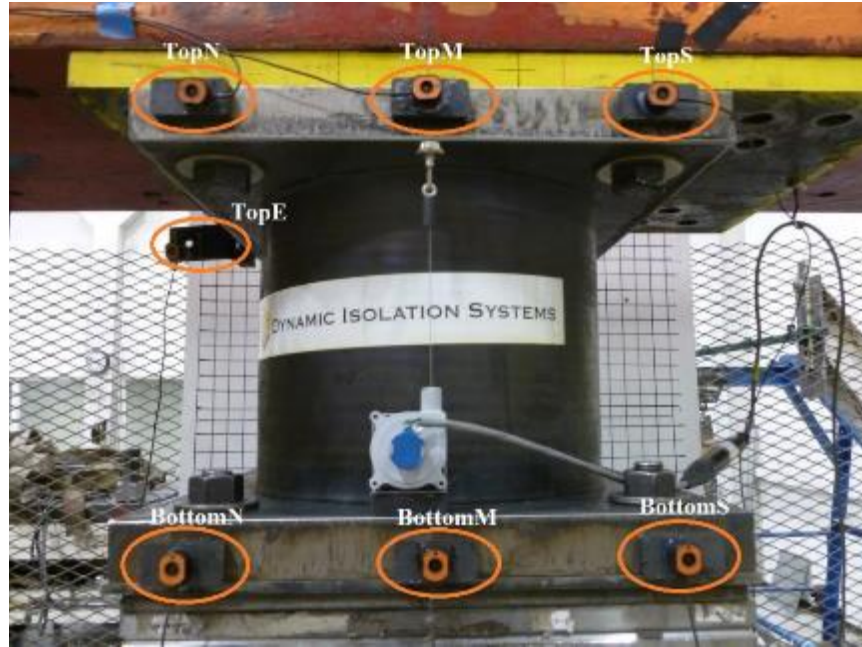


Figure 6-15 Locations monitored by the Krypton camera during testing

6.4.6 Video monitoring system

A video monitoring system was assembled to capture the behavior of the elastomeric bearings during the experiments. Details and close-up views of the cameras are presented in Table 6-9 and Figure 6-16, respectively. Cameras were installed at five locations. Four cameras, that included three CCD camera and one Hi-Definition GoPro camera, were installed on each column of the SBTM supporting the loading beam, as shown in Figure 6-17. One camera was installed on the west side of SBTM on a tripod. For the first few tests, a Canon camcorder was used, which was replaced by a Sony PTZ camera for subsequent experiments.

Table 6-9 Details of the camera used for video monitoring system

Camera	Model	Quantity	Resolution (pixels)
CCD	V-806b	3	510×492
PTZ	Sony EVID90	1	720×480
GoPro	Hero3 Black Edition	1	1920×1080
Camcorder	Canon Vixia HF G30	1	1920×1080



a) CCD Camera

b) PTZ camera

c) GoPro

Figure 6-16 Cameras used for the video monitoring system



Figure 6-17 Location of the four cameras on the columns of the SBTM

6.4.7 Concrete strength tester

As a final step in the experiments, all the bearings were subjected to gradually increasing compression load using a Concrete Strength Tester (CST) manufactured by FORNEY. The maximum applied compressive load was limited by the capacity of the CST, which was 400 kips in compression. The CST is shown in Figure 6-18. Four linear potentiometers manufactured by ETI systems (model no: LCP12A-50) were installed at four uniformly spaced locations around the perimeter of the circular bearings to capture the spatial distribution of the axial deformation. The locations of the four potentiometers and close-up view of a potentiometer is shown in Figure 6-19. The stroke of each linear potentiometer was ± 25 mm. The data sheet for the potentiometer is presented in Appendix A6.2.

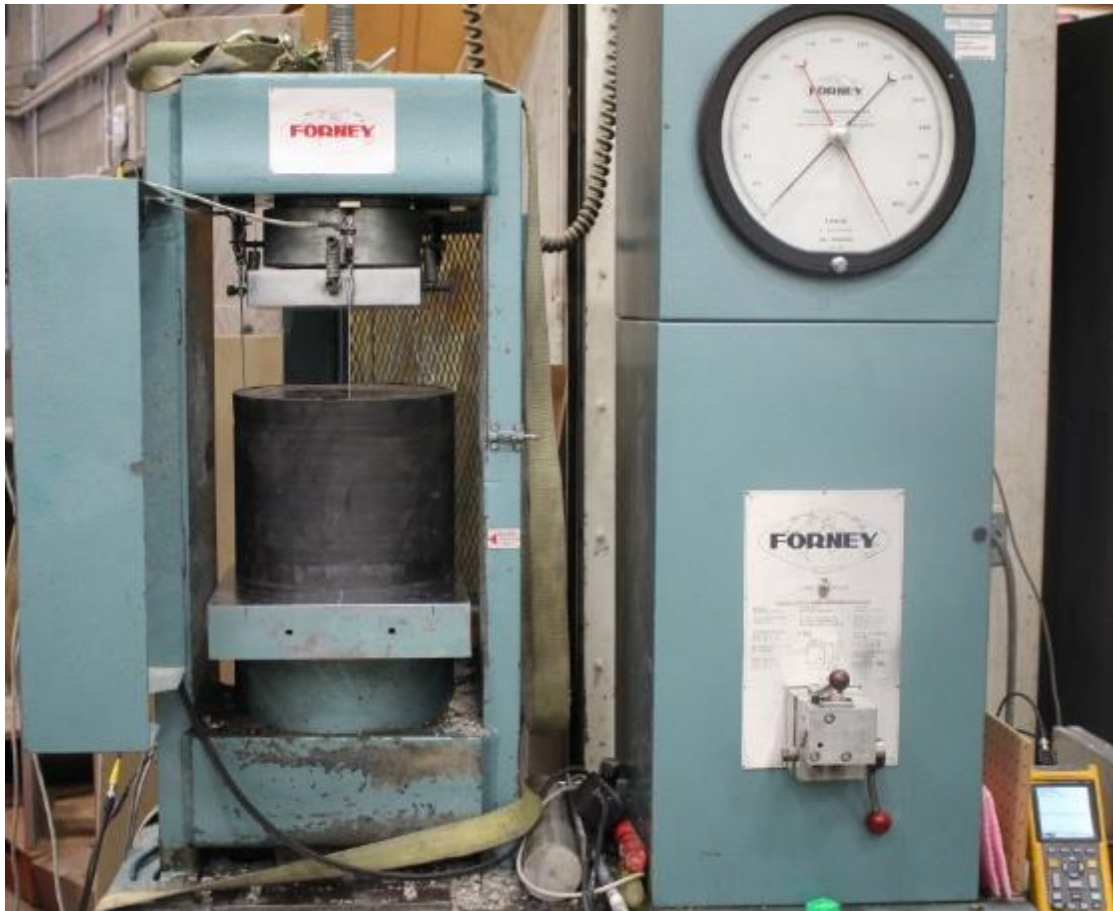
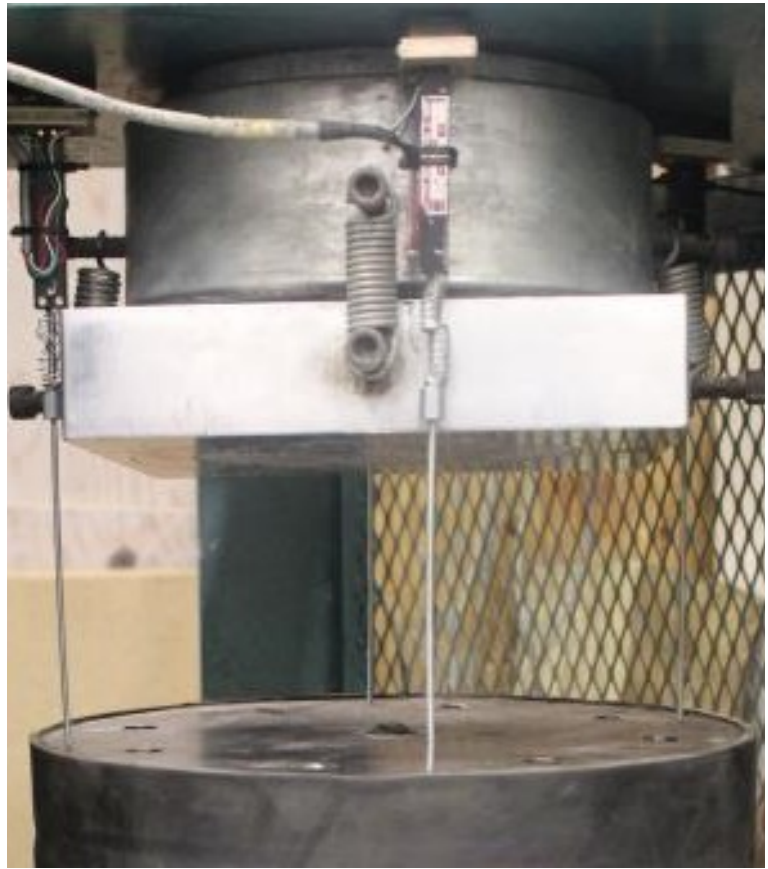


Figure 6-18 Compression Strength Tester at SEESL, University at Buffalo



a) Linear potentiometer



b) Location of four linear potentiometers

Figure 6-19 Potentiometers

7 EXPERIMENTAL RESULTS

7.1 Introduction

The results of testing of elastomeric bearings are presented in this chapter. The experimental plan and the test set-up were presented in Chapter 6. The primary goals of the experimental program were to characterize the behavior of elastomeric bearings in tension and to study the effects of different loading protocols on response in tension. A mathematical model of an elastomeric bearing in cyclic tension was developed in Chapter 3. The validity of the mathematical model is investigated and recommendations are made based on the experimental data presented in this chapter.

Data processing is discussed in Section 7.2. The results of the characterization tests are presented in Section 0. The effect of lateral offset on tensile properties and the effect of tensile loading history on cavitation are presented in Section 7.4 and Section 7.5, respectively. Section 7.5 discusses the effect of cavitation on the mechanical properties of elastomeric bearings. Section 0 provides details on failure of elastomeric bearings in tension. Section 0 presents the conclusions of the experimental study.

7.2 Data Processing

7.2.1 General

A MATLAB code is used to post-process the test data. Filtering techniques are employed to remove noise from the data. Redundant measurements of response quantities obtained from different channels are compared.

7.2.2 Filtering

A fifth-order low-pass Butterworth filter is used in conjunction with `filtfilt`, a zero-phase filter function in MATLAB, to remove high frequency noise.

The filtering procedures involves two types of frequencies: 1) the forcing frequency of the applied signal, and 2) the sampling frequency (number of recorded data points per second). Most of the tests were quasi-static (slow) tests, conducted at a forcing frequency of 0.01 Hz (10 sec time period). A few tests were conducted at 0.1 Hz and 1 Hz. The shear tests performed at 1 Hz could not be completed as the Single Bearing Testing Machine (SBTM) could not maintain the axial loads at corresponding high velocities. The sampling frequency for the tests is adjusted according to the forcing frequency so that 1000 data points are obtained in each cycle. Sampling frequencies of 10 Hz, 100 Hz, 1000 Hz are used for forcing frequencies of 0.01 Hz, 0.1 Hz, and 1 Hz, respectively.

A normalized cutoff frequency of 0.5 Hz is used to filter the response in shear. This choice of cutoff frequency for tensile response presents a unique challenge due to the rapid change in tensile stiffness following cavitation. The effect of cutoff frequency on the response of elastomeric bearing DA3 in shear and tension is shown in Figure 7-1 and Figure 7-2, respectively. A high cutoff frequency (e.g., 5 Hz) captures the change in stiffness adequately but fails to remove occasional spikes in the response, whereas a low cutoff frequency (e.g., 0.25 Hz) leads to excessive smoothing and cannot capture the sudden change in the tensile response around cavitation. Cutoff frequencies between 1 to 5 Hz are selected by trial and error to filter axial response for each test.

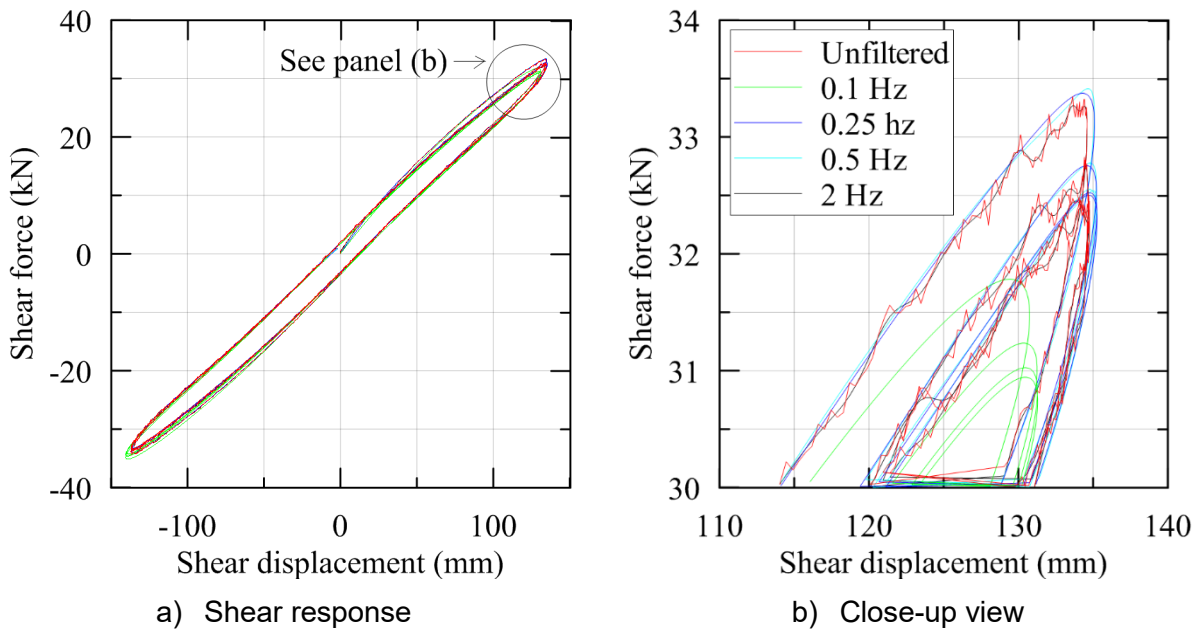


Figure 7-1 Effect of cutoff frequency on the shear response (bearing DA3, test 1)

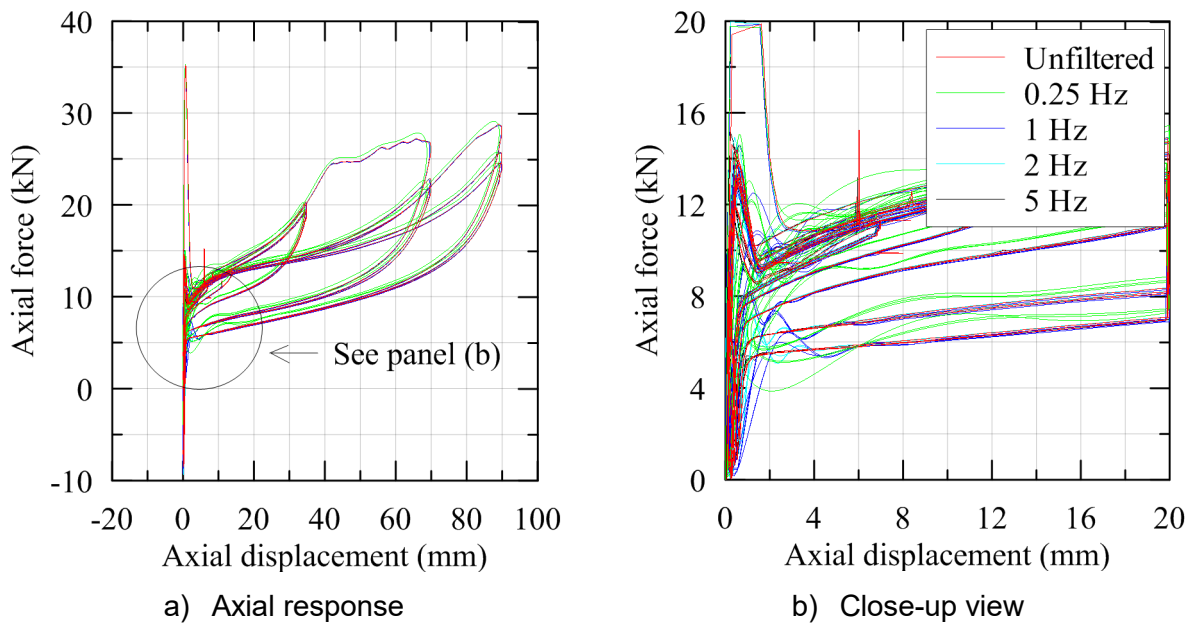


Figure 7-2 Effect of cutoff frequency on the tensile response (bearing DA3, test 6)

7.2.3 Axial displacement

The axial displacement of a bearing is measured using: 1) LVDTs inside the two vertical Parker actuators located to its north and south, 2) string potentiometers located to its east and west sides, and 3) a Krypton camera tracking three LEDs on each of the top and bottom bearing plates on its west sides, and a LED located on the north corner of its east side. The location of the Parker actuators and string potentiometers are shown in a top view of the SBTM in Figure 7-3; the locations of the LEDs for the Krypton tracking system are shown in Figure 7-4.

The axial deformation at the center of a bearing cannot be measured directly. Past experiments using the SBTM have reported bearing rotation about the two horizontal axes (e.g., Kasalanati (1998), Warn (2006)). Rotation across the two ends of the loading beam axis (X-direction) is caused by a time-delay in the signals between the master and slave vertical actuators. The inclination of the horizontal actuators also contributes to the rotation of loading beam. Rotation across the two sides of the loading beam (Y-direction) is due to rotation of loading beam about its axis. Axial displacements measured across a bearing using string potentiometers and Krypton camera are interpolated to obtain the axial deformation at the center of the bearing.

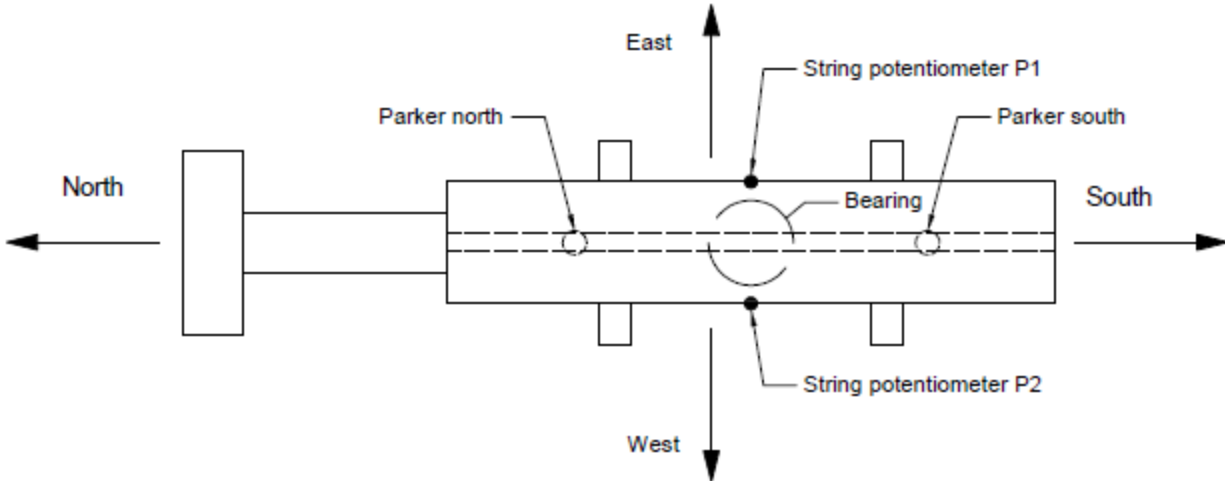


Figure 7-3 Top view of the instrumentation setup of SBTM

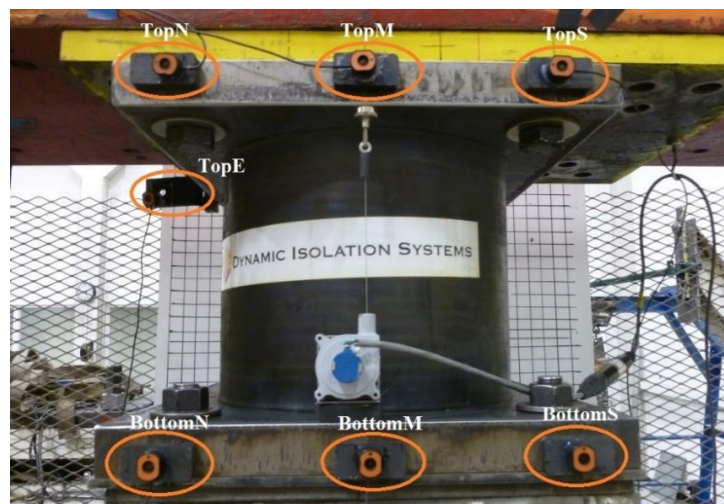


Figure 7-4 Locations of LEDs for Krypton tracking system

The vertical Parker actuators measure displacement that is different from the axial deformation of the bearing due to the inclination of the actuators with respect to the vertical plane. The rotation of the loading beam across its two ends also contributes to the difference in measurements between the two actuators. For lateral offset testing, the vertical actuators report the inclined components of the axial deformation in the bearing.

The displacements obtained from the string potentiometers on the two sides of a bearing are interpolated to obtain the axial deformation at the center of the bearing. A comparison of the axial deformation obtained using two string potentiometers (P_1 and P_2 shown in Figure 7-3) and their average value (P_{avg}) are enabled by Figure 7-5 and Figure 7-6, for compressive and tensile tests, respectively. A significant difference is observed between the values obtained from two potentiometers, P_1 and P_2 . Although the transverse rotation across the east and west side of a bearing was less than 1° , this small rotation resulted in a large difference between the displacements measured by the string potentiometers P_1 and P_2 due to the length of the bearing plates. The difference in displacement on the east and west sides of a bearing depend only on the rotation of the loading beam. For compressive tests, where the magnitude of the axial deformation is small, the percent difference between the axial displacements measured on the east and west of a bearing is much greater than in the tensile tests for which the magnitude of the axial deformation is larger.

The loading beam rotates if the cavitation pattern is not symmetric, which also contributes to the difference in the tensile displacements measured using the string potentiometers.

The Krypton camera tracked the coordinates of the seven LEDs installed on the bearing plates. The rotations of the bearing along two horizontal axes are calculated at each time step from the coordinates of the LEDs. The vertical displacement cannot be measured at the center of the bearing. The coordinates of the center of the top bearing plate are obtained by interpolating the coordinates of the LEDs, which allows the calculation of the axial deformation at the center of the bearing.

The axial deformations of a bearing obtained using potentiometers and the Krypton camera are presented in Figure 7-7 and Figure 7-8 for compressive and tensile tests, respectively. Small differences are observed. The average of two potentiometer measurements accounts for the rotation of the bearing across the sides of the loading beam but does not account for the rotation along the length of the loading beam. Moreover, potentiometer measurements also include minor slippage at the connection of the upper and lower bearing plates to the SBTM. When the measurements of the Krypton camera are used to calculate the axial deformation as the difference of coordinates at the top and bottom nodes of the bearing, they exclude any contribution of slippage at the bearing plate and SBTM connections. Accordingly, the Krypton camera measurements are used for the calculation of deformations in bearings.

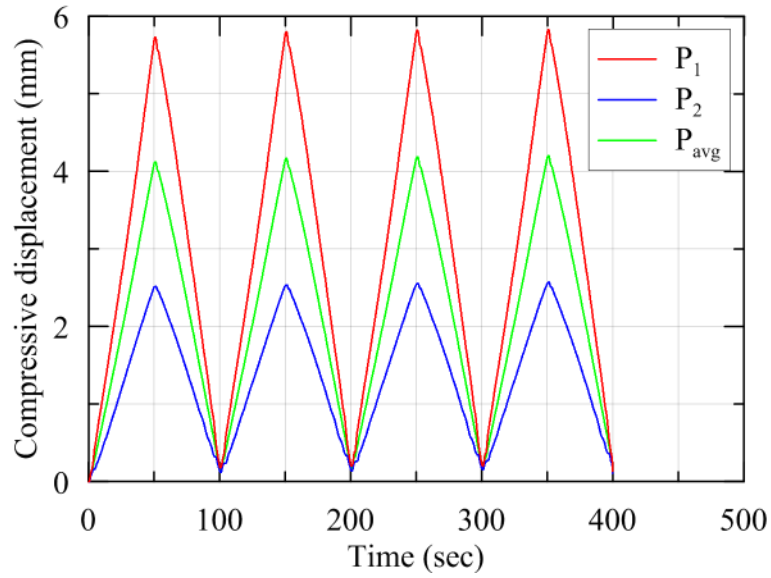


Figure 7-5 Axial deformation obtained using string potentiometers (bearing DA3, test 2)

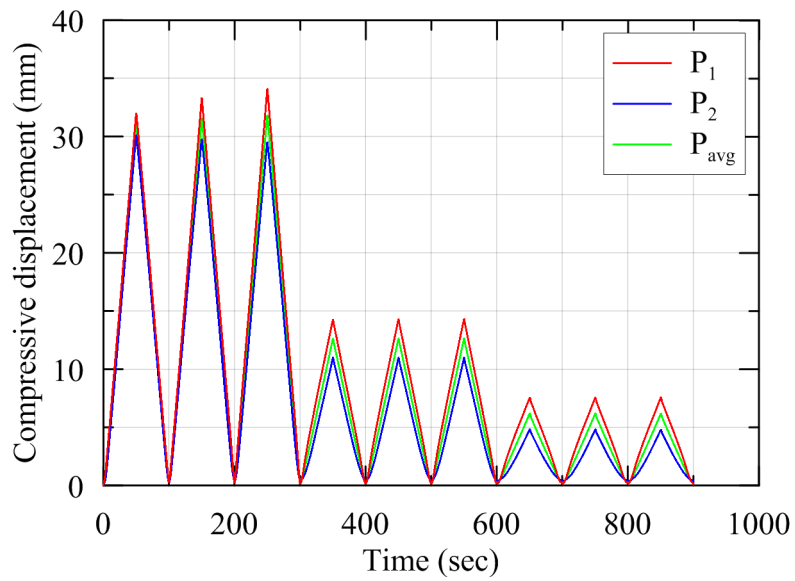


Figure 7-6 Axial deformation obtained using string potentiometers (bearing MA3, test 3)

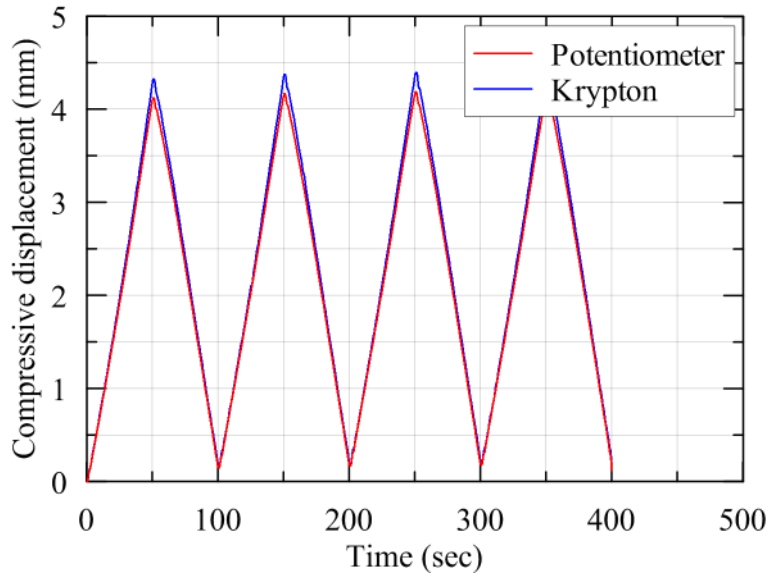


Figure 7-7 Axial deformation obtained using potentiometers and Krypton camera (bearing DA3, test 2)

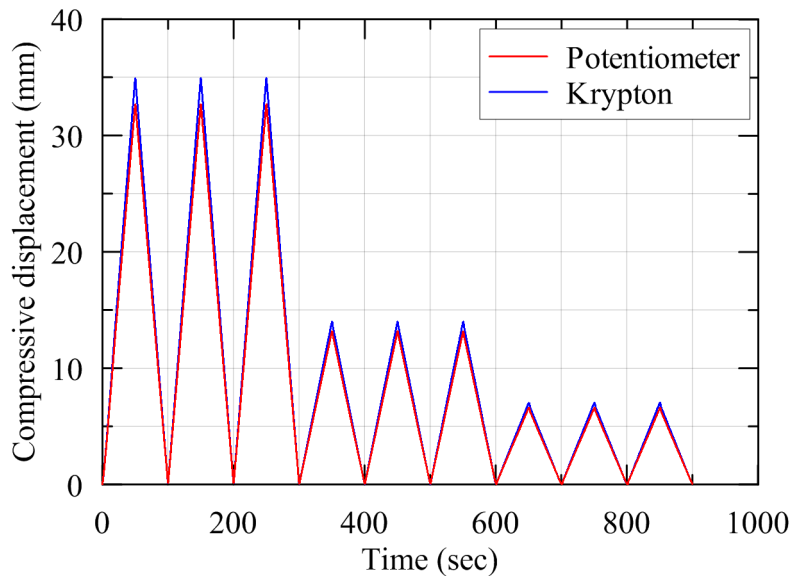


Figure 7-8 Axial deformation obtained using potentiometers and Krypton camera (bearing DA3, test 3)

7.2.4 Actuator comparison

The results of a test in which a substantial difference is observed between the values of shear force obtained using the horizontal actuator and the five channel load cell, are presented in Figure 7-9 and Figure 7-10. The shear modulus calculated using the measurements from the five channel load cell is smaller than the value calculated using the measurements from the horizontal actuator. The accuracy of measurements obtained using load cells depends on the procedure used to calibrate the load cell. A detailed discussion of the calibration of this load cell is presented in Warn (2006), which points out errors associated with the shear force calibration procedure. Forces measured by the load cell, especially in shear, contain calibration errors and errors due to cross talk between channels of the load cell. The cross talk between channels was expected to be greater in the shear and lateral offset tests than in the axial tests.

The horizontal MTS actuator has two data channels. There is no cross talk between these channels. For shear force, the measurement obtained from the horizontal actuator load cell is used. For axial force, the measurement from the five channel load cell is used.

In addition to measurements obtained using the Krypton camera, the shear displacement is also measured using the LVDT in the horizontal MTS actuator. A small difference is observed in the two measurements, as shown in Figure 7-11 and Figure 7-12.

Redundant measurements were not available for axial loads. The cross talk between the channels in the load cell during unidirectional axial loading only was expected to be small. The measurement of axial load using the five channel load cell is expected to be accurate. In summary, the shear and axial force acting on a bearing are obtained from the horizontal MTS actuator and the five channel load cell, respectively. The Krypton camera is used to measure displacements.

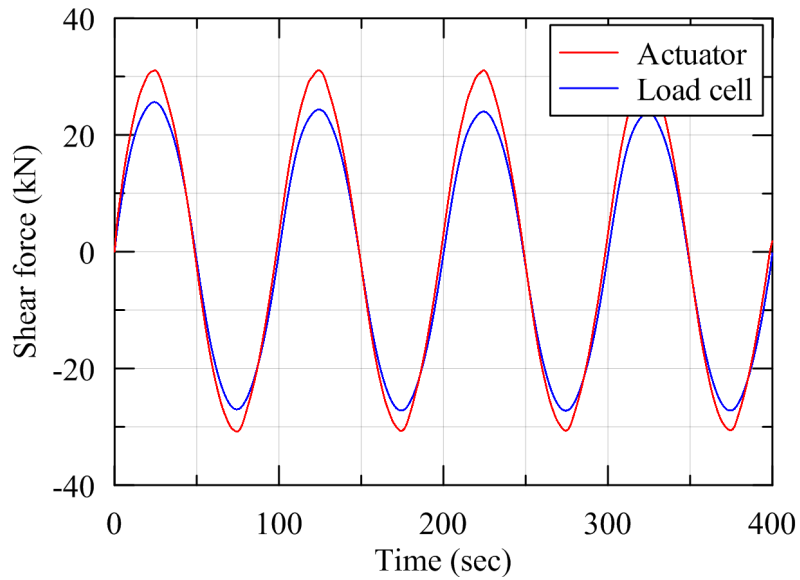


Figure 7-9 Shear force obtained using the MTS actuator and five channel load cell (bearing DB4, test 4a)

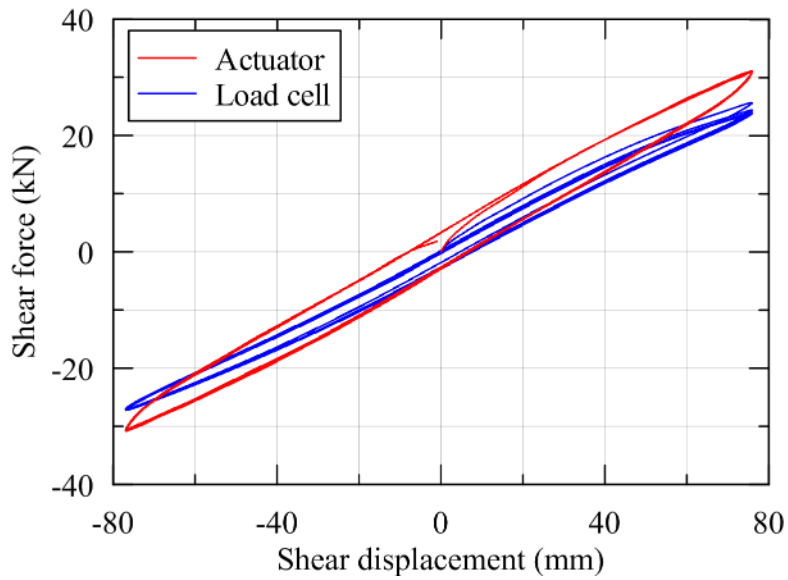


Figure 7-10 Shear force-displacement response obtained using the MTS actuator and the five channel load cell (bearing DB4, test 4a)

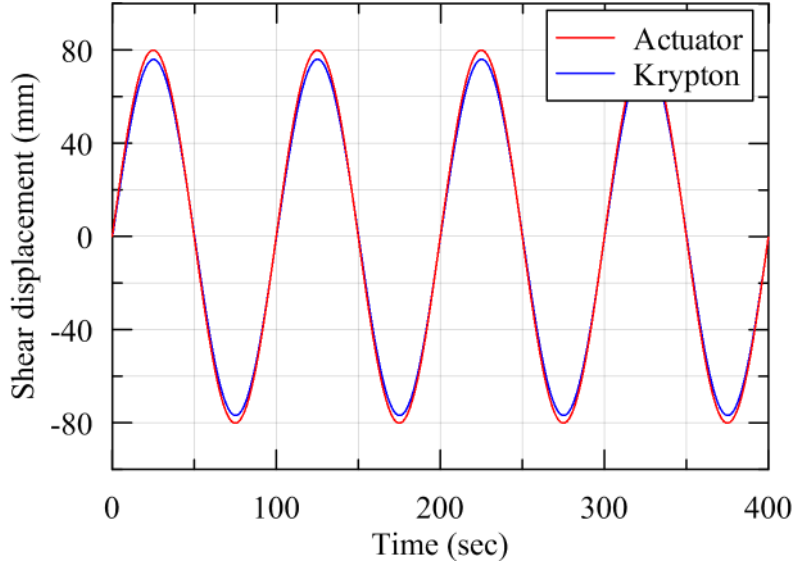


Figure 7-11 Shear displacement obtained using the MTS actuator and the Krypton camera (bearing DB4, test 4a)

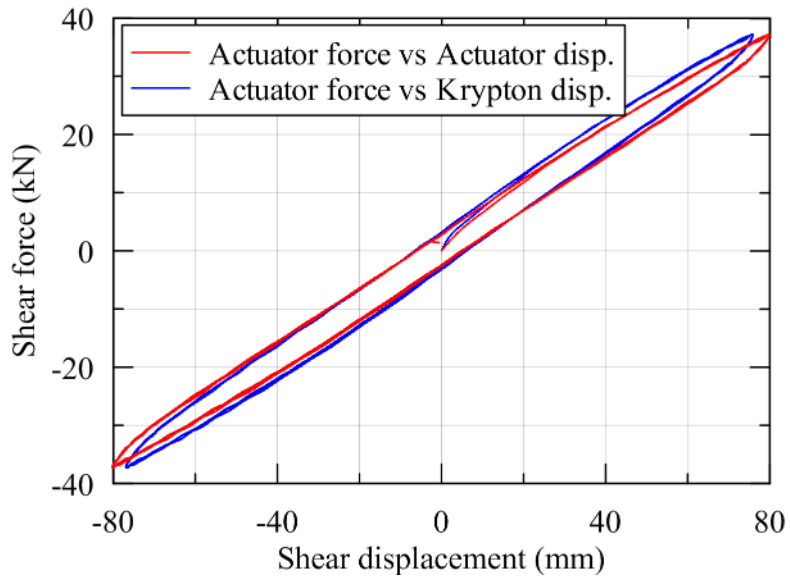


Figure 7-12 Shear force-displacement loops obtained using the MTS actuator and the Krypton camera (bearing DB4, test 4a)

7.3 Characterization Testing

7.3.1 General

Characterization tests were conducted to determine the mechanical properties of the elastomeric bearings in shear, compression, and tension. Benchmark shear and compression tests were performed on all sixteen bearings. Additional shear tests were conducted on selected bearings under varying conditions of stress and strain to obtain the variation of shear modulus with stress and strain. Tensile characterization tests were performed on two bearings. The results of the characterization tests are presented in the following sections.

7.3.2 Shear properties

The benchmark shear tests were conducted at 100% shear strain under an axial load of 70 kN, which corresponds to an approximate axial pressure of 1 MPa. Although the service axial pressure on elastomeric bearings used for seismic isolation of nuclear power plants is expected to be greater than 1 MPa, the maximum axial load that could be applied was limited by the moment capacity (due to shearing forces) of the five channel load cell. Most of the benchmark shear tests were conducted at excitation frequency of 0.01 Hz. A few shear benchmark tests were conducted at 0.1 and 1.0 Hz to investigate the effect of excitation frequency on shear modulus.

An idealized force-displacement curve for an elastomeric bearing in shear is presented in Figure 7-13.

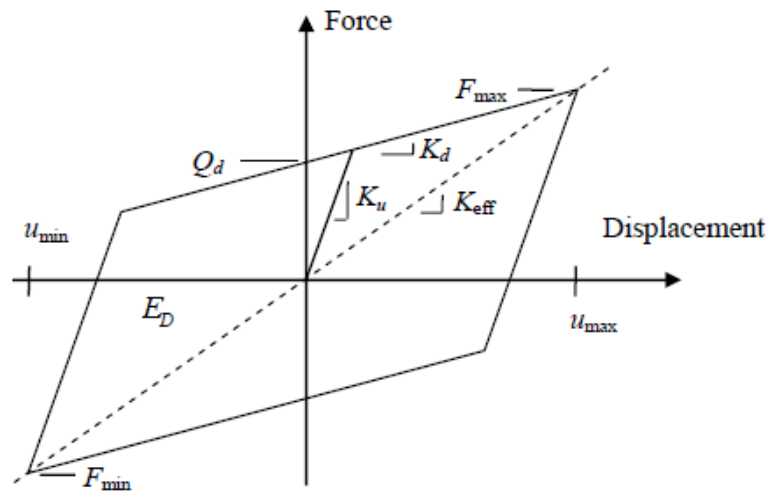


Figure 7-13 Idealized force-displacement behavior of an elastomeric bearing in shear (Warn and Whittaker, 2006)

The effective shear stiffness is calculated as:

$$K_{eff} = \frac{|F_{max}| + |F_{min}|}{|u_{max}| + |u_{min}|} \quad (7.1)$$

where u_{max} and u_{min} are the maximum and the minimum shear displacements, and F_{max} and F_{min} are the corresponding forces, as shown in Figure 7-13.

The effective shear modulus is determined as:

$$G_{\text{eff}} = \frac{K_{\text{eff}} T_r}{A_b} \quad (7.2)$$

where T_r is the total thickness of rubber, and A_b is the bonded rubber area that includes one half of the cover rubber.

The characteristic strength, Q_d , is estimated as:

$$Q_d = \frac{|F^+(u=0)| + |F^-(u=0)|}{2} \quad (7.3)$$

where $F^+(u=0)$ and $F^-(u=0)$ are the positive and negative zero displacement force intercepts, respectively, on the shear force-displacement hysteresis curve. The equivalent viscous damping is obtained by equating the energy dissipated in a cycle of loading to the energy dissipated in an equivalent viscous system. The equivalent damping ratio, ζ_{eq} , of a hysteretic system presented in Figure 7-14 is given as (Chopra, 2007):

$$\beta_{\text{eff}} = \frac{1}{4\pi} \frac{E_D}{E_{s0}} \quad (7.4)$$

The energy dissipated per cycle, E_D , is determined by numerically integrating the shear force-displacement response using a trapezoidal algorithm. The term $E_{s0} = K_{\text{eff}} u_0^2 / 2$ is the strain energy enclosed by the maximum displacements in each cycle, as shown in Figure 7-14. The deformation amplitude u_0 is taken as the average of the absolute values of u_{max} and u_{min} to account for any difference in the positive and negative amplitudes, and K_{eff} is the effective stiffness obtained at displacement amplitude u_0 .

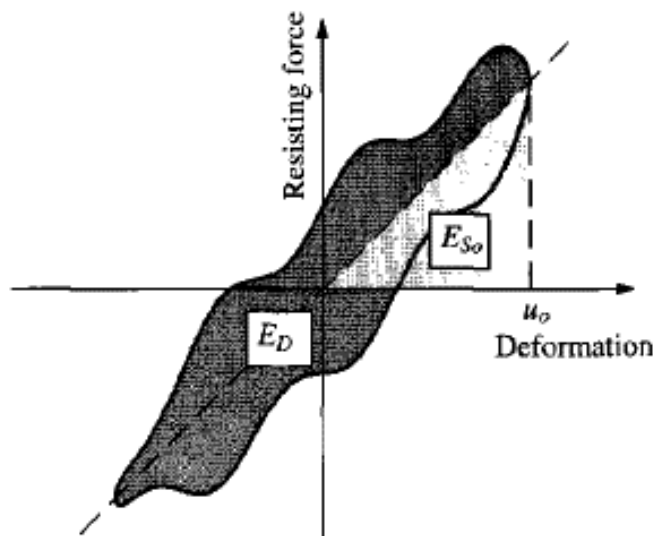


Figure 7-14 A general hysteretic system (Chopra, 2007)

The effective damping in shear is calculated as:

$$\beta_{eff} = \frac{2}{\pi} \left[\frac{E_D}{K_{eff} (|u_{max}| + |u_{min}|)^2} \right] \quad (7.5)$$

The shear properties of each bearing obtained from benchmark shear characterization tests are summarized in Table 7-1.

The target shear strain of 100% was applied using the horizontal actuator. The shear strain between the top and bottom nodes of the bearings obtained using the Krypton system are slightly different than 100% because of the inclination of the horizontal actuator to the horizontal plane. The shear strains reported in Table 7-1, which are calculated from Krypton measurements, are slightly different from the targets values identified in Chapter 6. For the Mageba type A bearings (MA), characterization shear tests could not be performed at 100% shear strain because the vertical actuators were unable to maintain the axial load during testing at strains greater than 75%. For bearings DB1, DB2, DB3, MB2, and MB4, characterization tests were not performed before cavitation and only the post-cavitation values are reported. Although, cavitation was not expected to affect the shear properties substantially, in few cases, misleading values of shear modulus are obtained because of slippage across the two parts of a ruptured bearing. Shear modulus is obtained from the displacement-controlled shear tests. The low shear modulus and high damping of MB2 is due to slippage and bearing damage.

A summary of the shear properties for each type of bearing, calculated by averaging the values in Table 7-1, is presented in Table 7-2. The averaged properties presented in Table 7-2 do not include values from the post-cavitation tests.

For a LDR bearing, the characteristic shear strength is estimated per Chapter 3 as:

$$Q_d = \frac{\pi}{2} \times \beta_{eff} \times K_{eff} \times D \quad (7.6)$$

where D is the displacement at which β_{eff} and K_{eff} are calculated. The theoretical values of the characteristic strength of all bearings are calculated using the information presented in Table 7-1. The experimental and theoretical values of characteristic strength are presented in Table 7-3. The differences are small.

The statistical distributions of effective shear modulus and damping ratios for the DIS and Mageba bearings are presented in Figure 7-15 and Figure 7-16, respectively. Unlike Table 7-2, where data consisted of only pre-cavitation values, the statistical distributions presented in Figure 7-15 and Figure 7-16 include values from pre- and post-cavitation tests. A small dispersion is observed in the shear modulus of the DIS bearings and the mean and median shear moduli are close to the shear modulus reported by DIS (=0.45 MPa). A greater dispersion is observed in the shear moduli of the Mageba bearings. The magnitude and dispersion of the damping ratio for the Mageba bearings are greater than those for the DIS bearings.

Table 7-1 Shear properties obtained from shear characterization tests (contd.)

Bearing	Test	Cycle	f (Hz)	ρ (MPa)	γ (%)	K_{eff} (kN/mm)	G_{eff} (MPa)	Q_d (kN)	E_D (J)	β_{eff} (%)
DA1	6a	1	0.01	1	97	0.203	0.4	2.06	975	4.1
		2	0.01	1	97	0.201	0.4	2.02	957	4.1
		3	0.01	1	97	0.2	0.4	1.99	948	4.1
		4	0.01	1	97	0.2	0.4	1.74	928	4
DA2	1	1	0.01	1	97	0.219	0.43	1.86	981	3.9
		2	0.01	1	97	0.215	0.42	1.75	862	3.5
		3	0.01	1	97	0.215	0.42	1.72	853	3.4
		4	0.01	1	97	0.214	0.42	1.43	836	3.4
DA3	1	1	0.01	1	97	0.214	0.42	2.61	1276	5.1
		2	0.01	1	97	0.211	0.42	2.5	1157	4.7
		3	0.01	1	97	0.21	0.41	2.46	1140	4.7
		4	0.01	1	97	0.209	0.41	2.08	1118	4.6
DA4	1	1	0.01	1	97	0.195	0.39	2.06	986	4.3
		2	0.01	1	97	0.193	0.38	2	939	4.2
		3	0.01	1	97	0.193	0.38	1.98	932	4.2
		4	0.01	1	97	0.192	0.38	1.74	923	4.1
DB1 ¹	2	1	0.01	1	95	0.389	0.44	1.98	492	3.5
		2	0.01	1	96	0.389	0.44	1.77	481	3.4
		3	0.01	1	96	0.388	0.44	1.74	472	3.3
		4	0.01	1	96	0.387	0.44	1.28	468	3.3
DB2 ¹	2	1	0.01	1	96	0.338	0.38	2.47	620	5
		2	0.01	1	96	0.336	0.38	2.28	595	4.8
		3	0.01	1	96	0.336	0.38	2.23	579	4.7
		4	0.01	1	96	0.336	0.38	1.87	576	4.6
DB3 ¹	2a	1	0.01	1	96	0.365	0.41	3.09	754	5.6
		2	0.01	1	96	0.363	0.41	2.96	759	5.7
		3	0.01	1	96	0.362	0.41	2.97	751	5.6
		4	0.01	1	96	0.361	0.41	2.41	741	5.6
DB4	1	1	0.01	1	96	0.403	0.45	1.71	496	3.4
		2	0.01	1	96	0.397	0.45	1.64	446	3.1
		3	0.01	1	96	0.397	0.45	1.58	433	3
		4	0.01	1	96	0.396	0.45	1.3	426	2.9
MA1	5c	1	0.01	1	73	0.413	0.8	4.55	1464	5.4
		2	0.01	1	73	0.412	0.8	4.25	1381	5.1
		3	0.01	1	73	0.412	0.79	4.21	1357	5
		4	0.01	1	73	0.411	0.79	3.74	1330	5
MA2	1a	1	0.01	1	70	0.383	0.74	2.84	949	4.2
		2	0.01	1	70	0.381	0.73	2.73	888	3.9
		3	0.01	1	70	0.38	0.73	2.69	868	3.8
		4	0.01	1	70	0.379	0.73	2.45	847	3.8
MA3	1	1	0.01	1	69	0.425	0.82	2.74	1142	4.6
		2	0.01	1	69	0.411	0.79	2.48	855	3.5
		3	0.01	1	69	0.407	0.78	2.39	807	3.3
		4	0.01	1	69	0.405	0.78	2.11	778	3.2
MA4	1	1	0.01	1	69	0.44	0.85	3.99	1460	5.6

Table 7-1 Shear properties obtained from shear characterization tests (contd.)

Bearing	Test	Cycle	f (Hz)	p (MPa)	γ (%)	K_{eff} (kN/mm)	G_{eff} (MPa)	Q_d (kN)	E_D (J)	β_{eff} (%)
		2	0.01	1	69	0.425	0.82	3.59	1187	4.7
		3	0.01	1	69	0.421	0.81	3.48	1138	4.6
		4	0.01	1	69	0.418	0.81	2.87	1111	4.5
MB1	3	1	0.01	1	94	0.714	0.79	3.88	1218	4.8
		2	0.01	1	94	0.69	0.76	3.72	1035	4.2
		3	0.01	1	94	0.683	0.75	3.64	988	4.1
		4	0.01	1	94	0.678	0.75	3.38	963	4
MB2 ¹	3	1	0.01	1	94	0.65	0.72	10.38	2107	9.1
		2	0.01	1	94	0.636	0.7	11.45	1621	7.1
		3	0.01	1	94	0.628	0.69	12.11	1588	7.1
		4	0.01	1	94	0.624	0.69	11.07	1577	7.1
MB3	1	1	0.01	1	94	0.735	0.81	2.99	1102	4.2
		2	0.01	1	94	0.707	0.78	2.79	816	3.3
		3	0.01	1	94	0.698	0.77	2.69	765	3.1
		4	0.01	1	94	0.693	0.76	2.25	732	3
MB4 ¹	3	1	0.01	1	95	0.591	0.65	4.37	1097	5.2
		2	0.01	1	95	0.589	0.65	4.19	1044	4.9
		3	0.01	1	95	0.587	0.65	4.14	1023	4.8
		4	0.01	1	95	0.586	0.65	3.96	1009	4.8

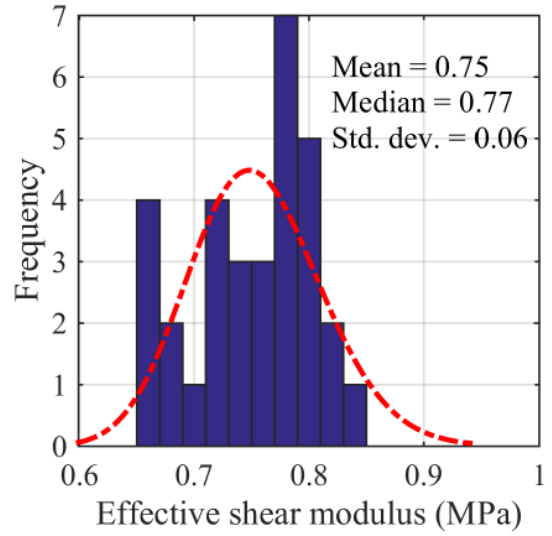
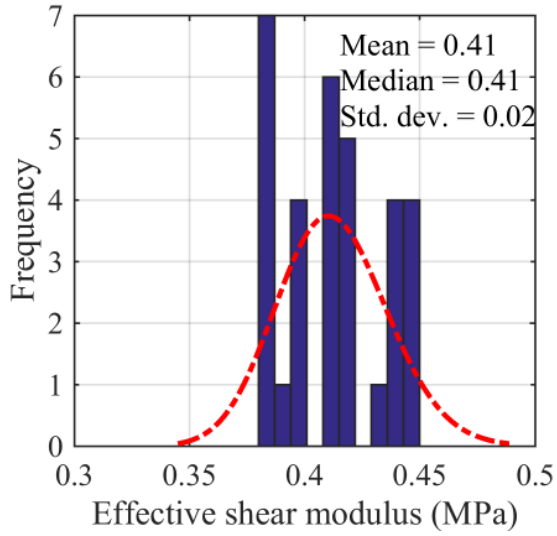
1. Post-cavitation properties

Table 7-2 Averaged shear properties of bearings

Bearing	K_{eff} (kN/mm)	G_{eff} (MPa)	Q_d (kN)	β_{eff} (%)
DA	0.205	0.41	2.0	4.2
DB	0.398	0.45	1.6	3.1
MA	0.408	0.79	3.2	3.5
MB	0.700	0.77	3.2	3.8

Table 7-3 Summary of averaged shear properties

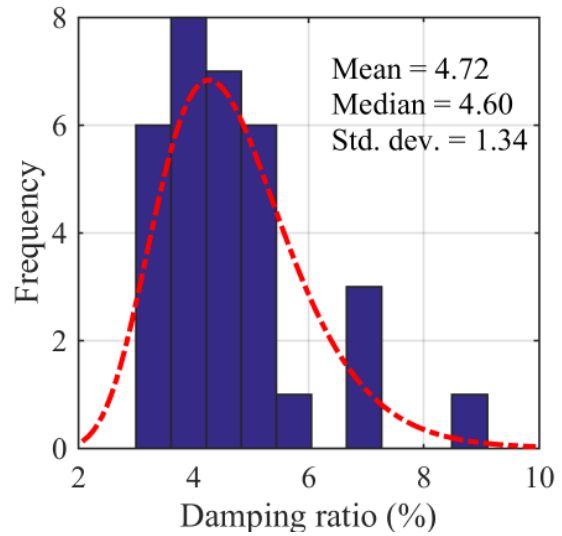
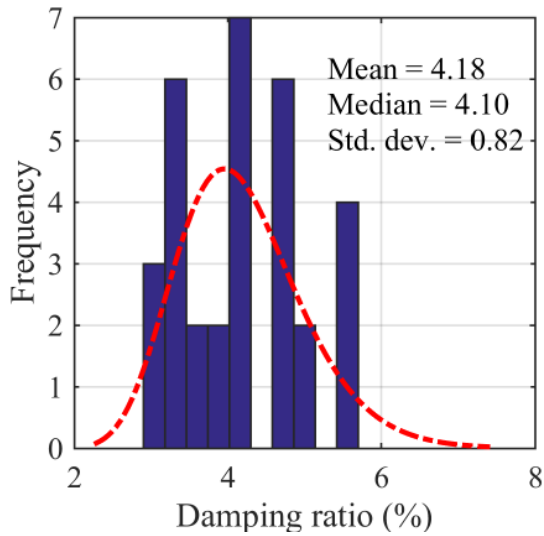
Bearing	$Q_{d_Experimental}$ (kN)	$Q_{d_Theoretical}$ (kN)	Difference (%)
DA	2.0	1.9	6
DB	1.6	1.6	3
MA	3.2	3.1	2
MB	3.2	3.4	6



a) DIS bearings

b) Mageba bearings

Figure 7-15 Statistical distributions of shear moduli



a) DIS bearings

b) Mageba bearings

Figure 7-16 Statistical distributions of damping ratios

The effect of the forcing frequency on shear modulus was investigated by performing shear characterization tests on bearing MA1 at 0.01 Hz and 0.1 Hz. Results are presented in Table 7-4 and Figure 7-17. No variation in shear modulus is observed with frequency. Shear characterization tests could not be performed at frequency of 1 Hz because the vertical actuators were unable to maintain the axial loads at the high velocities.

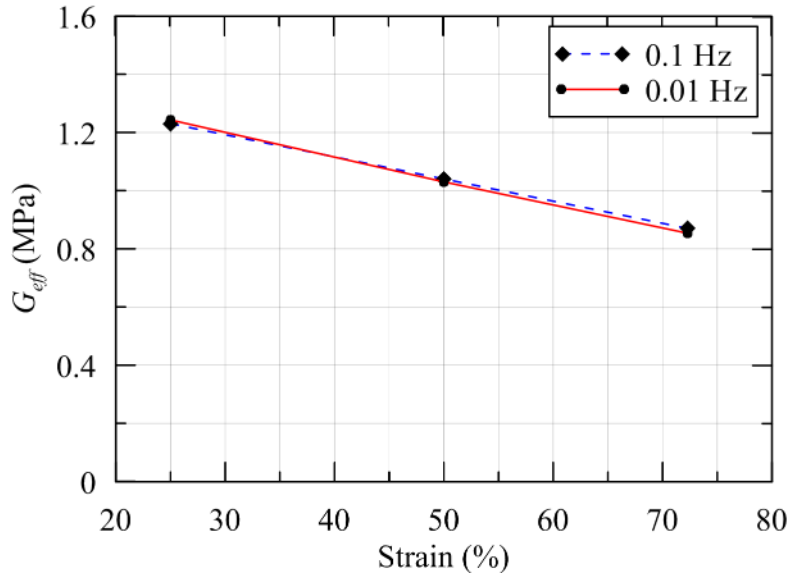


Figure 7-17 Variation of effective shear modulus of MA1 with frequency and strain

Table 7-4 Effect of frequency on effective shear modulus

Strain (%)	Effective shear modulus (MPa)	
	$f = 0.01$ Hz	$f = 0.1$ Hz
25	1.24	1.23
50	1.03	1.04
72.3	0.85	0.87

The variation of shear modulus with shear strain for the DIS and the Mageba bearings are presented in Figure 7-18 and Figure 7-19, respectively. The suffixes in the legend entries refer to pre- and post-cavitation values.

Shear modulus decreases with increasing shear strain, which is consistent with observations from past experiments. It has been observed that the shear modulus of the rubber in elastomeric bearings decreases up to a moderate shear strain, remains constant, and then increases at high values of shear strain (e.g, Clark *et al.* (1997); Constantinou *et al.* (2007), (Kelly, 1993)). The variation of shear modulus with shear strain could only be obtained up to a shear strain of 120%, limited by the moment capacity of the five channel load cell. A shear strain of 100% is chosen for all of the benchmark shear characterization tests. The variations of shear modulus with axial pressure are presented in Figure 7-20 and Figure 7-21 for the DIS and Mageba bearings, respectively.

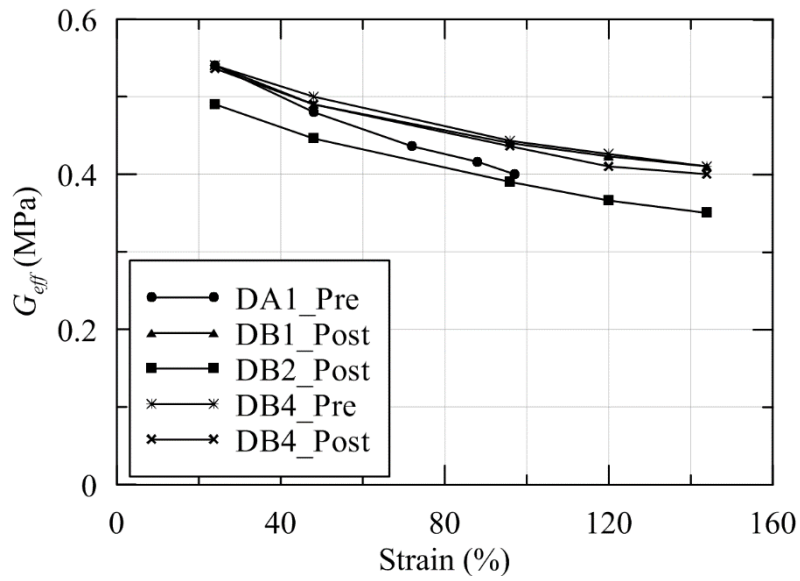


Figure 7-18 Variation of shear modulus of DIS bearings with shear strain

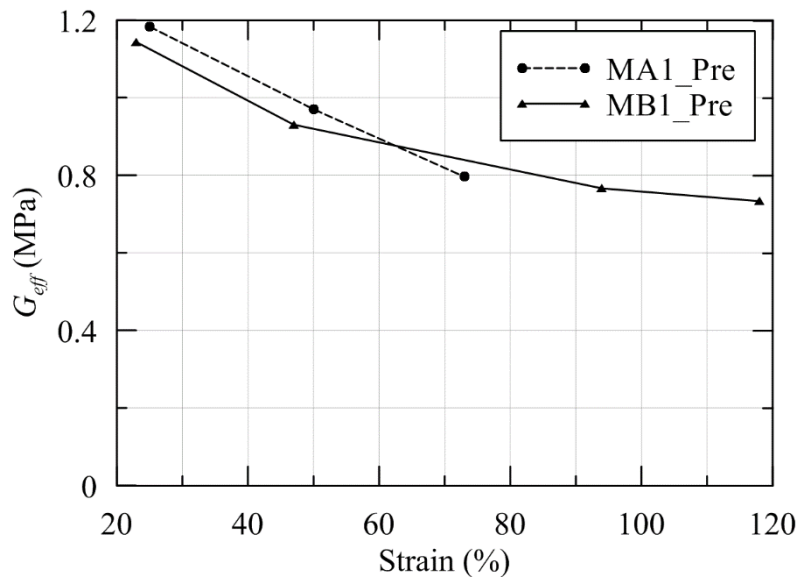


Figure 7-19 Variation of effective shear modulus of Mageba bearings with shear strain

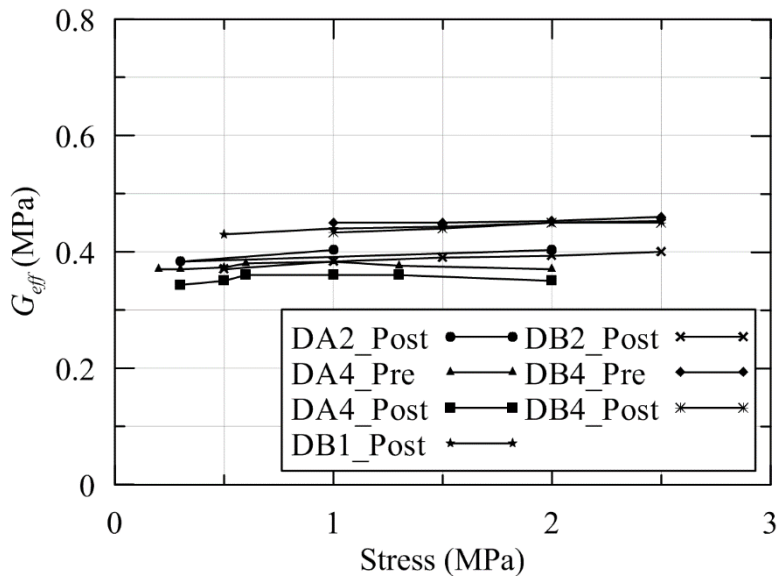


Figure 7-20 Variation of effective shear modulus of DIS bearings with axial pressure

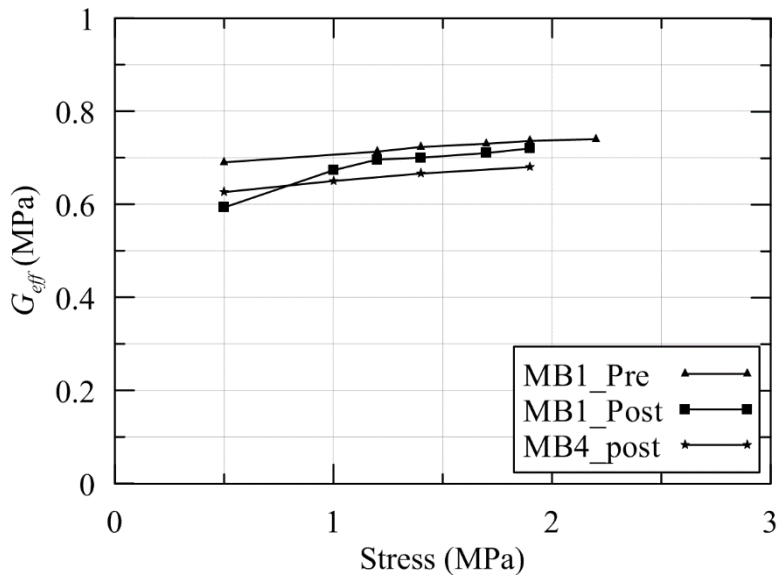


Figure 7-21 Variation of effective shear modulus of Mageba bearings with axial pressure

7.3.3 Compression properties

Compressive stiffness is determined using benchmark compression tests in which the bearing is subjected to force-controlled triangular cyclic loading of amplitude 300 kN that corresponds approximately to an axial pressure of 4.3 MPa. The vertical stiffness, K_{v0} , is calculated as:

$$K_{v0} = \frac{P^+ - P^-}{\delta^+ - \delta^-} \quad (7.7)$$

where P^+ is an axial compressive load corresponding to a target pressure (p) plus an offset Δp , and P^- is an axial compressive load corresponding to $p - \Delta p$, and δ^+ and δ^- are the vertical deformations corresponding to P^+ and P^- , respectively, on the ascending branch of the hysteresis loop. The values of p and Δp are chosen to be 2 MPa and 1.5 MPa, respectively. Axial stiffness is calculated using the ascending branch of the force-deformation curve for each cycle. The effective damping in the vertical direction, β_v , is estimated using:

$$\beta_v = \frac{E_D}{2\pi(|P_{\max} - P_{\min}|)(|\delta_{\max} - \delta_{\min}|)} \quad (7.8)$$

where δ_{\max} and δ_{\min} are the maximum and minimum vertical deformations, and P_{\max} and P_{\min} are the corresponding axial loads, respectively; the energy dissipated per cycle, E_D , is defined in Section 7.3.2. The pre- and post-cavitation cyclic response in compression and the secant stiffness line used to calculate the compression stiffness are shown in Figure 7-22 for bearings DA1, DB4, MA3, and MB1. The shear properties of all bearings are summarized in Table 7-5.

Pre-cavitation characterization tests were not performed for bearings DB1, DB2, MB2, and MB4, and the data reported in Table 7-5 are from post-cavitation tests. The compression characterization test was not performed on bearing DB3.

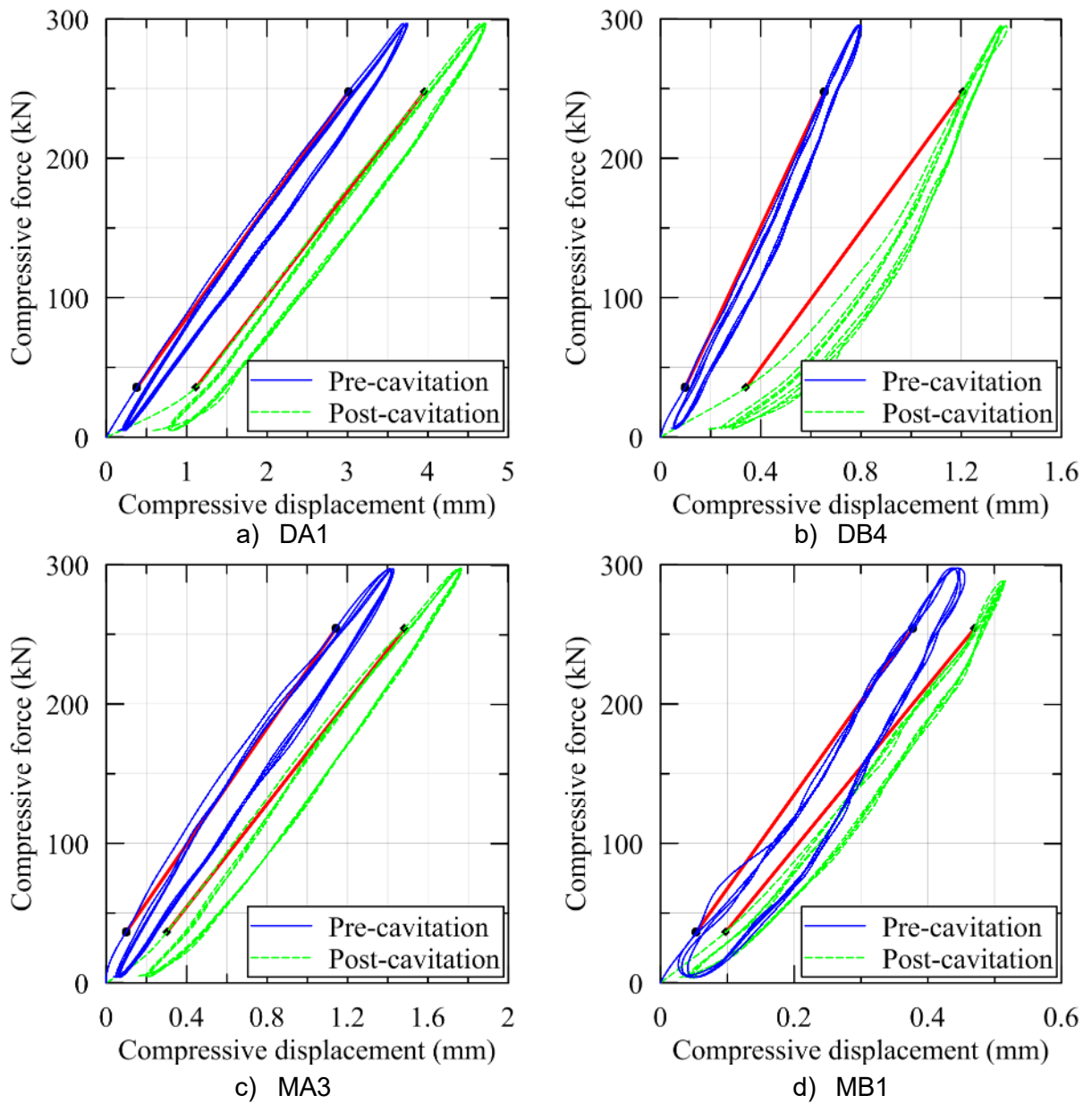


Figure 7-22 Compression characterization tests of bearings

Table 7-5 Compression properties obtained from characterization tests

Bearing	Test	Cycle	K_{v0} (kN/mm)	E_D (J)	β_v (%)
DA1	7	1	79	82	1.2
		2	83	65	0.9
		3	82	63	0.9
		4	81	61	0.9
DA2	2	1	71	114	1.4
		2	72	95	1.2
		3	71	92	1.2
		4	72	91	1.1
DA3	2	1	70	110	1.4
		2	71	87	1.1
		3	70	84	1.1
		4	70	81	1
DA4	6	1	74	90	1.2
		2	76	73	1
		3	76	67	0.9
		4	76	67	0.9
DB1 ¹	13	1	248	22	0.9
		2	254	17	0.7
		3	259	16	0.7
		4	265	17	0.7
DB2 ¹	13	1	284	23	1.1
		2	285	17	0.9
		3	286	15	0.8
		4	291	16	0.9
DB4	10	1	402	19	1.2
		2	399	15	1.1
		3	400	15	1
		4	425	15	1
MA1	7	1	194	36	1
		2	204	25	0.8
		3	200	25	0.8
		4	205	24	0.7
MA2	2	1	223	51	1.8
		2	211	39	1.4
		3	215	39	1.4
		4	215	38	1.5
MA3	2	1	209	47	1.7
		2	205	37	1.4
		3	214	34	1.3
		4	212	35	1.4
MA4	2	1	194	55	1.9
		2	198	43	1.5
		3	196	42	1.4
		4	197	41	1.4
MB1	11	1	657	19	2.3
		2	699	18	2.3

Table 7-5 Compression properties obtained from characterization tests (contd.)

Bearing	Test	Cycle	K_{v0} (kN/mm)	E_D (J)	β_v (%)
		3	702	16	2.1
		4	712	16	2.3
MB2 ¹	6	1	575	10	0.9
		2	626	5	0.5
		3	604	4	0.4
		4	617	5	0.5
MB3	2	1	792	18	2.6
		2	853	14	2.3
		3	881	13	2.3
		4	886	14	2.4
MB4 ¹	6	1	504	18	1.4
		2	538	13	1.2
		3	514	12	1.1
		4	547	12	1

1. Post-cavitation properties

The averaged compression properties of all four types of bearing are summarized in Table 7-6. The averaged properties do not include post-cavitation values.

Table 7-6 Summary of averaged compression properties of bearings

Bearing	K_{v0} (kN/mm)	E_D (J)	β_v (%)
DA	75	83	1.1
DB	355	20	1.0
MA	235	37	1.4
MB	727	15	2.0

Others (e.g. Warn (2006)) have concluded that the vertical stiffness of an elastomeric bearing calculated using the expression that considers limited compressibility of rubber layers matches reasonably with experimentally obtained values. This conclusion is revisited using the experimental data obtained here. The theoretical values of compression stiffness are calculated using Equation (6.6) for each bearing type and are compared with experimental values in Table 7-7. The average shear moduli from Table 7-2 are used for calculations of compression stiffness. The theoretical predictions are similar to the experimental results with differences less than 10%, except for type DA.

Table 7-7 Theoretical and experimentally obtained compressive stiffness

Bearing	K_{v0} (kN/mm)		
	Experimental	Theoretical	% difference
DA	75	80	7
DB	355	377	6
MA	235	206	12
MB	727	705	3

7.3.4 Tensile properties

The benchmark tensile characterization tests were performed on two bearings. The bearings were subjected to a force-controlled triangular loading of amplitude 25 kN. The amplitude was chosen as approximately one quarter of the estimated cavitation strength to ensure that no cavitation occurred. The tensile properties of the remaining bearings are obtained from tensile tests other than benchmark tensile characterizations tests. The tensile stiffness and damping ratio were obtained using Equations (7.7) and (7.8). The values of p and Δp are 0.3 MPa and 0.25 MPa, respectively. The tensile properties of the bearings are summarized in Table 7-8. The mechanical properties associated with the first tensile load-deformation cycle are presented.

Table 7-8 Summary of tensile properties obtained from tensile tests

Bearing	Test	Cycle	Δ (%)	ε_t (%)	F_c (kN)	u_c (mm)	K_v (kN/mm)	W_D (J)	β_v (%)
DA1 ¹	9	1	0	1	50	1.2	75	22	5.4
DA2	3a	1	0	5	95	4.4	88	198	6.8
DA3	3	1	0	25	86	2.9	76	890	26
DA4 ¹	14	1	0	5	65	2.0	51	71	2.5
DB1 ¹	14	1	0	4	85	4	96	45	3.1
DB2 ¹	1	1	187	4	85	1.2	160	81	4.8
DB3	1a	1	0	4	85	1.0	231	136	11
DB4	11a	1	0	4	110	2.5	236	52	2.7
MA1	8	1	0	failure	19	n.a.	25	n.a.	n.a.
MA2	3	1	0	4	136	6.0	180	198	4
MA3	3	1	0	24	192	2.5	378	3143	8.8
MA4 ¹	3	1	0	1	42	4	173	103	n.a.
MB1	12	1	0	4	120	3.0	377	105	4.8
MB2	1	1	0	3	202	1.0	945	215	8
MB3	3	1	0	3	170	2.0	429	110	4.2
MB4	1	1	0	failure	200	2.5	930	n.a.	n.a.

1. Bearings that either failed prematurely or for which tensile properties are not available at zero lateral offset

The experimental value of tensile stiffness varies significantly for given type of bearing. The value of secant tensile stiffness is sensitive to the length and location of the chord chosen on the tensile load-deformation curve. The variations in tensile properties, including tensile stiffness and cavitation force, can be attributed to the manufacturing quality control. Better quality control would ensure that bearings of the same material and geometric construction would have similar mechanical properties. A summary of averaged tensile properties is presented in Table 7-9. The average properties in Table 7-9 do not include values of the bearings marked with the superscript 1 in Table 7-8.

Table 7-9 Average tensile properties of bearings

Bearing	F_c (kN)	u_c (mm)	K_{v0} (kN/mm)
DA	91	3.7	82
DB	98	1.8	234
MA	164	4.3	279
MB	173	2.1	670

The load-deformation behavior of an elastomeric bearing in tension is generally assumed to be elastic up to cavitation with pre-cavitation tensile stiffness equal to the compressive stiffness. The validity of this assumption is investigated here. The average tensile stiffness of each bearing type is compared with its compressive stiffness in Table 7-10.

Table 7-10 Compressive and tensile stiffness of bearings

Bearing	K_{v0} (kN/mm)		
	Compression	Tension	% difference
DA	75	82	9
DB	355	234	34
MA	235	279	19
MB	727	670	8

There are differences between the values of tensile and compressive stiffness. However, the assumption of equal axial stiffness in tension and compression allows the use of a linear model up to cavitation without much loss of accuracy.

The cavitation strength of each bearing is determined from the tension tests. Significant scatter is observed in the experimentally recorded value. Ideally, the cavitation strength should be obtained by applying a tensile load to a virgin bearing at zero lateral offset. However, this was not possible for all of the bearings because the experimental program had multiple objectives, each requiring a different protocol. Some bearings were likely to have suffered cavitation damage due to tests performed before the tensile tests, and in a few cases, the cavitation strength could only be obtained at lateral offsets. Importantly, the cavitation strength is obtained by visual inspection of the tensile load-deformation curve: identifying the point at which a substantial reduction in tensile stiffness occurs. Visual determination introduces significant scatter in the cavitation strength, but there is no more reliable a strategy.

Table 7-11 summarizes experimentally and theoretically determined cavitation strengths. The response of four of the sixteen bearings (DA1, DA3, MA1, and MA4) suggest premature failure. If the outliers in the values of cavitation force are not considered, the experimental values show good agreement with the theoretical predictions ($=3GA$).

7.4 Effect of Lateral Offset on Tensile Properties

The coupling of the horizontal and vertical response of an elastomeric bearing in compression is well established and empirical relationships have been validated by Warn *et al.* (2007). Coupling of horizontal and vertical motion in tension was investigated here by subjecting bearings to tensile loading at different offset shear strains. The effect of lateral offset is assessed by three tensile characteristics: 1) pre- and post-cavitation tensile stiffness, 2) cavitation strength, and 3) hysteretic behavior in tension.

To determine the effect of lateral offset on pre-cavitation stiffness, four bearings were subjected to force-controlled cyclic tensile loading at different lateral offsets. The amplitude of the loading was approximately half of the estimated cavitation strength. The load-deformation behavior of the two bearings in cyclic tension at different lateral offsets is presented in Figure 7-23, where Δ is the lateral offset and R is the radius of the bearing. The variation of tensile stiffness of bearings DA1 and DA4 with lateral offset is shown in Figure 7-24. Although it is difficult to define and locate the exact point on the tensile force-deformation curve that corresponds to cavitation, the cavitation strength characterized by a sharp reduction in tensile stiffness, in Figure 7-23a

and Figure 7-23b can be seen to be decreasing with lateral offset. This trend is consistent with the findings of Iwabe *et al.* (2000) and Kato *et al.* (2003).

Table 7-11 Experimental and theoretical cavitation strengths

Bearing	$F_{c_experimental}$ (kN)	G_{eff} (MPa)	Area (mm ²)	$F_{c_analytical}$ (kN)	$F_{c_experimental} / F_{c_analytical}$
DA1 ¹	50	0.40	68900	83	0.60
DA2	95	0.42	68900	87	1.09
DA3 ¹	86	0.42	68900	86	1.00
DA4	65	0.38	68900	79	0.82
DB1	85	0.44	68900	91	0.93
DB2 ²	85	0.39	68900	81	1.05
DB3	85	0.41	68900	85	1.00
DB4	110	0.45	68900	93	1.18
MA1 ¹	19	0.80	70215	168	0.11
MA2	136	0.73	70215	154	0.88
MA3	192	0.80	70215	168	1.15
MA4 ¹	42	0.83	70215	174	0.24
MB1	120	0.77	70215	161	0.74
MB2	202	0.70	70215	148	1.36
MB3	170	0.79	70215	166	1.03
MB4	200	0.65	70215	137	1.46

1. Premature failure

2. Cavitation force obtained at lateral offset $\Delta=R$

The tensile stiffness decreases with an increasing number of loading cycles. The reduction in stiffness depends on the change in tensile strain amplitude between consecutive cycles. If the tensile strain amplitude does not change significantly, the reduction in tensile stiffness is insignificant. Figure 7-25 shows the variation in tensile stiffness with number of cycles at different lateral offsets for bearing DA1. The bearing is subjected to force-controlled cyclic tests of an amplitude that was approximately one half of the cavitation strength. The tensile stiffness in Figure 7-25 does not change significantly because of small increments in the tensile strain amplitude of consecutive cycles. This can be contrasted against a case where the tensile stiffness decreases substantially if the tensile strain amplitude between consecutive cycles increases significantly. Figure 7-26 shows the variation of tensile stiffness with number of cycles for bearing DB4, which was subjected to displacement-controlled cyclic tensile tests with strain amplitude increasing after every three cycles.

The effect of lateral offset on the hysteretic behavior of an elastomeric bearing in tension is difficult to assess because a tensile test with any substantial hysteresis involves irreversible damage due to cavitation. The hysteretic behaviors of an elastomeric bearing with different lateral offsets will inevitably be different and it is not possible to isolate on the load-deformation curve the effect of lateral offset from cavitation damage. If a force-controlled test does not involve cavitation, increasing lateral offset increases hysteretic energy dissipation, as observed in Figure 7-23a and Figure 7-23b.

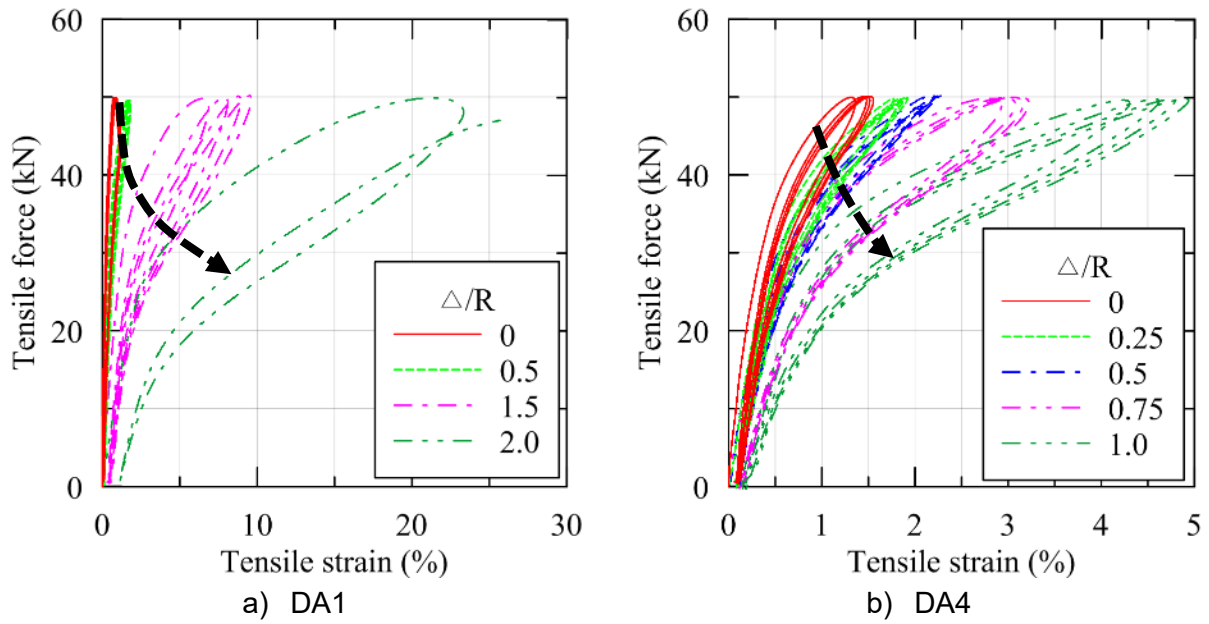


Figure 7-23 Load-deformation behavior in cyclic tensile loading at different lateral offsets

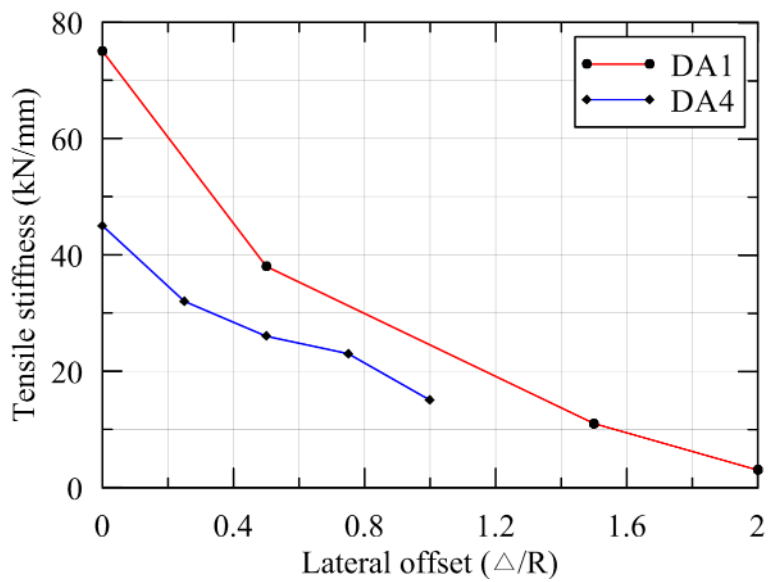


Figure 7-24 Variation of tensile stiffness with lateral offset strain

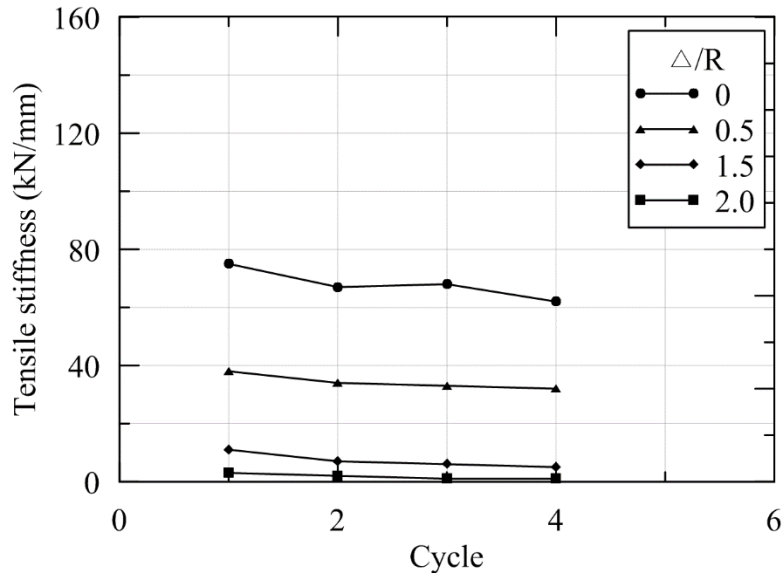


Figure 7-25 Variation of tensile stiffness with number of cycles for bearing DA1

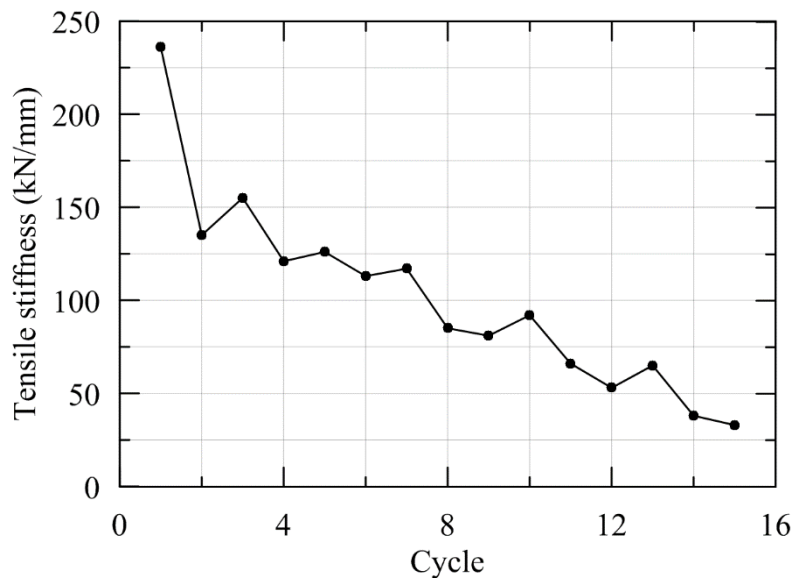


Figure 7-26 Variation of tensile stiffness with number of cycles for bearing DB4 ($\Delta/R = 0$)

To isolate the effect of lateral offset from tensile damage on hysteresis behavior of an elastomeric bearing, damage was induced in bearing DB1 by subjecting it to a tensile strain of 50%. It is known that if the strain amplitudes of the subsequent tensile tests are less than the maximum prior value of tensile strain, no additional damage is induced. Two cyclic tensile tests are performed on the same bearing with and without a lateral offset with tensile strain amplitude of 50%, so that any difference in hysteresis would only be because of lateral offset and not cavitation. Results are presented in Figure 7-27. The hysteretic behaviors are very similar despite the significant difference in lateral offset.

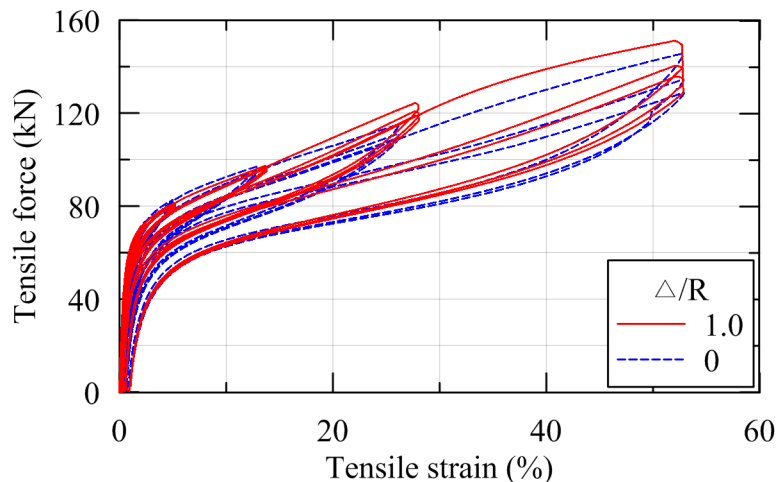


Figure 7-27 Effect of lateral offset on tensile hysteresis

7.5 Effect of Tensile Loading History on Cavitation

Past experiments have shown that damage in an elastomeric bearing accumulates with tensile deformation. Chapter 3 describes the mechanism of damage initiation and propagation, and proposes a mathematical model that predicts the behavior of an elastomeric bearing under cyclic tensile loading. Tests were performed to validate this mathematical model. The following assumptions are investigated:

1. Cavitation strength decreases (damage increases) with increasing values of tensile strain in each loading cycle
2. No additional damage is observed if the tensile strain is less than its prior maximum value
3. If the maximum prior value of tensile strain is exceeded, the formation of new cavities leads to additional damage, and cavitation strength is further decreased
4. Cavitation strength converges to a certain minimum value

Two test sequences, increasing triangular (IT) and decreasing triangular (DT), were used in which the tensile deformation amplitude was increased and decreased, respectively, after every three cycles. According to the mathematical model developed in Chapter 3, tensile properties such as the reduced cavitation strength, the post-cavitation stiffness and the minimum value of cavitation strength, should only depend on the prior maximum value of tensile strain and not on the sequence of loading. The behavior of elastomeric bearings under cyclic tensile loading is presented in Figure 7-28 through Figure 7-30.

Differences are observed between the behaviors shown in Figure 7-28 through Figure 7-30 and behaviors observed in past experiments (e.g. Iwabe *et al.* (2000), Kato *et al.* (2003), Warn (2006)). It was observed in previous experimental studies that if the tensile strain exceeds the prior maximum value, the prior maximum value of the tensile force is recovered, and subsequently, tensile force increases with tensile strain. However, a substantial reduction in force is observed between consecutive cycles for the bearings tested here, and the tensile force is not recovered after tensile strain exceeds the prior maximum value. The reason for this different behavior is not known.

The same tensile tests were conducted at the beginning of the experiment on a trial bearing (bearing in Figure 7.7 of Constantinou *et al.* (2007)) to ensure proper functioning of instrumentation, data acquisition, and actuator feedback control mechanism. The trial bearing was subjected to multiple IT and DT sequences of loading as described in Section 6.4. Results are presented in Figure 7-31.

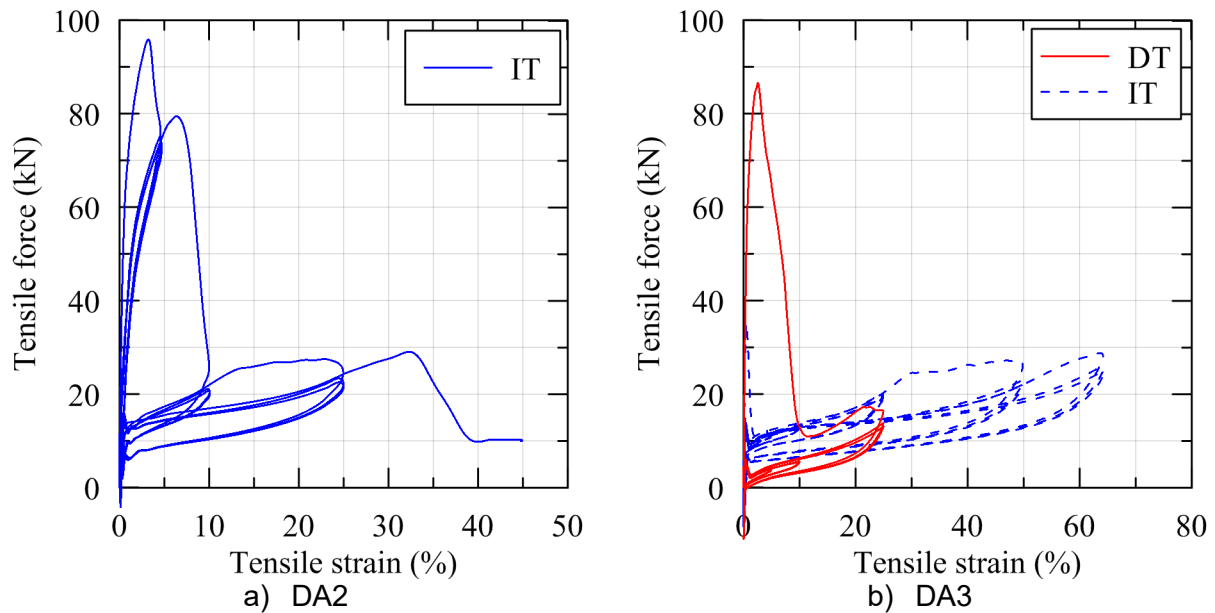


Figure 7-28 Behavior of DIS bearings under cyclic tensile loading

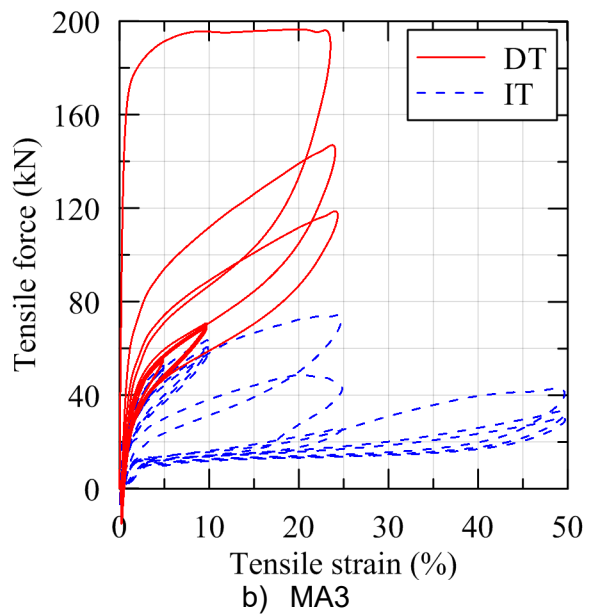
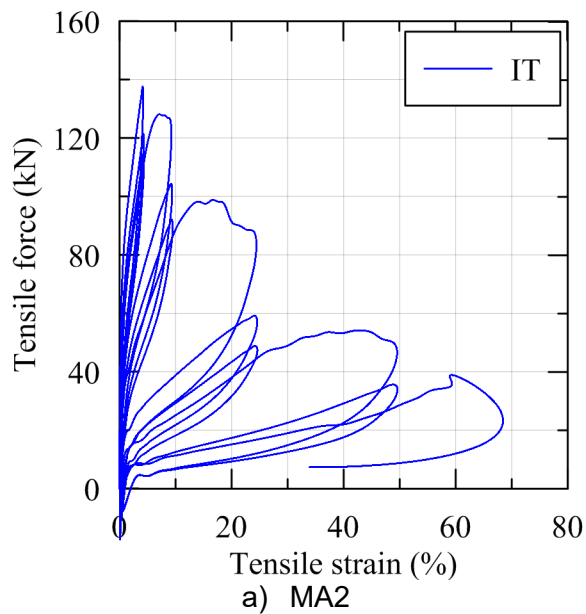


Figure 7-29 Behavior of Mageba bearings under cyclic tensile loading

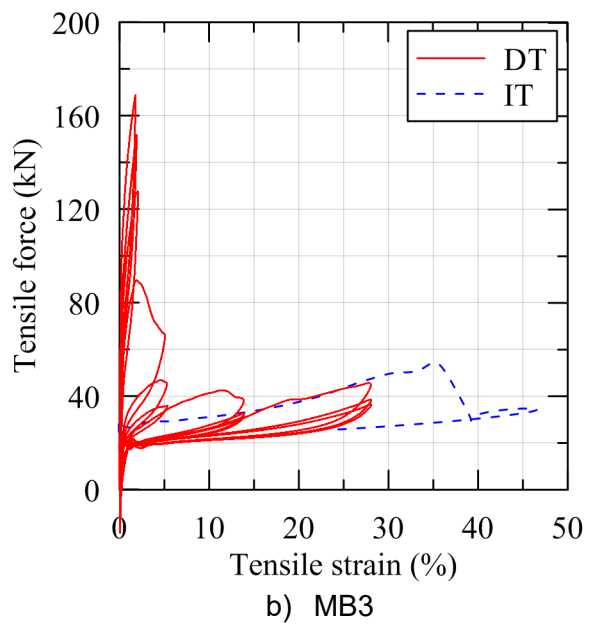
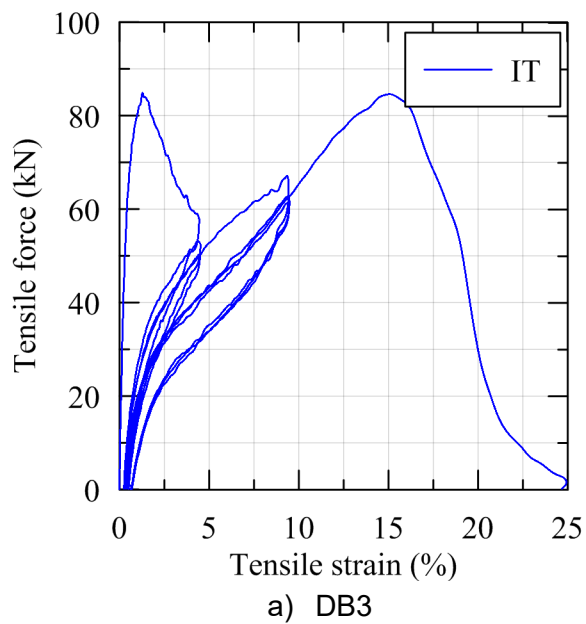


Figure 7-30 Behavior of DIS and Mageba bearings under cyclic tensile loading

The trial bearing follows an expected behavior that is consistent with past experimental studies and the model proposed in Chapter 3. This strongly suggests that the inconsistent tensile behavior is related to the properties of the bearing and not the experimental program. A variety of factors, including inadequate quality control, high damping, and insufficient curing, could lead to the observed tensile behavior.

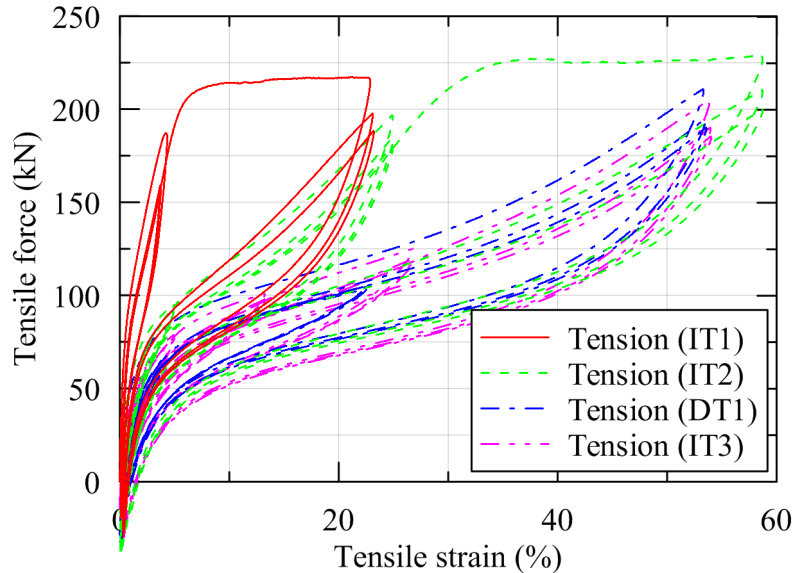


Figure 7-31 Behavior of the trial bearing under cyclic tensile loading

The residual strength observed in the tensile load-deformation curves of Figure 7-28 through Figure 7-30 is due to the resistance of the 4 mm cover rubber around the perimeter of the circular bearings.

Some bearings ruptured into two pieces following cavitation. The distances from the rupture planes from the bottom of the bearing are presented in Table 7-12. The total height of the bearing includes rubber layers, shim plates, and the two internal bearing plates (see Figure 4-11)

Table 7-12 Location of rupture plane in bearings failed due to cavitation

Bearing	Failure height (inches)	Bearing	Failure height (inches)	Bearing	Failure height (inches)	Bearing	Failure height (inches)
DA1	1.75	DB1	n.a. ¹	MA1	4.75	MB1	2
DA2	4.75	DB2	3.5	MA2	3	MB2	3.75
DA3	4	DB3	n.a.	MA3	4	MB3	3.25
DA4	4.5	DB4	n.a.	MA4	3.5	MB4	3.5

1. not available for bearings that did not rupture in two pieces

7.6 Effect of Cavitation on Mechanical Properties

7.6.1 General

The mechanical properties (e.g., shear modulus, axial stiffness) of all sixteen bearings were monitored during the experiments. The effects of cavitation on mechanical properties were investigated through characterization tests before and after cavitation, including shear and compression tests. Results are presented in the following sections.

7.6.2 Shear properties

The shear modulus and damping ratio of the bearings were monitored using shear characterization tests performed at 100% shear strain under an axial compressive pressure of 1 MPa. Additional shear tests were conducted at other shear strain amplitudes and axial loads to investigate if the change in shear modulus following cavitation was sensitive to the shear strain and axial load. The changes in the shear properties of the bearings are summarized in Table 7-13.

Table 7-13 Pre- and post-cavitation shear properties of elastomeric bearings

Bearing	G_{eff} (MPa)				β_{eff} (MPa)	
	Pre	Post	Ratio	% change	Pre	Post
DA1	0.40	0.37	0.93	8	4	5.1
DA2	0.42	0.40	0.95	5	4	4.4
DA3	0.42	0.40	0.96	4	5	3.8
DA4	0.38	0.36	0.94	6	4	4.9
DB1	n.a. ¹	0.44	n.a.	n.a.	n.a.	3.5
DB2	n.a.	0.39	n.a.	n.a.	n.a.	4.2
DB3	n.a.	0.41	n.a.	n.a.	n.a.	5.6
DB4	0.45	0.43	0.96	4	3	3.8
MA1	0.80	n.a.	n.a.	n.a.	5	n.a.
MA2	0.73	0.68	0.93	7	4	5.3
MA3	0.80	0.74	0.92	8	4	4.2
MA4	0.83	0.77	0.93	7	5	5.6
MB1	0.77	0.67	0.88	12	4	5.0
MB2	n.a.	0.70	n.a.	n.a.	n.a.	7.8
MB3	0.79	0.71	0.90	10	4	5.6
MB4	n.a.	0.65	n.a.	n.a.	n.a.	5.0

1. not available for bearings on which pre-cavitation characterization tests were not performed

Others (e.g., Iwabe *et al.* (2000)) have concluded that cavitation has no substantial effect on the shear modulus of a bearing because friction between the rubber layers provide adequate resistance to shear under nominal axial compressive loads. The frictional resistance depends on normal pressure and the contact area between the adjoining surfaces. The effect of cavitation on shear modulus may change with the magnitude of the axial compressive load maintained during the shear tests and the shear strain at which effective shear modulus is

calculated. To investigate this, cyclic shear tests were conducted before and after cavitation at various shear strain amplitudes and axial pressures. Results are presented in Figure 7-32 through Figure 7-35.

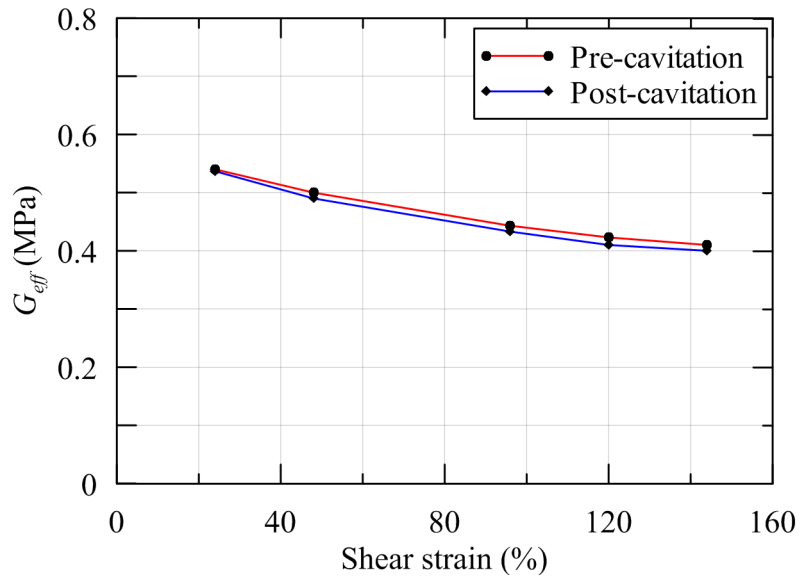


Figure 7-32 Variation of effective shear modulus with shear strain for bearing DB4

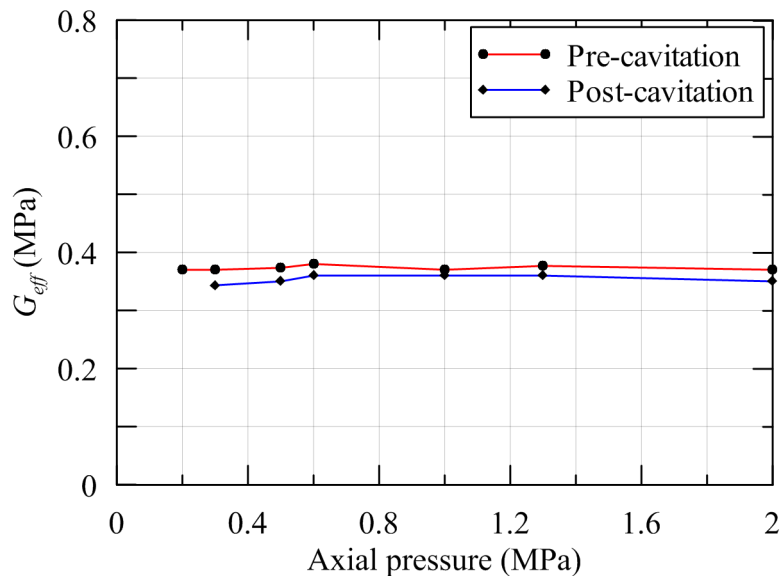


Figure 7-33 Variation of effective shear modulus with axial pressure for bearing DA4

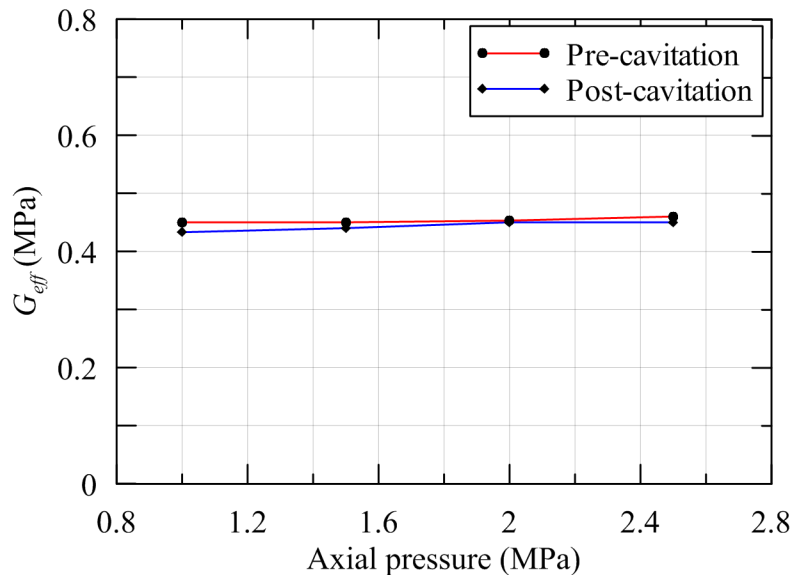


Figure 7-34 Variation of effective shear modulus with axial pressure for bearing DB4

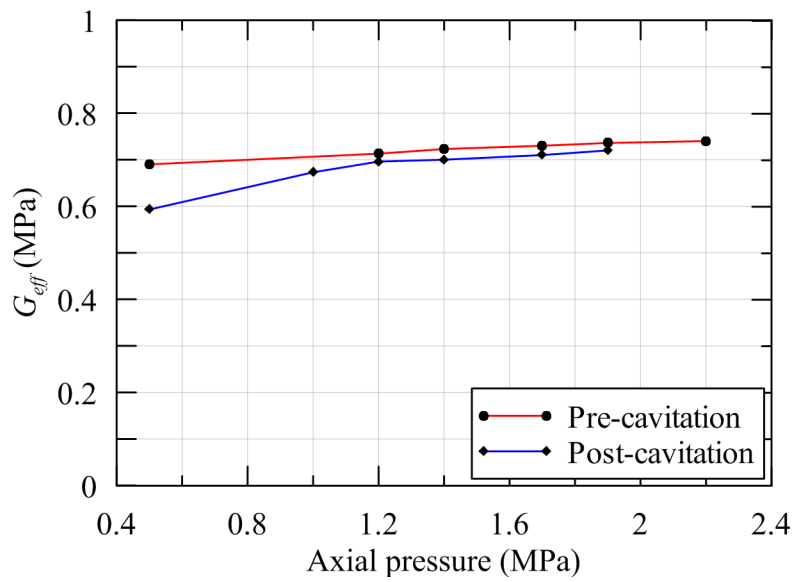


Figure 7-35 Variation of effective shear modulus with axial pressure for bearing MB1

The effect of cavitation on the shear modulus of a bearing is consistent over the range of shear strain and axial pressure considered. At very low values of axial pressure (< 0.5 MPa), differences between the pre- and post-cavitation shear modulus are seen because of the relative movement across the failure surface after cavitation, as seen in Figure 7-36. Slip is unlikely under a service axial pressure (≥ 3 MPa). Cavitation has no significant effect on the effective shear modulus of a bearing for shear strain less than 150% and axial compressive pressure greater than 1 MPa.



Figure 7-36 Slippage across the damaged interface of bearing MA4 in a shear test (axial pressure = 0.5 MPa)

A coefficient of friction between the two layers of rubber across a failure surface can be estimated from the data. When the bearing is in motion under constant velocity, the friction force is equal to the applied shear force. The coefficient of friction, μ_k , is obtained as:

$$\mu_k = \frac{F_s}{N} \quad (7.9)$$

where F_s is the applied shear force and N is constant axial load maintained during the shear test.

Slip across the failure surface surface is indicated by a plateau on the shear force-displacement curve in Figure 7-37 and this force is used to estimate μ_k : see Table 7-14.

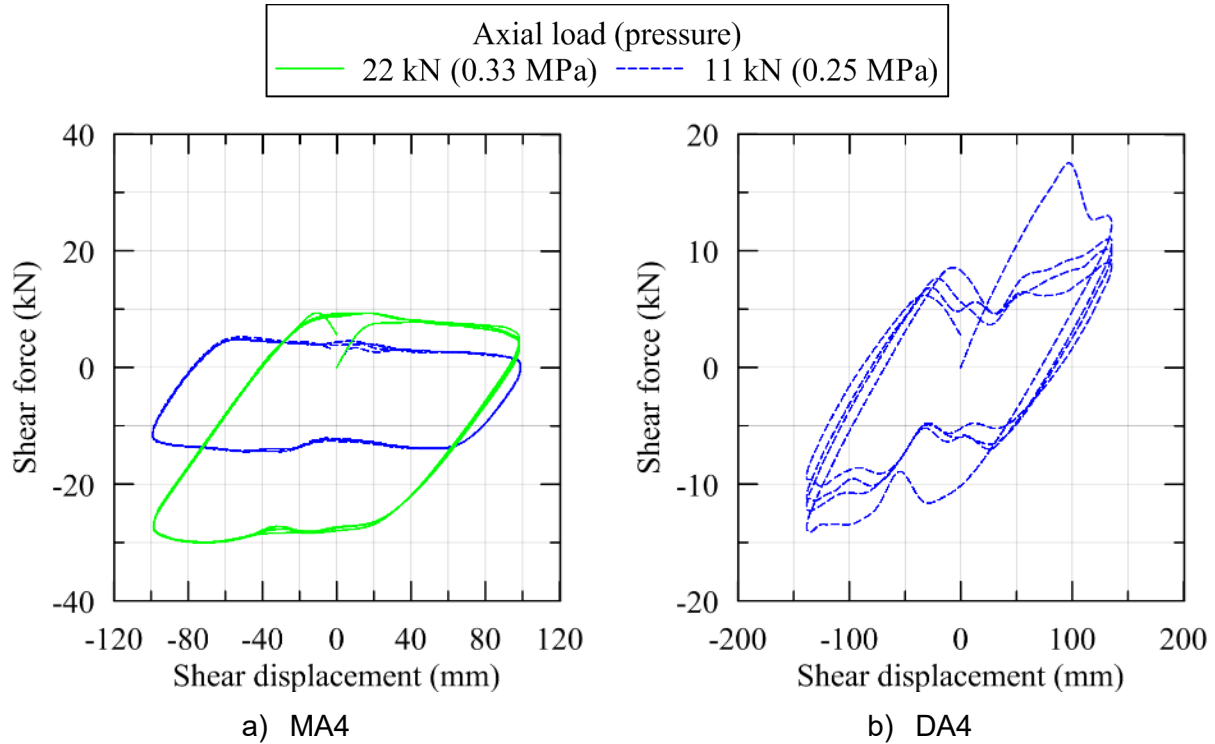


Figure 7-37 Shear response of bearing MA4 at different axial loads

Table 7-14 Coefficient of kinetic friction between rubber layers

Test no. ¹	Axial load (kN)	Shear force (kN)	Coefficient of friction
MA4_6	11	4	0.36
MA4_7	22	8	0.36
DA4_19	11	5	0.45

1. See Appendix A.1

7.6.3 Axial properties

Force-controlled compression characterization tests were performed to calculate compressive stiffness and damping ratio before and after cavitation. The changes in axial properties in compression are summarized in Table 7-15. A very small reduction in compressive stiffness is observed after cavitation. The pre- and post-cavitation values of the damping ratio in compression vary between 1 and 2% of critical.

7.6.4 Critical buckling load capacity

A series of monotonic compression tests were performed at the end of the testing program to investigate the effect of cavitation on the buckling load capacity of bearings. The critical buckling load of all bearings are estimated from load-deformation curves of the bearings as described in Section 6.4.7. The rated compressive load capacity of the testing machine is 1780 kN and its displacement capacity is 1.5 inches. Only eight of the sixteen bearings could be loaded in compression to failure. The buckling load for the remaining eight bearings exceeded 1780 kN.

The ruptured halves of the bearings that failed during cavitation were re-assembled and a compressive load was applied.

Table 7-15 Pre- and post-cavitation axial properties of elastomeric bearings

Bearing	K_{v0} (MPa)				β_v (MPa)	
	Pre	Post	Ratio	% change	Pre	Post
DA1	81	76	0.94	6	1.0	1.1
DA2	71	68	0.96	4	1.3	1.3
DA3	71	69	0.97	3	1.2	1.3
DA4	75	74	0.99	1	1.0	1.1
DB1	n.a. ¹	254	n.a.	n.a.	n.a.	0.8
DB2	n.a.	285	n.a.	n.a.	n.a.	0.9
DB3	n.a.	n.a.	n.a.	n.a.	n.a.	n.a.
DB4	400	273	0.68	32	1.1	0.9
MA1	199	n.a.	n.a.	n.a.	0.9	n.a.
MA2	216	161	0.74	26	1.5	1.1
MA3	209	191	0.91	9	1.5	1.5
MA4	196	180	0.92	8	1.6	1.4
MB1	686	605	0.88	12	2.2	1.0
MB2	n.a.	602	n.a.	n.a.	n.a.	0.6
MB3	842	765	0.91	9	2.4	0.9
MB4	n.a.	519	n.a.	n.a.	n.a.	1.2

1. not available

Compressive load-deformation plots for the four types of bearing are presented in Figure 7-38 through Figure 7-41. The initial plateau in the plots is due to a gap that the loading head of the testing machine had to overcome to engage the bearing. The axial displacement was measured using four linear potentiometers located symmetrically around the bearing. The potentiometers record displacement of the same sign up to buckling. However, after buckling begins, the signs might reverse due to rotation of the bearing. Axial deformation is taken as the average of the four potentiometer readings. The apparent hardening in the load-deformation curves results from the bearing being restrained laterally by the side walls of the testing machine following buckling.

The point on a load-deformation curve that corresponds to the beginning of buckling is shown with a solid black circle in Figure 7-38 and Figure 7-40. For the DB and MB bearings, the critical buckling loads were greater than the capacity of the testing machine (= 1780 kN) and they could not be failed in compression.

The theoretical values of critical buckling load obtained using the pre-cavitation and post-cavitation values of the effective shear modulus are presented in Table 7-16. No significant change in the buckling capacities of bearing types DA and MA due to cavitation is observed. Although failure could not be obtained for bearing type DB, they sustained a compressive load of 1700 kN, which is close to their theoretical buckling load, suggesting that there was no significant effect of cavitation on bearing type DB.

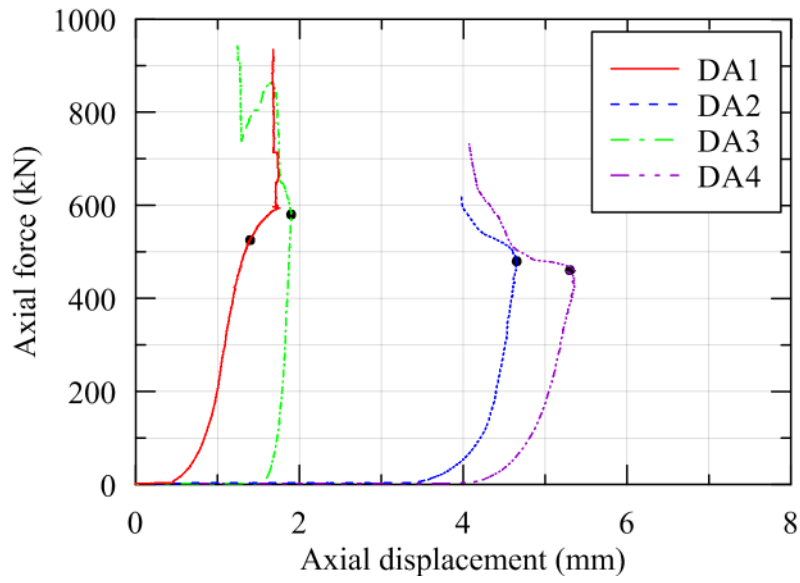


Figure 7-38 Compression failure tests of DA bearings

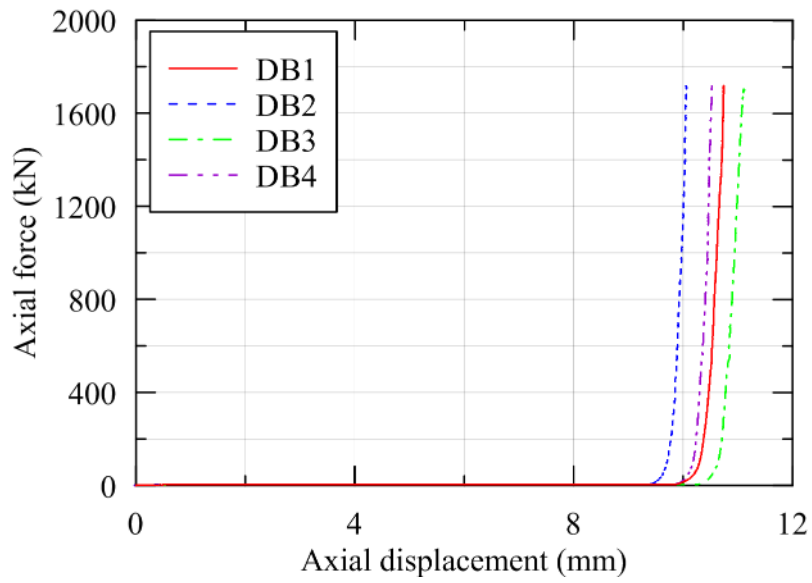


Figure 7-39 Compression failure tests of DB bearings

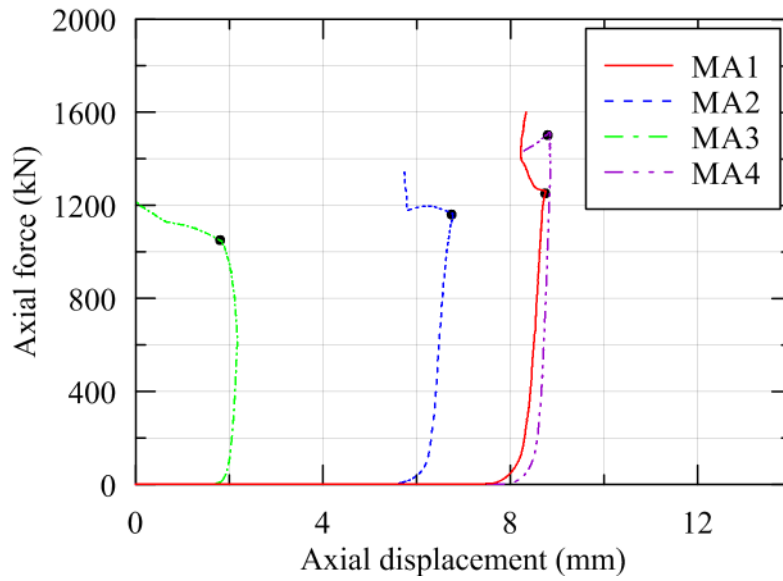


Figure 7-40 Compression failure tests of MA bearings

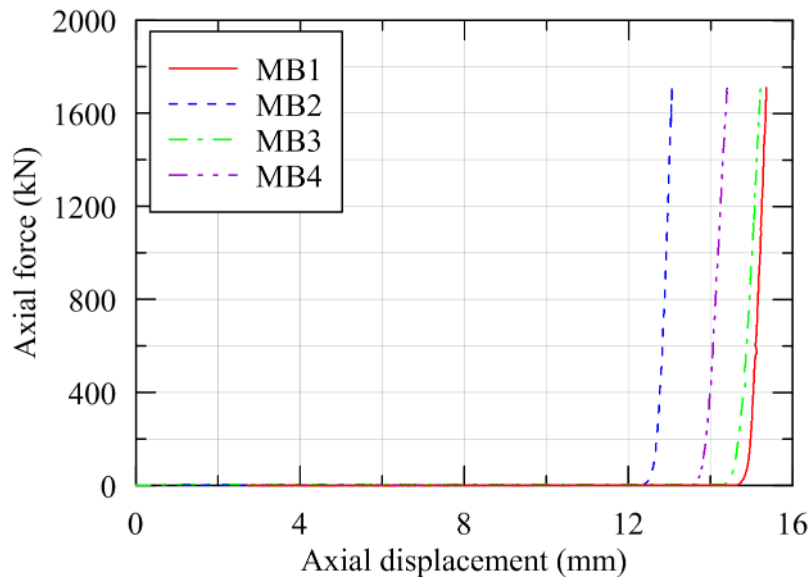


Figure 7-41 Compression failure tests of MB bearings

Table 7-16 Theoretical and experimental values of critical buckling load

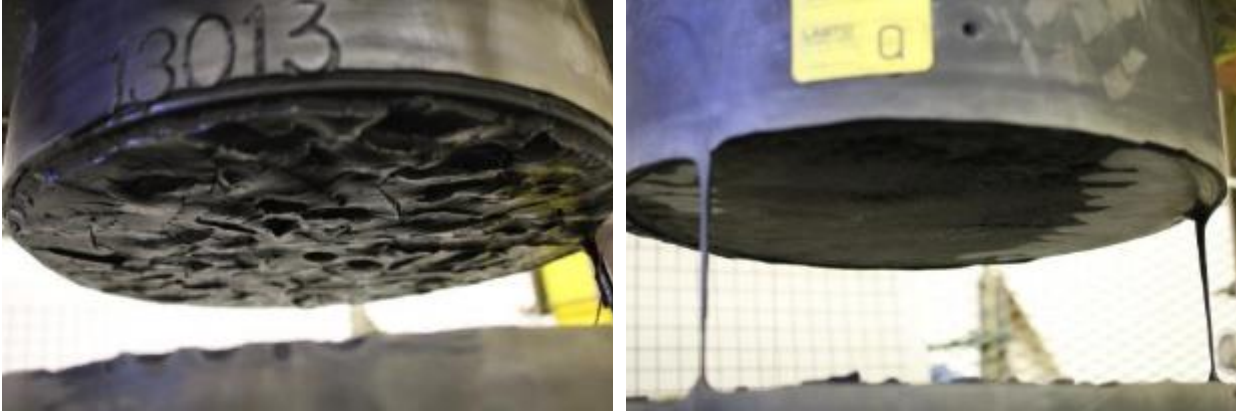
Bearing	G_{eff} (MPa)		P_{cr} theoretical (kN)		P_{cr} experimental (kN)
	Before	After	Before	After	
DA1	0.40	0.37	621	596	525
DA2	0.42	0.40	659	634	580
DA3	0.42	0.40	646	634	480
DA4	0.38	0.36	596	583	460
DB1	n.a.	0.44	n.a.	1770	>1780
DB2	n.a.	0.39	n.a.	1579	>1780
DB3	n.a.	0.41	n.a.	1675	>1780
DB4	0.45	0.43	1801	1739	>1780
MA1	0.80	n.a.	1349	n.a.	1250
MA2	0.73	0.68	1280	1196	1160
MA3	0.80	0.74	1363	1308	1050
MA4	0.83	0.77	1403	1321	1500
MB1	0.77	0.67	3147	2880	>1780
MB2	n.a.	0.70	n.a.	2971	>1780
MB3	0.79	0.71	3205	3060	>1780
MB4	n.a.	0.65	n.a.	2819	>1780

7.7 Failure mode in tension

The failure mode of a bearing is defined here as the loading conditions under which the bearing fails (e.g., pure tension, tension with lateral offset). The failure mechanism describes how the failure begins. The description of failure for each bearing in tension is presented in Appendix A.6.

The most common failure type in the DIS bearings was the formation of cavities in the rubber layer, whereas the Magedba bearings failed due to debonding at the interface of a rubber layer and a steel shim. Failure through formation of cavities in the volume of the rubber is the much preferred mechanism. These two failure mechanisms are shown in Figure 7-42.

Four of the sixteen bearings, DA1 (0.53), DA4 (0.55), MA1 (0.09), and MA4 (0.23), failed prematurely (failure occurred below theoretical cavitation force), where the value in parentheses is the ratio of the experimental to theoretical cavitation strengths. Although most of the experimental work (e.g., Iwabe *et al.* (2000), Kato *et al.* (2003), Warn (2006)) on cyclic loading of elastomeric bearings report a tensile deformation capacity of more than 100%, few bearings here achieved this. The hysteretic behavior was also different than what has been observed in past experimental studies, which might be related to manufacturing quality control. For example, three of the sixteen bearings tested here had misaligned tapped-holes at the bottom and top of the internal bearing plates, which led to initial torsional deformation after installation in SBTM. Bearing MA4, which had the greatest misalignment, is shown in Figure 7-43.



a) Cavities in the rubber volume (DA2) b) Debonding at rubber-shim interface (MA4)

Figure 7-42 Failure mechanism in rubber bearings under tension

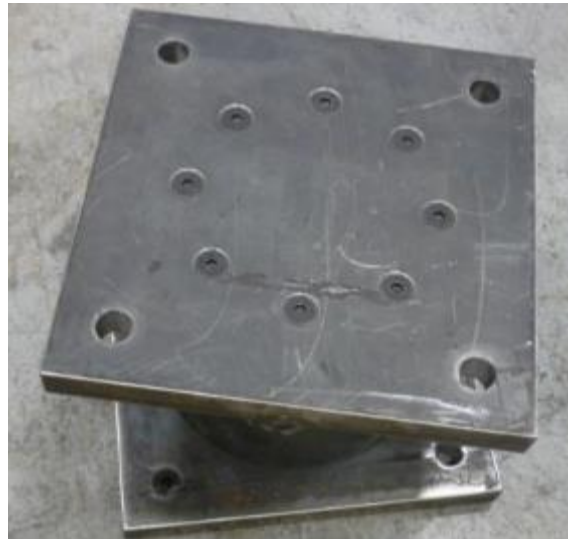


Figure 7-43 Misaligned grooves in top and bottom bearing plates of the bearing MA4

7.8 Validation of Mathematical Model

The mechanism of damage initiation and propagation due to cavitation in an elastomeric bearing was described in Section 3.2.4 through 3.2.6 and a mathematical model was proposed that predicts the behavior of an elastomeric bearing under cyclic tensile loading. The following assumptions are investigated:

1. Cavitation strength decreases (damage increases) with increasing values of tensile strain amplitude of each cycle
2. No additional damage is observed if the tensile strain is less than its prior maximum value
3. If the prior maximum value of tensile strain is exceeded, the formation of new cavities leads to additional damage, and cavitation strength is further decreased
4. Cavitation strength converges to a minimum value

A comparison of the experimental behavior and numerical results obtained using the phenomenological model described in Section 3.2.7 is presented in Figure 7-44 for all sixteen bearings, where F / F_c is the tensile force normalized by the cavitation strength. The values of the parameters used for the tensile model are: cavitation parameter, $k = 20$, 2) strength degradation parameter, $a = 1.0$, and 3) damage index, $\phi_{max} = 0.9$.

The numerical results are in reasonable agreement with the experimental behavior in most cases. Differences are observed in a few cases between the behaviors shown in Figure 7-44 and those observed from past experiments (e.g. Iwabe *et al.* (2000), Warn (2006), Kato *et al.* (2003)). It has been observed in previous experimental studies that if the tensile strain exceeds the prior maximum value, the prior maximum value of the tensile force is recovered, and subsequently, tensile force increases with tensile strain. However, a reduction in force is observed between consecutive cycles for a few of the bearings tested here, and the tensile force is not recovered after tensile strain exceeds the prior maximum value. The reduction might be due to initiation of tensile failure. It is difficult to locate the precise point of failure on the load-deformation curve up to which the phenomenological model can be applied. A consistent failure strain in tension is not observed among all the bearings. The tensile strain capacities of the bearings are smaller than those reported by others (e.g., Iwabe *et al.* (2000), Warn (2006), Kato *et al.* (2003)).

7.9 Conclusions and Recommendations

The key conclusions of the experiments are:

1. The value of $3GA$ is a reasonable estimate of the cavitation strength of a bearing.
2. The pre-cavitation tensile stiffness of a bearing decreases with an increasing number of loading cycles. The magnitude of the reduction depends on the prior maximum value of the tensile strain.
3. The pre-cavitation tensile stiffness decreases with an increase in coexisting shear strain.
4. Cavitation strength decreases with co-existing shear strain.
5. The sequence of loading does not change the behavior of elastomeric bearing under cyclic tension.
6. There is an insignificant change from a practical perspective in the compressive stiffness of a bearing following cavitation.
7. Cavitation has no significant effect on the effective shear modulus of a bearing for shear strain less than 150% under axial compressive pressure greater than 1 MPa.
8. No significant reduction in the buckling load of a bearing is observed due to prior cavitation.

Good quality assurance (QA) and quality control (QC) is key to the use of elastomeric bearings to seismically isolate nuclear power plants. Mathematical models are formulated based on physics and behaviors observed in experiments. These mathematical models are developed using a set of generalized assumptions about the expected behavior of elastomeric bearings. The desirable behavior of an elastomeric bearing in tension includes:

1. Cavitation at a well-defined force that is reproducible across similar bearings
2. Sufficient tensile deformation capacity
3. Ability to recover strength if tensile deformation exceeds the prior maximum value
4. Final failure through formation of cavities in the volume of the rubber and not through debonding at the interface of a rubber layer and a steel shim.

The bearings tested for the study described in this report showed different characteristics from those tested previously, including a) smaller tensile strain capacity, b) reduction in peak tensile force in consecutive cycles to a specified tensile displacement, and c) reduction in tensile resistance for loading to tensile strain that exceed a prior maximum value. These differences might have arisen because bearing manufacturers very rarely fabricate isolators of the relatively small size tested here. The infrequent manufacture of small runs of bearings with geometries most different from commercial product make it extremely difficult to achieve the high quality expected of isolators for nuclear power plant applications.

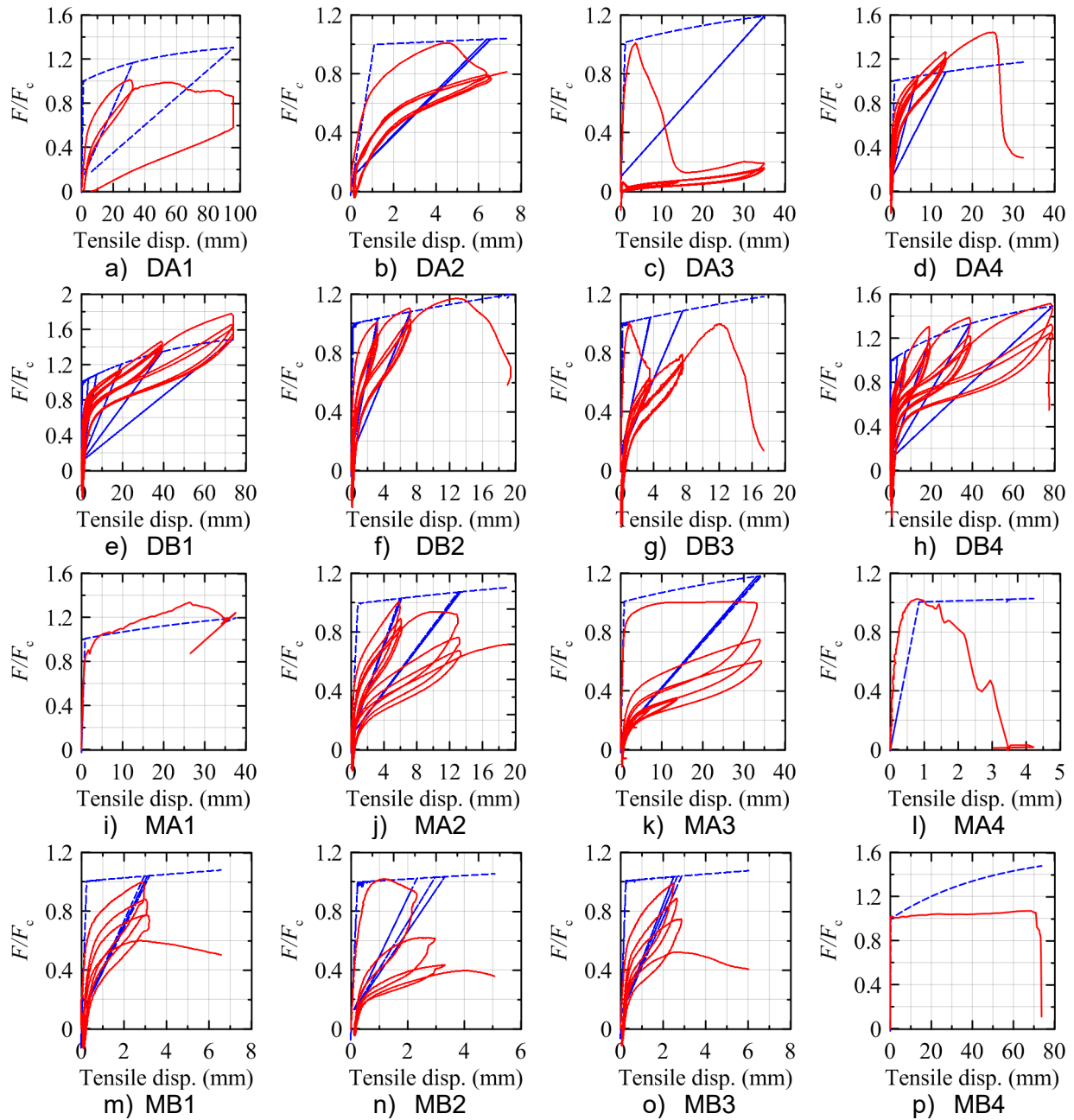


Figure 7-44 Validation of the mathematical model in tension, normalized force versus displacement

8 RESPONSE OF THE TWO-NODE MACRO MODEL OF BASE-ISOLATED NUCLEAR POWER PLANT

8.1 Introduction

The effects of changes in the mechanical properties of elastomeric bearings on the response of base-isolated nuclear power plant (NPP) structures are investigated here using the advanced numerical model of elastomeric bearings presented in Chapter 3. A macro model is used for response-history analysis of base-isolated NPPs. Ground motions are selected and scaled to be consistent with response spectra for design basis and beyond design basis earthquake shaking at the site of the Diablo Canyon Nuclear Generating Station. Ten isolation systems of two periods and five characteristic strengths are analyzed. The responses obtained using simplified and advanced isolator models are compared. Individual and cumulative effects of including each characteristic of elastomeric bearing on the response of base-isolated NPP under extreme loading are assessed.

8.2 Numerical Model

A two-node macro model of a NPP structure, shown in Figure 8-1, is created in OpenSees for response-history analysis. The lumped mass at the top node (node 2) represents the superstructure assigned to one isolator; the superstructure is assumed to be rigid for the purpose of these analyses. A LR¹ isolator joins the two nodes: *LeadRubberX*. All six degrees of freedom of the bottom node (node 1) are fixed to the ground, as are the three rotational degrees of freedom at the top node. Although this model cannot capture the effects of rocking and local axial force effects on isolators that are expected in an isolated system, its analysis does allow recommendations to be made about the importance of the characteristics of LR bearings.

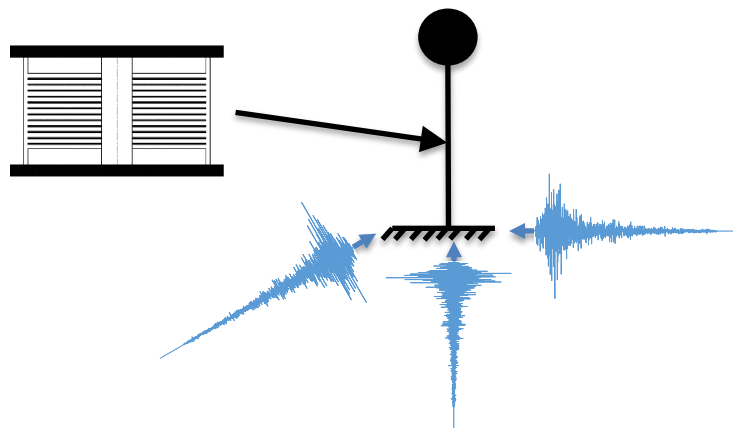


Figure 8-1 Two-node macro model of a base-isolated NPP

¹ Lead-rubber and low damping rubber elastomeric bearings are considered appropriate for use in safety-related nuclear structures in the United States at the time of this writing. Lead-rubber bearings are considered here because the seismic displacements at the Diablo Canyon site were anticipated to be large for design basis shaking.

Ten macro models of base-isolated NPPs are created: two isolation time periods ($T = 2, 3$ seconds) and five ratios of characteristic strength to supported weight ($Q_d / W = 0.03, 0.06, 0.09, 0.12, \text{ and } 0.15$). The models are denoted by $TxQy$, where x identifies the value of T and y identifies the percentage of Q_d / W . Table 8-1 summarizes the isolator properties assumed for analysis.

Table 8-1 Geometrical and mechanical properties of elastomeric bearings

Property	Notation (units)	Value
Single rubber layer thickness	t_r (mm)	10
Number of rubber layers	n	31
Total rubber thickness	T_r (mm)	310
Steel shim thickness	t_s (mm)	4.75
Outer diameter	D_o (mm)	1219
Lead core diameter	D_i (mm)	Varies ¹
Cover thickness	t_c (mm)	19
Yield stress of lead	σ_L (MPa)	8.5
Static pressure due to gravity loads	p_{static} (MPa)	3.0
Shear modulus	G (MPa)	Varies ²

1, 2: Calculated for each model

A static (gravity load) pressure on the bearing of 3 MPa is used for all analyses. The total gravity weight W on the bearing is calculated by multiplying the static pressure by the bonded rubber area. The total weight W is divided by g to obtain the equivalent mass M , which is lumped in the three translational directions at node 2 for response-history analyses. The diameter of the lead core is back calculated from Q_d / W , assuming an initial yield stress of 8.5 MPa. The effective shear modulus is calculated from the isolation time period T of the model. The geometric and mechanical properties of LR bearing are computed from the given values of Q_d / W and T as:

$$W = p_{static} \frac{\pi}{4} D_o^2; A_L = \frac{(Q_d / W) \times W}{\sigma_L}; D_i = \sqrt{4 \frac{A_L}{\pi}}; A = \frac{\pi}{4} [(D_o + t_c)^2 - D_i^2] \quad (8.1)$$

$$T_r = n t_r; M = \frac{W}{g}; K_{H0} = \frac{4\pi^2 M}{T^2}; G = \frac{K_{H0} T_r}{A}$$

where A_L is the area of the lead core, and all other variables are defined above. The geometric and material properties of the ten LR bearings are summarized in Table 8-2.

The parameters of the tensile model, k , a , and ϕ_{max} are set equal to 20, 1.0, and 0.75, respectively, for all models. A sensitivity analyses performed in Section 5.6.2 showed that the tensile response of an elastomeric bearing is not sensitive to either a or ϕ_{max} , and the values $a = 1.0$ and $\phi_{max} = 0.75$ recover the results of experiments. For the large diameter bearings considered here, a very sharp reduction in the tensile stiffness following cavitation is expected, which is captured by $k = 20$.

Table 8-2 Geometric and material properties of LR bearing models

Property	Notations (units)	T2Q3	T2Q6	T2Q9	T2Q12	T2Q15	T3Q3	T3Q6	T3Q9	T3Q12	T3Q15
Lead core diameter	D_i (mm)	125	168	195	216	231	100	136	161	180	195
Shear modulus	G (MPa)	0.92	0.92	0.93	0.94	0.94	0.41	0.41	0.41	0.41	0.41
Horizontal stiffness	K_{H0} (MN/m)	3.52	3.52	3.52	3.52	3.52	1.57	1.57	1.57	1.57	1.57
Vertical stiffness	K_{v0} (MN/m)	4061	4002	3959	3926	3899	3004	2956	2923	2897	2875
Buckling load	P_{cr0} (MN)	67.5	67.3	67.1	67.0	66.9	38.6	38.4	38.3	38.2	38.1
Cavitation force	F_c (MN)	3.28	3.28	3.28	3.28	3.28	1.46	1.46	1.46	1.46	1.46

The mechanical behaviors of LR bearings that are investigated here are:

1. Strength degradation in shear due to heating of the lead core (LR bearings)
2. Variation in buckling load due to horizontal displacement
3. Cavitation and post-cavitation behavior due to tensile loading
4. Variation in axial stiffness due to horizontal displacement
5. Variation in shear stiffness due to axial load

The *LeadRubberX* element permits the user to include each of these behaviors, or a combination thereof, in an analysis through a set of tags.

OpenSees does not provide option to specify modal damping. The *Rayleigh* damping, instead, is used, and the multipliers to the mass and stiffness matrices are calculated by assigning 2% damping to the 1st (torsion) and 6th (axial) modes. This ensures that effective damping corresponding to frequencies between these two modes would have an effective damping ratio smaller than 2%. The effect of Rayleigh damping is expected to be insignificant on the shear response where substantial damping is provided by energy dissipation in the lead core. The response in the axial direction, which is modeled as nonlinear elastic behavior, is expected to be more sensitive to the choice of Rayleigh damping coefficients. The coefficients, α_M and β_K , are calculated as:

$$\alpha_M = \frac{2\xi\omega_i\omega_j}{\omega_i + \omega_j}; \beta_K = \frac{2\xi}{\omega_i + \omega_j} \quad (8.2)$$

where ω_i and ω_j are the angular frequencies of the vibration modes in which damping of $\xi = 2\%$ is assigned, which correspond to the axial and torsional mode of vibration here. The effective damping ratio in the n^{th} mode of vibration is calculated as:

$$\xi_n = \frac{\alpha_M}{2\omega_n} + \frac{\beta_K}{2}\omega_n \quad (8.3)$$

where ω_n is the angular frequency of the n^{th} mode. Rayleigh damping depends on the instantaneous stiffness and changes at each step of a nonlinear analysis. A summary of the estimates of the Rayleigh damping based on the initial and post-yield (or post-cavitation) stiffness are obtained in different modes of oscillation of isolation system for isolation periods of 2 and 3 seconds, and are presented in Table 8-3.

Table 8-3 Rayleigh damping ratios in the six directions of motion of the isolation system

Number	Direction	$T = 2$ sec				$T = 3$ sec			
		Angular frequency ω (rad/sec)		Damping ratio ξ (%)		Angular frequency ω (rad/sec)		Damping ratio ξ (%)	
		Elastic	Post-elastic	Elastic	Post-elastic	Elastic	Post-elastic	Elastic	Post-elastic
1	Axial	106.7	5.4	2.0	0.6	91.1	3.6	2.0	0.6
2	Shear1	9.9	3.1	0.5	0.9	6.6	2.1	0.4	0.9
3	Shear2	9.9	3.1	0.5	0.9	6.6	2.1	0.4	0.9
4	Torsion	1.4	1.4	2.0	2.0	0.9	0.9	2.0	2.0
5	Rotation1	19.1	19.1	0.5	0.5	16.4	16.4	0.5	0.5
6	Rotation2	19.1	19.1	0.5	0.5	16.4	16.4	0.5	0.5

The set of 30 three-component ground motions selected and spectrally matched by Kumar (2015) to be consistent with uniform hazard response spectra (UHRS) for design-basis earthquake (DBE) shaking at the site of the Diablo Canyon Nuclear Generating Station are used for response-history analysis (Figure 8-2). The UHRS are calculated for a return period of 10,000 years and 5% damping. Response-history analysis is performed using these 30 sets of ground motions for each of the ten models at intensities of 100% DBE, 150% DBE, 167% DBE, and 200% DBE shaking. The intensities of 150% DBE and 167% DBE correspond to beyond design basis earthquake in Department of Energy (DOE) and United States Nuclear Regulatory Commission (USNRC) space, respectively; see Huang *et al.* (2009) and Huang *et al.* (2013). The mean 2% damped vertical spectrum is provided to aid later interpretation of the vertical response of the isolation systems.

The results of the response-history analyses are presented in the following sections. The peak responses for each ground motion set are assumed to distribute lognormally with arithmetic mean μ , median θ , and logarithmic standard deviation σ , which are computed as:

$$\mu = \frac{1}{n} \sum_{i=1}^n y_i \quad \theta = \exp\left(\frac{1}{n} \sum_{i=1}^n \ln y_i\right) \quad \sigma = \sqrt{\frac{1}{n-1} \sum_{i=1}^n (\ln y_i - \ln \theta)^2} \quad (8.4)$$

where n is the total number of ground motion sets (=30), and y_i is the peak response for i th ground motion set. The p th percentile (e.g., 50, 90, 99) value, y_p , is calculated as the inverse of the lognormal cumulative distribution function F per Mathworks (2014):

$$y_p = F^{-1}(p | \ln \theta, \sigma) = \{y_p : F(y_p | \ln \theta, \sigma) = p\} \quad (8.5)$$

These percentiles can be calculated with the aid of normal probability table. MATLAB provides a command *logninv* to compute *p*th percentile values of a lognormal distribution.

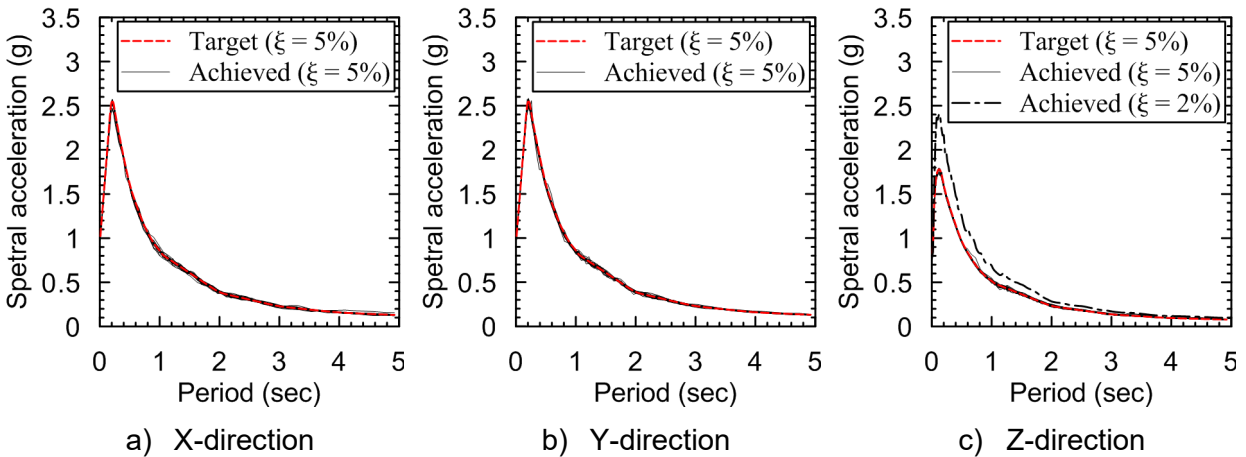


Figure 8-2 Acceleration response spectra of ground motions

8.3 Results of Analysis using the Simplified Isolator Model

The simplified model of LR bearing shown in Figure 8-3, with equal axial stiffness in compression and tension (and independent of shear displacement), represents the state-of-the-practice for response-history analysis of seismically isolated structures using contemporary software.

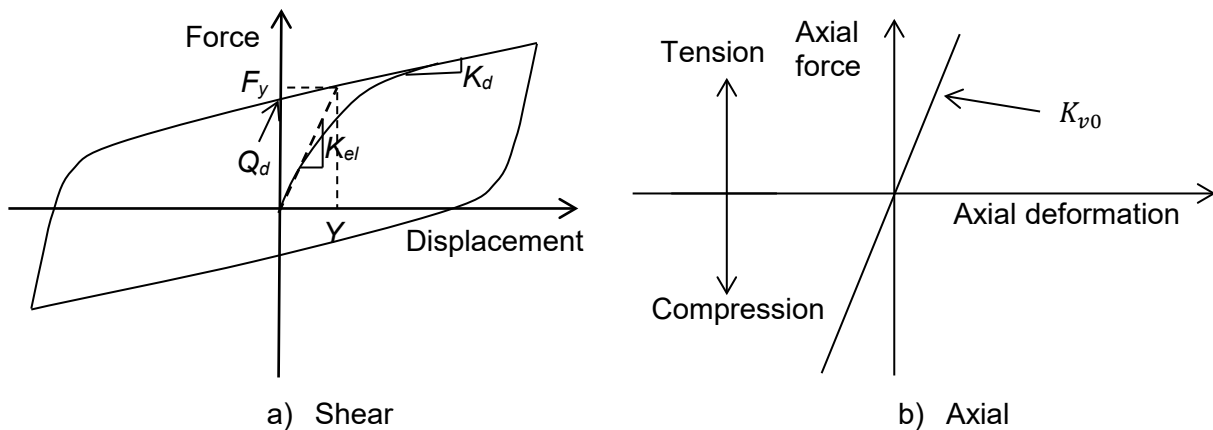


Figure 8-3 Simplified model of LR bearing

The simplified model does not consider any of the five characteristics identified in Section 8.2. For analysis using the simplified model as implemented in *LeadRubberX*, all tags are set to 0. The results of the response-history analyses are presented in Table 8-4 through Table 8-9. The results of the response-history analyses of the base-isolated NPP using the advanced isolator model are benchmarked against those using the simplified isolator model.

Mean and 50th, 90th and 99th percentile responses are presented in these tables, noting that the 90th and 99th percentile responses, for beyond design basis and design basis shaking, respectively, are important thresholds for seismically isolated nuclear structures (Huang *et al.*, 2009; Huang *et al.*, 2013). Vector sums of the shear displacements and forces are calculated at

each time step in an analysis and the peak values for a given ground motion are used to form the distributions of response. The forces are normalized by the total weight W on the bearing, which is approximately equal to 3500 kN for all of the models.

Table 8-4 Percentiles of peak horizontal displacement (mm) for 30 ground motion sets; simplified model¹

Model	100% DBE			150% DBE			167% DBE			200% DBE						
	μ	50 th	90 th	σ	99 th	90 th	μ	50 th	90 th	σ	90 th	μ	50 th	90 th	σ	
T2Q3	437	434	500	0.11	561	837	726	721	837	0.12	828	823	956	1026	1200	0.12
T2Q6	346	344	400	0.12	453	686	597	594	686	0.11	688	684	788	867	999	0.11
T2Q9	289	286	346	0.15	404	600	519	516	600	0.12	602	598	693	761	882	0.11
T2Q12	247	243	307	0.18	370	544	459	455	544	0.14	538	534	629	687	800	0.12
T2Q15	220	216	276	0.19	338	496	410	405	496	0.16	483	478	578	626	743	0.13
T3Q3	506	503	573	0.10	638	963	851	847	963	0.10	979	974	1101	1235	1382	0.09
T3Q6	381	378	449	0.13	517	779	684	680	779	0.11	794	790	902	1006	1147	0.10
T3Q9	321	317	393	0.17	469	674	572	567	674	0.13	669	664	781	864	994	0.11
T3Q12	283	278	357	0.19	438	613	506	500	613	0.16	589	582	705	756	898	0.13
T2Q15	261	256	331	0.20	409	571	459	452	571	0.18	537	530	657	685	833	0.15

1. The horizontal displacement corresponding to 100 (200, 300)% shear strain in the elastomer is 310 (620, 930) mm.

Table 8-5 Percentiles of peak horizontal shearing force (%W) for 30 ground motion sets; simplified model^{1, 2}

Model	100% DBE			150% DBE			167% DBE			200% DBE						
	μ	50 th	90 th	σ	99 th	90 th	μ	50 th	90 th	σ	90 th	μ	50 th	90 th	σ	
T2Q3	46	45	52	0.11	58	86	75	74	86	0.11	85	84	98	105	122	0.12
T2Q6	39	38	44	0.11	50	73	64	63	73	0.11	73	72	83	91	104	0.11
T2Q9	36	35	41	0.12	46	66	58	58	66	0.11	66	66	76	82	94	0.11
T2Q12	35	34	40	0.12	45	63	54	54	63	0.12	62	62	71	77	89	0.11
T2Q15	35	35	40	0.11	45	61	53	52	61	0.12	59	59	69	74	85	0.11
T3Q3	25	25	28	0.09	31	45	40	40	45	0.10	45	45	51	57	64	0.09
T3Q6	22	22	25	0.10	28	39	35	35	39	0.08	40	40	45	49	55	0.09
T3Q9	22	22	25	0.11	28	37	33	33	37	0.10	37	37	42	46	51	0.09
T3Q12	23	23	26	0.09	29	37	33	33	37	0.11	36	36	41	44	50	0.10
T2Q15	25	25	28	0.09	31	38	33	33	38	0.11	37	37	42	43	50	0.11

1. The gravity weight W on the bearing is approximately 3500 kN

2. The characteristic strength, Q_d , ranges between 3%W (e.g., T2Q3) and 15%W (e.g., T3Q15).

Table 8-6 Percentiles of peak compressive displacement (mm) for 30 ground motion sets; simplified model¹

Model	100% DBE			150% DBE			167% DBE			200% DBE			
	μ	50 th	90 th	μ	50 th	90 th	μ	50 th	90 th	μ	50 th	90 th	σ
T2Q3	2.5	2.5	2.9	3.3	3.3	3.9	3.6	3.6	4.3	4.1	4.1	5.0	0.15
T2Q6	2.6	2.6	3.0	3.4	3.4	4.0	3.7	3.7	4.4	4.3	4.2	5.1	0.14
T2Q9	2.6	2.6	3.0	3.4	3.5	4.1	3.8	3.8	4.5	4.4	4.4	5.2	0.13
T2Q12	2.7	2.7	3.1	3.5	3.6	4.2	3.9	3.9	4.6	4.5	4.5	5.3	0.13
T2Q15	2.8	2.8	3.1	3.4	3.7	4.2	4.0	4.0	4.6	4.6	4.6	5.3	0.12
T3Q3	3.7	3.7	4.3	4.9	5.0	5.9	5.4	5.3	6.4	6.2	6.2	7.4	0.15
T3Q6	3.8	3.8	4.4	4.9	5.1	6.0	5.5	5.5	6.5	6.4	6.3	7.5	0.14
T3Q9	3.9	3.9	4.5	5.0	5.2	6.1	5.7	5.6	6.6	6.5	6.5	7.7	0.14
T3Q12	3.9	3.9	4.5	5.0	5.3	6.1	5.7	5.7	6.7	6.6	6.6	7.7	0.13
T2Q15	4.0	4.0	4.6	5.2	5.4	6.3	5.8	5.8	6.8	6.7	6.7	7.9	0.14

1. The horizontal displacement corresponding to 100 (200, 300)% shear strain in the elastomer is 310 (620, 930) mm.

Table 8-7 Percentiles of peak compressive force (%W) for 30 ground motion sets; simplified model^{1,2}

Model	100% DBE			150% DBE			167% DBE			200% DBE			
	μ	50 th	90 th	μ	50 th	90 th	μ	50 th	90 th	μ	50 th	90 th	σ
T2Q3	290	288	337	385	381	456	417	413	496	480	475	574	0.15
T2Q6	293	291	337	389	386	456	422	418	497	486	481	575	0.14
T2Q9	296	294	339	394	391	459	427	424	499	492	487	578	0.13
T2Q12	298	297	340	397	395	460	431	428	501	496	492	581	0.13
T2Q15	300	299	338	400	398	457	434	432	497	500	497	576	0.12
T3Q3	313	311	365	420	416	497	456	452	542	527	521	630	0.15
T3Q6	314	312	362	421	417	493	457	453	537	528	523	624	0.14
T3Q9	314	312	362	422	418	492	458	454	537	529	524	623	0.14
T3Q12	313	311	357	419	416	486	455	452	529	525	521	614	0.13
T2Q15	312	310	359	417	414	488	453	450	532	523	518	618	0.14

1. The gravity weight W on the bearing is approximately 5270 kN

2. The characteristic strength, Q_d , ranges between 6%W (e.g., T2Q6) and 18%W (e.g., T3Q18).

Table 8-8 Percentiles of peak tensile displacement (mm) for 30 ground motion sets; simplified model¹

Model	50% DBE			100% DBE			150% DBE			200% DBE							
	μ	50 th	90 th	99 th	σ	μ	50 th	90 th	σ	μ	50 th	90 th	σ	μ	50 th	90 th	σ
T2Q3	0.8	0.7	1.8	4.2	0.80	1.6	1.5	2.6	0.40	1.9	1.8	2.9	0.37	2.5	2.3	3.6	0.34
T2Q6	0.8	0.6	3.3	13.2	1.32	1.7	1.6	2.6	0.41	2.0	1.8	3.0	0.37	2.5	2.4	3.7	0.34
T2Q9	0.8	0.7	2.0	4.8	0.83	1.7	1.6	2.8	0.45	2.0	1.9	3.1	0.41	2.6	2.4	3.9	0.36
T2Q12	0.9	0.7	1.7	3.5	0.66	1.7	1.6	3.0	0.51	2.0	1.9	3.3	0.45	2.6	2.5	4.0	0.39
T2Q15	0.9	0.8	1.7	3.2	0.61	1.8	1.6	3.2	0.53	2.1	1.9	3.5	0.46	2.7	2.5	4.2	0.40
T3Q3	1.3	1.1	2.1	3.5	0.48	2.5	2.4	3.6	0.33	2.9	2.8	4.1	0.31	3.7	3.6	5.1	0.28
T3Q6	1.3	1.2	2.1	3.4	0.43	2.6	2.5	3.6	0.30	3.0	2.9	4.2	0.28	3.9	3.7	5.2	0.26
T3Q9	1.4	1.3	2.1	3.1	0.37	2.7	2.6	3.7	0.27	3.1	3.1	4.2	0.25	4.0	3.9	5.3	0.24
T3Q12	1.4	1.3	2.0	2.8	0.32	2.7	2.7	3.6	0.24	3.2	3.1	4.2	0.23	4.1	4.0	5.2	0.21
T2Q15	1.5	1.4	2.1	2.9	0.32	2.8	2.7	3.7	0.24	3.3	3.2	4.3	0.23	4.2	4.1	5.4	0.22

1. The horizontal displacement corresponding to 100 (200, 300)% shear strain in the elastomer is 310 (620, 930) mm.

Table 8-9 Percentiles of peak tensile force (%W) for 30 ground motion sets; simplified model^{1, 2}

Model	50% DBE			100% DBE			150% DBE			200% DBE							
	μ	50 th	90 th	99 th	σ	μ	50 th	90 th	σ	μ	50 th	90 th	σ	μ	50 th	90 th	σ
T2Q3	99	82	227	522	0.80	202	189	317	0.40	237	223	361	0.37	305	290	448	0.34
T2Q6	100	74	403	1601	1.32	203	190	320	0.41	238	225	363	0.37	306	292	449	0.34
T2Q9	100	83	241	575	0.83	203	188	334	0.45	238	223	376	0.41	306	290	462	0.36
T2Q12	101	88	205	408	0.66	203	186	356	0.51	238	221	393	0.45	306	289	475	0.39
T2Q15	102	90	195	369	0.61	204	186	367	0.53	239	222	401	0.46	307	290	483	0.40
T3Q3	256	234	434	718	0.48	504	482	732	0.33	589	565	838	0.31	753	726	1045	0.28
T3Q6	263	244	424	667	0.43	515	495	725	0.30	600	579	831	0.28	766	743	1038	0.26
T3Q9	271	255	411	606	0.37	526	510	718	0.27	613	595	824	0.25	782	762	1031	0.24
T3Q12	269	257	386	540	0.32	524	510	692	0.24	610	595	796	0.23	779	762	1000	0.21
T2Q15	272	259	390	544	0.32	528	513	701	0.24	616	600	807	0.23	785	767	1013	0.22

1. The gravity weight W on the bearing is approximately 5270 kN

2. The characteristic strength, Q_d , ranges between 6%W (e.g., T2Q6) and 18%W (e.g., T3Q18).

8.4 Results of Analysis using the Advanced Isolator Model

The advanced isolator model considers the five characteristics of LR bearings identified in Section 8.2. The effect of each characteristic on the response of the isolated NPP is investigated. The responses distribute lognormally and the percentiles are calculated from the estimated distribution.

8.4.1 Strength degradation in shear due to heating of the lead core

The percentiles of peak horizontal displacement and shear force, with and without consideration of heating, are presented in Figure 8-4 and Figure 8-5, respectively. The responses of models T2Q3 and T3Q3 are not presented because the 90th percentile horizontal displacement at 167% DBE shaking is greater than 1000 mm, and larger diameter lead cores would be used to reduce these displacements. Percentile responses for models T2Q15 and T3Q15 are summarized in Appendix B.1 and not presented here.

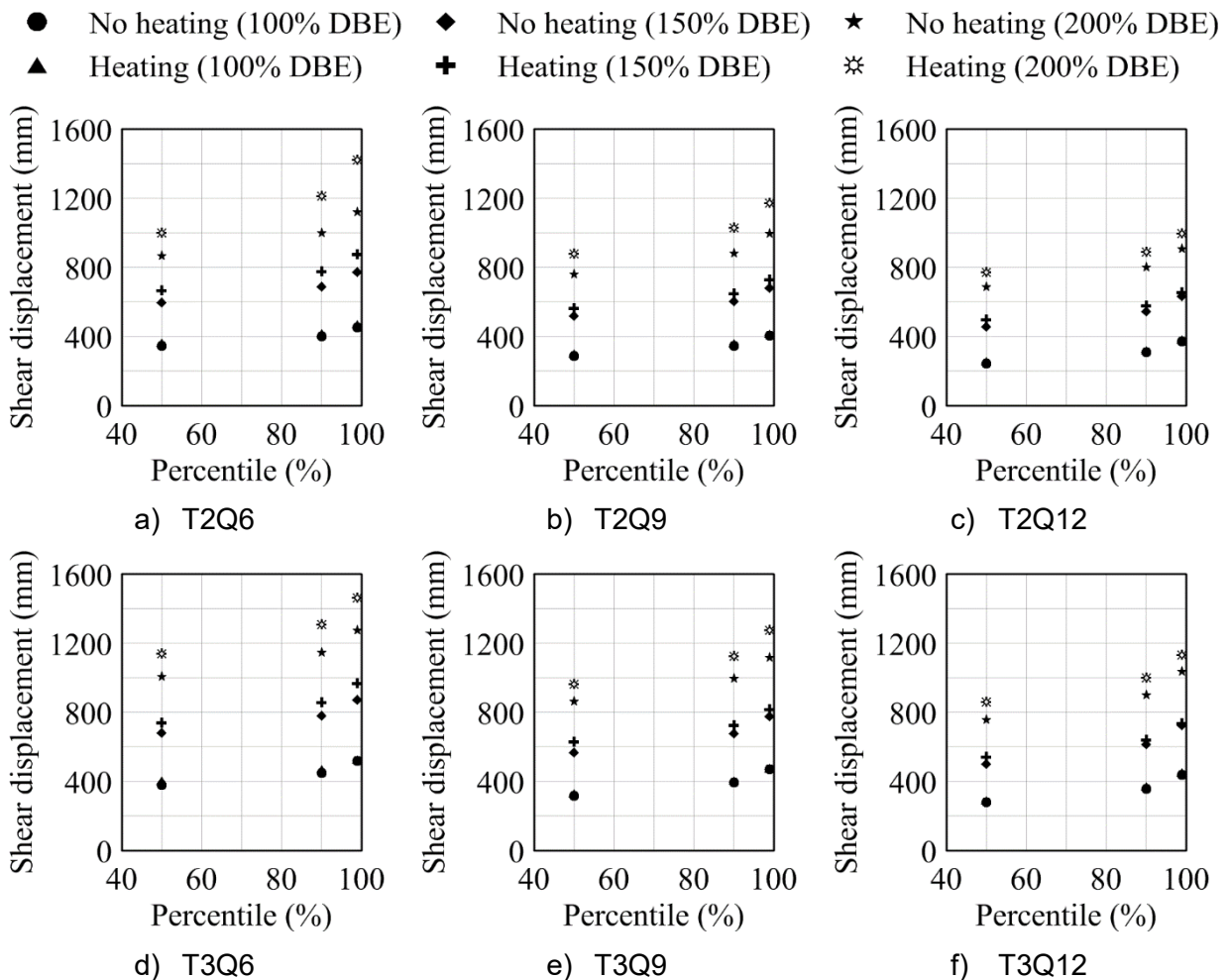


Figure 8-4 Percentiles of horizontal displacement for LR bearing models

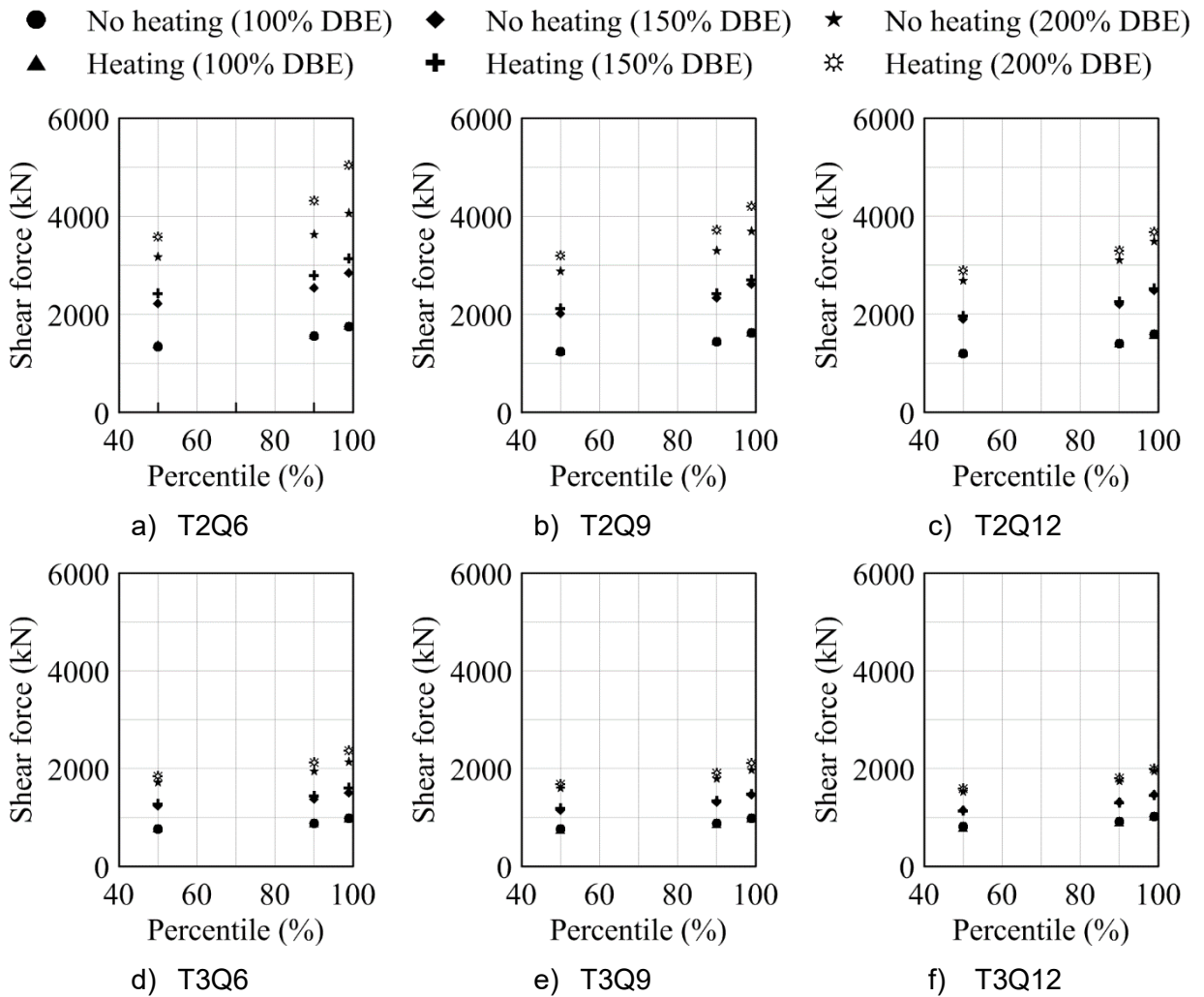


Figure 8-5 Percentiles of horizontal shear force for LR bearing models

The effect of heating of the lead core on median peak horizontal displacements and shear forces for 100% DBE shaking is negligible at the mean, and 50th, 90th and 99th percentiles. The effect of heating increases with the intensity of earthquake shaking. For a given Q_d / W , the effect of heating decreases with an increase in the isolation period T . For the same period, the effect of heating decreases with increasing Q_d / W . For those isolation systems with the highest Q_d / W (e.g., T2Q15, T3Q15), the shear forces decrease as a result of heating of the lead core.

The characteristic shear strength of a LR bearing varies substantially over the duration of earthquake shaking due to heating of the lead core. Of the ten isolation systems, T2Q6 and T3Q6 show the greatest reduction in characteristic shear strength. Plots of the ratio of the minimum characteristic shear strength to the initial strength, for each ground motion, and three intensities of shaking, are presented in Figure 8-6. A substantial reduction is observed in the characteristic shear strength with the average minimum value for the thirty ground motions falling below 50% of the initial value at 150% DBE shaking for isolation system T2Q6. Figure 8-7 plots the maximum temperature rise for each ground motion at three intensities of shaking. The maximum change in characteristic strength is observed for ground motions 5 and 30, for isolation systems T2Q6 and T3Q6, respectively. The temperature-rise time series for these two ground motions are presented in Figure 8-8 noting that the strong motion duration for the horizontal components of ground motions 5 and 30 are 50 seconds.

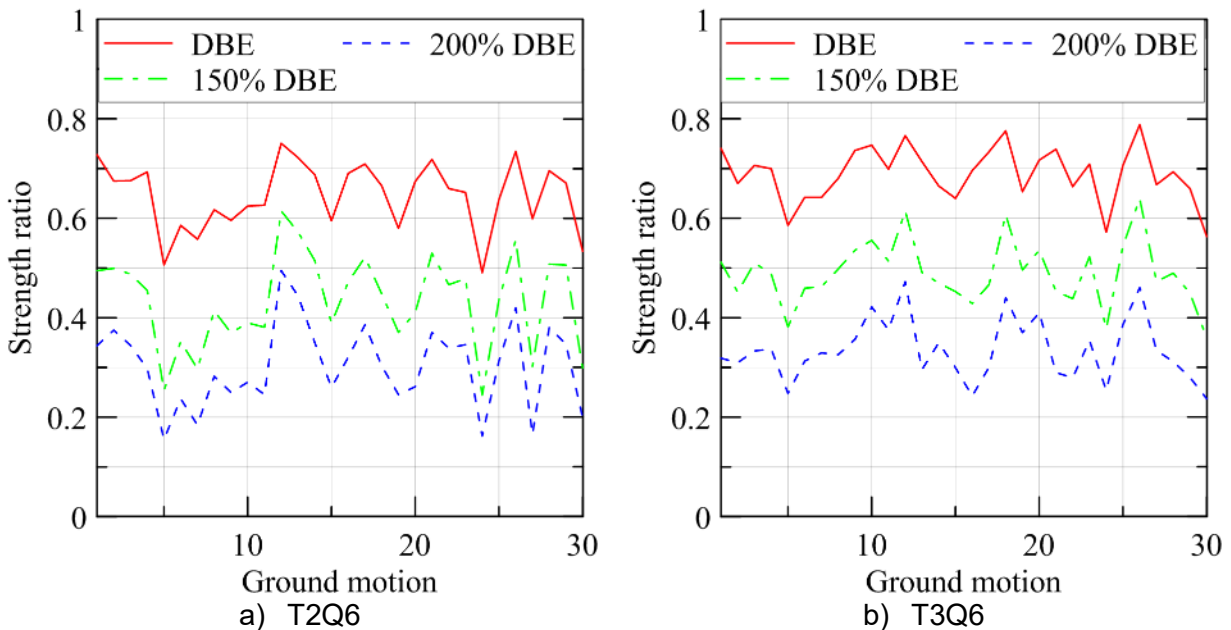


Figure 8-6 Ratio of minimum characteristic shear strength to initial strength

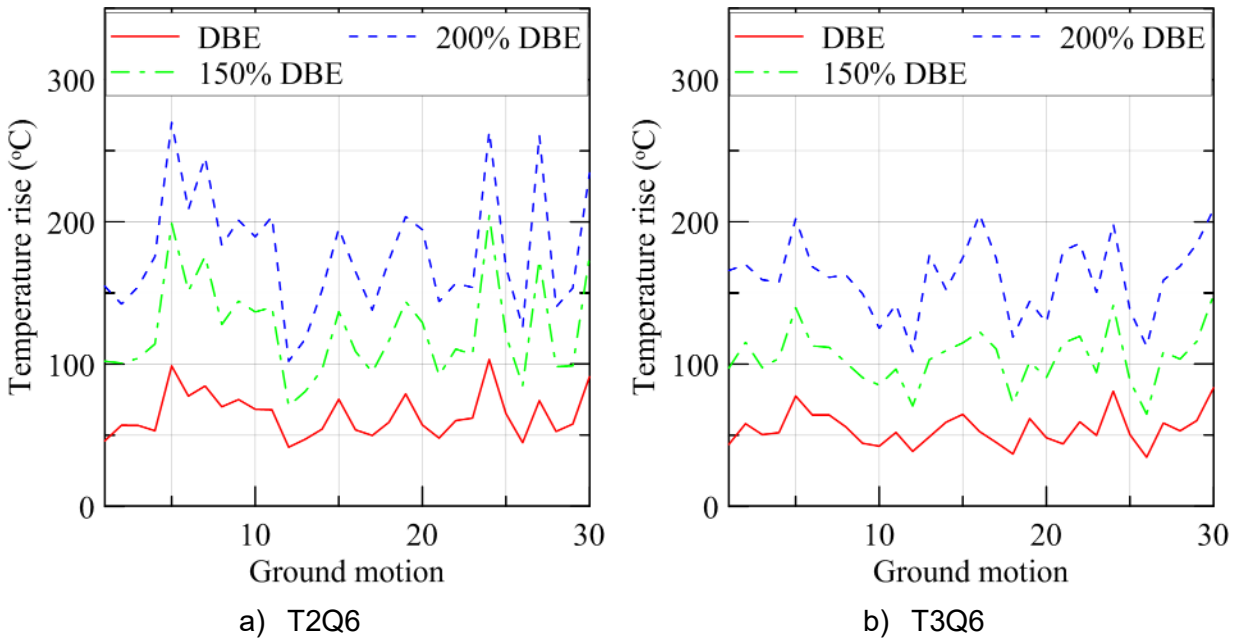


Figure 8-7 Maximum temperature rise in the lead core

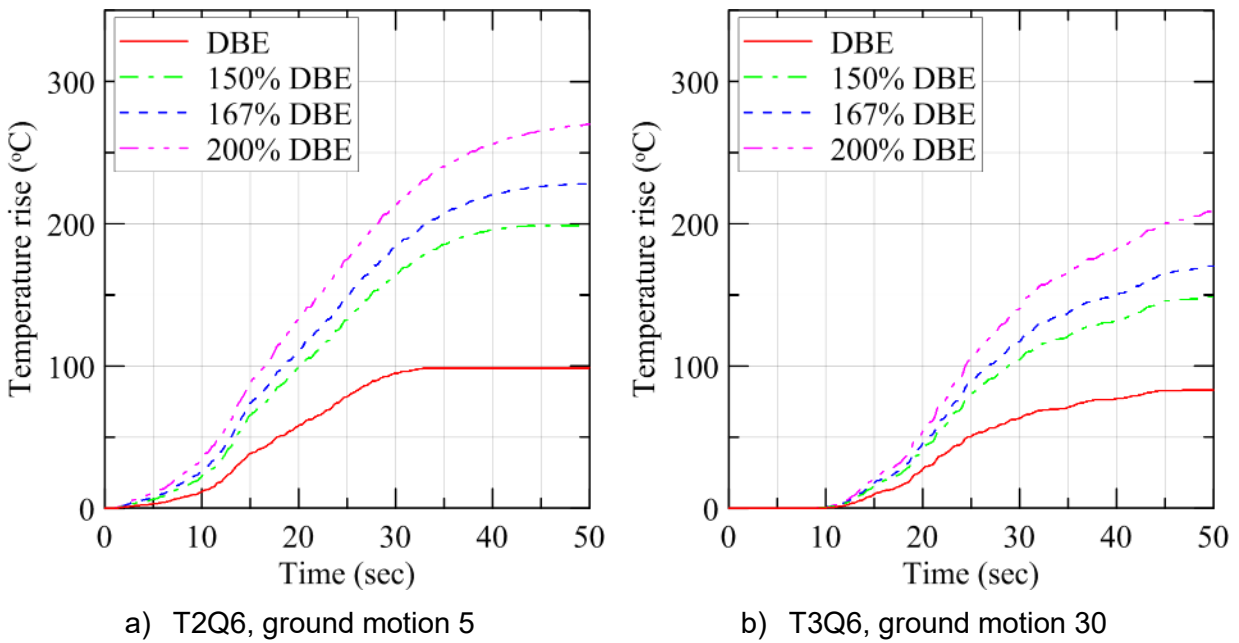


Figure 8-8 Histories of temperature increase in the lead cores

8.4.2 Variation in buckling load due to horizontal displacement

The numerical models of elastomeric bearings in contemporary software programs include a linear spring in the vertical direction. Buckling is not modeled. Three models of elastomeric bearings in compression can be modeled in *LeadRubberX*: 1) linear, 2) bilinear with a constant buckling load P_{cr0} , and 3) bilinear with a buckling load that is dependent on the co-existing horizontal displacement, P_{cr} . These three models are used for response-history analysis to identify the number of ground motions that would trigger buckling at the four intensities of shaking. For the third model, the buckling load calculation suggested by Warn *et al.* (2007) is:

$$P_{cr} = \begin{cases} P_{cr0} \frac{A_r}{A} & \frac{A_r}{A} \geq 0.2 \\ 0.2P_{cr0} & \frac{A_r}{A} < 0.2 \end{cases} \quad (8.6)$$

where P_{cr0} is the buckling load at zero displacement, and P_{cr} is the buckling load at overlapping area A_r of a bearing with an initial bonded rubber area of A .

Plots of the axial load ratio, which is the ratio of the minimum critical buckling load of a bearing over the duration of a ground motion, $P_{cr\min}$, as predicted by Equation (8.6) to the buckling load at zero displacement, P_{cr0} , are presented in Figure 8-9. The buckling load varies substantially over the duration of some of the earthquake ground motions. A bearing will never achieve its critical buckling load at zero horizontal displacement under three components of input as it will fail at a lower axial load at a nonzero horizontal displacement. For the constant buckling load model, the ratio is 1.0 for the duration of a ground motion. The use of a buckling load calculated at zero horizontal displacement might provide misleading expectations of the performance of isolators and an isolation system in design basis and more intense earthquake shaking.

The ratio of the instantaneous axial load to the instantaneous buckling load is computed at each time step in each response-history analysis, and the maximum value is recorded. If the ratio exceeds unity, the isolator has buckled. Plots of the maximum value of the ratio for each ground motion, at three intensities of shaking, are presented in Figure 8-10 and Figure 8-11 for the constant and displacement-dependent buckling load models, respectively, for T2Q6 and T3Q6.

The numbers of ground motions for which buckling is predicted using the constant and the displacement-dependent buckling load models are summarized in Table 8-10 and Table 8-11, respectively. The use of a buckling load calculated at zero displacement (i.e., P_{cr0}) may lead to substantially non-conservative judgments regarding performance of isolation systems, noting however that buckling of individual isolators in extreme shaking may not compromise the performance of an isolation system composed of 100s of isolators.

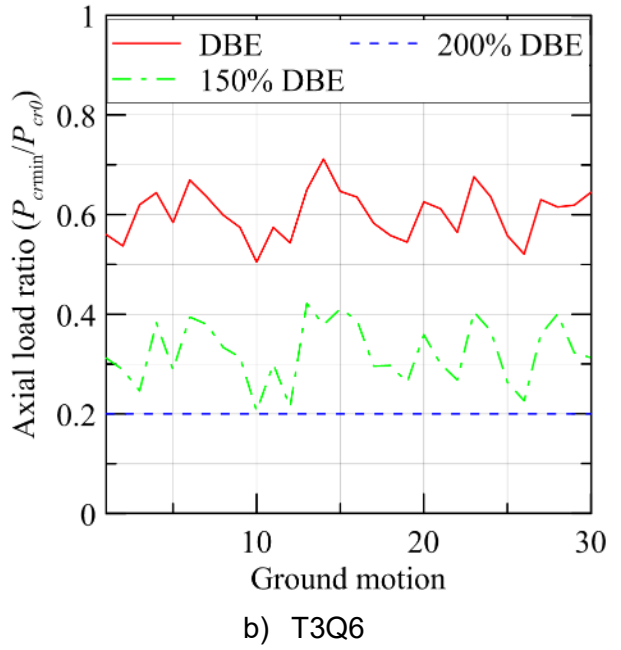
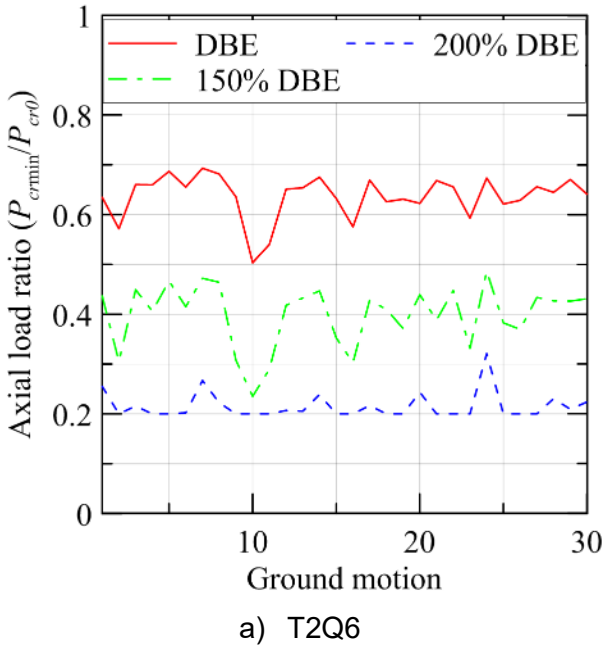


Figure 8-9 Normalized axial load ratios

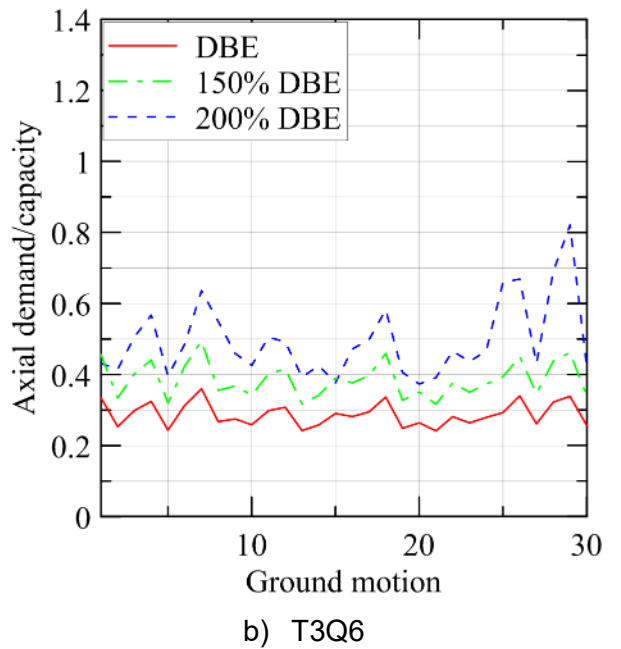
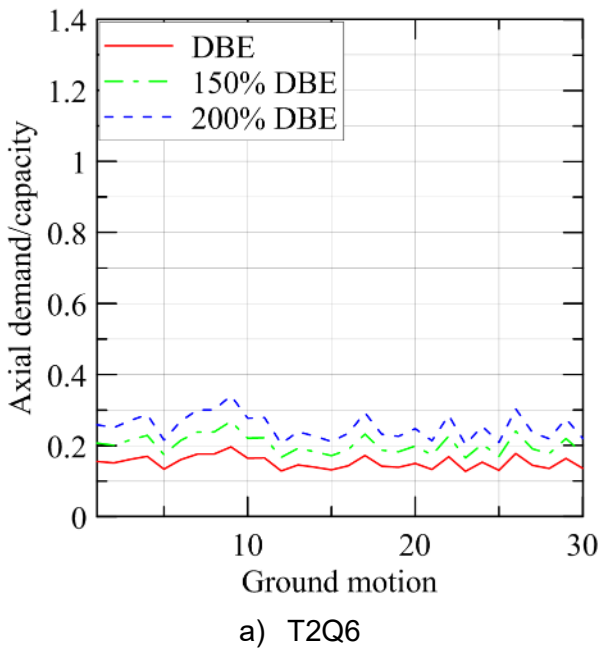


Figure 8-10 Demand-capacity ratios for the constant buckling load model, P_{cr0}

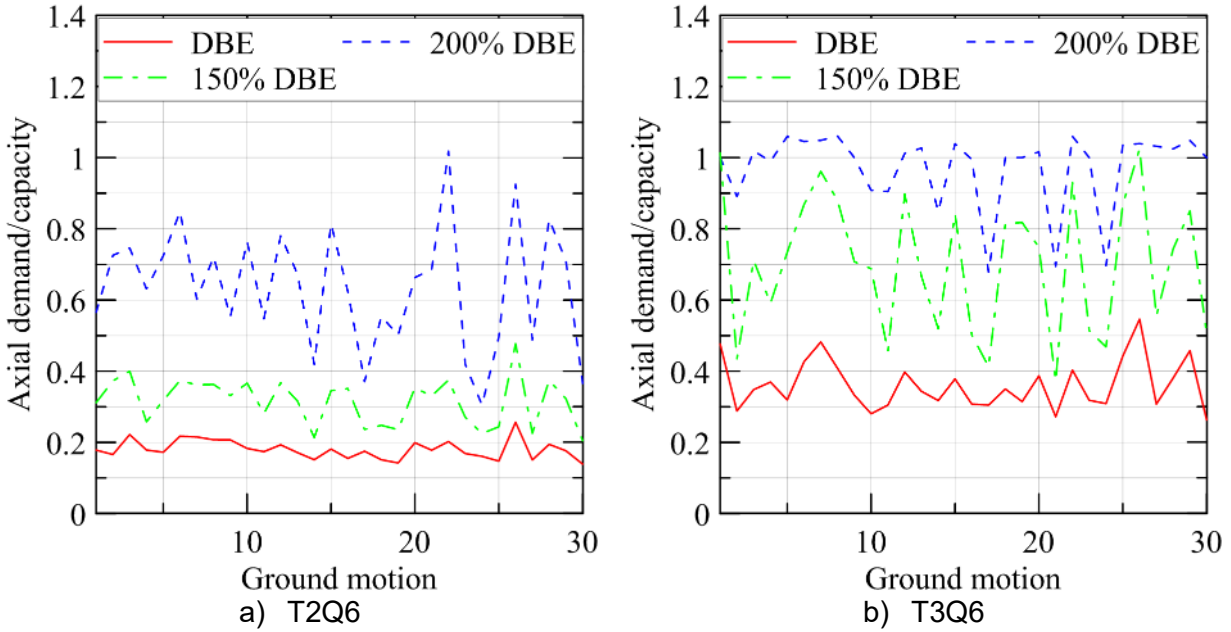


Figure 8-11 Demand-capacity ratios for the displacement-dependent buckling load model, P_{cr}

Table 8-10 Number of ground motions (of 30) triggering buckling failures; using P_{cr0}

Intensity (% DBE)	Isolation system									
	T2Q3	T2Q6	T2Q9	T2Q12	T2Q15	T3Q3	T3Q6	T3Q9	T3Q12	T3Q15
100	0	0	0	0	0	0	0	0	0	0
150	0	0	0	0	0	0	0	0	0	0
167	0	0	0	0	0	0	0	0	0	0
200	0	0	0	0	0	0	0	0	0	0

Table 8-11 Number of ground motions (of 30) triggering buckling failures; using P_{cr}

Intensity (% DBE)	Isolation system									
	T2Q3	T2Q6	T2Q9	T2Q12	T2Q15	T3Q3	T3Q6	T3Q9	T3Q12	T3Q15
100	0	0	0	0	0	7	0	0	0	0
150	0	0	0	0	0	24	2	1	0	0
167	0	0	0	0	0	30	12	3	1	1
200	5	1	0	0	0	30	20	17	10	4

8.4.3 Cavitation and post-cavitation behavior

A nonlinear elastic model is used to capture the behavior of elastomeric bearings in cyclic tension. The number of ground motions that produce cavitation damage at each intensity level are identified in Table 8-12. Nearly 50% of the ground motions result in cavitation at 100% DBE shaking for the 2 sec isolation systems, and all or nearly all of the ground motions result in cavitation at 150% DBE shaking for the 2 and 3 sec isolation systems. These high fractions are due to the intense vertical shaking at the Diablo Canyon site. The period of vibration in the axial direction for the 2 and 3 sec isolation systems are 0.06 and 0.07 sec, respectively, and the 2%

damped vertical spectral acceleration at these periods exceed 2.2g at 100% DBE shaking (see Figure 9-6c). (Note that the vertical DBE spectrum is for the surface free field and not a foundation input response spectrum: accounting for input at depth and incoherence should substantially reduce the vertical shaking effects.)

Table 8-12 Number of ground motions (of 30) that cavitate isolators

Intensity (% DBE)	Isolation system									
	T2Q3	T2Q6	T2Q9	T2Q12	T2Q15	T3Q3	T3Q6	T3Q9	T3Q12	T3Q15
100	12	14	14	16	16	27	27	27	27	27
150	27	27	27	27	28	30	30	30	30	30
167	28	28	28	28	28	30	30	30	30	30
200	30	30	30	29	29	30	30	30	30	30

8.4.4 Variation in axial stiffness due to horizontal displacement

The horizontal and vertical responses of an elastomeric bearing are coupled through the axial stiffness that in turn depends on the co-existing horizontal displacement. The expression for the elastic shear stiffness of a LR bearing is:

$$K_v = \frac{AE_c}{T_r} \left[1 + \frac{3}{\pi^2} \left(\frac{u_h}{r} \right)^2 \right]^{-1} = K_{v0} \left[1 + \frac{3}{\pi^2} \left(\frac{u_h}{r_g} \right)^2 \right]^{-1} \quad (8.7)$$

where E_c is the compression modulus (Constantinou *et al.*, 2007); u_h is the horizontal displacement; r_g is the radius of gyration of the bonded rubber area; and K_{v0} is the axial compressive stiffness at zero lateral displacement.

Axial stiffness (and buckling load) decreases with increasing horizontal displacement. Figure 8-12 shows the response of a LR bearing (LR5 in Warn (2006)) subject to a vertical acceleration history (in m^2/s) of $2.6 \sin(20\pi t)$ in the vertical direction. Two models for axial stiffness are considered here: 1) axial stiffness per Equation (8.7), and 2) axial stiffness per Equation (8.7) but capped by buckling and cavitation. Results are presented in Figure 8-12a and Figure 8-12b, respectively, for the three values of horizontal displacement, normalized by the outer diameter of the bearing, D_o , equal to 152 mm. The axial response of this bearing is substantially impacted by considerations of co-existing horizontal displacement, noting that the simplified model would predict response given by the red ($u_h / D_o = 0$) line in Figure 8-12a.

To understand the influence of co-existing horizontal displacement on the vertical response of an isolation system, analyses are performed for two representations of axial stiffness: 1) equal stiffness in compression and tension, calculated at zero horizontal displacement: K_{v0} in Equation (8.7), and 2) equal axial stiffness in compression and tension, but varying as a function of horizontal displacement: K_v in Equation (8.7). Cavitation and buckling are not considered. Results for a sample isolation system, T3Q6, are presented in Figure 8-13. The influence is negligible for 100% DBE shaking but considerable for beyond design basis shaking, with changes in axial displacement being greater than those in axial force. Results for the other isolation systems follow a similar trend.

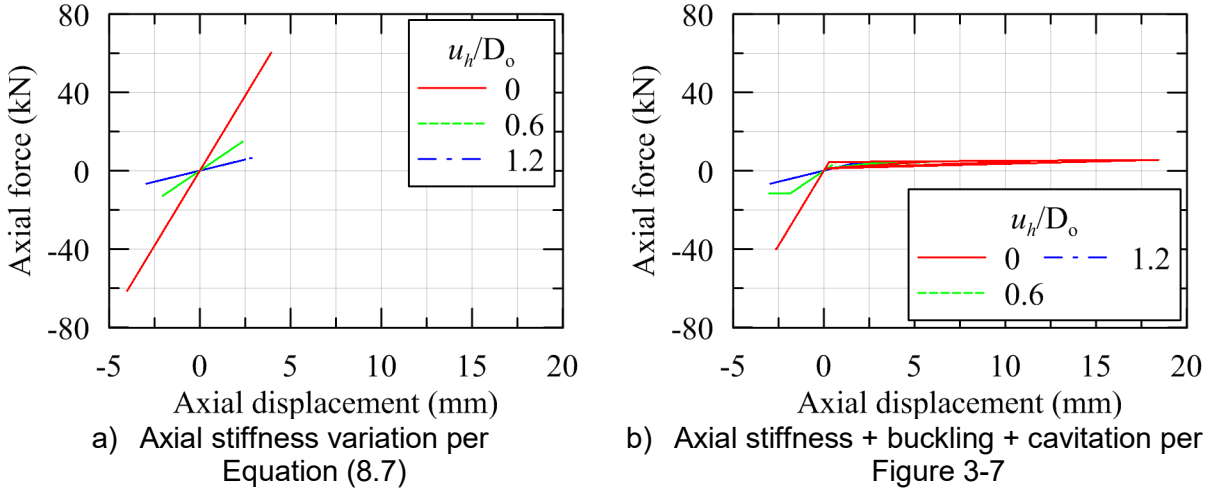


Figure 8-12 Axial response of bearing LR5 in Warn (2006) subject to harmonic vertical excitation

The variation in the stiffness ratio, which is the ratio of the minimum axial stiffness over the duration of a ground motion to the axial compressive stiffness at zero displacement, is shown in Figure 8-14a. The history of the ratio of the instantaneous axial compressive stiffness to the initial axial compressive stiffness for T3Q6 and ground motion 30 is shown in Figure 8-14b. The minimum axial compressive stiffness drops below 40% of the initial stiffness at 150+% DBE shaking. Although the variation in axial compressive stiffness has a notable effect on axial response, its effect on horizontal response is negligible here because the axial force varies at a much higher frequency than the isolation-system response in the horizontal direction².

8.4.5 Variation in shear stiffness due to axial load

The shear stiffness of an elastomeric bearing depends on the instantaneous axial load per:

$$K_H = \frac{GA}{T_r} \left[1 - \left(\frac{P}{P_{cr}} \right)^2 \right] = K_{H0} \left[1 - \left(\frac{P}{P_{cr}} \right)^2 \right] \quad (8.8)$$

where P is the instantaneous axial load; P_{cr} is the buckling load, and K_{H0} is the horizontal stiffness at zero axial load, and other variables were defined previously.

Two values for the buckling load can be used in Equation (8.8): 1) buckling load at zero lateral displacement, P_{cr0} , and 2) buckling load, P_{cr} , per Equation (8.6). Three models of the LR bearing are used to investigate the choice of shear stiffness model: 1) shear stiffness independent of axial load, 2) axial load dependence of shear stiffness using $P_{cr} = P_{cr0}$, and 3) axial load dependence of shear stiffness using the instantaneous buckling load, P_{cr} .

² The effect of changing axial compressive stiffness on shear response may be important if rocking-induced axial forces are significant because the rocking frequency may be of the order of the isolation-system frequency

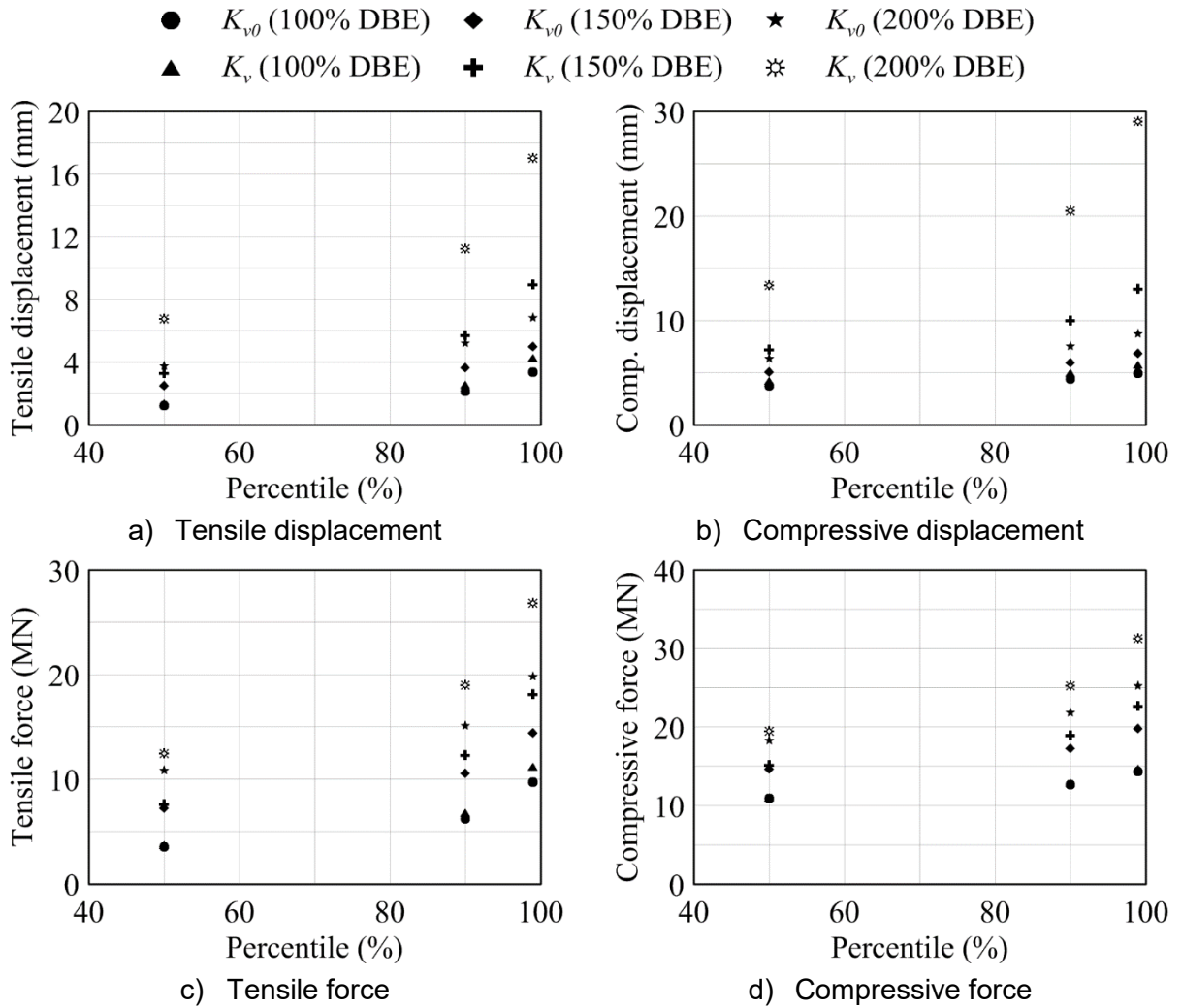


Figure 8-13 Influence of axial stiffness model on the vertical response of T3Q6

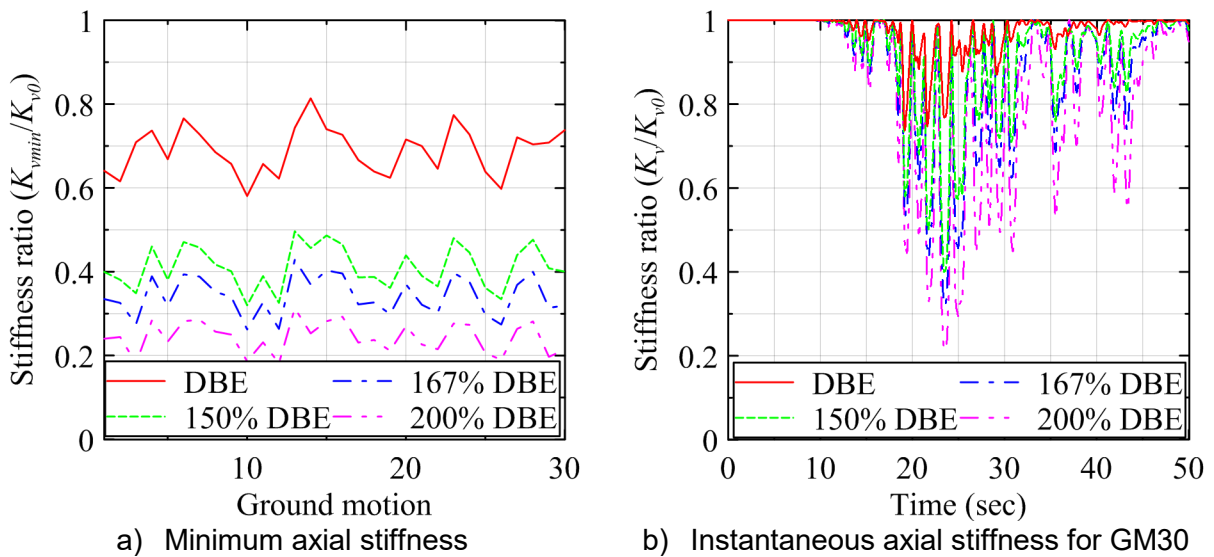


Figure 8-14 Effect of the variation of axial compressive stiffness on T3Q6

Figure 8-15a and Figure 8-15b present the results of response-history analysis of model T2Q6 using one ground motion from the set of 30, scaled to 167% DBE shaking. Models 1, 2, and 3 in the legend are: 1) shear stiffness K_{H0} independent of axial load, 2) shear stiffness dependent on axial load using K_H for the buckling load in Equation (8.6), and 3) shear stiffness K_H dependent on axial load using P_{cr} for the buckling load in Equation (8.6). The peak horizontal displacement is not affected by the choice of the model. The fluctuations in the hysteresis loops of models 2 and 3 occur at time instants near peak displacement but do not increase the shearing forces transmitted to the superstructure. Figure 8-15b presents fluctuations in the shear stiffness, calculated as the shear stiffness of models 2 and 3 normalized by the shear stiffness of model 1, which is 3.52 MN/m.

The outcomes of the response-history analysis of the ten base-isolated NPP models for the other ground motion sets, at all four intensities of shaking, are virtually identical to those seen in Figure 8-15, namely, that ignoring the effect of axial load on horizontal stiffness does not compromise the calculation of peak horizontal displacements or transmitted shear force to the superstructure.

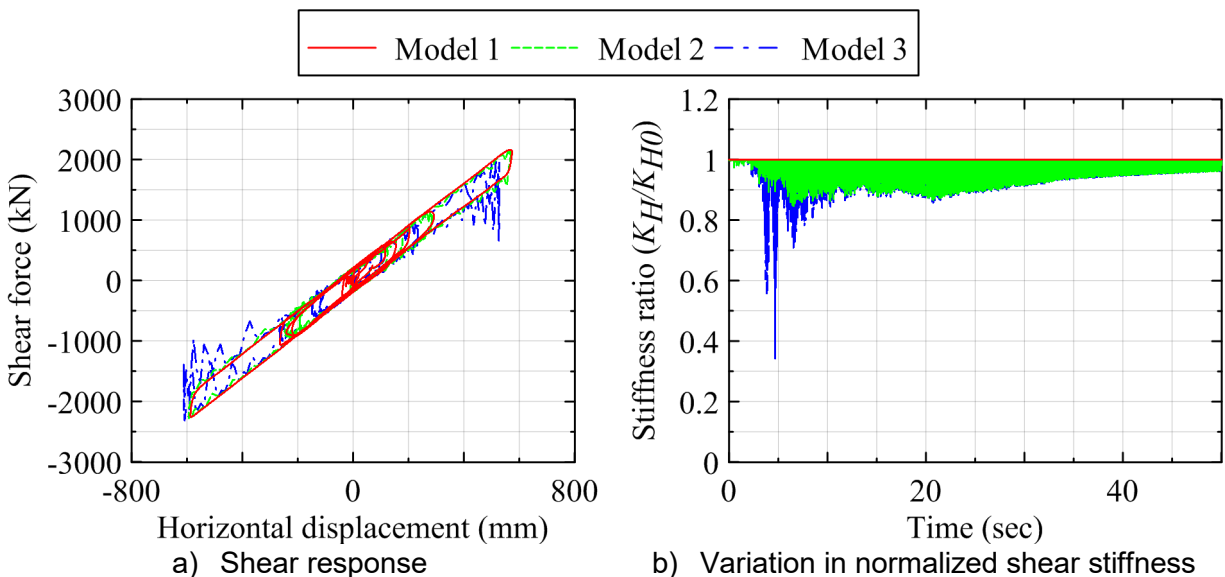


Figure 8-15 Response of T2Q6 to ground motion 1 at 167% DBE

8.4.6 Cumulative effects

The responses of the ten models considering all five characteristics listed in Section 8.2 are considered next. The ratios of the percentiles of the peak shear displacement for the simplified and advanced base-isolated NPP models, considered separately, at different intensities of shaking, are presented in Figure 8-16, where D is the displacement and its subscript denotes the intensity and the percentile of the peak shear displacement. Figure 8-17 presents horizontal displacements obtained using the advanced models normalized by the median DBE horizontal displacement calculated using the simplified model. The plots in the figures can be used to estimate horizontal displacements at 150+% DBE shaking for a range of isolation systems by calculating the median DBE horizontal displacement using the simplified isolator model. For example, the DBE median horizontal displacement obtained using the simplified model can be increased by the ratios presented in Figure 8-17 to address the five intra-earthquake changes in the mechanical properties of LR bearings enumerated in Section 8.2.

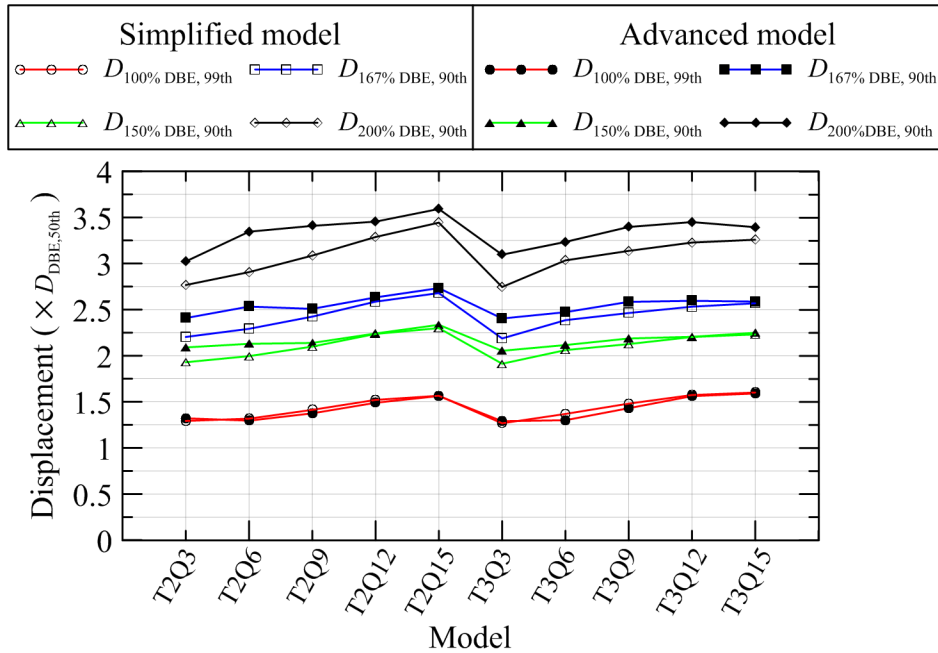


Figure 8-16 Ratios of percentiles of peak horizontal displacement to the median DBE displacement; simplified and advanced models

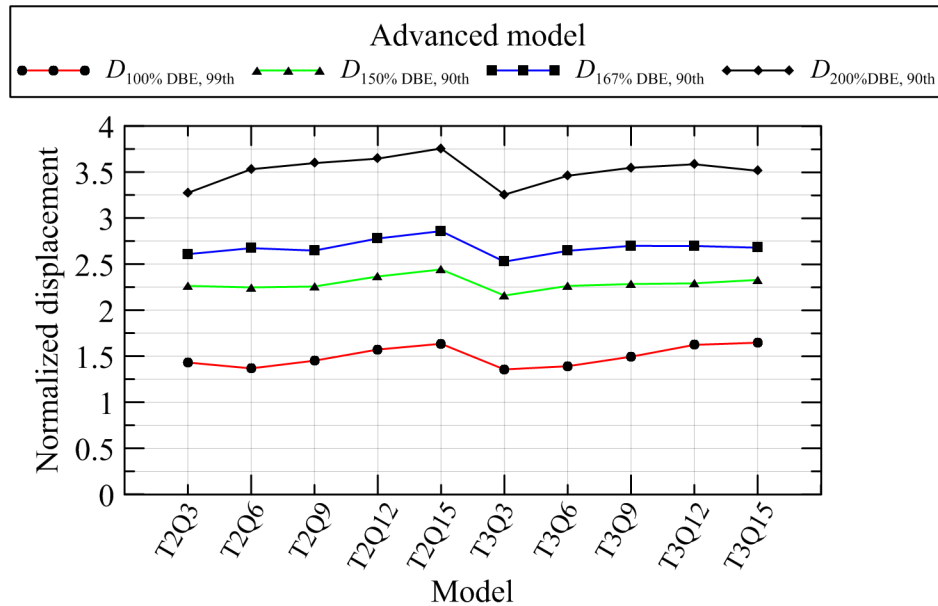


Figure 8-17 Ratios of the percentiles of peak horizontal displacement calculated using the advanced model to the median DBE displacement calculated using the simplified model

The numbers of ground motions for which cavitation and buckling are predicted are identified in Table 8-13 and Table 8-14, respectively, noting that simplified model of Section 8.3 cannot account for either behavior. The use of a displacement-dependent model for the calculation of buckling load predicts instabilities in many cases for intensities greater than DBE. Flexible (longer period) isolation systems with low strength (e.g., T3Q3) are more vulnerable to buckling. The results of response-history analyses for which buckling is predicted are not included in the calculation of the percentiles presented in Table 8-15 through Table 8-17. Only mean values are reported in shaded cells for these shaking intensities at which 15 or more (of 30) ground motions result in isolator buckling.

Table 8-13 Number of ground motion sets (of 30) for which cavitation is predicted; advanced model

Intensity (% DBE)	Isolation system									
	T2Q3	T2Q6	T2Q9	T2Q12	T2Q15	T3Q3	T3Q6	T3Q9	T3Q12	T3Q15
100	15	15	15	16	14	29	28	29	29	29
150	29	29	28	28	28	30	30	30	30	30
167	29	29	29	28	28	30	30	30	30	30
200	30	30	30	30	30	30	30	30	30	30

Table 8-14 Number of ground motion sets (of 30) for which buckling is predicted; advanced model

Intensity (% DBE)	Isolation system									
	T2Q3	T2Q6	T2Q9	T2Q12	T2Q15	T3Q3	T3Q6	T3Q9	T3Q12	T3Q15
100	0	0	0	0	0	0	0	0	0	0
150	0	0	0	0	0	15	7	2	1	0
167	3	0	0	0	0	24	19	10	8	8
200	12	8	2	2	0	29	27	22	24	19

Peak horizontal displacements are summarized in Table 8-15. The 90th percentile horizontal strain in the LR bearings at 167% DBE shaking are smaller than 300% for all isolation systems except those with low strength. The peak shearing and compressive forces normalized by the gravity load are presented in Table 8-16 and Table 8-17, respectively. Stiff (shorter period) isolation system transmits greater shear forces to the superstructure, with the mean values for T2Q3 and T2Q6 exceeding 100% at 200% DBE shaking. For the normalized compressive forces in Table 8-17, the increment above 100 represents the effect of the vertical ground motion. The high intensity of the vertical shaking at the site of the Diablo Canyon Nuclear Generating Station is reflected in these compressive forces, with mean values at 200% DBE above 600% for all models. This value is greater than that calculated by summing gravity and earthquake forces calculated using the peak spectral ordinate of the 2% damped vertical spectrum of Figure 9-6c ($5.4 W = W + 2*2.2 W$) because the vertical damping ratio falls below 2%. (The Rayleigh damping coefficients were selected by assigning 2% damping to the vertical frequency calculated using axial stiffness at zero horizontal displacement: the decrease in the vertical frequency due to a reduction in axial stiffness associated with horizontal displacement results in a smaller damping ratio than 2%.)

Peak tensile forces normalized by the initial cavitation force, F_c , are presented in Table 8-18. Mean values are reported because the data did not fit a lognormal distribution. The mean peak tensile forces exceed the cavitation force at 150%DBE shaking due to the intense vertical shaking at the Diablo Canyon site.

Table 8-15 Percentiles of peak horizontal displacement (mm) for 30 ground motion sets; advanced model

Model	100% DBE						150% DBE						167% DBE						200% DBE							
	50 th		90 th		99 th		50 th		90 th		99 th		50 th		90 th		99 th		50 th		90 th		99 th			
	μ	σ	μ	σ	μ	σ	μ	σ	μ	σ	μ	σ	μ	σ	μ	σ	μ	σ	μ	σ	μ	σ	μ	σ		
T2Q3	473	470	548	621	0.12	0.11	816	807	977	0.15	0.12	946	934	1148	0.16	0.13	1209	1148	1209	1148	1209	1148	1209	1148	1209	1148
T2Q6	365	363	419	470	0.11	0.11	669	664	774	0.12	0.12	784	777	918	0.13	0.13	1040	1029	1040	1029	1040	1029	1040	1029	1040	1029
T2Q9	305	302	360	415	0.14	0.14	563	559	646	0.11	0.11	663	659	758	0.11	0.11	889	881	889	881	889	881	889	881	889	881
T2Q12	261	257	320	383	0.17	0.17	497	493	575	0.12	0.12	587	583	675	0.11	0.11	773	768	773	768	773	768	773	768	773	768
T2Q15	229	225	288	353	0.19	0.19	444	440	526	0.14	0.14	527	523	617	0.13	0.13	702	697	702	697	702	697	702	697	702	697
T3Q3	535	533	608	676	0.10	0.10	978	--	--	--	--	1209	--	--	--	--	1584	--	--	1584	--	--	--	--	--	--
T3Q6	407	405	467	524	0.11	0.11	734	731	828	0.10	0.10	847	--	--	--	--	1148	--	--	1148	--	--	--	--	--	--
T3Q9	335	331	404	474	0.15	0.15	633	629	732	0.12	0.12	728	--	--	--	--	927	--	--	927	--	--	--	--	--	--
T3Q12	295	290	371	453	0.19	0.19	541	536	638	0.14	0.14	641	636	749	0.13	0.13	850	--	--	850	--	--	--	--	--	--
T3Q15	271	265	343	422	0.20	0.20	490	483	598	0.17	0.17	581	574	705	0.16	0.16	726	--	--	726	--	--	--	--	--	--

1. The horizontal displacement corresponding to 100 (200, 300)% shear strain in the elastomer is 310 (620, 930) mm.
2. Shaded cell data correspond to the cases where buckling is predicted in more than 15 ground motion sets; only mean values are reported.

Table 8-16 Percentiles of peak shearing force; advanced model (%W) for thirty ground motion sets; advanced model

Model	100% DBE						150% DBE						167% DBE						200% DBE						
	50 th		90 th		99 th		50 th		90 th		99 th		50 th		90 th		99 th		50 th		90 th		99 th		
	μ	σ	μ	σ	μ	σ	μ	σ	μ	σ	μ	σ	μ	σ	μ	σ	μ	σ	μ	σ	μ	σ	μ	σ	
T2Q3	48	48	56	63	0.11	0.11	80	79	94	0.13	0.13	91	91	109	0.15	0.15	116	--	--	116	--	--	--	--	--
T2Q6	40	39	45	50	0.11	0.11	68	68	78	0.11	0.11	79	78	90	0.11	0.11	102	101	102	101	102	101	102	101	102
T2Q9	36	36	41	46	0.11	0.11	60	60	68	0.10	0.10	70	69	79	0.10	0.10	90	89	90	89	90	89	90	89	90
T2Q12	34	34	40	45	0.12	0.12	56	55	64	0.11	0.11	64	64	73	0.11	0.11	81	81	81	81	81	81	81	81	81
T2Q15	34	34	40	45	0.12	0.12	53	53	61	0.11	0.11	60	60	69	0.11	0.11	76	76	76	76	76	76	76	76	76
T3Q3	25	25	28	31	0.09	0.09	40	--	--	--	--	46	--	--	--	--	58	--	--	58	--	--	--	--	--
T3Q6	22	22	25	27	0.09	0.09	35	35	38	0.08	0.08	37	--	--	--	--	48	--	--	48	--	--	--	--	--
T3Q9	22	21	25	28	0.11	0.11	34	33	38	0.10	0.10	37	--	--	--	--	42	--	--	42	--	--	--	--	--
T3Q12	22	22	26	29	0.11	0.11	32	32	37	0.11	0.11	36	36	41	0.11	0.11	41	--	--	41	--	--	--	--	--
T3Q15	24	24	27	30	0.10	0.10	32	32	37	0.11	0.11	36	36	42	0.12	0.12	41	--	--	41	--	--	--	--	--

1. The gravity weight W on the bearing is approximately 3500 kN.
2. The characteristic strength, Q_d , ranges between 3%W (e.g., T2Q3) to 15%W (e.g., T3Q15).
3. Shaded cell data correspond to the cases where buckling is predicted in more than 15 ground motion sets; only mean values are reported.

Table 8-17 Percentiles of peak compressive force (%W) for 30 ground motion sets; advanced model

Model	100% DBE			150% DBE			167% DBE			200% DBE												
	μ	50 th	99 th	μ	50 th	90 th	σ	90 th	μ	50 th	90 th	σ	90 th	μ	50 th	90 th	σ					
T2Q3	306	304	362	417	419	419	0.14	0.14	455	445	586	0.22	0.22	550	523	777	0.31	637	629	865	0.28	
T2Q6	305	301	361	419	419	419	0.14	0.14	457	441	618	0.26	0.26	546	530	737	0.26	629	649	899	0.28	
T2Q9	303	299	360	418	418	418	0.14	0.14	467	437	667	0.33	0.33	522	503	723	0.28	649	626	899	0.28	
T2Q12	303	300	365	428	428	428	0.15	0.15	461	442	633	0.28	0.28	565	529	823	0.34	647	618	909	0.30	
T2Q15	302	299	361	421	421	421	0.15	0.15	474	445	674	0.32	0.32	539	515	754	0.30	691	651	1021	0.35	
T3Q3	354	343	464	594	594	594	0.24	0.24	517	--	--	--	--	571	--	--	--	752	--	--	--	--
T3Q6	343	333	443	560	560	560	0.22	0.22	503	485	688	0.27	0.27	569	--	--	--	517	--	--	--	--
T3Q9	343	334	445	563	563	563	0.22	0.22	565	543	787	0.29	0.29	557	--	--	--	590	--	--	--	--
T3Q12	330	326	402	477	477	477	0.16	0.16	561	542	762	0.26	0.26	563	552	721	0.21	558	--	--	--	--
T3Q15	338	331	426	522	522	522	0.20	0.20	529	515	690	0.23	0.23	570	554	755	0.24	669	--	--	--	--

1. The gravity weight W on the bearing is approximately 3500 kN

2. Shaded cell data correspond to the cases where buckling is predicted in more than 15 ground motion sets; only mean values are reported.

Table 8-18 Mean peak tensile force (% F_c); of 30 ground motion sets; advanced model

Model	Shaking intensity					
	100% DBE	150% DBE	167% DBE	200% DBE	100% DBE	200% DBE
T2Q3	87	100	102	104	87	104
T2Q6	84	99	101	103	84	103
T2Q9	84	99	101	103	84	103
T2Q12	81	98	101	104	81	104
T2Q15	81	99	101	103	81	103
T3Q3	98	103	104	105	98	105
T3Q6	98	103	104	103	98	103
T3Q9	98	103	104	105	98	105
T3Q12	98	103	103	104	98	104
T3Q15	99	103	104	105	99	105

1. The cavitation force, F_c , corresponds to 3276 kN and 1456 kN for 2 and 3 sec isolation period models, respectively

8.5 Summary and Conclusions

Ten models of a base-isolated NPP are analyzed using thirty sets of ground motions that are selected and scaled to be consistent with uniform hazard response spectra for a return period of 10,000 years (or DBE shaking) at the site of the Diablo Canyon Nuclear Generating Station. A two-node macro model is used for response-history analysis. Two types of LR bearing models are analyzed. The first is the simplified model that is widely used and implemented in contemporary software programs, whereas the second is an advanced model that addresses five mechanical characteristics of elastomeric bearings under extreme loading:

1. Strength degradation in shear due to heating of the lead core (LR bearings only)
2. Variation in buckling load due to horizontal displacement
3. Cavitation and post-cavitation behavior due to tensile loading
4. Variation in axial stiffness due to horizontal displacement
5. Variation in shear stiffness due to axial load

The advanced model, which was verified and validated per ASME best practices, is implemented as user element *LeadRubberX* in OpenSees. The influence of each characteristic and of the combination of the five characteristics are investigated and results are compared with those obtained using the simplified model. The main conclusions of the study, which are specific to a region of moderate to high seismic hazard, are:

1. Heating of the lead core has a relatively small effect (< 10%) on horizontal DBE shear displacements but the influence increases at higher intensities of shaking.
2. Peak horizontal displacement is more sensitive to the heating of lead cores than peak shear force.
3. For a given isolation period, the effect of lead core heating decreases with an increase in the ratio of characteristic strength to weight, whereas for a given value of the ratio, the effect decreases with an increase in isolation period.
4. The characteristic strength of a LR bearing may degrade substantially during extreme earthquake shaking, with values falling below half the initial value for 150+% DBE shaking.
5. The temperature in a lead core may rise by 100+ °C for 150+% DBE shaking.
6. The axial response of a NPP base-isolated with LR bearings is not affected by changes in the mechanical properties of the lead core due to heating.
7. The buckling load of a LR bearing varies substantially during earthquake shaking. The displacement-dependent model for buckling load predicts failure for many more ground motions than the constant buckling load model, and is recommended for use in practice.
8. No effect of the variation in axial compression stiffness with lateral displacement is observed on the axial response at DBE shaking. A moderate effect is observed at higher intensities of shaking.
9. The horizontal (shear) force response of a base-isolated NPP is not affected by variations in axial compressive stiffness due to lateral displacements.
10. Of the five characteristics of LR bearings discussed in Section 8.2, 1) strength degradation due to heating of the lead core, 2) variation in buckling load due to horizontal displacement, and 3) variation in axial stiffness due to horizontal displacement, affect the responses of a base-isolated NPP most significantly.

9 RESPONSE OF A LUMPED-MASS MODEL OF A BASE-ISOLATED NUCLEAR POWER PLANT

9.1 Introduction

The response of a base-isolated nuclear power plant (NPP) structure, calculated using a two-node macro model for the isolation system, was discussed in Chapter 8. A detailed stick model of a NPP nuclear island is presented in this chapter. The superstructure is represented by an equivalent lumped-mass model, supported by a rigid basemat. The entire nuclear island (NPP and basemat) is isolated using lead rubber (LR) bearings. Seismic isolation systems of two periods and three values of Q_d / W (supported weight to strength ratios) are prepared, for a total of six models. Response-history analysis of the six models is performed. Ground motions are selected and scaled to be consistent with response spectra for design basis and beyond design basis earthquake shaking at the site of the Diablo Canyon Nuclear Generating Station. Two mathematical models of LR bearings are used: 1) simplified, and 2) advanced. The simplified model represents the current state of modeling of LR bearings in contemporary structural analysis programs, whereas the advanced model includes those five characteristics of LR bearings that are expected to influence the response of a base-isolated NPP at higher intensities of earthquake shaking.

The stick model of the NPP presented in EPRI (2007) is described. Numerical models of the NPP are developed in OpenSees and SAP2000 based on the information presented in EPRI (2007). The OpenSees model is verified using results of modal analysis of the SAP2000 model presented in EPRI (2007).

9.2 Fixed-base Model of a Nuclear Power Plant

The details of the stick model of the sample Nuclear Power Plant (NPP) is reproduced here from EPRI (2007). The three-dimensional model of NPP was simplified to three concentric lumped-mass stick models of the Coupled Auxiliary and Shield Building (ASB), the Steel Containment Vessel (SCV), and the Containment Internal Structure (CIS). EPRI (2007) provides the equivalent nodal and element properties of the stick models created in SAP2000 (CSI, 2007). A schematic of the stick models is presented in Figure 9-1. The model presented in EPRI (2007) is a modified version of the original model in Orr (2003).

The layout of the reactor model is presented in Appendix C.1. The geometric and material properties of the stick models are reproduced in Appendix C.1. EPRI (2007) provides results of modal analysis of the fixed-based stick models performed in SAP2000 as ASB, SCV, and CIS.

The properties of the stick models presented in EPRI (2007) were used to create and verify the stick models in OpenSees and SAP2000. The properties of the stick model presented in EPRI (2007) uses the following convention:

1. The nodal properties are specified in global coordinates
2. The element and sectional properties are specified in local coordinates
3. The North-South and East-West directions are the X and Y directions, respectively

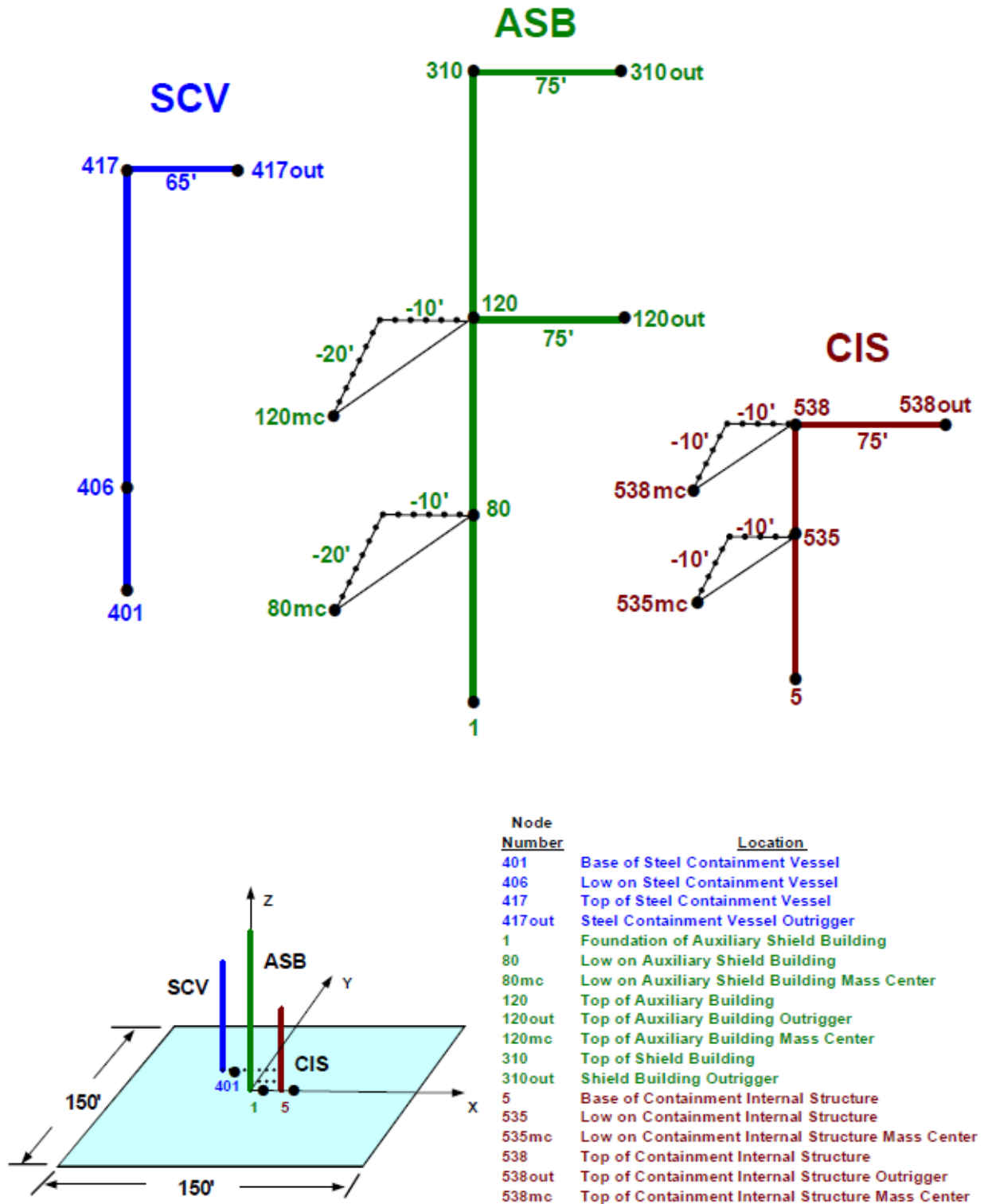


Figure 9-1 Stick model of the nuclear power plant (EPRI, 2007)

The stick models in SAP2000 created here adopt the same axes convention as EPRI (2007). However, the models in OpenSees use a different sign convention, as shown in Figure 9-2, which is the default axes convention used by OpenSees. The development of the SAP2000 and the OpenSees models are described in the following sections.

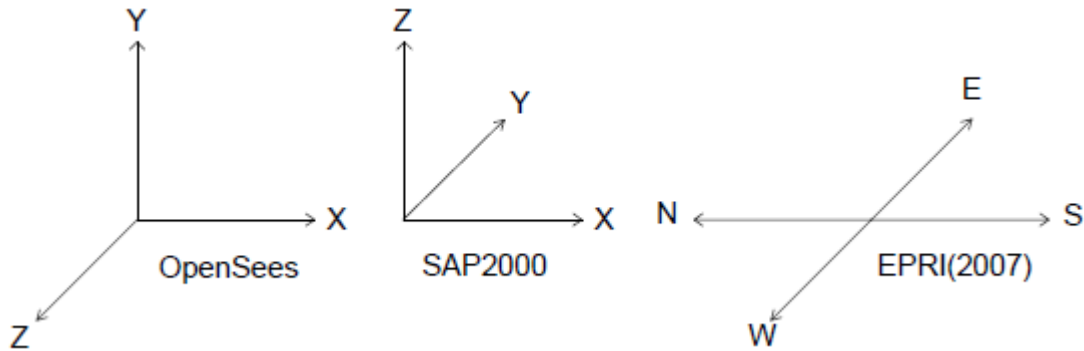


Figure 9-2 Orientation of the coordinate axes

9.2.1 Modal analysis

9.2.1.1 SAP2000 model

The fixed-base models of the ASB, CIS, and SCV were created in SAP2000. Modal analyses of the fixed-base models of ASB, SCV, and CIS were performed and the results are presented in Appendix C.3.

9.2.1.2 OpenSees model

The OpenSees model uses a different coordinate system than the SAP2000 model. The +Y and +Z axes in OpenSees correspond to the +Z and -Y axes in SAP2000, respectively, as shown in Figure 9-2. The material and geometric properties of the stick model provided in EPRI (2007) were transferred to the coordinate axes used for the OpenSees model. A linear geometric transformation is used in OpenSees, which is shown in Figure 9-3. This geometric transformation ensures the same orientation of local coordinate axes for an element's section in OpenSees and SAP2000. OpenSees provides an option to orient local axes in an element through the vector $Vecxz$. The local X axis is always defined by the two element nodes. A user must specify the $Vecxz$ such that it not parallel to the local X axis. The local y axis is obtained as the cross product of X and $Vecxz$. The local Z axis is obtained as the cross product of y and $Vecxz$ per the right-hand rule. A linear geometric transformation is assigned in OpenSees by specifying \bar{X} , \bar{Y} , and \bar{Z} of $Vecxz$. The orientation of the local axes in OpenSees for horizontal and vertical elements is shown in Figure 9-3. The vector $Vecxz$ (0, 0, -1) for the horizontal and vertical elements were chosen such that local axes in OpenSees have the same orientation as the default orientation of the local axes in SAP2000.

The *forceBeamColumn* element in OpenSees was used to model the elements connecting two nodes of the stick model. The element *rigidLink* was used for rigid components. Eigen analysis was performed to obtain modal periods and frequencies. The frequencies and periods of the first twenty modes of the stick models in OpenSees are presented in Table 9-1.

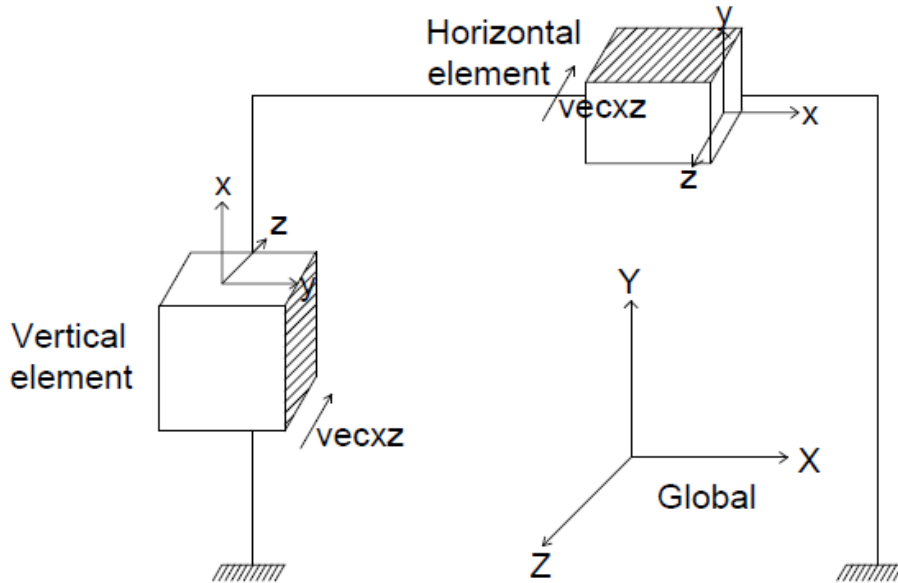


Figure 9-3 Orientation of local axes in OpenSees

Table 9-1 Modal properties of the stick models in OpenSees

Mode	ASB		SCV		CIS	
	Period (sec)	Freq. (Hz)	Period (sec)	Freq. (Hz)	Period (sec)	Freq. (Hz)
1	0.356	2.808	0.274	3.654	0.081	12.340
2	0.330	3.032	0.180	5.548	0.078	12.860
3	0.203	4.923	0.158	6.323	0.066	15.172
4	0.159	6.291	0.157	6.371	0.062	16.083
5	0.159	6.308	0.104	9.628	0.058	17.334
6	0.142	7.043	0.083	12.048	0.050	19.865
7	0.118	8.459	0.062	16.216	0.049	20.509
8	0.117	8.531	0.053	18.910	0.037	26.898
9	0.104	9.610	0.053	18.974	0.035	28.586
10	0.080	12.542	0.038	26.652	0.032	31.157
11	0.074	13.531	0.032	31.381	0.031	31.890
12	0.072	13.918	0.031	31.979	0.031	32.277
13	0.067	14.824	0.028	35.821	0.029	34.664
14	0.057	17.515	0.027	36.515	0.028	36.198
15	0.052	19.365	0.027	36.560	0.027	36.422
16	0.051	19.420	0.023	44.318	0.027	37.560
17	0.051	19.633	0.019	52.361	0.025	39.606
18	0.045	22.389	0.019	53.014	0.025	40.063
19	0.043	23.210	0.017	60.243	0.022	44.713
20	0.039	25.508	0.016	61.638	0.019	53.071

9.2.1.3 Verification

The results of the modal analyses of the stick models created in OpenSees and SAP2000, and the SAP2000 results of EPRI (2007) are presented in Table 9-2, Table 9-3, and Table 9-4. A very good agreement between modal periods and frequencies is achieved.

Table 9-2 Modal properties of Auxiliary Shield Building (ASB)

Mode	Axis		Direction	Period (sec)			Frequency (Hz)		
	OpenSees	SAP2000		OpenSees	SAP2000	EPRI	OpenSees	SAP2000	EPRI
2	X	X	Horizontal	0.330	0.323	0.312	3.032	3.097	3.2
5	X	X	Horizontal	0.159	0.136	-	6.308	7.336	-
10	X	X	Horizontal	0.080	0.070	-	12.542	14.197	-
1	Z	Y	Horizontal	0.356	0.362	0.333	2.808	2.762	3.0
4	Z	Y	Horizontal	0.159	0.142	-	6.291	7.026	-
9	Z	Y	Horizontal	0.104	0.072	-	9.610	13.938	-
6	Y	Z	Vertical	0.142	0.093	0.101	7.043	10.704	9.9
16	Y	Z	Vertical	0.051	0.043	-	19.420	23.251	-

Table 9-3 Modal properties of Steel Containment Vessel (SCV)

Mode	Axis		Direction	Period (sec)			Frequency (Hz)		
	OpenSees	SAP2000		OpenSees	SAP2000	EPRI	OpenSees	SAP2000	EPRI
2	X	X	Horizontal	0.180	0.180	0.181	5.548	5.548	5.5
5	X	X	Horizontal	0.104	0.104	0.105	9.628	9.628	9.5
9	X	X	Horizontal	0.053	0.053	0.101	18.973	18.973	9.9
3	Z	Y	Horizontal	0.158	0.158	0.164	6.322	6.325	6.10
1	Z	Y	Horizontal	0.274	0.275	-	3.654	3.632	-
8	Z	Y	Horizontal	0.053	0.053	-	18.910	18.910	-
7	Y	Z	Vertical	0.062	0.062	0.063	16.216	16.216	16.0
10	Y	Z	Vertical	0.038	0.038	-	26.652	26.652	-

Table 9-4 Modal properties of Containment Internal Structure (CIS)

Mode	Axis		Direction	Period (sec)			Frequency (Hz)		
	OpenSees	SAP2000		OpenSees	SAP2000	EPRI	OpenSees	SAP2000	EPRI
2	X	X	Horizontal	0.078	0.079	0.075	12.860	12.608	13.3
6	X	X	Horizontal	0.050	0.048	0.050	19.865	20.648	20.1
9	X	X	Horizontal	0.035	0.036	0.035	28.586	27.866	28.9
1	Z	Y	Horizontal	0.081	0.086	0.083	12.340	11.682	12.0
4	Z	Y	Horizontal	0.062	0.060	0.067	16.083	16.538	14.9
8	Z	Y	Horizontal	0.037	0.039	0.057	26.898	25.879	17.5
11	Y	Z	Vertical	0.031	0.025	0.024	31.890	40.062	41.4
14	Y	Z	Vertical	0.028	0.015	-	36.198	65.950	-
18	Y	Z	Vertical	0.025	0.008	-	40.063	129.955	-

9.3 Base-isolated Model of the Nuclear Power Plant

The stick model of the NPP is isolated through a common basemat slab on LR bearings, as shown in Figure 9-4. The dimensions of the concrete basemat slab are assumed to be 100m×60m×2.5m and the mat is assumed to be rigid in its plane. A symmetric layout of isolators is used beneath the basemat with the distance between the centers of adjacent bearings equal to 5 m, which requires a total of $N_b = 273$ isolators, as shown in Figure 9-5. The spacing between the bearings is in part dictated by the requirement to provide adequate space for maneuvering of fork lifts to perform maintenance and replacement of bearings.

Six models of base-isolated NPPs are created: two isolation time periods ($T = 2, 3$ seconds) and five ratios of characteristic strength to supported weight ($Q_d / W = 0.06, 0.12, \text{ and } 0.18$). The models are denoted by $TxQy$, where X identifies the value of T and y identifies the percentage of Q_d / W . Table 9-5 summarizes the isolator properties assumed for analysis.

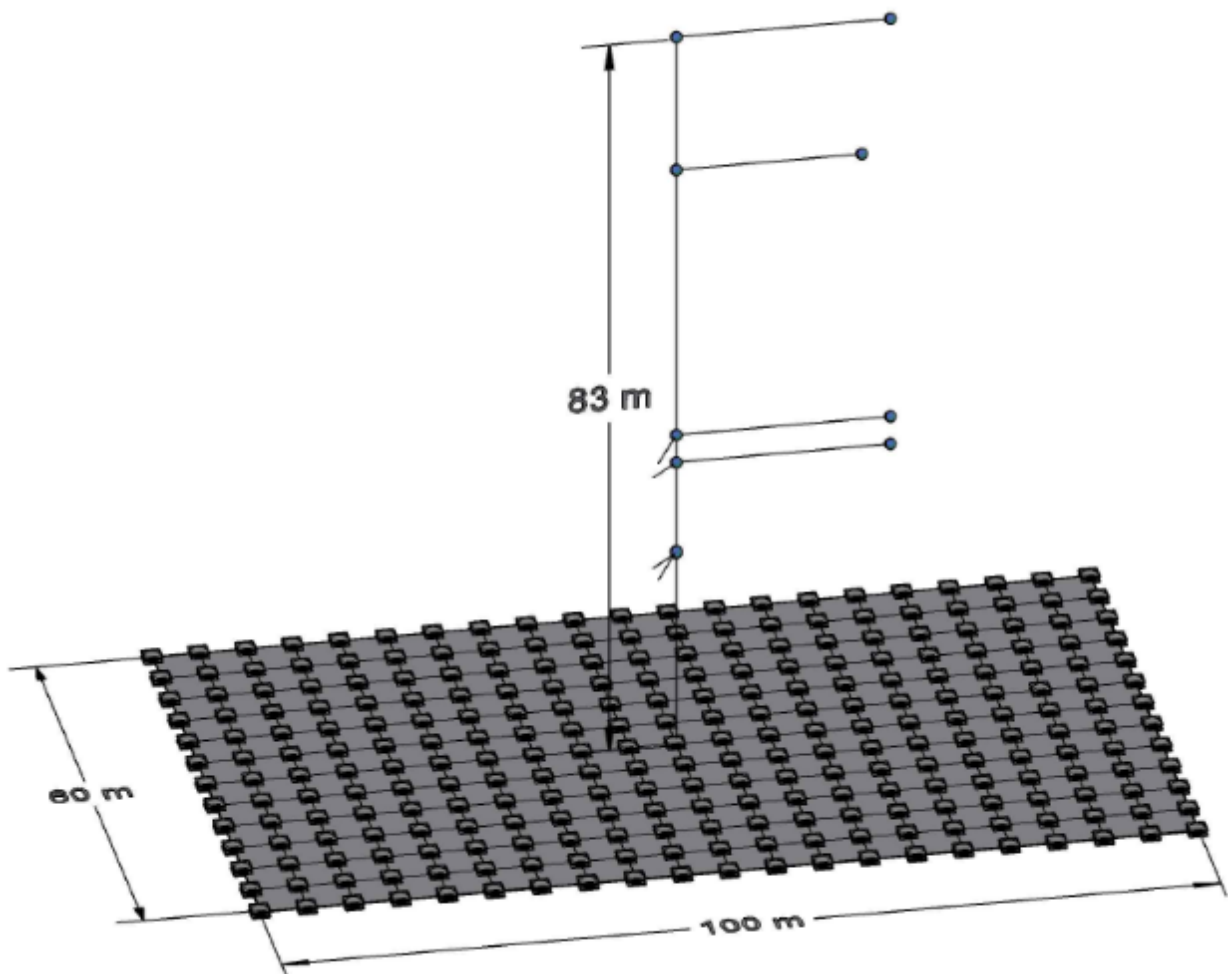


Figure 9-4 Stick model of a base-isolated NPP in OpenSees

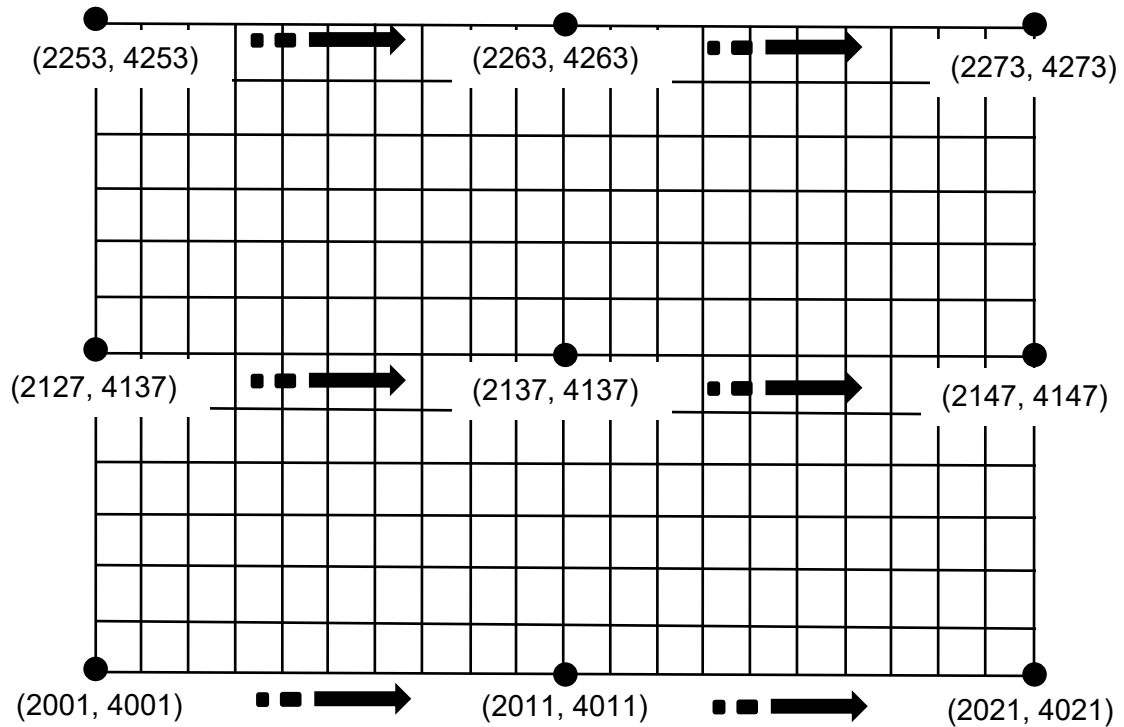


Figure 9-5 Plan view of the layout of isolated basemat showing (node, bearing) pairs

Table 9-5 Geometrical and mechanical properties of elastomeric bearings

Property	Notation (units)	Value
Mass of the superstructure	M_s (kg)	146284555
Number of LR bearings	N_b	273
Single rubber layer thickness	t_r (mm)	10
Number of rubber layers	n	31
Total rubber thickness	T_r (mm)	310
Steel shim thickness	t_s (mm)	4.75
Outer diameter	D_o (mm)	Varies ¹
Lead core diameter	D_i (mm)	Varies ¹
Cover thickness	t_c (mm)	19
Yield stress of lead	σ_L (MPa)	8.5
Static pressure due to gravity loads	p_{static} (MPa)	3.0
Shear modulus	G (MPa)	Varies ²

1, 2: Calculated for each model

A static (gravity) pressure on the bearing of 3 MPa is used for all analyses. The gravity weight W on a bearing is calculated by dividing the total weight of the superstructure ($M_s \times g$) by the number of bearings, N_b , in the isolation system. The weight W is divided by g to obtain the equivalent mass M in the three translational directions at the top node (node 2) of the bearings. The diameter of the lead core is back calculated from Q_d / W , assuming an initial yield stress of

8.5 MPa. The bonded rubber area (and hence the outer diameter) is calculated by dividing the gravity weight W on the bearing by the static pressure p_{static} . The effective shear modulus is calculated from the isolation time period T of the model. The geometric and mechanical properties of the LR bearings are computed from the given values of Q_d / W and T as:

$$W = \frac{M_s g}{N_b}; A_L = \frac{(Q_d / W) \times W}{\sigma_L}; D_i = \sqrt{4 \frac{A_L}{\pi}}; \quad (9.1)$$

$$M = \frac{W}{g}; A_b = \frac{W}{p_{static}}; D_o = \sqrt{\frac{4A_b}{\pi} + D_i^2} - t_c \quad (9.2)$$

$$T_r = nT_r; K_{H0} = \frac{4\pi^2 M}{T^2}; G = \frac{K_{H0} T_r}{A_b} \quad (9.3)$$

where A_L is the area of the lead core; A_b is the bonded rubber area, t_c is the rubber cover thickness; and all other variables are defined previously. The geometric and material properties of the six LR bearings are summarized in Table 9-6.

Table 9-6 Geometric and material properties of LR bearing isolation system models

Property	Notation (units)	T2Q6	T2Q12	T2Q18	T3Q6	T3Q12	T3Q18
Lead core diameter	D_i (mm)	217	277	310	172	228	262
Outer diameter	D_o (mm)	1494	1494	1494	1494	1494	1494
Shear modulus	G (MPa)	0.93	0.94	0.95	0.41	0.41	0.42
Horizontal stiffness	K_{H0} (MN/m)	5.29	5.29	5.29	2.35	2.35	2.35
Vertical stiffness	K_{v0} (MN/m)	6623	6506	6431	5272	5175	5109
Buckling load	P_{cr0} (MN)	130	130	130	77	77	77
Cavitation force	F_c (MN)	4.92	4.92	4.92	2.19	2.19	2.19

The parameters of the tensile model (see Chapter 3), k , a , and ϕ_{max} are set equal to 20, 1.0, and 0.75, respectively, for all models. A sensitivity analyses was performed in Section 5.6.2, which showed that the tensile response of an elastomeric bearing is not sensitive to either a or ϕ_{max} , and the values $a = 1.0$ and $\phi_{max} = 0.75$ recover the results of experiments. For the large diameter bearings considered here, a very sharp reduction in the tensile stiffness following cavitation is expected, which is captured by $k = 20$.

9.4 Response-history Analysis

The effect of five characteristics of LR bearings on the response of base-isolated NPP are investigated:

1. Strength degradation in shear due to heating of the lead core (LR bearings)
2. Variation in buckling load due to horizontal displacement
3. Cavitation and post-cavitation behavior due to tensile loading
4. Variation in axial stiffness due to horizontal displacement
5. Variation in shear stiffness due to axial load

The *LeadRubberX* element permits the user to include each of these behaviors, or a combination thereof, in an analysis through a set of tags. OpenSees does not provide an option for modal damping; *Rayleigh* damping is used instead, and the multipliers to the mass and stiffness matrices are calculated by assigning 2% damping to the 1st (torsion) and 6th (axial) modes.

The set of 30 three-component ground motions selected and spectrally matched by Kumar (2015) to be consistent with uniform hazard response spectra (UHRS) for design basis earthquake (DBE) shaking at the site of the Diablo Canyon Nuclear Generating Station are used for response-history analysis (Figure 9-6). The UHRS are calculated for a return period of 10,000 years and 5% damping.

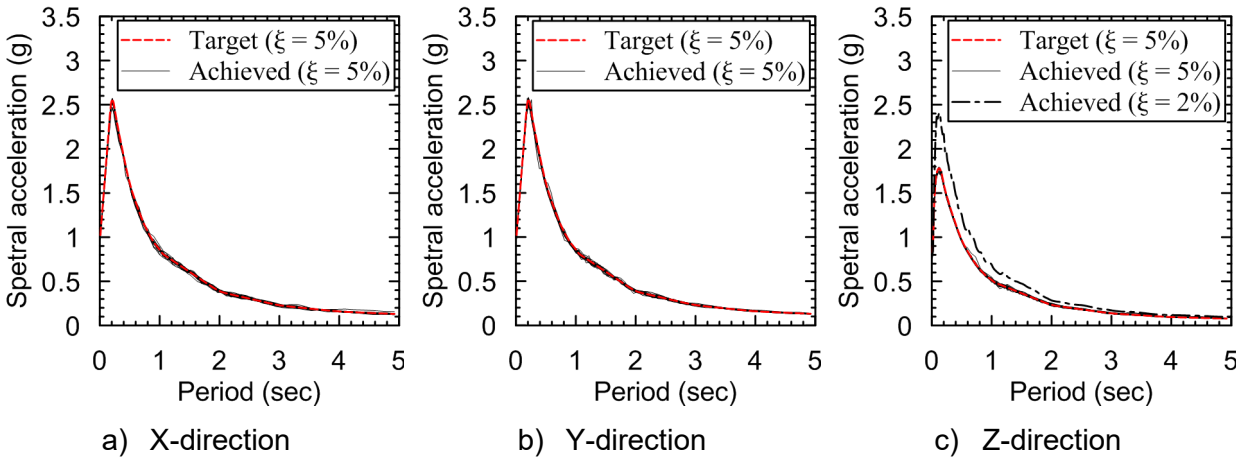


Figure 9-6 Acceleration response spectra of ground motions

Response-history analysis is performed using these 30 sets of ground motions for each of the ten models at intensities of 50% DBE, 100% DBE, 150% DBE, and 200% DBE shaking. The intensity of 150% DBE corresponds to beyond design basis earthquake in Department of Energy (DOE) space (see Huang *et al.* (2009) and Huang *et al.* (2013)). The intensity of 50% DBE is representative of low and moderate seismic hazard at Central and East United States (CEUS) sites. The mean 2% damped vertical spectrum is provided to aid later interpretation of the vertical response of the isolation systems.

The results of the response-history analyses are presented in the following sections. The force and displacement responses of LR bearings are monitored at the center and the four corners of the basemat. The acceleration, velocity and displacement response of the nodes shown with solid circles in Figure 9-4 are monitored.

The peak responses for each ground motion set are assumed to distribute lognormally with arithmetic mean μ , median θ , and logarithmic standard deviation σ , which are computed as:

$$\mu = \frac{1}{n} \sum_{i=1}^n y_i \quad \theta = \exp\left(\frac{1}{n} \sum_{i=1}^n \ln y_i\right) \quad \sigma = \sqrt{\frac{1}{n-1} \sum_{i=1}^n (\ln y_i - \ln \theta)^2} \quad (9.4)$$

where n is the total number of ground motion sets (=30), and y_i is the peak response for i th ground motion set.

The p th percentile (e.g., 50, 90, 99) value, y_p , is calculated as the inverse of the lognormal cumulative distribution function F per Mathworks (2014):

$$y_p = F^{-1}(p | \ln \theta, \sigma) = \{y_p : F(y_p | \ln \theta, \sigma) = p\} \quad (9.5)$$

These percentiles can be calculated with the aid of normal probability table. MATLAB provides a command *logninv* to compute p th percentile values of a lognormal distribution.

9.5 Results of Analysis using the Simplified Isolator Model

The simplified model does not consider any of the five characteristics identified in Section 9.4. For analysis using the simplified model, all tags are set to 0 in *LeadRubberX*. The peak horizontal, compressive and tensile displacements of the bearings at the center (4137) and below the four corners (4001, 4021, 4253, and 4273) of the isolated basemat are presented in Table 9-7 for model T2Q6. In this table, u_c and u_t are the compressive and tensile deformations, u_h and ε_h are the vector sum of deformations and strains, respectively, along the two orthogonal horizontal axes, and D_o is the bonded rubber diameter of the LR bearing. The rigid diaphragm constraint assigned to the basemat ensures that the top node of each bearing connected to the basemat move as if in a rigid plane along the horizontal direction. The peak tensile and compressive deformations in the outer bearings are greater than those near the center of the isolation system due to the rocking motion of the superstructure. The compressive deformation in the bearings due to gravity load is approximately 0.8 mm.

The rotations of the superstructure at the basemat level are summarized in Table 9-8, where θ_z^{\max} is the mean peak torsion about the vertical Z axis, and ϕ_x^{\max} and ϕ_y^{\max} are the mean rotations about horizontal X and Y , respectively, for the 30 ground motion sets. Angles are calculated by the inverse sine of the peak differential displacements between nodes at the opposite corners of the basemat divided by the distance between them. Although these values are small, they result in finite relative horizontal and vertical displacements over the plan dimension of the basemat.

The mean peak zero-period and spectral accelerations in the three orthogonal directions, at the center of basemat, for the 30 ground motion sets are presented in Table 9-9 and Table 9-10, respectively. The zero-period spectral accelerations are consistent with the values obtained from the response spectra in Figure 9-6. Spectral acceleration in the vertical direction is sensitive to how damping is defined for the response-history analysis. The effect of damping on the response of lumped-mass stick model is discussed in a later section.

Mean and 50th, 90th and 99th percentile responses are presented in Appendix C.5, noting that the 90th and 99th percentile responses, for beyond design basis and design basis shaking, respectively, are important thresholds for seismically isolated nuclear structures (Huang *et al.*, 2009; Huang *et al.*, 2013). The horizontal response of isolation system is assumed to be represented by the bearing at the center of the basemat. Vector sums of the shear displacements and forces are calculated at each time step in an analysis and the peak values for a given ground motion are used to form the distributions of response.

Table 9-7 Mean peak displacements (mm) for the 30 ground motion sets at the center and four corners of the basemat (model T2Q6); simplified model

Bearing	100% DBE					200% DBE				
	u_c^{\max}	u_t^{\max}	u_h^{\max}	ε_h^{\max}	u_h^{\max} / D_o	u_c^{\max}	u_t^{\max}	u_h^{\max}	ε_h^{\max}	u_h^{\max} / D_o
4137	1.9	0.3	340	110	0.23	3.0	0.8	851	275	0.57
4001	2.0	0.4	340	110	0.23	3.2	1.6	853	275	0.57
4021	2.0	0.4	335	108	0.22	3.3	1.6	830	268	0.56
4253	2.0	0.4	347	112	0.23	3.2	1.6	875	282	0.59
4273	2.0	0.4	341	110	0.23	3.2	1.6	855	276	0.57

Table 9-8 Mean peak rotations (degrees) for the 30 ground motion sets; simplified model

Model	50% DBE			100% DBE			150% DBE			200% DBE		
	θ_z^{\max}	ϕ_x^{\max}	ϕ_y^{\max}	θ_z^{\max}	ϕ_x^{\max}	ϕ_y^{\max}	θ_z^{\max}	ϕ_x^{\max}	ϕ_y^{\max}	θ_z^{\max}	ϕ_x^{\max}	ϕ_y^{\max}
T2Q6	0.004	0.0003	0.0002	0.016	0.0005	0.0003	0.031	0.0007	0.0004	0.047	0.0010	0.0006
T2Q12	0.003	0.0004	0.0002	0.009	0.0005	0.0003	0.018	0.0007	0.0004	0.031	0.0009	0.0006
T2Q18	0.003	0.0004	0.0003	0.007	0.0006	0.0004	0.013	0.0008	0.0005	0.022	0.0010	0.0006
T3Q6	0.005	0.0002	0.0001	0.013	0.0004	0.0002	0.025	0.0005	0.0003	0.041	0.0007	0.0004
T3Q12	0.005	0.0003	0.0002	0.009	0.0005	0.0003	0.016	0.0006	0.0004	0.026	0.0008	0.0005
T3Q18	0.005	0.0004	0.0003	0.009	0.0006	0.0004	0.014	0.0007	0.0004	0.021	0.0009	0.0005

1. An angle of 0.01 degrees correspond to 17 mm of horizontal displacement over a basemat length of 100 m.
2. An angle of 0.0005 degrees correspond to 1 mm of vertical displacement over a basemat length of 100 m.

Table 9-9 Mean peak zero-period accelerations (g) for the 30 ground motion sets at center of basemat (node 2137); simplified model

Model	50% DBE			100% DBE			150% DBE			200% DBE		
	a_x^{\max}	a_y^{\max}	a_z^{\max}	a_x^{\max}	a_y^{\max}	a_z^{\max}	a_x^{\max}	a_y^{\max}	a_z^{\max}	a_x^{\max}	a_y^{\max}	a_z^{\max}
T2Q6	0.16	0.17	0.56	0.33	0.35	1.11	0.52	0.55	1.66	0.76	0.78	2.23
T2Q12	0.2	0.22	0.56	0.31	0.34	1.12	0.46	0.5	1.65	0.65	0.69	2.23
T2Q18	0.25	0.27	0.56	0.34	0.39	1.12	0.47	0.52	1.68	0.63	1.21	2.25
T3Q6	0.12	0.12	0.6	0.2	0.21	1.19	0.3	0.31	1.79	0.39	0.42	2.34
T3Q12	0.17	0.18	0.6	0.23	0.24	1.2	0.3	0.33	1.8	0.4	0.42	2.4
T3Q18	0.22	0.23	0.6	0.27	0.3	1.21	0.35	0.36	1.81	0.41	0.44	2.41

Table 9-10 Mean peak spectral accelerations (g) for the 30 ground motion sets at center of basemat (node 2137); simplified model

Model	50% DBE			100% DBE			150% DBE			200% DBE		
	a_x^{\max}	a_y^{\max}	a_z^{\max}	a_x^{\max}	a_y^{\max}	a_z^{\max}	a_x^{\max}	a_y^{\max}	a_z^{\max}	a_x^{\max}	a_y^{\max}	a_z^{\max}
T2Q6	0.54	0.55	2.14	1.17	1.15	4.28	2.15	2.11	6.35	3.46	3.33	8.56
T2Q12	0.8	0.91	2.14	1.08	1.1	4.28	1.48	1.49	6.37	2.3	2.26	8.56
T2Q18	1.07	1.14	2.14	1.35	1.48	4.28	1.61	1.65	6.42	1.99	3.29	8.71
T3Q6	0.43	0.42	2.06	0.56	0.59	4.13	0.88	0.93	6.19	1.36	1.42	8.08
T3Q12	0.76	0.69	2.06	0.86	0.84	4.11	0.96	1	6.17	1.12	1.16	8.22
T3Q18	1.06	0.92	2.05	1.19	1.1	4.11	1.3	1.26	6.16	1.39	1.41	8.22

9.6 Results of Analysis using the Advanced Isolator Model

The advanced isolator model considers the five characteristics of LR bearings identified in Section 9.4. The response of base-isolated NPP considering all five characteristics is considered next.

The peak horizontal, compressive and tensile displacements of the bearings are summarized in Table 9-11. All of the bearings undergo approximately the same shear deformation. Rocking of the superstructure induces additional tensile and compressive deformation in the outer bearings.

The rotations of the superstructure at the basemat level are summarized in Table 9-12. A substantial increase in rotation about the horizontal axes is observed with respect to the simplified isolator model of Table 9-9, which is due to cavitation and buckling producing larger axial deformations in the bearings at the higher intensities of ground motion.

The mean peak zero-period and spectral accelerations in the three orthogonal directions, at the center of the basemat, for the 30 ground motion sets, are presented in Table 9-13 and Table 9-14, respectively. The advanced isolator models result in higher accelerations than the simplified isolator models (Table 9-9 and Table 9-10). A substantial increase in the vertical acceleration is observed at higher intensities of ground motion. Spectral acceleration in the vertical direction is sensitive to how damping is defined for the response-history analysis. The effect of damping on the response of lumped-mass stick model is discussed in a later section.

The stick model, unlike the two-node macro model, provides information on cavitation and buckling of individual bearings in an isolation system. The isolation system consists a total of 273 bearings. The outer bearings are more vulnerable to cavitation and buckling than those bearings near the center of the basemat. The number of bearings (of 273) that underwent cavitation and buckling were recorded for each ground motion set. The median numbers for the 30 ground motion sets, at each intensity, are presented in Table 9-15 and Table 9-16 for buckling and cavitation, respectively. All six isolation systems provide adequate safety against buckling even at the higher intensities of shaking, except for T3Q6 at 200%DBE. The flexible (longer period) isolation systems with low strength (e.g., T3Q6) are more vulnerable to buckling. Bearings in the isolation system cavitate at intensities of 100+% DBE shaking due to the intense vertical shaking at the Diablo Canyon site. The period of vibration in the axial direction for the 2 and 3 sec isolation systems are 0.06 and 0.07 sec, respectively, and the 2% damped vertical spectral acceleration at these periods exceed 2.2g at 100% DBE shaking (see Figure 9-6c). (Note that the vertical DBE spectrum is for the surface free field and not a foundation input response spectrum: accounting for input at depth and incoherence should substantially reduce the vertical shaking effects.) Cavitation in bearings can be reduced by increasing the shear modulus, but this option is limited by a manufacturer's ability to produce natural rubber bearings of high shear modulus that do not exhibit scragging or age-related stiffening.

Table 9-11 Mean peak displacements (mm) for 30 ground motion sets at the center and four corners of the basemat (model T2Q6); advanced model

Bearing	100% DBE					200% DBE				
	u_c^{\max}	u_t^{\max}	u_h^{\max}	ε_h^{\max}	u_h^{\max} / D_o	u_c^{\max}	u_t^{\max}	u_h^{\max}	ε_h^{\max}	u_h^{\max} / D_o
4137	2.0	0.3	359	116	0.24	6.3	6.1	981	316	0.66
4001	2.3	0.5	359	116	0.24	8.4	10.0	979	316	0.66
4021	2.2	0.5	352	114	0.24	7.7	10.3	958	309	0.64
4253	2.2	0.4	366	118	0.24	8.1	9.8	1008	325	0.67
4273	2.2	0.4	360	116	0.24	8.0	9.5	988	319	0.66

Table 9-12 Mean peak rotations (degrees) for 30 ground motion sets; advanced model

Model	50% DBE			100% DBE			150% DBE			200% DBE		
	θ_z^{\max}	ϕ_x^{\max}	ϕ_y^{\max}	θ_z^{\max}	ϕ_x^{\max}	ϕ_y^{\max}	θ_z^{\max}	ϕ_x^{\max}	ϕ_y^{\max}	θ_z^{\max}	ϕ_x^{\max}	ϕ_y^{\max}
T2Q6	0.005	0.0003	0.0002	0.018	0.0006	0.0003	0.036	0.0017	0.0013	0.06	0.0056	0.0052
T2Q12	0.003	0.0003	0.0002	0.01	0.0006	0.0003	0.022	0.0014	0.001	0.04	0.0047	0.0042
T2Q18	0.003	0.0004	0.0002	0.007	0.0006	0.0004	0.015	0.0014	0.001	0.028	0.0042	0.0035
T3Q6	0.005	0.0002	0.0001	0.015	0.0006	0.0004	0.033	0.0032	0.003	0.07	0.0072	0.0086
T3Q12	0.005	0.0003	0.0002	0.01	0.0006	0.0004	0.019	0.0032	0.0025	0.034	0.0064	0.0068
T3Q18	0.005	0.0004	0.0002	0.009	0.0008	0.0005	0.015	0.0035	0.0027	0.025	0.0066	0.0062

1. An angle of 0.01 degrees correspond to 17 mm of horizontal displacement over a basemat length of 100 m.
2. An angle of 0.0005 degrees correspond to 1 mm of vertical displacement over a basemat length of 100 m.

Table 9-13 Mean peak zero-period accelerations (g) for 30 ground motion sets at the center of the basemat (node 2137); advanced model

Model	50% DBE			100% DBE			150% DBE			200% DBE		
	a_x^{\max}	a_y^{\max}	a_z^{\max}	a_x^{\max}	a_y^{\max}	a_z^{\max}	a_x^{\max}	a_y^{\max}	a_z^{\max}	a_x^{\max}	a_y^{\max}	a_z^{\max}
T2Q6	0.16	0.18	0.56	0.34	0.36	1.13	0.62	0.67	1.89	1.08	1.2	3.54
T2Q12	0.19	0.22	0.56	0.31	0.34	1.12	0.53	0.6	1.87	0.98	1.1	3.4
T2Q18	0.25	0.26	0.56	0.33	0.38	1.12	0.5	0.6	1.88	0.89	1.03	3.28
T3Q6	0.11	0.12	0.6	0.21	0.23	1.27	0.49	0.59	2.56	0.98	1.13	4.81
T3Q12	0.17	0.18	0.6	0.23	0.26	1.24	0.5	0.64	2.58	0.92	1.04	4.38
T3Q18	0.21	0.22	0.6	0.27	0.31	1.26	0.54	0.7	2.55	0.91	1.1	4.27

Table 9-14 Mean peak spectral accelerations (g) for 30 ground motion sets at center of basemat (node 2137); advanced model

Model	50% DBE			100% DBE			150% DBE			200% DBE		
	a_x^{\max}	a_y^{\max}	a_z^{\max}	a_x^{\max}	a_y^{\max}	a_z^{\max}	a_x^{\max}	a_y^{\max}	a_z^{\max}	a_x^{\max}	a_y^{\max}	a_z^{\max}
T2Q6	0.52	0.54	2.14	1.33	1.29	4.35	3.01	2.72	6.77	4.97	4.62	12.97
T2Q12	0.78	0.88	2.14	1.02	1.06	4.31	1.72	1.82	6.7	3.3	3.38	11.64
T2Q18	1.03	1.11	2.14	1.28	1.38	4.3	1.51	1.78	6.79	2.38	2.85	11.16
T3Q6	0.41	0.4	2.06	0.57	0.66	4.17	1.32	1.81	8.91	2.51	3.22	14.43
T3Q12	0.72	0.65	2.05	0.78	0.8	4.07	1.17	1.99	8.62	2.25	2.99	13.81
T3Q18	1.00	0.88	2.05	1.07	1.04	4.1	1.38	2.24	8.2	2.18	3.27	13.71

Table 9-15 Median number of bearings (of 273) for 30 ground motion sets for which buckling is predicted; advanced model

Intensity (% DBE)	Isolation system					
	T2Q6	T2Q12	T3Q18	T3Q6	T3Q12	T3Q18
50	0	0	0	0	0	0
100	0	0	0	0	0	0
150	0	0	0	0	0	0
200	0	0	0	43	0	0

Table 9-16 Median number of bearings (of 273) for 30 ground motion sets for which cavitation is predicted; advanced model

Intensity (% DBE)	Isolation system					
	T2Q6	T2Q12	T2Q18	T3Q6	T3Q12	T3Q18
50	0	0	0	0	0	0
100	0	0	0	250	243	240
150	273	261	266	273	273	273
200	273	273	273	273	273	273

The ratios of the percentiles of peak shear displacement for the simplified and advanced base-isolated NPP models, considered separately, at different intensities of shaking, are presented in Figure 9-7, where D is the displacement and its subscript denotes the intensity and the percentile of the peak shear displacement. Figure 9-8 presents horizontal displacements obtained using the advanced models normalized by the median DBE horizontal displacement calculated using the simplified model. The plots in the figures can be used to estimate horizontal displacements at 150+% DBE shaking for a range of isolation systems by calculating the median DBE horizontal displacement. For example, the DBE median horizontal displacement obtained using a simplified model can be increased by the ratios presented in Figure 9-8 to address the five intra-earthquake changes in the mechanical properties of LR bearings enumerated in Section 9.4. Note that the ground motions used for these analyses were spectrally matched and do not consider differences in the intensity of shaking along the perpendicular horizontal axes that is observed in recorded ground motions (Huang *et al.*, 2009).

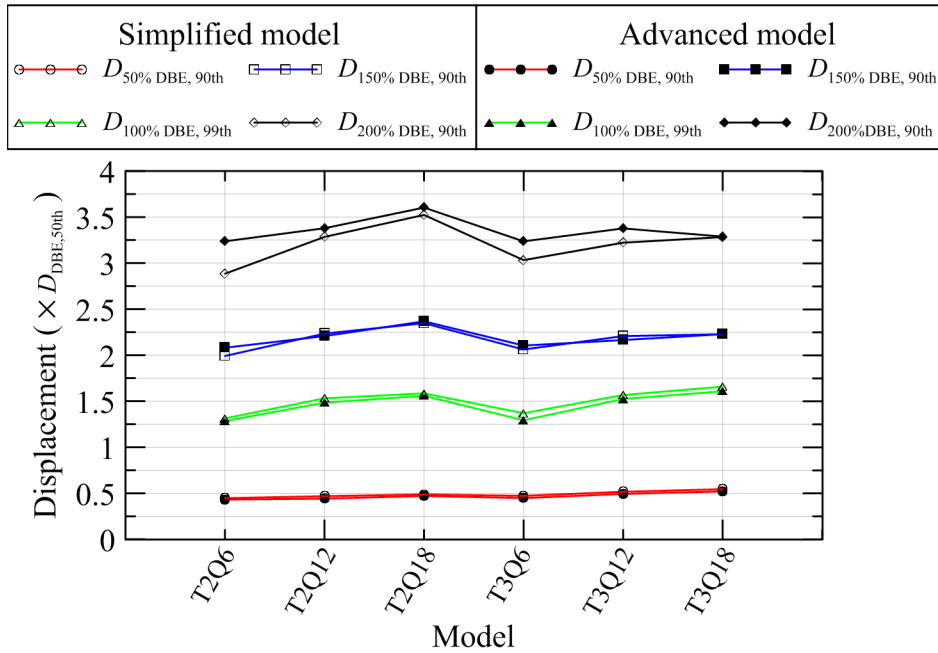


Figure 9-7 Ratios of percentiles of peak horizontal displacement to the median DBE displacement; simplified and advanced models

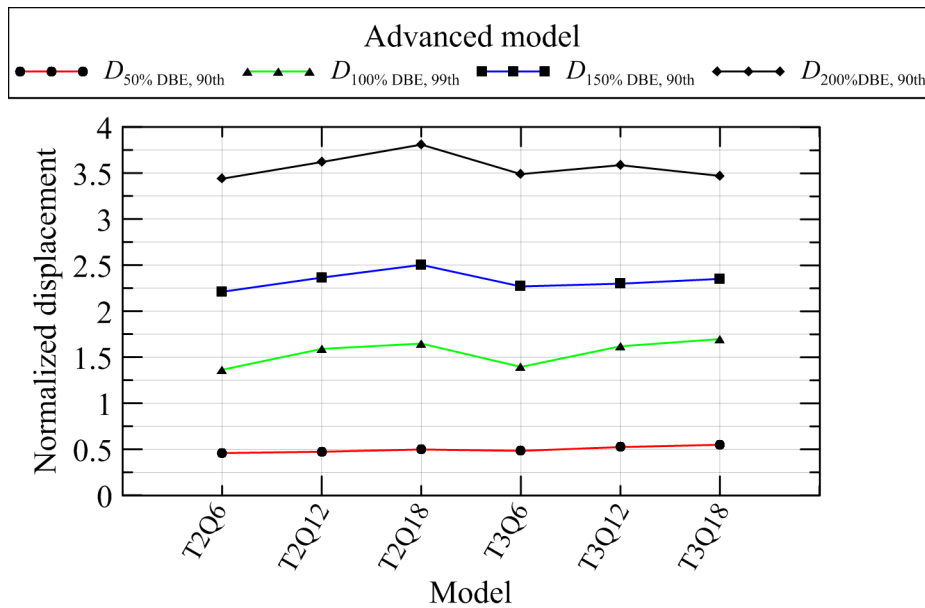


Figure 9-8 Ratios of the percentiles of peak horizontal displacement calculated using the advanced model to the median DBE displacement calculated using the simplified model

9.7 Comparison with Macro-model Analysis

The ratios of the percentiles of the peak horizontal displacement of the two-node macro model to those of the stick model using the simplified and advanced models of LR bearings, at different intensities of shaking, are presented in Figure 9-9 and Figure 9-10, respectively. The differences are small for all three intensities of shaking for the simplified model. Larger differences are observed at 200% DBE shaking using the advanced isolator model due to buckling in the two-node macro model. Differences are most pronounced for models T3Q6 and T3Q12, which are more prone to buckling due to their lower compressive load capacity and higher displacement demands. The shear stiffness (and hence shear displacement) of an elastomeric bearing depends on the axial load. The post-buckling¹ shear response of the two-node macro model, which consists of a single LR bearing, is not reliable in terms of system behavior, whereas the isolation system of the stick model of the base-isolated NPP comprises many bearings, so when one bearing fails, the load is redistributed amongst other bearings in the isolation system. The post-buckling shear response of the stick model will be more reliable than that of the two-node macro model. Results of analysis using the two-node macro model are in better agreement with the stick model for stiffer (smaller period) isolation systems with higher strength (e.g., T2Q12). The stick model of a base-isolated NPP provides additional information on torsional and rocking response and the spatial distribution of cavitation and buckling in the bearings.

¹ The post-buckling capacity of an isolator is assumed to be a small fraction of the buckling load at zero horizontal displacement and a small compressive stiffness is assigned to avoid convergence issues.

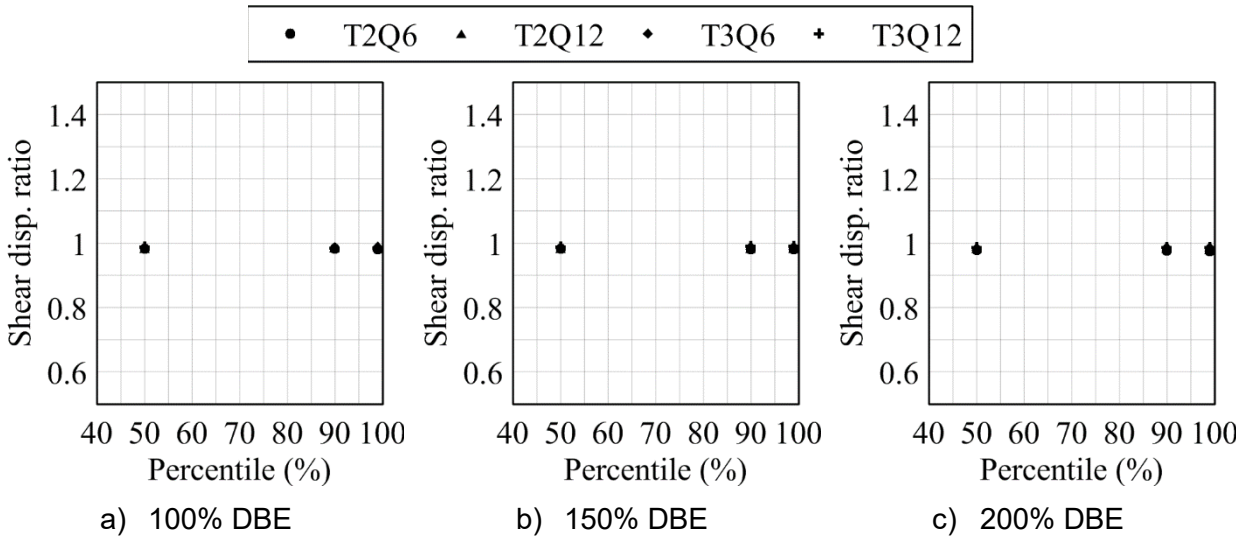


Figure 9-9 Ratios of the percentiles of peak horizontal displacement calculated using the stick model to the two-node macro model; simplified model

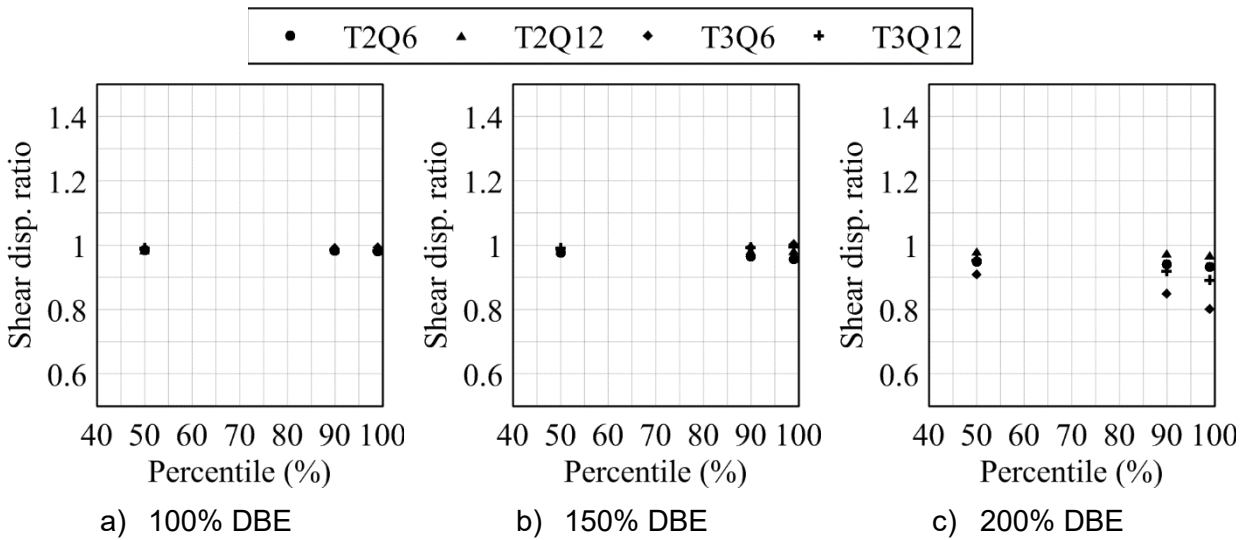


Figure 9-10 Ratios of the percentiles of peak horizontal displacement calculated using the stick model to the two-node macro model; advanced model

9.8 Vertical Accelerations in the Superstructure

The base isolation of a nuclear power plant significantly reduces seismic demand in the horizontal plane but may amplify demand in the vertical direction depending on a) the frequency content of the ground motion, and b) the mechanical properties of the isolation system. Table 9-17 and Table 9-18 present the mean peak ground accelerations and the mean peak zero-period accelerations at the center of the basemat of the base-isolated NPPs, respectively, from response-history analysis of the lumped-mass stick model for the 30 ground motion sets at the site of the Diablo Canyon Nuclear Generating Station (see Section 9.4). The variations of these accelerations along the height of the fixed-base and base-isolated superstructure (T2Q6) are plotted in Figure 9-11. The addition of an isolation system substantially increases response in the Z (vertical) direction. Ground motion 1 (GM1) and the acceleration response at the center of the basemat of the base-isolated NPP (T2Q6) subjected to GM1 are plotted in Figure 9-12. The corresponding response spectra are plotted in Figure 9-13.

The vertical accelerations at locations high in the superstructure (e.g., node 310, 417 in Figure 9-1) are much greater than the peak vertical ground acceleration. This is attributed to 1) the modal properties of this superstructure, and 2) how damping is modeled, both of which are described in the following sections.

Table 9-17 Mean peak ground acceleration (g) for 30 ground motion sets

50% DBE			100% DBE			150% DBE			200% DBE		
a_x^{\max}	a_y^{\max}	a_z^{\max}	a_x^{\max}	a_y^{\max}	a_z^{\max}	a_x^{\max}	a_y^{\max}	a_z^{\max}	a_x^{\max}	a_y^{\max}	a_z^{\max}
0.52	0.52	0.41	1.03	1.04	0.82	1.55	1.56	1.23	2.06	2.08	1.64

Table 9-18 Mean peak zero-period accelerations (g) for 30 ground motion sets at the center of the basemat; base-isolated NPP

Model	50% DBE			100% DBE			150% DBE			200% DBE		
	a_x^{\max}	a_y^{\max}	a_z^{\max}	a_x^{\max}	a_y^{\max}	a_z^{\max}	a_x^{\max}	a_y^{\max}	a_z^{\max}	a_x^{\max}	a_y^{\max}	a_z^{\max}
T2Q6	0.16	0.17	0.56	0.33	0.35	1.11	0.52	0.55	1.66	0.76	0.78	2.23
T2Q12	0.2	0.22	0.56	0.31	0.34	1.12	0.46	0.5	1.65	0.65	0.69	2.23
T2Q18	0.25	0.27	0.56	0.34	0.39	1.12	0.47	0.52	1.68	0.63	1.21	2.25
T3Q6	0.12	0.12	0.6	0.2	0.21	1.19	0.3	0.31	1.79	0.39	0.42	2.34
T3Q12	0.17	0.18	0.6	0.23	0.24	1.2	0.3	0.33	1.8	0.4	0.42	2.4
T3Q18	0.22	0.23	0.6	0.27	0.3	1.21	0.35	0.36	1.81	0.41	0.44	2.41

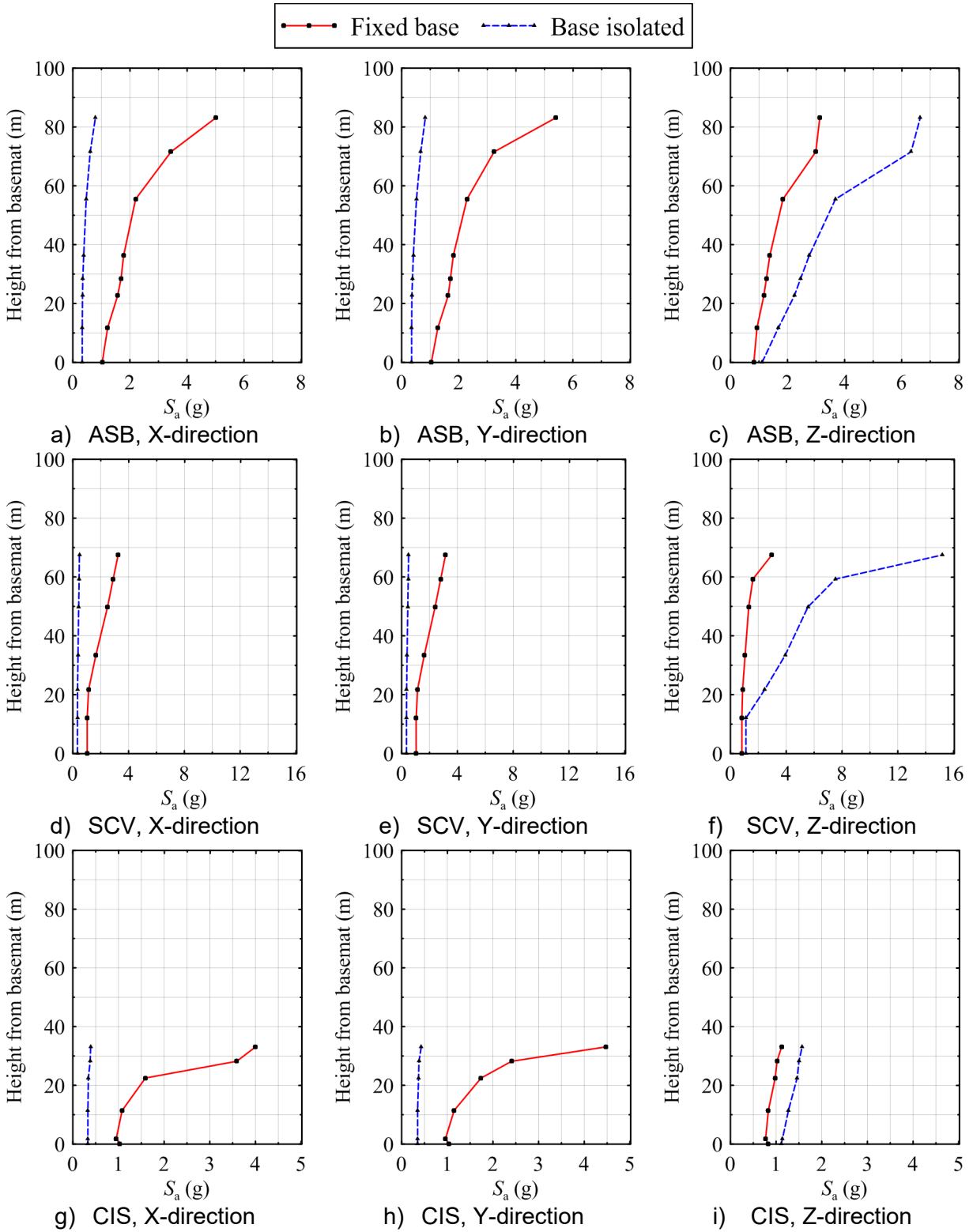


Figure 9-11 Mean peak zero-period accelerations (g) for 30 ground motion sets in the superstructure along the height for the model T2Q6; 100% DBE shaking

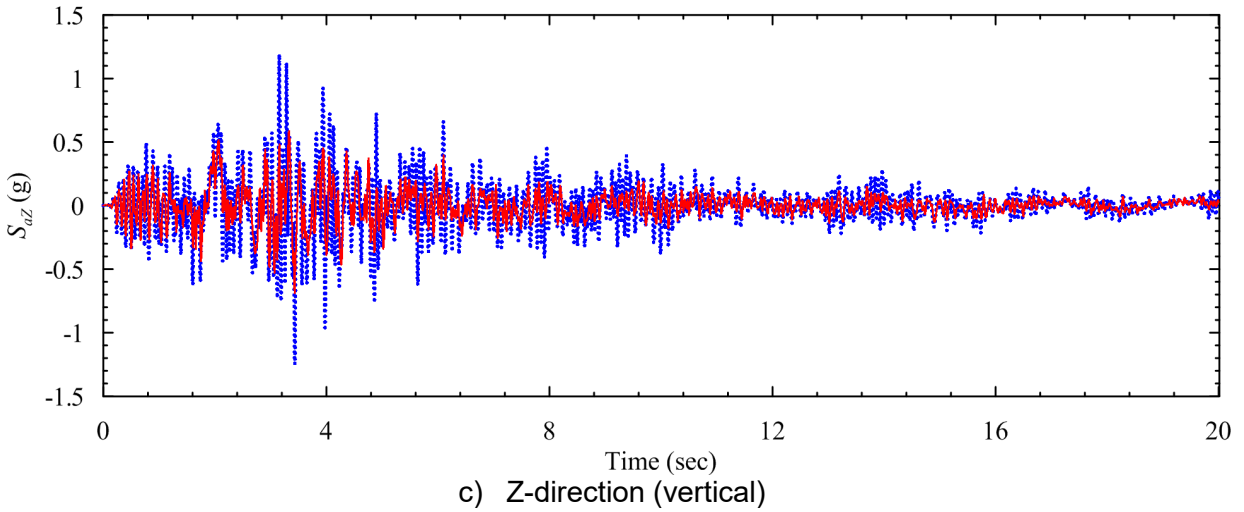
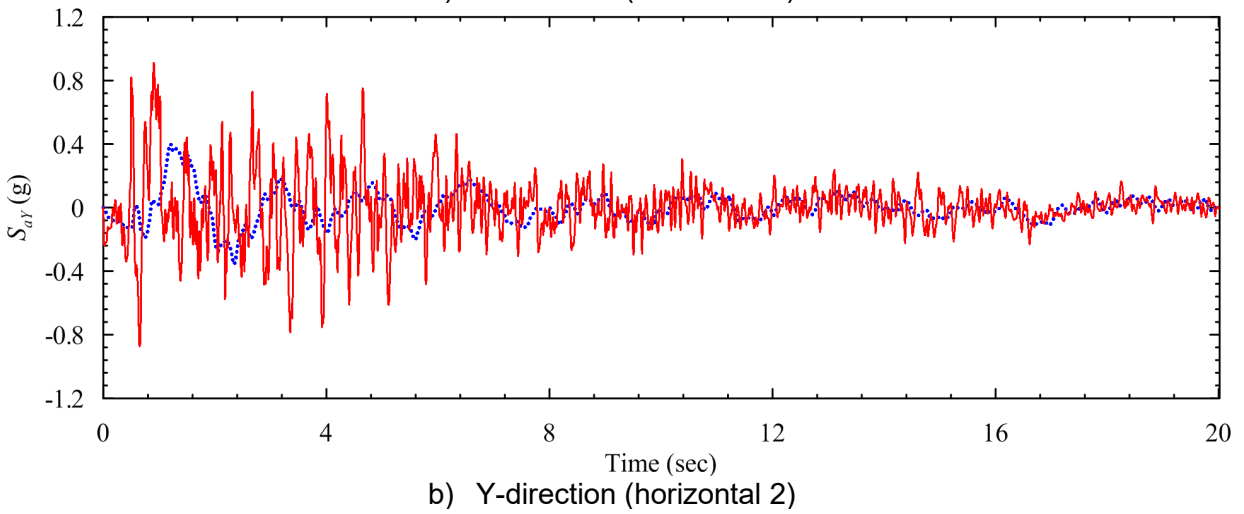
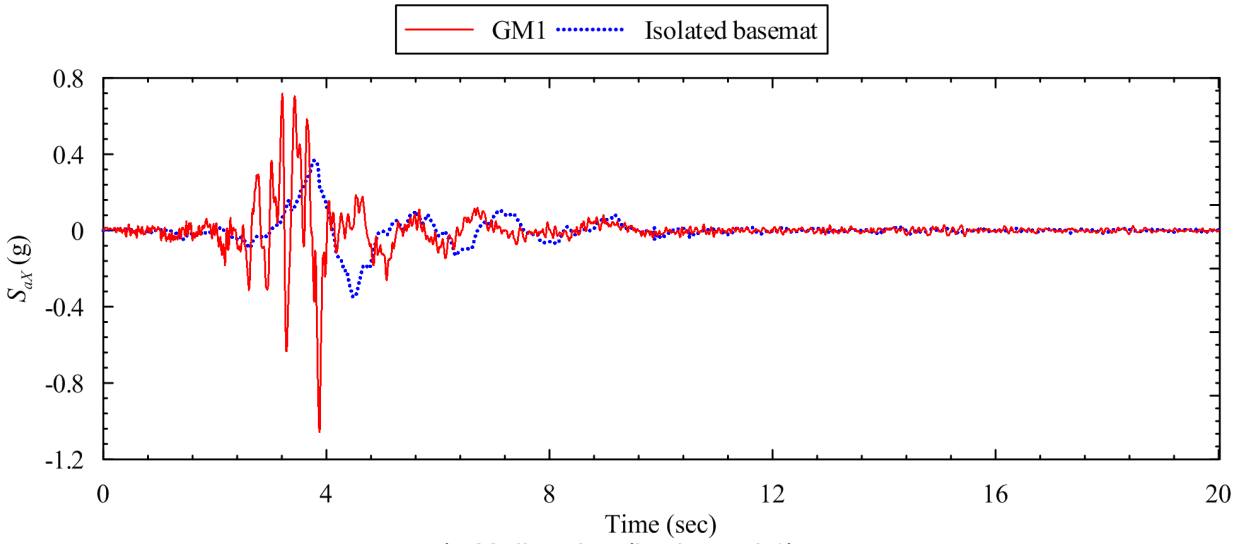


Figure 9-12 Acceleration histories at node 2137 of model T2Q6 subject to GM1; 100% DBE shaking

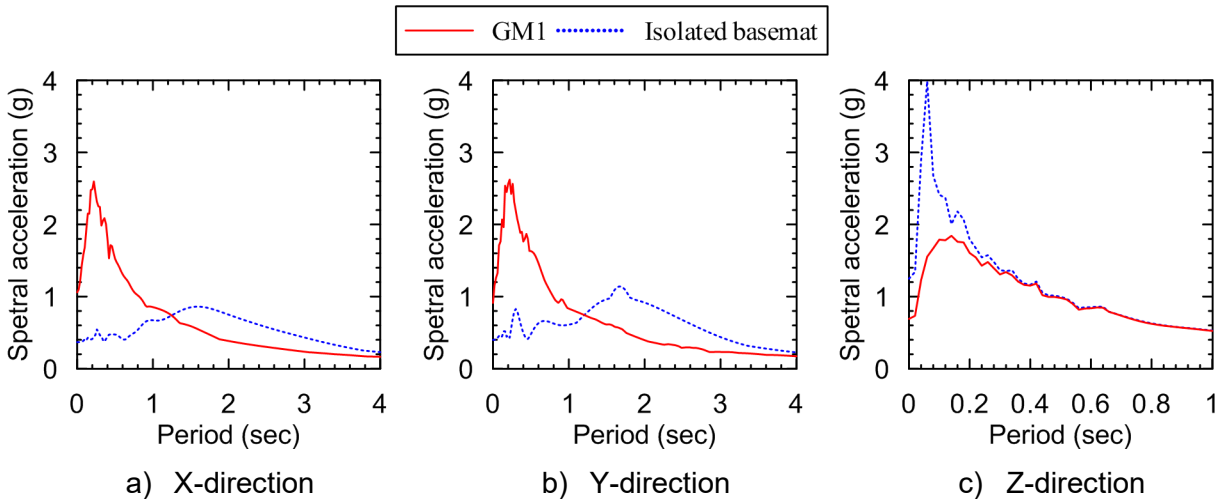


Figure 9-13 Acceleration response spectra at node 2137 of model T2Q6 subject to GM1; 100% DBE shaking

9.8.1 Modal properties

The power spectral densities of the ground acceleration (GM1) and the isolated basemat acceleration (model T2Q6) are shown in Figure 9-14. The vertical frequency of the isolation system at zero lateral displacement is 16 Hz. The predominant frequency² of the vertical accelerations of the ground motion and isolated basemat are 7 Hz and 16 Hz, respectively. The superstructure experiences the vertical acceleration of the isolated basemat. The first vertical frequency of the fixed-base SCV and the CIS, and the second vertical frequency of the ASB are 16, 32, and 19 Hz, respectively (Table 9-2 through Table 9-4). An input excitation frequency close to these natural frequencies will result in a significant amplification of motion, which is why the vertical accelerations of the SCV and ASB are high, but that of the CIS is (relatively) low, as shown in Figure 9-11.

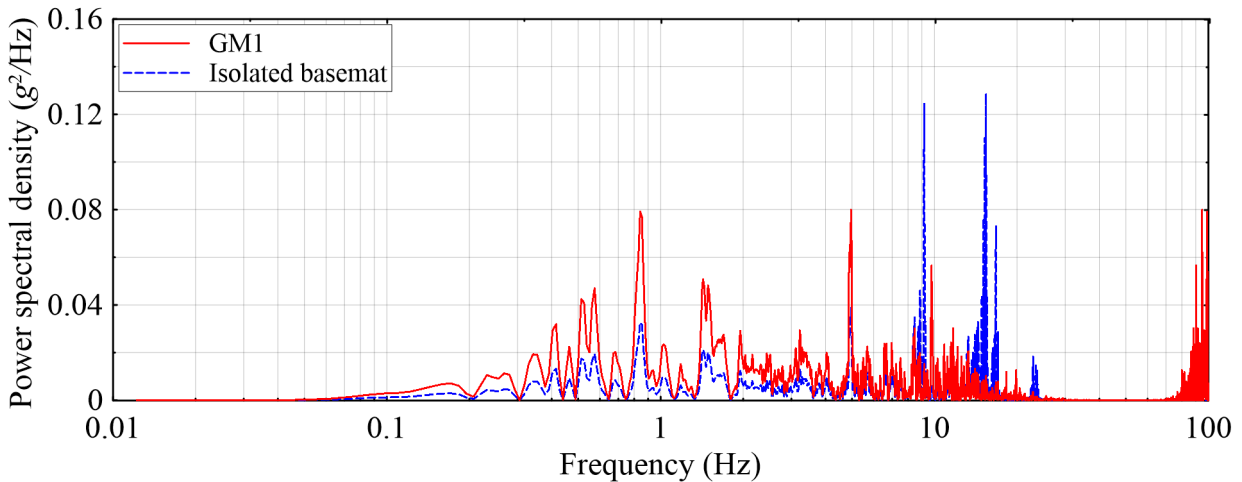


Figure 9-14 Power spectral density of vertical acceleration for model T2Q6 subject to GM1; 100% DBE shaking

² Frequency corresponding to the peak value of the Fourier amplitude spectrum.

9.8.2 Damping

Damping of the horizontal response of a LR-isolated NPP is provided by hysteretic energy dissipation in the lead cores of the bearings. Damping will be in the range of 10% to 30% of critical. A bidirectional hysteretic model is used in the horizontal direction for response-history analysis to capture energy dissipation (damping) explicitly.

Damping in the LR isolators in the vertical direction will be of the order of 2% to 4% of critical, and this can be considered viscous. OpenSees provides three options for including viscous damping in dynamic analysis: 1) mass-proportional, 2) stiffness-proportional, and 3) Rayleigh. The general formulation of the damping matrix C is:

$$C = \alpha M + \beta K \quad (9.6)$$

where M and K are the global mass and stiffness matrices, respectively, and α and β are proportionality coefficients, which are calculated by assigning damping ratios to selected modes. The coefficients α and β are zero for stiffness and mass proportional damping, respectively.

The effects of these three damping models on the response of the lumped-mass stick model of base-isolated NPP are investigated here. The responses of the base-isolated NPP in the horizontal and vertical directions are mostly due to shear and axial deformations in the LR bearings. The multipliers to the mass and stiffness matrices, α and β , were calculated using Equation (8.2) by assigning 2% damping to the modes (frequencies) corresponding to the vertical ($f = 17.7$ Hz) and torsional excitation ($f = 0.27$ Hz) of the single LR bearing (i.e., two-node macro model³). This ensured that the contribution of Rayleigh damping to the modes corresponding to response of base-isolated NPP in the shearing and torsional directions were bounded and small. The variation of modal damping ratio with frequency is presented in Figure 9-15 for the three damping models. The mass and stiffness proportional damping models overdamps the lower and higher modes of vibration, respectively, of the structure.

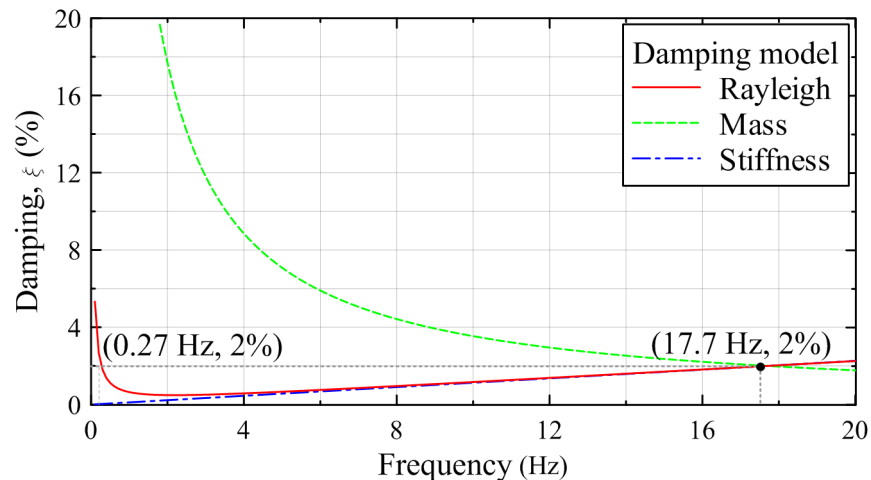


Figure 9-15 Variation of modal damping ratios with frequency

³ The two-node macro model is a simplified representation of the lumped-mass stick model of a base-isolated NPP and both models have the same isolation frequencies in the horizontal and vertical directions.

The damping ratios corresponding to the vertical and horizontal isolation frequencies of the lumped-mass stick model are presented in Table 9-19. The isolation systems *T2Qy* and *T3Qy* have horizontal isolation periods of 2 sec and 3 sec, respectively. The damping ratios corresponding to the horizontal and vertical frequencies of the superstructure (i.e., ASB, SCV, CIS) are presented in Table 9-20 through Table 9-22. The damping ratio corresponding to the horizontal isolation frequency of the isolation system is excessive for mass proportional damping, but small and tiny for Rayleigh and stiffness proportional damping, respectively. Similarly, the damping ratios corresponding to horizontal and vertical frequencies of the reinforced concrete superstructure, where an expected value is between 4% and 7%, generally fall well outside this range.

Response-history analysis of the the lumped-mass stick model of the base-isolated NPP was performed using the three viscous damping models described above. The mean peak zero-period accelerations and the percentiles of the peak horizontal displacements at the center of the basemat are presented in Table 9-23 through Table 9-25 and Table 9-26 through Table 9-28, respectively. No effect of the choice of damping model is observed on basemat acceleration, but much smaller horizontal displacements of the basemat are obtained when mass proportional damping is used. There is no meaningful difference between the horizontal displacements obtained using the Rayleigh and stiffness proportional damping.

The variations of mean peak zero-period acceleration along the height of the superstructure are plotted in Figure 9-16. All three damping models provide similar accelerations along the height of the superstructure. This counterintuitive observation can be explained using mean floor spectra at the center of the isolated basemat. Figure 9-17 presents such spectra for the 30 ground motion sets for the three damping models, for the ASB, SCV and CIS, in the X-, Y- and Z-directions. The fundamental frequency for the substructure (e.g., CIS) in the direction considered (e.g., Z-direction, CIS, in Figure 9-17i) is identified: see Table 9-20 through Table 9-22 for details. The floor spectra are generated for the damping calculated for each model at the fundamental frequency. The damping ratios in the legends of Figure 9.17 are those reported in Table 9-20 through Table 9-22. The first mode responses are similar in each direction for each substructure, except for the ASB and CIS in the Z-direction. The relative spectral amplitudes of Figure 9-17c and Figure 9-17i are consistent with the zero-period accelerations plotted in Figure 9-16c and Figure 9-16i, respectively. It is highly unlikely this outcome would be observed for substructures in other NPPs.

Although Rayleigh and stiffness proportional damping are suitable for the calculation of isolation level response as both provide similar estimate of acceleration and displacement response (see Table 9-23 through Table 9-28), none of the three formulations discussed here adequately damp the superstructure response. An alternate method to assign damping is discussed in the following subsection to address this issue.

Table 9-19 Damping ratios corresponding to isolation frequency

Direction	Frequency (Hz)	Damping (%)		
		Rayleigh ($\alpha = 0.067, \beta = 3.5 \times 10^{-4}$)	Mass proportional ($\alpha = 4.45$)	Stiffness proportional ($\beta = 3.6 \times 10^{-4}$)
Vertical	17.7	2.0	2.0	2.0
Horizontal (T2Qy)	0.5	1.12	70.8	0.06
Horizontal (T3Qy)	0.33	1.65	107.3	0.04

Table 9-20 Damping ratios corresponding to the frequencies of the ASB

Direction	Frequency (Hz)	Damping (%)		
		Rayleigh	Mass	Stiffness
Horizontal 1	3.0	0.5	11.8	0.3
Horizontal 2	2.8	0.5	12.6	0.3
Vertical	7.0	0.9	5.1	0.8

Table 9-21 Damping ratios corresponding to the frequencies of the SCV

Direction	Frequency (Hz)	Damping (%)		
		Rayleigh	Mass	Stiffness
Horizontal 1	5.5	0.7	6.4	0.6
Horizontal 2	3.6	0.5	9.8	0.4
Vertical	16.2	1.8	2.2	1.8

Table 9-22 Damping ratios corresponding to the frequencies of the CIS

Direction	Frequency (Hz)	Damping (%)		
		Rayleigh	Mass	Stiffness
Horizontal 1	12.9	1.5	2.7	1.5
Horizontal 2	12.3	1.4	2.9	1.4
Vertical	31.9	3.6	1.1	3.6

Table 9-23 Mean peak zero-period accelerations (g) for 30 ground motion sets at the center of the basemat (node 2137); Rayleigh damping

Model	50% DBE			100% DBE			150% DBE			200% DBE		
	a_x^{\max}	a_y^{\max}	a_z^{\max}	a_x^{\max}	a_y^{\max}	a_z^{\max}	a_x^{\max}	a_y^{\max}	a_z^{\max}	a_x^{\max}	a_y^{\max}	a_z^{\max}
T2Q6	0.16	0.17	0.56	0.33	0.35	1.11	0.52	0.55	1.66	0.76	0.78	2.23
T2Q12	0.2	0.22	0.56	0.31	0.34	1.12	0.46	0.5	1.65	0.65	0.69	2.23
T2Q18	0.25	0.27	0.56	0.34	0.39	1.12	0.47	0.52	1.68	0.63	1.21	2.25
T3Q6	0.12	0.12	0.6	0.2	0.21	1.19	0.3	0.31	1.79	0.39	0.42	2.34
T3Q12	0.17	0.18	0.6	0.23	0.24	1.2	0.3	0.33	1.8	0.4	0.42	2.4
T3Q18	0.22	0.23	0.6	0.27	0.3	1.21	0.35	0.36	1.81	0.41	0.44	2.41

Table 9-24 Mean peak zero-period accelerations (g) for 30 ground motion sets at the center of the basemat (node 2137); mass proportional damping

Model	50% DBE			100% DBE			150% DBE			200% DBE		
	a_x^{\max}	a_y^{\max}	a_z^{\max}	a_x^{\max}	a_y^{\max}	a_z^{\max}	a_x^{\max}	a_y^{\max}	a_z^{\max}	a_x^{\max}	a_y^{\max}	a_z^{\max}
T2Q6	0.19	0.2	0.56	0.35	0.35	1.12	0.51	0.51	1.68	0.67	0.67	2.24
T2Q12	0.23	0.24	0.56	0.38	0.39	1.12	0.53	0.54	1.69	0.69	0.7	2.25
T2Q18	0.27	0.27	0.56	0.42	0.43	1.13	0.57	0.59	1.69	0.72	0.74	2.25
T3Q6	0.17	0.18	0.61	0.31	0.31	1.22	0.44	0.44	1.84	0.58	0.57	2.45
T3Q12	0.2	0.21	0.61	0.34	0.35	1.23	0.48	0.48	1.84	0.61	0.61	2.46
T3Q18	0.22	0.23	0.61	0.38	0.39	1.23	0.51	0.53	1.84	0.64	0.66	2.46

Table 9-25 Mean peak zero-period accelerations (g) for 30 ground motion sets at the center of the basemat (node 2137); stiffness proportional damping

Model	50% DBE			100% DBE			150% DBE			200% DBE		
	a_x^{\max}	a_y^{\max}	a_z^{\max}	a_x^{\max}	a_y^{\max}	a_z^{\max}	a_x^{\max}	a_y^{\max}	a_z^{\max}	a_x^{\max}	a_y^{\max}	a_z^{\max}
T2Q6	0.16	0.17	0.56	0.34	0.36	1.12	0.56	0.59	1.67	0.82	0.84	2.23
T2Q12	0.2	0.22	0.56	0.32	0.35	1.12	0.49	0.53	1.68	0.69	0.73	2.24
T2Q18	0.26	0.27	0.56	0.34	0.39	1.12	0.48	0.52	1.68	0.62	0.68	2.24
T3Q6	0.12	0.12	0.6	0.2	0.21	1.19	0.3	0.32	1.79	0.41	0.45	2.39
T3Q12	0.17	0.18	0.6	0.23	0.24	1.19	0.31	0.33	1.8	0.39	0.42	2.4
T3Q18	0.22	0.23	0.6	0.28	0.3	1.21	0.34	0.36	1.81	0.42	0.45	2.41

Table 9-26 Percentiles of peak horizontal displacement (mm) for 30 ground motion sets at the center of the basemat (node 2137); Rayleigh damping

Model	50% DBE			100% DBE			150% DBE			200% DBE			
	μ	50 th	90 th	σ	50 th	90 th	σ	50 th	90 th	σ	50 th	90 th	σ
T2Q6	121	119	151	0.18	340	338	393	0.12	571	547	887	0.38	851
T2Q12	87	86	112	0.21	243	239	302	0.18	436	408	780	0.51	669
T2Q18	76	75	94	0.18	197	193	249	0.2	364	358	453	0.18	567
T3Q6	140	138	176	0.19	376	373	443	0.14	674	670	769	0.11	964
T3Q12	113	110	142	0.2	280	275	352	0.19	500	494	607	0.16	752
T3Q18	104	103	129	0.18	238	230	329	0.28	420	412	528	0.19	616

Table 9-27 Percentiles of peak horizontal displacement (mm) for 30 ground motion sets at the center of the basemat (node 2137); mass proportional damping

Model	50% DBE			100% DBE			150% DBE			200% DBE			
	μ	50 th	90 th	σ	50 th	90 th	σ	50 th	90 th	σ	50 th	90 th	σ
T2Q6	53	52	68	0.21	123	122	152	0.17	197	195	239	0.16	272
T2Q12	45	44	56	0.18	106	103	135	0.21	175	172	218	0.18	247
T2Q18	41	41	49	0.16	95	93	123	0.21	159	155	203	0.21	228
T3Q6	62	61	80	0.21	143	141	180	0.19	230	226	288	0.19	318
T3Q12	57	56	70	0.18	125	122	160	0.21	204	200	257	0.2	288
T3Q18	55	55	67	0.15	118	115	148	0.2	188	184	240	0.21	265

Table 9-28 Percentiles of peak horizontal displacement (mm) for 30 ground motion sets at the center of the basemat (node 2137); stiffness proportional damping

Model	50% DBE			100% DBE			150% DBE			200% DBE			
	μ	50 th	90 th	σ	50 th	90 th	σ	50 th	90 th	σ	50 th	90 th	σ
T2Q6	125	123	155	0.18	354	352	410	0.12	621	617	714	0.11	918
T2Q12	89	87	114	0.21	249	245	310	0.18	468	463	554	0.14	709
T2Q18	77	76	96	0.18	196	188	278	0.3	374	368	466	0.18	564
T3Q6	142	140	179	0.19	387	384	455	0.13	697	693	797	0.11	1034
T3Q12	114	112	144	0.2	280	269	408	0.33	510	504	619	0.16	755
T3Q18	106	104	131	0.18	246	240	317	0.22	412	390	659	0.41	648

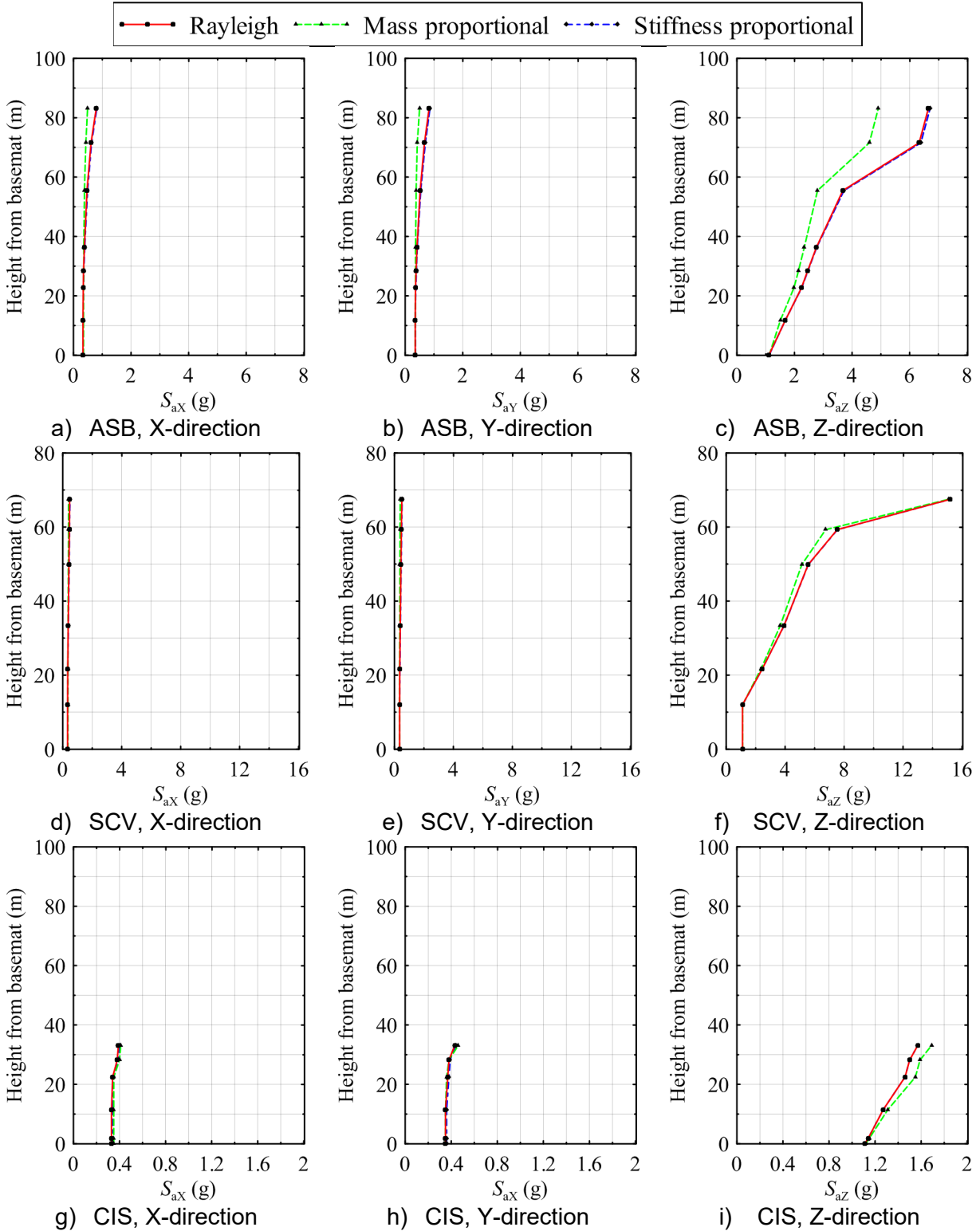


Figure 9-16 Mean peak zero-period accelerations (g) for 30 ground motion sets in the superstructure along the height of the base-isolated NPP model T2Q6; 100% DBE shaking

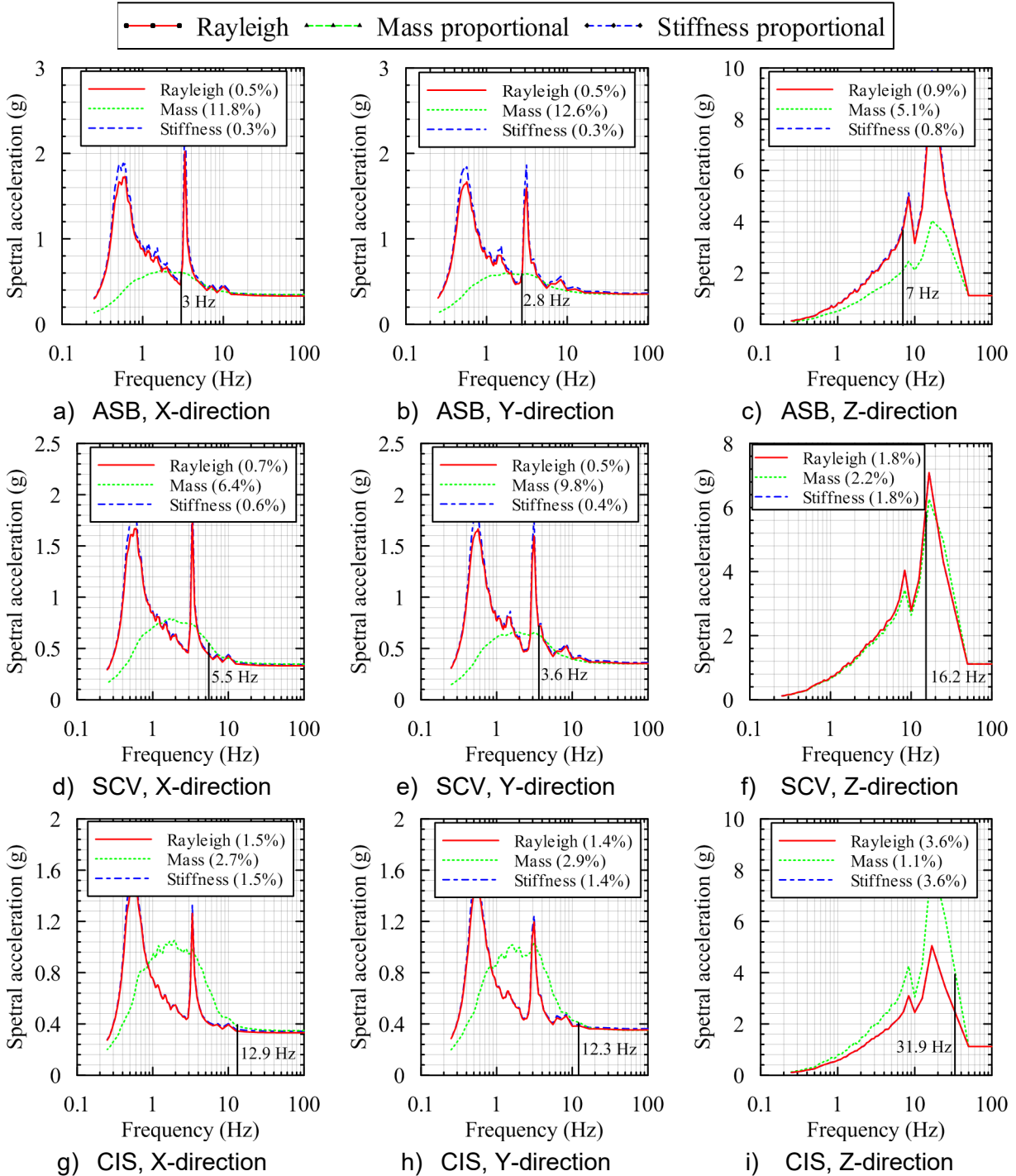


Figure 9-17 Mean floor response spectra for 30 ground motion sets at the center of the isolated basemat (node 2137) for three damping models and corresponding modal damping ratios in the superstructure; T2Q6, 100% DBE shaking

9.8.3 Substructuring

An alternative approach is explored here to capture the vertical acceleration response at higher locations in the superstructure, where the increases in acceleration response of Figure 9-11c), f) and i) might result from an inadequate treatment of damping. This analysis approach uses a substructuring technique in which the six components of acceleration response are obtained at the center of the isolated basemat (node 2137) and used as input excitations for the response-history analysis of the three fixed-base components of the superstructure (i.e., ASB, CIS, and SCV). The response-history analyses of the three superstructure components are performed in OpenSees and SAP2000. These models are designated as the equivalent fixed-base (EFB) models in OpenSees (EFB_OpenSees) and SAP2000 (EFB_SAP2000). The results of the response-history analysis of these models are benchmarked against the response of the lumped-mass stick model of base-isolated NPP (Stick_model_OpenSees) presented in Section 9.5. The simplified isolator model is used for all analyses because the focus here is on utility of the substructuring approach.

The Rayleigh damping formulation is used in OpenSees and the proportionality coefficients are calculated for EFB_OpenSees by assigning 5% damping (i.e., between 4% and 7%) to the first horizontal and vertical translational modes of vibration of each superstructure. This ensures that the contribution of Rayleigh damping to other modes in the horizontal and vertical directions are bounded and small. Table 9-29 presents the damping ratios in the first mode of vibration along the three orthogonal directions of the ASB, SCV, and CIS.

Table 9-29 Rayleigh damping in the horizontal and vertical modes of the fixed-base superstructures in OpenSees

Direction	ASB		SCV		CIS	
	Frequency (Hz)	Damping (%)	Frequency (Hz)	Damping (%)	Frequency (Hz)	Damping (%)
Horizontal 1	3.0	4.9	5.5	4.1	12.9	4.9
Horizontal 2	2.8	5.0	3.6	5.0	12.3	5.0
Vertical	7.0	5.0	16.2	5.0	31.9	5.0

The results of the response-history analysis obtained using OpenSees (EFB_OpenSees) and base-isolated NPP in Section 9.5 and their differences are presented in Table 9-30, Table 9-31, and Table 9-32 respectively, for node 417, which is located at the uppermost point of the SCV. A substantial reduction of the order of 30% is observed in the vertical acceleration across all shaking intensities when the equivalent fixed-based model approach is used. The reductions in the horizontal accelerations are small, except at smaller shaking intensities.

SAP2000 provides the option to assign modal damping in response-history analysis of a MDOF system. Damping of 5% is used for all modes in the SAP2000 model. Acceleration histories at node 417 in the SCV obtained using EFB_OpenSees, EFB_SAP2000 and the base-isolated OpenSees model, for isolation system T2Q6 subject to ground motion 1, are plotted in Figure 9-18. The difference in responses obtained using 5% modal damping in SAP2000 and 5% Rayleigh damping in OpenSees are negligible in all three directions, which suggests that the Rayleigh damping in OpenSees and modal damping in SAP2000 provides similar results for the EFB models. Moreover, it suggests that Rayleigh damping based on vertical frequency does not overdamp response in the horizontal directions though this is dependent on the vertical and horizontal frequencies of the ASB, SCV, and CIS. Results of analysis of the EFB_OpenSees

model are presented in Table 9-33 through Table 9-35 and Figure 9-19 for the uppermost point in the ASB (node 310), and Table 9-36 through Table 9-38 and Figure 9-20 for the uppermost point in the CIS (node 538). A reduction of the order of 30% is observed in the ASB when the substructuring approach is used. The reductions in the horizontal accelerations are small. Unlike the SCV and ASB, the accelerations in the three orthogonal directions at node 538 in the CIS obtained using the substructuring approach are similar to that obtained from the lumped-mass stick model of base-isolated NPP.

Table 9-30 Mean peak zero-period accelerations (g) for 30 ground motion sets at node 417; lumped-mass stick model

Model	50% DBE			100% DBE			150% DBE			200% DBE		
	a_x^{\max}	a_y^{\max}	a_z^{\max}	a_x^{\max}	a_y^{\max}	a_z^{\max}	a_x^{\max}	a_y^{\max}	a_z^{\max}	a_x^{\max}	a_y^{\max}	a_z^{\max}
T2Q6	0.29	0.32	7.6	0.47	0.5	15.2	0.68	0.7	22.46	0.91	0.94	30.4
T2Q12	0.36	0.39	7.6	0.57	0.63	15.21	0.75	0.78	22.57	0.94	0.98	30.41
T2Q18	0.42	0.45	7.61	0.63	0.73	15.21	0.85	0.95	22.82	1.05	1.62	30.4
T3Q6	0.17	0.19	6.71	0.27	0.3	13.42	0.38	0.41	20.13	0.5	0.53	26.36
T3Q12	0.23	0.24	6.61	0.34	0.38	13.22	0.45	0.48	19.84	0.53	0.59	26.45
T3Q18	0.27	0.29	6.53	0.4	0.43	13.05	0.5	0.56	19.58	0.61	0.65	26.11

Table 9-31 Mean peak zero-period accelerations (g) for 30 ground motion sets at node 417; equivalent fixed-base model in OpenSees (EFB_OpenSees)

Model	50% DBE			100% DBE			150% DBE			200% DBE		
	a_x^{\max}	a_y^{\max}	a_z^{\max}	a_x^{\max}	a_y^{\max}	a_z^{\max}	a_x^{\max}	a_y^{\max}	a_z^{\max}	a_x^{\max}	a_y^{\max}	a_z^{\max}
T2Q6	0.22	0.28	4.94	0.38	0.47	9.88	0.58	0.67	14.57	0.82	0.93	19.76
T2Q12	0.28	0.34	4.95	0.44	0.56	9.9	0.59	0.74	14.85	0.76	0.94	19.8
T2Q18	0.35	0.39	4.96	0.5	0.63	9.91	0.65	0.85	14.87	0.81	1.03	19.83
T3Q6	0.14	0.18	4.88	0.23	0.28	9.77	0.33	0.4	14.65	0.44	0.55	19.53
T3Q12	0.2	0.24	4.84	0.29	0.36	9.68	0.37	0.47	14.51	0.46	0.58	19.35
T3Q18	0.25	0.29	4.8	0.34	0.42	9.6	0.43	0.53	14.4	0.52	0.64	19.19

Table 9-32 Percentage reduction in means of peak zero-period accelerations (g) for 30 ground motion sets at node 417 obtained using the lumped-mass stick model and the equivalent fixed-base model in OpenSees (EFB_OpenSees)

Model	50% DBE			100% DBE			150% DBE			200% DBE		
	a_x^{\max}	a_y^{\max}	a_z^{\max}	a_x^{\max}	a_y^{\max}	a_z^{\max}	a_x^{\max}	a_y^{\max}	a_z^{\max}	a_x^{\max}	a_y^{\max}	a_z^{\max}
T2Q6	24	13	35	19	6	35	15	4	35	10	1	35
T2Q12	22	13	35	23	11	35	21	5	34	19	4	35
T2Q18	17	13	35	21	14	35	24	11	35	23	36	35
T3Q6	18	5	27	15	7	27	13	2	27	12	4	26
T3Q12	13	0	27	15	5	27	18	2	27	13	2	27
T3Q18	7	0	26	15	2	26	14	5	26	15	2	27

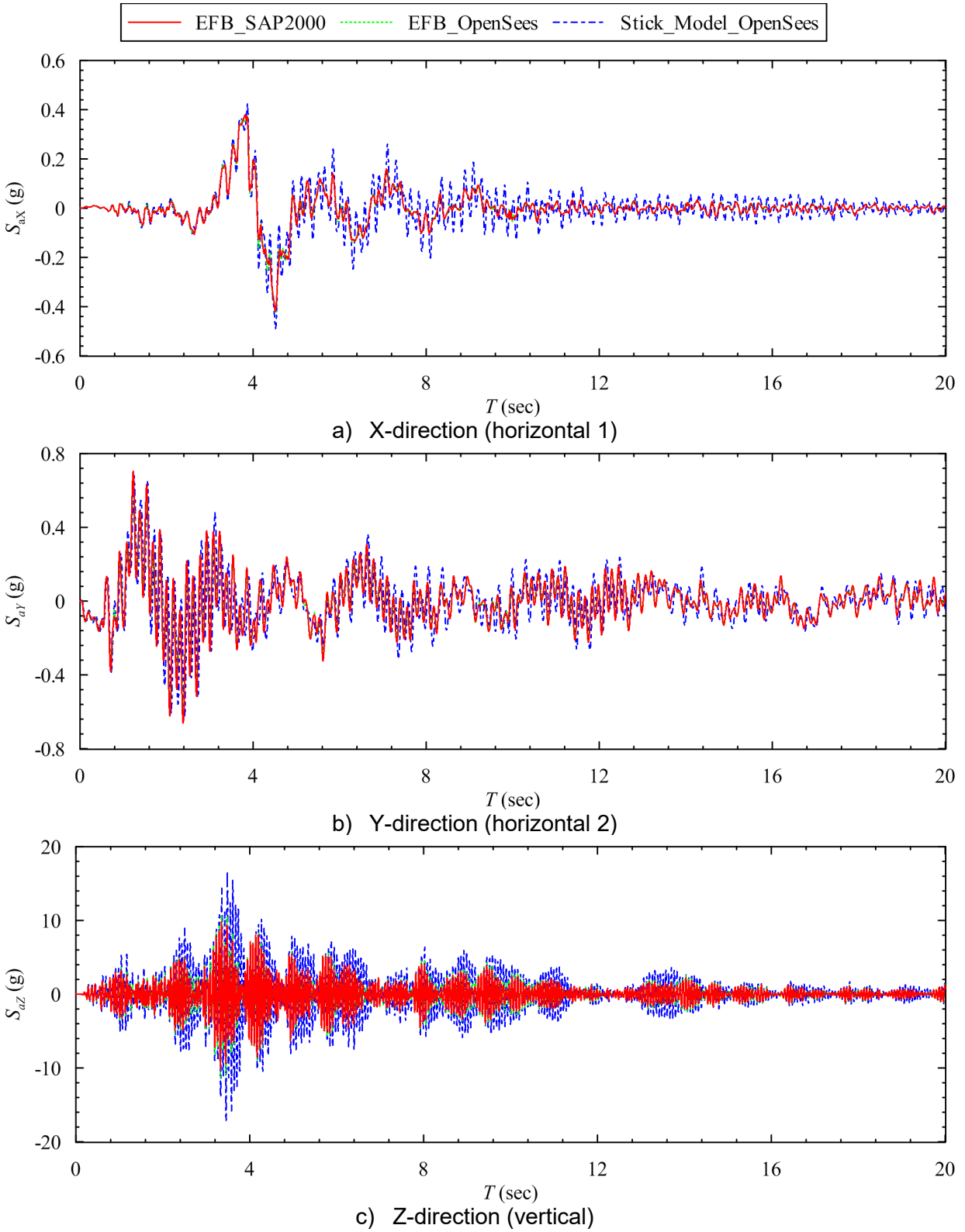


Figure 9-18 Acceleration histories at node 417 of model T2Q6 subject to GM1; 100% DBE shaking

Table 9-33 Mean peak zero-period accelerations (g) for 30 ground motion sets at node 310; lumped-mass stick model

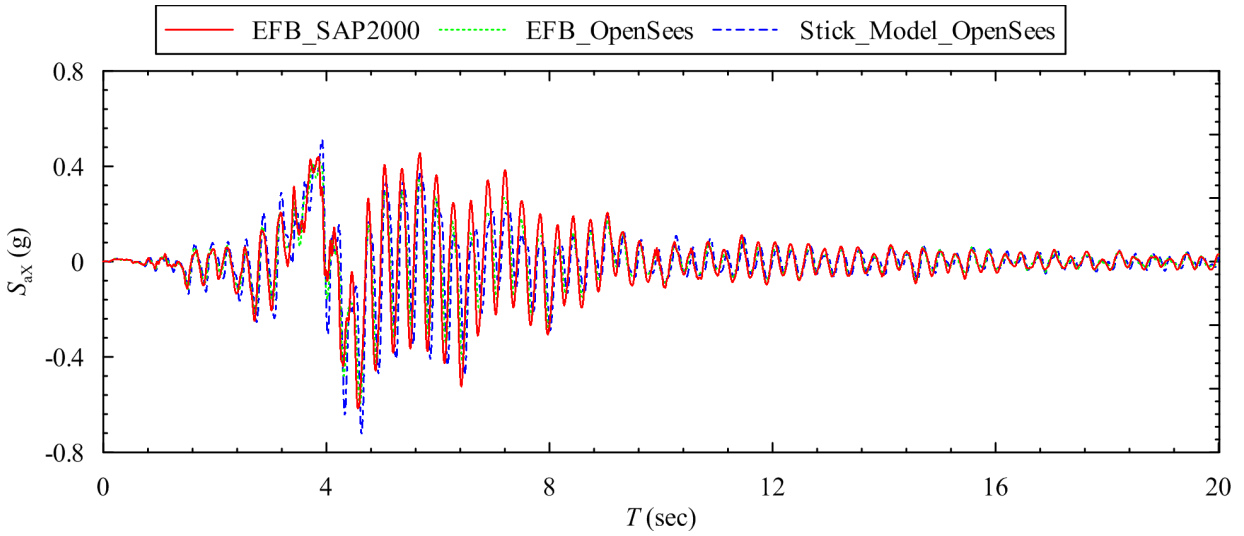
Model	50% DBE			100% DBE			150% DBE			200% DBE		
	a_x^{\max}	a_y^{\max}	a_z^{\max}	a_x^{\max}	a_y^{\max}	a_z^{\max}	a_x^{\max}	a_y^{\max}	a_z^{\max}	a_x^{\max}	a_y^{\max}	a_z^{\max}
T2Q6	0.6	0.62	3.33	0.79	0.83	6.65	0.97	1.05	9.84	1.22	1.32	13.31
T2Q12	0.83	0.92	3.33	1.2	1.24	6.65	1.35	1.43	9.72	1.55	1.63	13.1
T2Q18	0.95	1.09	3.32	1.5	1.58	6.65	1.8	1.87	9.97	2	2.42	13.33
T3Q6	0.39	0.41	3.31	0.57	0.59	6.61	0.7	0.71	9.92	0.79	0.82	12.9
T3Q12	0.51	0.57	3.31	0.79	0.82	6.62	0.97	1.03	9.92	1.14	1.17	13.23
T3Q18	0.58	0.65	3.31	0.9	0.99	6.62	1.18	1.23	9.93	1.35	1.42	13.14

Table 9-34 Mean peak zero-period accelerations (g) for 30 ground motion sets at node 310; equivalent fixed-base model in OpenSees (EFB_OpenSees)

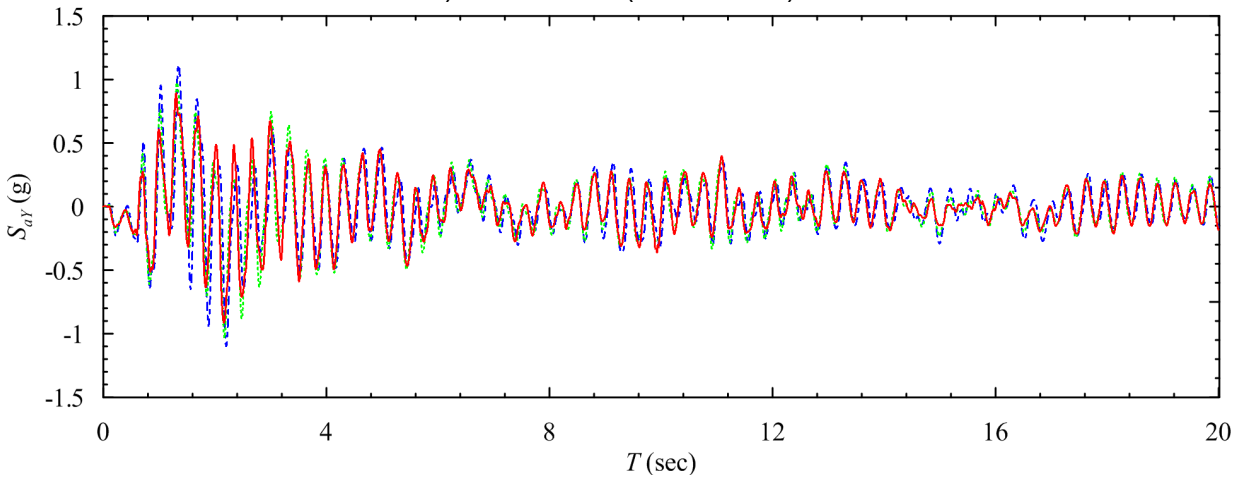
Model	50% DBE			100% DBE			150% DBE			200% DBE		
	a_x^{\max}	a_y^{\max}	a_z^{\max}	a_x^{\max}	a_y^{\max}	a_z^{\max}	a_x^{\max}	a_y^{\max}	a_z^{\max}	a_x^{\max}	a_y^{\max}	a_z^{\max}
T2Q6	0.53	0.59	2.25	0.7	0.8	4.5	0.89	1.03	6.71	1.14	1.31	9
T2Q12	0.73	0.86	2.25	1.06	1.18	4.51	1.21	1.39	6.76	1.4	1.61	9.01
T2Q18	0.85	1.02	2.25	1.3	1.48	4.51	1.59	1.76	6.76	1.75	2	9.02
T3Q6	0.37	0.4	2.44	0.52	0.59	4.88	0.65	0.72	7.32	0.75	0.86	9.76
T3Q12	0.48	0.57	2.46	0.73	0.81	4.92	0.89	1.02	7.37	1.05	1.19	9.83
T3Q18	0.55	0.64	2.47	0.85	0.97	4.94	1.09	1.22	7.42	1.26	1.43	9.88

Table 9-35 Percentage reduction in means of peak zero-period accelerations (g) for 30 ground motion sets at node 310 obtained using the lumped-mass stick model and the equivalent fixed-base model in OpenSees (EFB_OpenSees)

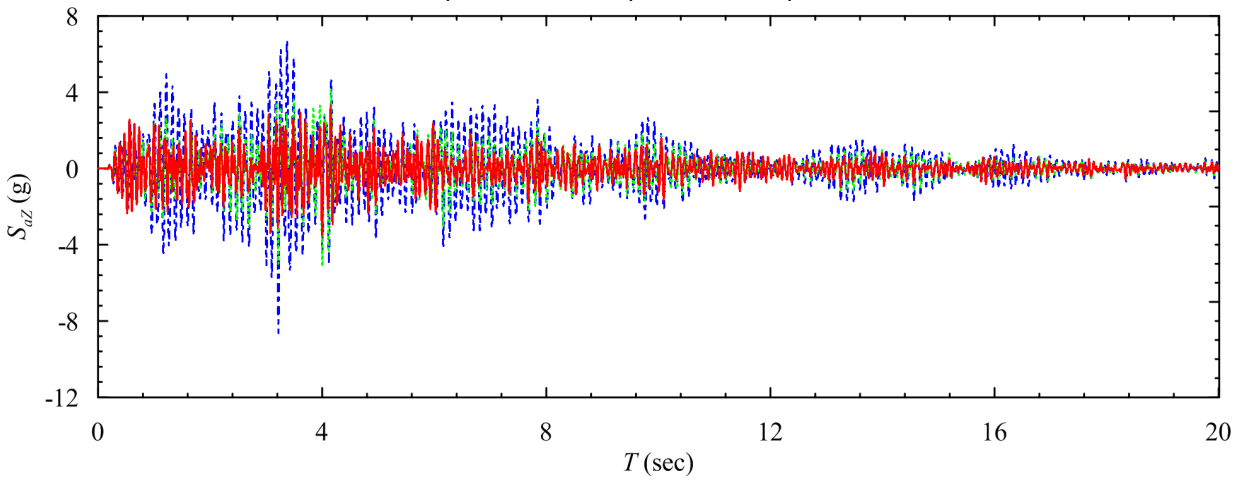
Model	50% DBE			100% DBE			150% DBE			200% DBE		
	a_x^{\max}	a_y^{\max}	a_z^{\max}	a_x^{\max}	a_y^{\max}	a_z^{\max}	a_x^{\max}	a_y^{\max}	a_z^{\max}	a_x^{\max}	a_y^{\max}	a_z^{\max}
T2Q6	12	5	32	11	4	32	8	2	32	7	1	32
T2Q12	12	7	32	12	5	32	10	3	30	10	1	31
T2Q18	11	6	32	13	6	32	12	6	32	13	17	32
T3Q6	5	2	26	9	0	26	7	1	26	5	5	24
T3Q12	6	0	26	8	1	26	8	1	26	8	2	26
T3Q18	5	2	25	6	2	25	8	1	25	7	1	25



a) X-direction (horizontal 1)



b) Y-direction (horizontal 2)



c) Z-direction (vertical)

Figure 9-19 Acceleration histories at node 310 of model T2Q6 subject to GM1; 100% DBE shaking

Table 9-36 Mean peak zero-period accelerations (g) for 30 ground motion sets at node 538; lumped-mass stick model

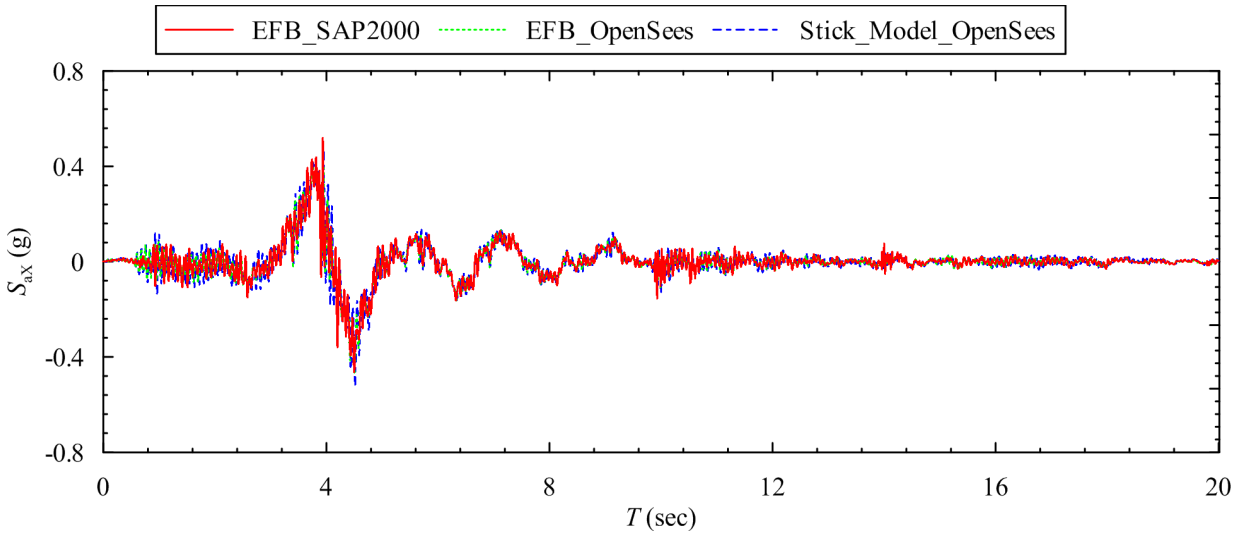
Model	50% DBE			100% DBE			150% DBE			200% DBE		
	a_x^{\max}	a_y^{\max}	a_z^{\max}	a_x^{\max}	a_y^{\max}	a_z^{\max}	a_x^{\max}	a_y^{\max}	a_z^{\max}	a_x^{\max}	a_y^{\max}	a_z^{\max}
T2Q6	0.19	0.23	0.78	0.39	0.43	1.57	0.61	0.67	2.34	0.87	0.95	3.14
T2Q12	0.25	0.28	0.78	0.39	0.44	1.57	0.57	0.61	2.32	0.78	0.88	3.13
T2Q18	0.3	0.33	0.78	0.43	0.49	1.57	0.58	0.66	2.35	0.77	1.34	3.07
T3Q6	0.13	0.14	0.77	0.23	0.25	1.53	0.36	0.44	2.3	0.51	0.68	3
T3Q12	0.18	0.2	0.77	0.26	0.28	1.54	0.36	0.4	2.31	0.5	0.58	3.08
T3Q18	0.23	0.25	0.77	0.31	0.33	1.54	0.39	0.44	2.32	0.5	0.56	3.09

Table 9-37 Mean peak zero-period accelerations (g) for 30 ground motion sets at node 538; equivalent fixed-base model in OpenSees (EFB_OpenSees)

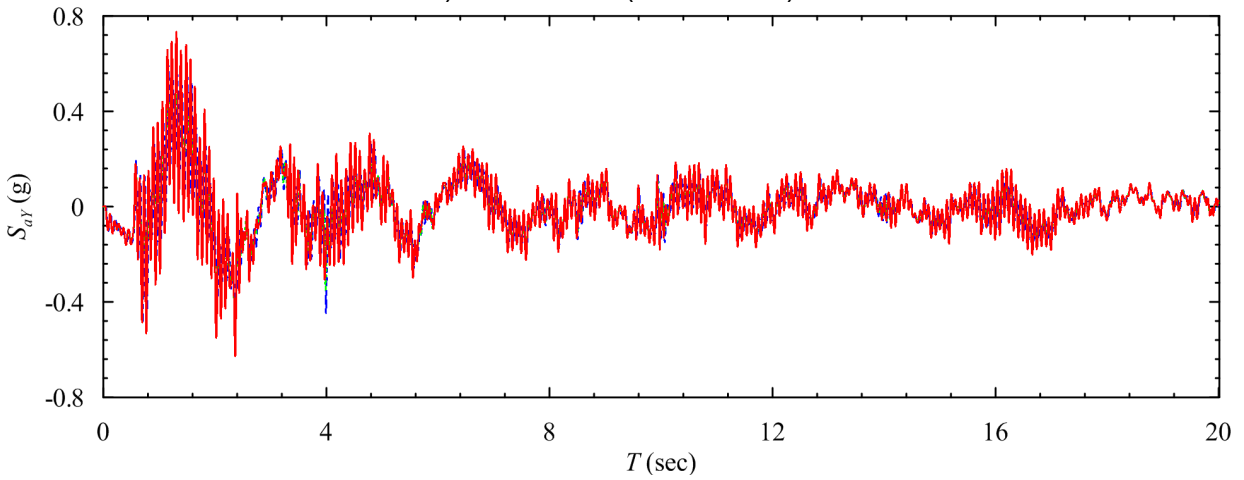
Model	50% DBE			100% DBE			150% DBE			200% DBE		
	a_x^{\max}	a_y^{\max}	a_z^{\max}	a_x^{\max}	a_y^{\max}	a_z^{\max}	a_x^{\max}	a_y^{\max}	a_z^{\max}	a_x^{\max}	a_y^{\max}	a_z^{\max}
T2Q6	0.19	0.21	0.78	0.37	0.41	1.56	0.58	0.62	2.33	0.84	0.88	3.12
T2Q12	0.24	0.27	0.78	0.38	0.42	1.56	0.56	0.6	2.34	0.75	0.82	3.12
T2Q18	0.3	0.33	0.78	0.42	0.48	1.56	0.56	0.64	2.34	0.75	0.82	3.12
T3Q6	0.13	0.14	0.77	0.22	0.24	1.53	0.33	0.36	2.3	0.46	0.51	3.06
T3Q12	0.18	0.2	0.77	0.25	0.28	1.54	0.34	0.37	2.3	0.46	0.48	3.07
T3Q18	0.23	0.25	0.77	0.32	0.35	1.54	0.38	0.42	2.31	0.52	0.54	3.08

Table 9-38 Percentage reduction in means of peak zero-period accelerations (g) for 30 ground motion sets at node 538 obtained using the lumped-mass stick model and the equivalent fixed-base model in OpenSees (EFB_OpenSees)

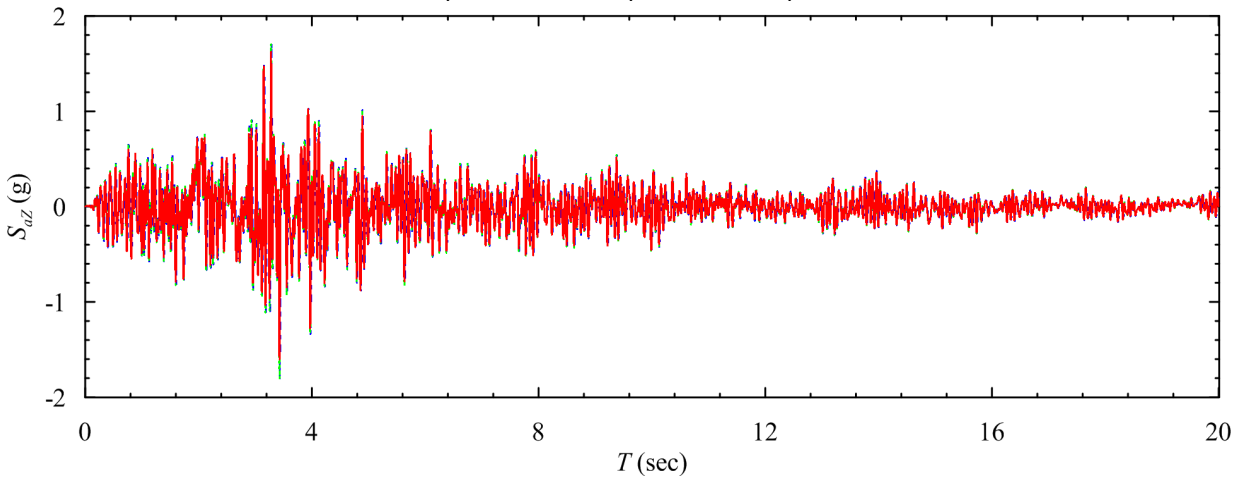
Model	50% DBE			100% DBE			150% DBE			200% DBE		
	a_x^{\max}	a_y^{\max}	a_z^{\max}	a_x^{\max}	a_y^{\max}	a_z^{\max}	a_x^{\max}	a_y^{\max}	a_z^{\max}	a_x^{\max}	a_y^{\max}	a_z^{\max}
T2Q6	0	9	0	5	5	1	5	7	0	3	7	1
T2Q12	4	4	0	3	5	1	2	2	1	4	7	0
T2Q18	0	0	0	2	2	1	3	3	0	3	39	2
T3Q6	0	0	0	4	4	0	8	18	0	10	25	2
T3Q12	0	0	0	4	0	0	6	8	0	8	17	0
T3Q18	0	0	0	3	6	0	3	5	0	4	4	0



a) X-direction (horizontal 1)



b) Y-direction (horizontal 2)



c) Z-direction (vertical)

Figure 9-20 Acceleration histories at node 538 of model T2Q6 subject to GM1; 100% DBE shaking

The substructuring technique provides a rational basis to model damping in a nonlinear response-history analysis of a base-isolated NPP by allowing the use of different damping values for the isolation system and the superstructure. For the model of the base-isolated NPP considered here, the nonlinearities are present only in the isolation bearings, and the superstructure is modeled as elastic. The response-history analysis of the superstructure using the basemat level input excitation is linear and the use of a classical damping matrix does not numerically damp the response.

The substructuring technique results in vertical acceleration response in the ASB and CIS that is substantially smaller than that of lumped-mass stick model in Section 9.5. One could argue that the vertical acceleration response is still too demanding on structures, systems and components. One solution would be to modify the design of the bearings in the isolation system so that the vertical frequency of the isolation system is removed from the vertical frequency of the superstructure. Another solution is to add damping in the vertical direction using supplemental devices. To investigate the latter, response-history analysis of the lumped-mass stick model of the base-isolated NPP was performed with the Rayleigh damping of 2% and 10% of critical. The acceleration response at the node 2137 (isolated basemat), 310 (ASB), 417 (SCV), and 538 (CIS) for these two damping values and the respective percentage difference are presented in Table 9-39 through Table 9-50. Increasing the damping from 2% to 10% of critical reduces the acceleration demands by between 25% and 75% in the three orthogonal directions. The percentage reduction is greater in the SCV and ASB in the vertical direction, which is expected because the relative reduction in the acceleration response due to damping is greater for systems whose frequencies are close to the excitation frequency.

Table 9-39 Mean peak zero-period accelerations (g) for 30 ground motion sets at node 2137 (isolated basemat); lumped-mass stick model, 2% Rayleigh damping

Model	50% DBE			100% DBE			150% DBE			200% DBE		
	a_x^{\max}	a_y^{\max}	a_z^{\max}	a_x^{\max}	a_y^{\max}	a_z^{\max}	a_x^{\max}	a_y^{\max}	a_z^{\max}	a_x^{\max}	a_y^{\max}	a_z^{\max}
T2Q6	0.16	0.17	0.56	0.33	0.35	1.11	0.52	0.55	1.66	0.76	0.78	2.23
T2Q12	0.2	0.22	0.56	0.31	0.34	1.12	0.46	0.5	1.65	0.65	0.69	2.23
T2Q18	0.25	0.27	0.56	0.34	0.39	1.12	0.47	0.52	1.68	0.63	1.21	2.25
T3Q6	0.12	0.12	0.6	0.2	0.21	1.19	0.3	0.31	1.79	0.39	0.42	2.34
T3Q12	0.17	0.18	0.6	0.23	0.24	1.2	0.3	0.33	1.8	0.4	0.42	2.4
T3Q18	0.22	0.23	0.6	0.27	0.3	1.21	0.35	0.36	1.81	0.41	0.44	2.41

Table 9-40 Mean peak zero-period accelerations (g) for 30 ground motion sets at node 2137 (isolated basemat); lumped-mass stick model, 10% Rayleigh damping

Model	50% DBE			100% DBE			150% DBE			200% DBE		
	a_x^{\max}	a_y^{\max}	a_z^{\max}	a_x^{\max}	a_y^{\max}	a_z^{\max}	a_x^{\max}	a_y^{\max}	a_z^{\max}	a_x^{\max}	a_y^{\max}	a_z^{\max}
T2Q6	0.14	0.16	0.45	0.29	0.3	0.89	0.45	0.47	1.33	0.64	0.67	1.8
T2Q12	0.18	0.21	0.43	0.29	0.33	0.9	0.43	0.45	1.31	0.58	0.6	1.74
T2Q18	0.22	0.24	0.44	0.3	0.33	0.85	0.4	0.43	1.26	0.55	0.56	1.68
T3Q6	0.11	0.11	0.46	0.18	0.2	0.93	0.27	0.28	1.39	0.36	0.38	1.85
T3Q12	0.16	0.17	0.46	0.22	0.22	0.91	0.26	0.28	1.28	0.34	0.36	1.75
T3Q18	0.2	0.21	0.46	0.25	0.28	0.9	0.32	0.34	1.39	0.38	0.43	1.79

Table 9-41 Percentage reduction in means of peak zero-period accelerations (g) for 30 ground motion sets at node 2137 (isolated basemat) obtained using 2% and 10% Rayleigh damping, lumped-mass stick model

Model	50% DBE			100% DBE			150% DBE			200% DBE		
	a_x^{\max}	a_y^{\max}	a_z^{\max}	a_x^{\max}	a_y^{\max}	a_z^{\max}	a_x^{\max}	a_y^{\max}	a_z^{\max}	a_x^{\max}	a_y^{\max}	a_z^{\max}
T2Q6	13	6	20	12	14	20	13	15	20	16	14	19
T2Q12	10	5	23	6	3	20	7	10	21	11	13	22
T2Q18	12	11	21	12	15	24	15	17	25	13	54	25
T3Q6	8	8	23	10	5	22	10	10	22	8	10	21
T3Q12	6	6	23	4	8	24	13	15	29	15	14	27
T3Q18	9	9	23	7	7	26	9	6	23	7	2	26

Table 9-42 Mean peak zero-period accelerations (g) for 30 ground motion sets at node 310; lumped-mass stick model (ASB), 2% Rayleigh damping

Model	50% DBE			100% DBE			150% DBE			200% DBE		
	a_x^{\max}	a_y^{\max}	a_z^{\max}	a_x^{\max}	a_y^{\max}	a_z^{\max}	a_x^{\max}	a_y^{\max}	a_z^{\max}	a_x^{\max}	a_y^{\max}	a_z^{\max}
T2Q6	0.6	0.62	3.33	0.79	0.83	6.65	0.97	1.05	9.84	1.22	1.32	13.31
T2Q12	0.83	0.92	3.33	1.2	1.24	6.65	1.35	1.43	9.72	1.55	1.63	13.1
T2Q18	0.95	1.09	3.32	1.5	1.58	6.65	1.8	1.87	9.97	2	2.42	13.33
T3Q6	0.39	0.41	3.31	0.57	0.59	6.61	0.7	0.71	9.92	0.79	0.82	12.9
T3Q12	0.51	0.57	3.31	0.79	0.82	6.62	0.97	1.03	9.92	1.14	1.17	13.23
T3Q18	0.58	0.65	3.31	0.9	0.99	6.62	1.18	1.23	9.93	1.35	1.42	13.14

Table 9-43 Mean peak zero-period accelerations (g) for 30 ground motion sets at node 310; lumped-mass stick model (ASB), 10% Rayleigh damping

Model	50% DBE			100% DBE			150% DBE			200% DBE		
	a_x^{\max}	a_y^{\max}	a_z^{\max}	a_x^{\max}	a_y^{\max}	a_z^{\max}	a_x^{\max}	a_y^{\max}	a_z^{\max}	a_x^{\max}	a_y^{\max}	a_z^{\max}
T2Q6	0.43	0.46	1.82	0.55	0.6	3.55	0.69	0.77	5.38	0.88	0.97	7.29
T2Q12	0.6	0.68	1.75	0.87	0.93	3.64	1.02	1.07	5.33	1.11	1.18	7.07
T2Q18	0.66	0.8	1.8	1.04	1.08	3.43	1.17	1.27	5.01	1.36	1.4	6.83
T3Q6	0.28	0.3	1.82	0.4	0.43	3.64	0.5	0.52	5.46	0.57	0.61	7.28
T3Q12	0.36	0.42	1.82	0.54	0.58	3.58	0.64	0.67	5.11	0.76	0.81	6.81
T3Q18	0.41	0.47	1.82	0.61	0.69	3.56	0.82	0.87	5.42	0.94	1	7.02

Table 9-44 Percentage reduction in means of peak zero-period accelerations (g) for 30 ground motion sets at node 310 (ASB) obtained using 2% and 10% Rayleigh damping, lumped-mass stick model

Model	50% DBE			100% DBE			150% DBE			200% DBE		
	a_x^{\max}	a_y^{\max}	a_z^{\max}	a_x^{\max}	a_y^{\max}	a_z^{\max}	a_x^{\max}	a_y^{\max}	a_z^{\max}	a_x^{\max}	a_y^{\max}	a_z^{\max}
T2Q6	28	26	45	30	28	47	29	27	45	28	27	45
T2Q12	28	26	47	28	25	45	24	25	45	28	28	46
T2Q18	31	27	46	31	32	48	35	32	50	32	42	49
T3Q6	28	27	45	30	27	45	29	27	45	28	26	44
T3Q12	29	26	45	32	29	46	34	35	48	33	31	49
T3Q18	29	28	45	32	30	46	31	29	45	30	30	47

Table 9-45 Mean peak zero-period accelerations (g) for 30 ground motion sets at node 417 (SCV); lumped-mass stick model, 2% Rayleigh damping

Model	50% DBE			100% DBE			150% DBE			200% DBE		
	a_x^{\max}	a_y^{\max}	a_z^{\max}	a_x^{\max}	a_y^{\max}	a_z^{\max}	a_x^{\max}	a_y^{\max}	a_z^{\max}	a_x^{\max}	a_y^{\max}	a_z^{\max}
T2Q6	0.29	0.32	7.6	0.47	0.5	15.2	0.68	0.7	22.46	0.91	0.94	30.4
T2Q12	0.36	0.39	7.6	0.57	0.63	15.21	0.75	0.78	22.57	0.94	0.98	30.41
T2Q18	0.42	0.45	7.61	0.63	0.73	15.21	0.85	0.95	22.82	1.05	1.62	30.4
T3Q6	0.17	0.19	6.71	0.27	0.3	13.42	0.38	0.41	20.13	0.5	0.53	26.36
T3Q12	0.23	0.24	6.61	0.34	0.38	13.22	0.45	0.48	19.84	0.53	0.59	26.45
T3Q18	0.27	0.29	6.53	0.4	0.43	13.05	0.5	0.56	19.58	0.61	0.65	26.11

Table 9-46 Mean peak zero-period accelerations (g) for 30 ground motion sets at node 417 (SCV); lumped-mass stick model, 10% Rayleigh damping

Model	50% DBE			100% DBE			150% DBE			200% DBE		
	a_x^{\max}	a_y^{\max}	a_z^{\max}	a_x^{\max}	a_y^{\max}	a_z^{\max}	a_x^{\max}	a_y^{\max}	a_z^{\max}	a_x^{\max}	a_y^{\max}	a_z^{\max}
T2Q6	0.2	0.21	1.97	0.34	0.36	3.9	0.5	0.52	5.82	0.69	0.72	7.96
T2Q12	0.27	0.27	1.94	0.41	0.43	3.97	0.54	0.57	5.82	0.68	0.71	7.76
T2Q18	0.31	0.31	1.92	0.45	0.45	3.75	0.56	0.6	5.52	0.73	0.72	7.25
T3Q6	0.13	0.14	1.8	0.21	0.22	3.6	0.3	0.32	5.4	0.4	0.42	7.2
T3Q12	0.18	0.19	1.79	0.26	0.27	3.57	0.32	0.33	4.94	0.4	0.42	6.74
T3Q18	0.23	0.23	1.77	0.3	0.32	3.48	0.39	0.4	5.22	0.46	0.48	6.89

Table 9-47 Percentage reduction in means of peak zero-period accelerations (g) for 30 ground motion sets at node 417 (SCV) obtained using 2% and 10% Rayleigh damping, lumped-mass stick model

Model	50% DBE			100% DBE			150% DBE			200% DBE		
	a_x^{\max}	a_y^{\max}	a_z^{\max}	a_x^{\max}	a_y^{\max}	a_z^{\max}	a_x^{\max}	a_y^{\max}	a_z^{\max}	a_x^{\max}	a_y^{\max}	a_z^{\max}
T2Q6	31	34	74	28	28	74	26	26	74	24	23	74
T2Q12	25	31	74	28	32	74	28	27	74	28	28	74
T2Q18	26	31	75	29	38	75	34	37	76	30	56	76
T3Q6	24	26	73	22	27	73	21	22	73	20	21	73
T3Q12	22	21	73	24	29	73	29	31	75	25	29	75
T3Q18	15	21	73	25	26	73	22	29	73	25	26	74

Table 9-48 Mean peak zero-period accelerations (g) for 30 ground motion sets at node 538 (CIS); lumped-mass stick model, 2% Rayleigh damping

Model	50% DBE			100% DBE			150% DBE			200% DBE		
	a_x^{\max}	a_y^{\max}	a_z^{\max}	a_x^{\max}	a_y^{\max}	a_z^{\max}	a_x^{\max}	a_y^{\max}	a_z^{\max}	a_x^{\max}	a_y^{\max}	a_z^{\max}
T2Q6	0.19	0.23	0.78	0.39	0.43	1.57	0.61	0.67	2.34	0.87	0.95	3.14
T2Q12	0.25	0.28	0.78	0.39	0.44	1.57	0.57	0.61	2.32	0.78	0.88	3.13
T2Q18	0.3	0.33	0.78	0.43	0.49	1.57	0.58	0.66	2.35	0.77	1.34	3.07
T3Q6	0.13	0.14	0.77	0.23	0.25	1.53	0.36	0.44	2.3	0.51	0.68	3
T3Q12	0.18	0.2	0.77	0.26	0.28	1.54	0.36	0.4	2.31	0.5	0.58	3.08
T3Q18	0.23	0.25	0.77	0.31	0.33	1.54	0.39	0.44	2.32	0.5	0.56	3.09

Table 9-49 Mean peak zero-period accelerations (g) for 30 ground motion sets at node 538 (CIS); lumped-mass stick model, 10% Rayleigh damping

Model	50% DBE			100% DBE			150% DBE			200% DBE		
	a_x^{\max}	a_y^{\max}	a_z^{\max}	a_x^{\max}	a_y^{\max}	a_z^{\max}	a_x^{\max}	a_y^{\max}	a_z^{\max}	a_x^{\max}	a_y^{\max}	a_z^{\max}
T2Q6	0.15	0.17	0.55	0.3	0.32	1.1	0.47	0.51	1.63	0.67	0.72	2.23
T2Q12	0.2	0.23	0.54	0.31	0.36	1.11	0.46	0.48	1.62	0.6	0.64	2.16
T2Q18	0.24	0.26	0.55	0.33	0.37	1.04	0.43	0.47	1.55	0.59	0.61	2.07
T3Q6	0.11	0.12	0.55	0.19	0.21	1.09	0.28	0.3	1.64	0.39	0.42	2.18
T3Q12	0.16	0.18	0.55	0.23	0.23	1.07	0.28	0.29	1.5	0.36	0.39	2.07
T3Q18	0.21	0.21	0.54	0.26	0.29	1.07	0.33	0.36	1.63	0.4	0.42	2.12

Table 9-50 Percentage reduction in means of peak zero-period accelerations (g) for 30 ground motion sets at node 538 (CIS) obtained using 2% and 10% Rayleigh damping, lumped-mass stick model

Model	50% DBE			100% DBE			150% DBE			200% DBE		
	a_x^{\max}	a_y^{\max}	a_z^{\max}	a_x^{\max}	a_y^{\max}	a_z^{\max}	a_x^{\max}	a_y^{\max}	a_z^{\max}	a_x^{\max}	a_y^{\max}	a_z^{\max}
T2Q6	21	26	29	23	26	30	23	24	30	23	24	29
T2Q12	20	18	31	21	18	29	19	21	30	23	27	31
T2Q18	20	21	29	23	24	34	26	29	34	23	54	33
T3Q6	15	14	29	17	16	29	22	32	29	24	38	27
T3Q12	11	10	29	12	18	31	22	28	35	28	33	33
T3Q18	9	16	30	16	12	31	15	18	30	20	25	31

9.9 Conclusions

Most of the conclusions related to the horizontal displacement response of the base-isolated NPP calculated using the two-node macro model are valid for the stick model. The conclusions listed below add to those presented in Chapter 8 and are somewhat specific to the Diablo Canyon site and the NPP studied:

1. All of the isolation systems considered here provide an adequate margin of safety against buckling at 200% DBE shaking, except for T3Q6.
2. Bearings cavitate at 150% and 100% DBE shaking for isolation systems of periods 2 and 3 sec, respectively. Bearings around the perimeter of the isolation system are more prone to cavitation due to rocking of the superstructure.
3. The peak horizontal displacements obtained using the two-node macro NPP model are in good agreement with those for the lumped-mass stick NPP model for the simplified and advanced isolator representations for 150% DBE shaking and smaller if the horizontal displacement of lumped-mass stick model is represented by the center of the basemat.
4. The base-isolated NPP undergoes appreciable torsional motion at shaking intensities greater than 150% DBE. For example, the contribution of torsion to the horizontal displacement in the bearings around the perimeter of T3Q6 exceeds 10% at 200% DBE shaking.
5. Although the two-node macro model can be used to estimate the horizontal displacement response of a base-isolated NPP, a three-dimensional model that explicitly considers all of the bearings in the isolation system is required to estimate demands on individual bearings, and to investigate rocking and torsional responses.
6. The torsional response increases with increasing shear displacement in the bearings and eccentricity in the structure. Isolations systems with higher strengths (e.g., T2Q18, T3Q18) exhibit a smaller torsional response.
7. The use of the simplified LR bearing model will underestimate the torsional and rocking response of a base-isolated NPP.
8. Rayleigh and stiffness proportional damping are suitable for the calculation of isolation level response as both provide similar estimates of basemat acceleration and isolator displacement response.
9. The vertical acceleration response in the superstructure is sensitive to the definition of damping in the structural model. Rayleigh, mass proportional and stiffness proportional damping models anchored to the isolation frequencies do not appropriately damp the superstructure.
10. The substructuring technique provides a rational basis to model damping for the nonlinear response-history analysis of a base-isolated NPP by allowing the use of different damping values for the isolation system and the superstructure.

10 SUMMARY, CONCLUSIONS AND RECOMMENDATIONS

10.1 Summary

Mission-critical infrastructure in the form of buildings and bridges has been seismically isolated in the United States. Isolation tools and technology developed in the United States have been used to protect infrastructure abroad, including LNG tanks and offshore oil and gas platforms. Safety-related nuclear facilities have been seismically isolated in France and South Africa at sites of low to moderate seismic hazard. The bearings used in those plants were synthetic rubber isolators and would not be used for seismic isolation of structures in the United States. This because of the reported and documented long-term changes in the mechanical properties of the elastomers, specifically the synthetic rubber, which is a neoprene and has stiffened significantly (37%) over time, changing the properties of the isolation system.

Issues related to the application of elastomeric seismic isolation bearings to Nuclear Power Plants (NPPs) in the United States were investigated. Sites in regions of high seismic hazard were emphasized because they pose the greatest challenges in terms of demands on isolators for design basis and beyond design basis earthquake shaking. Mathematical models of low damping rubber (LDR) and lead rubber (LR) bearings suitable for analysis of safety-related nuclear structures subjected to design basis and beyond design basis earthquake shaking were developed to accommodate the following five characteristics or behaviors that may be important for US plants sited in regions of high seismic hazard:

1. Strength degradation in shear due to heating of the lead core (LR bearings)
2. Variation in buckling load due to horizontal displacement
3. Cavitation and post-cavitation behavior due to tensile loading
4. Variation in axial stiffness due to horizontal displacement
5. Variation in shear stiffness due to axial load

These *advanced* mathematical models, *ElastomericX* and *LeadRubberX*, extended the available robust formulation in shear and compression and implemented a new phenomenological model for behavior in tension. *LeadRubberX* includes an algorithm to address heating of the lead core in a LR bearing. The mathematical models were implemented in OpenSees (McKenna *et al.*, 2006) and ABAQUS (Dassault, 2010e) as user elements, and are being implemented in LS-DYNA (LSTC, 2012a) at the time of this writing, to enable use by researchers, regulators and the design professional community. The models were verified and validated following ASME best practices (ASME, 2006). A mathematical model for high-damping rubber bearings, HDRX, was implemented in OpenSees; the model includes many of the features of *ElastomericX* but implements the Grant *et al.* (2004) model in shear. HDRX was written for completeness and not in support of application to nuclear facilities in the United States.

The mathematical models in the shear (horizontal) and axial directions were validated using existing experimental data. A series of experiments were conducted at the University at Buffalo to characterize behavior of elastomeric bearings in tension and tension/shear. Sixteen low damping rubber bearings from two manufacturers, with similar geometric properties but different shear moduli, were tested under various loading conditions to identify those factors that affect cavitation in an elastomeric bearing. The effect of cavitation on the shear and axial properties of elastomeric bearings was investigated by performing post-cavitation tests. The test data was used to validate a phenomenological model of an elastomeric bearing in tension.

A model of a base-isolated nuclear island was analyzed using response-history techniques. The NPP nuclear island model was derived from an early version of the Westinghouse AP1000 reactor (Orr, 2003) but is considered to be representative of large light water reactors currently under construction at Vogtle and Summer in the United States. The set of 30 three-component ground motions selected and spectrally matched by Kumar (2015) to be consistent with uniform hazard response spectra (UHRS) for design basis earthquake (DBE) shaking at the site of the Diablo Canyon Nuclear Generating Station were used for response-history analysis. The ground motions were amplitude scaled by 1.0, 1.5, 1.67 and 2.0 to represent DBE shaking (1.0) and three representations of beyond design basis earthquake (BDBE, 1.5, 1.67 and 2.0) shaking at Diablo Canyon. The return period of DBE shaking at Diablo Canyon is 10,000 years. Two times DBE shaking at Diablo Canyon is associated with a return period of approximately 100,000 years.

Two representations of the base-isolated NPP were considered: 1) a two-node macro model, involving a macro seismic isolator and a supported mass equal to that of the model NPP, and 2) a lumped-mass stick model, involving 273 isolators distributed across the footprint of the basemat and lumped mass stick models representing the auxiliary building containment vessel and containment internal structure. The isolators were LR bearings modeled using both the simplified and the advanced representations of behavior. The simplified model, with equal axial stiffness in compression and tension (and independent of shear displacement), represents the state-of-the-art for response-history analyses of seismically isolated structures using contemporary software programs. The advanced isolator model considers the five characteristics of LR bearings identified above. Isolation systems of different combinations of isolated time-period (T) and supported weight to strength ratios (Q_d / W) were analyzed. The effect of each of the five characteristics on the response of the isolated structure was quantified. Results calculated using the simplified and advanced models were compared and contrasted. The lumped-mass stick models of the base-isolated NPP provided additional information on torsional and rocking response and the spatial distribution of cavitation and buckling in the bearings comprising the isolation system. Floor response spectra in two orthogonal horizontal directions were obtained at different locations in the stick model. Vertical accelerations in the superstructure of the base-isolated NPP were sensitive to the definition of damping. A substructuring method was proposed that allowed the use of different damping values for the isolation system and the superstructure and provided a more realistic estimate of vertical acceleration without overdamping the horizontal response. The reported data allow a reader to judge which representation of an isolated NPP (macro model or lumped-mass stick) and which features, if any, of the advanced isolator model are needed to compute response for different intensities of earthquake shaking.

10.2 Conclusions

The key conclusions of the research presented in this report are:

1. The value of $3GA$ is a reasonable estimate of the cavitation strength of an elastomeric bearing, where G is the shear modulus and A is the bonded area.
2. There is no significant change in the shear modulus, compressive stiffness, and buckling load of a bearing after cavitation.
3. Of the five characteristics of LR bearings discussed, 1) strength degradation due to heating of the lead core, 2) variation in buckling load due to horizontal displacement, and 3) variation in axial stiffness due to horizontal displacement, affect most significantly the responses of base-isolated NPPs.

4. Heating of the lead core in a LR bearing has a relatively small effect (< 10%) on horizontal DBE (shear) displacements but the influence increases at higher intensities of shaking.
5. For a given isolation period, the effect of lead core heating decreases with an increase in the ratio of characteristic strength to weight, whereas for a given value of the ratio, the effect decreases with an increase in isolation period.
6. The characteristic strength of a LR bearing may degrade substantially during extreme earthquake shaking, with values falling below half the initial value for 150+% DBE shaking. The temperature in a lead core may rise by 100+ °C for 150+% DBE shaking.
7. The influence of the variation in axial stiffness with horizontal displacement on the axial response is negligible for DBE shaking but considerable for beyond design basis shaking, with percentage changes in axial displacement being greater than those in axial force.
8. The two-node macro model can be used to estimate the horizontal displacement response of a base-isolated NPP, but a three-dimensional model that explicitly considers all of the bearings in the isolation system is required to estimate demands on individual bearings, and to investigate rocking and torsional response.
9. The buckling load of a LR bearing varies substantially during earthquake shaking. The displacement-dependent model for buckling load predicts failure for many more ground motions than the constant buckling load model, and is thus recommended for use in practice.
10. The torsional response of a base-isolated NPP nuclear island structure may be significant at high intensities of shaking due to high shear displacement demand and eccentricity in the structure. For example, the contribution of torsion to the horizontal displacement in the bearings around perimeter of T3Q6 exceeds 10% at 200% DBE shaking.
11. The use of the simplified LR bearing model will underestimate the torsional and rocking response of a base-isolated NPP nuclear island structure, with the differences becoming significant at the higher intensities of ground shaking.
12. The superstructure response of the lumped-mass stick model representation of a base-isolated NPP nuclear island structure is sensitive to the definition of damping (e.g., Rayleigh, mass proportional, stiffness proportional). A substructuring approach that allows the analyst to specify reasonable level of damping to all modes of interest in the superstructure should be used in response-history analysis.

10.3 Recommendations for Future Research

The following recommendations are made for future studies:

1. Experiments were performed on bearings with very thin rubber layers (4 mm and 7 mm), which likely affected their response under cyclic tensile loading. Full-size bearings representative of those to be used for base-isolated NPPs should be tested using protocols similar to those described in this report.
2. Response-history analysis was performed for the site of the Diablo Canyon Nuclear Generating Station: a site of high seismic hazard. These analysis results could inform preliminary decisions regarding required model complexity at sites of lower hazard. However, similar response-history analyses should be performed for representative sites of low and moderate seismic hazard in the Central and East United States (CEUS) to better inform decision making.
3. The lumped-mass stick model appears to provide adequate information on the response of the isolation system and loads and displacements on individual isolators. Response-

history analysis of a detailed finite element model of base-isolated NPP should be performed to investigate the accuracy of the superstructure responses calculated obtained using the stick model.

11 REFERENCES

- [1] American Association of State Highway and Transportation Officials (AASHTO). (2010). "Guide specifications for seismic isolation design." Washington, D.C.
- [2] AIAA (1998). "Guide for the verification and validation of computational fluid dynamics simulations." *AIAA-G-077-1998*, American Institute of Aeronautics and Astronautics, Reston, VA.
- [3] Aiken, I. D., Kelly, J. M., and Tajirian, F. F. (1989). "Mechanics of low shape factor elastomeric seismic isolation bearings." Technical Report UCB/EERC-89/13, Earthquake Engineering Research Center, University of California, Berkeley, CA.
- [4] ANSYS, Inc. (ANSYS) (2011). Computer Program ANSYS® Academic Research, Canonsburg, PA.
- [5] American Society of Civil Engineers (ASCE). (2010). "Minimum design loads for buildings and other structures." *ASCE/SEI Standard 7-10*, Reston, VA.
- [6] American Society of Civil Engineers (ASCE). (2017). "Seismic analysis of safety-related nuclear structures and commentary." *ASCE/SEI Standard 4-16*, Reston, VA.
- [7] American Society of Mechanical Engineers (ASME). (2006). "Guide for verification and validation in computational solid mechanics." *ASME V&V 10-2006*, New York, NY.
- [8] Austin, N., Hattori, S., Rodwell, E., and Womack, G. (1991). "UK contribution to CEGB-EPRI-CRIEPI program on seismic isolation." *Nuclear Engineering and Design*, 127(3), 253-264.
- [9] Buckle, I., Nagarajaiah, S., and Ferrell, K. (2002). "Stability of elastomeric isolation bearings: experimental study." *Journal of Structural Engineering*, 128(1), 3-11.
- [10] Buckle, I. G. (1985). "New Zealand seismic base isolation concepts and their application to nuclear engineering." *Nuclear Engineering and Design*, 84(3), 313-326.
- [11] Buckle, I. G., and Liu, H. (1993). "Stability of elastomeric seismic isolation systems." *Proceedings: 1st Seminar on Seismic Isolation, Passive Energy Dissipation, and Control*, Redwood City, CA, 293-305.
- [12] Chalhoub, M. S., and Kelly, J. M. (1990). "Effect of bulk compressibility on the stiffness of cylindrical base isolation bearings." *International Journal of Solids and Structures*, 26(7), 743-760.
- [13] Chopra, A. K. (2007). "Dynamics of structures: theory and applications to earthquake engineering." Prentice Hall, NJ, USA.
- [14] Ciesielski, A. (1999). "An introduction to rubber technology." Smithers Rapra Technology.

- [15] Clark, P. W., Aiken, I. D., Kelly, J. M., Gluekler, E. L., and Tajirian, F. F. (1995). "Tests of reduced-scale seismic isolation bearings for the U.S. advanced liquid metal reactor (ALMR) program." *Proceedings: Joint ASME/JSME Pressure Vessels and Piping Conference*, Honolulu, HI.
- [16] Clark, P. W. (1996). "Experimental studies of the ultimate behavior of seismically-isolated structures." Ph.D. Dissertation, University of California, Berkeley, CA.
- [17] Clark, P. W., Aiken, I. D., and Kelly, J. M. (1997). "Experimental studies of the ultimate behavior of seismically-isolated structures." Technical Report UCB/EERC-97/18, Earthquake Engineering Research Center, University of California, Berkeley, CA.
- [18] Constantinou, M., Kalpakidis, I., Filiatrault, A., and Lay, R. A. E. (2011). "LRFD-based analysis and design procedures for bridge bearings and seismic isolators." Technical Report MCEER-11-0004, University at Buffalo, State University of New York, Buffalo, NY.
- [19] Constantinou, M. C., and Adnane, M. A. (1987). "Dynamics of soil-base-isolated-structure systems: Evaluation of two models for yielding systems." Report No. 4 to NSF, Drexel University, PA.
- [20] Constantinou, M. C., Kartoum, A., and Kelly, J. M. (1992). "Analysis of compression of hollow circular elastomeric bearings." *Engineering Structures*, 14(2), 103-111.
- [21] Constantinou, M. C., Tsopelas, P., and Kasalanati, A. (1996). "Longevity and reliability of sliding isolation systems." *Proceedings: 4th National Workshop on Bridge Research in Progress*, University at Buffalo, State University of New York, Buffalo, NY, 299-304.
- [22] Constantinou, M. C., Whittaker, A. S., Kalpakidis, I., Fenz, D. M., and Warn, G. P. (2007). "Performance of seismic isolation hardware under service and seismic loading." Technical Report MCEER-07-0012, University at Buffalo, State University of New York, Buffalo, NY.
- [23] Cook, R. D. (2001). "Concepts and applications of finite elements." John Wiley & Sons.
- [24] Computer & Structures Inc. (CSI) (2006). Computer Program PERFORM-3D, Berkeley, CA.
- [25] Computer & Structures Inc. (CSI) (2007). "SAP2000 user's manual—version 11.0." Berkeley, CA.
- [26] Dassault Systèmes (Dassault) (2010a). "ABAQUS 6.10 analysis user's manual." *Abaqus 6.10 Documentation*, Providence, RI.
- [27] Dassault Systèmes (Dassault) (2010b). "ABAQUS/CAE 6.10 user's manual." *Abaqus 6.10 Documentation*, Providence, RI.
- [28] Dassault Systèmes (Dassault) (2010c). "ABAQUS 6.10 user subroutines reference manual." *Abaqus 6.10 Documentation*, Providence, RI.

- [29] Dassault Systèmes (Dassault) (2010d). "Abaqus CAE workshop: Large strain elasticity ", Providence, RI.
- [30] Dassault Systèmes (Dassault) (2010e). Computer Program ABAQUS/CAE, Providence, RI.
- [31] Dassault Systèmes (Dassault) (2010f). "ABAQUS 6.10 verification manual." *Abaqus 6.10 Documentation*, Providence, RI.
- [32] Dassault Systèmes (Dassault) (2010g). "ABAQUS 6.10 benchmarks manual." *Abaqus 6.10 Documentation*, Providence, RI.
- [33] Dassault Systèmes (Dassault) (2012). "Writing user subroutines with ABAQUS." *Workshop by Simulia services*, Providence, RI.
- [34] Delfosse, G. (1977). "The GAPEC system: a new highly effective aseismic system." *Proceedings: 6th World Conference on Earthquake Engineering*, New Delhi, India.
- [35] Derham, C. F., and Plunkett, A. P. (1976). "Fire resistance of steel-laminated natural rubber bearings." *Natural Rubber Technology*, 7(2), 29-37.
- [36] Dynamic Isolation Systems (DIS). (1983). "A prototype nuclear reactor feasibility study for base isolation using lead-rubber bearings." *Report R807-02*, Berkeley, CA.
- [37] Defense Modeling and Simulation Office (DMSO). (1994). "Modeling and simulation management." *DoD Directive No. 5000.59*, Department of Defense, Washington, DC.
- [38] Dorfmann, A., and Burtscher, S. L. (2000). "Aspects of cavitation damage in seismic bearings." *Journal of Structural Engineering*, 126(5), 573-579.
- [39] Dorfmann, A. (2003). "Stress softening of elastomers in hydrostatic tension." *Acta Mechanica*, 165(3-4), 117-137.
- [40] Eidingen, J. M., and Kelly, J. M. (1985). "Seismic isolation for nuclear power plants: technical and non-technical aspects in decision making." *Nuclear Engineering and Design*, 84(3), 383-409.
- [41] Electric Power Research Institute (EPRI). (2007). "Program on technology innovation: validation of CLASSI and SASSI codes to treat seismic wave incoherence in soil-structure interaction (SSI) analysis of nuclear power plant structures." *EPRI Technical Report 1015111*, Palo Alto, CA.
- [42] Energy Technology Engineering Center (ETEC). (1988). "Seismic technology program plan for advanced reactors." *Volume 1 & 2*, Ventura County, CA.
- [43] Feng, D., Miyama, T., Lu, X., and Ikenaga, M. (2004). "A shaking table test study on shear tensile properties of lead rubber bearings." *Proceedings: 13th World Conference on Earthquake Engineering*, August 1-6, 2004, Vancouver, Canada.

- [44] Fenves, G. L., McKenna, F., Scott, M. H., and Takahashi, Y. (2004). "An object-oriented software environment for collaborative network simulation." *Proceedings: 13th World Conference on Earthquake Engineering*, Vancouver, B.C., Canada.
- [45] Forni, M. (2010). "Seismic isolation of advanced NPPs: State of the art and most recent designs." <<http://www.iter-consult.it/Meetings&Courses/ITM%20Tivoli/Presentazioni%20pdf/Seismic%20isolatio n%20of%20advanced%20NPPs%20%28ENEA%29.pdf>>.
- [46] Forni, M., and Poggianti, A. (2011). "Seismic isolation of nuclear power plants." *Proceedings: 13th International Conference on Civil, Structural and Environmental Engineering Computing*, Crete, Greece.
- [47] Freskakis, G. N., and Sigal, G. B. (1985). "Seismic isolation systems for LMFBR plants." *Proceedings: 8th International Conference on Structural Mechanics in Reactor Technology (SMiRT 8)*, Brussels, Belgium.
- [48] GE Hitachi Nuclear Energy (GE) (2012). <<http://www.nrc.gov/reactors/advanced/prism.html>>.
- [49] Gent, A. (1990). "Cavitation in rubber: a cautionary tale." *Rubber Chemistry and Technology*, 63, 49.
- [50] Gent, A. N., and Lindley, P. B. (1959a). "The compression of bonded rubber blocks." *Proceedings of the Institution of Mechanical Engineers*, 173(1959), 111-122.
- [51] Gent, A. N., and Lindley, P. B. (1959b). "Internal rupture of bonded rubber cylinders in tension." *Proceedings of the Royal Society of London, Series A, Mathematical and Physical Sciences*, 249(1257), 195-205.
- [52] Gent, A. N. (2001). "Engineering with rubber: how to design rubber components." Hanser Gardner Publications, Munich.
- [53] Gluekler, E. L., Bigelow, C. C., DeVita, V., Kelly, J. M., Seidensticker, R. W., and Tajirian, F. F. (1989). "Seismic isolation development for the US advanced liquid-metal reactor program." *Proceedings: 1st International Seminar on Seismic Base Isolation of Nuclear Power Facilities*, Netherlands, 295-301.
- [54] Gluekler, E. L. (1997). "U.S. advanced liquid metal reactor (ALMR)." *Progress in Nuclear Energy*, 31(1-2), 43-61.
- [55] Grant, D., Fenves, G., and Auricchio, F. (2005). "Modelling and analysis of high-damping rubber bearings for the seismic protection of bridges." Technical Report ROSE-2005/01, ROSE School, Pavia, Italy.
- [56] Grant, D. N., Fenves, G. L., and Whittaker, A. S. (2004). "Bidirectional modeling of high-damping rubber bearings." *Journal of Earthquake Engineering*, 8(SP 1), 161-185.

- [57] Gueraud, R., Noel-Leroux, J. P., Livolant, M., and Michalopoulos, A. P. (1985). "Seismic isolation using sliding-elastomer bearing pads [nuclear plants]." *Nuclear Engineering and Design*, 84(3), 363-377.
- [58] Hadjian, A. H., and Tseng, W. S. (1983). "Issues in seismic isolation of nuclear power plants." *Nuclear Engineering and Design*, 84(3), 433-438.
- [59] Haringx, J. A. (1948). "On highly compressible helical springs and rubber rods, and their application for vibration-free mountings." *Philips Research Reports*(3), 401-449.
- [60] Huang, Y.-N., Whittaker, A. S., and Luco, N. (2008). "Performance assessment of conventional and base-isolated nuclear power plants for earthquake and blast loadings." Technical Report MCEER-08-0019, University at Buffalo, State University of New York, Buffalo, NY.
- [61] Huang, Y.-N., Whittaker, A. S., Kennedy, R. P., and Mayes, R. L. (2009). "Assessment of base-isolated nuclear structures for design and beyond-design basis earthquake shaking." Technical Report MCEER-09-0008, University at Buffalo, State University of New York, Buffalo, NY.
- [62] Huang, Y.-N., Whittaker, A. S., Kennedy, R. P., and Mayes, R. L. (2010). "Response of base-isolated nuclear structures for design and beyond-design basis earthquake shaking." *Proceedings: ASME 2010 Pressure Vessels and Piping Division/K-PVP Conference, PVP2010, July 18, 2010 - July 22, 2010*, American Society of Mechanical Engineers, Bellevue, WA, United states, 135-143.
- [63] Huang, Y.-N., Whittaker, A. S., and Luco, N. (2011a). "A probabilistic seismic risk assessment procedure for nuclear power plants: (I) Methodology." *Nuclear Engineering and Design*, 241, 3996-4003.
- [64] Huang, Y.-N., Whittaker, A. S., and Luco, N. (2011b). "A probabilistic seismic risk assessment procedure for nuclear power plants: (II) Application." *Nuclear Engineering and Design*, 241, 3985-3995.
- [65] Huang, Y.-N., Whittaker, A. S., Luco, N., and Hamburger, R. O. (2011c). "Scaling earthquake ground motions for performance-based assessment of buildings." *Journal of Structural Engineering*, 137(3), 311-321.
- [66] Huang, Y.-N., Whittaker, A. S., Kennedy, R. P., and Mayes, R. L. (2013). "Response of base-isolated nuclear structures for design and beyond-design basis earthquake shaking." *Earthquake Engineering & Structural Dynamics*, 42(3), 339-356.
- [67] Institute of Electrical and Electronics Engineers (IEEE). (1984). "IEEE standard dictionary of electrical and electronics terms." *ANSI/IEEE Standard 100-1984*, New York, NY.
- [68] Institute of Electrical and Electronics Engineers (IEEE). (1991). "IEEE standard glossary of software engineering terminology." *IEEE Standard 610.12-1990*, New York, NY.

- [69] Ikonomou, A. S. (1985). "Alexisimon isolation engineering for nuclear power plants." *Nuclear Engineering and Design*, 85(2), 201-216.
- [70] Inagaki, T., Watanabe, Y., Ueta, M., Tarutani, K., Shibata, Y., Okada, K., and Hayashi, Y. (1996). "Design of seismic isolated demonstration FBR plant." *Proceedings: ASME Pressure Vessels and Piping Conference. Part 1 (of 2)*, ASME, Montreal, Canada, 129-138.
- [71] Ishida, K., Yabana, S., and Shibata, H. (1995). "Distinctive features of proposed technical guidelines for the design of seismically isolated fast breeder (FBR) plants." *Proceedings: Joint ASME/JSME Pressure Vessels and Piping Conference*, American Society of Mechanical Engineers, Honolulu, HI.
- [72] Iwabe, N., Takayama, M., Kani, N., and Wada, A. (2000). "Experimental study on the effect of tension for rubber bearings." *Proceedings: 12th World Conference on Earthquake Engineering*, New Zealand.
- [73] Japan Electric Association (JEA). (2000). "Technical guidelines on seismic base isolated system for structural safety and design of nuclear power plants." *JEAG 4614-2000*, Japan.
- [74] Jolivet, F., and Richli, M. (1977). "Aseismic foundation system for nuclear power stations." *Proceedings: 4th International Conference on Structural Mechanics in Reactor Technology (SMiRT 4)*, San Francisco, CA, 12.
- [75] Japan Road Association (JRA). (2011). "Bearing support design guide for highway bridges (In Japanese)." Japan.
- [76] Kalpakidis, I. V., and Constantinou, M. C. (2008). "Effects of heating and load history on the behavior of lead-rubber bearings." Technical Report MCEER-08-0027, University at Buffalo, State University of New York, Buffalo, NY.
- [77] Kalpakidis, I. V., and Constantinou, M. C. (2009a). "Effects of heating on the behavior of lead-rubber bearings. II: Verification of theory." *Journal of Structural Engineering*, 135(12), 1450-1461.
- [78] Kalpakidis, I. V., and Constantinou, M. C. (2009b). "Effects of heating on the behavior of lead-rubber bearings. I: Theory." *Journal of Structural Engineering*, 135(12), 1440-1449.
- [79] Kalpakidis, I. V., Constantinou, M. C., and Whittaker, A. S. (2010). "Modeling strength degradation in lead-rubber bearings under earthquake shaking." *Earthquake Engineering and Structural Dynamics*, 39(13), 1533-1549.
- [80] Kammerer, A. M., Whittaker, A. S., and Constantinou, M. C. (2019). "Technical considerations for seismic isolation of nuclear facilities." NUREG/CR-7253, United States Nuclear Regulatory Commission, Washington, DC.
- [81] Kasalanati, A. (1998). "Experimental study of bridge elastomeric and other isolation and energy dissipation systems with emphasis on uplift prevention and high velocity

- near-source seismic excitation." Ph.D. Dissertation, University at Buffalo, State University of New York, Buffalo, NY.
- [82] Kato, R., Oka, K., and Takayama, M. (2003). "The tensile tests of natural rubber bearings focused on the effect of the steel flange plates." *Proceedings: Pressure Vessels and Piping Conference*, American Society of Mechanical Engineers, Cleveland, OH, 81-88.
- [83] Kelly, J. M. (1979). "Aseismic base isolation: a review." *Proceedings: 2nd U.S. National Conference on Earthquake Engineering*, EERI, Berkeley, CA.
- [84] Kelly, J. M., Tajirian, F. F., Gluekler, E. L., and Veljovich, W. (1990). "Performance margins of seismic isolator bearings." *Proceedings: International Fast Reactor Safety Meeting*, LaGrange Park, IL, 393-411.
- [85] Kelly, J. M. (1993). "Earthquake-resistant design with rubber." Springer-Verlag, London.
- [86] Kelly, J. M. (2003). "Tension buckling in multilayer elastomeric bearings." *Journal of Engineering Mechanics*, 129(12), 1363-1368.
- [87] Koh, C. G., and Kelly, J. M. (1987). "Effects of axial load on elastomeric isolation bearings." Technical Report EERC/UBC-86/12, Earthquake Engineering Research Center, University of California, Berkeley, CA.
- [88] Koh, C. G., and Kelly, J. M. (1988). "A simple mechanical model for elastomeric bearings used in base isolation." *International Journal of Mechanical Sciences*, 30(12), 933-943.
- [89] Kumar, M. (2014). Computer Program ElastomericX, LeadRubberX, and HDR: User elements in OpenSees for analysis of elastomeric seismic isolation bearings under extreme loading, OpenSees, Buffalo, NY, (<http://opensees.berkeley.edu/wiki/index.php>).
- [90] Kumar, M. (2015). "Seismic isolation of nuclear power plants using sliding bearings." Ph.D. Dissertation, University at Buffalo, State University of New York, Buffalo, NY.
- [91] Kumar, M., Whittaker, A. S., and Constantinou, M. C. (2015). "Seismic isolation of nuclear power plants using elastomeric bearings." Technical Report MCEER-15-0008, University at Buffalo, State University of New York, Buffalo, NY.
- [92] Kumar, M., Whittaker, A. S., and Constantinou, M. C. (2019). "Seismic isolation of nuclear power plants using sliding bearings." NUREG/CR-7254, United States Nuclear Regulatory Commission, Washington, DC.
- [93] Kunar, R. R., and Maini, T. (1979). "A review of seismic isolation for nuclear structures." Report NP-1220-SR, Electric Power Research Institute, United Kingdom.
- [94] EDF (Labbe, P.) (2010). "Pioneering actual use of seismic isolation for nuclear facilities." *First kashiwazaki international symposium on seismic safety of nuclear*

installations, <http://www.jnes.go.jp/seismic-symposium10/presentationdata/7_ws2/WS2-02.pdf>.

- [95] Lee, D. E. (1993). "The base isolation of Koeberg nuclear power station 14 years after installation." *Proceedings: Post-SMiRT Conference Seminar on Isolation, Energy Dissipation and Control of Vibrations of Structures*, Capri, Italy.
- [96] Livermore Software Technology Corporation (LSTC) (2012a). Computer Program LS-DYNA, Livermore, CA.
- [97] Livermore Software Technology Corporation (LSTC) (2012b). "LS-DYNA keyword user's manual, volume 2: material models." Livermore, CA.
- [98] Malushte, S. R., and Whittaker, A. S. (2005). "Survey of past base isolation applications in nuclear power plants and challenges to industry/regulatory acceptance." *Proceedings: 18th International Conference on Structural Mechanics in Reactor Technology (SMiRT 18)*, Beijing, China, 3404-3410.
- [99] Mangerig, I., and Mano, T. (2009). "Characteristics of various elastomeric bearings in tension." *Steel Construction*, 2(3), 161-166.
- [100] Martelli, A. (1988). "Some remarks on the use and perspectives of seismic isolation for fast reactors." *Proceedings: Seismic, Shock and Vibration Isolation*, American Society of Mechanical Engineers, Pittsburgh, PA, 83-88.
- [101] Martelli, A., Masoni, P., Forni, M., Indirli, M., Spadoni, B., Di Pasquale, G., Lucarelli, V., Sano, T., Bonacina, G., and Castoldi, A. (1989). "ENEA activities on seismic isolation of nuclear and nonnuclear structures." *Nuclear Engineering and Design*, 127(3), 265-272.
- [102] Martelli, A., Masoni, P., Forni, M., Indirli, M., Spadoni, B., Pasquale, G. d., Lucarelli, V., Sano, T., Bonacina, G., and Castoldi, A. (1991). "ENEA activities on seismic isolation of nuclear and non-nuclear structures." *Nuclear Engineering and Design*, 127(3), 265-272.
- [103] Martelli, A., Forni, M., Bettinali, F., Bonacina, G., Bergamo, G., Castellano, M. G., Medeot, R., Marioni, A., Sano, T., and Pugliese, A. (1999). "New activities performed in Italy on innovative anti-seismic techniques for civil and industrial structures." *Proceedings: Seismic Engineering: The ASME Pressure Vessels and Piping Conference*, American Society of Mechanical Engineers, Boston, MA, 311-326.
- [104] The Mathworks Inc. (Mathworks) (2014). Computer Program Matlab R2014a, Natick, MA.
- [105] Mazzoni, S., McKenna, F., Scott, M. H., and Fenves, G. L. (2006). "OpenSees command language manual." Pacific Earthquake Engineering Research Center, University of California, Berkeley, CA.
- [106] McKenna, F., Fenves, G., and Scott, M. (2006). Computer Program OpenSees: Open System for Earthquake Engineering Simulation, Pacific Earthquake Engineering

Research Center, University of California, Berkeley,
CA, (<http://opensees.berkeley.edu>).

- [107] Mooney, M. (1940). "A theory of large elastic deformation." *Journal of Applied Physics*, 11(9), 582-592.
- [108] Nagarajaiah, S., Reinhorn, A. M., and Constantinou, M. C. (1989). "Nonlinear dynamic analysis of three-dimensional base-isolated structures (3D-BASIS)." Technical Report NCEER-89-0019, University at Buffalo, State University of New York, Buffalo, NY.
- [109] Nagarajaiah, S., Reinhorn, A. M., and Constantinou, M. C. (1991). "Nonlinear dynamic analysis of three-dimensional base isolated structures (3D-BASIS): part 2." Technical Report NCEER-91-0005, University at Buffalo, State University of New York, Buffalo, NY.
- [110] United States Nuclear Regulatory Commission (NRC). (1994). "Preapplication Safety Evaluation Report for the Power Reactor Innovative Small Module (PRISM) Liquid-Metal Reactor." *NUREG-1368*, Washington, DC.
- [111] Fressynet (NUVIA) (2011). "Earthquake-proof pads of JHR project: IAEA workshop on construction technologies for nuclear power plants."
<<http://www.iaea.org/NuclearPower/Downloads/Technology/meetings/2011-Dec-12-16-WS-Paris/2.08-NUVIA-SeismicIsolation.pdf>>.
- [112] Oberkampf, W. L., Trucano, T. G., and Hirsch, C. (2004). "Verification, validation, and predictive capability in computational engineering and physics." *Applied Mechanics Reviews*, 57(1-6), 345-384.
- [113] Oberkampf, W. L., and Roy, C. J. (2010). "Verification and validation in scientific computing." Cambridge University Press, Cambridge.
- [114] Ogden, R. W. (1972). "Large deformation isotropic elasticity - on the correlation of theory and experiment for incompressible rubberlike solids." *Proceedings of the Royal Society A: Mathematical, Physical & Engineering Sciences*, 326(1567), 565-584.
- [115] Orr, R. (2003). "AP1000 inputs for 2D SASSI analyses." Westinghouse Electric Company, Cranberry Township, PA.
- [116] Park, Y. J., Wen, Y. K., and Ang, A. H. S. (1986). "Random vibration of hysteretic systems under bi-directional ground motions." *Earthquake Engineering and Structural Dynamics*, 14(4), 543-557.
- [117] Plichon, C. (1975). "Hooped rubber bearings and frictional plates: a modern antiseismic engineering technique." *Proceedings: Specialist Meeting of the Anti-Seismic Design of Nuclear Installations*, Paris, France.
- [118] Plichon, C., and Jolivet, F. (1978). "Aseismic foundation systems for nuclear power plants." *Proceedings: Institute of Mechanical Engineering Conference on Engineering Design for Earthquake Environments*, London, UK.

- [119] Plichon, C., Gueraud, R., Richli, M., and Casagrande, J. (1980). "Protection of nuclear power plants against seism." *Nuclear Technology*, 49(2), 295-306.
- [120] (Poggianti, S.) (2011). "Updated design of the IRIS nuclear reactor seismic isolation system and seismic analysis in beyond project design condition." *ENEA*, <http://www.enea.it/it/Ricerca_sviluppo/documenti/ricerca-di-sistema-elettrico/nuovo-nucleare-fissione/lp2/rds-92-lp2.pdf>.
- [121] Rivlin, R. S. (1948). "Large elastic deformations of isotropic materials." *Royal Society of London, Philosophical Transactions Series A*, 240(823), 509-525.
- [122] Roache, P. J. (1998). "Verification and validation in computational science and engineering." Hermosa Albuquerque, NM.
- [123] Roche-Rivera, R. G. (2013). "NPP testbeds for SI project." *Personal Communication*
- [124] Roy, C. J., and Oberkampf, W. L. (2011). "A comprehensive framework for verification, validation, and uncertainty quantification in scientific computing." *Computer Methods in Applied Mechanics and Engineering*, 200(25–28), 2131-2144.
- [125] Ryan, K. L., Kelly, J. M., and Chopra, A. K. (2005). "Nonlinear model for lead-rubber bearings including axial-load effects." *Journal of Engineering Mechanics*, 131(12), 1270-1278.
- [126] Schellenberg, A. (2006). Computer Program elastomericBearing element for analysis of elastomeric bearings in OpenSees, Pacific Earthquake Engineering Research Center, Berkeley, CA (http://opensees.berkeley.edu/wiki/index.php/Elastomeric_Bearing_Element).
- [127] Structural Engineering and Earthquake Simulation Laboratory (SEESL). (2010). "Lab manual." Department of Civil, Structural and Environmental Engineering, University at Buffalo.
- [128] Structural Engineering and Earthquake Simulation Laboratory (SEESL) (2014). <<http://nees.buffalo.edu/training/krypton/geoloc%20English.PDF>>. (19 June, 2014).
- [129] Toshiba Coportation (Shimizu) (2009). "4S seismic base isolation design description." <<http://pbadupws.nrc.gov/docs/ML0906/ML090650235.pdf>>.
- [130] Shiojiri, H. (1991). "CRIEPI test program for seismic isolation of the FBR." *Nuclear Engineering and Design*, 127(3), 393-407.
- [131] Shoji, G., Saito, K., Kameda, T., and Fueki, T. (2004). "Seismic performance of a laminated rubber bearing under tensile axial loading." *Proceedings: 13th World Conference on Earthquake Engineering*, August 1-6, 2004, Vancouver, Canada.
- [132] Skinner, R. I., Bycroft, G. N., and McVerry, G. H. (1976a). "A practical system for isolating nuclear power plants from earthquake attack." *Nuclear Engineering and Design*, 36(2), 287-297.

- [133] Skinner, R. I., Tyler, R. G., and Hodder, S. B. (1976b). "Isolation of nuclear power plants from earthquake attack." *Bulletin of the New Zealand National Society for Earthquake Engineering*, 9(4), 199-204.
- [134] Snyder, C. R., and Tajirian, F. F. (1990). "Seismic design of the ALMR." *Proceedings: Annual Meeting of the American Nuclear Society*, USA, 304-306.
- [135] Stanton, J. F., and Roeder, C. W. (1982). "Elastomeric bearings design, construction, and materials: NCHRP Report 248." Report 0077-5614, Transportation Research Boards, Washington, DC.
- [136] Stevenson, J. D. (1978). "The economic effect of increased seismic load on nuclear power plant design and construction costs." *Nuclear Engineering and Design*, 48(1), 231-243.
- [137] Tajirian, F. F., and Kelly, J. M. (1989). "Seismic isolation of nuclear plants: a world overview." *Proceedings: Seismic Engineering: Research and Practice*, American Society of Civil Engineers, San Francisco, CA, 799-808.
- [138] Tajirian, F. F., Kelly, J. M., and Aiken, I. D. (1990). "Seismic isolation for advanced nuclear power stations." *Earthquake Spectra*, 6(2), 371-401.
- [139] Thacker, B. H., Doebling, S. W., Hemez, F. M., Anderson, M. C., Pepin, J. E., and Rodriguez, E. A. (2004). "Concepts of model verification and validation." Los Alamos National Lab., Los Alamos, NM (US).
- [140] Trucano, T. G., Pilch, M., and Oberkampf, W. L. (2003). "On the role of code comparisons in verification and validation." *Sandia National Laboratories, SAND2003-2752*.
- [141] Tsopelas, P. C., Roussis, P. C., Constantinou, M. C., Buchanan, R., and Reinhorn, A. M. (2005). "3D-BASIS-ME-MB: Computer program for nonlinear dynamic analysis of seismically isolated structures." Technical Report MCEER-05-0009, University at Buffalo, State University of New York, Buffalo, NY.
- [142] Vaidya, N. R., and Eggenberger, A. J. (1984). "Feasibility evaluation of base isolation for the aseismic design of structures." D'Appolonia, United States, 130p.
- [143] Warn, G. P., and Whittaker, A. S. (2004). "Performance estimates in seismically isolated bridge structures." *Engineering Structures*, 26(9), 1261-1278.
- [144] Warn, G. P. (2006). "The coupled horizontal-vertical response of elastomeric and lead-rubber seismic isolation bearings." Ph.D. Dissertation, University at Buffalo, State University of New York, Buffalo, NY.
- [145] Warn, G. P., and Whittaker, A. S. (2006). "A study of the coupled horizontal-vertical behavior of elastomeric and lead-rubber seismic isolation bearings." Technical Report MCEER-06-0011, University at Buffalo, State University of New York, Buffalo, NY.

- [146] Warn, G. P., Whittaker, A. S., and Constantinou, M. C. (2007). "Vertical stiffness of elastomeric and lead-rubber seismic isolation bearings." *Journal of Structural Engineering*, 133(9), 1227-1236.
- [147] Weisman, J., and Warn, G. P. (2012). "Stability of elastomeric and lead-rubber seismic isolation bearings." *Journal of Structural Engineering*, 138(2), 215-223.
- [148] Wen, Y.-K. (1976). "Method for random vibration of hysteretic systems." *Journal of the Engineering Mechanics Division*, 102(2), 249-263.
- [149] Wilson, E. L. (1997). Computer Program SAP2000: Integrated finite element analysis and design of structures, Computers & Structures, Inc, Berkeley, CA.
- [150] Wilson, E. L. (2002). "Three-dimensional static and dynamic analysis of structures: a physical approach with emphasis on earthquake engineering." Computers & Structures, Inc, Berkeley, CA.
- [151] Wu, T., Hsieh, B. J., and Seidensticker, R. W. (1987). "Comparative studies of isolation systems applied to a compact LMR reactor module." *Proceedings: 9th International Conference on Structural Mechanics in Reactor Technology (SMiRT 9)*, Switzerland, 471-476.
- [152] Argonne National Lab., IL (USA) (Wu, T., Chang, Y., and Seidensticker, R.) (1988). "Benefits of vertical and horizontal seismic isolation for LMR (liquid metal reactor) nuclear reactor units." <<http://www.osti.gov/bridge/servlets/purl/5075844-gbNSA2/5075844.pdf>>.
- [153] Yamamoto, S., Kikuchi, M., Ueda, M., and Aiken, I. D. (2009). "A mechanical model for elastomeric seismic isolation bearings including the influence of axial load." *Earthquake Engineering & Structural Dynamics*, 38(2), 157-180.
- [154] Yang, Q. R., Liu, W. G., He, W. F., and Feng, D. M. (2010). "Tensile stiffness and deformation model of rubber isolators in tension and tension-shear states." *Journal of Engineering Mechanics*, 136(4), 429-437.
- [155] Yeoh, O. H. (1993). "Some forms of the strain energy function for rubber." *Rubber Chemistry and Technology*, 66(5), 754-771.
- [156] Yoo, B., Cho, M., Lee, J., and Koo, G. (1999). "Integrated horizontal and vertical seismic isolation bearing." *US Patent 5881507*, Korea Electric Power Corporation, USA.
- [157] Yoo, B., and Kulak, R. F. (2002). "Application of seismic isolation to the star-LM reactor." *Proceedings: 10th International Conference on Nuclear Engineering (ICONE 10)*, American Society of Mechanical Engineers, Arlington, VA, 691-697.

APPENDIX A EXPERIMENTAL PROGRAM AND RESULTS

A.1 Experimental Program

The detailed sequence proposed for the testing program is presented here. The characterization tests before and after cavitation are shaded grey. Some bearings failed prematurely and the entire number of planned experiments could not be completed for those bearings. Experiments that were planned but could not be performed are shaded orange.

Table A-1 Single bearing test sequence

Test no.	Test type	Bearing	Type	Signal ¹	Preload P_o (kN)	Axial load amplitude ² P (kN)	Static lateral offset Δ (mm)	Displ. Amplitude u, δ (mm)	Freq. f (Hz)	No. of cycles
1	1	DA1	Shear	S	70	n.a.	n.a.	±35	0.01	4
2	1	DA1	Shear	S	70	n.a.	n.a.	±35	1	4
3	1	DA1	Shear	S	70	n.a.	n.a.	±70	0.01	4
4	1	DA1	Shear	S	70	n.a.	n.a.	±70	1	4
5	1	DA1	Shear	S	70	n.a.	n.a.	±105	0.01	4
6	1	DA1	Shear	S	70	n.a.	n.a.	±127	0.01	4
6a	1	DA1	Shear	S	70	n.a.	n.a.	±140	0.01	4
7	1	DA1	Compression	T	0	300	n.a.	n.a.	0.01	4
8	1	DA1	Tension	T	0	-25	n.a.	n.a.	0.01	4
9	2	DA1	Tension	T	0	-50 kN	0	n.a.	0.01	4
10	2	DA1	Tension	T	0	-50 kN	75	n.a.	0.01	4
11	2	DA1	Tension	T	0	-50 kN	150	n.a.	0.01	4
12	2	DA1	Tension	T	0	-50 kN	225	n.a.	0.01	4
13	2	DA1	Tension	T	0	-50 kN	300	n.a.	0.01	4
14	1	DA1	Shear	S	70	n.a.	n.a.	±140	0.01	4
15	1	DA1	Compression	T	0	300	n.a.	n.a.	0.01	4
	2	DA1	Tension	IT	0	n.a.	0	7, 14, 35, 70, 140	0.01	3
	1	DA1	Shear	S	70	n.a.	n.a.	±140	0.01	4
	1	DA1	Compression	T	0	300	n.a.	n.a.	0.01	4
16	5	DA1	Compression	L	0	n.a.	0	Failure	n.a.	n.a.
1	2	DB1	Tension	IT	0	n.a.	150	4, 8, 20, 40, 80	0.01	3
2	1	DB1	Shear	S	70	n.a.	n.a.	±80	0.01	4
3	1	DB1	Shear	S	35	n.a.	n.a.	±80	0.01	4
4	1	DB1	Shear	S	70	n.a.	n.a.	±80	0.01	4
5	1	DB1	Shear	S	105	n.a.	n.a.	±80	0.01	4
6	1	DB1	Shear	S	140	n.a.	n.a.	±80	0.01	4
7	1	DB1	Shear	S	175	n.a.	n.a.	±80	0.01	4
8	1	DB1	Shear	S	70	n.a.	n.a.	±20	0.01	4

Table A-1 Single bearing test sequence (contd.)

Test no.	Test type	Bearing	Type	Signal ¹	Preload P_o (kN)	Axial load amplitude ² P (kN)	Static lateral offset Δ (mm)	Displ. Amplitude u, δ (mm)	Freq. f (Hz)	No. of cycles
9	1	DB1	Shear	S	70	n.a.	n.a.	±40	0.01	4
10	1	DB1	Shear	S	70	n.a.	n.a.	±80	0.01	4
11	1	DB1	Shear	S	70	n.a.	n.a.	±100	0.01	4
12	1	DB1	Shear	S	70	n.a.	n.a.	±120	0.01	4
13	1	DB1	Compression	T	0	300	n.a.	n.a.	0.01	4
14	3	DB1	Tension	IT	0	n.a.	0	4, 8, 20, 40, 80, 86	0.01	3
15	5	DB1	Compression	L	0	n.a.	0	Failure	n.a.	n.a.
1	1	MA1	Shear	S	70	n.a.	n.a.	±35	0.01	4
2	1	MA1	Shear	S	70	n.a.	n.a.	±35	1	4
3	1	MA1	Shear	S	70	n.a.	n.a.	±70	0.01	4
4	1	MA1	Shear	S	70	n.a.	n.a.	±70	1	4
5	1	MA1	Shear	S	70	n.a.	n.a.	±101.6	0.01	4
6	1	MA1	Shear	S	70	n.a.	n.a.	±101.6	1	4
	1	MA1	Shear	S	70	n.a.	n.a.	±105	0.01	4
	1	MA1	Shear	S	70	n.a.	n.a.	±140	0.01	4
7	1	MA1	Compression	T	0	300	n.a.	n.a.	0.01	4
8	1	MA1	Tension	T	0	-25	n.a.	n.a.	0.01	4
	2	MA1	Tension	T	0	-50 kN	0	n.a.	0.01	4
	2	MA1	Tension	T	0	-50 kN	75	n.a.	0.01	4
	2	MA1	Tension	T	0	-50 kN	150	n.a.	0.01	4
	2	MA1	Tension	T	0	-50 kN	225	n.a.	0.01	4
	2	MA1	Tension	T	0	-50 kN	300	n.a.	0.01	4
	2	MA1	Shear	S	70	n.a.	n.a.	±140	0.01	4
	2	MA1	Compression	T	0	300	n.a.	n.a.	0.01	4
9	5	MA1	Compression	L	0	n.a.	0	Failure	n.a.	n.a.
1	1	MB1	Shear	S	70	n.a.	n.a.	±20	0.01	4
2	1	MB1	Shear	S	70	n.a.	n.a.	±40	0.01	4

Table A-1 Single bearing test sequence (contd.)

Test no.	Test type	Bearing	Type	Signal ¹	Preload P_o (kN)	Axial load amplitude ² P (kN)	Static lateral offset Δ (mm)	Displ. Amplitude u, δ (mm)	Freq. f (Hz)	No. of cycles
3	1	MB1	Shear	S	70	n.a.	n.a.	±80	0.01	4
4	1	MB1	Shear	S	70	n.a.	n.a.	±120	0.01	4
5	1	MB1	Shear	S	70	n.a.	n.a.	±140	0.01	4
6	1	MB1	Shear	S	35	n.a.	n.a.	±80	0.01	4
7	1	MB1	Shear	S	87	n.a.	n.a.	±80	0.01	4
8	1	MB1	Shear	S	105	n.a.	n.a.	±80	0.01	4
9	1	MB1	Shear	S	122	n.a.	n.a.	±80	0.01	4
10	1	MB1	Shear	S	140	n.a.	n.a.	±80	0.01	4
11	1	MB1	Shear	S	157	n.a.	n.a.	±80	0.01	4
12	1	MB1	Compression	T	0	300	n.a.	n.a.	0.01	4
13	3	MB1	Tension	IT	0	n.a.	0	4, 8, 20, 40, 80	0.01	3
14	1	MB1	Shear	S	35	n.a.	n.a.	±80	0.01	4
15	1	MB1	Shear	S	70	n.a.	n.a.	±80	0.01	4
16	1	MB1	Shear	S	105	n.a.	n.a.	±80	0.01	4
17	1	MB1	Shear	S	140	n.a.	n.a.	±80	0.01	4
18	1	MB1	Shear	S	175	n.a.	n.a.	±80	0.01	4
19	1	MB1	Compression	T	0	300	n.a.	n.a.	0.01	4
20	5	MB1	Tension	L	0	n.a.	0	Failure	n.a.	n.a.
1	1	DA2	Shear	S	70	n.a.	n.a.	±140	0.01	4
2	1	DA2	Compression	T	0	300	n.a.	n.a.	0.01	4
3	4	DA2	Tension	IT	0	n.a.	0	7, 14, 35, 70, 91	0.01	3
4	1	DA2	Shear	S	140	n.a.	n.a.	±140	0.01	4
5	1	DA2	Shear	S	15.7	n.a.	n.a.	±140	0.01	4
6	1	DA2	Shear	S	5	n.a.	n.a.	±140	0.01	4
7	1	DA2	Compression	T	0	300	n.a.	n.a.	0.01	4
	4	DA2	Tension	DT	0	n.a.	0	91, 70, 35, 14, 7	0.01	3
	1	DA2	Shear	S	70	n.a.	n.a.	±140	0.01	4

Table A-1 Single bearing test sequence (contd.)

Test no.	Test type	Bearing	Type	Signal ¹	Preload P_o (kN)	Axial load amplitude ² P (kN)	Static lateral offset Δ (mm)	Displ. Amplitude u, δ (mm)	Freq. f (Hz)	No. of cycles
1	1	DA2	Compression	T	0	300	n.a.	n.a.	0.01	4
8	5	DA2	Compression	L	0	n.a.	300	Failure	n.a.	n.a.
1	2	DB2	Tension	IT	0	n.a.	150	4, 8, 20, 40, 80	0.01	3
2	1	DB2	Shear	S	70	n.a.	n.a.	±80	0.01	4
3	1	DB2	Shear	S	35	n.a.	n.a.	±80	0.01	4
4	1	DB2	Shear	S	70	n.a.	n.a.	±80	0.01	4
5	1	DB2	Shear	S	105	n.a.	n.a.	±80	0.01	4
6	1	DB2	Shear	S	140	n.a.	n.a.	±80	0.01	4
7	1	DB2	Shear	S	175	n.a.	n.a.	±80	0.01	4
8	1	DB2	Shear	S	70	n.a.	n.a.	±20	0.01	4
9	1	DB2	Shear	S	70	n.a.	n.a.	±40	0.01	4
10	1	DB2	Shear	S	70	n.a.	n.a.	±80	0.01	4
11	1	DB2	Shear	S	70	n.a.	n.a.	±100	0.01	4
12	1	DB2	Shear	S	70	n.a.	n.a.	±120	0.01	4
13	1	DB2	Compression	T	0	300	n.a.	n.a.	0.01	4
14	5	DB2	Compression	L	0	n.a.	0	Failure	n.a.	n.a.
1	1	MA2	Shear	S	70	n.a.	n.a.	±140	0.01	1
1a	1	MA2	Shear	S	70	n.a.	n.a.	±101.6	0.01	4
2	1	MA2	Compression	T	0	300	n.a.	n.a.	0.01	4
3	4	MA2	Tension	IT	0	n.a.	0	7, 14, 35, 70, 91	0.01	3
4	1	MA2	Shear	S	70	n.a.	n.a.	±101.6	0.01	4
5	1	MA2	Compression	T	0	300	n.a.	n.a.	0.01	4
	4	MA2	Tension	DT	0	n.a.	0	91, 70, 35, 14, 7	0.01	3
	1	MA2	Shear	S	70	n.a.	n.a.	±140	0.01	4
	1	MA2	Compression	T	0	300	n.a.	n.a.	0.01	4
6	5	MA2	Compression	L	0	n.a.	300	Failure	n.a.	n.a.

Table A-1 Single bearing test sequence (contd.)

Test no.	Test type	Bearing	Type	Signal ¹	Preload P_o (kN)	Axial load amplitude ² P (kN)	Static lateral offset Δ (mm)	Displ. Amplitude u, δ (mm)	Freq. f (Hz)	No. of cycles
1	3	MB2	Tension	IT	0	n.a.	0	4, 8, 20, 40, 80	0.01	3
2	1	MB2	Shear	S	35	n.a.	n.a.	±80	0.01	4
3	1	MB2	Shear	S	70	n.a.	n.a.	±80	0.01	4
4	1	MB2	Shear	S	105	n.a.	n.a.	±80	0.01	4
5	1	MB2	Shear	S	140	n.a.	n.a.	±80	0.01	4
6	5	MB2	Compression	T	0	300	n.a.	n.a.	0.01	4
		MB2	Compression	L	0	n.a.	0	Failure	n.a.	n.a.
1	1	DA3	Shear	S	70	n.a.	n.a.	±140	0.01	4
2	1	DA3	Compression	T	0	300	n.a.	n.a.	0.01	4
3	4	DA3	Tension	DT	0	n.a.	0	70, 35, 14, 7	0.01	3
4	1	DA3	Shear	S	70	n.a.	n.a.	±140	0.01	4
5	1	DA3	Compression	T	0	300	n.a.	n.a.	0.01	4
6	4	DA3	Tension	IT	0	n.a.	0	7, 14, 35, 70, 91	0.01	3
7	1	DA3	Shear	S	70	n.a.	n.a.	±140	0.01	4
8	1	DA3	Compression	T	0	300	n.a.	n.a.	0.01	4
9	5	DA3	Compression	L	0	n.a.	0	Failure	n.a.	n.a.
1	4	DB3	Tension	IT	0	n.a.	0	4, 8, 20, 40	0.01	3
2	1	DB3	Shear	S	70	n.a.	n.a.	±80	0.01	4
3	1	DB3	Compression	T	0	300	n.a.	n.a.	0.01	4
	1	DB3	Tension	DT	0	n.a.	0	40, 20, 8, 4	0.01	3
	1	DB3	Shear	S	70	n.a.	n.a.	±80	0.01	4
	1	DB3	Compression	T	0	300	n.a.	n.a.	0.01	4
4	5	DB3	Compression	L	0	n.a.	0	Failure	n.a.	n.a.
1	1	MA3	Shear	S	150	n.a.	n.a.	±140	0.01	4
2	1	MA3	Compression	T	24	300	n.a.	n.a.	0.01	4

Table A-1 Single bearing test sequence (contd.)

Test no.	Test type	Bearing	Type	Signal ¹	Preload P_o (kN)	Axial load amplitude ² P (kN)	Static lateral offset Δ (mm)	Displ. Amplitude u, δ (mm)	Freq. f (Hz)	No. of cycles
3	4	MA3	Tension	DT	0	n.a.	0	70, 35, 14, 7	0.01	3
4	1	MA3	Shear	S	150	n.a.	n.a.	±140	0.01	4
5	1	MA3	Compression	T	24	300	n.a.	n.a.	0.01	4
6	4	MA3	Tension	IT	0	n.a.	0	7, 14, 35, 70, 91	0.01	3
7	1	MA3	Shear	S	150	n.a.	n.a.	±140	0.01	4
8	1	MA3	Compression	T	24	300	n.a.	n.a.	0.01	4
9	5	MA3	Compression	L	24	n.a.	0	Failure	n.a.	n.a.
1	1	MB3	Shear	S	70	n.a.	n.a.	±80	0.01	4
2	1	MB3	Compression	T	0	300	n.a.	n.a.	0.01	4
3	4	MB3	Tension	IT	0	n.a.	0	4, 8, 20, 40,	0.01	3
4	1	MB3	Shear	S	70	n.a.	n.a.	±80	0.01	4
5	1	MB3	Compression	T	0	300	n.a.	n.a.	0.01	4
6	4	MB3	Tension	DT	0	n.a.	0	80, 40, 20, 8, 4	0.01	3
7	1	MB3	Shear	S	70	n.a.	n.a.	±80	0.01	4
8	1	MB3	Compression	T	0	300	n.a.	n.a.	0.01	4
9	5	MB3	Compression	L	0	n.a.	0	Failure	n.a.	n.a.
1	1	DA4	Shear	S	70	n.a.	n.a.	±140	0.01	4
2	1	DA4	Shear	S	44.5	n.a.	n.a.	±140	0.01	4
3	1	DA4	Shear	S	33.4	n.a.	n.a.	±140	0.01	4
4	1	DA4	Shear	S	22.2	n.a.	n.a.	±140	0.01	4
5	1	DA4	Shear	S	11.1	n.a.	n.a.	±140	0.01	4
5a	1	DA4	Shear	S	89	n.a.	n.a.	±140	0.01	4
5b	1	DA4	Shear	S	140	n.a.	n.a.	±140	0.01	4
6	1	DA4	Compression	T	0	300	n.a.	n.a.	0.01	4
7	2	DA4	Tension	T	0	-50 kN	0	n.a.	0.01	4
8	2	DA4	Tension	T	0	-50 kN	37.5	n.a.	0.01	4
9	2	DA4	Tension	T	0	-50 kN	75	n.a.	0.01	4

Table A-1 Single bearing test sequence (contd.)

Test no.	Test type	Bearing	Type	Signal ¹	Preload P_o (kN)	Axial load amplitude ² P (kN)	Static lateral offset Δ (mm)	Displ. Amplitude u, δ (mm)	Freq. f (Hz)	No. of cycles
10	2	DA4	Tension	T	0	-50 kN	112.5	n.a.	0.01	4
11	2	DA4	Tension	T	0	-50 kN	150	n.a.	0.01	4
12	1	DA4	Shear	S	70	n.a.	n.a.	±140	0.01	4
13	1	DA4	Compression	T	0	300	n.a.	n.a.	0.01	4
14	2	DA4	Tension	IT	0	n.a.	0	7, 14, 35, 70, 91	0.01	3
15	1	DA4	Shear	S	70	n.a.	n.a.	±140	0.01	4
16	1	DA4	Shear	S	44.5	n.a.	n.a.	±140	0.01	4
17	1	DA4	Shear	S	33.4	n.a.	n.a.	±140	0.01	4
18	1	DA4	Shear	S	22.2	n.a.	n.a.	±140	0.01	4
19	1	DA4	Shear	S	11.1	n.a.	n.a.	±140	0.01	4
19a	1	DA4	Shear	S	89	n.a.	n.a.	±140	0.01	4
19b	1	DA4	Shear	S	140	n.a.	n.a.	±140	0.01	4
20	1	DA4	Compression	T	0	300	n.a.	n.a.	0.01	4
21	5	DA4	Compression	L	0	n.a.	0	Failure	n.a.	n.a.
1	1	DB4	Shear	S	70	n.a.	n.a.	±80	0.01	4
2	1	DB4	Shear	S	105	n.a.	n.a.	±80	0.01	4
3	1	DB4	Shear	S	140	n.a.	n.a.	±80	0.01	4
4	1	DB4	Shear	S	175	n.a.	n.a.	±80	0.01	4
5	1	DB4	Shear	S	70	n.a.	n.a.	±20	0.01	4
6	1	DB4	Shear	S	70	n.a.	n.a.	±40	0.01	4
7	1	DB4	Shear	S	70	n.a.	n.a.	±80	0.01	4
8	1	DB4	Shear	S	70	n.a.	n.a.	±100	0.01	4
9	1	DB4	Shear	S	70	n.a.	n.a.	±120	0.01	4
10	1	DB4	Compression	T	0	300	n.a.	n.a.	0.01	4
11	3	DB4	Tension	IT	0	n.a.	0	4, 8, 20, 40, 80	0.01	3
12	1	DB4	Shear	S	70	n.a.	n.a.	±80	0.01	4
13	1	DB4	Shear	S	105	n.a.	n.a.	±80	0.01	4
14	1	DB4	Shear	S	140	n.a.	n.a.	±80	0.01	4

Table A-1 Single bearing test sequence (contd.)

Test no.	Test type	Bearing	Type	Signal ¹	Preload P_o (kN)	Axial load amplitude ² P (kN)	Static lateral offset Δ (mm)	Displ. Amplitude u, δ (mm)	Freq. f (Hz)	No. of cycles
15	1	DB4	Shear	S	175	n.a.	n.a.	±80	0.01	4
16	1	DB4	Shear	S	70	n.a.	n.a.	±20	0.01	4
17	1	DB4	Shear	S	70	n.a.	n.a.	±40	0.01	4
18	1	DB4	Shear	S	70	n.a.	n.a.	±80	0.01	4
19	1	DB4	Shear	S	70	n.a.	n.a.	±100	0.01	4
20	1	DB4	Shear	S	70	n.a.	n.a.	±120	0.01	4
21	3	DB4	Tension	IT	0	n.a.	0	4, 8, 20, 40, 80	0.01	3
21	1	DB4	Compression	T	24	300	n.a.	n.a.	0.01	4
22	6	DB4	Compression	L	0	n.a.	300	Failure	n.a.	n.a.
1	1	MA4	Shear	S	70	n.a.	n.a.	±101.6	0.01	4
2	1	MA4	Compression	T	0	300	n.a.	n.a.	0.01	4
3	2	MA4	Tension	T	0	-50 kN	0	n.a.	0.01	4
	1	MA4	Tension	T	0	-50 kN	37.5	n.a.	0.01	4
	1	MA4	Tension	T	0	-50 kN	75	n.a.	0.01	4
	1	MA4	Tension	T	0	-50 kN	112.5	n.a.	0.01	4
	1	MA4	Tension	T	0	-50 kN	150	n.a.	0.01	4
	1	MA4	Shear	S	70	n.a.	n.a.	±101.6	0.01	4
	1	MA4	Compression	T	0	300	n.a.	n.a.	0.01	4
	3	MA4	Tension	IT	0	n.a.	0	7, 14, 35, 70, 91	0.01	3
	1	MA4	Shear	S	70	n.a.	n.a.	±101.6	0.01	4
	1	MA4	Compression	T	0	300	n.a.	n.a.	0.01	4
4	1	MA4	Shear	S	70	n.a.	n.a.	±101.6	0.01	4
5	1	MA4	Shear	S	44.5	n.a.	n.a.	±101.6	0.01	4
6	1	MA4	Shear	S	33.4	n.a.	n.a.	±101.6	0.01	4
7	1	MA4	Shear	S	22.2	n.a.	n.a.	±101.6	0.01	4
8	1	MA4	Shear	S	11.1	n.a.	n.a.	±101.6	0.01	4
9	1	MA4	Compression	T	0	300	n.a.	±101.6	0.01	4
10	5	MA4	Compression	L	0	n.a.	300	Failure	n.a.	n.a.

Table A-1 Single bearing test sequence (contd.)

Test no.	Test type	Bearing	Type	Signal ¹	Preload P_o (kN)	Axial load amplitude ² P (kN)	Static lateral offset Δ (mm)	Displ. Amplitude u, δ (mm)	Freq. f (Hz)	No. of cycles
1	3	MB4	Tension	DT	0	n.a.	0	80, 40, 20, 8, 4	0.01	3
2	1	MB4	Shear	S	35	n.a.	n.a.	±80	0.01	4
3	1	MB4	Shear	S	70	n.a.	n.a.	±80	0.01	4
4	1	MB4	Shear	S	105	n.a.	n.a.	±80	0.01	4
5	1	MB4	Shear	S	140	n.a.	n.a.	±80	0.01	4
6	3	MB4	Compression	T	0	300	n.a.	n.a.	0.01	4
7	5	MB4	Compression	L	0	n.a.	0	Failure	n.a.	n.a.

1. S = Sinusoidal, T = Triangular, IT = Increasing Triangular, DT = Decreasing Triangular

2. Negative value indicates loading in tension

A.2 Original Load Cell Design Sheet (source: nees.buffalo.edu)



UNIVERSITY AT BUFFALO
State University of New York

SCHOOL OF ENGINEERING
AND APPLIED SCIENCES



Department of Civil, Structural, and Environmental Engineering

212 Ketter Hall, North Campus, Buffalo, NY 14260-4300
http://www.civil.buffalo.edu/

Fax: (716) 645-3733
Andrei M. Reinhorn, P.E., Ph.D.
Professor of Structural Engineering

Tel: (716) 645 2114, x 2419
e-mail: reinhorn@buffalo.edu

26-Mar-92

FIVE AXES LOAD CELL USING TUBE STRUCTURE

Designed by Prof. Andrei M. Reinhorn, Assisted by Prof. Joe Bracci (Texas A&M University)

Height of load cell total	HH	13.00	in				
Size of top plate (square)	BB	16.00	in				
		Capacity		SI	Max Output		
Axial Load Capacity	N	50.00	Kips	222.7	kN	10.0	V
Moment Capacity	M	200.00	Kips-in	22.6	kN-m	10.0	V
Shear Capacity	S	20.00	Kips	89.1	kN	10.0	V
		Design data					
Outside Diameter	Do	8.00	in				
Outside Diameter Gap	Dg	5.00	in				
Inside diameter	d	4.00	in				
Height of gap	hg	3.00	in				
Height of pipe section	H	9.00	in				
Thickness of top plate	t	2.00	in				
Cross section area	A	7.07	in ²		37.7	in ²	
Moment of inertia	I	18.11	in ⁴		188.5	in ⁴	
Modulus of section	W	7.25	in ³		75.4	in ³	
		Performance					
Axial Strain	en	235.8	µSt	2	2.9	mV	4241
Moment strain	em	920.1	µSt	4	18.4	mV	679
Shear strain	es	122.6	µSt	4	4.9	mV	2549
Gage factor	-	2.0	-				Ampl.Fact= 1.25
Excitation Voltage	Vo	10.0	V	Nr of arms	Max Output	Amplification for full scale	
		Total Strains					
Modulus of elasticity	E	30000.0	ksi		30.0	Msi	
Steel yield stress	fy	36.0	ksi				
Allowable yield strain	ey	1200.0	µSt				
Total principal strain	et	1168.8	µSt				
		Natural Freq.					
Horizontal Stiffness	Kh	5.37E+03	kips/in				
Vertical Stiffness	Kv	2.36E+04	kips/in				
Horizontal Frequency	fx	51	Hz				
Vertical Frequency	fy	68	Hz				
		Bolts					
Number of bolts	nrb	8					High Strength (Tens=180 ksi)
Bolt diameter	db	0.625	in				(Shear=162 ksi)
Bolt circle diameter	Db	6.00	in				
Distance between bolts	s	1.73	in				
Bolts tension Capacity	Nb	441.8	Kips	Single bolt:	55	Kips	
Bolts shear capacity	Sb	397.6	Kips	Single bolt:	50	Kips	

Colored data can be adjusted

NOTE: OUTPUT=10V*GF=2*µSt*#GAGES/4 = 10*2*463*2.6(MU=0.3)/4

NOTE: OUTPUT=10V*GF=2*µSt*#GAGES/4 = 10*2*728*4/4

A.3 String Potentiometer Data Sheet (source: www.celesco.com)

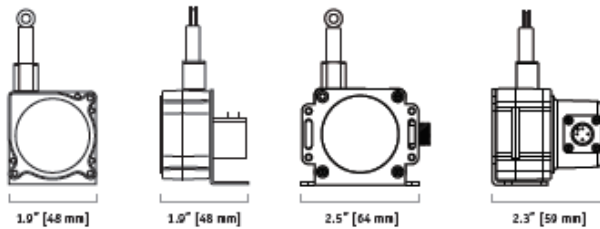
SP1

Compact String Pot • Voltage Divider Output

Linear Position to 50 Inches (1270 mm)

Rugged Polycarbonate Enclosure • IP67 Optional
Mounting Bracket & Optional Sensor Cover w/Connector

IN STOCK for Quick Delivery!



COMPLETE SPECIFICATIONS

Full Stroke Range Options	0-4.75, 0-12.5, 0-25, 0-50 inches
Output Signal	voltage divider (potentiometer)
Accuracy	±0.25 to ±1.00% (see ordering info)
Repeatability	± 0.05% full stroke
Resolution	essentially infinite
Measuring Cable	0.019-in. dia. nylon-coated stainless steel
Measuring Cable Tension	7 oz. (1.9 N) ±25%
Maximum Cable Acceleration, SP1-xx	15 g
Maximum Cable Acceleration, SP1-xx-3	13 g
Enclosure Material	polycarbonate
Sensor	plastic-hybrid precision potentiometer
Weight, max. (includes bracket)	.4 lbs (.19 kg)

ELECTRICAL

Input Resistance	10K ohms, ±10%
Power Rating, Watts	2.0 at 70°F derated to 0 at 250°
Recommended Maximum Input Voltage	30 V (AC/DC)
Output Signal Change Over Full Stroke Range	94% ±4% of input voltage
Electrical Connection, SP1-xx	solder terminals
Electrical Connection, SP1-xx-3	4-pin, M12 connector

ENVIRONMENTAL

Enclosure	IP 50 (SP1-xx), IP67 (SP1-xx-3)
Operating Temperature, SP1-xx	0° to 160°F (-18° to 70°C)
Operating Temperature, SP1-xx-3	-40° to 160°F (-40° to 70°C)
Vibration	up to 10 g to 2000 Hz maximum

20630 Plummer Street • Chatsworth, CA 91311
tel: 800.423.5483 • +1.818.701.2750 • fax: +1.818.701.2700



This compact stringpot with "voltage divider" output, provides the ultimate in ease-of-use and flexibility for measurement ranges up to 50 inches. Made of rugged polycarbonate, the SP1 fits in small spaces, doesn't need perfect alignment and ships with a stainless steel mounting bracket to let the user easily orient this sensor in just about any direction imaginable.

The SP1 comes in two different versions: one complete with a connector, mating plug and sensor cover to protect against IP67 (wet) environments and the other, a lower cost, open sensor design priced for both the budget conscious single piece user and the OEM alike.

ORDERING INFORMATION

full stroke range	Part No.	Part No.	accuracy	cycle life
4.75 in (120 mm)	SP1-4	SP1-4-3	1.00%	2.5M
12.5 in (317 mm)	SP1-12	SP1-12-3	25%	500K
25 in (635 mm)	SP1-25	SP1-25-3	25%	500K
50 in (1270 mm)	SP1-50	SP1-50-3	25%	250K

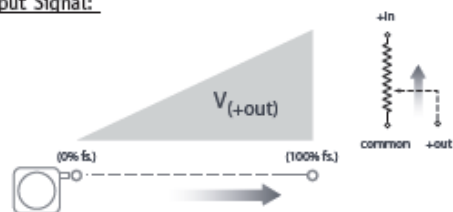
optional cordset



Part No. 9036810-0040

For all SP1-xx-3 versions, an optional convenient 13-ft. long cordset is available for short-run connections.

Output Signal:



celesco.com • info@celesco.com

SP1 | 1

A.4 Linear Potentiometer Data Sheet (source: www.etisystems.com)

REV. BY DATE	APPRVL. REV. NOTE:	P/N	LCP12
M BT 03/27/00	ADDED NOTE:		

THIS DOCUMENT CONTAINS PROPRIETARY DATA OF ETI SYSTEMS. REPRODUCTION OR USE OF ANY PART THERE OF MAY BE MADE EXCEPT BY WRITTEN PERMISSION.

SPECIFICATIONS

RESOLUTION ----- INFINITE

OUTPUT SMOOTHNESS ----- LESS THAN 0.1% INPUT VOLTAGE

CONTACT RESIST. VARIATION ----- LESS THAN 2%

DIELECTRIC STRENGTH ----- 500 VAC MIN.

INSULATION RESISTANCE ----- 1000 MEGOHMS AT 500 VDC MIN.

FRICITION ----- 1.8 oz. (3.6 oz FOR LCP12-100)

STOP STRENGTH ----- 20 OZ. MIN.

RESISTANCE TEMPCO ----- ±400 PPM/°C

WEIGHT ----- 10 TO 35 GRAMS

LIFE EXPECTANCY ----- 20 MILLION STROKES

MATERIALS

BODY ----- ALUMINUM (BLACK ANODIZE)

LID ----- HIGH TEMP. PLASTIC

SHAFT ----- STAINLESS STEEL

TERMINALS ----- BRASS GOLD PLATED

RESISTANCE ELEMENT ----- CONDUCTIVE PLASTIC

OPTIONS AVAILABLE

SPECIAL ENDED SHAFTS

SPECIAL RESISTANCE VALUES

SPECIAL LINEARITY

NON STANDARD STROKES

SPRING RETURNS

MODEL NO.	LCP12-12	LCP12-25	LCP12-50	LCP12-76	LCP12-100
STD. RESIS. VALUES	500, 1K, 2K 5K, 10K	500, 1K, 2K 5K, 10K, 20K	1K, 2K, 5K 10K, 20K	1K, 2K, 5K 10K, 20K	1K, 2K, 5K 10K, 20K
RESISTANCE TOL.	±20% ±1.5%	±20% ±0.7%	±20% ±0.5%	±20% ±0.5%	±20% ±0.5%
LINEARITY (IND.)					
POWER RATING	0.2 WATT	0.4 WATT	0.7 WATT	1.2 WATT	1.2 WATT
STROKE MECH-F-1-0	1/2"	2"	3"	4"	
STROKE ELECT ±.02	2.00	3.00	4.00	5.00	
"A" DIM ±0.04	1.50	2.75	3.76	4.76	
"B" DIM ±0.02	1.26	1.77	2.75	3.76	4.76

SHAFT STYLES

LCP12P-(STROKE)-(RES.) (P) PLAIN

LCP12A - - - (A) 5/16"

LCP12B - - - (B) #5-40 THREAD

LCP12C - - - (C) CHAMFERED 0.030" DIA. X 45°

LCP12S - - - (S) SPRING RETURN

LCP12S-76 OR -100 (RES) 1 1/4" FOR 3" & 4" STROKE SPRING RETURN.

NOTE: FOR SPRING RETURN WITH THREAD, SEE DWG. LCP12ST

ETI SYSTEMS CARLSBAD CALIFORNIA

DATE: 3-29-88

BY: _____

APPRVD: _____

BT: _____

SCALE: NONE

CODE IDENT: 19477

ETI SYSTEMS CARLSBAD CALIFORNIA

LINEAR MOTION POTENTIOMETER

LCP12

A.5 Effect on tensile behavior of a central hole in a bearing

Large diameter elastomeric bearings are generally fabricated using a central mandrel that 1) enables the stacking of the alternate layers of rubber and steel shims prior to vulcanization, and 2) facilitates efficient heating of the bearing for vulcanization. Upon removal, the resulting hole can be filled with a lead plug to form a LR bearing.

The behaviors of LR and LDR bearings in tension have been assumed to be identical because the lead plug is not actively engaged. The effect of the central hole on tensile behavior has been assumed to be negligible but is studied here because excessive values of tensile stress and/or shear strain could trigger premature failure due to cavitation or debonding of the rubber from a shim plate.

Axisymmetric finite element analysis was performed to investigate the effect of the central hole on distributions of tensile stress and shear strain. Analysis of one 7-mm thick constrained rubber layers from the DIS bearing type DA (see Table 6-2) was performed using ABAQUS (Dassault, 2010e). The elastomer was modeled as an elastic material with Young's modulus = 1.35 MPa and Poisson's ratio = 0.49. The model is shown in Figure A.1. The central hole, when modeled, was 20 mm in diameter. The X-Y coordinate system is shown; the origin (0, 0) is identified by the solid circle.

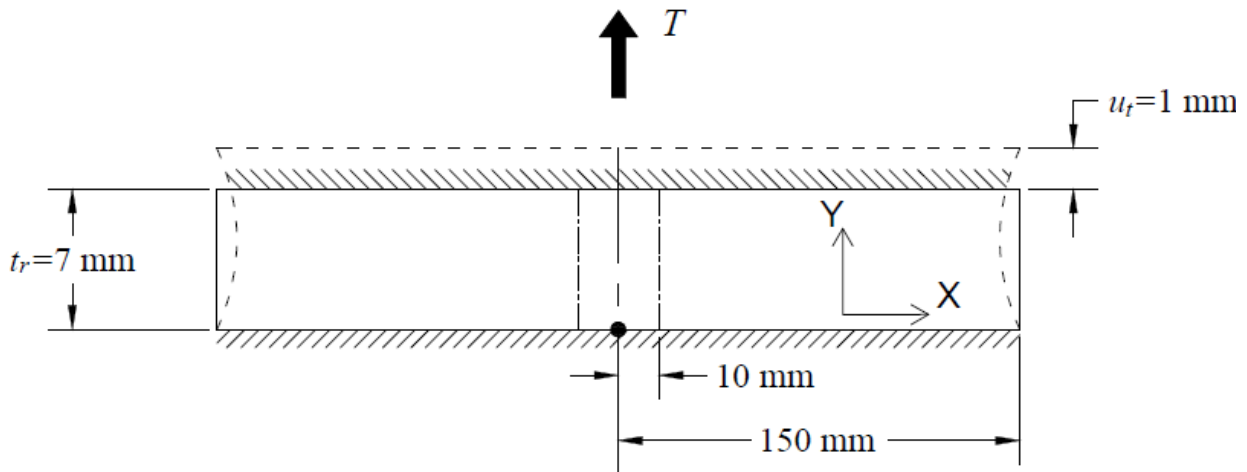


Figure A-1 Tension in a single constrained rubber layer

Consider the distribution of normal stress and shear strain at the rubber-shim interface of a constrained rubber layer that is shown in Figure A.2b and Figure A.2c; this layer has no central hole. The applied axial displacement, $u_t = 1$ mm. The horizontal axis is distance X normalized by one half of the outside diameter, D_o , of the rubber layer.

The following boundary conditions are imposed:

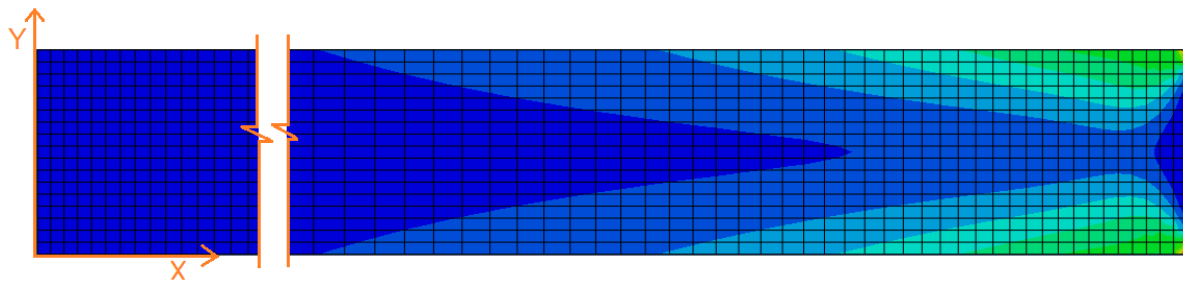
- Zero displacements in the two horizontal directions ($U_1 = 0$ and $U_2 = 0$) at $Y = 0$.
- Zero displacement in the X direction ($U_1 = 0$) at $Y = t_r$.

For this example, the distribution of normal stress is approximately parabolic, with a maximum value at the center of the bearing. The shear strain is small and approximately constant near the center of the bearing, and has a maximum value at the free edge.

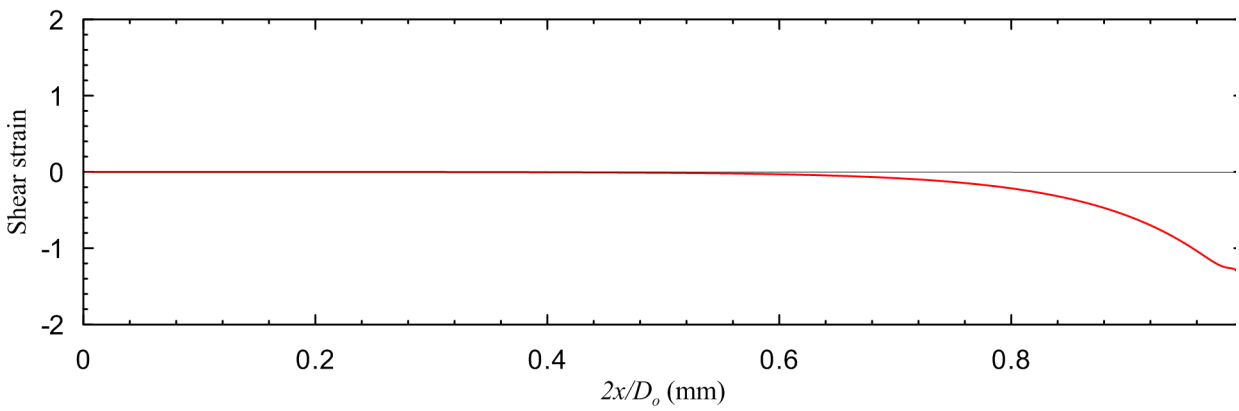
Consider now the distribution of normal stress and shear strain at the rubber-shim interface of a constrained rubber layer with a central hole of radius 10 mm that is shown in Figure A.3. The elastomer and the boundary conditions are those reported above. The introduction of a central hole does not change the shear strain at the outer radius ($X = 150$ mm). The inclusion of a central hole leads to a significant (50%) increase in the maximum shear strain, with the peak value observed at the inner radius ($X = 10$ mm). The distributions of shear and normal stress in a constrained rubber layer with and without a central hole are presented together in Figure A.4.

There are two mode of failures of elastomeric bearings in tension: 1) formation of cavities in the rubber volume, and 2) debonding at the rubber-shim interface. The first mode of failure depends on the hydrostatic stress. As the inclusion of a central hole does not change the maximum value of normal stress in the three orthogonal direction, the cavitation strength of an elastomeric bearing will not be significantly affected by the hole. Bearings with a central hole will have a lower tensile strength if failure occurs due to debonding (prior to cavitation) because the hole increases the maximum shear strain. The probable location of the debonding is rubber-shim interface at the inner perimeter.

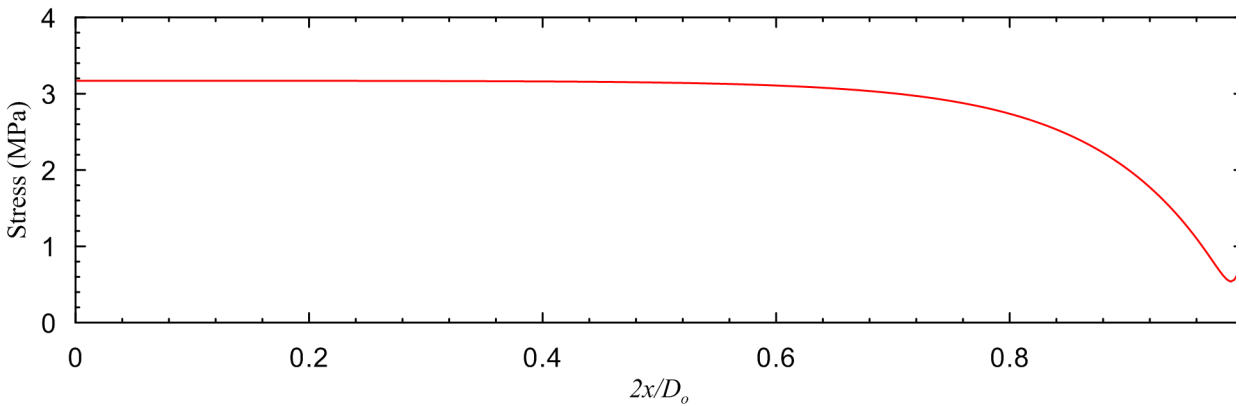
The lead core in a LR bearing does not contribute to the compressive and tensile capacity. The results of tensile tests on elastomeric bearings with a central hole are likely better correlated to the behavior of LR bearing in tension than tests on bearings without a hole.



a) Model of the rubber layer

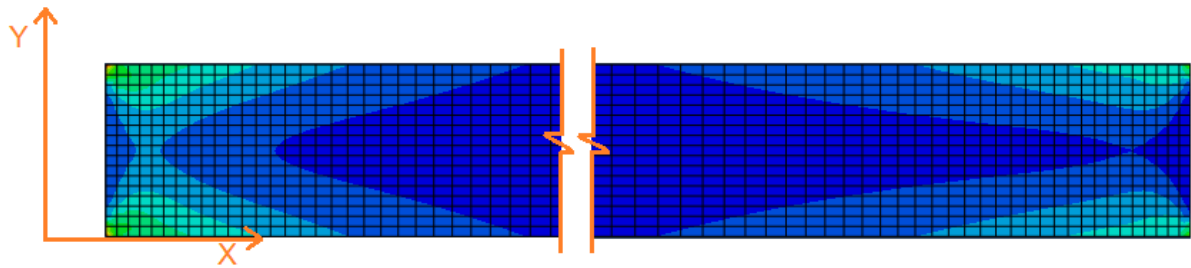


b) Shear strain at rubber-shim interface

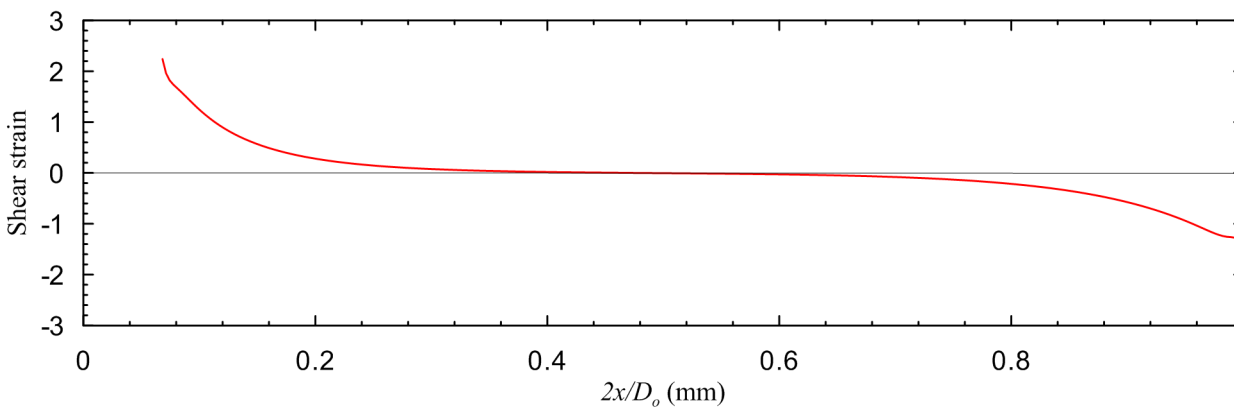


c) Tensile stress at rubber shim interface

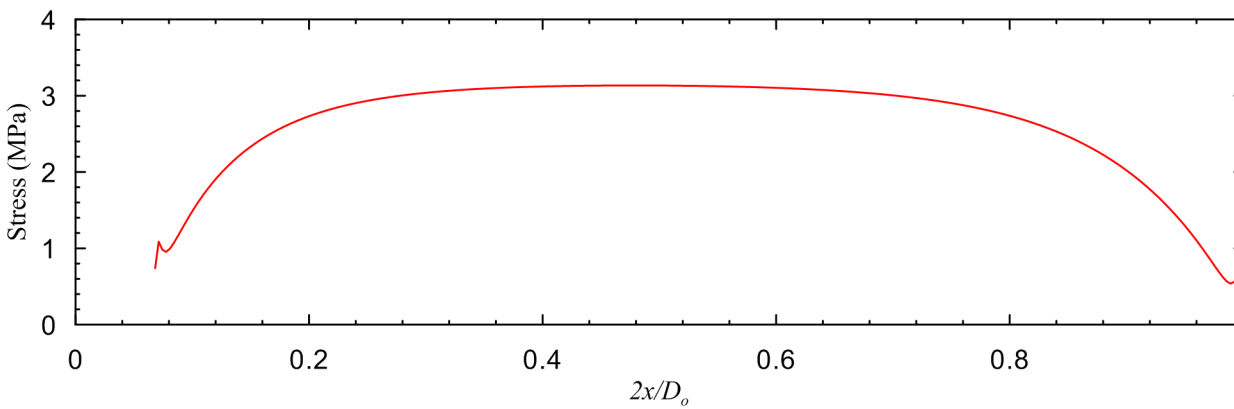
Figure A-2 Shear strain and tensile stress in a constrained solid rubber layer in tension



a) Model of the annular rubber layer



b) Shear strain at rubber-shim interface



c) Tensile stress at rubber shim interface

Figure A-3 Shear strain and tensile stress in a constrained annular rubber layer in tension

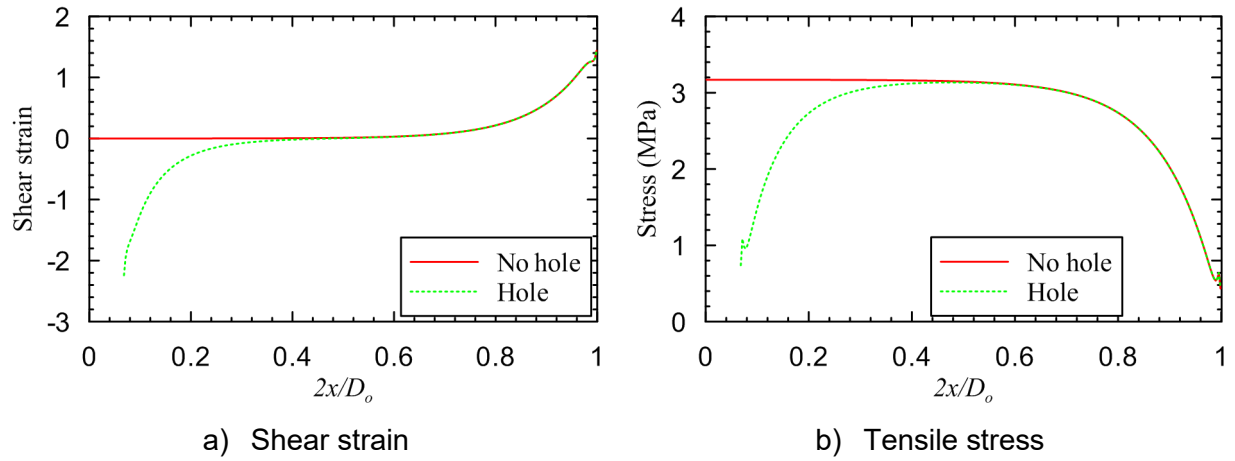


Figure A-4 Distribution of shear strain in the radial direction

A.6 Failure Mode in Tension

The description of the failure of each bearing in tension is presented here. The mode is defined here as the loading conditions under which the bearing failed (e.g., pure tension, tension with lateral offset). The mechanism describes how failure began.

Table A-2 Failure states of bearings under tensile load




Failure description	Image of failure
<p>Bearing: DA1 Test no: DA1_13</p> <p>Failure mode: tension with lateral offset Failure mechanism: cavities in rubber layer</p> <p>Image note: 214% lateral offset, 25% tensile strain</p>	
<p>Bearing: DA2 Test no: DA2_3a</p> <p>Failure mode: tension Failure mechanism: cavities in rubber layer</p> <p>Image note: 50% tensile strain</p>	
<p>Bearing: DA3 Test no: DA3_06</p> <p>Failure mode: tension Failure mechanism: unknown</p> <p>Image note: 65% tensile strain</p>	

Table A-2 Failure states of bearings under tensile load (contd.)





Failure description	Image of failure
<p>Bearing: DA4 Test no: DA4_14</p> <p>Failure mode: tension Failure mechanism: unknown</p> <p>Image note: 25% tensile strain</p>	
<p>Bearing: DB1 Test no: DB1_1a</p> <p>Failure mode: no failure</p> <p>Image note: 187% lateral offset 10% tensile strain</p>	
<p>Bearing: DB1 Test no: DB1_14</p> <p>Failure mode: no failure</p> <p>Image note: 93% tensile strain</p>	
<p>Bearing: DB2 Test no: DB2_01</p> <p>Failure mode: tension with lateral offset Failure mechanism: cavities in rubber layer</p> <p>Image note: 187% lateral offset</p>	

Table A-2 Failure states of bearings under tensile load (contd.)

Failure description	Image of failure
<p>Bearing: DB3 Test no: DB3_1a</p> <p>Failure mode: tension Failure mechanism: unknown</p>	<p>No rupture</p>
<p>Bearing: DB4 Test no: DB4_11a</p> <p>Failure mode: no failure</p> <p>Image note: 100% tensile strain</p>	
<p>Bearing: DB4 Test no: DB4_21</p> <p>Failure mode: no failure</p> <p>Image note: 187% lateral offset and 50% tensile strain</p>	
<p>Bearing: DB4 Test no: DB4_21</p> <p>Failure mode: no failure</p> <p>Image note: 187% lateral offset and 100% tensile strain</p>	

Table A-2 Failure states of bearings under tensile load (contd.)

Failure description	Image of failure
<p>Bearing: MA1 Test no: MA1_08</p> <p>Failure mode: tension Failure mechanism: debonding</p> <p>Image note: 25% tensile strain</p>	
<p>Bearing: MA2 Test no: MA2_03</p> <p>Failure mode: tension Failure mechanism: debonding</p> <p>Image note: 65% tensile strain</p>	
<p>Bearing: MA3 Test no: MA3_06</p> <p>Failure mode: tension Failure mechanism: unknown</p> <p>Image note: 50% tensile strain</p>	

Table A-2 Failure states of bearings under tensile load (contd.)




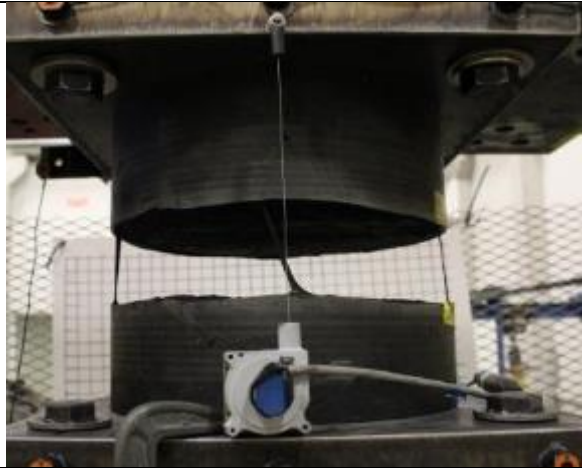
Failure description	Image of failure
<p>Bearing: MA4 Test no: MA4_03</p> <p>Failure mode: tension Failure mechanism: debonding</p> <p>Image note: 50% tensile strain</p>	
<p>Bearing: MB1 Test no: MB1_12</p> <p>Failure mode: tension Failure mechanism: unknown</p>	<p>Image not available</p>
<p>Bearing: MB2 Test no: MB2_01</p> <p>Failure mode: tension Failure mechanism: debonding</p> <p>Image note: 100% tensile strain</p>	
<p>Bearing: MB3 Test no: MB3_06</p> <p>Failure mode: tension Failure mechanism: debonding</p> <p>Image note: 50% tensile strain</p>	

Table A-2 Failure states of bearings under tensile load (contd.)

Failure description	Image of failure
<p>Bearing: MB4 Test no: MB4_01</p> <p>Failure mode: tension Failure mechanism: debonding</p> <p>Image note: 100% tensile strain</p>	 A photograph showing a large, dark, cylindrical bearing component suspended from a metal frame. The bearing is under tensile load, as indicated by the thin wire or cable attached to its top. The bearing shows signs of failure, specifically debonding, which is visible as a dark, irregular shape on its surface. The background is a white, grid-like safety fence. A white electrical plug is visible in the foreground, connected to the bearing's support structure.

APPENDIX B RESPONSE OF THE TWO-NODE MACRO MODEL OF BASE-ISOLATED NUCLEAR POWER PLANT

B.1 Strength Degradation in Shear due to Heating of the Lead Core

The percentiles of peak horizontal displacement and shear force with consideration of heating are presented here. The peak responses for each ground motion set are assumed to distribute lognormally with arithmetic mean μ , median θ , and logarithmic standard deviation σ , which are computed as:

$$\mu = \frac{1}{n} \sum_{i=1}^n y_i \quad \theta = \exp\left(\frac{1}{n} \sum_{i=1}^n \ln y_i\right) \quad \sigma = \sqrt{\frac{1}{n-1} \sum_{i=1}^n (\ln y_i - \ln \theta)^2}$$

where n is the total number of ground motion sets (=30), and y_i is the peak response for i th ground motion set. If a data set Y distributes lognormally then $\log Y$ follows a normal (Gaussian) distribution, and is referred to associated normal distribution of Y . The mean and standard deviation of associated normal distribution are $\log \theta$ and σ , respectively. The Standardized normal distribution¹ table can be used to calculate the standard normal variable u_p that corresponds to p th percentile. The p th percentile response of Y is calculated as:

$$y_p = F^{-1}(p | \ln \theta, \sigma) = \{y_p : F(y_p | \ln \theta, \sigma) = p\}$$

The value of u_p for 50th (median), 90th, and 99th percentiles can be obtained as 0, 1.29, and 2.33 respectively, from standard normal distribution table. For model T2Q3 in Table B.1 at 100% DBE, median $\theta = 471$ and $\sigma = 0.22$, which gives the 90th and 99th percentile response as:

$$y_{90} = \exp(\ln 471 + 1.29 \times 0.22) = 550 \text{ mm}$$

$$y_{99} = \exp(\ln 471 + 2.33 \times 0.22) = 623 \text{ mm}$$

¹ If Y is a normal random variable with distribution $N(\mu, \sigma)$, then $U = (Y - \mu) / \sigma$ is the standardized normal random variable with distribution $N(0, 1)$. The cumulative distribution probability of U can be obtained from standard normal distribution table.

Table B-1 Percentiles of peak horizontal displacement (mm) for 30 ground motion sets; heating effects¹

Model	100% DBE			150% DBE			167% DBE			200% DBE				
	50 th	90 th	99 th	50 th	90 th	99 th	50 th	90 th	99 th	50 th	90 th	99 th	σ	
T2Q3	471	549	622	806	982	1154	923	1132	1336	0.16	1150	1420	1688	0.17
T2Q6	363	419	470	666	773	873	777	919	1054	0.13	1000	1214	1421	0.15
T2Q9	302	360	415	560	646	725	661	757	845	0.11	877	1029	1172	0.12
T2Q12	257	320	383	494	576	653	584	677	763	0.12	771	888	996	0.11
T2Q15	226	289	353	441	527	611	523	617	706	0.13	698	811	916	0.12
T3Q3	529	609	683	957	1087	1207	1113	1270	1415	0.10	1425	1638	1834	0.11
T3Q6	405	468	527	737	855	966	862	1000	1127	0.12	1140	1308	1463	0.11
T3Q9	331	404	474	626	724	815	738	856	965	0.12	963	1124	1276	0.12
T3Q12	290	370	452	539	639	734	644	752	853	0.12	858	999	1130	0.12
T3Q15	266	343	422	483	596	707	570	686	798	0.14	768	900	1024	0.12

1. The horizontal displacement corresponding to 100 (200, 300)% shear strain in the elastomer is 310 (620, 930) mm.

Table B-2 Percentiles of peak horizontal shearing force (%W) for 30 ground motion sets; heating effects^{1, 2}

Model	100% DBE			150% DBE			167% DBE			200% DBE				
	50 th	90 th	99 th	50 th	90 th	99 th	50 th	90 th	99 th	50 th	90 th	99 th	σ	
T2Q3	48	56	63	82	99	117	93	114	135	0.16	116	143	170	0.17
T2Q6	40	45	51	69	80	90	80	94	107	0.13	102	123	144	0.15
T2Q9	36	41	47	60	69	77	70	80	89	0.10	91	106	120	0.12
T2Q12	34	40	45	56	64	72	64	74	83	0.11	82	94	105	0.11
T2Q15	34	40	45	53	61	69	61	70	79	0.11	77	88	99	0.11
T3Q3	25	29	32	44	50	55	50	58	64	0.10	64	74	82	0.11
T3Q6	22	25	28	36	41	46	41	47	53	0.10	53	61	68	0.11
T3Q9	22	25	28	34	38	42	38	43	48	0.09	48	54	60	0.10
T3Q12	22	26	29	32	37	41	36	41	46	0.10	45	51	57	0.10
T3Q15	24	27	30	32	37	42	36	41	46	0.11	44	50	55	0.10

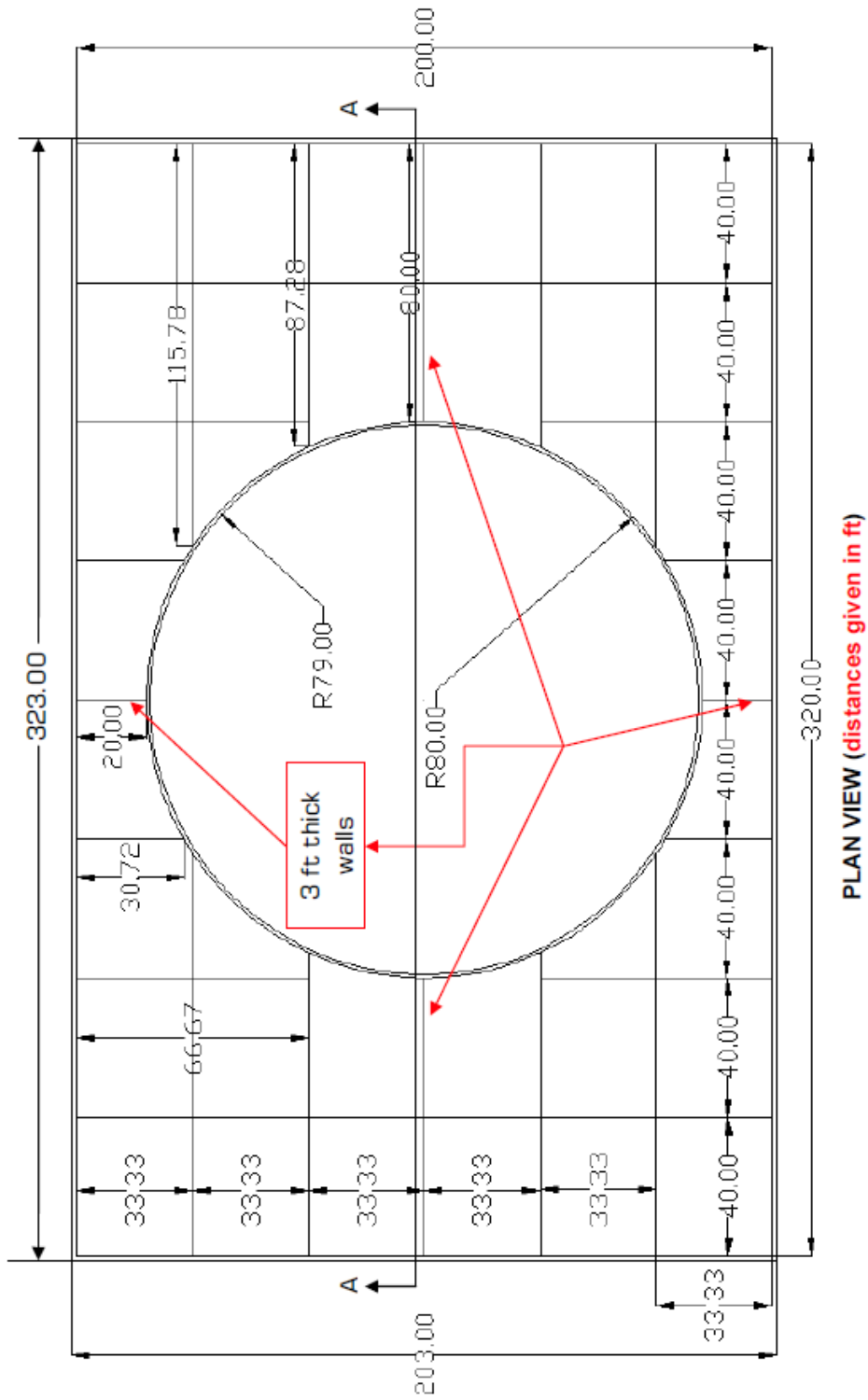
1. The gravity weight W on the bearing is approximately 3500 kN.

2. The characteristic strength, Q_d , ranges between 3%W (e.g., T2Q3) and 15%W (e.g., T3Q15).

APPENDIX C RESPONSE OF THE LUMPED-MASS STICK MODEL OF BASE-ISOLATED NUCLEAR POWER PLANT

C.1 Model of Nuclear Power Plant

The finite element model provided by Roche-Rivera (2013) provides dimensions of the sample nuclear power plant that is studied in this report. Figure C.1 and C.2 reproduce information from Roche-Rivera (2013).



Notes for Auxiliary Building:

- Interior walls except those highlighted above have a thickness = 2 ft.
- Exterior walls have a thickness of 3 ft.

Figure C-1 The plan view of the representative reactor model (Roche-Rivera, 2013)

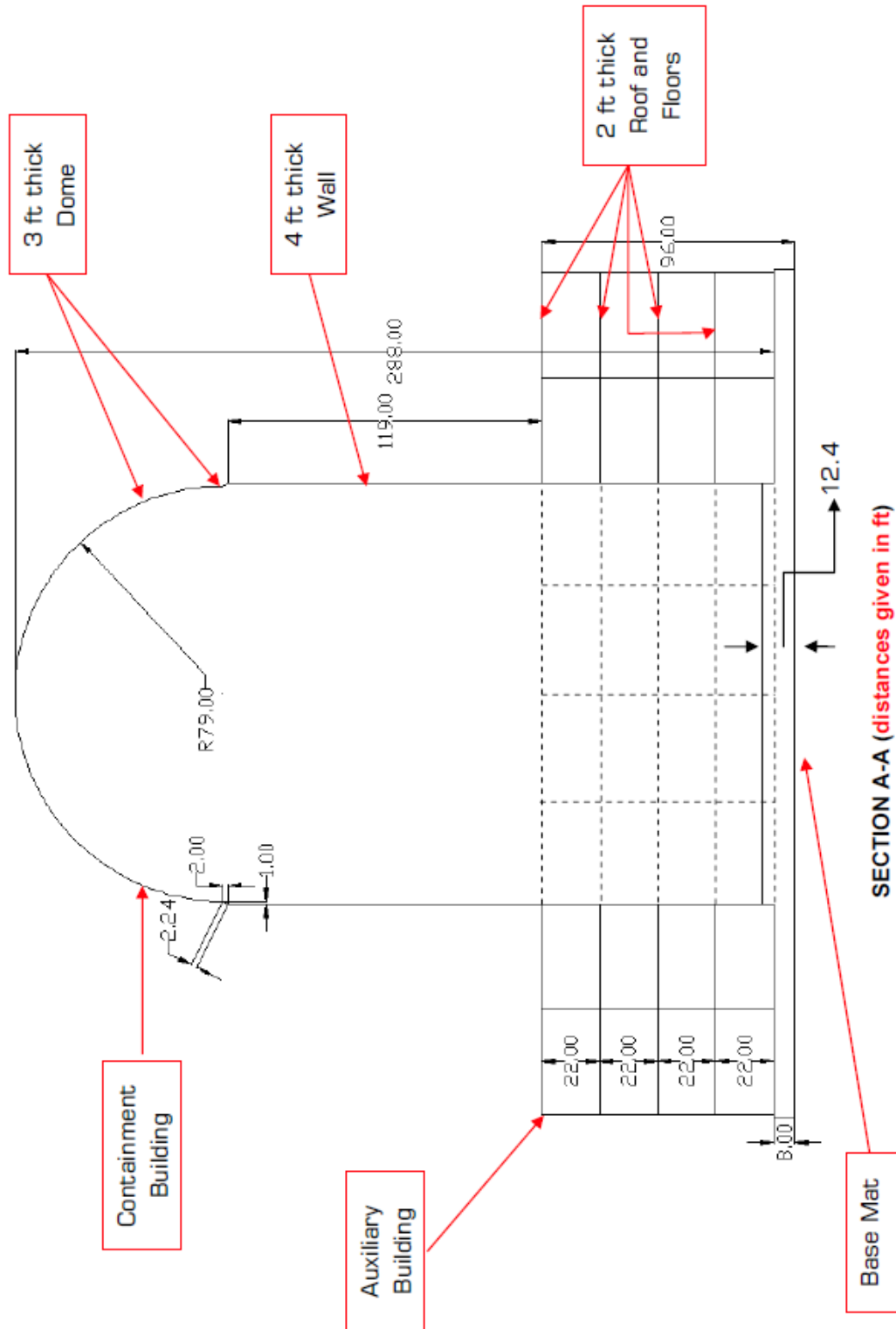


Figure C-2 The plan view of the representative reactor model

C.2 Geometric and Material Properties of the Stick Model

The geometric and material properties of the three lumped-mass stick models of the Auxiliary Shield Building (ASB), Containment Internal Structure (CIS), and Steel Containment Vessel (SCV) are reproduced from EPRI (2007) in this appendix in Tables C.1 and C.2.

Table C-1 Nodes and mass properties for structural model (units: kip, feet, seconds)

				North-South Model			East-West Model		
NODE	X	Y	Z	MX	MZ	Iy	MY	MZ	Ix
ASB									
1	0	0	60.50						
11	0	0	66.50	236.400	236.400	1641500	236.400	236.400	466740
21	0	0	81.50	494.260	494.260	3612000	494.260	494.260	847820
31	0	0	91.50	307.080	439.280	1938300	307.080	439.280	456250
41	0	0	99.00	330.460	330.460	2619900	330.460	330.460	484190
51	0	0	106.17	210.100	210.100	1287500	210.100	210.100	390700
61	0	0	116.50	597.740	465.540	2526200	597.740	465.540	764330
80	0	0	134.87	0	441.849	3448492	0	441.849	710952
80mc	-10	-20	134.87	441.849	0	0	441.849	0	0
90	0	0	145.37	165.406	165.406	933560	165.406	165.406	293100
100	0	0	153.98	190.099	190.099	1022510	190.099	190.099	316650
110	0	0	164.51	164.371	164.371	422680	164.371	164.371	271344
120	0	0	179.56	0	200.431	323582	0	200.431	349825
120out	75	0	179.56	0	0	0	0	0	0
120mc	-10	-20	179.56	200.431	0.00	0.00	200.431	0.00	0.00
130	0	0	200.00	126.050	126.050	317710	126.050	126.050	317710
140	0	0	220.00	132.470	132.470	333900	132.470	132.470	333900
150	0	0	242.50	140.260	140.260	353540	140.260	140.260	353540
160	0	0	265.00	231.223	231.223	529020	231.223	231.223	529020
309	0	0	295.23	263.980	433.530	276470	263.980	433.530	276470
310	0	0	333.13	135.590	91.320	63050	135.590	91.320	63050
310out	75	0	333.13	0	0	0	0	0	0
320	0	0	296.77	0.000	0.000	0	0.000	0.000	0

Table C.1 Nodes and mass properties for structural model (contd.)

				North-South Model			East-West Model		
NODE	X	Y	Z	MX	MZ	Iy	MY	MZ	Ix
CIS									
5	0	0	60.5						
500	0	0	66.5	595.3	593.4	568000	595.3	595.3	568000
531	0	0	82.5	927.6	927.6	1422000	927.6	927.6	137100
532	0	0	98	468.7	468.7	70800	468.7	468.7	680000
533	0	0	103	146.3	286.2	185000	146.3	286.2	177000
534	0	0	107.17	319.1	238.7	358900	319.1	238.7	319130
535	0	0	134.25	0	238.6	282150	0	238.6	255550
535mc	-10	-10	134.25	298.2	0	0	298.2	0	0
536	0	0	153	14.6	14.6	2019	14.6	14.6	2504
537	0	0	153	30.8	30.8	6065	30.8	30.8	4321
538	0	0	169	0	9.4	748	0	9.4	696
538out	75	0	169	0	0	0	0	0	0
538mc	-10	-10	169	9.4	0	0	9.4	0	0

				North-South Model			East-West Model		
NODE	X	Y	Z	MX	MZ	Iy	MY	MZ	Ix
SCV									
401	0	0	100.000	1.739	1.739	3636	1.739	1.739	3636
402	0	0	104.125	5.541	5.541	11732	5.541	5.541	11732
403	0	0	110.500						
404	0	0	112.500	15.388	15.388	33362	15.388	15.388	33362
406	0	0	131.677	17.907	17.907	37914	17.907	17.907	37914
407	0	0	138.583						
408	0	0	141.500	17.904	17.904	38689	17.904	17.904	38689
409	0	0	162.000	18.349	18.349	38850	18.349	18.349	38850
410	0	0	169.927	28.994	28.994	61388	28.994	28.994	61388
411	0	0	200.000	28.340	28.340	60003	28.340	28.340	60003
412	0	0	224.000	40.251	51.739	81602	51.522	51.739	81602
413	0	0	224.208	15.746	15.746	33338	15.746	15.746	33338
414	0	0	255.021	11.271	11.271	21897	11.271	11.271	21897
415	0	0	265.833	10.288	10.288	14610	10.288	10.288	14610
416	0	0	273.833	10.070	10.070	8149	10.070	10.070	8149
417	0	0	281.901	5.618	5.618	0	5.618	5.618	0
417out	65	0	281.901	0	0	0	0	0	0
425	0	0	224.000	28.439	16.951		17.168	16.951	

Note: All values are in kip, seconds, feet units.
 Assume: $I_z = I_x + I_y$.

Table C-2 Element properties for structural model (units: kip, feet, seconds)

		North-South Model				East-West Model				
ELEM	NODES		A	IYY	AshearY	A	IZZ	AshearZ	Material	Modal Damping
ASB										
1	1	11	15484.0 0	9717600 0	10322.67	15484.00	11236800	10322.67	Concrete	4 %
2	11	21	3462.50	6266240	1366.35	3462.50	4061440	1011.30	Concrete	4 %
3	21	31	3462.50	6266240	1366.35	3462.50	4061440	1011.30	Concrete	4 %
4	31	41	3462.50	6266240	1366.35	3462.50	4061440	1011.30	Concrete	4 %
5	41	51	3293.30	5744880	1214.35	3293.30	3562800	1008.14	Concrete	4 %
6	51	61	3293.30	5744880	1214.35	3293.30	3562800	1008.14	Concrete	4 %
7	61	80	3293.30	5744880	1214.35	3293.30	3562800	1008.14	Concrete	4 %
	80	80mc	Rigid Link							
31	80	90	3197.52	4196560	1185.61	3197.52	4412370	1360.04	Concrete	4 %
32	90	100	3197.52	4196560	1185.61	3197.52	4412370	1360.04	Concrete	4 %
33	100	110	2501.52	3676560	874.54	2501.52	3311570	1121.07	Concrete	4 %
34	110	120	1954.00	3083632	810.51	1954.00	3290960	746.70	Concrete	4 %
	120	120out	Rigid Link							
	120	120mc	Rigid Link							
35	120	130	1338.00	2700000	535.20	1338.00	2700000	535.20	Concrete	4 %
36	130	140	1338.00	2700000	535.20	1338.00	2700000	535.20	Concrete	4 %
37	140	150	1338.00	2700000	535.20	1338.00	2700000	535.20	Concrete	4 %
38	150	160	1338.00	2700000	535.20	1338.00	2700000	535.20	Concrete	4 %
301	160	309	50.45	1	0.000	50.45	1	0.000	Concrete	4 %
302	320	309	13.59	2680	10.872	13.59	2681.6	10.872	Concrete	4 %
303	309	310	704.50	431720	281.800	704.50	431720	281.800	Concrete	4 %
	310	310out	Rigid Link							
	160	320	Rigid	Rigid	Rigid	Rigid	Rigid	Rigid		

Table C.2 Element properties for structural model (contd.)

		North-South Model				East-West Model				
ELEM	NODES		A	IYY	AshearY	A	IZZ	AshearZ	Material	Modal Damping
CIS										
500	5	500	15175	1.24E+07	9228.29	15175	1.11E+07	8311.88	Concrete	4 %
501	500	531	15175	1.24E+07	9228.29	15175	1.11E+07	8311.88	Concrete	4 %
502	531	532	6732	4.50E+06	2976.99	6732	3.33E+6	2965.86	Concrete	4 %
503	532	533	7944	6.74E+06	4411.70	7944	5.95E+06	3948.04	Concrete	4 %
504	533	534	5160	4.60E+06	3026.91	5160	2.93E+06	2702.19	Concrete	4 %
505	534	535	1705	7.83E+05	613.65	1705	5.75E+05	405.33	Concrete	4 %
	535	535mc	Rigid Link							
506	535	536	326	3.15E+03	13.10	326	1.77E+04	67.36	Concrete	4 %
507	535	537	484	3.89E+04	93.98	484	1.58E+04	64.30	Concrete	4 %
508	537	538	164	2.11E+03	29.24	164	2.47E+03	17.16	Concrete	4 %
	538	538out	Rigid Link							
	538	538mc	Rigid Link							
506	535	536	326	3.15E+03	13.10	326	1.77E+04	67.36	Concrete	4 %
507	535	537	484	3.89E+04	93.98	484	1.58E+04	64.30	Concrete	4 %
508	537	538	164	2.11E+03	29.24	164	2.47E+03	17.16	Concrete	4 %

Table C.2 Element properties for structural model (contd.)

ELEM	NODES		North-South Model			East-West Model			Material	Modal Damping
			A	IYY	AshearY	A	IZZ	AshearZ		
SCV										
401	401	402	14.49	29,107	27.6	14.49	29,107	27.6	Steel	4 %
402	402	403	59.63	126,243	29.81	59.63	126,243	29.81	Steel	4 %
403	403	404	59.63	126,243	29.81	59.63	126,243	29.81	Steel	4 %
405	404	406	59.63	126,243	29.81	59.63	126,243	29.81	Steel	4 %
406	406	407	59.63	126,243	29.81	59.63	126,243	29.81	Steel	4 %
407	407	408	59.63	126,243	29.81	59.63	126,243	29.81	Steel	4 %
408	408	409	59.63	126,243	29.81	59.63	126,243	29.81	Steel	4 %
409	409	410	59.63	126,243	29.81	59.63	126,243	29.81	Steel	4 %
410	410	411	59.63	126,243	29.81	59.63	126,243	29.81	Steel	4 %
411	411	412	59.63	126,243	29.81	59.63	126,243	29.81	Steel	4 %
412	412	413	59.63	126,243	29.81	59.63	126,243	29.81	Steel	4 %
413	413	414	13.15	110,115	27.1	13.15	110,115	27.1	Steel	4 %
414	414	415	4.58	83,714	24.6	4.58	83,714	24.6	Steel	4 %
415	415	416	1.74	46,047	19.89	1.74	46,047	19.89	Steel	4 %
416	416	417	0.55	13,850	8.56	0.55	13,850	8.56	Steel	4 %
	417	417out	Rigid Link							
	Spring		Kz	Kx		Kz	Ky			
	412	425	27630	80439		27630	9467			4 %

Notes:

All values are in kip, seconds, feet units

Material properties:

Concrete:

Elastic modulus = 519,120 ksf
 Poisson's ratio = 0.17

Steel:

Elastic modulus = 4,248,000 ksf
 Poisson's ratio = 0.30

C.3 Modal Analysis of Lumped-Mass Stick Model

The fixed-base models of the ASB, CIS, and SCV are created in SAP2000. Modal analyses of the fixed-base models of ASB, SCV, and CIS are performed and results are presented below.

Table C-3 Modal properties of the Auxiliary Shield Building (ASB)

Mode	Period (sec)	Freq. (Hz)	UX	UY	UZ	SumUX	SumUY	SumUZ
1	0.362	2.762	0.000	0.405	0.000	0.000	0.405	0.000
2	0.323	3.097	0.447	0.000	0.000	0.447	0.405	0.000
3	0.158	6.345	0.008	0.000	0.000	0.455	0.405	0.000
4	0.142	7.026	0.001	0.177	0.000	0.456	0.583	0.000
5	0.136	7.336	0.369	0.000	0.000	0.825	0.583	0.000
6	0.093	10.704	0.000	0.000	0.573	0.825	0.583	0.573
7	0.082	12.239	0.000	0.000	0.000	0.825	0.584	0.573
8	0.076	13.090	0.014	0.000	0.000	0.839	0.584	0.573
9	0.072	13.938	0.000	0.181	0.000	0.839	0.765	0.573
10	0.070	14.197	0.038	0.000	0.000	0.877	0.765	0.573
11	0.064	15.624	0.000	0.105	0.000	0.877	0.870	0.573
12	0.051	19.656	0.027	0.000	0.000	0.904	0.870	0.573
13	0.049	20.275	0.000	0.005	0.000	0.904	0.875	0.573
14	0.045	22.124	0.000	0.000	0.000	0.904	0.875	0.573
15	0.043	23.064	0.003	0.000	0.000	0.907	0.875	0.573
16	0.043	23.251	0.000	0.000	0.282	0.907	0.875	0.855
17	0.040	24.998	0.015	0.000	0.000	0.923	0.875	0.855
18	0.039	25.757	0.000	0.000	0.000	0.923	0.875	0.855
19	0.039	25.871	0.000	0.022	0.000	0.923	0.897	0.855
20	0.033	30.346	0.000	0.001	0.000	0.923	0.898	0.855

Table C-4 Modal properties of the Steel Containment Vessel (SCV)

Mode	Period (sec)	Freq. (Hz)	UX	UY	UZ	SumUX	SumUY	SumUZ
1	0.275	3.632	0.000	0.157	0.000	0.000	0.157	0.000
2	0.180	5.548	0.716	0.000	0.000	0.716	0.157	0.000
3	0.158	6.325	0.000	0.603	0.000	0.716	0.760	0.000
4	0.157	6.371	0.000	0.000	0.092	0.716	0.760	0.092
5	0.104	9.628	0.043	0.000	0.000	0.759	0.760	0.092
6	0.083	12.048	0.000	0.000	0.000	0.759	0.760	0.092
7	0.062	16.216	0.000	0.000	0.674	0.759	0.760	0.766
8	0.053	18.910	0.000	0.148	0.000	0.759	0.908	0.766
9	0.053	18.973	0.152	0.000	0.000	0.911	0.908	0.766
10	0.038	26.652	0.000	0.000	0.135	0.911	0.908	0.901
11	0.032	31.388	0.000	0.020	0.000	0.911	0.929	0.901
12	0.031	31.976	0.015	0.000	0.000	0.926	0.929	0.901
13	0.028	35.829	0.000	0.011	0.000	0.926	0.939	0.901
14	0.027	36.515	0.000	0.000	0.000	0.926	0.939	0.901
15	0.027	36.559	0.015	0.000	0.000	0.941	0.939	0.901
16	0.023	44.318	0.000	0.000	0.014	0.941	0.939	0.914
17	0.019	52.367	0.000	0.024	0.000	0.941	0.964	0.914
18	0.019	53.011	0.024	0.000	0.000	0.964	0.964	0.914
19	0.017	60.245	0.000	0.000	0.000	0.964	0.964	0.914
20	0.016	61.637	0.000	0.000	0.048	0.964	0.964	0.963

Table C-5 Modal properties of the Containment Internal Structure (CIS)

Mode	Period (sec)	Freq. (Hz)	UX	UY	UZ	SumUX	SumUY	SumUZ
1	0.086	11.682	0.002	0.212	0.000	0.002	0.212	0.000
2	0.079	12.608	0.227	0.002	0.000	0.229	0.214	0.000
3	0.061	16.423	0.005	0.014	0.000	0.235	0.227	0.000
4	0.060	16.538	0.003	0.048	0.000	0.238	0.275	0.000
5	0.054	18.566	0.026	0.011	0.000	0.264	0.286	0.000
6	0.048	20.648	0.129	0.002	0.000	0.393	0.289	0.000
7	0.045	22.350	0.001	0.041	0.000	0.394	0.330	0.000
8	0.039	25.879	0.010	0.241	0.000	0.404	0.571	0.000
9	0.036	27.866	0.148	0.107	0.000	0.552	0.678	0.000
10	0.034	29.032	0.145	0.041	0.000	0.698	0.718	0.000
11	0.025	40.062	0.000	0.000	0.504	0.698	0.718	0.504
12	0.020	51.211	0.039	0.083	0.000	0.736	0.802	0.504
13	0.018	54.918	0.107	0.053	0.000	0.843	0.855	0.504
14	0.015	65.950	0.000	0.000	0.264	0.843	0.855	0.768
15	0.012	83.236	0.076	0.062	0.000	0.918	0.916	0.768
16	0.011	91.693	0.000	0.000	0.007	0.918	0.916	0.775
17	0.010	99.850	0.051	0.057	0.000	0.969	0.973	0.775
18	0.008	129.955	0.000	0.000	0.127	0.969	0.973	0.902
19	0.007	138.466	0.000	0.000	0.005	0.969	0.973	0.907
20	0.004	284.819	0.000	0.000	0.093	0.969	0.973	1.000

C.4 Simplified Calculation of Modal Frequencies

A simplified model of the base-isolated nuclear power plant is presented in Figure C.3 to estimate the horizontal, vertical, torsional and rocking frequencies.

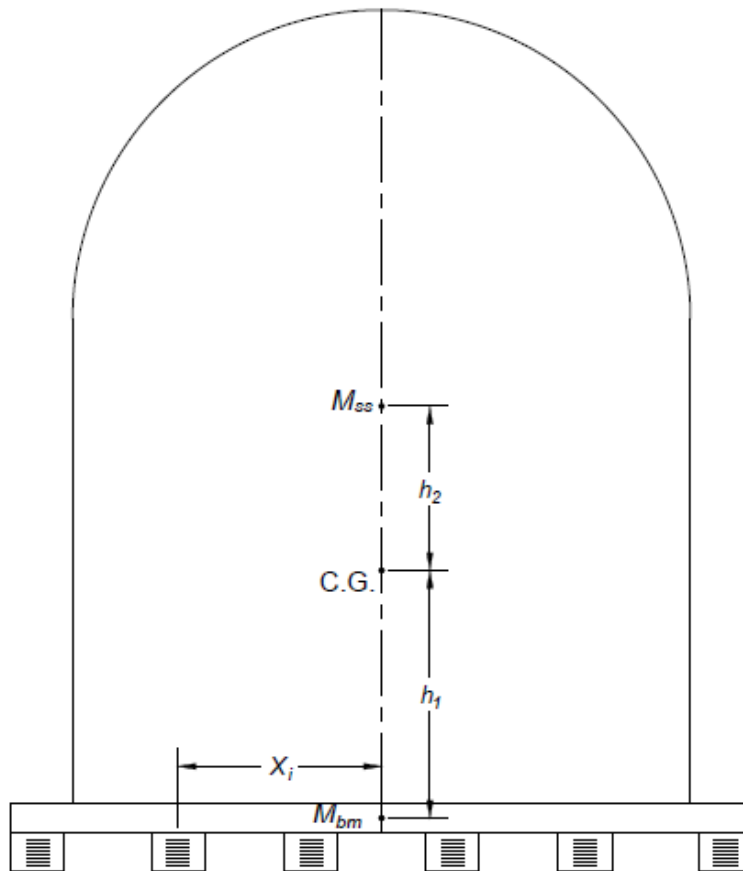


Figure C-3 A two-dimensional representation of base-isolated NPP

The basemat and superstructure is considered rigid and their masses are lumped at their respective center of gravities. The center of gravities of the different component of the base-isolated NPP are calculated using nodal properties presented in Table C.2, and are presented in Table C.6. The dimensions of the concrete basemat slab is 100m×60m×2.5m and the mat is assumed to be rigid in its plane. A symmetric layout of isolators is used beneath the basemat with the distance between the centers of adjacent bearings equal to 5 m, which requires a total of $N_b = 273$ isolators. This results in 13 and 21 rows of LR bearings in the two orthogonal horizontal directions. The layout of isolators is shown in Figure 9-5.

The modal frequencies are obtained using the properties of LR bearings presented in Table 9-5 and Table 9-6 for the isolation system T2Q6. The horizontal and vertical stiffnesses, K_{H0} and K_{V0} , of LR bearings are 5.29 MN/m and 6623 MN/m, respectively. The rocking frequency is obtained for the rotational motion of the superstructure along the shorter dimension (60 m) of the basemat, which gives smaller frequency than the rotation about the larger dimension (100 m).

The modal frequencies are calculated as:

$$f_{horizontal} = \frac{1}{2\pi} \sqrt{\frac{\sum_{i=1}^{N_b} K_{H0}}{M_{bm} + M_{ss}}} = 0.5 \text{ Hz}$$

$$f_{vertical} = \frac{1}{2\pi} \sqrt{\frac{\sum_{i=1}^{N_b} K_{V0}}{M_{bm} + M_{ss}}} = 17.7 \text{ Hz}$$

$$f_{rocking} = \frac{1}{2\pi} \sqrt{\frac{\sum_{i=1}^{N_b} K_{V0} X_i^2}{M_{bm} h_1^2 + M_{ss} h_2^2}} = 35.2 \text{ Hz}$$

where h_1 and h_2 are the distances of the center of gravities of basemat and superstructure from the center of gravity of whole superstructure.

Table C-6 Location of the center of gravities

Structure		Total mass (kg)	C.G.	Total height (m)
Superstructure (ss)	ASB	65571108	28.3	83.1
	SCV	3733776	40.9	67.5
	CIS	40979671	9.5	33.1
	Total	110284555	21.8	83.1
Basemat (bm)		36000000	1.25	2.5
Base-isolated NPP (Superstructure+basemat)		146284555	17.4 ¹	85.6

1. Distance from the C.G. of the basemat

C.5 Responses of the Base-isolated Nuclear Power Plant

The responses of the base-isolated NPP using the simplified and advanced LR bearing models are presented in this appendix. Mean (μ), median θ (50th), and 90th and 99th percentiles response are tabulated together with σ , which logarithmic standard deviation. The calculation of percentile responses are described in Appendix B.1 and Section 9.4.

The simplified isolator model uses a linear elastic model in the axial direction, and results in same σ in displacement and force response in Table C.8 through C.11. A large dispersion (σ) in the tensile response (Table C.8 and C.9) of the base-isolated NPP models for 30 ground motion sets is due to fact that some ground motions produce tensile response that is negligible or very close to zero. Cavitation is observed in the bearings of base-isolated NPP using advanced isolator model at 200% DBE shaking, hence the maximum tensile force response is close to the cavitation force in LR bearings for all ground motions. This results in a very small dispersion in tensile force response at 200% DBE shaking in Table C.20.

Table C-7 Percentiles of peak horizontal displacement (mm) for 30 ground motion sets; simplified model¹

Model	50% DBE			100% DBE			150% DBE			200% DBE						
	μ	50 th	90 th	σ	μ	50 th	90 th	σ	μ	50 th	90 th	σ	μ	50 th	90 th	σ
T2Q6	121	119	151	0.18	340	338	393	0.12	586	583	673	0.11	854	849	975	0.11
T2Q12	87	86	112	0.21	243	239	302	0.18	451	447	534	0.14	680	675	785	0.12
T2Q18	76	75	94	0.18	197	193	249	0.2	364	358	453	0.18	567	561	680	0.15
T3Q6	140	138	176	0.19	376	373	443	0.14	674	670	769	0.11	996	991	1131	0.1
T3Q12	113	110	142	0.2	280	275	352	0.19	500	494	607	0.16	752	745	886	0.14
T3Q18	104	103	129	0.18	243	237	313	0.22	420	412	528	0.19	634	626	778	0.17

1. The horizontal displacement corresponding to 100 (200, 300)% shear strain in the elastomer is 310 (620, 930) mm.

Table C-8 Percentiles of peak horizontal shearing force (%W) for 30 ground motion sets; simplified model^{1, 2}

Model	50% DBE			100% DBE			150% DBE			200% DBE						
	μ	50 th	90 th	σ	μ	50 th	90 th	σ	μ	50 th	90 th	σ	μ	50 th	90 th	σ
T2Q6	17	17	20	0.12	38	38	43	0.11	62	62	71	0.11	89	88	101	0.11
T2Q12	20	20	22	0.09	34	34	39	0.12	53	53	61	0.11	76	75	87	0.11
T2Q18	25	25	27	0.06	36	36	40	0.1	51	51	59	0.12	70	69	81	0.12
T3Q6	12	12	13	0.09	22	22	25	0.11	35	35	39	0.09	49	48	55	0.09
T3Q12	17	17	18	0.06	23	23	26	0.09	32	32	37	0.11	43	43	49	0.11
T3Q18	22	22	23	0.04	28	28	31	0.08	35	35	39	0.09	43	43	50	0.11

1. The gravity weight W on the bearing is approximately 5270 kN

2. The characteristic strength, Q_d , ranges between 6%W (e.g., T2Q6) and 18%W (e.g., T3Q18).

Table C-9 Percentiles of peak compressive displacement (mm) for 30 ground motion sets; simplified model¹

Model	50% DBE			100% DBE			150% DBE			200% DBE			
	μ	50 th	90 th	99 th	σ	μ	50 th	90 th	σ	μ	50 th	90 th	σ
T2Q6	1.3	1.3	1.5	1.6	0.07	1.9	1.9	2.1	0.1	2.4	2.4	2.8	0.12
T2Q12	1.4	1.3	1.5	1.6	0.07	1.9	1.9	2.2	0.1	2.4	2.4	2.8	0.12
T2Q18	1.4	1.4	1.5	1.6	0.07	1.9	1.9	2.2	0.1	2.5	2.4	2.8	0.12
T3Q6	1.8	1.7	1.9	2.1	0.08	2.5	2.5	2.8	0.11	3.2	3.2	3.7	0.13
T3Q12	1.8	1.8	2	2.1	0.08	2.5	2.5	2.9	0.11	3.3	3.2	3.8	0.12
T3Q18	1.8	1.8	2	2.1	0.08	2.6	2.5	2.9	0.11	3.3	3.3	3.9	0.12

1. The horizontal displacement corresponding to 100 (200, 300)% shear strain in the elastomer is 310 (620, 930) mm.

Table C-10 Percentiles of peak compressive force (%W) for 30 ground motion sets; simplified model^{1, 2}

Model	50% DBE			100% DBE			150% DBE			200% DBE			
	μ	50 th	90 th	99 th	σ	μ	50 th	90 th	σ	μ	50 th	90 th	σ
T2Q6	167	167	183	198	0.07	235	233	267	0.1	302	300	351	0.12
T2Q12	167	167	183	198	0.07	235	234	267	0.1	302	300	351	0.12
T2Q18	167	167	183	198	0.07	235	234	267	0.1	302	300	351	0.12
T3Q6	171	171	188	204	0.08	243	242	277	0.11	314	312	366	0.13
T3Q12	172	171	189	204	0.08	244	242	278	0.11	316	313	367	0.12
T3Q18	172	172	189	205	0.08	245	243	279	0.11	317	314	368	0.12

1. The gravity weight W on the bearing is approximately 5270 kN

2. The characteristic strength, Q_d , ranges between 6%W (e.g., T2Q6) and 18%W (e.g., T3Q18).

Table C-11 Percentiles of peak tensile displacement (mm) for 30 ground motion sets; simplified model¹

Model	50% DBE			100% DBE			150% DBE			200% DBE							
	μ	50 th	90 th	99 th	σ	μ	50 th	90 th	σ	μ	50 th	90 th	σ	μ	50 th	90 th	σ
T2Q6	0.3	0.2	0.9	2.8	1.13	0.3	0.2	0.9	1.11	0.8	0.7	1.6	0.61	1.4	1.3	2.2	0.4
T2Q12	0.3	0.2	0.9	3	1.16	0.3	0.2	0.9	1.12	0.8	0.7	1.6	0.59	1.4	1.3	2.2	0.39
T2Q18	0.3	0.2	0.8	2.6	1.1	0.3	0.2	0.9	1.14	0.9	0.8	1.6	0.58	1.4	1.3	2.2	0.39
T3Q6	0.3	0.3	0.5	0.7	0.41	0.4	0.4	1.3	0.99	1.2	1.1	1.7	0.3	1.9	1.9	2.5	0.23
T3Q12	0.3	0.3	0.5	0.7	0.41	0.5	0.4	1.1	0.81	1.2	1.2	1.7	0.29	2	1.9	2.6	0.23
T3Q18	0.3	0.3	0.5	0.7	0.4	0.5	0.4	1	0.71	1.2	1.2	1.7	0.28	2	1.9	2.6	0.23

1. The horizontal displacement corresponding to 100 (200, 300)% shear strain in the elastomer is 310 (620, 930) mm.

Table C-12 Percentiles of peak tensile force (%W) for 30 ground motion sets; simplified model^{1, 2}

Model	50% DBE			100% DBE			150% DBE			200% DBE							
	μ	50 th	90 th	99 th	σ	μ	50 th	90 th	σ	μ	50 th	90 th	σ	μ	50 th	90 th	σ
T2Q6	32	25	106	347	1.13	39	26	109	1.11	104	92	201	0.61	173	161	270	0.4
T2Q12	32	25	110	370	1.16	39	26	111	1.12	105	93	197	0.59	173	162	268	0.39
T2Q18	32	25	102	322	1.1	39	26	113	1.14	105	93	195	0.58	173	162	267	0.39
T3Q6	28	26	44	68	0.41	44	35	124	0.99	116	111	163	0.3	188	183	247	0.23
T3Q12	28	26	44	67	0.41	44	37	104	0.81	117	112	163	0.29	189	184	247	0.23
T3Q18	28	26	43	66	0.4	45	38	94	0.71	117	113	162	0.28	189	185	247	0.23

1. The gravity weight W on the bearing is approximately 5270 kN

2. The characteristic strength, Q_d , ranges between 6%W (e.g., T2Q6) and 18%W (e.g., T3Q18).

Table C-13 Percentiles of peak torsion (degrees) for 30 ground motion sets; simplified model¹

Model	50% DBE			100% DBE			150% DBE			200% DBE							
	μ	50 th	90 th	σ	μ	50 th	90 th	σ	μ	50 th	90 th	σ	μ	50 th	90 th	σ	
T2Q6	0.004	0.004	0.007	0.10	0.36	0.016	0.015	0.024	0.37	0.031	0.029	0.045	0.34	0.047	0.045	0.068	0.32
T2Q12	0.003	0.003	0.005	0.007	0.33	0.009	0.008	0.013	0.36	0.018	0.017	0.027	0.36	0.031	0.029	0.047	0.37
T2Q18	0.003	0.003	0.005	0.006	0.28	0.007	0.007	0.010	0.32	0.013	0.012	0.020	0.36	0.022	0.021	0.033	0.36
T3Q6	0.005	0.005	0.006	0.008	0.24	0.013	0.013	0.018	0.29	0.025	0.024	0.036	0.3	0.041	0.040	0.057	0.28
T3Q12	0.005	0.004	0.006	0.009	0.28	0.009	0.009	0.012	0.24	0.016	0.016	0.022	0.27	0.026	0.025	0.037	0.29
T3Q18	0.005	0.005	0.007	0.010	0.28	0.009	0.009	0.012	0.24	0.014	0.014	0.018	0.24	0.021	0.020	0.028	0.26

1. An angle of 0.01 degrees correspond to 17 mm of horizontal displacement over a basemat length of 100 m.

Table C-14 Percentiles of peak rotation (degrees) about X axis for 30 ground motion sets; simplified model¹

Model	50% DBE			100% DBE			150% DBE			200% DBE							
	μ	50 th	90 th	σ	μ	50 th	90 th	σ	μ	50 th	90 th	σ	μ	50 th	90 th	σ	
T2Q6	0.0003	0.0003	0.0003	0.0004	0.16	0.0005	0.0005	0.0006	0.17	0.0007	0.0007	0.0008	0.14	0.0010	0.0010	0.0011	0.1
T2Q12	0.0004	0.0004	0.0004	0.0005	0.17	0.0005	0.0005	0.0006	0.16	0.0007	0.0007	0.0009	0.18	0.0009	0.0009	0.0012	0.17
T2Q18	0.0004	0.0004	0.0005	0.0006	0.17	0.0006	0.0006	0.0008	0.16	0.0008	0.0008	0.0010	0.16	0.0010	0.0010	0.0012	0.17
T3Q6	0.0002	0.0002	0.0003	0.0004	0.19	0.0004	0.0004	0.0005	0.17	0.0005	0.0005	0.0006	0.13	0.0007	0.0007	0.0009	0.11
T3Q12	0.0003	0.0003	0.0004	0.0005	0.13	0.0005	0.0005	0.0006	0.19	0.0006	0.0006	0.0008	0.17	0.0008	0.0008	0.0009	0.17
T3Q18	0.0004	0.0004	0.0005	0.0005	0.12	0.0006	0.0006	0.0007	0.16	0.0007	0.0007	0.0009	0.19	0.0009	0.0009	0.0011	0.17

1. An angle of 0.0005 degrees correspond to 1 mm of vertical displacement over a basemat length of 100 m.

Table C-15 Percentiles of peak rotation (degrees) about Y axis for 30 ground motion sets; simplified model¹

Model	50% DBE			100% DBE			150% DBE			200% DBE							
	μ	50 th	90 th	σ	μ	50 th	90 th	σ	μ	50 th	90 th	σ	μ	50 th	90 th	σ	
T2Q6	0.0002	0.0002	0.0002	0.0002	0.15	0.0003	0.0003	0.0003	0.13	0.0004	0.0004	0.0005	0.1	0.0006	0.0006	0.0007	0.08
T2Q12	0.0002	0.0002	0.0003	0.0003	0.15	0.0003	0.0003	0.0004	0.15	0.0004	0.0004	0.0005	0.14	0.0006	0.0006	0.0007	0.13
T2Q18	0.0003	0.0003	0.0003	0.0004	0.15	0.0004	0.0004	0.0004	0.15	0.0005	0.0005	0.0006	0.15	0.0006	0.0006	0.0007	0.15
T3Q6	0.0001	0.0001	0.0002	0.0002	0.13	0.0002	0.0002	0.0003	0.16	0.0003	0.0003	0.0004	0.17	0.0004	0.0004	0.0005	0.16
T3Q12	0.0002	0.0002	0.0002	0.0003	0.12	0.0003	0.0003	0.0003	0.13	0.0004	0.0004	0.0005	0.16	0.0005	0.0005	0.0006	0.16
T3Q18	0.0003	0.0003	0.0003	0.0003	0.1	0.0004	0.0003	0.0004	0.11	0.0004	0.0004	0.0005	0.13	0.0005	0.0005	0.0006	0.15

1. An angle of 0.0005 degrees correspond to 1 mm of vertical displacement over a basemat length of 100 m.

Table C-16 Percentiles of peak horizontal displacement (mm) for 30 ground motion sets; advanced model¹

Model	50% DBE			100% DBE			150% DBE			200% DBE							
	μ	50 th	90 th	99 th	σ	μ	50 th	90 th	σ	μ	50 th	90 th	σ	μ	50 th	90 th	σ
T2Q6	125	123	155	187	0.18	359	357	411	0.11	652	648	747	0.11	981	972	1162	0.14
T2Q12	89	87	113	141	0.21	256	253	316	0.18	488	484	565	0.12	756	751	865	0.11
T2Q18	77	76	96	116	0.18	204	200	258	0.2	394	389	483	0.17	630	625	735	0.13
T3Q6	143	141	180	219	0.19	402	399	462	0.11	735	730	846	0.12	1141	1134	1301	0.11
T3Q12	114	112	144	177	0.2	292	287	365	0.19	536	532	632	0.13	854	848	986	0.12
T3Q18	105	103	130	157	0.18	250	245	322	0.21	446	438	557	0.19	690	684	822	0.14

1. The horizontal displacement corresponding to 100 (200, 300)% shear strain in the elastomer is 310 (620, 930) mm.

Table C-17 Percentiles of peak horizontal shearing force (%W) for 30 ground motion sets; advanced model^{1, 2}

Model	50% DBE			100% DBE			150% DBE			200% DBE							
	μ	50 th	90 th	99 th	σ	μ	50 th	90 th	σ	μ	50 th	90 th	σ	μ	50 th	90 th	σ
T2Q6	17	17	20	22	0.12	39	39	44	0.11	67	67	76	0.1	98	97	115	0.13
T2Q12	20	19	22	24	0.09	34	34	39	0.12	55	54	63	0.11	80	80	91	0.11
T2Q18	24	24	26	28	0.07	35	35	40	0.1	51	50	59	0.12	72	71	82	0.11
T3Q6	11	11	13	14	0.1	22	22	25	0.1	36	35	40	0.1	51	51	58	0.1
T3Q12	16	16	17	19	0.06	22	22	25	0.11	32	32	36	0.11	45	44	50	0.1
T3Q18	21	21	23	24	0.05	26	26	29	0.09	33	33	38	0.11	42	42	48	0.11

1. The gravity weight W on the bearing is approximately 5270 kN

2. The characteristic strength, Q_d , ranges between 6%W (e.g., T2Q6) and 18%W (e.g., T3Q18).

Table C-18 Percentiles of peak compressive displacement (mm) for 30 ground motion sets; advanced model¹

Model	50% DBE			100% DBE			150% DBE			200% DBE			
	μ	50 th	90 th	99 th	σ	μ	50 th	90 th	σ	μ	50 th	90 th	σ
T2Q6	1.3	1.3	1.5	1.6	0.07	2	2	2.4	0.13	3.4	3.3	4.4	0.23
T2Q12	1.4	1.4	1.5	1.6	0.07	2	1.9	2.2	0.1	2.9	2.9	3.7	0.19
T2Q18	1.4	1.4	1.5	1.6	0.07	1.9	1.9	2.2	0.1	2.8	2.8	3.4	0.17
T3Q6	1.8	1.8	1.9	2.1	0.08	2.8	2.8	3.3	0.14	5.4	5.3	7.1	0.23
T3Q12	1.8	1.8	2	2.1	0.08	2.7	2.6	3.1	0.12	4.6	4.5	5.9	0.2
T3Q18	1.8	1.8	2	2.2	0.08	2.7	2.7	3.1	0.12	4.3	4.3	5.4	0.19

1. The buckling deformations are approximately 20 mm and 15 mm for T2Qy, and T3Qy, respectively.

Table C-19 Percentiles of peak compressive force (%W) for 30 ground motion sets; advanced model^{1, 2}

Model	50% DBE			100% DBE			150% DBE			200% DBE			
	μ	50 th	90 th	99 th	σ	μ	50 th	90 th	σ	μ	50 th	90 th	σ
T2Q6	167	167	183	198	0.07	237	236	270	0.11	322	319	377	0.13
T2Q12	167	167	183	198	0.07	235	234	267	0.1	318	315	380	0.15
T2Q18	168	167	183	198	0.07	235	234	267	0.1	319	316	386	0.16
T3Q6	172	171	189	205	0.08	250	249	290	0.12	375	371	453	0.16
T3Q12	172	171	189	205	0.08	248	246	284	0.11	383	378	466	0.16
T3Q18	172	172	189	205	0.08	249	247	288	0.12	381	376	465	0.17

1. The gravity weight W on the bearing is approximately 5270 kN

2. The buckling loads are approximately 130 MN and 77 MN for T2Qy, and T3Qy, respectively.

Table C-20 Percentiles of peak tensile displacement (mm) for 30 ground motion sets; advanced model¹

Model	50% DBE				100% DBE				150% DBE				200% DBE				
	μ	50 th	90 th	99 th	σ	μ	50 th	90 th	σ	μ	50 th	90 th	σ	μ	50 th	90 th	σ
T2Q6	0.3	0.2	0.7	1.9	0.95	0.3	0.2	0.9	1.08	1.4	1.2	2.4	0.53	6.1	4.9	11.8	0.69
T2Q12	0.3	0.2	0.8	2.6	1.1	0.3	0.2	1.4	1.51	1.2	1.1	2.3	0.59	5.1	4.2	9.6	0.64
T2Q18	0.3	0.2	1.1	4.6	1.36	0.3	0.2	1	1.18	1.3	1	2.5	0.67	4.4	3.6	8.5	0.66
T3Q6	0.3	0.3	0.4	0.7	0.39	0.6	0.5	1.3	0.73	4.5	3.8	8.4	0.61	15.9	14.3	26.4	0.48
T3Q12	0.3	0.3	0.5	0.7	0.4	0.6	0.5	1.1	0.65	4	3.4	7.4	0.6	12.3	10.8	20.8	0.52
T3Q18	0.3	0.3	0.5	0.7	0.4	0.6	0.5	1.2	0.71	3.7	3.2	6.7	0.57	10.8	9.7	17.6	0.47

1. The cavitation deformations are approximately 0.8 mm and 0.4 mm for T2Qy, and T3Qy, respectively.

Table C-21 Percentiles of peak tensile force (%W) for 30 ground motion sets; advanced model^{1, 2}

Model	50% DBE				100% DBE				150% DBE				200% DBE				
	μ	50 th	90 th	99 th	σ	μ	50 th	90 th	σ	μ	50 th	90 th	σ	μ	50 th	90 th	σ
T2Q6	32	26	87	234	0.95	38	27	107	1.07	87	86	103	0.14	95	95	98	0.02
T2Q12	32	25	103	324	1.1	39	24	163	1.5	84	82	115	0.26	95	95	97	0.02
T2Q18	32	24	136	566	1.36	39	26	117	1.17	84	80	123	0.34	95	95	99	0.04
T3Q6	28	26	43	65	0.39	37	34	63	0.48	42	42	42	0.01	43	43	44	0.02
T3Q12	28	26	43	66	0.4	36	33	59	0.45	42	42	42	0.01	43	43	44	0.02
T3Q18	28	26	43	65	0.4	35	33	61	0.49	42	42	43	0.01	43	43	43	0.01

1. The gravity weight W on the bearing is approximately 5270 kN.

2. The cavitation loads, F_c , are approximately 4920 and 2190 MN for T2Qy, and T3Qy, respectively.

Table C-22 Percentiles of peak torsion (degrees) for 30 ground motion sets; simplified model¹

Model	50% DBE			100% DBE			150% DBE			200% DBE			
	μ	50 th	90 th	σ	99 th	90 th	μ	50 th	90 th	μ	50 th	90 th	σ
T2Q6	0.005	0.004	0.007	0.01	0.35	0.018	0.017	0.026	0.34	0.036	0.035	0.051	0.29
T2Q12	0.003	0.003	0.005	0.007	0.33	0.01	0.009	0.014	0.34	0.022	0.021	0.033	0.34
T2Q18	0.003	0.003	0.005	0.007	0.33	0.007	0.007	0.011	0.32	0.015	0.015	0.022	0.33
T3Q6	0.005	0.005	0.006	0.008	0.25	0.015	0.014	0.021	0.3	0.033	0.031	0.045	0.28
T3Q12	0.005	0.005	0.006	0.008	0.27	0.01	0.009	0.013	0.25	0.019	0.018	0.026	0.28
T3Q18	0.005	0.005	0.007	0.01	0.29	0.009	0.009	0.012	0.24	0.015	0.015	0.02	0.26

1. An angle of 0.01 degrees correspond to 17 mm of horizontal displacement over a basemat length of 100 m.

Table C-23 Percentiles of peak rotation (degrees) about X axis for 30 ground motion sets; simplified model¹

Model	50% DBE			100% DBE			150% DBE			200% DBE			
	μ	50 th	90 th	σ	99 th	90 th	μ	50 th	90 th	μ	50 th	90 th	σ
T2Q6	0.0003	0.0003	0.0004	0.17	0.0006	0.0006	0.0008	0.22	0.0017	0.0015	0.0024	0.36	0.0056
T2Q12	0.0003	0.0003	0.0004	0.0005	0.17	0.0006	0.0005	0.0007	0.19	0.0014	0.0012	0.0022	0.45
T2Q18	0.0004	0.0004	0.0005	0.0006	0.17	0.0006	0.0006	0.0008	0.18	0.0014	0.0012	0.0023	0.5
T3Q6	0.0002	0.0002	0.0003	0.0004	0.2	0.0006	0.0006	0.0008	0.32	0.0032	0.0029	0.0053	0.48
T3Q12	0.0003	0.0003	0.0004	0.0005	0.14	0.0006	0.0006	0.0009	0.31	0.0032	0.0028	0.0059	0.58
T3Q18	0.0004	0.0004	0.0005	0.0005	0.12	0.0008	0.0008	0.0011	0.29	0.0035	0.0031	0.006	0.52

1. An angle of 0.0005 degrees correspond to 1 mm of vertical displacement over a basemat length of 100 m.

Table C-24 Percentiles of peak rotation (degrees) about Y axis for 30 ground motion sets; simplified model¹

Model	50% DBE			100% DBE			150% DBE			200% DBE			
	μ	50 th	90 th	σ	99 th	90 th	μ	50 th	90 th	μ	50 th	90 th	σ
T2Q6	0.0002	0.0002	0.0002	0.16	0.0003	0.0003	0.0004	0.16	0.0013	0.0012	0.0023	0.52	0.0052
T2Q12	0.0002	0.0002	0.0002	0.0003	0.15	0.0003	0.0003	0.0004	0.19	0.001	0.0009	0.0018	0.56
T2Q18	0.0002	0.0002	0.0003	0.0003	0.15	0.0004	0.0004	0.0004	0.16	0.001	0.0009	0.0018	0.56
T3Q6	0.0001	0.0001	0.0002	0.0002	0.13	0.0004	0.0004	0.0007	0.54	0.003	0.0024	0.0053	0.61
T3Q12	0.0002	0.0002	0.0002	0.0003	0.11	0.0004	0.0004	0.0006	0.39	0.0025	0.0021	0.0047	0.63
T3Q18	0.0002	0.0002	0.0003	0.0003	0.1	0.0005	0.0005	0.0008	0.43	0.0027	0.0023	0.005	0.62

1. An angle of 0.0005 degrees correspond to 1 mm of vertical displacement over a basemat length of 100 m.

Table C-27 Number of bearings (of 273) for which buckling is predicted due to each ground motion set at four shaking intensities; advanced model

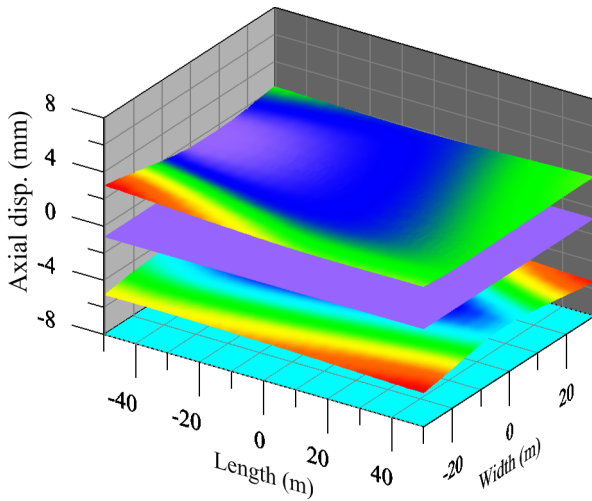
GM	T2Q6			T2Q12			T2Q18			T3Q6			T3Q12			T3Q18		
	50% DBE	100% DBE	200% DBE	50% DBE	100% DBE	200% DBE	50% DBE	100% DBE	200% DBE	50% DBE	100% DBE	200% DBE	50% DBE	100% DBE	200% DBE	50% DBE	100% DBE	200% DBE
1	0	0	0	0	0	0	0	0	0	0	273	0	0	0	0	0	0	0
2	0	0	0	0	0	0	0	0	0	0	173	0	0	0	0	0	0	0
3	0	0	0	0	0	0	0	0	0	0	184	0	0	0	0	0	0	0
4	0	0	0	0	0	0	0	0	0	0	0	0	0	0	0	0	0	0
5	0	0	0	0	0	0	0	0	0	0	263	0	0	0	0	0	0	0
6	0	0	0	0	0	0	0	0	0	0	130	0	0	0	0	0	0	0
7	0	0	0	0	0	0	0	0	0	0	0	0	0	0	0	0	0	0
8	0	0	0	0	0	0	0	0	0	0	0	0	0	0	0	0	0	0
9	0	0	0	0	0	0	0	0	0	0	66	0	0	0	0	0	0	0
10	0	0	0	0	0	0	0	0	0	0	0	0	0	0	0	0	0	0
11	0	0	0	0	0	0	0	0	0	0	2	0	0	0	0	0	0	0
12	0	0	0	0	0	0	0	0	0	0	273	0	0	0	0	0	0	0
13	0	0	0	0	0	0	0	0	0	0	0	0	0	0	0	0	0	0
14	0	0	0	0	0	0	0	0	0	0	0	0	0	0	0	0	0	0
15	0	0	0	0	0	0	0	0	0	0	243	0	0	0	0	0	0	0
16	0	0	0	0	0	0	0	0	0	0	0	0	0	0	0	0	0	0
17	0	0	0	0	0	0	0	0	0	0	0	0	0	0	0	0	0	0
18	0	0	0	0	0	0	0	0	0	0	69	0	0	0	0	0	0	0
19	0	0	0	0	0	0	0	0	0	0	273	0	0	0	0	0	0	0
20	0	0	0	0	0	0	0	0	0	0	0	0	0	0	0	0	0	0
21	0	0	0	0	0	0	0	0	0	0	0	0	0	0	0	0	0	0
22	0	0	0	0	0	0	0	0	0	0	163	0	0	0	0	0	0	0
23	0	0	0	0	0	0	0	0	0	0	0	0	0	0	0	0	0	0
24	0	0	0	0	0	0	0	0	0	0	0	0	0	0	0	0	0	0
25	0	0	0	0	0	0	0	0	0	0	14	0	0	0	0	0	0	0
26	0	0	0	0	0	0	0	0	0	0	107	0	0	0	0	0	0	0
27	0	0	0	0	0	0	0	0	0	0	248	0	0	0	0	0	0	0
28	0	0	0	0	0	0	0	0	0	0	19	0	0	0	0	0	0	0
29	0	0	0	0	0	0	0	0	0	0	250	0	0	0	0	0	0	0
30	0	0	0	0	0	0	0	0	0	0	273	0	0	0	0	0	0	0

Table C-28 Number of bearings (of 273) for which cavitation is predicted due to each ground motion set at four shaking intensities; advanced model

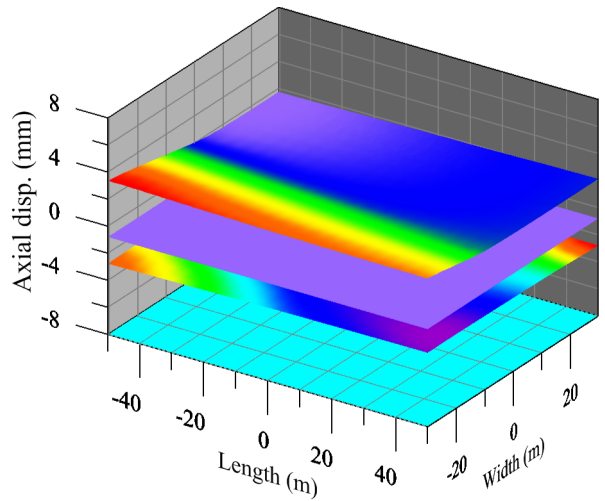
GM	T2Q6						T2Q12						T2Q18						T3Q6						T3Q12						T3Q18					
	50% DBE	100% DBE	150% DBE	200% DBE	50% DBE	100% DBE	150% DBE	200% DBE	50% DBE	100% DBE	150% DBE	200% DBE	50% DBE	100% DBE	150% DBE	200% DBE	50% DBE	100% DBE	150% DBE	200% DBE	50% DBE	100% DBE	150% DBE	200% DBE	50% DBE	100% DBE	150% DBE	200% DBE								
1	0	0	127	273	0	22	273	273	0	83	273	273	0	192	273	273	0	190	273	273	0	100	273	273	0	273	273	273								
2	0	0	273	273	0	0	140	273	0	0	126	273	0	0	190	273	273	0	246	273	273	0	273	273	273	0	273	273	273							
3	0	3	273	273	0	6	273	273	0	21	273	273	0	0	273	273	273	0	273	273	273	0	273	273	273	0	273	273	273							
4	0	0	273	273	0	0	273	273	0	0	273	273	0	0	273	273	273	0	273	273	273	0	273	273	273	0	273	273	273							
5	0	0	112	273	0	0	69	273	0	0	7	198	0	0	20	273	273	0	20	273	273	0	0	273	273	0	0	273	273							
6	0	0	273	273	0	0	256	273	0	0	258	273	0	0	273	273	273	0	273	273	273	0	273	273	273	0	273	273	273							
7	0	0	273	273	0	0	273	273	0	7	273	273	0	0	273	273	273	0	273	273	273	0	273	273	273	0	273	273	273							
8	0	0	273	273	0	0	273	273	0	7	273	273	0	0	273	273	273	0	273	273	273	0	273	273	273	0	273	273	273							
9	0	0	273	273	0	0	273	273	0	0	273	273	0	0	37	273	273	0	37	273	273	0	0	273	273	0	0	273	273							
10	0	0	273	273	0	0	273	273	0	0	273	273	0	0	273	273	273	0	273	273	273	0	257	273	273	0	273	273	273							
11	0	0	273	273	0	0	273	273	0	1	273	273	0	0	273	273	273	0	273	273	273	0	273	273	273	0	273	273	273							
12	0	51	273	273	0	49	273	273	0	28	273	273	0	0	268	273	273	0	268	273	273	0	273	273	273	0	273	273	273							
13	0	0	273	273	0	0	250	273	0	0	221	273	0	0	28	273	273	0	28	273	273	0	5	273	273	0	6	273	273							
14	0	0	130	273	0	0	116	273	0	0	137	273	0	0	195	273	273	0	195	273	273	0	211	273	273	0	245	273	273							
15	0	0	111	273	0	0	27	273	0	0	44	273	0	0	141	273	273	0	141	273	273	0	178	273	273	0	201	273	273							
16	0	0	13	273	0	0	103	273	0	0	127	273	0	0	273	273	273	0	273	273	273	0	273	273	273	0	273	273	273							
17	0	0	269	273	0	0	265	273	0	1	273	273	0	1	262	273	273	0	262	273	273	0	234	273	273	0	229	273	273							
18	0	0	273	273	0	0	273	273	0	0	273	273	0	0	188	273	273	0	188	273	273	0	267	273	273	0	257	273	273							
19	0	0	195	273	0	0	57	273	0	0	35	273	0	0	0	273	273	0	0	273	273	0	0	273	273	0	86	273	273							
20	0	0	192	273	0	0	167	273	0	0	158	273	0	0	273	273	273	0	273	273	273	0	223	273	273	0	208	273	273							
21	0	0	85	273	0	0	0	273	0	0	0	104	0	0	0	240	273	0	0	240	273	0	0	273	273	0	0	234	273							
22	0	36	273	273	0	20	273	273	0	1	273	273	0	1	257	273	273	0	257	273	273	0	273	273	273	0	273	273	273							
23	0	0	18	271	0	0	0	269	0	0	69	273	0	0	0	273	273	0	0	273	273	0	24	273	273	0	39	273	273							
24	0	0	0	267	0	0	19	242	0	0	82	273	0	0	4	273	273	0	4	273	273	0	3	273	273	0	52	273	273							
25	0	0	249	273	0	0	233	273	0	0	214	273	0	0	254	273	273	0	254	273	273	0	251	273	273	0	269	273	273							
26	0	177	273	273	0	180	273	273	0	174	273	273	0	0	273	273	273	0	273	273	273	0	255	273	273	0	273	273	273							
27	0	0	273	273	0	0	209	273	0	2	188	273	0	0	149	273	273	0	149	273	273	0	138	273	273	0	149	273	273							
28	0	0	273	273	0	0	273	273	0	0	273	273	0	0	270	273	273	0	270	273	273	0	266	273	273	0	235	273	273							
29	0	33	273	273	0	3	273	273	0	2	273	273	0	0	273	273	273	0	273	273	273	0	273	273	273	0	273	273	273							
30	0	0	24	273	0	0	25	273	0	0	76	273	0	0	0	273	273	0	0	273	273	0	0	273	273	0	0	273	273							

C.6 Basemat Response

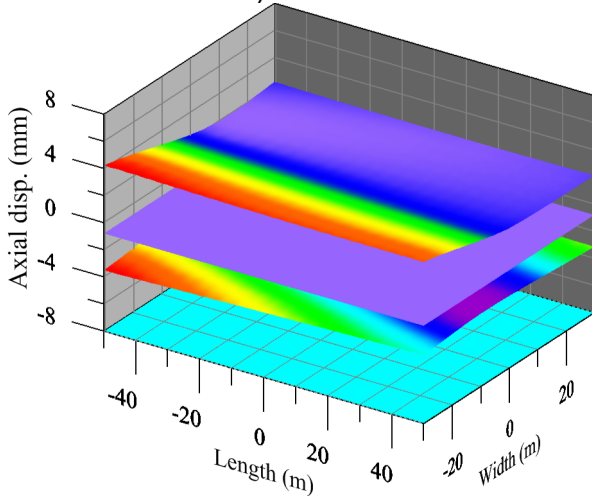
Displacement profiles for mean peak tensile (positive) and compressive (negative) displacement of bearings for 30 ground motion sets are presented here at a shaking intensity of 200% DBE. The outer bearings experience higher axial displacements than the inner bearings due to rocking and torsion of superstructure.



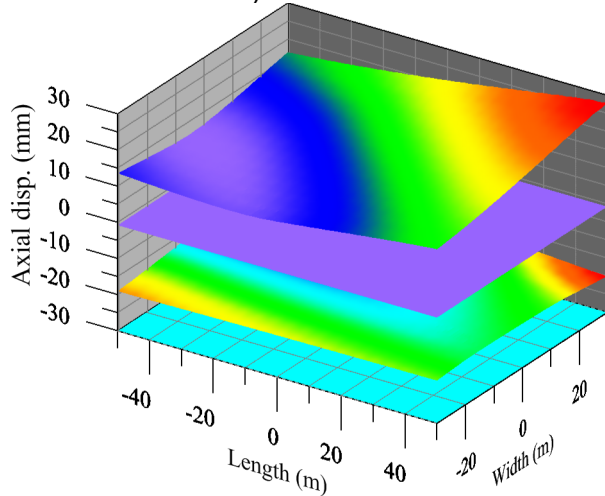
a) T2Q6



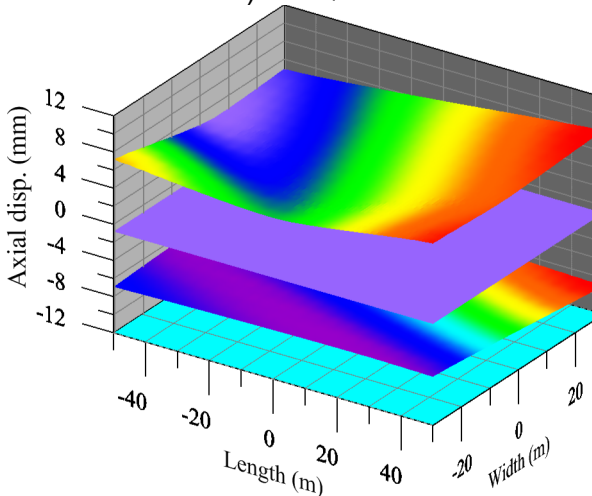
b) T2Q12



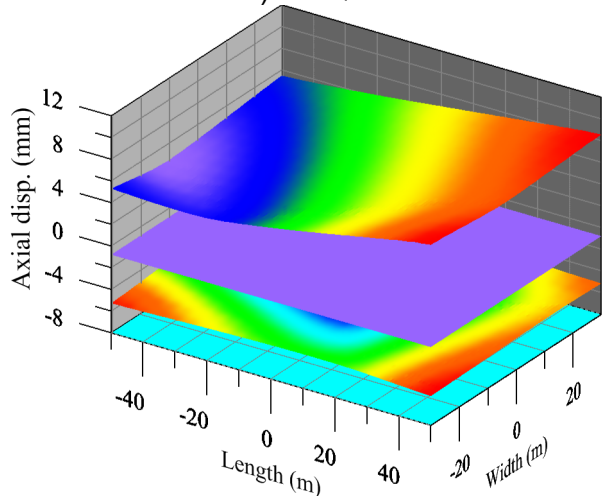
c) T2Q18



d) T3Q6



e) T3Q12



f) T3Q18

Figure C-4 Spatial profile for mean of peak axial displacements (mm) for sets of 30 ground motion sets, 200% DBE

C.7 Superstructure Response

Figures C.4 and C.5 present the variations of zero-period acceleration along the height of the superstructure for the ASB, CIS, and SCV, and isolation systems T2Q6 and T2Q12.

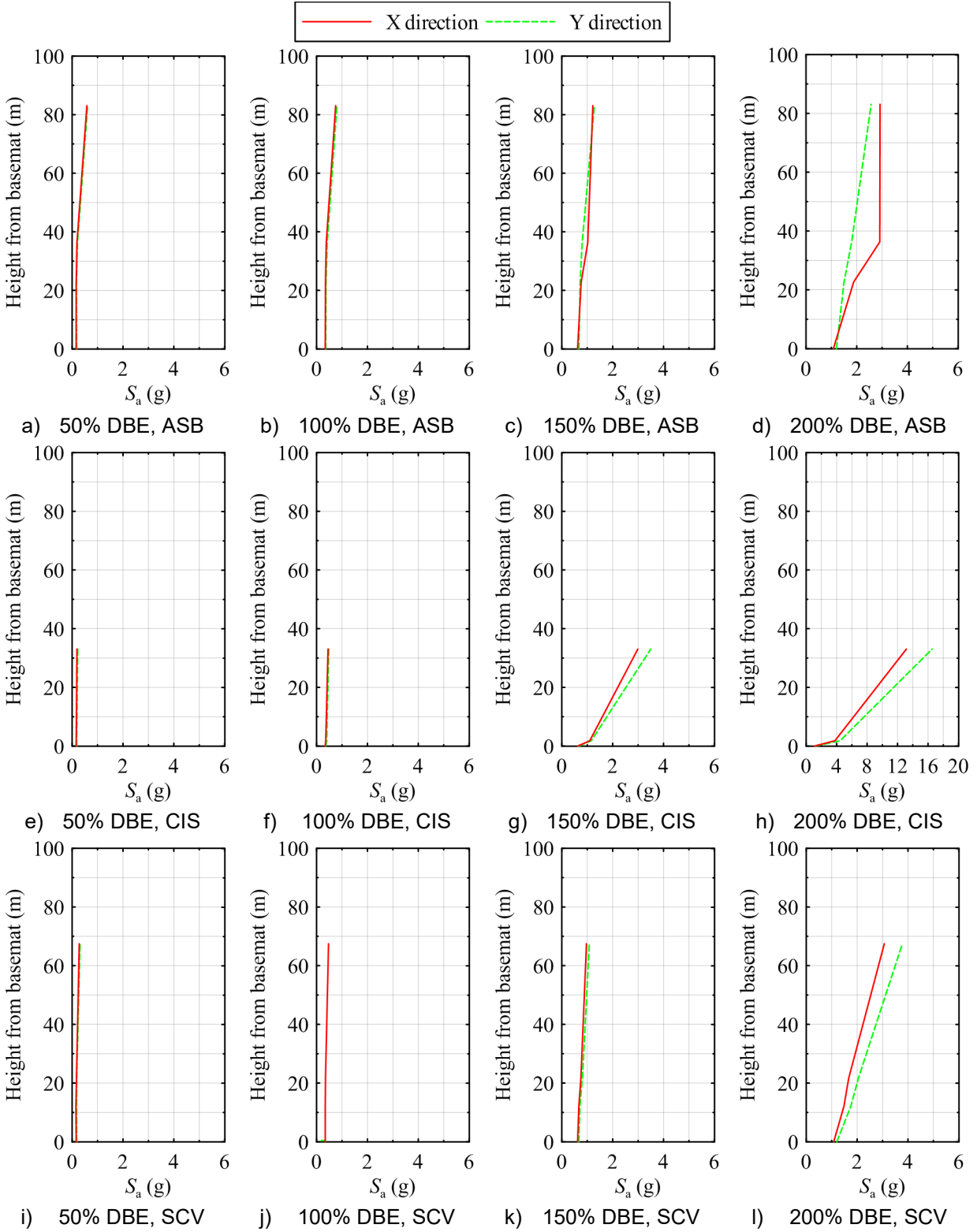


Figure C-5 Mean peak zero-period accelerations (g) for the 30 ground motion sets, T2Q6

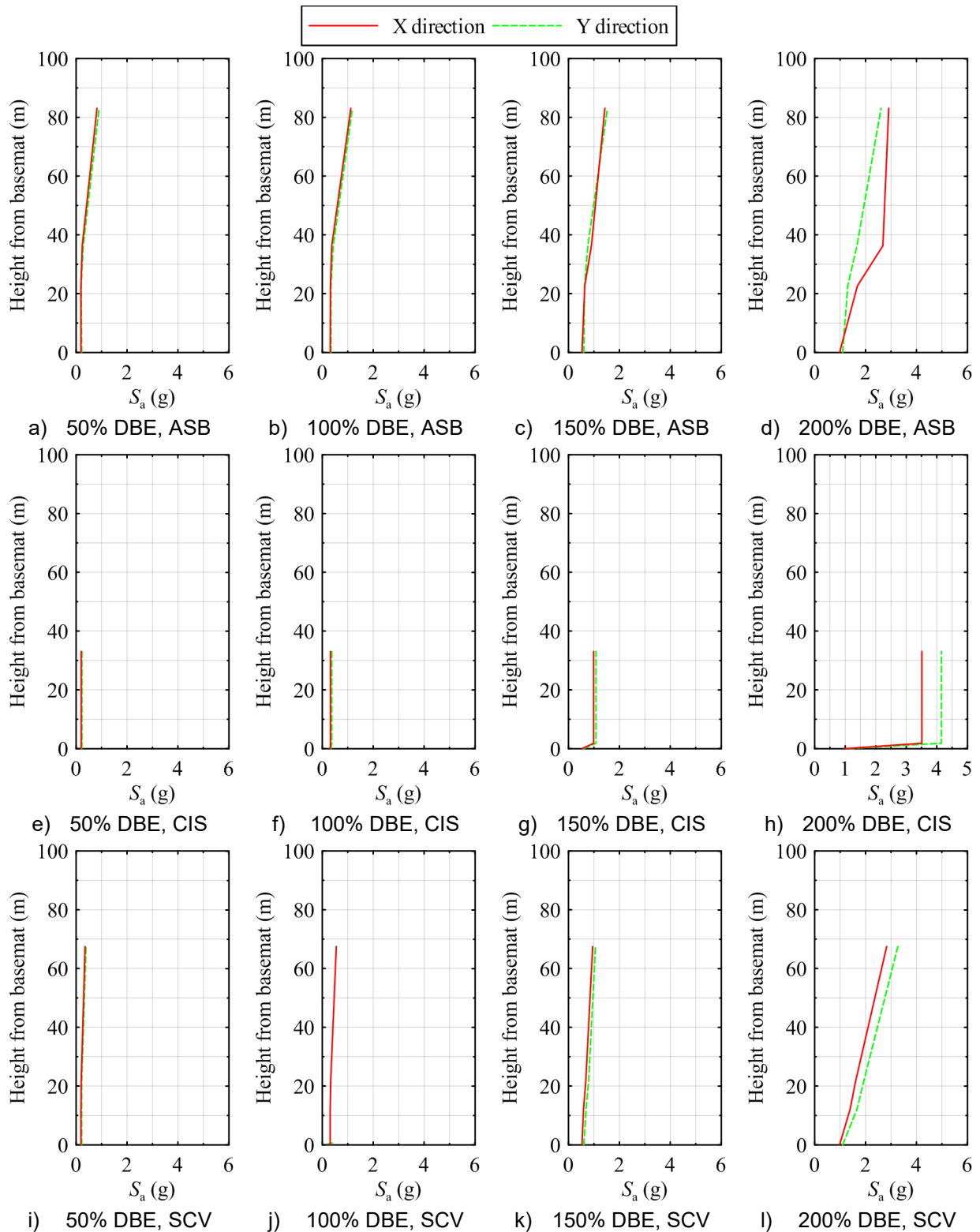


Figure C-6 Mean peak zero-period accelerations (g) for the 30 ground motion sets, T2Q12

C.8 Floor Response Spectra

C.8.1 Simplified isolator model

Floor response spectra (damping = 5%) at the center of the basemat (node 2137) is presented in Figure C.6 through C.8 for simplified isolator model.

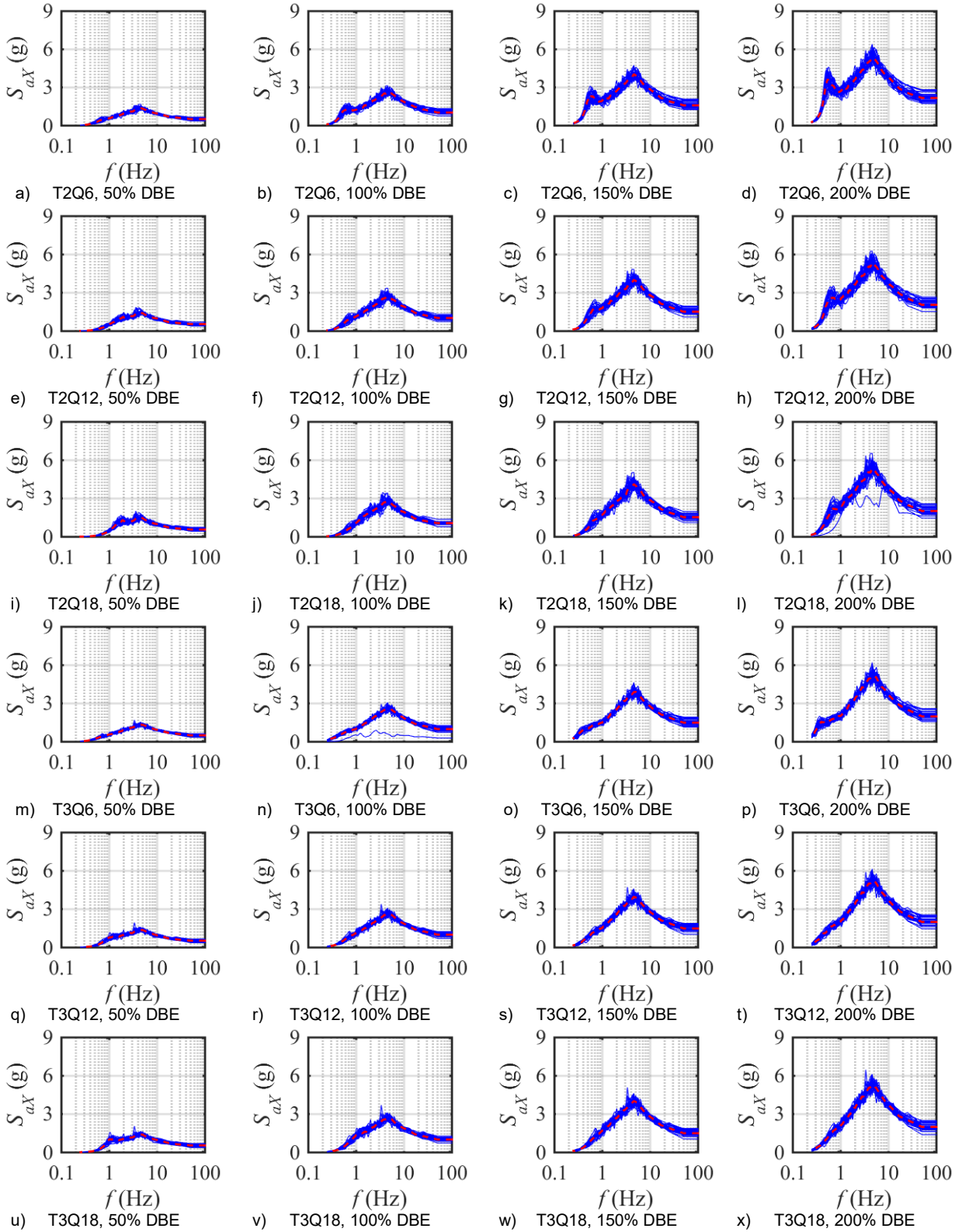


Figure C-7 Floor response spectra, simplified model, node 2137, X direction

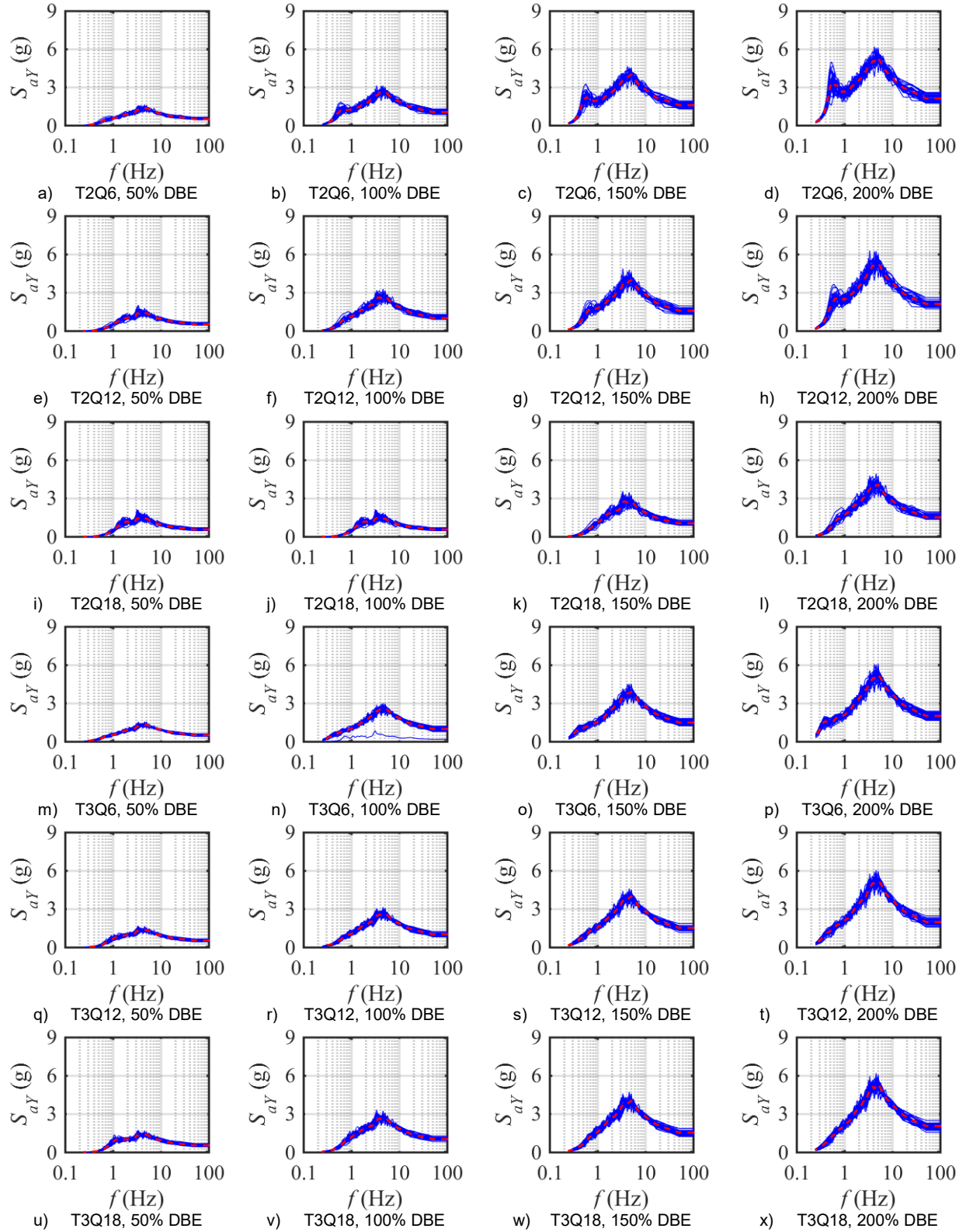


Figure C-8 Floor response spectra, simplified model, node 2137, Y direction

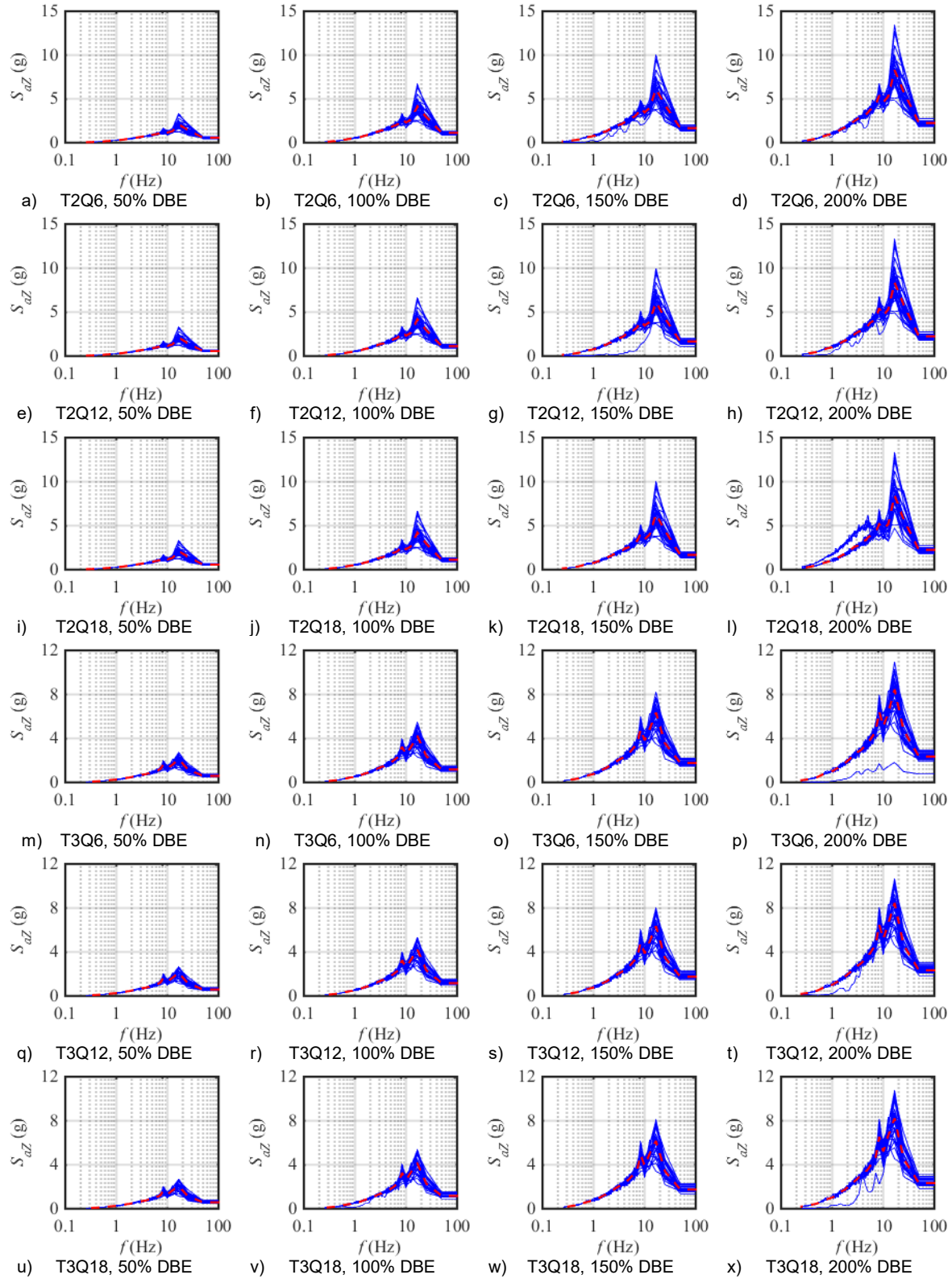


Figure C-9 Floor response spectra, simplified model, node 2137, Z direction

C.8.2 Advanced isolator model

Floor response spectra (damping = 5%) at the center of the basemat (node 2137) is presented in Figure C.9 through C.11 for advanced isolator model. Greater amplitude and record-to-record variability in the response spectra is observed with respect to results calculated using the simplified model. The effects of the five characteristics of LR bearings discussed in Section 9.4 become significant at the higher intensities of earthquake shaking.

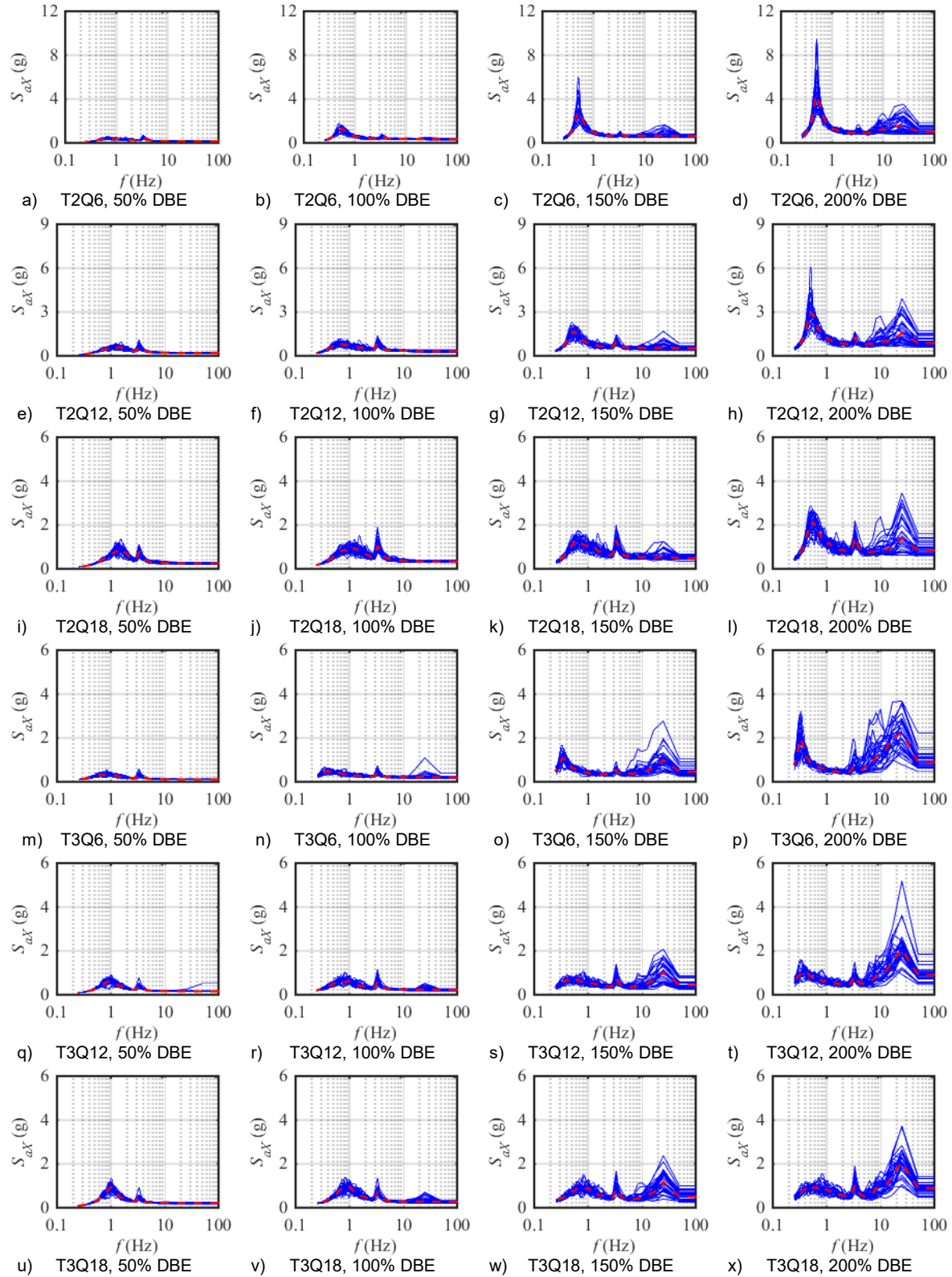


Figure C-10 Floor response spectra, advanced model, node 2137, X direction

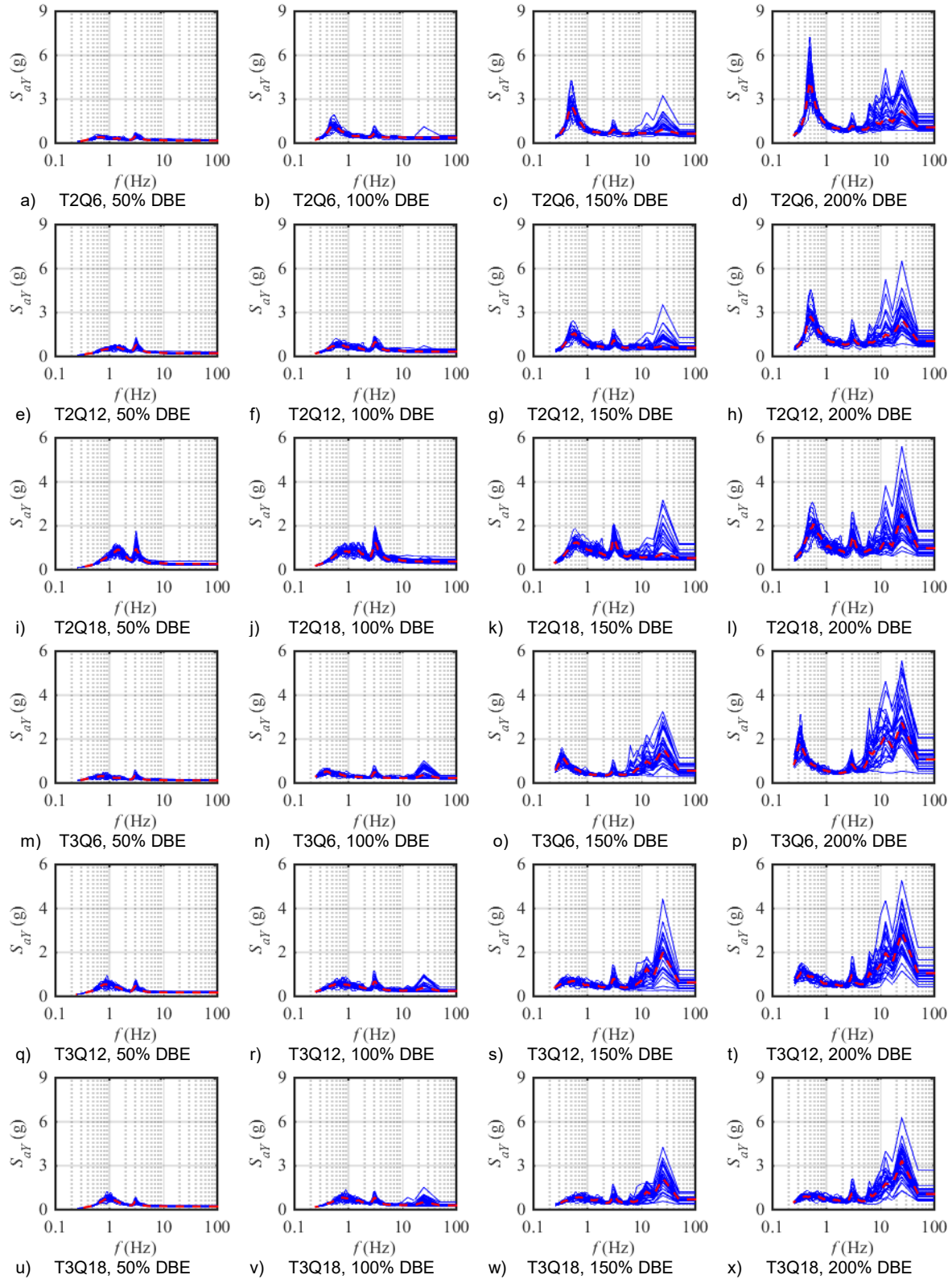


Figure C-11 Floor response spectra, advanced model, node 2137, Y direction

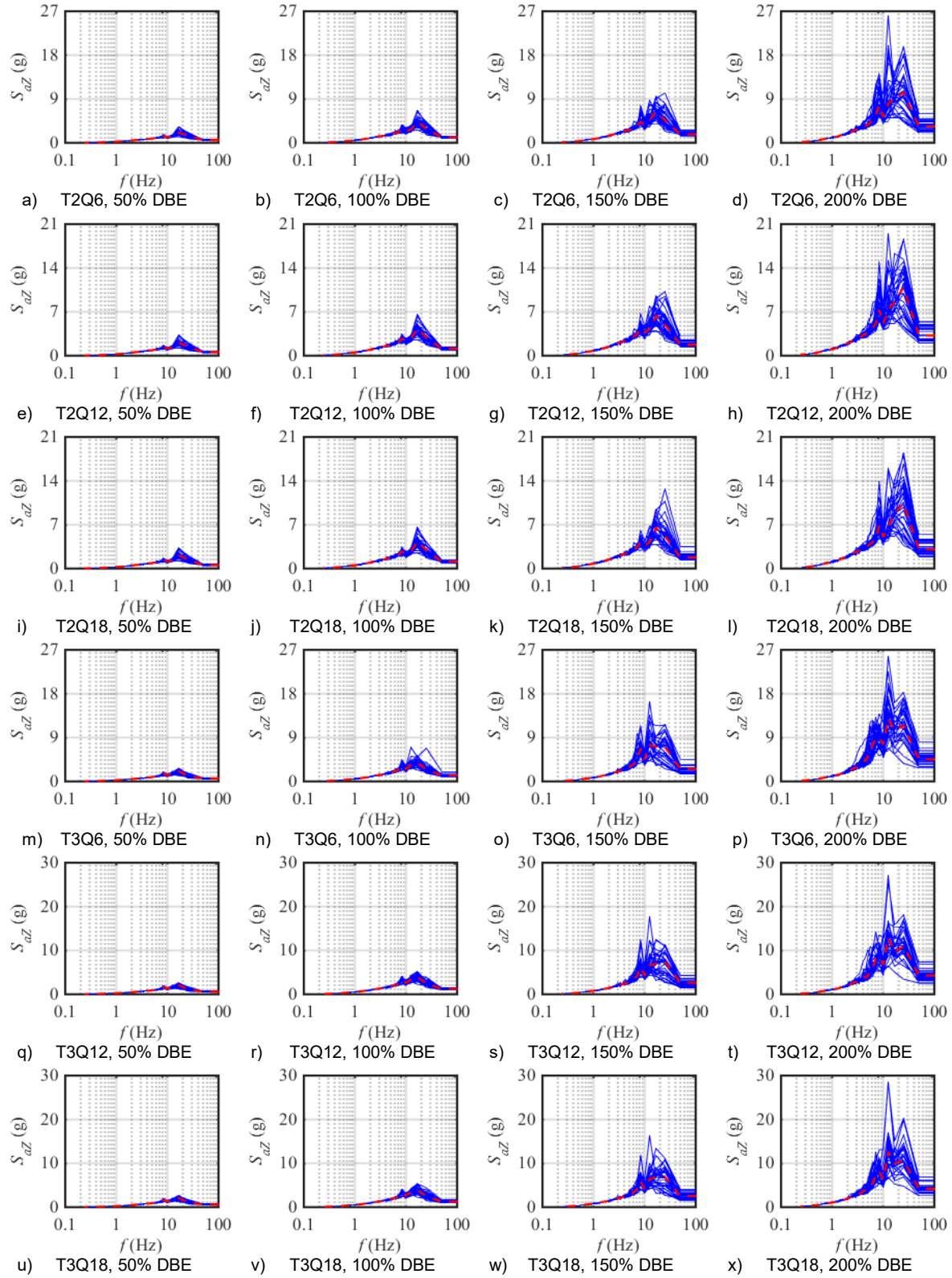


Figure C-12 Floor response spectra, advanced model, node 2137, Z direction

BIBLIOGRAPHIC DATA SHEET

(See instructions on the reverse)

NUREG/CR-7255

2. TITLE AND SUBTITLE

Seismic Isolation of Nuclear Power Plants using Elastomeric Bearings

3. DATE REPORT PUBLISHED

MONTH	YEAR
Febraury	2019

4. FIN OR GRANT NUMBER

5. AUTHOR(S)

M. Kumar
A. Whittaker
M. Constantinou

6. TYPE OF REPORT

Technical

7. PERIOD COVERED (Inclusive Dates)

8. PERFORMING ORGANIZATION - NAME AND ADDRESS (If NRC, provide Division, Office or Region, U. S. Nuclear Regulatory Commission, and mailing address; if contractor, provide name and mailing address.)

Multidisciplinary Center for Earthquake Engineering Research (MCEER)
University at Buffalo, State University of New York
212 Ketter Hall
Buffalo, NY 142601

9. SPONSORING ORGANIZATION - NAME AND ADDRESS (If NRC, type "Same as above", if contractor, provide NRC Division, Office or Region, U. S. Nuclear Regulatory Commission, and mailing address.)

Division of Engineering
Office of Nuclear Regulatory Research
U.S. Nuclear Regulatory Commission
Washington, DC 20555-0001

10. SUPPLEMENTARY NOTES

11. ABSTRACT (200 words or less)

Seismic isolation using low damping rubber (LDR) and lead-rubber (LR) bearings is a viable strategy for mitigating the effects of extreme earthquake shaking on safety-related nuclear structures. Although seismic isolation has been deployed in nuclear structures in France and South Africa, it has not seen widespread use. This has been attributed to, in part, limited new build nuclear construction in the past 30 years and a lack of guidelines, codes and standards for the analysis, design and construction of isolation systems specific to nuclear structures.

The effects of variation in mechanical properties of lead-rubber bearing on the response of base-isolated nuclear power plants (NPPs) were investigated using an advanced numerical model of lead-rubber bearing. The model was verified and validated, and implemented in OpenSees and ABAQUS. A series of experiments were conducted at University at Buffalo to characterize the behavior of elastomeric bearings in tension. The test data was used to validate a phenomenological model of an elastomeric bearing in tension. The value of three times the shear modulus of rubber in the elastomeric bearing was found to be a reasonable estimate of the cavitation stress of a bearing. The sequence of loading did not change the behavior of an elastomeric bearing under cyclic tension, and there was no significant change in the shear modulus, compressive stiffness, and buckling load of a bearing following cavitation.

12. KEY WORDS/DESCRIPTORS (List words or phrases that will assist researchers in locating the report.)

Seismic Isolation, Seismic Safety of Nuclear Power Plants, Risk-informed Performance-based Design, Elastomeric Bearings.

13. AVAILABILITY STATEMENT

unlimited

14. SECURITY CLASSIFICATION

(This Page)

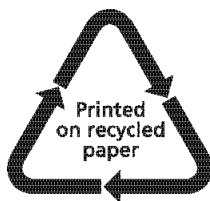
unclassified

(This Report)

unclassified

15. NUMBER OF PAGES

16. PRICE



Federal Recycling Program



**UNITED STATES
NUCLEAR REGULATORY COMMISSION
WASHINGTON, DC 20555-0001**

OFFICIAL BUSINESS



@NRCgov



NUREG/CR-7255

Seismic Isolation of Nuclear Power Plants using Elastomeric Bearings

February 2019